REVIEW OF JT-60U EXPERIMENTAL RESULTS

FROM MARCH TO OCTOBER, 1991

June 1992

JT-60 Team

日 本 原 子 力 研 究 所
Japan Atomic Energy Research Institute

Review of JT-60U Experimental Results
from March to October, 1991

JT-60 Team[*]

Department of Fusion Plasma Research
Department of Fusion Facility
Naka Fusion Research Establishment
Japan Atomic Energy Research Institute
Naka-machi, Naka-gun, Ibaraki-ken

Experimental results achieved in the initial operation of JT-60U are described in this paper. Experiments of JT-60U were initiated in March 1991, and deuterium experiments started in the middle of July. Multivariable non-interacting control was adopted to allow independent control over the strong mutual coupling between the ohmic heating coils and the vertical field coils. Well controlled divertor discharges were successfully obtained using this method and discharges with plasma current up to 5MA were achieved. H-mode experiments were performed in the region of I_p=1-4MA, B_T=1.7-4T, q_{eff}=3-5 and P_{NB}=6-22MW. Most of the H-mode data published so far from H-mode tokamaks are in low toroidal field (<3T) except for those with limiter H-mode in JT-60(LHCD) and TFTR. In JT-60U, clear L- to H- transitions and density/temperature profiles with steep edge gradients were observed in divertor configuration at 4T. The maximum enhancement factor of H-mode was 1.5 for the non-steady state case and 1.3 for the quasi-steady state case. The causes of this modest improvement in confinement are discussed. The high-q and high-β_p regime with hot ion enhanced confinement was investigated for concept development of steady-state reactors like SSTR. The maximum β_p reached 2.25, the maximum T_i of 20keV was achieved and τ_E^{dia} was improved to about 2.9 times as large as that of ITER89-P scaling. The maximum neutron rate of 1.3×10^{16}n/s was also obtained in the

highest-β_p discharge. The corresponding Q_{DD} and the equivalent Q_{DT} were 8.9×10^{-4} and ~0.20, respectively. Heat load localized in both toroidal and poloidal directions was shown to be in a good agreement for the first time with calculated heat load profile due to ripple trapped particle loss. The divertor heat flux was analyzed to establish a scaling law on the heat flux peaking factor which is the reciprocal of the scrape-off-layer thickness. Achieved values of the first experiment of the JT-60U LHCD in 1991 were $P_{LH}=1.5MW$, driven current $I_{RF}=2MA$, current drive efficiency $\eta_{CD}(\equiv\bar{n}_e R_p I_{RF}/P_{LH})=0.25\times10^{20}m^{-2}A/W$ and current driven product $CDP(\equiv\bar{n}_e R_p I_{RF})=3\times10^{20}m^{-2}MA$.

*JT-60 Team :

H. Akasaka, K. Akiba, M. Akiba, N. Akino, T. Ando, K. Annou, T. Aoyagi, T. Arai, K. Arakawa, M. Araki, N. Asakura, M. Azumi, S. Chiba, M. Dairaku, N. Ebisawa, T. Fujii, T. Fukuda, A. Funahashi, H. Furukawa, H. Gunji, J.C.M. de Haas, K. Hamamatsu, M. Hanada, K. Haraguchi, H. Hiratsuka, T. Hirayama, S. Hiroki, M. Honda, M. Honda, H. Horiike, S. Hoshi, N. Hosogane, D. Humphreys, S. Ide, Y. Ikeda, Y. Ikeda, Y. Ikeda, T. Imai, T. Inoue, N. Isaji, M. Isaka, N. Isei, S. Ishida, K. Itami, N. Ichige, M. Ito, T. Ito, R. Jinbou, Y. Kamada, A. Kaminaga, T. Kashimura, M. Kawai, Y. Kawamata, Y. Kawano, M. Kikuchi, H. Kimura, T. Kimura, H. Kishimoto, S. Kitamura, A. Kitsunezaki, K. Kiyono, K. Kodama, T. Koike, Y. Koide, S. Kogure, M. Komata, I. Kondo, T. Kondo, S. Konoshima, H. Kubo, S. Kunieda, K. Kurihara, M. Kuriyama, M. Kusaka, Y. Kusama, S. Maebara, K. Maeno, T. Matoba, M. Matsukawa, M. Matsuoka, Y. Matsuzaki, S. Miura, Y. Miura, N. Miya, K. Miyachi, K. Miyake, Y. Miyo, M. Mizuno, K. Mogaki, S. Moriyama, Y. Murakami, M. Nagami, A. Nagashima, K. Nagashima, T. Nagashima, S. Nagaya, K. Nagayama, O. Naito, H. Nakamura, T. Nakafuji*, S. Nakajima, H. Nemoto, M. Nemoto, Y. Neyatani, H. Ninomiya, T. Nishitani, H. Nobusaka, H. Nomoto, S. Numazawa, K. Odajima, N. Ogiwara, Y. Ohara, T. Ohga, T. Ohshima, M. Ohta, S. Ohuchi, Y. Ohuchi, A. Oikawa, H. Oohara, M. Oozeki, Y. Okumura, K. Omori, S. Omori, Y. Omori, T. Ozeki, M. Saido, M. Saigusa, N. Saito, K. Sakamoto, A. Sakasai, S. Sakata, T. Sakuma, T. Sasajima, M. Sato, M. Sato, M. Sawahata, M. Seimiya, M. Seki, S. Seki, K. Shibanuma, M. Shimada, K. Shimizu, M. Shimizu, Y. Shimomura, M. Shimono, S. Shinozaki, H. Shirai, H. Shirakata, M. Shitomi, K. Suganuma, T. Sugie, H. Sunaoshi, N. Suzuki, Y. Suzuki, M. Takahashi, S. Takahashi, T. Takahashi, A. Takasa, M. Takasaki, H. Takatsu, T. Takayasu, H. Takeuchi, A. Takeshita, T. Takizuka, S. Tamura, S. Tanaka, T. Tanaka, Y. Tanaka, K. Tani, T. Tani, M. Terakado, T. Terakado, K. Tobita, T. Totsuka, N. Toyoshima, T. Tsugita, S. Tsuji, Y. Tsukahara, M. Tsuneoka, A. Tsurumi, K. Uehara, S. Uno, Y. Uramoto, H. Usami, K. Ushigusa, K. Usui, M. Yagi, J. Yagyu, K. Yamagishi, M. Yamamoto, T. Yamamoto, O. Yamashita, T. Yamazaki, T. Yasuda, K. Yokokura, H. Yoshida, R. Yoshino, Y. Yoshioka, I. Yonekawa, K. Watanabe, S.W. Wolfe.

JT-60U 1991年3月-10月期実験結果のレビュー

日本原子力研究所那珂研究所炉心プラズマ研究部・核融合装置試験部
JT-60チーム*

　本論文では，JT-60Uの初期運転において得られた実験結果を述べる。JT-60Uは，軽水素ガスを用いたジュール加熱実験を3月末から開始し，その後重水素放電を7月中旬に開始した。プラズマ制御に関しては，ジュール加熱コイルと垂直磁場コイルの間に強い結合がある状態でも，プラズマ電流と水平位置を独立に制御するために多変数非干渉制御を採用した。この方法を用いて良く制御されたダイバータ放電が得られ，現在までに5MA放電を得ている。Hモード実験は，$I_P = 1-4 MA$，$B_T = 1.7-4 T$，$q_{eff} = 3-5$，$P_{NB} = 6-22 MW$の範囲で行った。従来のHモードデータは，JT-60のLHCDとTFTRのリミターHモードを除いて3T以下の低いトロイダル磁場であるが，JT-60Uでは明確なL-H遷移と急峻な端部の密度／温度勾配の形成が4Tで見られた。Hモードの最大の閉じ込め改善度は，過渡的な場合に1.5で定常状態で1.3である。この緩やかな閉じ込め改善の理由について議論している。SSTRのような定常炉概念の構築のために高イオン温度・高q高β_p領域の閉じ込めを調べ，最大のβ_pとして2.25を，最大イオン温度として20keV 以上を得た。また，閉じ込め改善度はITERパワー則の2.9倍を得ている。この高β_p領域で得られた最大中性子発生率は 1.3×10^{16}／秒であり，これは$Q_{DD} = 8.9 \times 10^{-3}$，等価な$Q_{DT} \sim 0.2$に相当する。ダイバータ熱流束を調べ，スクレープオフ層の熱流厚さの逆数を熱流束のピーキング係数として比例則を求めた。トロイダルとポロイダル両方に局在化した熱負荷が，リップル損失として明確に同定され，これは主にリップル補捉に基づく熱負荷であり，計算結果と一致している。1991年のJT-60UのLHCDの最初の実験で得られたパラメータは，$P_{LH} = 1.5 MW$，駆動電流$I_{RF} = 2 MA$，電流駆動効率n_{CD} $(= \bar{n}_e R_P I_{RF}/P_{LH}) = 0.25 \times 10^{20} m^{-2} A/W$及び電流駆動積CDP$(= \bar{n}_e R_P I_{RF}) = 3 \times 10^{20} m^{-2} M$であった。

那珂研究所：〒311-01　茨城県那珂郡那珂町大字向山801-1

* J T - 6 0 チーム

青柳　哲男・赤坂　博美・秋野　　昇・秋場　賢一・秋場　真人・朝倉　伸幸・安積　正史
新井　　貴・荒川喜代次・荒木　政則・安東　俊郎・安納　勝人・池田　幸治・池田　佳隆
池田裕二朗・井坂　正義・伊佐治信明・石田　真一・伊世井宣明・伊丹　　潔・井手　俊介
市毛　尚志・伊藤　孝雄・伊藤　　優・井上多加志・今井　　剛・上原　和也・宇佐美広次
牛草　健吉・薄井　勝富・宇野　定則・浦本　保幸・海老沢　昇・及川　　晃・大内　章寿
大内　　豊・大賀　徳道・大島　貴幸・大関　正弘・大田　　充・大原比呂志・大森憲一郎
大森　俊造・大森　栄和・荻原　徳男・奥村　義和・小関　隆久・小田島和男・小原　祥裕
樫村　隆則・鎌田　　裕・神永　敦嗣・河合視己人・河野　康則・川俣　陽一・菊池　　満
岸本　　浩・北村　　繁・狐崎　晶雄・木村　豊秋・木村　晴行・清野　公広・日下　　誠
草間　義紀・国枝　俊介・久保　博孝・栗原　研一・栗山　正明・軍司　秀穂・小池　常之
小出　芳彦・小暮　重幸・児玉　幸三・木島　　滋・小又　将夫・近藤　育朗・近藤　　貴
斉藤　直之・西堂　雅博・三枝　幹雄・逆井　　章・坂田　信也・坂本　慶司・佐久間　猛
笹島　唯之・佐藤　正泰・佐藤　　稔・沢畠　正之・都　　守正・篠崎　信一・柴沼　　清
嶋田　道也・清水　勝宏・清水　正亜・下野　　貢・下村　安夫・白井　　浩・白形　弘文
神保龍太郎・菅沼　和明・杉江　達夫・鈴木　紀男・鈴木　靖生・砂押　秀則・清宮　宗孝
関　　正美・関　　省吾・高佐　　明・高崎　　學・高津　英幸・高橋　春次・高橋虎之介
高橋　　実・高安　利男・滝塚　知典・竹内　　浩・竹下　　明・田中　　茂・田中竹次郎
田中　裕二・谷　　啓二・谷　　孝志・田村　早苗・大楽　正幸・千葉　真一・塚原　美光
次田　友宜・辻　　俊二・恒岡まさき・鶴見　　聰・寺門　恒久・寺門　正之・戸塚　俊之
飛田　健次・豊島　　昇・中島　信治・内藤　　磨・中藤　隆志・中村　博雄・長島　　章
永島　圭介・永島　　孝・永谷　　進・永見　正幸・長山　　清・西谷　健夫・二宮　博正
沼澤　　呈・根本　裕功・根本　正博・閨谷　　譲・信坂　裕通・野本　弘樹・花田磨砂也
濱松　清隆・原口　和三・平塚　　一・平山　俊雄・廣木　成治・福田　武司・藤井　常幸
船橋　昭昌・古川　　弘・細金　延幸・星　　静男・堀池　　寛・本田　正男・本多　光輝
前原　　直・前野　勝樹・松岡　　守・松川　　誠・松崎　　誼・的場　　徹・三浦　良和
三浦　早苗・水野　　誠・宮　　直之・三宅　一幸・宮地　謙吾・三代　康彦・村上　義夫
藻垣　和彦・森山　伸一・矢木　雅敏・柳生　純一・安田　泰三・山岸耕二郎・山崎　　武
山下　　修・山本　　巧・山本　正弘・横倉　賢治・吉岡　祐二・吉田　英俊・芳野　隆治
米川　　出・渡邊　和弘・J. C. M. de Haas ・D. Humphreys, ・S. W. Wolfe

Contents

目　　　次

Executive Summary

Experimental results achieved in the initial operation of JT-60U are described in this paper. Construction of the JT-60U to allow higher plasma current, deuterium operation and higher heating power was completed in March 1991 and ohmic experiments with hydrogen gas were initiated at the end of March. After commissioning the diagnostics and the NBI system, deuterium discharges started in the middle of July and deuterium experiments with NB power of up to 22 MW started in late August. In October, hydrogen discharges were made before an annual vacuum break in November. The main objectives of experiments in 1991 were to study the basic performance of JT- 60U and the following experiments were performed: 1) optimization of plasma control, 2) confinement improvement and studies of its characteristics, 3) MHD and disruption studies, 4) impurity control and divertor studies, 5) studies of ripple loss, high energy particle and D-D reaction product and 6) LHCD experiments.

Optimizations of break-down, current ramp-up and divertor configuration were performed. Multivariable non-interacting control was adopted to allow independent control over the strong mutual coupling between the ohmic heating coils and the vertical field coils. Well controlled divertor discharges were successfully demonstrated by this method and 4 MA discharges were accomplished in only 12 days of operation. Discharges with plasma currents of up to 5 MA were achieved and method of obtaining 6 MA discharges was clear.

H-mode experiments were performed in the region of I_p=1-4 MA, B_T=1.7-4 T, q_{eff}=3-5 and P_{NB}=6-22 MW. Most of the H-mode data published so far from H-mode tokamaks are in low toroidal field (<3T) except for those with limiter H-mode in JT-60 (LHCD) and TFTR. In JT-60U, clear L- to H-transitions and density/temperature profiles with steep edge gradients were observed in divertor configuration at 4 T. A quasi-steady state H-mode with ELMs was obtained in discharges with B_T=1.7-2.5 T after wall conditioning. However, the ELM-free phase was still short (< 0.2 s) and confinement enhancement in the H-mode compared to the L-mode scaling was still low. The maximum enhancement factor was 1.5 for the non-steady state case and 1.3 for the quasi-steady state case. The causes of this modest improvement in confinement are discussed.

The high-q and high-β_p regime with hot ion enhanced confinement was investigated for concept development of steady-state reactors like SSTR. The maximum β_p reached 2.25, the maximum T_i of 20 keV was achieved and τ_E^{dia} was improved to about 2.9 times as large as that of ITER89-P scaling. The maximum neutron rate obtained in this high-β_p regime was 1.3 x 10^{16} n/s, which corresponds to Q_{DD}=8.9 x 10^{-3} and the equivalent Q_{DT}~ 0.2.

Energy confinement time of L-mode discharges is compared with ITER L-mode scaling. The energy confinement time of low plasma current (3 MA) and full size elliptic plasmas with vertical elongation of 1.6 is roughly consistent with the prediction of ITER89-P law, but that of high plasma current (3-4 MA) is a little shorter than the prediction. One explanation is that the

current penetration is not enough in high plasma current discharges. On the other hand, L-mode confinement of the small a_p configuration (a_p=0.8 m, A=4) is 1.3 times ITER89-P law which exceeds the prediction of the Goldston scaling giving stronger aspect ratio dependence of the fusion product than the ITER89-P law.

Effects of a current profile l_i and an effective safety factor q_{eff} on MHD characteristics and plasma confinement were studied to obtain a systematic understanding of macroscopic instabilities, and a clear correlation between MHD and confinement with the separate role of micro turbulence distinguished. In a l_i-q_{eff} plot, the stable region and the sawtooth region are clearly separated. The dependence of sawtooth inversion/mixing radii on l_i and q_{eff} is demonstrated, and energy confinement time is clearly correlated with l_i and q_{eff}. Phenomena of MARFE and detached plasma prior to disruptions were studied, and a reliable control of disruptions was demonstrated using the detachment phenomenon.

In JT-60U, to reduce carbon impurity production at the divertor tile edges, divertor tiles made of carbon-fiber composites were installed with good alignment (<0.5 mm) and tile edges were beveled. These feature and extensive divertor diagnostics enabled investigation of carbon impurity generation mechanism. In high density discharges, lower incident ion energy reduced carbon impurity generation at divertor plates. Carbon influx to the main plasma was further reduced due to higher shielding efficiency in the divertor and scrape-off layer plasmas. Remote radiative cooling power increased with $n_e q_{eff}$. The divertor heat flux was analyzed to establish a scaling law on the heat flux peaking factor which is the reciprocal of the scrape-off-layer thickness. The experimentally-derived scaling law is $P_{NB}^{0.49\pm0.18} \bar{n}_e^{-0.45\pm0.22} q_{eff}^{-0.67\pm0.18}$. All these results suggest that high density, high q_{eff} operation mitigates divertor heat load, divertor plate erosion and impurity concentration.

Heat load localized in both toroidal and poloidal directions was shown to be in a good agreement for the first time with calculated heat load profile due to ripple trapped particle loss. The confinement and slowing down of the 1MeV triton produced by d(d,p)t reactions have been investigated through the burnup of the 1 MeV tritons in the D-D plasma. The slowing down was classical in both ohmically and neutral beam heated plasmas.

In the first campaign of the JT-60U LHCD in 1991, the emphasis of the experiment was placed on the physics understandings of the LHCD such as the identification of the LH wave dispersion relation, effect of the accessibility and behavior of the fast electrons measured by the hard X-ray and soft X-ray signal (energy spectra, profiles and time response). Achieved values of the experiment were P_{LH}=1.5 MW, driven current I_{RF}=2 MA, current drive efficiency $\eta_{CD}(\equiv \bar{n}_e R_p I_{RF}/P_{LH})$=0.25x10^{20} m^{-2}A/W and current driven product CDP ($\equiv \bar{n}_e R_p I_{RF}$)=3x10^{20} m^{-2}MA.

1 Machine and Diagnostics Status

1.1 Machine Status

This section presents the status of the JT-60U device in 1991. Figure 1 shows the cross sectional view of the JT-60U device [1-2]. The JT-60U uses the original toroidal field coils, high power heating systems and power supply systems after minor modification. The poloidal field coils and the vacuum vessel were superseded by new ones to allow single-null open divertor plasmas with plasma currents of up to 6 MA, plasma volumes of up to 110 m^3, aspect ratios of 3.4-4.0 and plasma elongations of 1.4 to 1.8. Table 1 shows the main parameters of JT-60U and achieved values in this year operation.

The poloidal field coil (PF coil) system consists of an ohmic heating coil (F), a vertical field coil (V), a horizontal field coil (H), a divertor coil (D) and a sector coil (DCW). Main parameters of PF coils are shown in Table 2. To obtain 6 MA discharges, the capacity of the F-coil was increased to 42 V·s by increasing its current rating from 92 kA to 120 kA, and the V-coil was designed to have a flux swing capacity of 19 V·s by eliminating return conductors. The V-coil was also designed to produce 3 types of divertor configurations as illustrated in Fig. 2. The V-coil is divided into 4 blocks and the plasma configuration can be selected by the tap change in the coil feeder. In the standard mode (case A in Fig. 2), the divertor plasma with elongation of 1.4-1.6 and an aspect ratio of ~3.4 can be produced. In the elongated mode (case B), the divertor plasma with elongation of 1.6-1.8 and an aspect ratio of 3.8-4 can be produced. Case C permits continuous control of the elongation and the triangularity, but this option requires an additional power supply, so that the standard mode and the elongated mode have been examined in 1991. The H-coil power supply was superseded by a 24 phase converter from a 12 phase converter for rapid current control of H-coil to increase the vertical instability control capability.
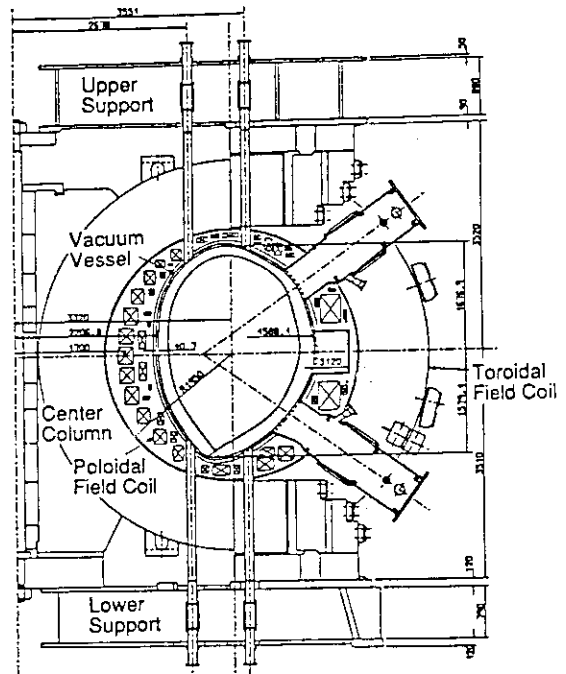
Fig. 1 Cross sectional view of the JT-60U device.

Table 1 Main parameters of JT-60U.

Parameters	Design value	Achieved value
Plasma current		
Divertor	6 MA at 4.2 T	5 MA at 4 T
Limiter	6.5 MA at 4.2 T	3 MA at 4 T
Major radius	3.2 - 3.4 m	3.05 - 3.35 m
Minor radius		
Horizontal	0.8 - 1.1 m	0.75 - 1.0 m
Vertical	1.4 - 1.5 m	1.15-1.5 m
Elongation	1.4 - 1.8	1.4-1.7
Plasma volume	80-110 m^3	50-100 m^3
Discharge duration	15 s	15 s
Flux swing	61 V·s	40 V·s
Neutral beam		
Torus input power	40 MW	22 MW
Beam energy	120 keV	95 keV
ICRF		
Torus input power	< 5 MW	
Frequency	110 - 130 MHz	
LHCD		
Torus input power	< 10 MW	1.5 MW
Frequency	1.7 - 2.3 GHz	
Pellet injection	< 2.3 km/s, 4 mm^3	

Moreover, the cycle time of feedback control of vertical position was shortened to 0.25 ms from 1ms by using three MC88100 based RISC computers and VME buses [3].

A continuous chamber with a multi-arc shape and so called double-skin structure were chosen to obtain a large vacuum vessel with sufficient strength within the bore of the existing toroidal field coils [1,4]. This structure consists of inner and outer skins and poloidally-oriented square pipes made of Inconel. To reduce carbon bloom, a carbon-fiber composite (C/C) with thermal conductivity of up to 300 W/m°C is used for the divertor plates. These plates are set continuously, and the difference in height between neighboring tiles is less than 0.5 mm. Moreover, edges of divertor tiles shingle in the toroidal direction to reduce heat flux density on the edges. Water cooling pipes are introduced into the vacuum vessel for the heat removal of the divertor plate to suppress thermal stress of vacuum vessel. The surface of the vacuum vessel except divertor plates is covered with isotropic graphite tiles. These tiles are inertially cooled and the heat is removed through the cooling channel after shots.

The vessel can be baked out up to 300 °C. Taylor discharge cleaning (TDC) method were prepared with a pressure of $0.2\text{-}1 \times 10^{-2}$ Pa, I_p=10-40 kA, B_T=0.7-1 T, a pulse duration of 30 ms and a repetition time of 1 s. Glow discharge cleaning device was also introduced at the middle of April. GDC was performed with a pressure of $\sim 2 \times 10^{-2}$ Pa, a discharge voltage of 500-600 V and a discharge current of 0.5-1.5 A.

The toroidal field coils and heating systems are those of the original JT- 60 with minor modification. The designed value of maximum toroidal field is 4.2 T at the major radius of 3.4 m but the maximum

Table 2 Main parameters of PF coils.

F coil	Flux swing A. turns	42 V·s 120 kA × 70 turns
V coil	Flux swing Vertical field A. turns	19 V·s 0.5 T 50 kA × 78 turns 60 kA × 58 turns
H coil	Horizontal field A. turns	0.06 T 30 kA × 26 turns
D coil	A. turns	110 kA × 10 turns
DCW coil	Sector turns No. of toroidal sectors Current	3 turns 4 20 kA
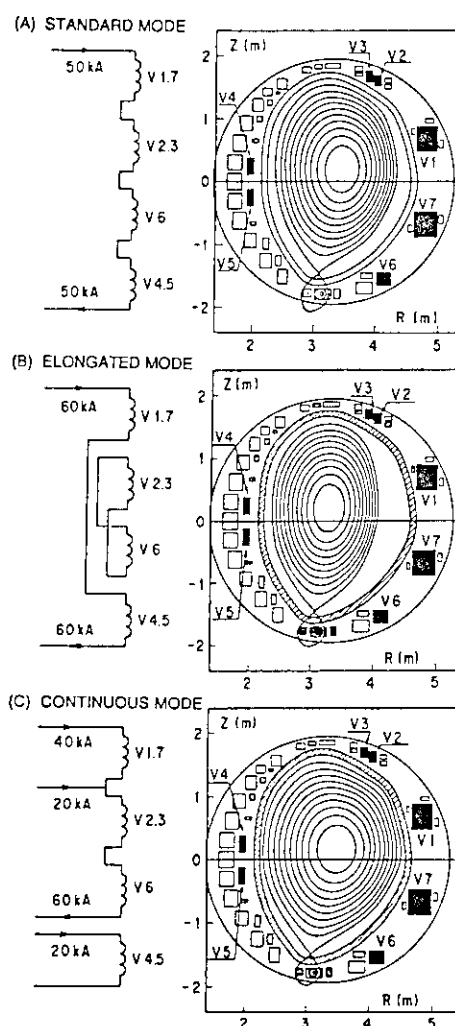
Fig. 2 Typical plasma configuration and connection of the vertical field coils.

toroidal field operated in this year was 4 T. Ten quasi-perpendicular neutral-beam injectors (~ 75°) can deliver up to 28 MW with accelerating D^0 beam voltage up to 120 kV (Fig. 3) [5]. The electrode of the ion sources in these beamlines were rearranged to match 120 keV deuterium operation. The maximum input power of NB obtained in this year operation was, however, 22 MW because the accelerating D^0 beam voltage obtained was ~100 keV due to the lack of beam source conditioning. One multi-junction launcher for lower hybrid current drive was installed in a diagonal port [6]. This launcher was designed to operate at the wide frequency range of 1.74 to 2.23 GHz and to control $N_{//}$ spectra with high directivity. This launcher was provided ~1.5 MW of torus input power for current drive studies. Neutron shields for deuterium operation were also prepared.

1.2 Diagnostics Status

Diagnostics installed on the JT- 60U are shown in Figs.3-7. Plasma density is measured by 2 vertical chords of sub-mm wave (FIR) inter-ferometers. Electron temperature profiles are measured by ~20 channels ECE michelson interferometers and 9 channels Thomson scattering as shown in Fig. 4. The charge exchange recombination spectrometer (CXRS) with 20 tangential and 8 poloidal channels is the main instrument for providing ion temperature profiles and plasma rotation velocity profiles as shown in Fig.4. The time resolution of ECE michelson interferometers is 20 ms and CXRS is ~50 ms. One channel of ECE grating polychromer with the time resolution of 20 μs measures fast behavior of electron temperature in central
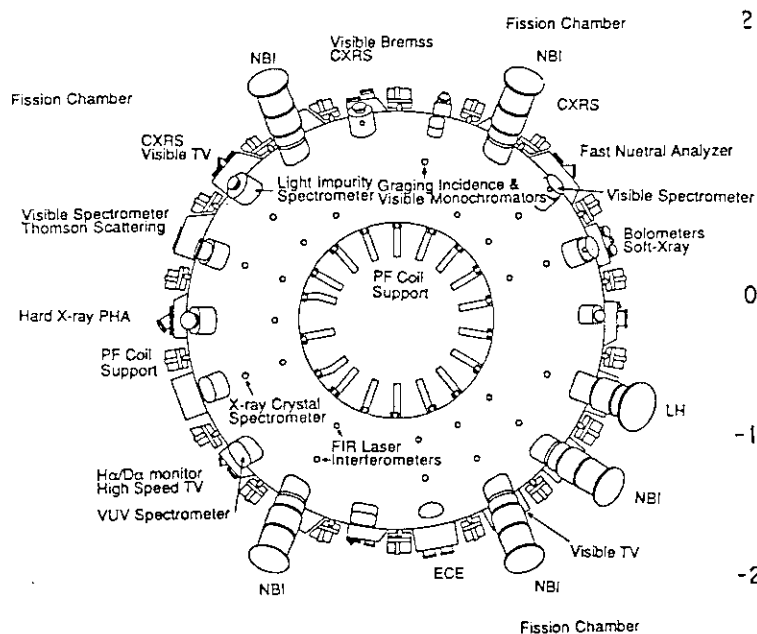
Fig. 3 Arrangement of NB injectors and main diagnostics.
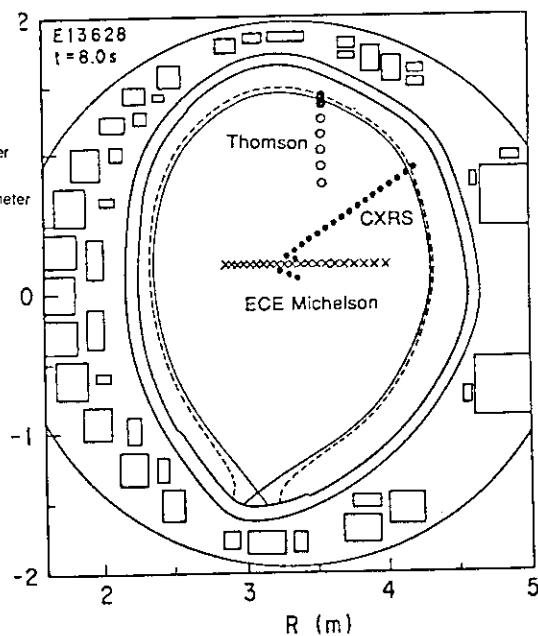
Fig. 4 Poloidal views of the Thomson scattering, ECE michelson interferometer and CXRS.

region. The electron density and temperature profiles on the divertor plate are measured by 15 channels Langmuir probes arrayed poloidally on the divertor plate.

Impurity species and concentrations in a main plasma are measured by 1 chord of VUV spectrometer (0.5-130 nm) and 1 chord of grazing incidence monochromater (10-130 nm) as shown in Fig. 5. The intensity profiles of impurity lines and ion temperatures of a divertor plasma are observed by filter optics (for CII, OII, D_α and D_β) and a VUV spectrometer, respectively. Radial profiles of Z_{eff} are measured by filters (10 viewing chords) and 1 vertical chord of visible monochromater as shown in Fig. 5.

Neutron flux is measured by 3 sets of detectors composed of a ^{235}U fission chamber, ^{238}U fission chamber and ^{3}He counter. These detectors were calibrated with a ^{252}Cf source placed at many positions inside the vacuum vessel.

Radiation loss profile is measured by 32 channel bolometers with spatial resolution of 10 cm at the plasma center as shown in Fig. 6. Spatial profile of soft X-ray intensity is measured by two arrays with 32-channel PIN diodes from horizontal port. The field of PIN diode view is the almost same with the bolometer view. H_α/D_α profiles are measured by 10 channels H_α/D_α PMTs arrayed poloidally as shown in Fig.7 and 6 vertical chords. The chords of hard X-ray PHA are also shown in Fig. 7. There are 15 one-turn loops and two sets of 17 magnetic probes to measure the tangential magnetic fields, 16 magnetic probes to measure the normal magnetic fields and diamagnetic loop [7].
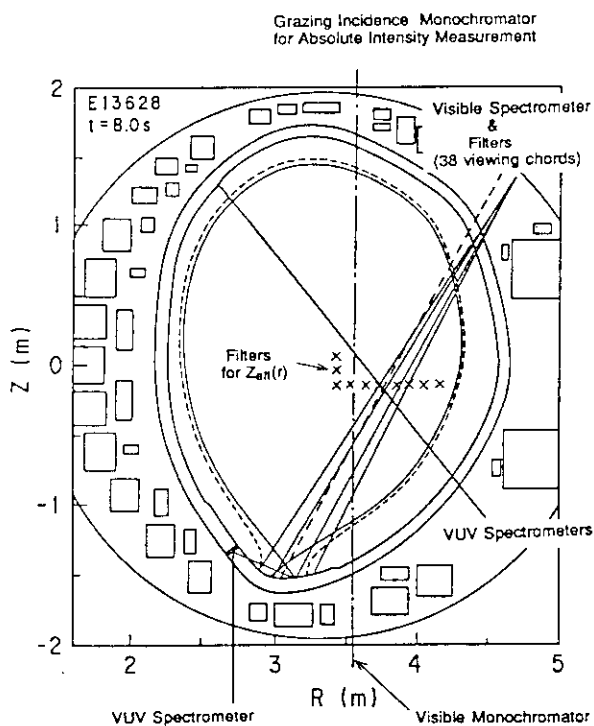
Fig. 5 Poloidal views of the impurity measurement system.
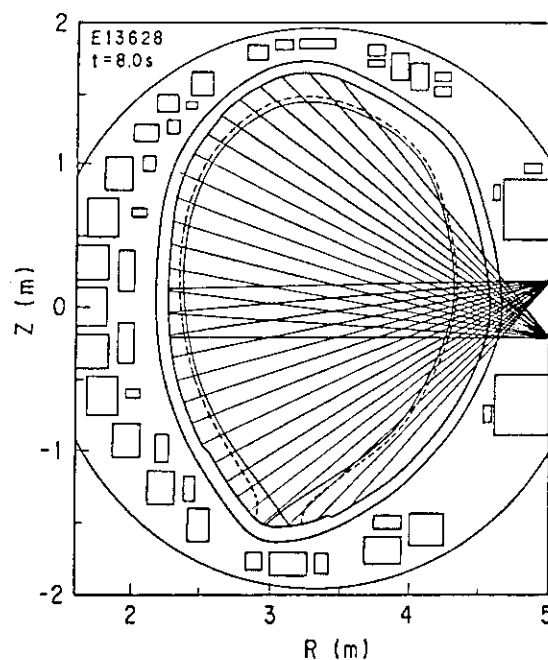
Fig. 6 Poloidal views of the bolometer array.
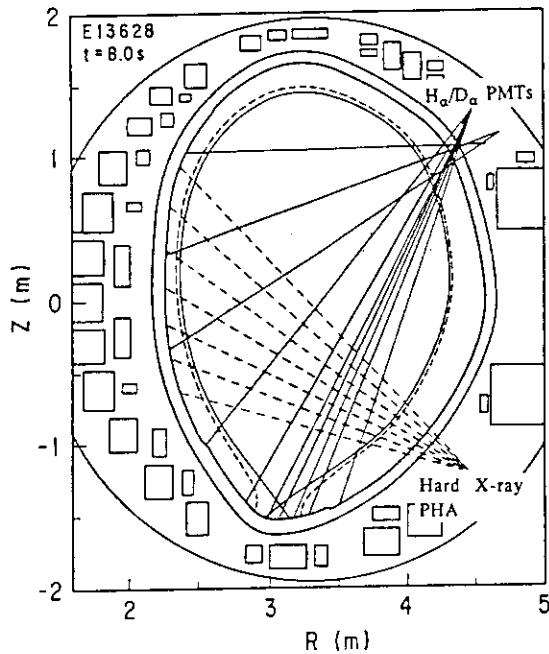
Fig. 7 Poloidal view of the H_α/D_α PMT's and hard X-ray PHA.

1.3 Overview of Operation

Construction of the JT- 60U was completed in March 1991 and ohmic experiments with hydrogen gas were initiated at the end of March. Optimizations of break-down, current ramp-up and divertor configuration has been performed. Multivariable non-interacting control was adopted to allow independent control despite the strong mutual coupling between the ohmic heating coils and the vertical field coils. Well controlled divertor discharges were successfully obtained using this method and discharges with plasma current of up to 4 MA were achieved after only 12 days of operation. After testing and developing the scientific and technical capabilities of the diagnostics and the NBI system, deuterium discharges started in July. After the conditioning of NB injection port, experiments with NB power of up to 22 MW started in late August. The main objective of NBI experiments has been to study the basic performance of JT- 60U and the following experiments have been performed : 1) H-mode experiments, 2) High-β_p/hot-ion discharges and 3) confinement studies of L-mode discharges [8]. In October, hydrogen discharges were made before an annual vacuum break in November. Discharges with plasma currents of up to 5 MA have been achieved and method of obtaining 6 MA discharges is clear. LHCD experiments have also been performed. Table 3 shows the overview of these operations.

References

[1] H. Ninomiya, et al., Plasma Devices and Operations, **1** (1990) 43.

[2] H. Horiike, et al., Fusion Engrg. Des. **16** (1991) 285.

[3] T. Kimura, et al., IEEE Trans on Nuclear Science **35** (1989) 1554.

[4] Y. Neyatani, et al., Plasma Devices and Operations, **1** (1991) 183.

[5] M. Kuriyama, et al., Proc. of 13th Symp. on Fusion Engineering, Knoxville (1989) p. 996.

[6] M. Seki, et al., Proc. of 16th Symp. on Fusion Tech. London (1990) Vol. 2, p.1060.

[7] Y. Neyatani, et al., 14th Symp. of Fusion Engineering, San Diego (1991).

[8] H. Ninomiya, et al., to be published in Phys. Fluids B.

Table 3 Overview of operation in 1991

Data	H/D	Number of shots	Conf. S/H	T(C)	Main items and results
3/26-28	H	0	S	300	Optimization of TDC, Cleaning of VV, Check of sequence
4/1-4	H	14	S	300	Cleaning of VV, Check of sequence, Optimization of break down
4/8-11	H	5	S	300	Cleaning of VV, Check of FBsequence, Optimization of current ramp-up
4/15-19	H	107	S	300	Check of FB sequence, Check of divertor configuration, Optimization of divertor discharge, 2.5 MA and 5 s discharge
4/22-25	H	58	S	300	Optimization of divertor discharge, 4 MA discharge, Measurement of divertor plasma density and temperature
6/5-7	H	36	S	300 150	Optimization of divertor discharge and FB control
6/11-14	H	43	S	300	NB port aging
6/18-21	H	42	H	150 300	Optimization of elongated divertor discharge, Check of diagnostics
6/25-28	H	72	H	150	Optimization of elongated divertor discharge, Check of diagnostics, NBport aging
7/18-19	D	12	S	300 150	Check of TFC displacement, Check of deutrium discharge
7/23-26	D	67	S	150 300	Check of deutrium discharge, Check of diagnostics, NB port aging
7/30-8/2	D	52	S	300	NB port aging
8/6-9	D	71	S	300	NB port aging, H-mode try (8/9)
8/26-30	D	75	S	300 150	Introduction of GDC, H-mode try, Check of neutron yield, $Sn = 2.5 \times 10^{15}$/s, Ripple loss
9/3-6	D	81	H	150 25	High-poloidal beta and hot ion discharge $Sn = 7.9 \times 10^5$ /s, Ti~16 keV
9/10-13	D	57	H	150	Optimization of confinement of 3-4 MA discharges, $Sn = 1.3 \times 10^{16}$/s, Wdia = 5.16 MJ
9/124-27	D	82	H	150	H-mode try in low Ip and low B_T region
10/1-4	D	71	H	150	H-mode try, quasi-stationary H-mode, H-factor~1.4
10/14-18	H	122	S	150	LH aging, Sawtooth supression, LH CD characteristics
10/22-25	H	103	S	150	LHCD and LHCD + NBI, 2 MA current drive, 5 MA discharge
10/29-11/1	H	81	H	150 25	Density limit, Divertor characteristics of high density plasma, Study of toroidal rotation, Optimization of current ramp-up

2 Plasma Control

2.1 Operation Regime of Plasma Parameters in JT-60U

M. Matsukawa, H. Ninomiya, N. Hosogane, K. Ushigusa, R. Yoshino, K. Tobita

A. Sakasai, T. Kondo and Y. Kamada

As mentioned in section 1.1, ohmic experiments with hydrogen gas were initiated at the end of March and deuterium discharges started in June. Experiments with NB power of up to 22 MW started in late August. In October, hydrogen discharges were again made before an annual vacuum break in November. LHCD experiments have been performed in this phase. The standard mode were mainly used in hydrogen discharges and the NB power-up phase. The elongated mode were used in deuterium experiments with high NB power.

The main objective of deuterium NB heating experiments were : 1) H-mode experiments, 2) High-β_p/hot-ion discharges and 3) confinement studies of L-mode discharges. H-mode experiments have been performed in the region of I_p=1-4 MA, B_T=1.7-4 T, q_{eff}=3-5 and P_{NB}=6-22 MW, where I_p is the plasma current and B_T is the toroidal field. q_{eff} is the effective safety factor defined as

$$q_{eff} = \frac{5a_p^2 B_T}{R_p I_p} \frac{1+\kappa^2}{2} \left[1+\left(\frac{R_p}{a_p}\right)^2 \left(1+\frac{(\beta_p+l_i/2)^2}{2}\right) \right] \left[1.24-0.54\kappa+0.3(\kappa^2+\delta^2)+0.13\delta \right] ,$$

where a_p is the plasma minor radius, R_p is the plasma major radius, κ is the plasma elongation, l_i is the plasma internal inductance, δ is the plasma triangularity and P_{NB} is the NB input power. In high-β_p/hot-ion discharges, relatively small plasmas of R_p~3.1 m, a_p~0.75 m, κ~1.6 and plasma volume V_p of ~50 m^3 were used as the target of high power NB of 15-22 MW to improve the deposition profile and heating density of NB near the central region. The plasma current was scanned from 0.8 to 2 MA with q_{eff} varying from 12 to 4. L-mode study has been performed in the region of R_p~3.2 m, a_p~0.9 m, κ~1.6 and B_T~4 T. Wall conditioning has been performed by a combination of baking of the vessel (~300 °C), Taylor discharge cleaning (TDC), glow discharge cleaning (GDC), helium clean-up discharges and disruptive discharges. Before the introduction of GDC, the oxygen concentration is about twice as large as that of carbon. After the introduction of GDC at the middle of August, the oxygen concentration decreases to the same level as carbon and Z_{eff} of ohmic and high power NB heated plasmas is 2.2-4.4.

Figure 1 shows a relation of toroidal field and plasma current for the standard mode. Toroidal field of 4 T was usually used for the optimization of plasma configuration and feedback control. High plasma current discharges were also performed at 4T in standard mode to avoid the risk of vertical positional instability. Maximum plasma current achieved was 5MA

with B_t of 4T, although the rated plasma current is 6MA with B_t of 4.2T. Figure 2 shows the case of elongated mode. In comparison with the standard mode, relatively many shots were performed with B_t of near 3T due to H-mode try. High-β_p plasma experiments are performed only in the elongated mode. The maximum plasma current in the elongated mode was 4MA. The enough stabilizing effect of the vacuum vessel for the vertical positional instability was observed in high-β_p plasma experiments. It is evaluated that the vacuum vessel has the stabilizing factor of larger than 0.4. Therefore, high plasma current operation in the elongated mode will be also achieved easily rather than its expectation.

Figure 3 and 4 show the relation between plasma major radius and its aspect ratio for both vertical field coil connections. In the case of the standard mode, plasma major radius is usually 3.2 to 3.5m and the aspect ratio is 3.2 to 3.8. On the other hand, plasma major radius is 3.0 to 3.4 and the aspect ratio is 3.3 to 4.2 in the case of elongated mode. Although the decrease of the major radius, the aspect ratio has increased. It implies that plasma volume decreased considerably in H-mode try and high β_p plasma experiments.

The operation region of $\bar{n}_e$ vs. I_p and $1/q_{cyn}$ vs. $\bar{n}_e R_p/B_T$ is shown in Figs. 5 and 6, where $\bar{n}_e$ is the line averaged electron density (m^{-3}) and q_{cyn} is the cylindrical safety factor defined by $q_{cyn} = 5a_p^2 \kappa B_T/R_p I_p$. The density limit experiments are mainly performed only in the elongated mode and the maximum Murakami parameter is 4.2 in ohmically heated discharges and 8.8 in neutral beam heated discharges. In the density limit experiments, the various condition of the vacuum vessel was tested. For example, the baking temperature of 300°c, 150°c and room temperature were used. Moreover, after TDC and GDC using hydrogen, deuterium and/or helium gases, and disruptive cleaning were also used. However, the density limit with gas puffing in the elongated mode was not optimized yet.

Figure 7 shows a relation of plasma current and P_{NB} for both connection. High power experiments are performed mainly in the elongated mode according to H-mode try and High-β_p experiments because the standard mode were mainly used in the NB power-up phase.

Operation regime performed from April to November in 1991 are summarized. There is no enough time to survey various kind of experimental condition so that the operational regime is not optimized until end of last experimental period. The tangential NBI, ICRF and the pellet injector need own optimal operational condition so that more wide operation regime will be required in next experimental period.
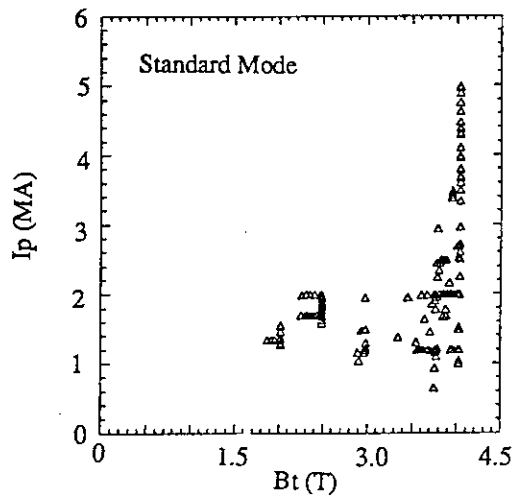
Fig.1 Toroidal field vs. Plasma current
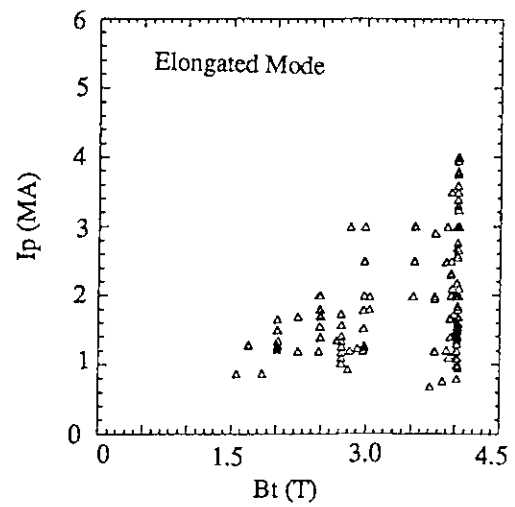
Fig.2 Toroidal field vs. Plasma current
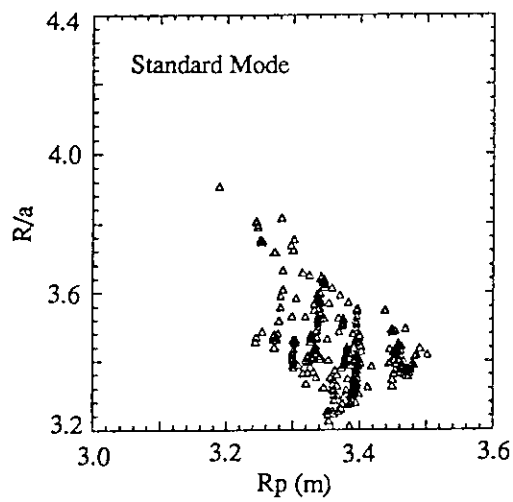
Fig.3 Major radius vs. aspect ratio
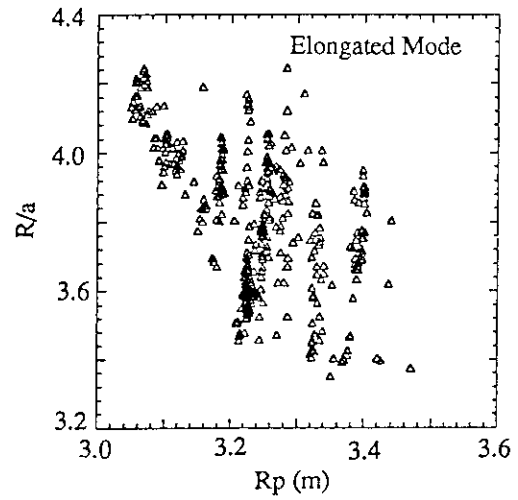
Fig.4 Major radius vs. aspect ratio

(a) Plasma current vs. density

(b) Hugill diagram
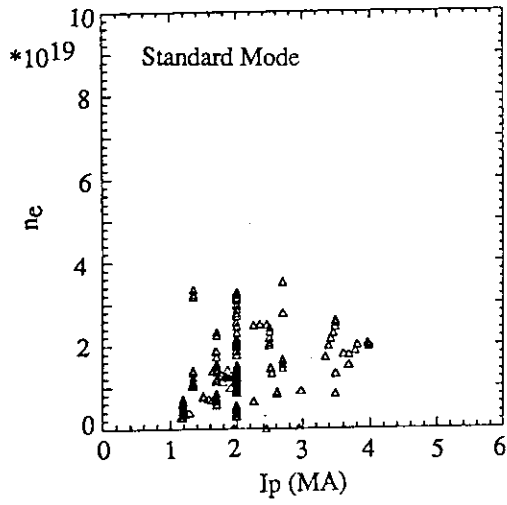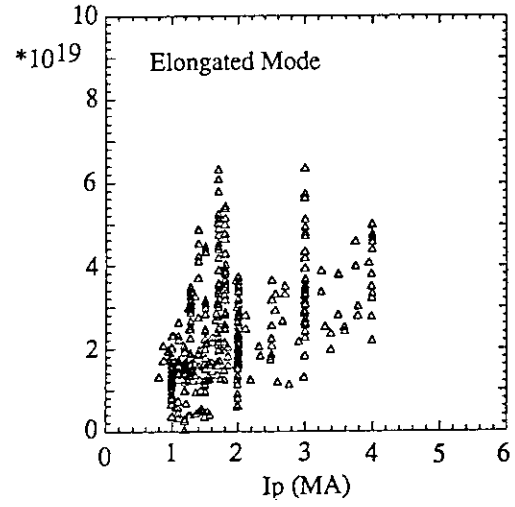
Fig.5 Plasma current and density

(a) Plasma current vs. density
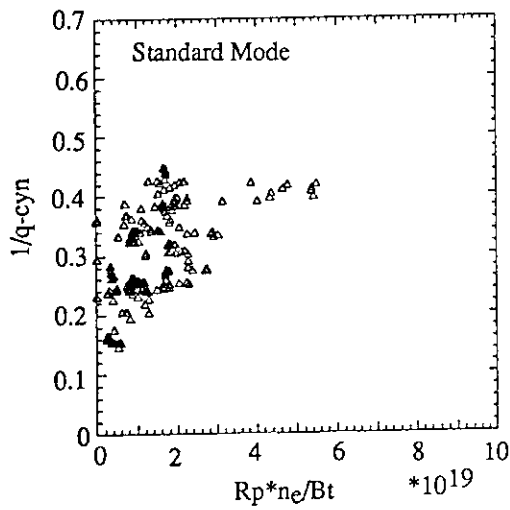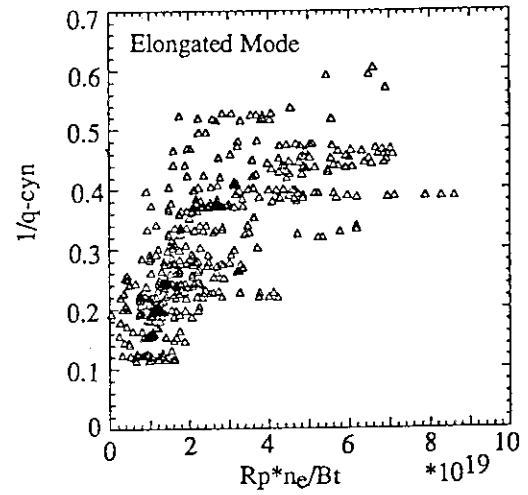
(b) Hugill diagram

Fig.6 Plasma current and density
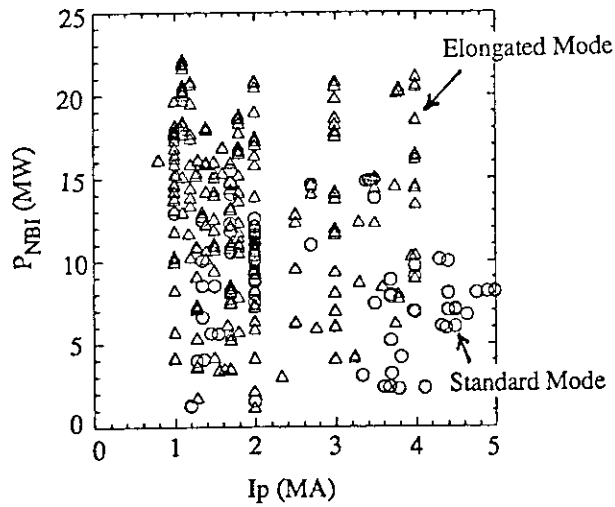
Fig.7 Plasma current vs. NBI power

2.2 Operation Regime from Aspect of Machine Capability

M.Matsukawa,H.Horiike,H.Ninomiya,N.Hosogane,K.Ushigusa,R.Yoshino,
K.Tobita,A.Sakasai, T.Kondo and Y.Kamada

1. Introduction

JT-60U has been designed to permit plasma current of 6MA with divertor configuration, but it should be noted that the operation regimes of the poloidal field coil (PFC) and the toroidal field coil (TFC) are to be limited in a designed region for avoidance from excessive stress. It is worth to confirm that the operated region did not exceed the limits. From the view point of machine safety, various operational limits should be summarized for the following experiments on JT-60U.

2. Overturning force of toroidal field coil

A most important issue in the limitations for machine operation is the overturning force of TFC. Because it causes the excessive stress on the brazed connection in TFC. In the initial operation of JT-60U in April, we set to 250 ton per one TFC as the maximum of it, that is the really operated maximum value on original JT-60. Then we reinforced the TFC by welding the neighboring coils on June, and the considerable decrease in displacement of the TFC was confirmed. Then, the maximum software interlock value of overturning force was raised up to 300 ton for 5MA operation. However, it must be stressed that the largest overturning force has happened just after a disruption. Moreover the instantaneous increase in the force is about 100 ton and it tends to increase with plasma current. Figure 1 shows a typical example of it.

3. Limitations for poloidal field coil

The vertical field coil of JT-60U is constructed from four coil blocks. And the two types of connection were used in actual experiments. They are named to be the standard divertor connection (ST) and the highly elongated mode connection (HE). Hence, we discuss the results for both vertical field coil connections.

3. 1 Standard divertor connection

The current limitations of PFC are basically determined by a function of the plasma current. Figures 2 to 4 show the operation regime of ohmic heating coil (F-coil), vertical field coil (V-coil) and divertor coil (D-coil) in the case of ST. Here, the horizontal field coil (H-coil) and sector coil (DCW-coil) are not shown, because they are restricted only by their maximum currents as shown in Table 1. The designed region is represented by hatching and they are significantly wider rather than actually operated region. One of the reasons is that the maximum plasma current has not reached to its rating of 6MA until the end of this experimental period. Hence, the maximum premagnetized current of F-coil was only 80kA. Nevertheless the efficiency of flux swing was enough to make a survey of the operational scenario of 6MA plasma. That resulted in the

premagnetization of 100kA at least must be required for 6MA operation as shown in Fig.2. The V-coil current increases linearly with plasma current as shown in Fig.3. The narrowness of operated region and relatively low poloidal beta value caused to this relation. Although the divertor coil current is limited only when F-coil current is positive (See Table 2), the operation regime is not so wide as shown in Fig.4. This is caused by other limitation factor, that is to keep the separatrix line onto the divertor plate. Therefore, the maximum height of X-point is limited to be 25 cm, and is not determined by the stress of D-coil for lower plasma current experiments.

3. 2 Highly elongated mode connection

Figures 5 to 7 show the operation regime of PFC in the case of HE. Although the operated region of F-coil against to plasma current is smaller than case of ST, V-coil and D-coil have relatively larger operated region. It is due to the hot ion mode plasma experiments that are performed with small divertor configurations at the inboard side of vacuum vessel as possible to avoid ripple losses and to get the good heating power deposition. These high poloidal beta plasmas required high currents of V-coil and D-coil.

4. Over turning force limit in 6MA operation

The time evolution of the over turning force on a shot of E014221 is as sown in Fig. 8, and the maximum overturning force of 250 ton appeared at the end of premagnetization with the F-coil current of 80kA. On the other hand, the minimum over turning force of -180 ton appeared at the plasma current ramp down phase. Then, the maximum over turning force of 370 ton is at least required in 6MA operation for the F-coil premagnetization of 100kA without a disruption. Considering the increase of over turning force due to a disruption, TFC must withstand it larger than 400 ton. The careful observation of TFC displacement is required to rise software interlock value.

5.Conclusion

Limitations of JT-60U are summarized from data performed in 1991's experimental period. It is confirmed that the no risky operations had been performed, and we are sure of that 6MA operation will be achieved in next experimental period.

Table 1 Maximum rating of poloidal field coils in JT-60U

	Standard divertor	Elongated divertor
F-coil	±120kA / ±2.5kV	±120kA / ±2.5kV
V-coil	-8.7kA,+50kA / ±5kV	-8.7kA,+60kA / ±5kV
H-coil	±30kA / ±1kV	±30kA / ±1kV
D-coil	+110kA / ±1kV	+110kA / ±1kV
DCW-coil	±15kA / ±1kV	±15kA / ±1kV

Table 2 Software interlock of PFC in real time control

	In the case of If>0	In the case of If<0
F-coil current	0<If(kA)<120	-120<If(kA)<0
Plsma current	Ip(MA)<4(1-If(kA)/120)	Ip(MA)<6
V-coil current	-10+6.66Ip(MA)<Iv(KA)	same to left
	Iv(kA)<4.735Ip(MA)+23.5	
	--------(for ST)	
	-10+8.33Ip(MA)<Iv(KA)	
	Iv(kA)<5Ip(MA)+30	
	-------(for HE)	
D-coil current	Id<52kA+0.145Ip	Id(kA)<110
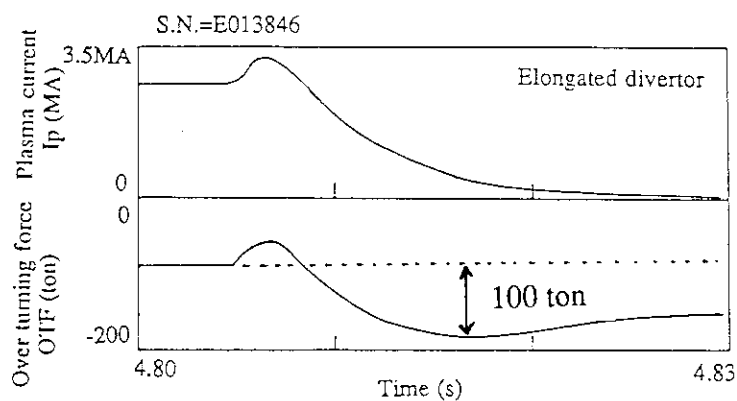
Fig.1 Overturning force during plasma disruption
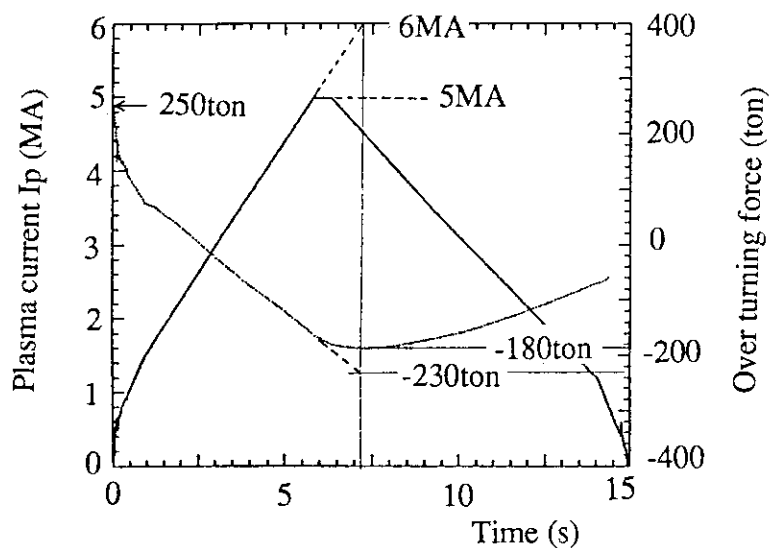
Fig.8 Time evolution of overturning force.

Fig.4 D-coil vs. Plasma current

Fig.3 V-coil vs. Plasma current

Fig.2 F-coil vs. Plasma current
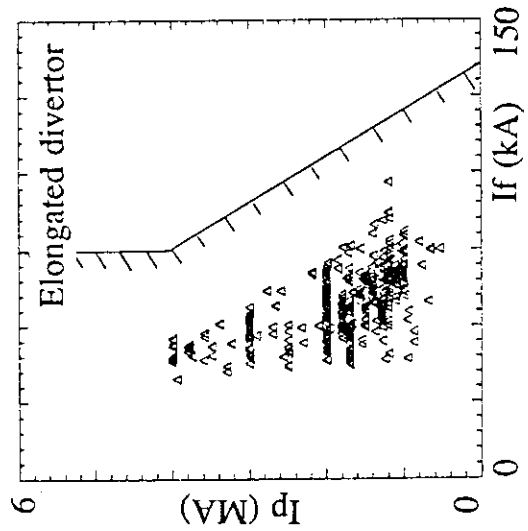
Fig.7 D-coil vs. Plasma current

Fig.6 V-coil vs. Plasma current
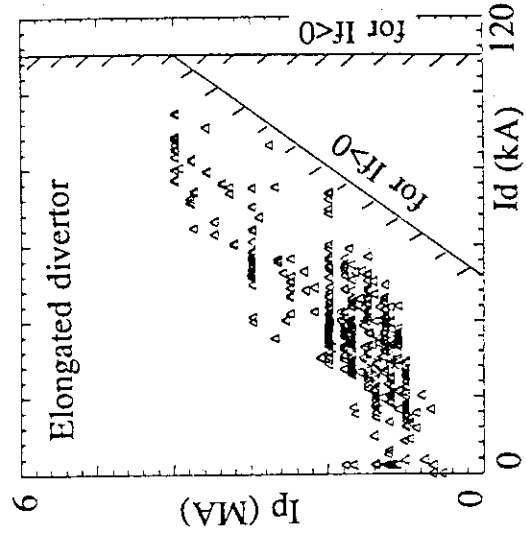
Fig.5 F-coil vs. Plasma current

2.3 Detecting Method of Plasma Position by Regression Analysis

M. Matsukawa, N. Hosogane and H. Ninomiya

1. Introduction

JT-60U has 17 tangential probes,16 normal probes and 15 flux loops as magnetic sensors for detecting the plasma shape. One may expect that to detect plasma position is very easy because a lot of sensors are available, but it is still important problem how we can obtain the reliable and accurate measurement formulas to be applicable to real time feedback control. From primer experience of the lower single null divertor operation in JT-60, we obtained the measurement formulas by regression analysis using calculated equilibrium database. They were made from probes signals and aimed basically to use for initial operations so that the accuracy was relatively sacrificed to ensure its reliability. Although the start up of JT-60U was carried out successfully, the detecting accuracy was not enough to control easily plasma position for various experimental requirements. Then we generated a equilibrium database by fast boundary identification code (FBI) from the really discharged data. It enable to test for various regression functions using not only magnetic probes but also flux loops without consideration of measurement error effect. This paper describes the stability and accuracy of used regression functions at start up. And the new regression functions with the probes and flux loops are also presented.

2.Obtaining the Regression Functions

Figure 1 shows the configuration of the magnetic sensors in JT-60U. From limitation of computer capability for real time feedback control, the number of available sensors is limited as mentioned later. The plasma current and poloidal field coil currents are also available. However, the poloidal field coil currents except divertor coil current can not be available due to the shielding effect of vacuum vessel.

Figure 2 shows the calculated region of ohmic heating coil and divertor coil current in the equilibrium database, that is selected to be close to the actual operational region. Here, both currents are normalized by the plasma current because the plasma shape is independent of the plasma current. Figure 3 shows the reference position of plasma geometrical center. The range of the poloidal beta and the plasma internal inductance are 0.2 to 1.5 and 0.5 to 1.5,respectively.

JT-60U has two types of vertical field coil connection for standard divertor and elongated divertor plasmas. Therefore, the equilibrium database were made for both type of plasmas. They have approximately one thousand equilibria of divertor and three thousands of limiter equilibria.

The set of predictor variables for regression analysis is as follows.

$$x_i \ (i = 1, 30) : \frac{B_{tj}}{I_p}, \frac{B_{nj}}{I_p}, (j = 1, 7), \frac{B_{tk}I_d}{I_p^2}, \frac{B_{nk}I_d}{I_p^2} \ \ (k = 1, 8)$$

Here, the numbers of B_t and B_n probe are determined by the limitation of hardware construction. These variables are selected by backward elimination procedure from whole set of sensors. (Draper and Smith,1966) It was done in order to decrease the number of predictor variables to calculate within one control cycle of 250 μs. And all regression functions of the plasma horizontal position Rp, the vertical position Zp and the height of X-point Xp, have to use same set of predictor variables. However, it should be stressed that the number of predictor variables of 30 is too large to obtain the reliable regression functions. In fact, all F-values which represent the level of significance do not satisfy its criterion of 2. (Sugiyama,1983) Therefore, we obtained the regression functions with stepwise procedure from these 30 predictor variables.

3. Experimental Results of Initial Operation

Figure 4 shows the deviation of measured plasma position as a function of the number of predictor variables in the case of standard divertor operation. Here, the deviation is calculated from the FBI database and the applied regression functions. In actual experiments, 8 predictor variables are used for detecting the plasma horizontal position Rp, 12 variables for the vertical position Zp and 8 variables for the height of X-point Xp. In the case of Rp, the number of predictor variables

is fairly good because the deviation increases rapidly after 10 variables. But in other cases, the used numbers are not so suitable to obtain accurate results. Figure 5 shows the deviation in the case of elongated plasma operation. The deviation of Xp is very large so that it seems to be difficult to operate sufficiently. In the case of the standard divertor, the comparison of the regression function with FBI database are shown as in Fig.6 to 8.

4. Revise of Regression Functions

Using FBI database, we can revise the regression functions. It is advantageous because the consideration for measurement errors does not required. Figure 9 to 11 show the comparison of the revised regression functions obtained from 30 variables for standard divertor. The deviation of Rp, Zp and Xp are 12mm, 6mm and 16mm with 7, 17 and 6 predictor variables, respectively. In comparison with figure 6 to 8, the detecting accuracy has considerably improved. Here, these number of predictor variables are determined to satisfy the criterion of F-value of 2. In the case of elongated divertor, the deviations are slightly larger than those of standard divertor. The deviation of Rp, Zp and Xp are 41mm, 35mm and 33mm. It might be partly due to the difference of distance between the probes and outer most plasma surface, and partly due to the wideness of operated region.

5. Comparison of Probes and Loops

It is very interesting problem how we can combine the magnetic probes and flux loops to increase in reliability and accuracy of the regression functions. However, the regression analysis based on the calculated equilibrium database resulted in that the flux loops does not have so much information rather than the magnetic probes. Moreover, the weight functions of the probes and the loops strongly depend on the difference of those sensing accuracy, and it causes the difficulty in the regression analysis. Thus, we did not use the flux loops on the initial operation. Nevertheless, it is absolutely clear that hybrid use of them may improve the accuracy of detecting plasma position. Therefore, we tested it using FBI database. Here, the following predictor variables are used in the regression analysis.

$$x_i \ (i=1,82) \quad : \quad \frac{B_{tj}}{I_p},(j=1,17), \ \frac{B_{nj}}{I_p},(j=1,16), \ \frac{B_{tj}I_d}{I_p^2},(j=1,17), \ \frac{B_{nj}I_d}{I_p^2},(j=1,16),$$

$$\frac{\left(\Phi^{j=3,1,1,3,8,13,12,11}-\Phi^{j=12,8,3,8,13,15,13,14}\right)}{I_p}, \ \frac{\left(\Phi^{j=3,1,1,3,8,13,12,11}-\Phi^{j=12,8,3,8,13,15,13,14}\right)I_d}{I_p^2}$$

The deviation of Rp, Zp and Xp are 7mm, 11mm and 15mm with 10,7 and 6 predictor variables, respectively. These are comparable to the results of revised regression functions as mentioned in section 4. Therefore the flux loops are thought to be effective when many of loops are used at same time like a FBI code.

6.Conclusion

The regression functions for detecting plasma position were investigated by stepwise regression procedure using FBI database. The accuracy of less than 2 cm could be expected for Rp,Zp and Xp with new functions in next experiments and it would enable to control easily plasma position.

REFERENCES

Draper N.R. and Smith H., (1966) Applied Regression Analysis, John Wiley & Sons Inc., New York.
Hosogane N., Ninomiya H. and Seki S., (1986) Nucl. Fusion **26**, 657.
Matsukawa M., Hosogane N., and Ninomiya H., (1991) JAERI-M(91-206)
Sugiyama, (1983) Tahenryou Data Kaiseki Nyuumon, p.133-136 (in Japanese), Asakura shoten,Tokyo
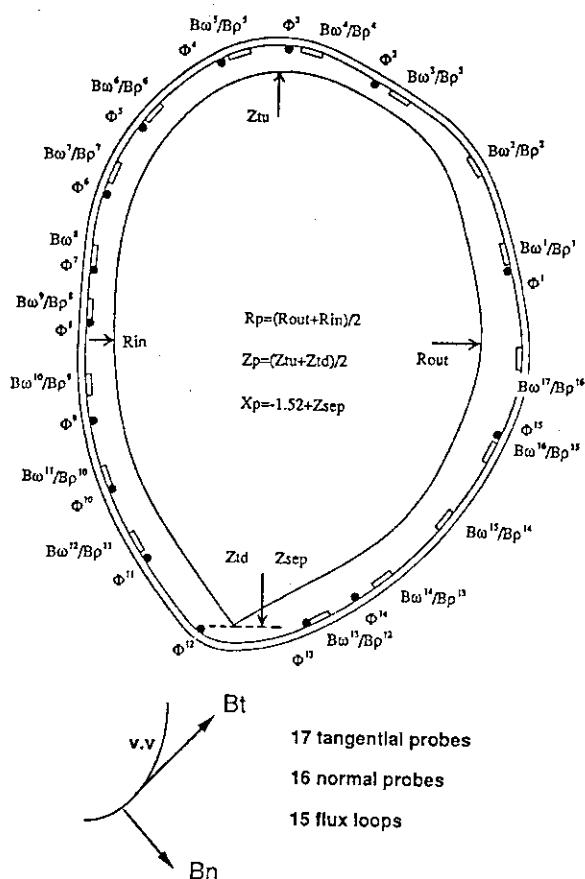
Fig.1 Arrangement of magnetic sensors.

$Rp=(Rout+Rin)/2$

$Zp=(Ztu+Ztd)/2$

$Xp=-1.52+Zsep$

17 tangential probes

16 normal probes

15 flux loops
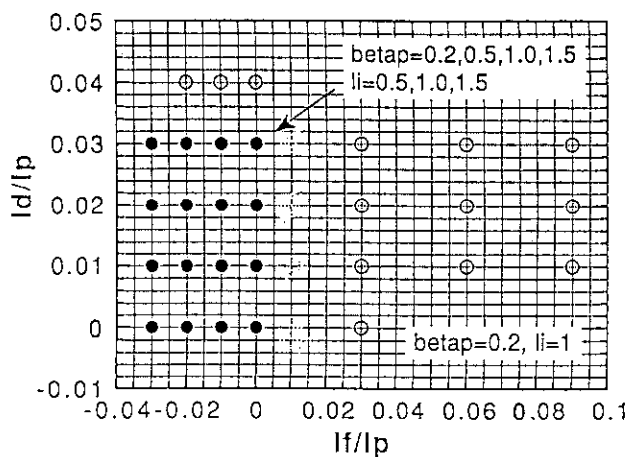
Fig.2 Operation regime of ohmic and vertical field coil.
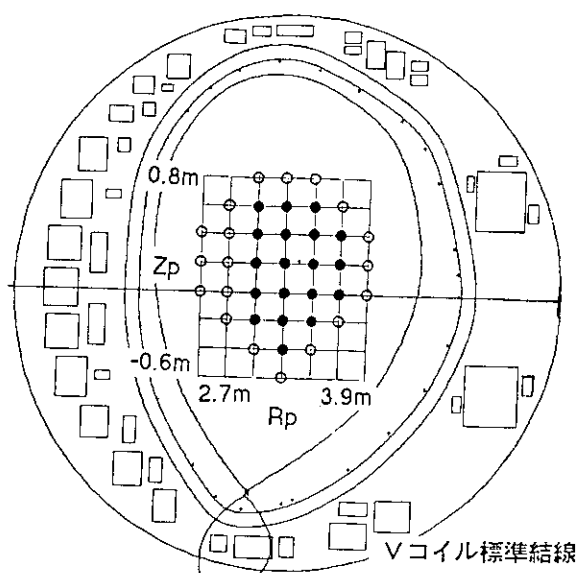
Fig.3 Reference of geometric center of plasma for standard divertor database.
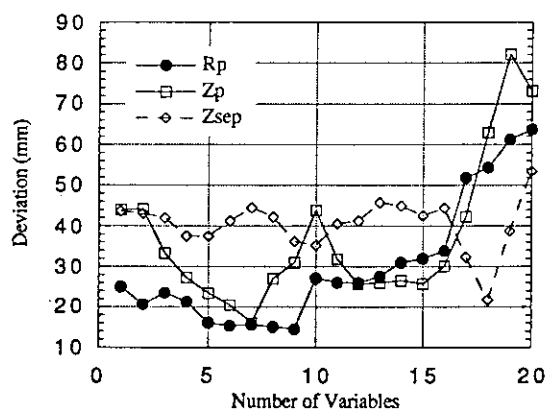
Fig.4 Deviation of measured position for standard divertor.
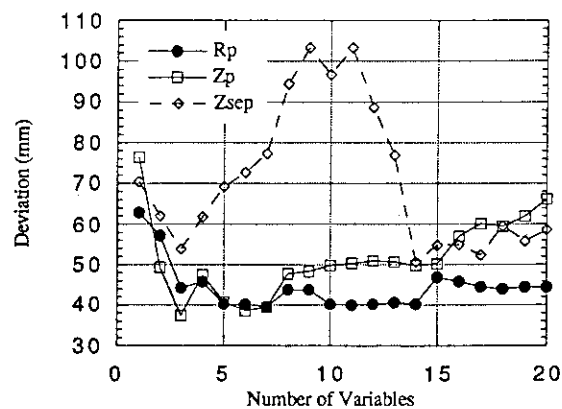
Fig.5 Deviation of measured position for elongated divertor.
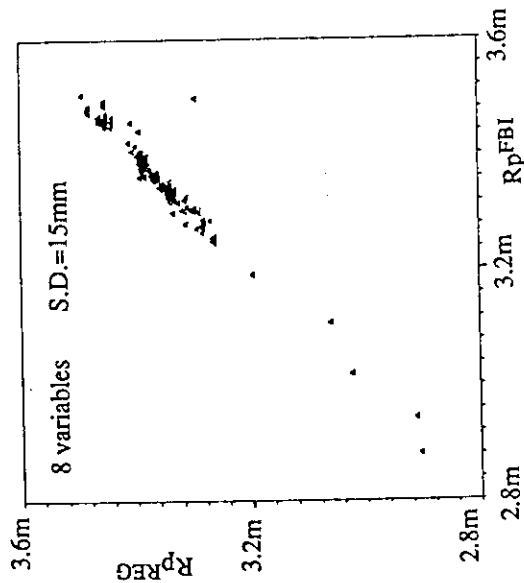
Fig.6 Coincidence of Rp using regression
function obtained from MHD database.
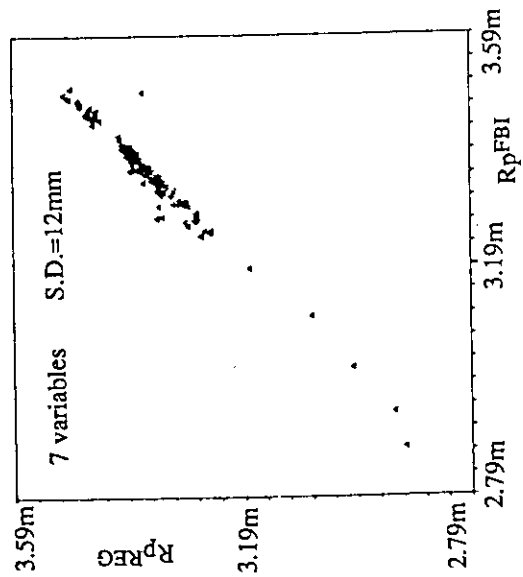
Fig.7 Coincidence of Zp using regression
function obtained from MHD database.
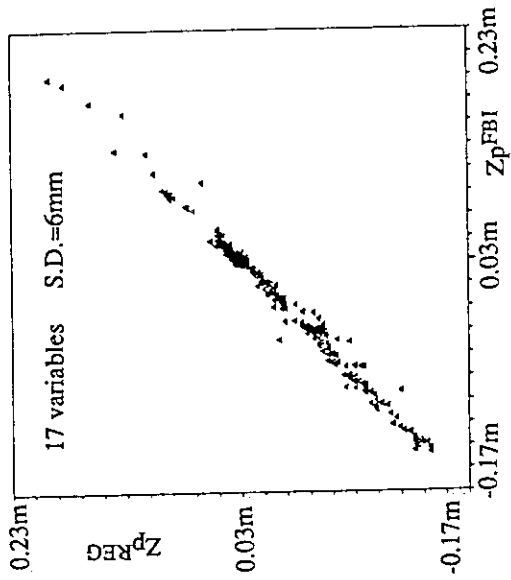
Fig.8 Coincidence of Xp using regression
function obtained from MHD database.

Fig.9 Coincidence of Rp using regression
function obtained from FBI database.

Fig.10 Coincidence of Zp using regression
function obtained from FBI database.
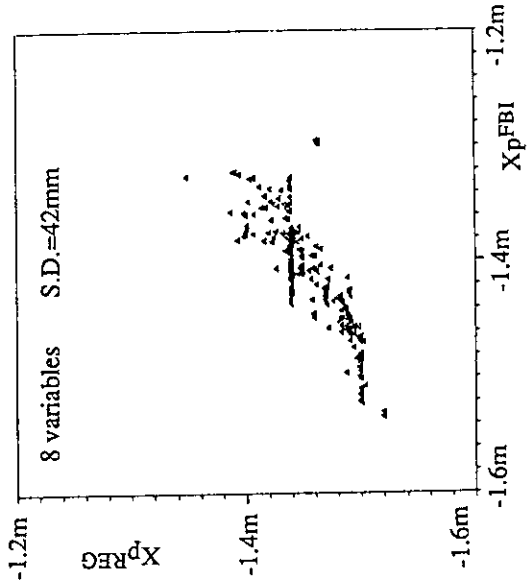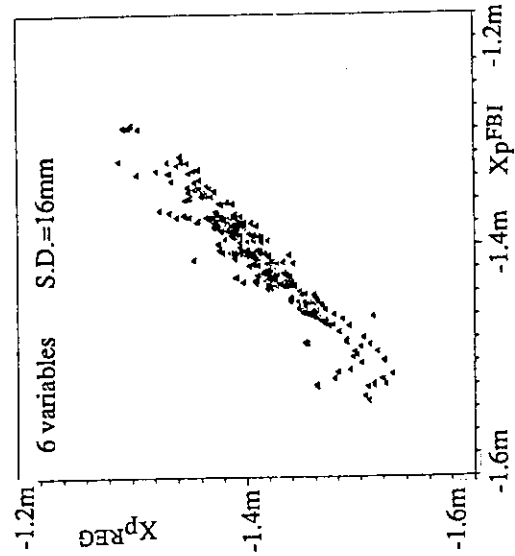
Fig.11 Coincidence of Xp using regression
function obtained from FBI database.

2.4 Estimation of Vessel Eddy Current by Magnetic Fitting Code in JT-60U

K. Ushigusa, M. Matsukawa and Y. Neyatani

The one-turn resistivity of the vacuum vessel in JT-60U is ~ 200μΩ in design value and was deduced experimentally to be ~ 160μΩ[1]. This resistivity is designed to be ~ 20μΩ in the ITER tokamak. A large toroidal current may flow in the vacuum vessel in such a low resistance vessel when the discharge is in a dynamical phase such as 1) major or minor disruption, 2) MHD unstable plasmas (locked mode or vertically unstable discharge), 3) plasma break down phase, 4) current ramp up phase, 5) misfired discharge and so on. In such dynamical phases, the identification of toroidal vessel current and its profile are important for a) the determination of the plasma boundary, b) the estimation of Shafranov lambda and the safety factor, c) the understanding of shell effect on MHD instabilities, d) the estimation of penetration of external field and so on. The understanding of vessel eddy current is quite important for the design of the next generation tokamak.

1. Description of magnetic fitting code

The electromagnetic interaction between plasmas and the vacuum vessel during disruptions has been studied in the Hitachi tokamaks by employing a magnetic fitting code[2]. A similar technique is used to identify vessel eddy current in JT-60U. JT-60U has thirty three magnetic probes and fifteen flux loops ψ. The location of these probes and loops is shown in Fig. 1. Seventeen of these probes measure the magnetic field tangential to the vessel (B_T), while the other sixteen probes measure the magnetic field normal to the vessel (B_N). All these measured quantities ($y_i \equiv (B_T, B_N, \psi)$; i = 1 ~ 48) are used in the fitting code. We model the vacuum vessel as one hundred filament coils along the vessel, and assume that the i-th filament current at the poloidal angle θ_i can be described by
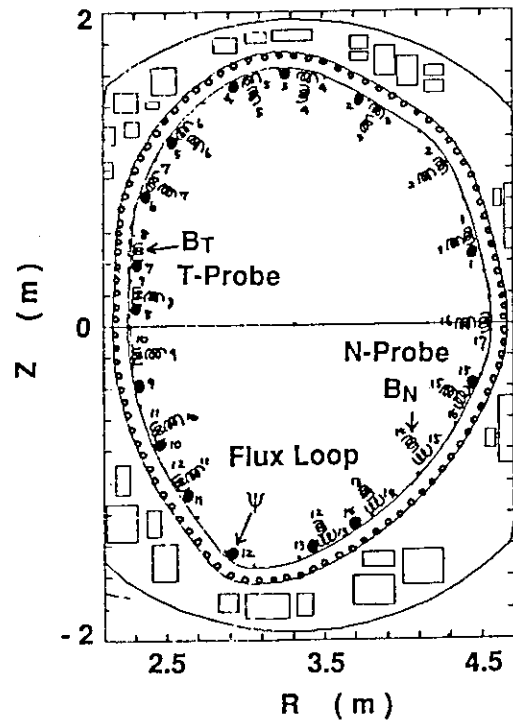
Fig.1 Locations of probes, flux loops and current filaments in the vessel.

$$I_{ED}(\theta_i) = I_{EDo} + \sum_{m=1}^{M} \left\{ A_m \cos(m\theta_i) + B_m \sin(m\theta_i) \right\} \qquad (1)$$

The plasma current is assumed to be typically four filament currents I_{pF}. In order to determine the unknown currents $(x_j \equiv (I_{pF}, I_{EDo}, A_m, B_m) ; j = 1 \sim 15$, typically), we use the conditional least squares method, which keeps the total filament current inside the plasma to be the measured plasma current. The unknown filament currents x_i are obtained by minimizing

$$\chi^2 = \sum_i w_i \left\{ \left[y_i^{mes} - \sum_j Q_{ij}^{ext} I_j^{ext} \right] - y_i^{cal} \right\}^2 - 2\lambda \left(I_p^{mes} - \sum_k I_{pFk} \right) \qquad (2)$$

where $y_i^{cal} = \sum_j Q_{ij} x_j$, Q_{ij} (Q_{ij}^{ext}) is the response matrix of i-th probe and j-th filament (external coil) ,w_i is the weight of each measured quantity and λ is the Lagrange unknown coefficient. At first, filament currents x_i are solved with a fixed initial position of plasma filaments and then the plasma boundary is determined. The plasma filaments are relocated on an ellipse with the same ellipticity as the solved boundary. The ellipse has a radius of typically 40% of minimal distance between the solved current center and the solved boundary, and its center is located in the solved current center. The calculation is iteratively performed until the center of the filament ellipse agrees with the solved current center within a fixed error (typically 0.5%).

2. Results

The toroidal eddy current in the plasma break-down and current ramp-up phases was examined in Fig. 2. The solid and broken lines of the top traces show Rogowskii coil currents inside and outside the vessel, respectively. The difference between these two signals corresponds to the toroidal eddy current (open circles in the second box of Fig. 2). About 0.2MA of toroidal eddy current flows in the vessel at the plasma break down phase. The fitting at t = 20 msec indicates that the plasma is initiated at the upper inside region of the vacuum vessel, and this is consistent with the location of minimum poloidal field at the break down phase[1]. It should be emphasized that the identification of the plasma boundary at the plasma breakdown phase is impossible without including the toroidal eddy current because the toroidal eddy current is much higher than the plasma current ($I_{ED}/I_p > 4$). The plasma boundary grows with the increase in plasma current as shown Fig.2(b) and (c). The fitting result indicates that the null point appears early in the current ramp up. This result is consistent with the observation from the visible TV. The visible TV always indicates the interaction of the plasma with the first wall at the lower outward region. This
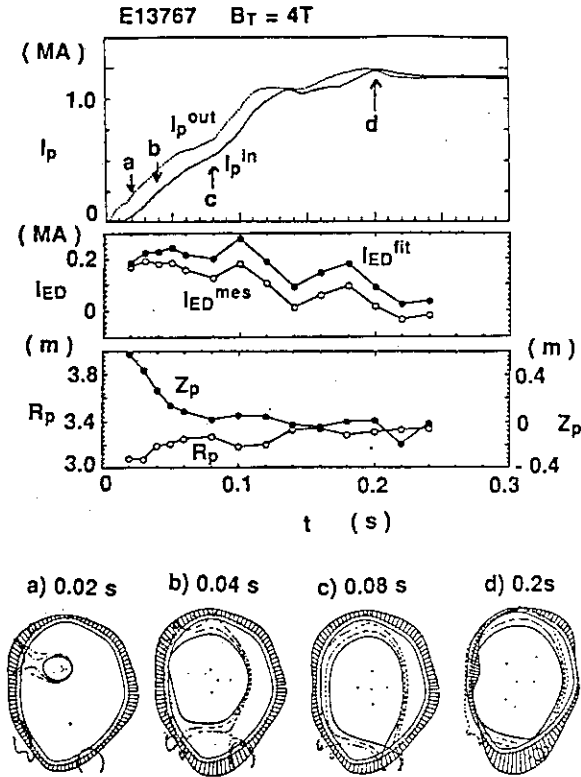
Fig. 2 Eddy current profile duringplasma breakdown and rampup phase.
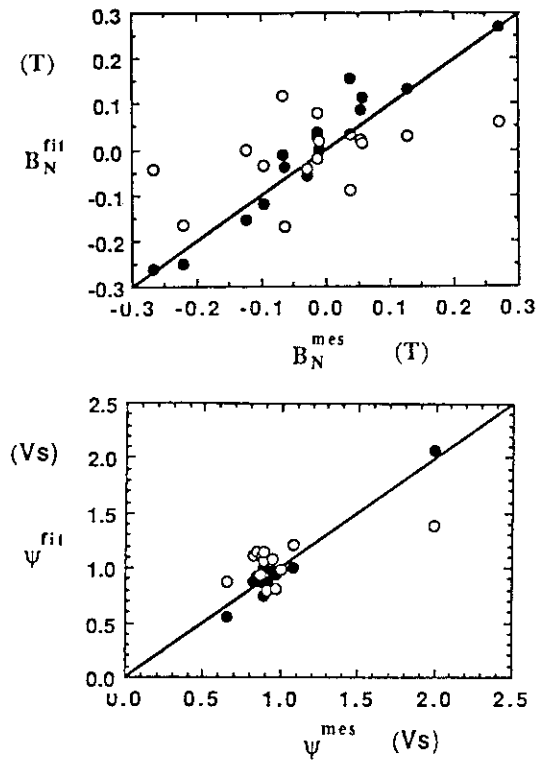
Fig. 3 Comparison of measured and fitted data. Solid and open circles are with and without eddy currents

null point is due to the primary winding current, which flows in the same direction as the plasma current at the early phase of the discharge. The fitting code can estimate the total toroidal eddy current I_{ED}^{fit} by integrating Eq.(1). The closed circles in the second trace of Fig. 2 show the fitted total eddy current. The fitted eddy current has a similar time evolution as the measured one; however, the fitted current is higher than the measured current by about 100kA. The reason for this difference will be discussed later.

Figure 3 shows a comparison of the measured and fitted normal magnetic field B_N and flux ψ, with and without inclusion of the eddy current, at a disruption where a large eddy current flows in the vessel ($I_{ED}/I_p \sim 1$). Solid and open circles show results with and without eddy current, respectively. By including eddy current, the correlation coefficient is improved to ~ 0.93 from ~ 0.22 for B_N and to ~ 0.96 from 0.4 for ψ. The measured fields and fluxes are fairly well reconstructed by including the eddy current.

The fitted total eddy current is compared with the measured eddy current in Fig. 4(a). The fitted eddy current agrees well with the measured current with about 10% error. Figure 4(b) shows the difference between fitted and measured currents as a function of the time derivative of the measured eddy current. The difference correlates to the inductive voltage which is the origin of eddy current. This suggests that there are other eddy current loops

outside the vessel because the fitting code regards eddy currents outside the vessel as part of the vessel eddy current.
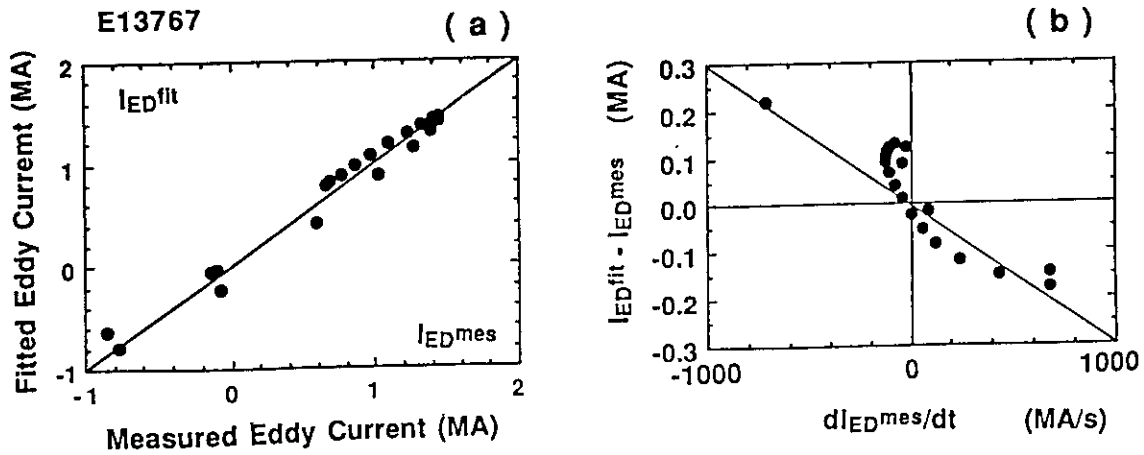
Fig. 4 (a) Fitted total eddy current against measured eddy current

(b) The difference between measured and fitted eddy current against time derivative of eddy current

3. Discussion and summary

A magnetic fitting code including vessel eddy currents is useful to estimate the toroidally symmetric eddy current profile in the vacuum vessel. The measured magnetic data were fairly well reconstructed by including vessel eddy currents and the fitted total eddy current agreed well with the measured current. The code can be also applied for misfired shots (no plasma current). In Sec. 7.2 , the eddy current profile in major disruption will be analyzed with this code.

The eddy current outside the vessel should be identified to estimate eddy current in the vessel more precisely[1]. For this improvement, the code requires more information about magnetic data far from the vessel. Several flux loops outside the torus are enough for this requirement. The location of these eddy current loops should be identified by applying the code to the power test for each poloidal coil. Only toroidally symmetric eddy current was assumed in the present work. Several sets of magnetic probes at different toroidal locations are required to include toroidally asymmetric eddy current.

References

[1] Yoshino, R., et al., Sec. 2.5 in this review paper

[2] Abe,M., Takeuchi, K., Fukumoto, H., et al., Jap. J. of Appl. Phys. 29(1990)395.

2.5 Eddy Currents and Their Effect on the Breakdown

R.Yoshino, U.Neyatani, K.Ushigusa, M.Matsukawa, M.Takahasi

1.Introduction

There are still many unresolved issues on the plasma initiation as follows, 1)which decides a time delay of the plasma initiation just after the rise of the one-turn voltage, 2)which decides the location of the initiation point of a plasma, 3)the process between the plasma initiation and the creation of the normal plasma with the Shafranov equilibrium, and the model of the required vertical magnetic field during this transition, 4)the minimum breakdown voltage and the minimum plasma current ramp up rate just after the plasma initiation, and which decides these operational limits.

In this paper, 1)toroidal eddy currents, that flow in the vacuum vessel and in the external of it, are investigated, 2)a standard scenario of the plasma initiation in JT-60U is presented, and 3)a magnetic field pattern just before the breakdown is analyzed including the eddy current effect.

2.One-turn Resistivity and Eddy Current Loops

Designed value of the one-turn resistivity of the vacuum vessel of JT-60U is 200$\mu\Omega$. However a measurement of that is essential to establish a model of toroidal eddy currents in the vacuum vessel. Then excitation tests of ohmic heating coil (F-coil) is executed. The leak of F-coil's magnetic flux into the vacuum vessel is negligibly small, so that the voltages of 15 channel flux loops are same at the flattop. Here flux loops are installed at the inside of vacuum vessel as shown in Fig.1. Total eddy current in the vacuum vessel is measured by a pair of Rogowski probes settled inside and outside of the vacuum vessel. Thus one-turn resistivity of 160$\mu\Omega$ is obtained from the loop voltage and the total eddy current as shown in Fig.2, that is 80% of the designed value. The one-turn voltage is measured at the inside surface of vacuum vessel, so that the measured voltage must be corrected by the width of vacuum vessel of 4cm. However this correction increases the one-turn resistivity only 1~2%.

To investigate the time delay in the rise of the one-turn loop voltages of the flux loops, excitation test of the vertical magnetic field coil is executed. Then it becomes clear that extra-eddy current loops with time constant of ~100ms is required at the external of the vacuum vessel as shown in Fig.3, to reconstruct the experimental results of the one-turn voltages. Here three sets of dipole eddy current loops are assumed near the center pole and top and bottom of vacuum vessel. Figure 4 shows the comparison of the experimental results and simulated ones, that are presented by solid lines and dotted lines. Good agreement is obtained between them. Eighteen toroidal coils may be possible candidates of

the extra-eddy current loops with making saddle type shells.

3.Plasma Initiation Scenario

A typical time evolution of the plasma initiation and the plasma current ramp up is shown in Fig.5. Poloidal magnetic field coil system of JT-60U consists of four types of coils such as F-coil, vertical magnetic field coil (V-coil), horizontal magnetic field coil (H-coil), and divertor coil (D-coil). The excitation levels of H-coil and D-coil just before the breakdown are negligibly small. However F-coil current is excited largely, that can be raised up to 110kA, and an excitation level of V-coil current is ~500A. One-turn voltage is raised by the preset program control of thyristor voltages of F-coil and V-coil. The maximum voltage of F-coil is 2.5kV, and that of V-coil is 5.0kV. Here an additional rise in the voltage of V-coil with the same voltage of F-coil is required to compensate the inductive coupling with F-coil. Feedback controls of the plasma current, the horizontal plasma position, and the vertical plasma position are started from 100 ms, 80 ms and 60 ms respectively.

A time evolution of the one-turn voltage is shown in Fig.6. The plasma density rises at t=10ms with the one-turn voltage of 15V, that is measured by #8 one-turn loop settled at the inboard side of the vacuum vessel. Then the plasma current rises at t=12ms. JT-60U has no quadruple magnetic field coil, so that the control of n-index as demonstrated in JT-60 is impossible. Thus high negative n-index field of V-coil, that is -0.8 with high elongation connection and -0.5 with standard connection, determines the n-index of the total poloidal coil system.

The plasma current rises at 10~40ms, and clouds of plasmas are observed by a fast TV camera at 2~3 ms before the rise of the plasma current. Then the magnetic field at t=7ms is investigated. A simulation study is performed with an assumption of three sets of dipole eddy current loops at the external of vacuum vessel as shown in Fig.3. Eddy currents in vacuum vessel is assumed by 100 filaments. With these assumptions, a miss-fired shot caused by an insufficient prefilling gas is reconstructed. Then a reasonable agreement is obtained between the experimental results (flux loop voltages, coil currents, and a total eddy current in the vacuum vessel) and the simulated ones. The investigated magnetic field is shown in Fig.7. A point of minimal field ~50 Gauss locates at the inboard-up of a chamber, that agrees well with the TV observations. These results suggests that the plasma is initiated from the minimal error field point. Further studies on the delayed plasma initiation will make clear of it.

4.Discussions

In the plasma initiation, a plasma attaches to the inboard-up of the first wall with an indistinct boundary is observed by the TV measurement. Then a plasma expands to a circle

core plasma with the Shafranov equilibrium. Study on this transition phase will make clear the required vertical magnetic field. In the case of detached plasmas observed just after the plasma initiation, an expansion is not observed, but a small core plasma seems to be born within a clouds of an initial plasma with an undistinguished boundary. High prefilling gas or high retention of the first wall with hydrogenic gas cause this phenomena with the long time delay of the plasma initiation. Power balance between the joule heating and the radiation loss may decide the detachment or the attachment just after the plasma initiation.

5.Conclusions

A one-turn resistivity of the vacuum vessel is measured to be 160μΩ, that is 80% of the design value. The investigation of the flux loop in the excitation test of the vertical magnetic field coil suggests the existence of the extra-eddy current loops in addition to the vacuum vessel. That can be simulated by three sets of dipole loops near the center pole and top and bottom of vacuum vessel. Saddle type shells produced by 18 toroidal coils are possible candidates.

Plasma initiation of JT-60U is estimated by magnetic probes, Rogowski probes, flux loop, and fast TV camera. Plasma seems to be generated from the minimal error field point with loop voltage of ~15V at the inboard-up of the chamber. Artificial extra-eddy current loops act the essential role to produce this minimal field point. The relation between the location of the minimal field and the plasma initiation point will be studied more systematically.
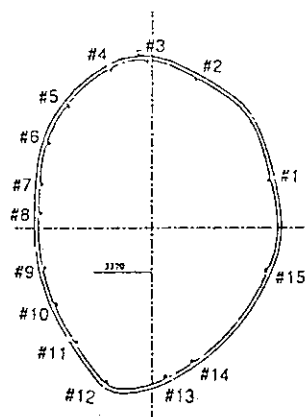
Fig.1   Flux loop channels
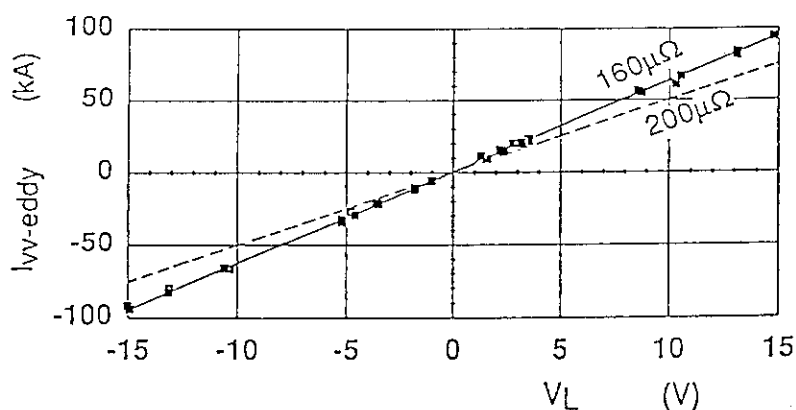
Fig.2   One-turn resistivity of the vacuum vessel.
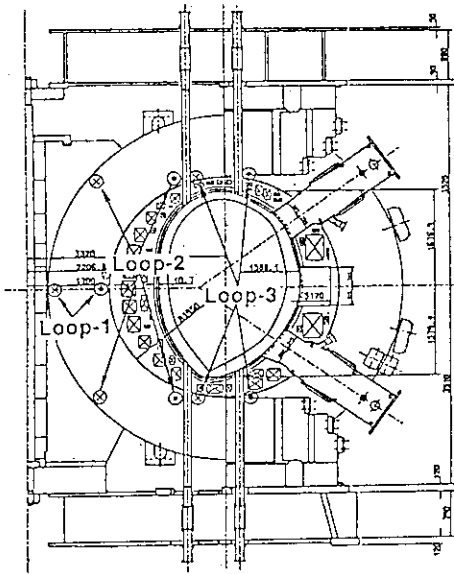
Fig.3 Extra-eddy current loops at the external of the vacuum vessel.
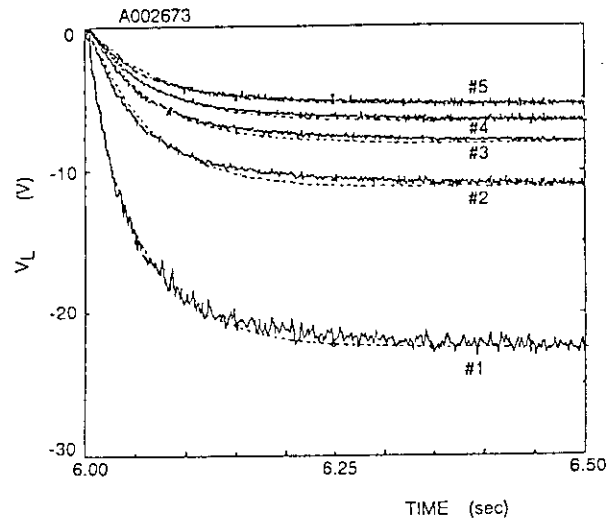
Fig.4 One-turn voltages of the flux loops in the excitation of the vertical magnetic field coil with -40kA/s.
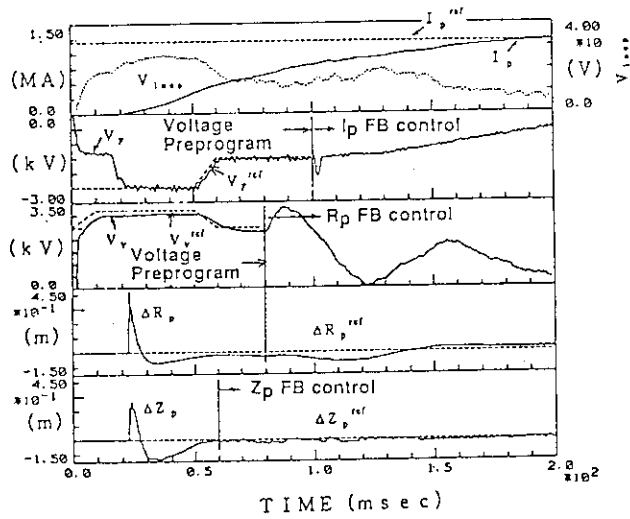
Fig.5 A typical case of the plasma initiation and the plasma current ramp up at t=0~200 ms.
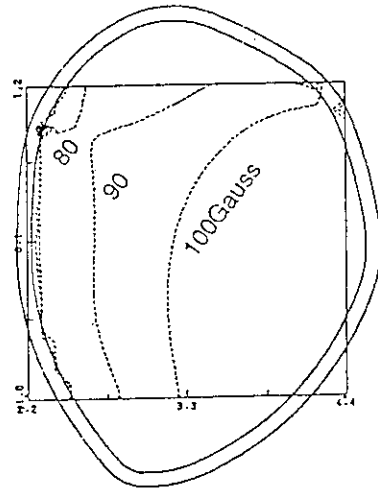
Fig.7 A magnetic field pattern at 7ms just before the breakdown.
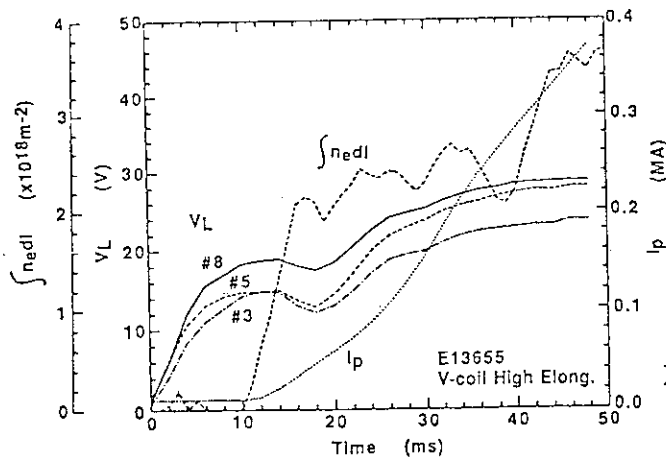
Fig.6 Time evolution of the one-turn voltages in the plasma initiation.

2.6 Plasma Current Ramp Up
with "Growing Plasma Method" on JT-60U

Ryuji Yoshino

1.Introduction

This paper presents the experimental results of the "growing plasma method", that has been newly developed in JT-60U to solve the following requirements on the plasma current ramp up. 1)Fast current ramp-up speed of >1MA/s is necessary to get a 6MA plasma with 5 s flattop, that is planned in the next experiment period, owing to the limit in a discharge duration of 15 s. 2)Locked mode disruptions occur at $dIp/dt>0.75MA/s$ in the usual current ramp up method with the constant plasma minor radius. Thus the avoidance of the mode locking is required by some modifications in the plasma current ramp up method. NBI heating is useful for this purpose[1], but raises the plasma density and limits the flexibility of the plasma operation. 3)High l_i with low plasma density of $\sim 0.5 \times 10^{19} m^{-3}$ is required at $I_p=1.5\sim2.5MA$ in LHCD experiments to get the sawtooth stabilization with the full current drive.

2. 5MA with Growing Plasma Method

A time evolution of a 5MA discharge obtained by the growing plasma method with dI_p/dt of 0.71MA/s is shown in Fig.1. Here a plasma grows up from a small diameter limiter plasma, that attaches to the inboard first wall, to a large diameter divertor plasma as is shown in Fig.2. A characteristic of the growing plasma method is the reduction in q_{eff} below 4 at the very early phase (t=0.25s) just after the plasma initiation with small plasma volume of $20m^3$ as shown in Fig.3. During the plasma current ramp-up, q_{eff} is controlled to be <4 by the increase in the plasma volume from $20m^3$ to $100m^3$, except the transition phase (t=1~2 s) from the limiter to the divertor configuration. Toroidal magnetic field is almost constant. Voltsecond is supplied by the ohmic heating coil and the vertical magnetic field coil. Their limits are 40.6Vs and 17.9Vs respectively. 40 volt second is already consumed to reach a 5MA plasma as shown in Fig.4. An extrapolation to 6MA suggests a spare of ~5Vs still exists at a 6MA plasma. However a flattop of the plasma current will be limited below 3 s by the maximum discharge duration of 15 s, if the normal plasma current ramp down rate of <-1.0MA/s is used. Thus a ramp up rate of >1MA/s is required to get a 6MA plasma with a 5 s flattop.

3. Stabilization of Locked Mode Disruptions

Locked mode disruptions are frequently observed in the plasma current ramp up. The operational region of the occurrence of locked mode disruptions is limited on an X_p

versus I_d/I_p diagram as $X_p<0.75*(I_d/I_p)*10^3-7.5$(cm) at $q_{eff}=3\sim4$ [2]. On the other hand plasmas ramped up by the growing plasma method are stable in this region. A time trace of a typical shot with dI_p/dt of 0.71MA/s is presented on the X_p versus I_d/I_p diagram as shown in Fig.5. Here a plasma deeply enters the unstable region for locked mode disruptions. The cause of this stabilization is not clear yet. One possible reason is relatively higher l_i explained in the next section, that is stable to the kink type instability. Another possibility is the faster toroidal plasma rotation speed owing to a smaller diameter.

4. Fast Current Ramp Up

The plasma current ramp up rate has been raised upto 2.0MA/s at Ip=0.7~3.5MA with the usage of the growing plasma method as shown in Fig.1. Minor disruptions caused by the mode locking in the divertor plasma phase, but they have not terminated a discharge. The decrease in l_i is small with the increase in the plasma current ramp up speed up to 2MA/s as shown in Fig.6(a). However the plasma minor radius a_p is small in the growing plasma method as shown in Fig.6(b). Then $l_i*a_p^2$ decreases with the increase in the plasma current ramp up rate as shown in Fig.6(c).

The possibility of the mode locking increases with the decrease in l_i, in the same unstable region on the X_p versus I_d/I_p diagram. Thus the increase in l_i is required to get more stable plasma current ramp up. For this purpose, the plasma diameter or q_{eff} should be decreased during the plasma current ramp up as shown in Fig.7. Here l_i of 1.45 s increases from 0.55 to 0.9 with the decrease in q_{eff} from 7.0~10.0 to 3.5 at dI_p/dt =0.75MA/s. These results shows that l_i can be controlled by the plasma current ramp up rate and the choice of q_{eff}.

Higher rate of >2MA/s has not been tried yet, but will be tried in the next experimental period from the following reasons. 1)Plasma current ramp up with small a_p and $q_{eff}<3$ will keep l_i of >0.65 and raise the limit on the plasma current ramp up speed as shown in Fig.6. Here the plasma current ramp up with q_{eff} of 2.5 has been obtained without large MHD instabilities. 2)Plasma operation with lower I_d/I_p will avoid the occurrence of mode locking and will expand the limit on dI_p/dt.

5. Discussions

In the growing plasma method, the heat flux onto the first wall is relatively high owing to the large input of the joule heating power with high one-turn voltage. However the impurity contamination is almost the same with plasmas ramped up by the normal plasma current ramp up. Plasma energy confinement is improved with the increase in l_i[3], that suggests the importance in the optimization to get high l_i plasmas from the start of a discharge. Here the growing plasma method is the useful method for this operation.

6. Conclusions

Plasma current ramp-up rate is raised upto 2MA/s at I_p=0.7~3.5MA by newly developed "growing plasma method". Effective safety factor q_{eff} is reduced below 4.0 with small minor radius at t=0.25s just after the plasma initiation. Reduction in the resistive voltsecond consumption is small owing to the high one-turn voltage. However the stability of plasma current ramp-up is raised dramatically with no major disruptions during current ramp up. Plasma internal inductance l_i can be controlled by the choice of plasma current ramp up speed and q_{eff}. Here q_{eff} can be modified by the plasma minor radius. Impurity contamination is same with that of normal current ramp up method, in spite of the higher heat flux onto the first wall.

References

[1]H.Ninomiya, et al., Nuclear Fusion 28 (1988) 1275.

[2]R.Yoshino, section 2.11 in this review paper .

[3]M.C.Zarnstorff, et al., Plasma Physics and Controlled Nuclear Fusion Research 1990 (Proc. 13th Int. Conf.,Washington D.C.,1990) 1,101
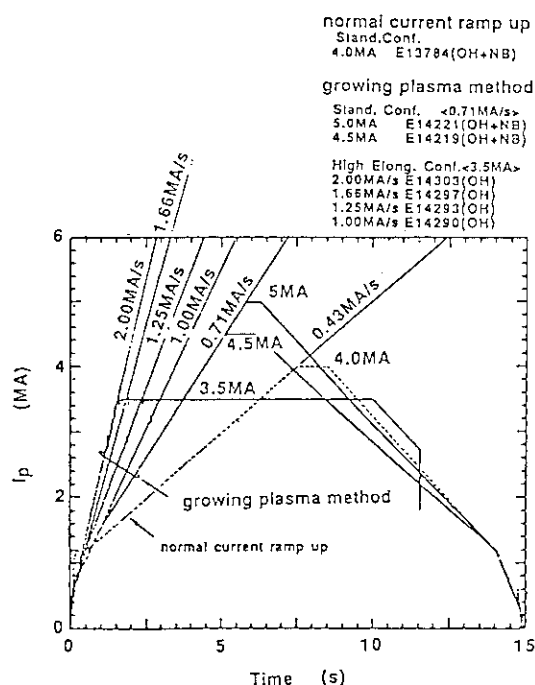
Fig.1 Discharges with the growing plasma method.

No	Time(s)	I_p(MA)	V_p(m³)	q_{eff}
1	0.25	0.79	20.0	4.1
2	0.60	1.15	27.1	3.7
3	1.00	1.53	38.2	3.5
4	1.50	1.89	51.5	4.5
5	2.00	2.25	59.6	4.0
6	3.00	2.97	77.6	3.5
7	4.00	3.69	90.3	3.0
8	5.00	4.39	94.1	2.7
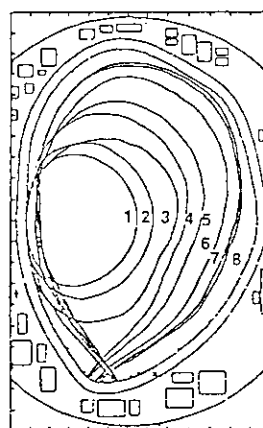
Fig.2 An evolution of the plasma configuration in a 5MA discharge presented in Fig.1.

Fig.4 Supply of the voltsecond in a 5MA discharge.
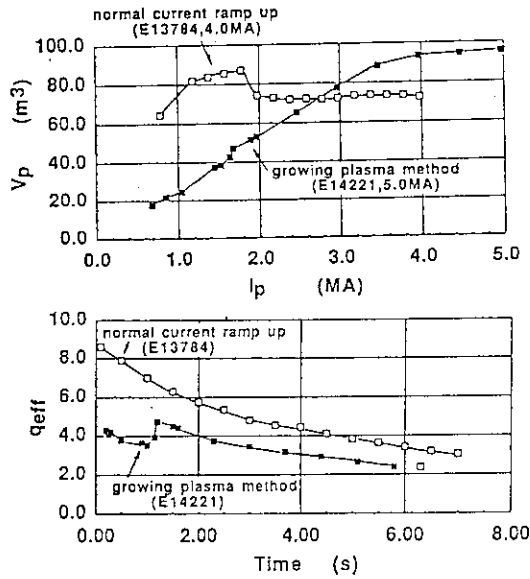
Fig.3 (a)plasma volume and (b)q_{eff} in a 5MA discharge ramped up by the growing plasma method.
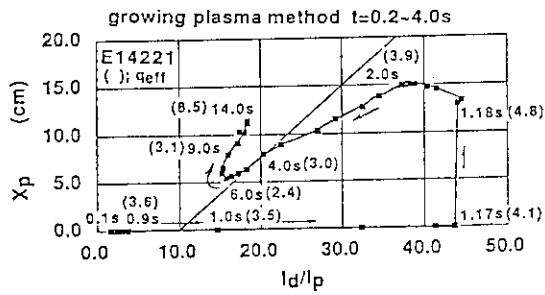
Fig.5 A trace of a dischage ramped up by the growing plasma method on a X_p versus I_d/I_p diagram.
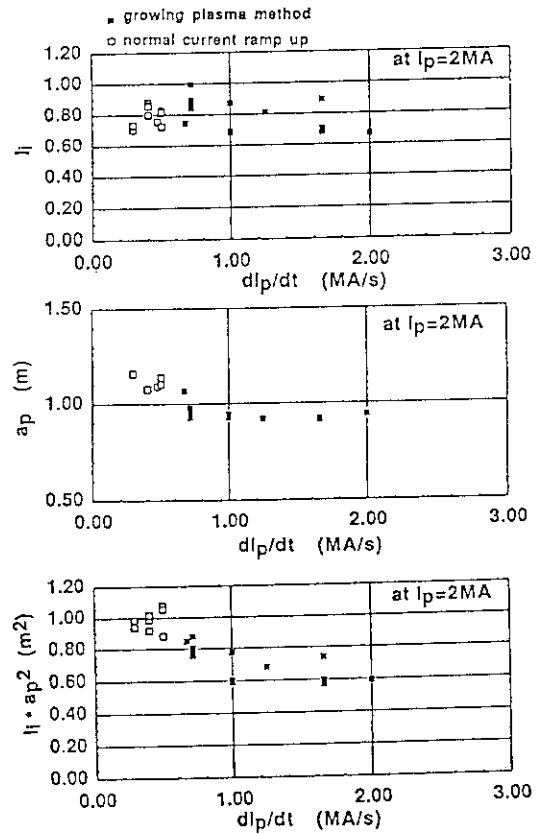
Fig.6 (a)l_i, (b)a_p and (b)$l_i*a_p^2$ in the scan of the plasma current ramp up rate.

Fig.7 Time evolution of l_i in the scan of q_{eff} with the plasma current ramp up rate of 0.75MA/s.

2.7 Multivariable Noninteracting Method in the Plasma Configuration Control

Ryuji Yoshino

1. Introduction

The control of the plasma configuration is indispensable to get the required plasma performances, such as the divertor effect, the minimization of the plasma wall interaction, and the confinement mode of the H-mode and L-mode[1]. From a view point to design a feedback control system of reactor grade plasmas, general control methods are desirable. Multivariable noninteracting control method is one of them, that was proposed for the swing of separatrix lines on the divertor plate with keeping the main plasma configuration in JT-60's outside null point divertor plasmas according to the simulational study[2]. Furthermore this control method was applied to ITER for the estimation of the required power supply voltages of poloidal magnetic field coils[3]. Then this control method has been demonstrated in the experiments on JT-60U as presented in this paper.

2. Noninteracting Control Method

The derivation of the matrix gain G of the plasma current and the plasma shape is presented in the reference [3] as,

$$RG=(MA+M_p)2\pi f \tag{1}$$

with

$$M_p = (\partial M_{pc}/\partial x, \ M_{pc}) \tag{2}$$
$$A = (A_x, A_p{}^V) \tag{3}$$
$$f = (f_x, \ f_p) \tag{4}$$

Where M_{pc} is a vector of the mutual inductance between the plasma current and PF coil currents, R is a diagonal matrix of the resistivity of PF coils, x is the control variables of the plasma shape. A_x presents the relation between the displacements of the control variables dx from the equilibrium state and that of PF coil currents dI as $dI=A_xI_pdx$. A_p presents the same relation between the plasma current dI_p and that of PF coil currents as $dI=A_pdI_p$. A diagonal matrix of f_x is the characteristic frequency of control variables, and f_p is the the control frequency of the plasma current.

The effect of eddy currents, that flow in the machine components such as the vacuum vessel, is not included explicitly in the above equation of a matrix gain, because the feedback control frequency of the plasma configuration is usually selected to be lower than the characteristic frequency of eddy currents. If it is selected to be too high, it becomes unstable owing to the time delay caused by the shielding effect of eddy currents. Thus the

optimum frequency of f, should be investigated by a simulation code, that includes the effect of eddy currents.

3. Feedback Control System of JT-60U

Four control variables of the plasma current (I_p), the vertical and the horizontal plasma position(R_p, Z_p), and the height of a null point from the divertor plate (X_p) are selected in JT-60U as shown in Fig.1. In JT-60U hybrid poloidal coil system consists of the primely coil (F-coil), the vertical magnetic field coil (V-coil), the horizontal magnetic field coil (H-coil), and the divertor coil (D-coil). Here the mutual inductance between F-coil and V-coil is very large, and is almost same with the self inductance of F-coil. Thus the control of I_p and R_p have the strong interaction between them. There also exists a large interaction between the control of Z_p and X_p.

Control system of the JT-60U plasma configuration is designed as presented in Fig.2. Control system consists of a plasma feedback computer made by 32-bit VME-based multiprocessor system with a sampling period of 250 μs and the DDC-controller of each coil power supply. The matrix of proportional gain, that is installed in a plasma feedback computer is simplified as presented in Fig.3 to shorten the calculation time and to avoid the complex in the decision of gain elements. Thus the plasma current I_p and the vertical and plasma position R_p are controlled by F- and V-coils. The horizontal plasma position Z_j and the height of a null point X_p are controlled by H- and D-coils. The differential gain, that is necessary to compensate the system time delay, is applied by a diagonal matrix.

4. Matrix Gain of JT-60U

The relation between the control variables and the poloidal magnetic field coil currents, that is presented by a matrix A, is essential to obtain a matrix gain, and is estimated for JT-60U plasmas from the following basic equations. 1)Ip; circuit equation of the plasma current, 2)Rp; Shafranov equilibrium equation, 3)Zp; force balance to the vertical plasma direction, and 4)X_p; a state equation derived from the large database[4] of the predicted equilibriums as, X_p=-2.9378(I_F/I_p)-17.7219(I_H/I_p)+10.8419(I_D/I_p)-0.10613 (m) in the standard V-coil connection.

Z_p can be presented by Z_p=-6.43145(I_H/I_p)+17.0511(I_D/I_p)-0.1159 (m) using the same derivation of X_p. Thus the X_p and Z_p is linearly independent, so that the noninteracting control of X_p and Z_p is possible. Then matrix gain can be calculated using the equation (1).

5. Decoupling of I_p and R_p

A matrix gain is tested in a simulation code, that assumes a plasma current by one filament at the plasma current center and simulates the eddy current in vacuum vessel with

100 filaments. This simulation code is enough to predict the control performance of I_p, R_p, and Z_p. However it is hard to estimate the controllability of X_p. Thus as the first step the noninteracting control between I_p and R_p has been studied.

The comparison of the independent control and noninteracting control has been executed in a divertor plasma using a swing of R_p with ±2cm and 10Hz as shown Fig.4. The large interaction with I_p control, that occurs inevitably in the independent control, can be suppressed about 5% by the noninteracting control. This result suggests that the noniteracting control method is very powerful method to minimize the interaction between I_p and R_p. The noninteracting control of Z_p and X_p will be tried in the next experimental period.

6. Conclusions

Multivariable noninteracting control method is examined in the control of JT-60U plasma configuration with a single null point divertor. The plasma current I_p and the vertical and plasma position R_p are controlled by F- and V-coils. The horizontal plasma position Z_j and the height of a null point X_p are controlled by H- and D-coils. Large interaction between I_p and R_p is dramatically decreased by the noninteracting control method. The application to Z_p and X_p will be tried in the next experiments period.

Multivariable noninteracting control methods is general, thus it will be applicable to each tokamak machine and especially to the next generation machine like ITER.

References

[1]R.Yoshino, et al., section **2.11** in this
   review paper.
[2]R.Yoshino, et al., "Control of Divertor
   Configuration in JT-60", Proc. 13th
   Symp. on Fusion Technology, Vol.1,
   (1984) 483
[3]R.Yoshino, et al., "Control of the Plasma
   Configuration in ITER" JAERI-M (1991)
[4]M.Matsukawa, et al., section **2.3** in this
   review paper.
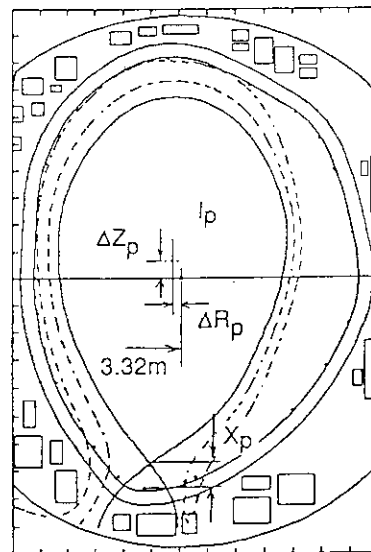
Fig.1　Control variables in the lower X-point divertor plasma.
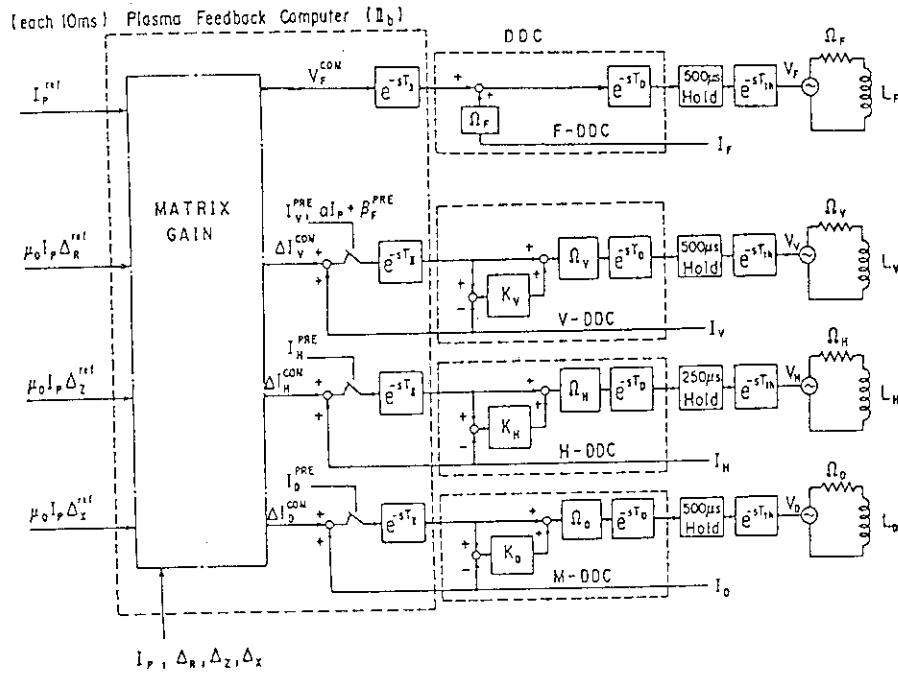
Fig.2　Feedback control system of the plasma configuration.

$$\begin{pmatrix} \delta V_F{}^{com} \\ \delta I_V{}^{com} \\ \delta I_H{}^{com} \\ \delta I_D{}^{com} \end{pmatrix} = \left(\begin{array}{cc|cc} * & * & \multicolumn{2}{c}{} \\ * & * & \multicolumn{2}{c}{0} \\ \hline \multicolumn{2}{c|}{} & * & * \\ \multicolumn{2}{c|}{0} & * & * \end{array} \right) \cdot \begin{pmatrix} \delta I_p \\ \mu_0 I_p \delta R_p \\ \mu_0 I_p \delta Z_p \\ \mu_0 I_p \delta X_p \end{pmatrix}$$

Fig.3
Matrix of the proportional gain in the control of the plasma configuration.
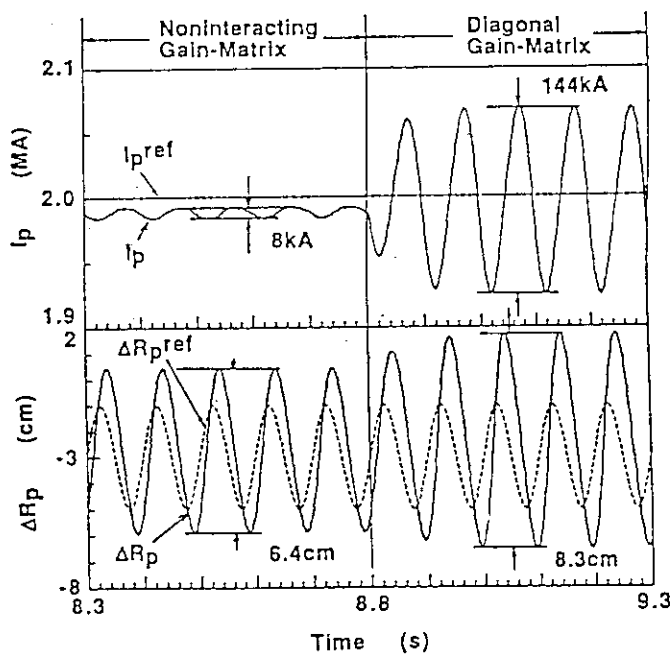
Fig.4
Swing of R_p with ±2cm and 10Hz. The noniteracting control method is compared with the usual independent control method. $R_p{}^{ref}$ is the reference vale of R_p. Refernce of Ip ($I_p{}^{ref}$) is kept 2.MA.

2.8　Vertical Stability Control Experiments

D. A. Humphreys and R. Yoshino

Introduction　The intrinsically destabilizing decay index required to create vertically elongated JT-60U plasmas ($\kappa \gtrsim 1.6$) results in a need for active control of the vertical position [1]. During initial operation of the machine from March to October of 1991, a range of experiments were conducted to investigate the vertical stability of JT-60U equilibria and assess the accuracy of existing simulation models. We describe two types of experiments: those for which vertical position feedback gain was set to zero over a fixed interval during a shot, and those in which β_p rose over the course of a shot due to applied NBI heating, resulting in onset of vertical instability.

Vertical motion of the plasma during these experiments was simulated with a rigid plasma model coupled to a discrete conductor array representing the vacuum vessel and poloidal field coil set. Both experimental and simulation results are presented.

Plasma-Conductor System Model　To simulate plasma vertical motion, we model the plasma as a rigid assembly of axisymmetric current-carrying filaments, free to move only in the vertical direction [2]. The total current is held fixed during plasma motion, an approximation which has been shown to be closer to the energy minimizing plasma mode than a flux conserving rigid vertical motion [3].

The conductor voltage equation appears as

$$\mathbf{M}\dot{\vec{I}} + \mathbf{R}\vec{I} + \left[\frac{\partial \vec{\psi}(p)}{\partial z}\frac{\partial z}{\partial \vec{I}}\right]\dot{\vec{I}} = \vec{V}.$$

where $\mathbf{M}$ and $\mathbf{R}$ are the conductor mutual inductance and resistance matrices, $\vec{V}$ is the applied voltage vector, and the third term represents plasma-conductor coupling and the effect of destabilizing decay index. The decay index effect is calculated from the massless plasma vertical force balance equation, thus assuming the plasma to be in quasiequilibrium at all times.

The dominant up-down antisymmetric mode of the vacuum vessel model alone has a decay time of about 10 ms, while that of the vessel and PF coils together has a decay time of about 1 sec.

Control Algorithm　Vertical stability control is provided by driving the horizontal field coil (H-coil) alone with a feedback relation which determines voltage demand as a function of estimated plasma vertical position. Proportional and derivative (velocity) feedback is provided. The overall feedback loop calculation and power supply delay has been estimated to be nominally about 2 ms. In addition, H-coil current feedback is applied, artificially reducing the effective resistance of H-coil to a negative value.

Using a single-pole model of the power supply delay [2], the feedback transfer function describing voltage applied to H-coil is given by

$$V_H(s) = R_H^{prog} I_H(s) - \frac{G_p(1 + \tau_d s)}{(1 + \tau_{ps} s)} z_{pred}(s)$$

where the predicted vertical position, z_{pred}, is a function of magnetic signals, and can therefore be expressed as a function of conductor currents, $\vec{I}$. G_p is the proportional gain, τ_d is the derivative gain time constant, and τ_{ps} is the power supply delay time, taken to be 2 ms. R_H^{prog} represents the programmed H-coil resistance reduction factor.

Feedback Turnoff Experiments A series of experiments were performed in which the proportional gain, G_p, was set to zero, removing all vertical position feedback for intervals of 300 ms or 600 ms. However, the value of R_H^{prog} was held fixed. During these periods the plasma moved monotonically away from the original equilibrium vertical position until control was restored. Examples of this motion are shown in Figs. 1 and 2, illustrating a typical 300 ms and 600 ms gain turnoff interval respectively. These figures show vertical position measured by magnetic signals, and compare the experimental data to simulations of the turnoff intervals using the rigid plasma model. The simulation reproduces the experimental motion within an uncertainty of a few millimeters, comparable to the accuracy of the position measurement itself.

Because there is no integral term ($\propto \int z \mathrm{dt}$) in the feedback law, a non-zero steady state voltage is applied to H-coil by the control system, resulting in the plasma being driven to a new equilibrium when G_p is zeroed. This process is stable for sufficiently low decay index due to the stabilizing effect of R_H^{prog}, as can be seen in the longer interval case of Fig. 2.

High β_p Unstable Plasmas During the course of several neutral beam-heated shots, β_p became sufficiently high that the preset control gains could not stabilize the plasma. These cases provided an opportunity to compare simulation predictions with actual unstable plasma behavior. Results of two shots with particularly clear underdamped vertical instability growth are shown in Figs. 3 and 4. Fig. 3 shows vertical position, simulation-predicted growth rates, and β_p evolution as a function of time. The actual maximum growth rate was found to be $\gamma_{exp} \simeq 8 \pm 130i$, and the predicted value was calculated to be $\gamma_{sim} \simeq 7 \pm 290i$. The plasma was lost at the end of the time interval shown. Experimental onset of instability and real growth rate coincide well with the predicted values. The discrepancy in the imaginary part is attributable to the single pole power supply model.

Fig. 4 shows vertical position and β_p as a function of time for a case in which β_p decreased before the plasma was lost, allowing control to be reestablished. The figure shows the onset of instability and restoration of control coinciding with the same approximate value of β_p. The actual maximum growth rate was found to be $\gamma_{exp} \simeq 15 \pm 190i$, and the predicted value was calculated to be $\gamma_{sim} \simeq 14 \pm 530i$. Again, the experimental real growth rate coincides well with the predicted value.

Summary Within expected uncertainty, to date the rigid plasma model has been able to reproduce typical JT-60U plasma behavior fairly well, and has proven sufficient to design control laws to stabilize elongations of $\kappa \gtrsim 1.6$ with $\beta_p \gtrsim 1.8$.

References

[1] Wesson, J. A., Nucl. Fus. **18** (1978), 87

[2] Humphreys, D. A., Hutchinson, I. H., Filament-Circuit Model Analysis of Alcator C-MOD Vertical Stability, PFC Rept. PFC/JA-89-28, Mass. Inst. of Tech., Cambridge, (1989)

[3] Hutchinson, I. H., Nucl. Fus. **29** (1989), 2107
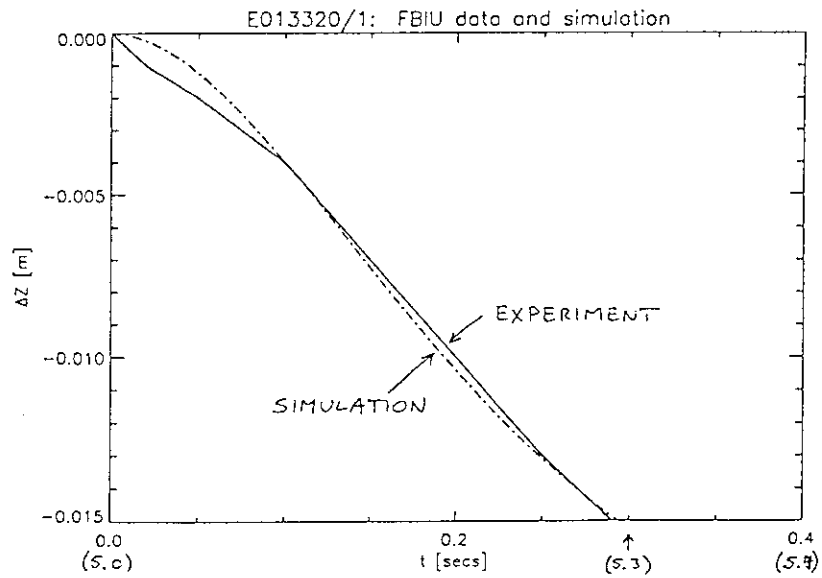
Figure 1: Feedback turnoff experiment of 300 ms duration.
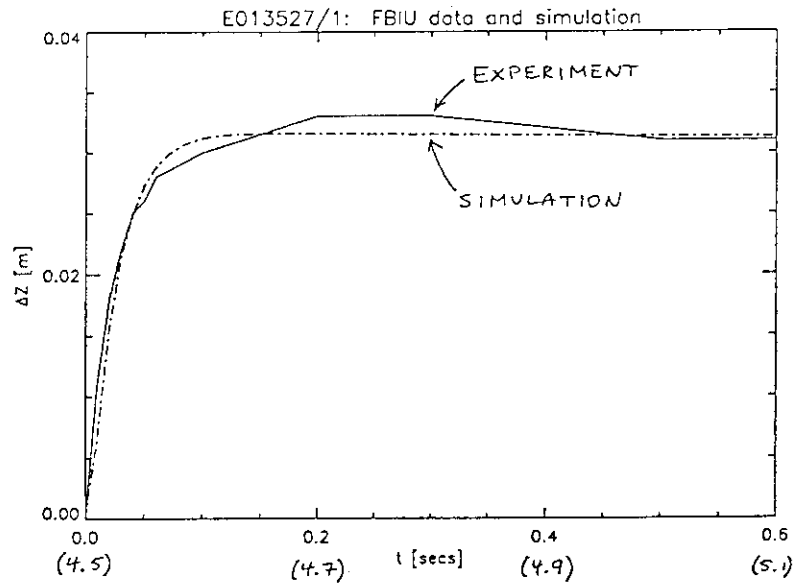
Figure 2: Feedback turnoff experiment of 600 ms duration.
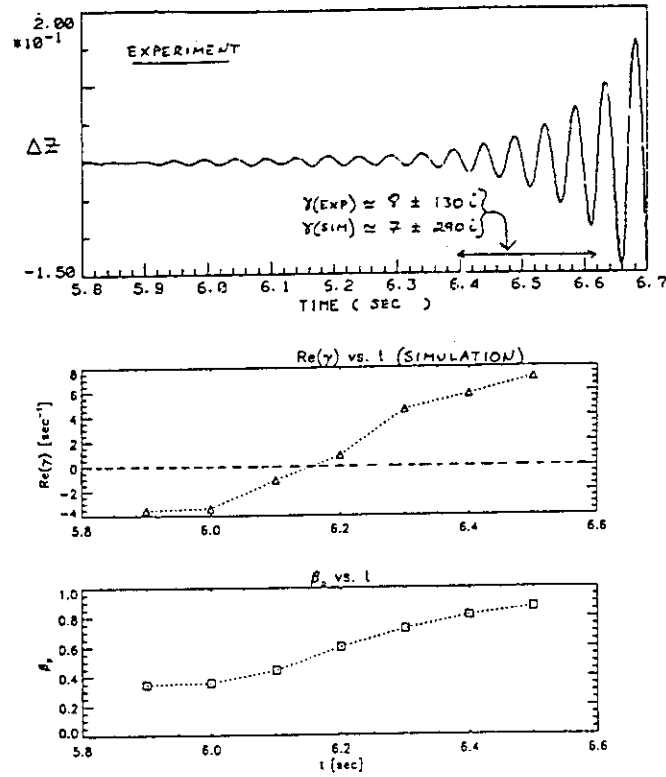
Figure 3: NBI heated high β_p case 1: (a) vertical position, (b) simulation calculated growth rate, (c) β_p evolution.
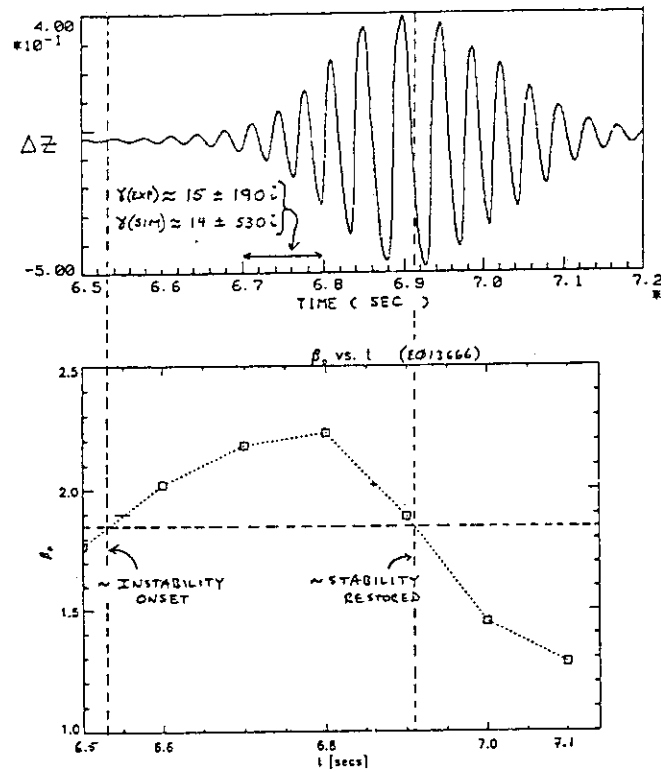
Figure 4: NBI heated high β_p case 2: (a) vertical position, (b) β_p evolution.

2.9 Vertical Stability Boundaries

D. A. Humphreys and R. Yoshino

Introduction Analysis of expected vertical stability limits for JT-60U has been carried out using the simple rigid plasma model and conductor array described in Section 2.1.8. Both a single filament and uniform current distribution multifilament plasma model are used along with the full conductor array to calculate critical decay indices for ideal MHD stability limits. The gain space is then searched to determine the maximum stabilizable value of the Shafranov $\Lambda \equiv \beta_p + l_i/2$.

Critical Decay Index For the purpose of this analysis, we write the stabilizing conductor array circuit equation including plasma coupling and destabilizing decay index, n, as

$$\mathbf{M}\dot{\vec{I}} + \mathbf{R}\vec{I} + \frac{2R_0}{\mu_0 \Gamma n}\vec{M}'_{vp}\vec{M}'_{pv}\vec{I} = \vec{V}, \tag{1}$$

assuming a massless (quasiequilibrium) plasma [1] (see also Section 2.1.8). Here $\vec{M}'_{vp}$ and $\vec{M}'_{pv}$ are the mutual inductance gradient vector (from conductor array to plasma) and its transpose respectively, and $\Gamma \equiv ln|\frac{8R_0}{a}| + \Lambda - 1.5$ is the Shafranov vertical field coefficient.

The critical decay index, n_c, describes the field curvature beyond which a plasma becomes vertically unstable on the ideal MHD timescale [2], corresponding to infinite growth rate for a massless plasma. Allowing $\gamma \to \infty$ as $n \to n_c$ in Eq. 1, it can be easily shown that for an array of stabilizing conducting elements, n_c is given by

$$n_c = -\frac{2R_0}{\mu_0 \Gamma}Tr(\mathbf{M}^{-1}\vec{M}'_{vp}\vec{M}'_{pv}), \tag{2}$$

where Tr indicates the matrix trace.

Fig. 1 shows critical decay index magnitude for both single filament (SF) and multifilament (MF) plasma models plotted as a function of Λ. Also shown (triangles) are experimental decay index magnitudes and Λ values achieved in JT-60U to date for $\kappa \simeq 1.6$ equilibria. The maximum n/n_c achieved corresponds to $n \sim 88\%$ of the multifilament critical index or 80% of the single filament critical index, at $\Lambda \simeq 2.7$. Extrapolating this data for $n = -1.6$, corresponding to elongation $\kappa \simeq 1.6$, $\Lambda \sim 3.5$ appears to be the theoretical upper limit achievable in JT-60U (corresponding to the single filament, or most favorable, model). Passive growth rate and active control calculations are necessary to determine a more realistic limit.

Passive and Active Calculations Single filament passive and active responses for fixed decay index are now examined to determine a more realistic upper limit to achievable Λ. Fig. 2 shows calculated single filament model passive growth rates for $n = -1.6$ as a function of Λ. Since the nominal feedback loop plus power supply delay time is about 2 ms, the $\gamma \simeq 500$ sec^{-1} crossover point provides an approximate measure of the controllability limit [2], and predicts $\Lambda_{max} \simeq 3.0$.

Figs. 3 and 4 show active stability boundaries calculated in $G_p - \tau_d$ space using the single pole, PD power supply model described in Section 2.1.8. Fig. 3, corresponding to $\Lambda = 3.0$, reveals a broad stable region, while Fig. 4 shows that $\Lambda = 3.1$ cannot be stabilized for any combination of values of G_p and τ_d.

Summary Critical decay indices and both passive and active growth rates have been calculated for high elongation JT-60U plasmas in order to determine stability and control boundaries for achieving maximum values of Shafranov Λ. This analysis indicates that $\Lambda \simeq 3.0$ represents an approximate upper bound to achievable Λ (within the limits of the simple rigid model and the accuracy of the conductor array model).

References

[1] Lazarus, E. A., Lister, J. B., et al, Nucl. Fus. **30** (1990), 1107

[2] Humphreys, D. A., Hutchinson, I. H., Filament-Circuit Model Analysis of Alcator C-MOD Vertical Stability, PFC Rept. PFC/JA-89-28, Mass. Inst. of Tech., Cambridge, (1989)
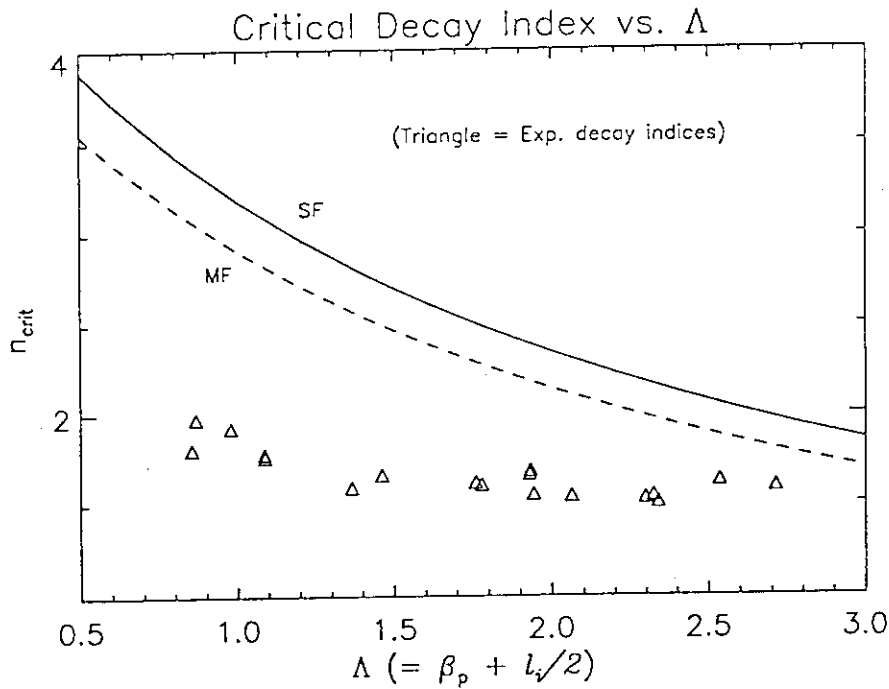
Figure 1: Critical decay index and experimentally achieved decay indices vs. Shafranov Λ.
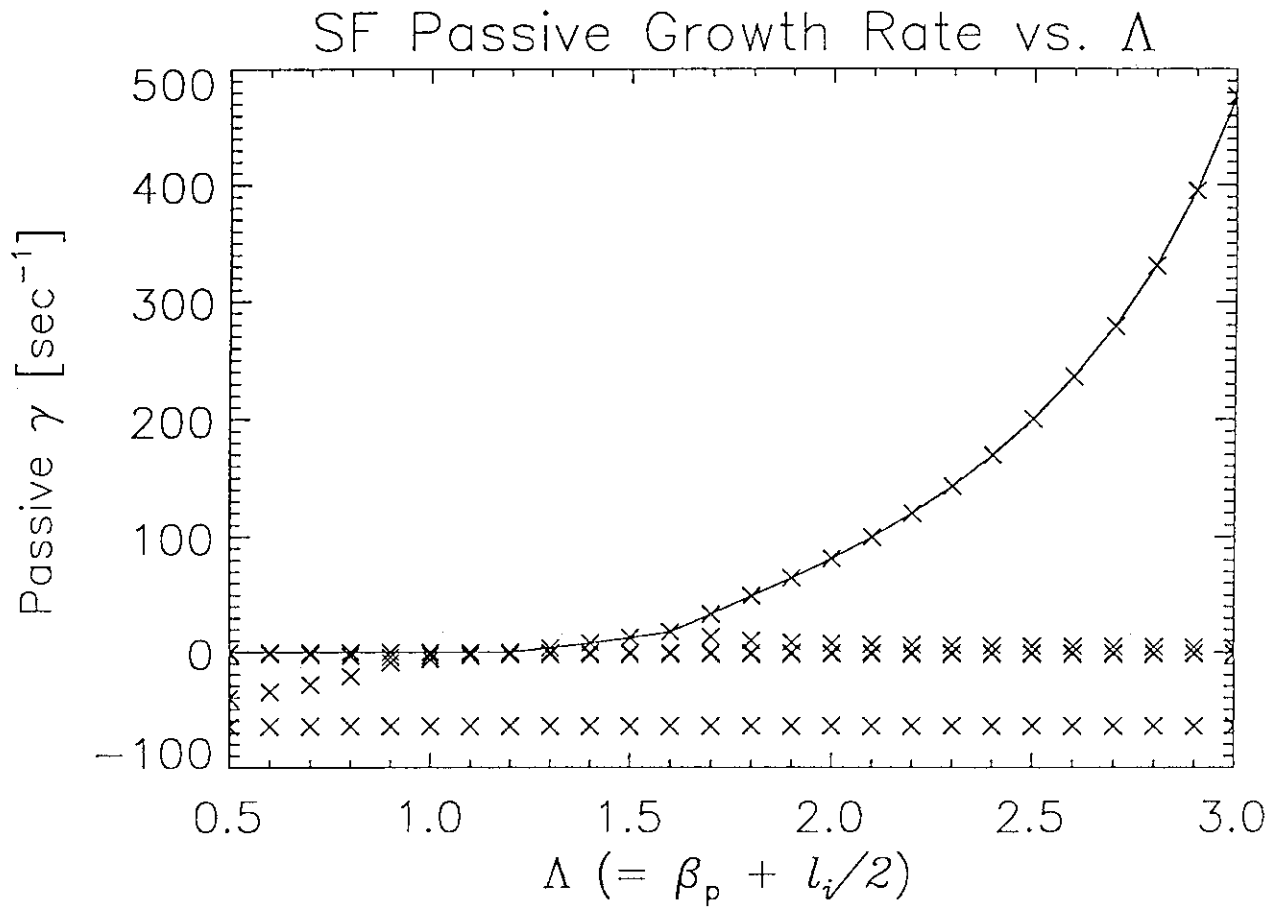
Figure 2: Passive growth rates as a function of Λ for n=-1.6.
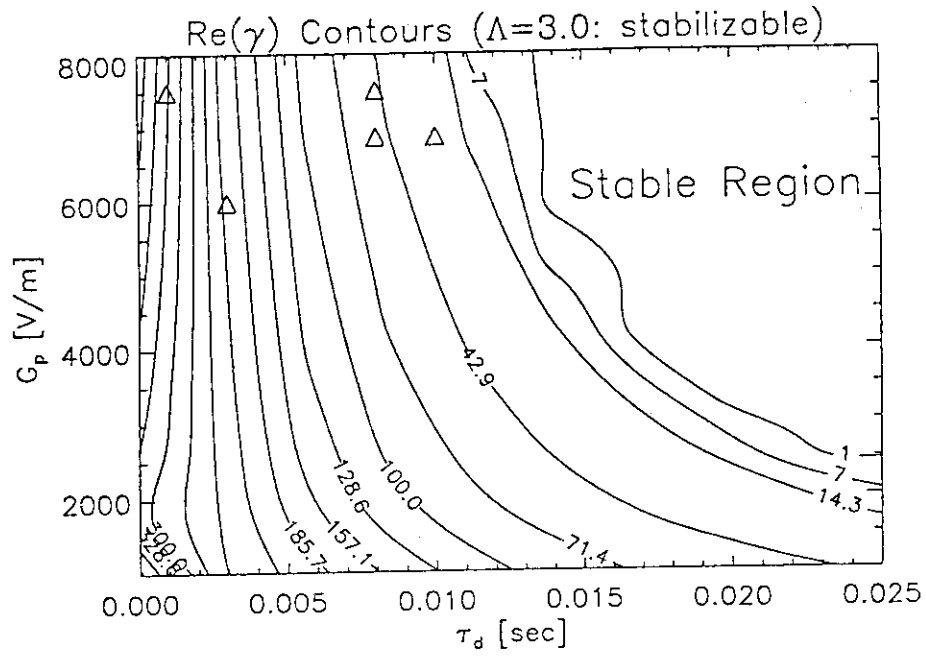
Figure 3: Contours of constant growth rate in G_p and τ_d space showing stability boundary for $\Lambda = 3.0$, $n = -1.6$. Triangles indicate typical operating points.
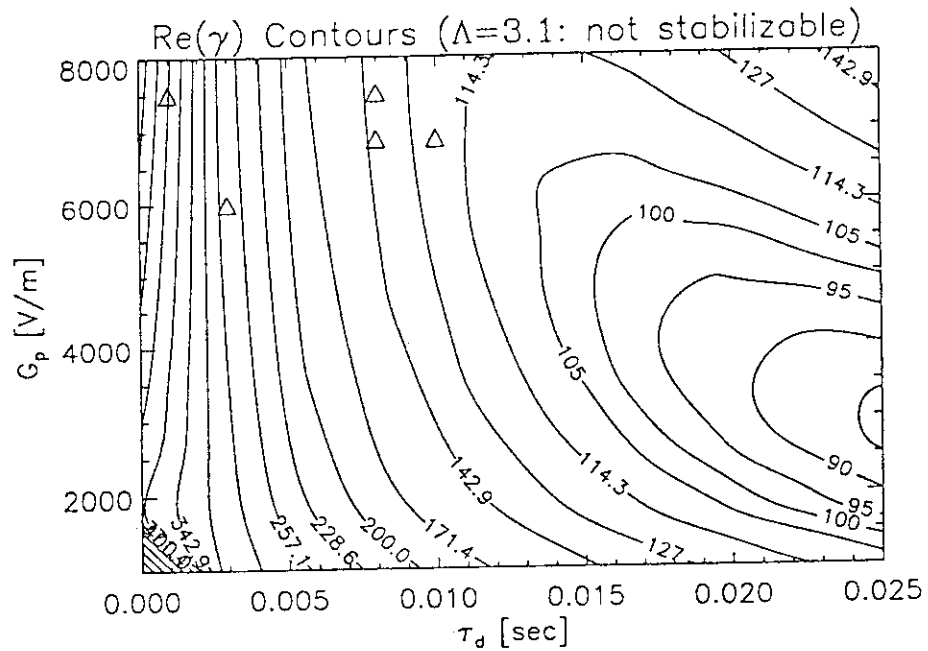
Figure 4: Contours of constant growth rate in G_p and τ_d space showing no region of stability for $\Lambda = 3.1$, $n = -1.6$. Triangles indicate typical operating points.

2.10 Detached Plasmas in JT-60U

Ryuji Yoshino

1.Introduction

Detached plasmas were observed in many tokamaks such as, TFTR[1], DITE[2], JET[3], and DIII-D[4]. General features of the detached plasma are the following. 1)The detachment is observed near the density limit, after MARFE and before a major disruption, so that it can be used as a pre-precursor. However the detachment is not observed in ASDEX[5] and JFT-2M[6], in spite of the detection of MARFE. 2)A shrinkage of the plasma current channel can be observed by TV, 3)Increase in the plasma internal inductance l_i and the sawtooth inversion radius, 4)A stable contraction is observed in the electron temperature profile, that leads to an increasingly unstable current profile, 5)Total radiated power nearly equals the input heating power with the poloidally symmetric radiation profile 6)Edge electron temperature of 6~7eV is measured in DITE. 7)The margin between the density, at which the detachment and the disruptions occurs, becomes small with the decrease in the safety factor. At low q (e.g. q(95%)=2.9) no-detachment or a short time detachment of <20ms is observed in DIII-D.

Detachment is also observed in JT-60U's limiter and divertor plasmas. A typical time evolution of the detachment during the plasma current ramp down is shown in Fig.1. It shows that 1)the detachment occurs after MARFE and 500ms before a major disruption, 2)light impurities of carbon (and oxygen) increase during the detachment, and 3)the repetitions of the detachment and the attachment occurs with high MHD activities is observed between the end of a detachment phase and a plasma current quench. General features of 2), 3) and 6) are also observed in this detachment.

To avoid disruptions of the density limit type, the detachment phase is very important as the pre-precursor. Especially large tokamaks like JT-60U have the possibility to get a good spatial resolution in the measurement of the detachment owing to the longer skin time. Thus the detached plasmas are investigated in this paper.

2.Time Delay of a Major Disruption from the Start of the Detachment

The detachment is observed in the density limit disruption, and also the moment of impurity influx during NBI heating and LH heating. Thus the data points of the detachment are scattered on the Hugill Diagram.

A time delay of the current quench in a major disruption from the start of the detachment is investigated as shown in Fig.2. The time delay increases with q_{eff}. No major disruption occurs at $q_{eff} > 7.5$, in spite of the occurrence of many minor disruptions. The limit in ohmic heating coil current terminates these discharges. When q_{eff} is 4~6.5, the time delay increases with l_i measured at the start of the detachment as shown in Fig.3. A time

delay of 0.6 s is obtained with l_i of 0.8. This suggests low l_i plasmas of 0.7~0.8, that is proposed for ITER fusion reactor plasmas, have a long time delay, that would enable the avoidance of major disruptions. Furthermore the flat current profile with low l_i during the plasma current ramp down would enable a stable soft landing.

3.Survival from the Detachment

Long stable detached plasma of ~1sec is obtained during the plasma current ramp up phase with joule heating alone. Joule heating at the plasma periphery seems to keep the power balance with the radiation loss and to suppress the shrink of the plasma current channel. Further heating by NBI and additional joule heating by the plasma current ramp up were performed to return the detached plasmas to the attached plasmas , and were found to be powerful method to avoid the disruption. However NBI heating increases the plasma density and induces a major disruption just after the stop of NBI heating. The plasma current ramp up cannot be used for the soft landing of a discharge. The maintenance of power balance at the plasma periphery is essential to avoid the disruptions. Thus RF heating of the peripheral region, the increase in the joule heating power density at the plasma periphery by the control of the plasma current and the plasma shape, and the decrease in the peripheral plasma density should be tried for this purpose. Especially the excitation of the weak MHD activities by the control of X_p and I_d/I_p' [7] is one method to decrease the plasma density, because the drop in the plasma density is frequently observed in a minor disruption caused by mode locking.

4. The Detachment just after the Plasma Initiation

Stable detached plasmas are observed in a plasma initiation and in the early phase of the plasma current ramp up, when a high retention of the hydrogenic particles is obtained for the first wall. Bad wall condition with the high impurity contamination such as oxygen also causes the detachment with a bright light surrounding a plasma, however that is not stable and is always disrupted. This difference in the plasma stability may be caused by the difference in the radiation power of hydrogen and oxygen. The diameter of the plasma current channel is extremely small in detached plasmas. When q_{cyl} reaches ~2.0, an explosion of the plasma volume occurs, and a detached plasma with small diameter changes to an attached plasma within 1 ms. This process is the inverse of the density limit disruption, where the plasma current channel shrinks until q_{cyl} decreases to ~2.0 then a major disruption terminates a discharge.

5.Reduction of Energy and Particle Flux to the Divertor Plate

In the case of detached plasmas produced by intense gas puffing or impurity influx, the particle and energy flux onto the divertor region is extremely reduced with nearly 100%

radiation loss of the main plasma. Thus the detachment can be used in a fusion reactor to change the heat flux onto the divertor plate to the radiation loss of the main plasma at the emergency such as the LOCA of the cooling pipe to the divertor plate. The long duration of the detachment obtained with low l_i plasmas is preferable for this operation.

6.Conclusions

Detached plasmas are frequently observed in JT-60U, just before the major disruptions caused by the density limit and the high impurity influx, and just after the plasma initiation with the high retention of the hydrogenic particles in the first wall. The following new information have been obtained. 1)A time delay of the current quench in a major disruption from the start of the detachment becomes long with the increase in q_{eff} and the decrease in l_i. Especially the long time delay with low li of ~0.8, that is propose for ITER fusion reactor plasmas, suggests the possibility to avoid the major disruptions. 2)Time delay seems to be decided by the power balance at the plasma periphery. Re-establishment of the power balance by the further heating of NBI or the plasma current ramp up avoids a major disruption by returning the detached plasmas to the attached plasmas. 3)Long stable detachment phase has the possibility to decrease immediately the energy flux onto the divertor plate at the emergency such as the LOCA of the cooling pipe of the divertor plate.

References

[1]   J.D.Strachan et al., Procc. European Conf. on Plasma Physics and Controlled Fusion, Budapest, Hungary (1985) 477.

[2]   G.M.McCracken et al., Journal of Nuclear Materials **145-147** (1987)181.

[3]   J.A.Wesson et al., Nuclear Fusion **29** (1989) 641.

[4]   T.W.Petrie et al., ITER Physics R&D Program Task PH17 U2.

[5]   H.Niedermeyer, et al., IPP III/90 (1983).

[6]   N.Suzuki private communication.

[7]   R.Yoshino, et al., section **2.11** in this review paper.
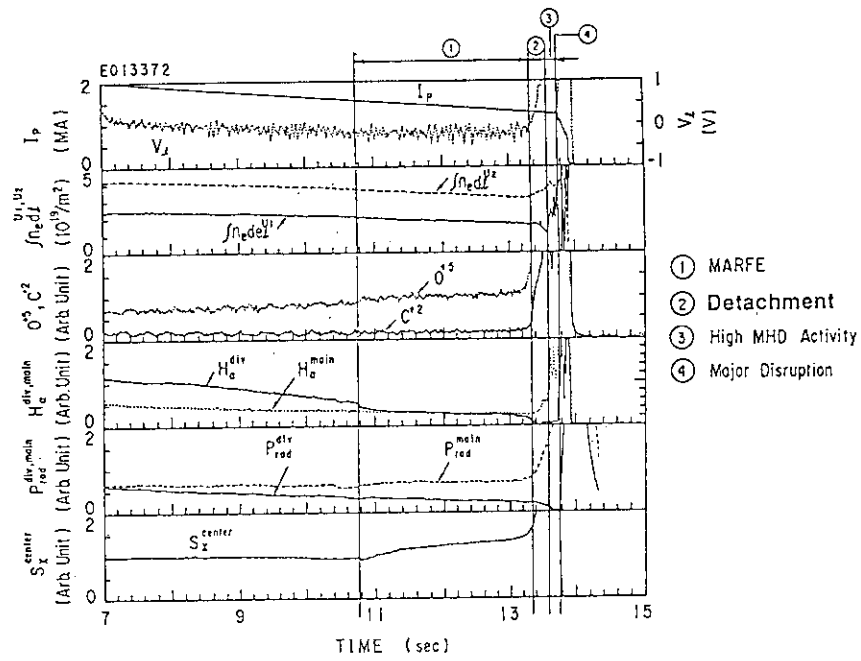
Fig.1 Detachment at the plasma current ramp down.
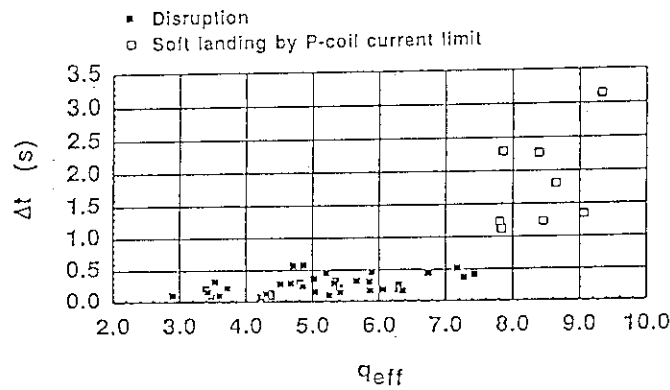
Fig.2 Time delay of the plasma current quench from the start of the detachment versus q_{eff} at the start of the detachment.
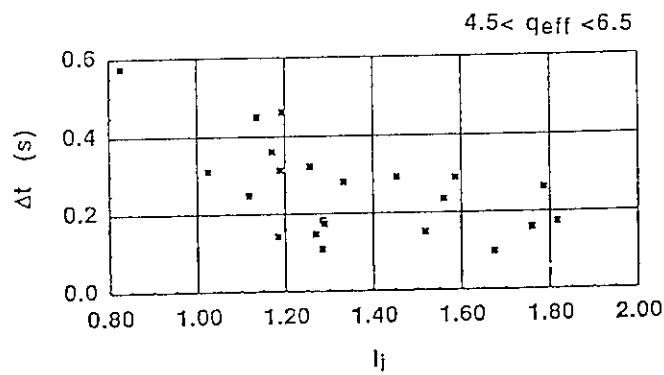
Fig.3 Time delay of the plasma current quench from the start of the detachment versus l_i at the start of the detachment at $4.5 < q_{eff} < 6.5$.

2.11 Locked Mode Disruptions and Duration of D_α drop in H-mode on an Xp versus I_d/I_p Diagram in JT-60U

Ryuji.Yoshino, Sean W Wolfe

1. Introduction

Locked mode disruptions are observed in many tokamak machines. The physical mechanism of that is considered to be the deceleration of the toroidal rotation speed by the damping effect of the resistive wall. Toroidaly asymmetric error magnetic field coupled with the MHD activities locks the rotation. Thus the final form of the magnetic field patter is always the same. This suggests that the error field can be investigated from the magnetic measurements of the mode locking. This error field has the possibility to effect the confinement mode. In JFT-2M NBI heating power threshold for H-mode plasma transition increases with the ergodic field coil current[1]. Then analyses of the error magnetic fields that cause locked mode disruptions are important to study their effect on the confinement mode. From this point of view, as the first step, the operational regions of locked mode disruptions and H-mode phenomena are studied in this paper.

2. Locked Mode Disruptions

Major disruptions caused by the locked mode are frequently observed in JT-60U divertor plasmas. A typical case of a locked mode disruption during the plasma current ramp up with joule heating alone is shown in Fig.1. After the rise of the divertor coil (D-coil) current, a mode locking with m=3 is observed in B_ρ magnetic probes from 2.58s. Plasma density decreases gradually from this time. Then a minor disruption occurs at t=2.72s with q_{eff} of 4.05, plasma densities of $1.33 \times 10^{19} m^{-3}$ (ch.1 at $1/3a_p$) and $1.59 \times 10^{19} m^{-3}$ (ch.2 at $2/3a_p$), and l_i of 0.87. Here q_{eff} is the effective safety factor. The soft X-ray signal from the center chord drops at this moment. Finally a discharge is terminated by a major disruption at t=2.89s with q_{eff}=4.15.

For an analysis of locked mode disruptions during joule heating alone, major disruptions that terminate a discharge and minor disruptions that induce the fluctuation in plasma current and the drop in the stored energy are selected as the data points. Then it is found that q_{eff} of these disruptions is mainly at $3<q_{eff}<4$. Of course data points exist at $q_{eff}=\sim5$ and <3, but their number is few. Locked modes are sometimes observed in density limit disruptions. However those locked modes are not investigated in this paper.

The effects of ohmic heating coil current and D-coil current on locked mode disruptions are investigated, and the occurrence of disruptions is found to be mainly limited to high D-coil current of >40kA. The height of the X-point is an important parameter of the configuration in JT-60U's lower X-point single null divertor plasma, and can be controlled

by D-coil current and horizontal magnetic field coil current. Thus X_p is not a linear function of I_d/I_p. Then the occurrence of disruptions can be plotted on an X_p versus I_d/I_p diagram as shown in Fig.2, where disruptions are presented by closed points and normal stable plasmas with $3 < q_{eff} < 4$ are plotted by open points. This diagram shows that disruptions are limited to high I_d/I_p and low X_p as $X_p(cm) < 0.75*(I_d/I_p)*10^3-7.5(cm)$. This result suggests that the error field produced by D-coil may trigger locked mode disruptions. These disruptions occur at relatively high density of $2 \times 10^{19} m^{-3}$. However low density of $0.5 \times 10^{19} m^{-3}$ is easily obtained outside of this unstable region with I_p of 2~2.5MA.

The avoidance of locked mode disruptions is indispensable for the design of ITER-like fusion reactor, in that the plasma current is designed to be ramped up with low l_i. Here newly developed growing plasma method has demonstrated the stabilization in the unstable region for locked mode[2].

3. D_α Drop in H-mode

Owing to the incomplete wall conditioning in the first year operation, a clear improvement in the energy confinement with H-mode transition has not been obtained yet[3]. However high reproducibility of the drop in D_α signal of the main plasma (D_α^{main}) with an increase in plasma density is obtained with NBI heating. A typical case of the D_α drop during NBI heating is shown in Fig.3. Here 7.5MW deuterium NBI is injected into a deuterium divertor plasma of 1.3MA with $q_{eff}=3.1$. The duration of the D_α drop is 145ms (t=8.23~8.37s), and there is a clear rise of plasma density in spite of several ELMs.

The duration of the D_α^{main} drop during the H-mode is analyzed on an X_p versus I_d/I_p diagram to study the relation with the unstable region for locked modes. In the selection of data points, the following criteria are settled on the relation between plasma density and the drop of D_α^{main}. "Plasma density must increase with the drop of D_α^{main}, and must decrease with the increase in D_α^{main}." The relation between the D_α^{main} drop duration and the location of the data points with respect to the unstable region for locked mode disruption is shown in Fig.4. Here $X_p > 0.75*(I_d/I_p)*10^3-7.5+5.0(cm)$ is required to get D_α^{main} drop duration of >50ms. Fig.5 shows data points where the D_α^{main} drop duration is longer than 50ms, that are clearly limited in the X_p versus I_d/I_p diagram. These figure show that improvement in particle confinement has not been obtained in the unstable region and the neighborhood of that region. Furthermore these figures suggest that the operational scan of H-mode experiments has not been completed yet, especially in the region of low X_p with low I_d/I_p.

Confinement modes of the H-mode and the L-mode may be controlled by the location on the X_p versus I_d/I_p diagram. Therefore a systematic study of this diagram is an

urgent issue.

4. Conclusions

Investigations of a region where locked mode disruptions frequently occur have been performed on an X_p versus I_d/I_p diagram. Locked mode disruptions have been found to occur mainly at $X_p < 0.75*(I_d/I_p)*10^3-7.5$(cm) when q_{eff} is 3~4. Low density plasma of $0.5 \times 10^{19} m^{-3}$ has been easily obtained outside of this unstable region. On the other hand plasmas of $2.0 \times 10^{19} m^{-3}$ are still unstable in this region. Furthermore the duration of the drop in the D_α signal of the main plasma during the H-mode is considered on the same X_p versus I_d/I_p diagram. Longer D_α drop durations of >50ms are found to be obtained in the limited region of $X_p > 0.75*(I_d/I_p)*10^3-7.5+5$(cm).

These experimental results suggest a relationship between the error field produced by the D-coil and the occurrence of locked mode disruptions, and an effect of the error field on the degradation of particle confinement. Thus this paper has established a new point of view for executing experiments and data analyses on locked mode disruptions and the H-mode.

References

[1]A.W.Leonard, et al., Nuclear Fusion, 31 (1991) 1511

[2]R.Yoshino, section **2.6** in this review paper.

[3]H.Ninomiya and JT-60 Team, 33rd Annual Meeting, APS Division of Plasma Physics (1991), to be submitted to Phys. Fluids B.
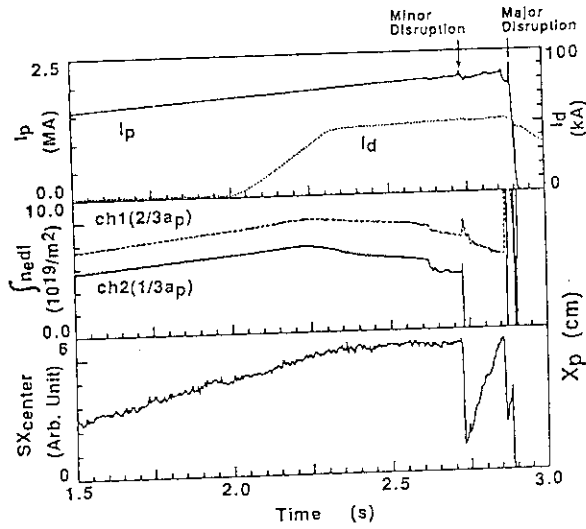
Fig.1 Time evolution of a typical locked mode disruption
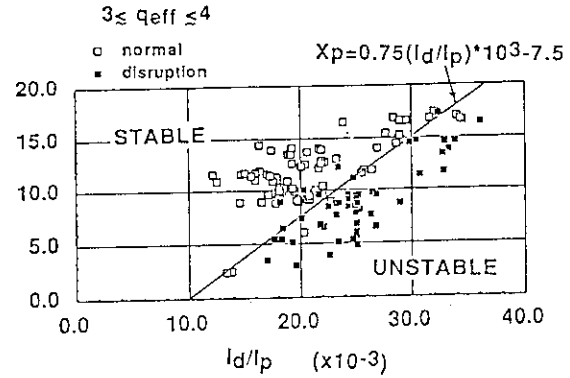
Fig.2 Operation region of Locked mode disruptions
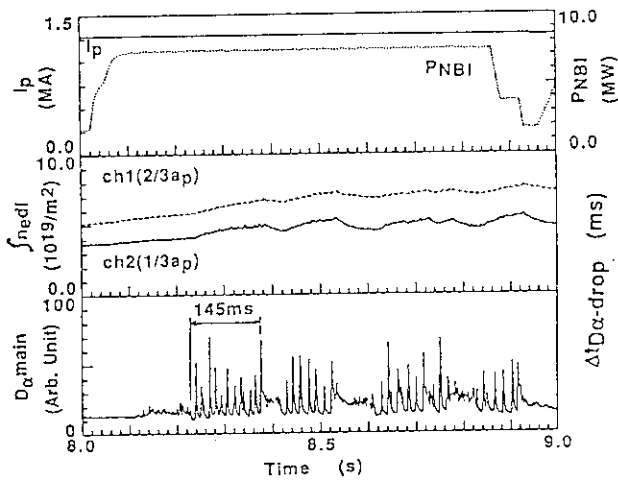
Fig.3 Time evolution of a H-mode attempt discharge.
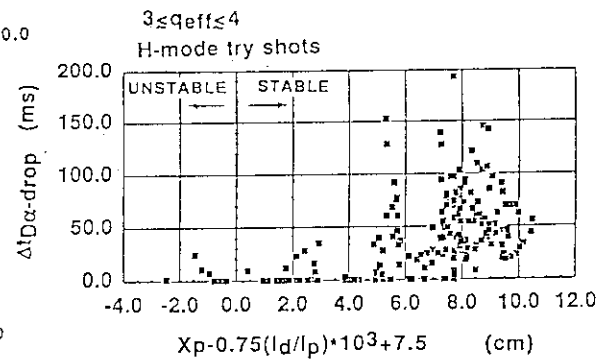
Fig.4 Drop-time of the main D_α signal versus X_p-0.75*(I_d/I_p)*10^3+7.5(cm).
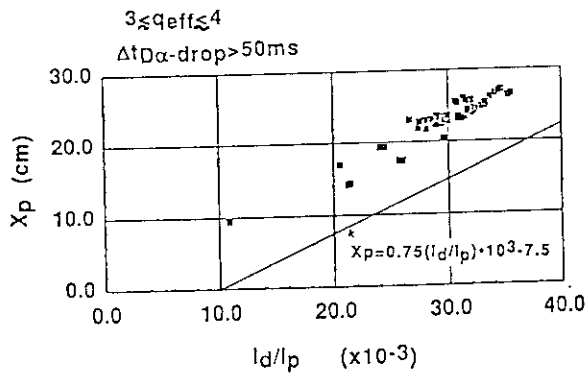
Fig.5 The location of the data points, D_α signal of which drop longer than 50ms, on the X_p versus I_d/I_p diagram.

2.12 Plasma Movement in Minor Disruptions

S.Nakajima, R.Yoshino, K.Ushigusa

1.Introduction

The investigation of the plasma movement in minor disruptions is necessary to determine the clearance between the plasma outermost surface and the first wall. If a plasma touches the first wall owing to a minor disruption, high impurity influx into a plasma induces a major disruption. The movement of plasma is determined by the stabilizing effect of the eddy currents and by the equilibrium control of the poloidal magnetic field coil currents. The effect of eddy currents is large at the high frequency. On the other hand the effect of control coils is large at the low frequency. Thus at the intermediate frequency, plasma movement becomes large. In the case of JT-60U, this unstable frequency band is 20~50Hz. This situation may be the same in the case of a

fusion reactor. The reduction in the resistivity of the vacuum vessel to $10\text{~}20\mu\Omega$ will increase the stabilizing effect of eddy currents. However the increase in the poloidal coil inductance will decrease the stabilizing effect of the control coil, if the voltage of the power supply is the same with the present large tokamaks.

Then we have started a study of the plasma movement in the high elongation configuration ($\kappa=1.6\text{~}1.7$) JT-60, selecting the fluctuation time scale of 10~25ms. Here the time constant of the eddy currents in the vacuum vessel is ~10ms. and the control time scale of the plasma shape is ~20ms.

A typical case of a minor disruption is shown in Fig.1, the plasma current rises suddenly and the horizontal plasma position shift to the inward side within 20ms.
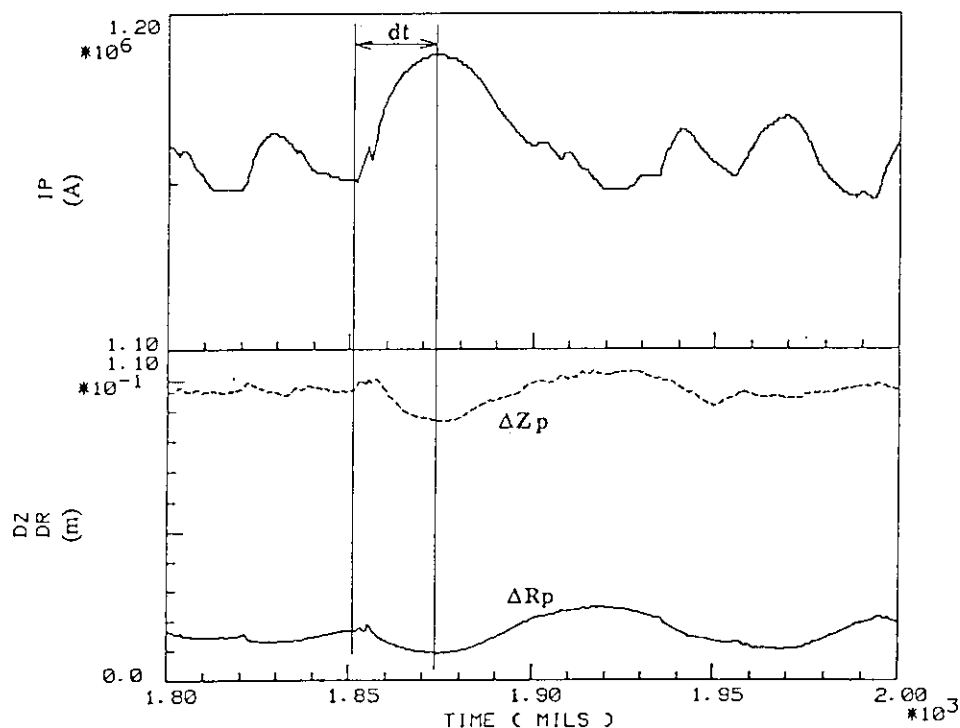
Fig.1 A typical time evolution of a minor disruption

2. Variations of plasma parameters

Variations of I_P, a_P, l_i, β_P, R_j, Z_j in minor disruptions are plotted in Figs 2. to 7. Most of changes occur within 10~20ms and the maximum variation of I_P, R_j, a_P. are 36%, 4%, and 13%, respectively. The relative variation of internal inductance ($dl_i/2$) is about one order larger than that of the poloidal beta.
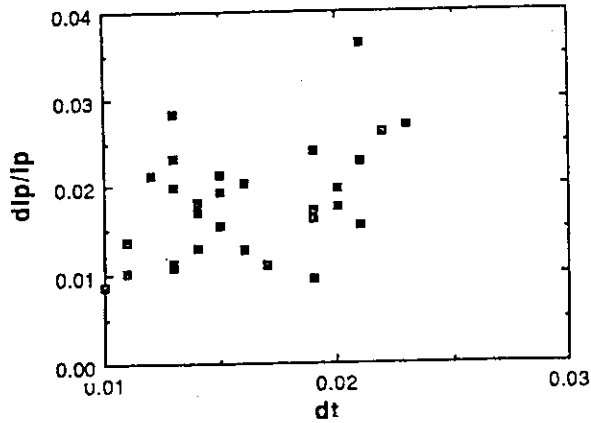
Fig.2 Variation of I_p
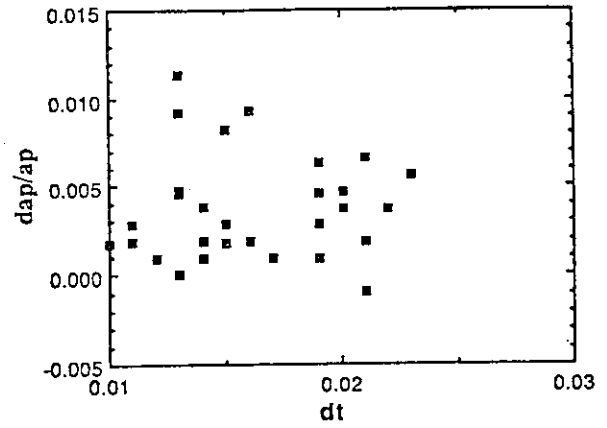
Fig.3 Variation of a_p
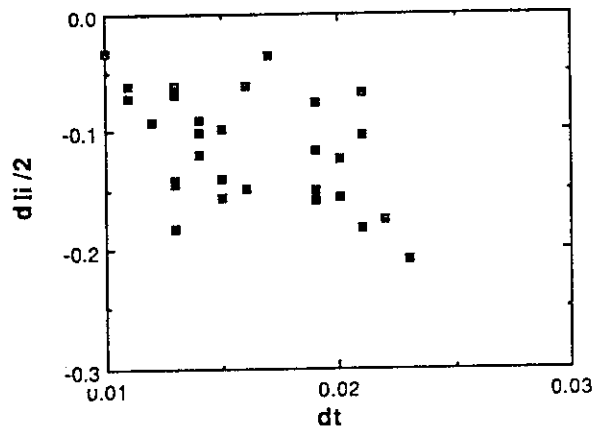
Fig.4 Variation of l_i
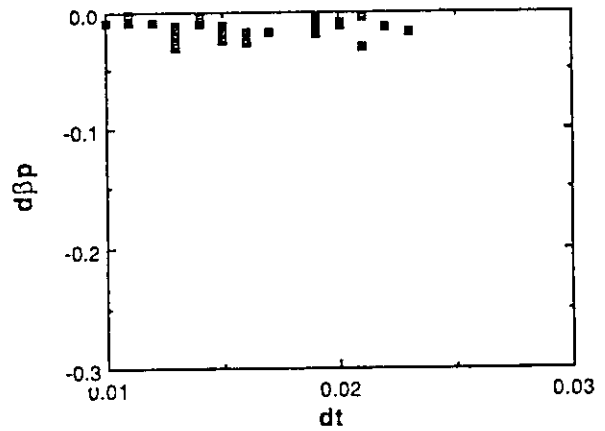
Fig.5 Variation of β_p
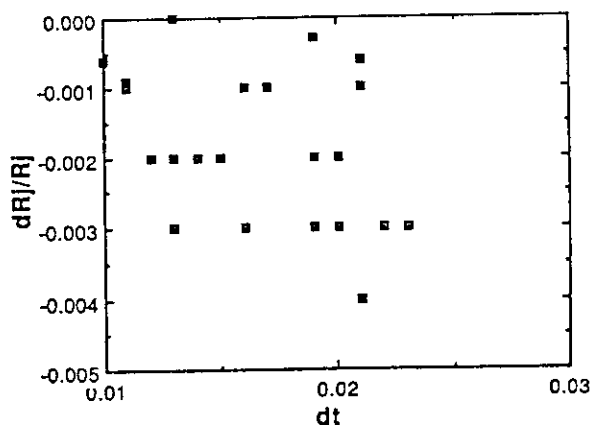
FIg.6 Variation of R_j
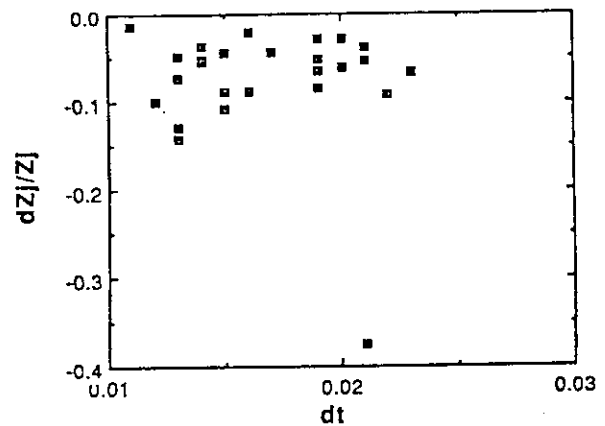
Fig.7 Variation of Z_j

3. Contribution of the poloidal beta and the internal inductance

Fig 8. shows comparison of the contribution of beta poloidal and internal inductance to the plasma movement in the assumption of the flux conservation. The internal inductance plays a major roll in a minor disruption.

From assumptions of $\delta F_R = 0$ and $L_P I_P =$constant. The effective contribution of l_i on R_j can be written as,

$$\frac{\frac{1}{2}+\beta_P}{A_0} \times \delta \frac{l_i}{2}$$

$$A_0 \equiv \ln \frac{\delta R_j}{a_p} + \frac{l_i}{2} - 2$$
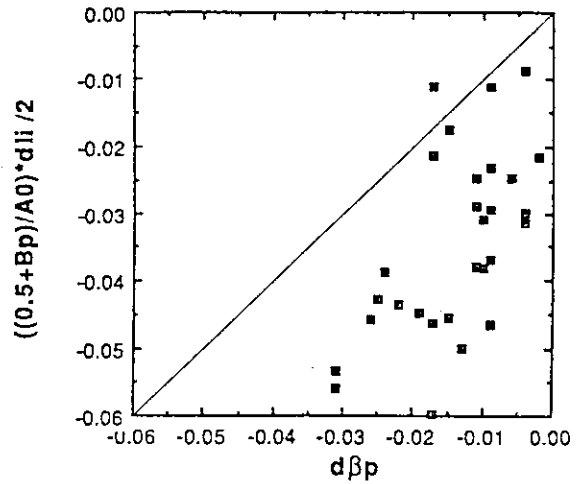
Fig.8 Contribution of the poloidal beta and the internal inductance

4. Force balance in the horizontal direction

Fig. 9 shows the the force balance in the horizontal direction with an assumption of one filament plasma current, that can be written as,

Fig.9 Force balance in the horizontal direction
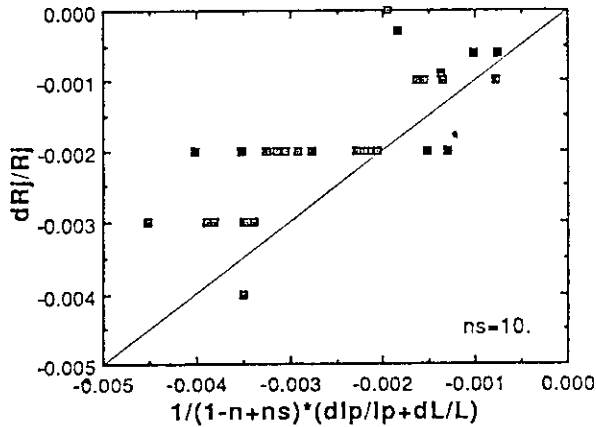
$$\frac{\delta R_j}{R_j} = \frac{1}{1-n+ns} \left(\frac{\delta I_p}{I_p} + \frac{\delta A_0}{A_0} \right)$$

$$A_0 \equiv \ln \frac{\delta R_j}{a_p} + \frac{l_i}{2} - \frac{3}{2} + \beta_p$$

Here n_s is the shielding effect of eddy currents that flows in the vacuum vessel and the other components. $n_s = 10.0$ is selected to fit the experimental data.

5. Flux conservation

Fig. 10 shows the flux conservation before and after a minor disruption. Here Ψ_{PSURF} is the flux at the plasma surface. Fig. 11 shows small drop in the flux.
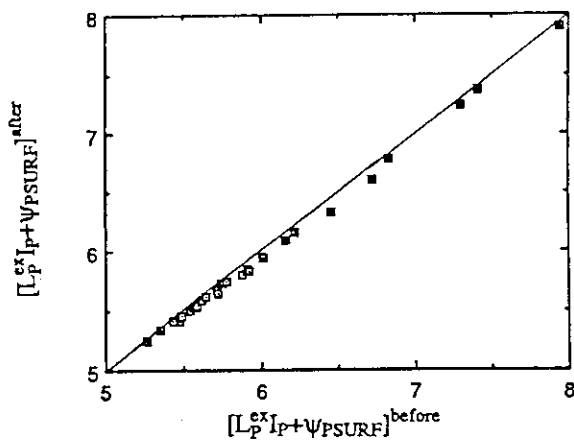
Fig.10 Flux conservation
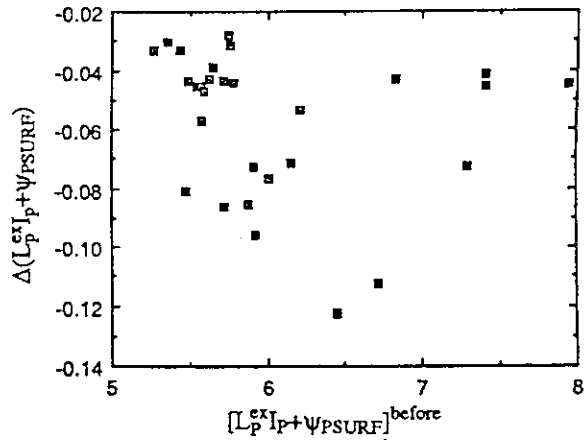
Fig.11 Flux consumption
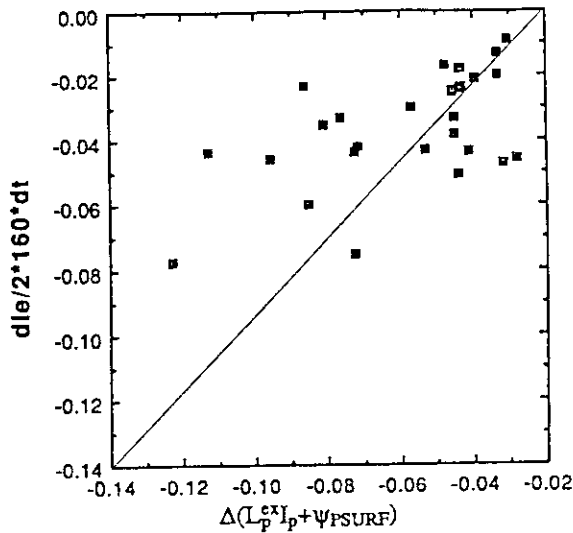
Fig.12 Flux consumption assuming 160 μΩ

of the one-turn resistance of the vessel

Flux conservation can be presented as,

$$L_p^{ex}I_p + (\psi_{PSURF} - \psi_0) = const$$

Where ψ_0 is the initial flux in the vacuum veassel. Then

$$[L_p^{ex}I_p + (\psi_{PSURF} - \psi_0)]^{after} =$$

$$[L_p^{ex}I_p + (\psi_{PSURF} - \psi_0)]^{before}$$

$$L_p^{ex} \equiv \mu_0 R_j (\ln \frac{8R_j}{a_p} - 2)$$

Fig.12 suggests that this flux consumed by eddy currents that flows in the vacuum vessel.

$$\psi_{eddy}^{loss} = \frac{\Delta Ie}{2} \times 160\mu\Omega \times \Delta t$$

Where ΔIe is the deviation of eddy currents that flows in the vacuum vessel.

6. Force balance in the vertical direction

Fig. 13 shows the equilibrium horizontal magnetic field just before a minor disruption and at a minor disruption. It shows that the difference in the equilibrium horizontal magnetic field B_Z^{eq} is small.

The B_Z^{eq} can be prsented as,

$$B_Z^{eq} = n_{index} \frac{\mu_0 I_p \Lambda_0}{4\pi R_j} \times \frac{Z_j}{R_j}$$

$$\Lambda_0 \equiv \ln \frac{8R_j}{a_p} + \frac{l_i}{2} - \frac{3}{2} + \beta_p$$

with an assumption of the force balance in the vertical direction.
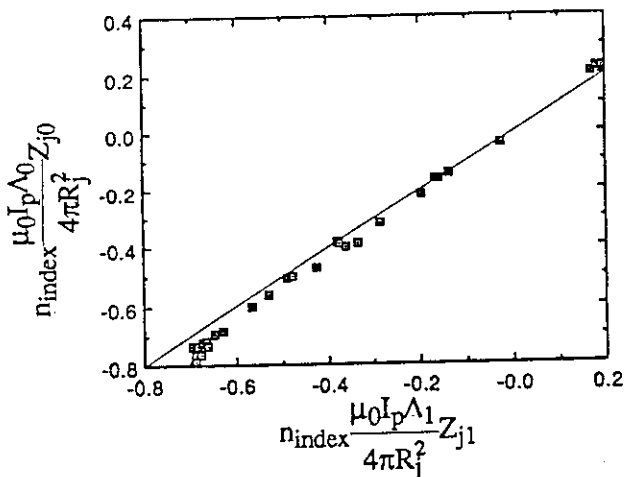
Fig.13 Force balance in the vertical direction

7. Conclusion

Plasma movement in minor disruptions has been studied to determine the required clearance between the plasma outermost surface and the first wall. The movement in Rj can be explained by the force balance equation of a plasma current with an assumption of a one filament plasma current and ns of eddy currents as ~10.0. The flux conservation is broken a little before and after a minor disruption, that may be consumed by resistivity drop of the vacuum vessel eddy currents'. The movement in Z_j can be also explained by the force balance equation.

3. Confinement

3.1 Progress towards High Fusion Product in JT-60

M. Kikuchi, T. Nishitani, S. Ishida, H. Yoshida, Y. Kamada, Y. Koide

Significant progress has been made in attaining high fusion product in JT-60U. Maximum $n_e(0)T_i(0)\tau_E$ of 3×10^{20}keVsec/m^3 has been obtained in 1.1MA high βp discharge. The calculated $n_i(0)T_i(0)\tau_E$ is 2×10^{20}keVsec/m^3. And the equivalent energy gain Q_{DT} of 0.2 has been obtained. Maximum volume averaged fusion product ($<nT>\tau_E$) is relatively insensitive to the plasma current and the performance enhancement is very large in low current regime compared with those expected from the L mode scaling.

1. Introduction

Attainment of the high fusion product in the range of Q=1 condition ($n_i(0)T_i(0)\tau_E \sim 10^{21}$keVsecm^{-3}) is one of major research goal of JT-60U research. To achieve this condition, energy confinement of the H mode level (2 times the L mode) is required in 6MA discharge. But the recent observation of the hot ion H mode relaxes the condition to H mode confinement with 4MA. Since the JT-60U tokamak is a high aspect ratio tokamak with A~4, it is expected from the L mode scalings such as ITER power law or Goldston scaling that high fusion product can be attainable in relatively low plasma current (fusion product~$I_p^2A^2$). For example, 2.3MA , A=4 plasma in JT-60U would have comparable fusion product capability to the I_p=3.1MA, B_t=2.8T, A=3.0 JET plasma which attained the Q~1 condition[1]. Reduction of the plasma current in the tokamak reactor is important for the efficient steady state operation and for the reductions of the electromagnetic force and runaway electron production due to plasma disruption. So it is very important to maximize the fusion product for a certain plasma current as well as the attainment of the high fusion product by increasing plasma current. The confinement quality at high aspect ratio is good enough especially in high βp mode in JT-60U and this experimental result is encouraging for the realization of the steady state tokamak reactor.

In this paper, achievement of the high fusion product is discussed in section 2. And the Ip dependence of the average fusion product and the confinement quality are discussed in section 3. Summary and future direction are described in the final section.

2. Attainment of the high fusion product

Various types of experiments are made to obtain high fusion product in JT-60U. Fig. 1 shows the ($n_e(0)\tau_E T_i(0)$, $T_i(0)$) diagram for the standard divertor L&H modes, elongated divertor L modes and high βp enhanced confinement modes. Maximum fusion product in the standard configuration experiments are limited to 4×10^{19} keVsecm^{-3} at $T_i(0)$=5keV. This is partly caused by the reduction of the net heating power due to large

ripple induced fast ion loss, by the transport enhancement with high hydrogen concentration (~30%) and by poor power deposition profile (off axis NB heating). In the elongated divertor L mode, fusion product of 6.6×10^{19}keVsm^{-3} is obtained at T_{i0}=15keV. Highest fusion product up to 3×10^{20}keVsecm^{-3} has been obtained in high βp mode. Relatively peaked density profile is inferred in high βp mode. Fusion product of the highest plasma stored energy shot is only 0.6×10^{20}keVsecm^{-3}.
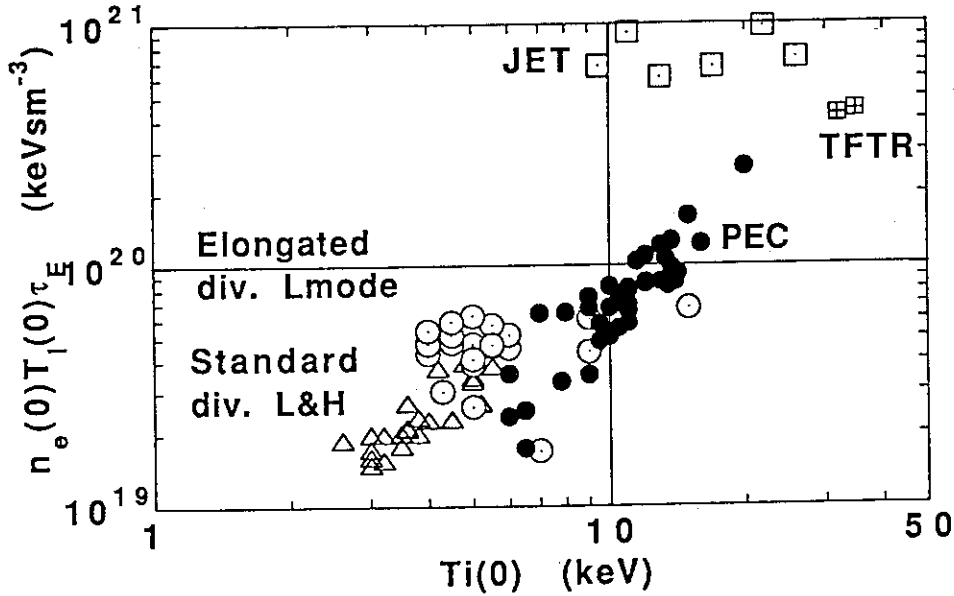
Fig. 1 Plasma performance in the $(n_e(0)T_i(0)\tau_E, T_i(0))$ diagram for various dischages

A detailed analysis of the highest fusion product shot (sec.4.6) shows central electron density of 4.8×10^{19}m^{-3} with density peakedness parameter $n_{e0}/<n_e>$=2.8 gives best fit to the diamagnetic and equilibrium stored energies, neutron rate and FIR measurement at r/a=0.6. This gives a fusion product of 3×10^{20}keVsm^{-3} with n_{e0}=4.8×10^{19}m^{-3}, T_{i0}= 25keV, τ_E=0.27s. In this case, 50% of the DD neutron comes from the beam-thermal reaction, 30% from thermal reaction and the rest from beam-beam reaction (Fig.2). And the equivalent Q_{DT} is 0.2 for D^0 injection into 50 : 50 D-T plasma.
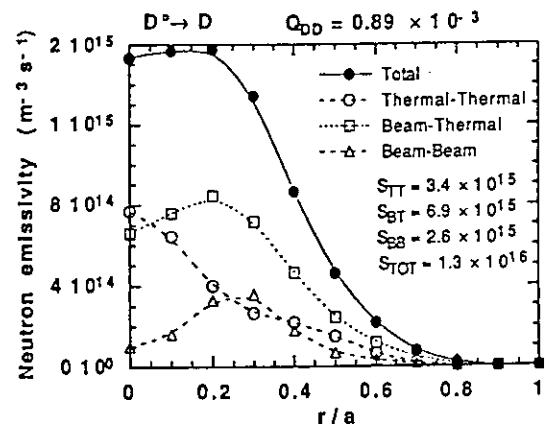
Fig. 2 Radial profile of the neutron emissivity for E13753

3. Average fusion product and the confinement quality factor

The volume averaged fusion product $<nT>\tau_E$ can be evaluated from the global

energy confinement time as follows,

$$<nT>\tau_E(keVsecm^{-3})=2.1\times10^{21}(W_{dla}/V)\tau_E^{dla}(MJsecm^{-3})$$

Fig. 3 shows volume averaged fusion product as a function of the plasma current together with those from other major tokamaks. As is clear from the figure, lower bound of the fusion product increases with plasma current. But the upper bound of the fusion product is relatively insensitive to the plasma current. In the lower bound, we see DIII-D and JET L mode database(low aspect ratio tokamaks). And the improvement of the average fusion product is clearly seen in the figure. Improvement factor of the fusion product over the low aspect ratio tokamak L mode reaches up to 50. Since optimization of the higher current discharges are not done in this short experimental period, continued effort to obtain higher fusion product will be continued in the next year.
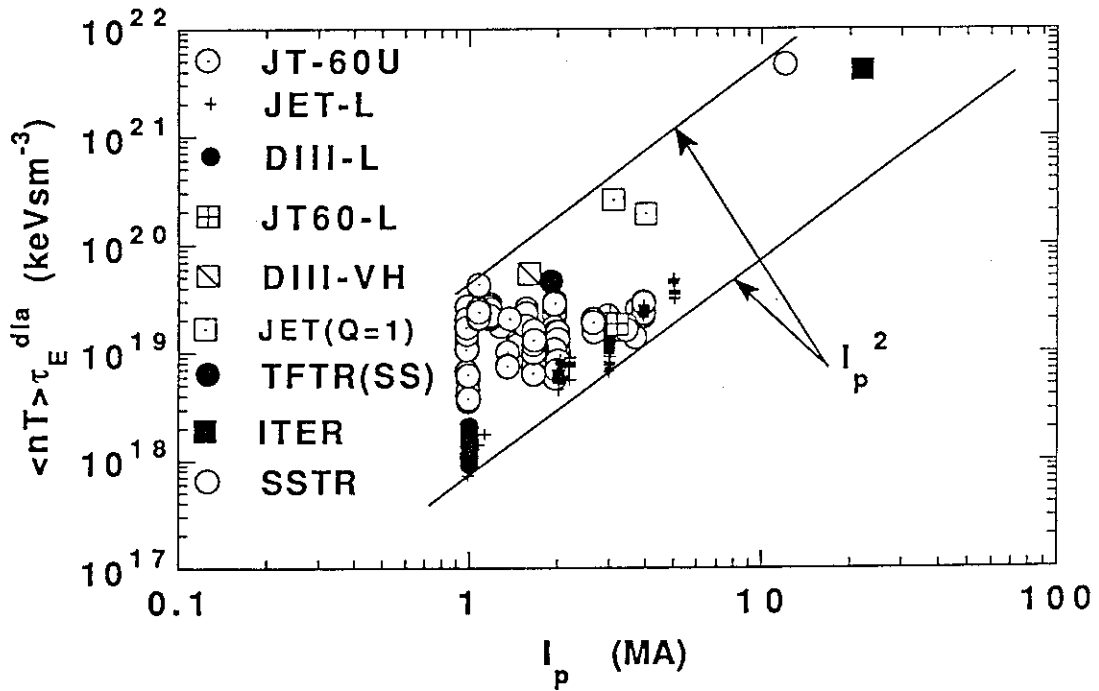
Fig. 3 Average fusion product with the plasma current for JT-60U and other machines

Let's move on to the quality of the confinement in view of the fusion product for the same plasma current. Here, we define confinement quality factor (CQ) as,

$$CQ \equiv \frac{<nT>\tau_E}{I_p^2}$$

The average fusion product of $40keVsec10^{20}m^{-3}$ is required for the fusion reactor. And the CQ of 0.08 is requested in ITER, while CQ of 0.27 is required for the SSTR. Fig. 4 shows the confinement quality factor as a function of the plasma current in JT-60U. Maximum CQ of 0.37 have been obtained in JT-60U, well above the requirement for the steady state tokamak reactor.
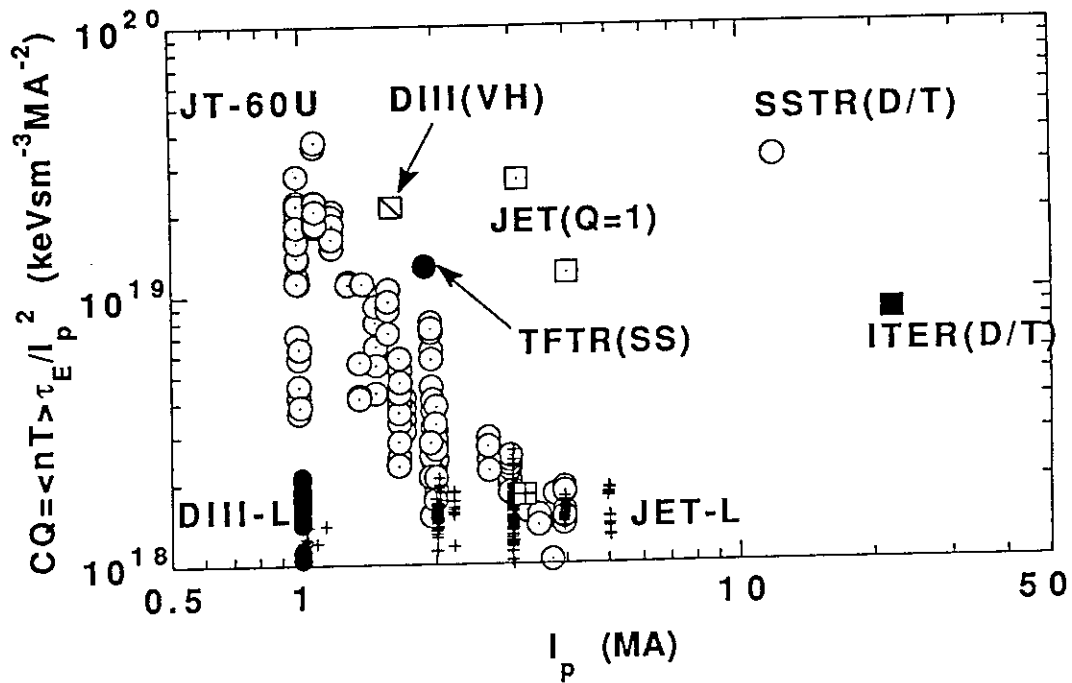
Fig. 4 Confinement quality factor with plasma current for JT-60U and other machines

4. Summary

The high power D^0 beam injection into JT-60U plasma produces a plasma whose fusion product of $3 \times 10^{20} keVsecm^{-3}$. This plasma is low plasma current high βp discharge which is suitable for the realization of the steady state operation. Fusion product is 50 times larger than that from the low aspect ratio L mode discharge with same plasma current. Confinement quality factor (CQ) of 0.37 keVsec$10^{20}m^{-3}$/MA^2 is obtained which may be encouraging for the steady state tokamak reactor concept.

Reference

[1] JET team, Nucl. Fusion 32(1992)187.

3.2 L and Transient H mode Confinements in the Standard Divertor

M. Kikuchi, Y. Kamada, T. Takizuka, H. Shirai, H. Yoshida, S. Tsuji

Energy confinement characteristics of the D^0 beam heated plasma is investigated in the Standard Divertor (SD) configuration. Plasma heating power of 5-15MW and plasma density of 2-$3.5\times10^{19}m^{-3}$ with $B_t=2$-$4.2T$ are investigated. H factor over the ITER power law varies from 1.5-0.7 monotonically decreasing with plasma current. H mode is obtained in medium to low field regime and a confinement enhancement factor up to 1.5 over the ITER L modes is obtained although ~10% of the heating power is lost by the ripple loss and the effective charge Z_{eff} is relatively high at 2.5-4.2.

1. Introduction

Study of the H mode confinement characteristics is one of major subject of JT-60U research. Various configurations are studied in the old JT-60, including outside divertor and lower X point divertor with and without T_i gettering. And it was found to be difficult to obtain good H mode (here, "H" means high confinement). Since then, JT-60 is upgraded to JT-60U[1] so that we can inject D^0 beam into D plasma which is believed to be important to obtain good H mode. In this paper, experimental studies of L and H modes are discussed in the standard divertor (SD) configuration done in 8/26-30 just after NB port aging. Very dirty wall condition forced us to spent ~3 weeks for the NB port aging ,which is usually finished within a few days in old JT-60, and the oxygen concentration in the plasma is of the order of 4 % during port aging, two times larger than that of old JT-60. The oxygen concentration is still high at 2% although He GDC of 1A has been applied during these experiments. Moreover, large hydrogen concentration of the order of 30% (=H/(H+D)) is measured by the H_α/D_α measurement (see section 8.2) for this experimental period. This hydrogen is likely to come from the NB port. These results are caused by the poor wall condition possibly due to the oil contamination during the start up phase of the tokamak. Last important issue is the orbital energy loss (up to 10%) of slowing-down fast ion due to large toroidal field ripple (section 10.1). Despite of such poor conditions, H mode confinement is obtained in low field ($B_t=2.5T$) condition. Experimental results are shown in section 2. The summary is given in the last section.

2. Energy confinement study in the Standard Divertor (SD) configuration

Fig. 1 shows (P_{abs},n_e) and (n_e,Z_{eff}) diagrams for this experiment. The plasma current and toroidal field are varied 1.4-3.5MA and 2-4T, respectively. The absorbed power and the line averaged plasma density are varied 3-15MW and 1.5-$3.5\times10^{19}m^{-3}$, respectively.

Confinement enhancement factor (H factor) over the ITER power law (ITER-P) is plotted as a function of the plasma current for 2-2.5T, 4T toroidal fields in Fig.2.

[2MA B_t scan] Experiments are started from B_t scan (B_t=2.5-4T, q_{eff}=3.3-6.0) with I_p=2MA. Major radius (R_p) and plasma volume (V_p) are kept relatively constant (R_p=3.32-3.38m, V_p=79-87m^3). The plasma is heated with net heating power of 7-11MW and the line average plasma density is 2-3.5x10^{19}m^{-3}. The effective charge Z_{eff} of the discharges are 2.8-4. The main plasma radiation is < 30% of the heating power while divertor radiation is < 45 % of the heating power. The H factor over ITER-P varies from 0.85-1.0 (see Fig.2). Fig. 3 show the power dependences of the energy confinement time for I_p=2MA discharges for B_t=2.5T and 4T, respectively. The power dependence of the energy confinement time is $\tau_E \sim P^{-0.47}$ which is close to the ITER power law ($\tau_E \sim P^{-0.5}$). The B_t dependence of the energy confinement time is $\tau_E \sim B_t^{0.22}$ which is close to the dependence of the ITER power law ($\tau_E \sim B_t^{0.2}$). The H mode power threshold study (see section 3.6) shows that the power threshold is $\sim 4B_t$ (=10MW for 2.5T and 16MW for 4T) which is marginal. As an important plasma parameter of the edge plasma confinement, the electron temperature at 95% plasma minor radius is measured with the edge Thomson scattering system. Measured T_e(r=0.95a_p) is 0.65-0.75 keV for P_{NB}=10-12MW, n_e=2.5-3.3x10^{19}m^{-3} at B_t=2.5T plasma while T_e(0.95a_p) is
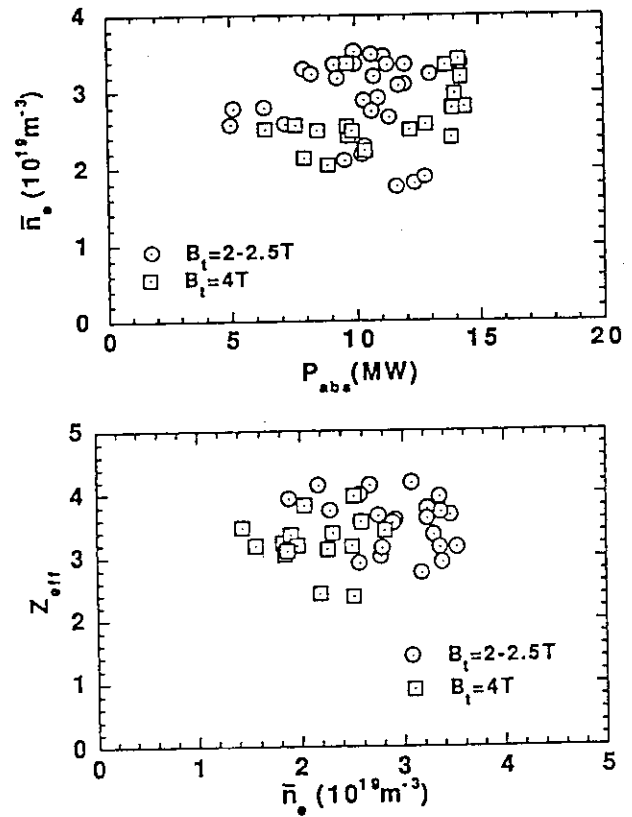
Fig. 1 Operation regime of NB heated plasmas in (P_{abs},$\bar{n}_e$) plane and the effective charge Z_{eff} as a function of $\bar{n}_e$.
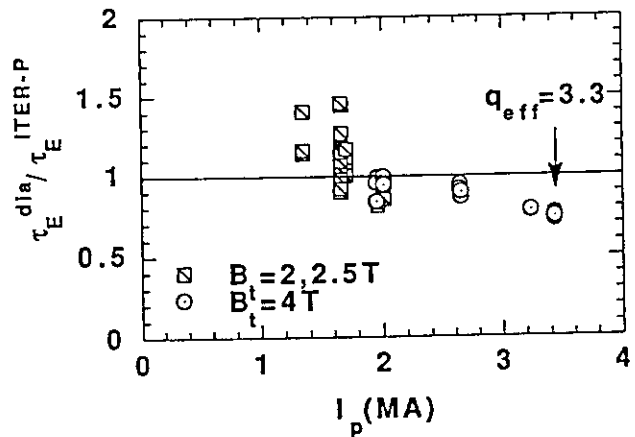
Fig. 2 Confinement enhancement factor over ITER power law as a function of plasma current.

somewhat lower for B_t=4T plasma ($T_e(0.95 a_p$)~0.57-0.59keV for n_e=2-2.2x10^{19} m^{-3}). In both cases, the electron collisionality ν_{*e} is ~0.3-0.6 (collisionless regime).

[**1.7MA, 2.5T small volume**]   Next, we moved to lower plasma current I_p=1.7MA with B_t=2.5T so that we can produce smaller plasmas with wider clearance to the outside wall in order to reduce plasma-wall interaction and hot spot due to ripple loss. The plasma volume is reduced to 65-71m^3. The Xpoint height is scanned between 1-16cm. H mode confinement is observed in a few shots. Fig. 4 shows typical waveform of the H mode discharge (E13632). Divertor D_α drops slightly at 4.18sec and the diamagnetic stored energy continues to rise until the occurrence of the strong ELM activity. Fig. 5 shows energy confinement time as a function of the net heating power compared with ITER-P and ITER-offset linear scalings. Although the duration of the H mode is short (<0.2sec), confinement enhancement factor up to 1.5 is obtained (E13635). Confinement enhancement is not good at high power, but the power degradation becomes weaker (τ_E~P$^{-0.23}$ in contrast to the 2MA power scan) which indicates an improvement due to H mode effect.   For this configuration, ripple loss of fast ion is estimated to be ~10% of the heating power (section 10.1). The edge electron temperature ($T_e(0.95a_p)$) is 0.74-0.77keV at P_{NB}=12.8-14.3MW, n_e= 2.5-3x10^{19}m^{-3} for L mode discharges and is 0.82-0.94keV at P_{NB}=15.4-15.9MW, n_e=
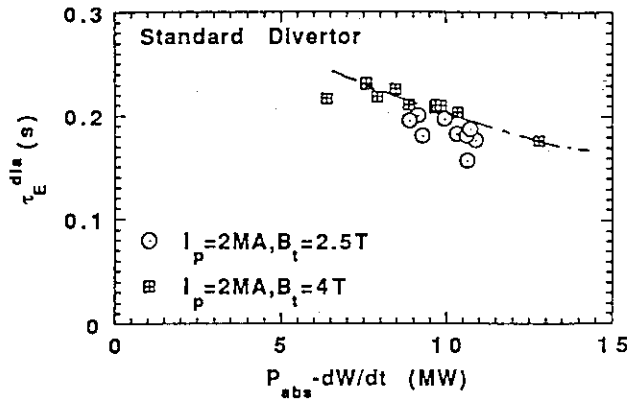
Fig. 3 Energy confinement time for 2MA power scan (Bt=2.5 and 4T).
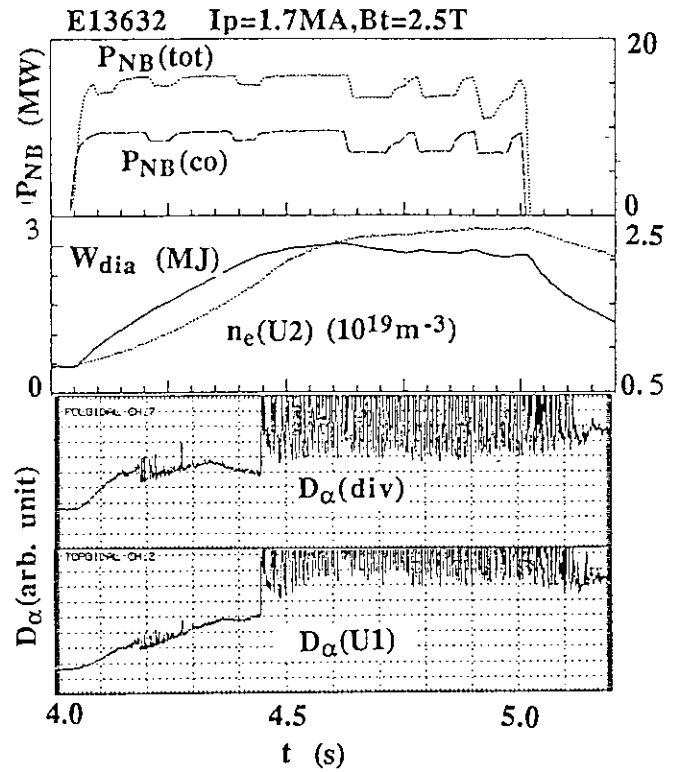
Fig. 4 Typical waveform of the H mode discharge.

1.9-2x10^{19}m^{-3} for H mode discharges. The electron collisionality of the L and H modes are typically 0.4 and 0.2 at 95% of the plasma minor radius, respectively.

The effect of the current profile on the energy confinement properties is discussed in section 3.5. This study clearly shows that $\tau_E \sim l_i$ in various L mode plasma where l_i is the internal inductance. Current profile of NB heated plasmas is not well penetrated to equilibrium profile expected from the temperature profile and the neoclassical resistivity since plasma current is build up with full aperture ($a_p \sim 1m$) with higher electron temperature (2-6keV). The internal inductance is thus lower than the equilibrium value which makes the L mode confinement lower than the previous scaling, such as ITER power law. Thus an H mode optimization with better current penetration (say, using the growing plasma method [2]) is important to get higher confinement time.
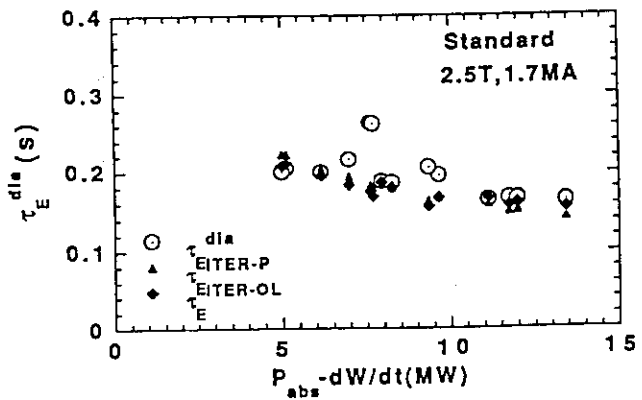
Fig. 5 Energy confinement time as a function of the heating power for a series of H mode discharges. Confinement enhancement is large for medium power.

3. Summary

Experimental study of the energy confinement for the standard divertor configuration has been made. H mode is obtained at low field regime (2.5-2T) and the H factor against ITER-P of 1.5 is reached. The edge temperature (at r=0.95a_p) up to 940eV has been obtained during the H mode whose electron collisionality is ~0.2. Optimizations of the H mode with respect to the current profile and impurity/recycling reduction are important in future.

References

[1] M. Kikuchi, T. Ando, et al., Fusion Technology Vol.1 (1989)287.

[2] M. Kikuchi , Nuclear Fusion 26(1986)223.

3.3 L and H modes at high Bt in the Elongated Divertor

M. Kikuchi, Y. Kamada, T. Takizuka, H. Shirai, H. Yoshida, O. Naitou, S. Tsuji

NB heated confinement characteristics in the elongated divertor is investigated up to 20MW in JT-60U. H mode transition is observed in 4MA, 4T discharges associated with main and divertor D_α drops and slight improvement in energy confinement (~10%) with clear formation of the edge temperature pedestal of the order of ~2.5cm which is much larger than the poloidal gyro radius of the thermal ion. Even in the L mode discharge which do not have D_α drop, formation of the edge temperature pedestal is observed. Energy confinement for small minor radius case (A=R/a~4) is better than that of Goldston (Aachen) scaling where ripple loss is small and power deposition profile is better.

1. Introduction

Study of the confinement characteristics at high aspect ratio is one of major subjects of JT-60U research (A=4, Ip=6MA, B_t=4.4T at R=3.25m) [1] since JET tokamak is characterized by its low aspect ratio (A=2.5) and high plasma current (Ip=6MA) with low toroidal field B_t=3.3T. In this paper, an overview of the energy confinement characteristics are discussed for elongated divertor (ED) configurations. Enhanced confinement regime at high βp is described in other papers. The energy confinement characteristics in full size ED configurations are discussed in section 2 and those in small minor radius case are discussed in section 3, respectively. A summary is given in the last section.

2. Energy confinement in the full size ED plasma

Typical equilibrium configuration of the ED discharge is shown in Fig.1. Experiments are performed for B_t(3.25m) = 4.1T to get confinement base for I_p = 1-4MA and P_{NB} = 5-20MW. Major radius (R_p), minor radius (a_p), vertical elongation (κ) and plasma volume (V_p) are typically 3.25m, 0.87m, 1.7 and 75m^3, respectively.

Deuterium neutral beam is injected perpendicularly from the upper and lower slant ports with the beam energy of 90keV. Neutral beam have three energy components (E, E/2, E/3) and power fractions are 78%, 15% and 7%, respectively.
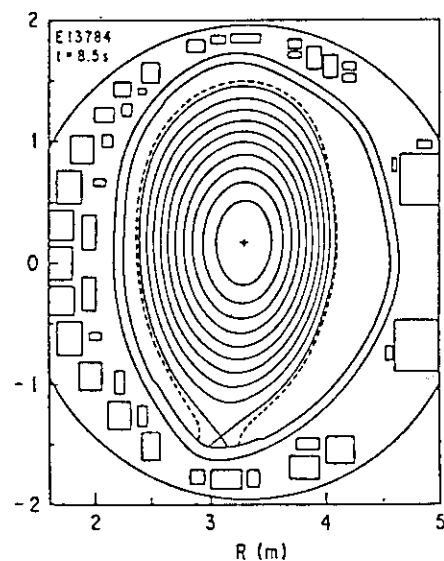
Fig. 1 Typical equilibrium of ED plasma

Fig. 2 shows waveform of a typical 4MA discharge. The effective charge Z_{eff} is 3.1 during 20MW beam heating. Divertor and main D_α shows clear drop during the NB heating accompanied by the increase of the diamagnetic stored energy W_{dia} which is a weak transition to the H mode. H mode threshold power (P_{th}) study (section 3.6) indicates H mode is obtained at $P_{abs}>16MW$ for $B_t=4T$ ($P_{th}\sim4B_t$). But the increase of W_{dia} is not significant and the discharge stays in the L mode confinement level partly due to large radiation fraction of the main plasma. Reduction of the D_α signal continues for 0.9s. The main plasma radiation continues to rise to 70% of the total heating power. The electron density and temperature profile at t=8.2s are shown in Fig.3. There is a clear formation of the edge T_e pedestal. And the density profile is flat for 0.5a<r<a. Magnetic fluctuation is also decreased after the transition ($\widetilde{B_p}/B_p=5\times10^{-5}$ before transition). These observations are typically seen in the H mode. Based on the Shaing's H mode theory [2], H mode bifurcation occurs in the collisionless regime from the parallel force balance between neoclassical viscosity and viscosity driven by the non-ambipolar ion orbit loss near the plasma edge. Hence the theoretical width of the edge transport barrier (δ_H) is of the order of poloidal gyro radius (~0.7cm for this case). The measured δ_H for the outside midplane is 2.5-3cm much larger than the poloidal gyro radius and is an order of the poloidal gyro radius of the slowing down fast ion. Since H mode is observed in
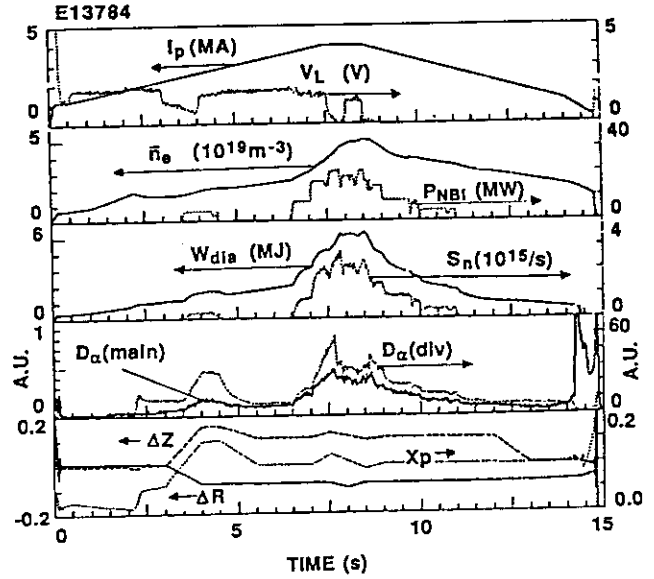
Fig. 2 Waveform of 4MA discharge
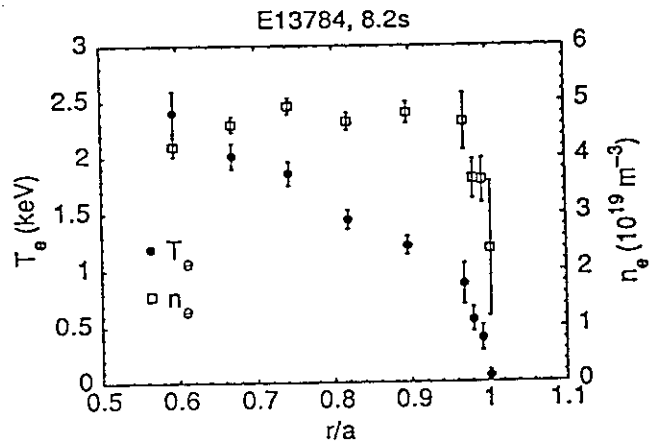
Fig. 3 Density and temperature profiles
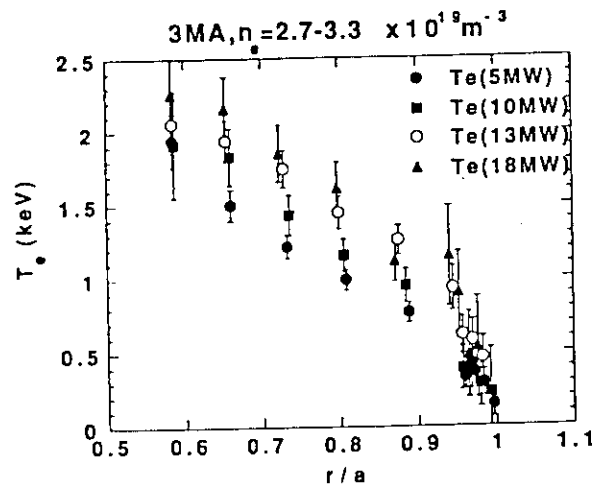
Fig. 4 Te profiles of 3MA power scan

collisional regime ($\nu_{*i}>1$) in JFT-2M[3], Shaing's H mode theory may be viable for the fast ion orbit loss near the plasma edge. For lower power level, such a transition is not observed. But the electron temperature profile shows formation of the edge pedestal. Fig. 4 shows edge temperature profiles for various heating powers. As the heating power increases, the edge temperature is increased to ~1keV in proportion to the heating power while inner temperature gradient stays relatively constant. Associated with this formation of the edge pedestal, toroidal rotation opposite to the beam injection has been observed (section 3.9) which shows strong velocity shear of the toroidal rotation.

Fig. 5 shows plasma stored energy as a function of net heating power for the plasma current of 1, 2, 3 and 4MA and a maximum plasma stored energy up to 4.4MJ have been achieved. Effective charge Z_{eff} and radiation power from the main plasma are relatively high (Z_{eff}~3-4, P_r^{main}/P_{net} = 0.2-0.5). The main plasma radiation may have non negligible effect on the energy confinement in high current regime. Further improvement will be done in the next year.

3. Small minor radius L mode with the aspect ratio of 4.

As a best target plasma with respect to the ripple loss and the power deposition, we have investigated the plasma with R_p=3.1m, a_p=0.77m with the aspect ratio of 4.0. Fig.6 shows the energy confinement time of the 2MA power scan compared with ITER power
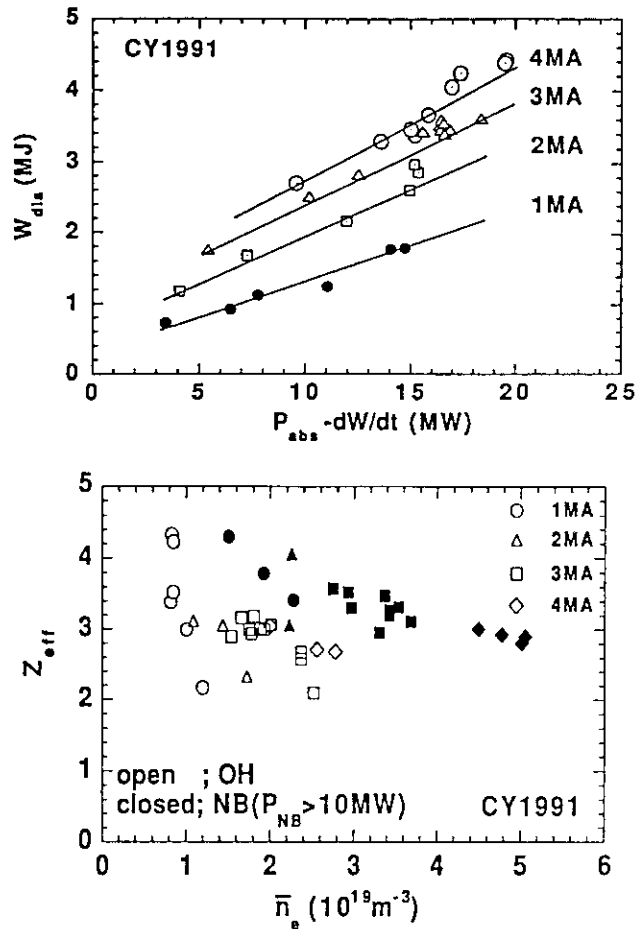
Fig. 5 W_{dia} with heating power for Ip=1-4MA and Z_{eff} for ohmic and NB heated plasmas.
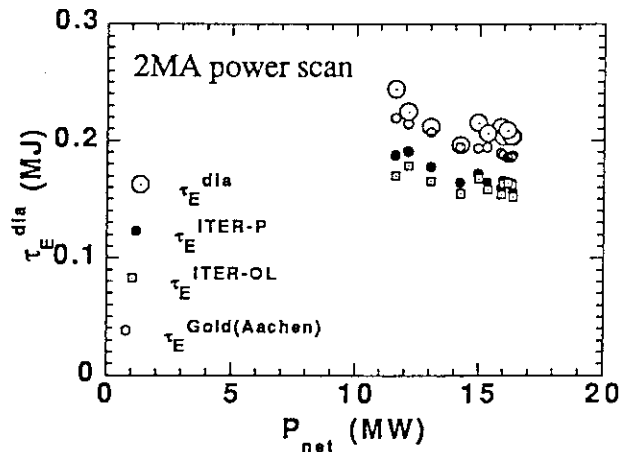
Fig. 6 τ_E with power for small ap L mode

law, ITER offset linear and Goldston
scalings. The energy confinement time is
better than that expected from the Goldston
scaling (1984, Aachen).

4. Confinement scaling comparison

Energy confinement times of the full
size and small a_p ED plasmas are compared
with ITER power law in Fig. 7 together with
old JT-60 data. Effective mass $A_i=1.9$ is
used throughout this study based on the
H_α/D_α measurement of 0.2. The energy
confinement time is slightly lower than the
ITER power law. This may be explained by
the effect of current profile (l_i) on energy
confinement since current penetration is poor
due to longer resistive diffusion time (section
3.5).
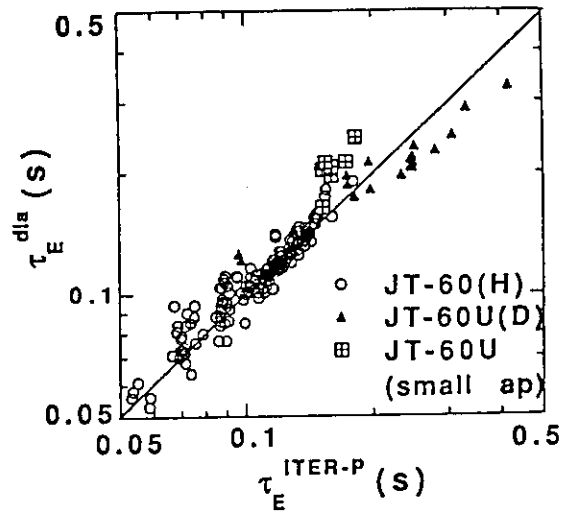
Fig. 7 τ_E^{dia} compared with ITER power law.

5. Summary

Global confinement and edge temperature profiles of elongated divertor plasma are
investigated in JT-60U. H mode transition has been observed in high field regime $B_t=4T$
with clear formation of the edge transport barrier, much larger than ion poloidal gyro
radius. But, edge pedestal is also found in the L mode power scan associated with the
counter plasma rotation. Further confinement optimization will be placed on reduction of
impurity / recycling, current profile control (higher l_i) and rotation/ radial electric field
control.

References

[1] M. Kikuchi, T. Ando, et al., Fusion Technology Vol.1 (1989)287.

[2] K.C. Shaing, E.C. Crume, Jr., P.R.L. 63(1989)2369.

[3] K. Ida, et al, 3rd Workshop on H mode Physics (JET Joint Undertaking, 1991).

3.4 Comparative Study of the D and H Plasma Confinement in JT-60U

T. Takizuka, H. Shirai, S. Tsuji, Y. Kamada, H. Yoshida, M. Kikuchi

1. Introduction

The effects of ion mass number, M_i, on the tokamak plasma confinement is one of unsolved issues in the magnetic confinement fusion research. Energy confinement time τ_E is believed in general to increase with the mass number. We have reported, therefore, the JT-60 performance converted from hydrogen plasma confinement into deuteron plasma confinement as $\tau_E(D) = 1.4 \times \tau_E(H)$ [1]. Statistical analyses of ITER L-mode confinement database have shown the M_i dependence of τ_E as $\tau_E \propto M_i^{0.3-0.5}$ [2,3]. The following is the present consensus among tokamak researchers [4]: On small and medium size tokamaks, this isotope scaling is almost uniformly seen. A comparison of confinement between JT-60 and TFTR supports the $M_i^{0.5}$ isotope scaling. Preliminary results in JET and DIII-D indicate a weaker isotope dependence in L-mode. We stress the importance of future studies of isotope scaling [4]. Also in the H-mode plasmas, isotope dependence of $M_i^{\sim 0.5}$ has been found from analyses of ITER H-mode database [5]. When we predict the confinement performance of D-T fusion reactors, we take value of $M_i = 2.5$ and obtain about 10% improvement in τ_E compared with τ_E in D plasmas. This 10% improvement is rather important for designing fusion reactors. Study of isotope dependence is of course indispensable to clarify the physical mechanism of the plasma transport.

In the present paper, we report for the first time the result of the isotope effects on the global energy confinement of L-mode plasmas in the JT-60U divertor configuration.

2. Results

Comparative experiments of D and H plasma confinement have been done in the JT-60U elongated divertor configuration. The major radius R is 3.20 - 3.25m, minor radius a is 0.87 - 0.92m, and elongation κ is 1.6- 1.7. The toroidal magnetic field at the plasma center, B_T, is about 4T. We survey the dependence of τ_E on the total heating power, P_h, and on the plasma current, I_p, for both D^0-beam-heated D plasmas and H^0-beam-heated H plasmas. Discharges are typical L-mode and no ELM is observed.

The concentration of H in a D plasma and that of D in a H plasma are estimated from the intensity ratio of H_α/D_α or D_α/H_α. The value of H_α/D_α in D plasmas is about 0.35, and that of D_α/H_α in H plasmas is about 0.55. The effective ion mass number is then evaluated as $M_{eff}^D = 1.75 - 1.85$ for D plasmas and $M_{eff}^H = 1.2 - 1.35$ for H plasmas. Effects of other impurities (mainly C and O) on the effective ion mass are ignored here. The values of line averaged electron density, n_{el}, in both D and H discharges are chosen to be almost the same for almost the same discharge condition ($I_p = 1, 2$ and 3MA, and $P_h = 3 - 11$MW) as shown in

Fig.1. Open symbols in the figure denote D plasmas and closed symbols indicate H plasmas. Triangles correspond to I_p=1MA discharges, circles to I_p=2MA, and squares to I_p=3MA. The total heating power, P_h, consists of joule heating power and deposited neutral beam heating power, which is estimated by subtracting the reionization fraction in the beam duct and shine-through fraction The latter fraction is roughly calculated by using a simple empirical scaling, $P_{shine-through} \propto \exp(-n_c{}^{D,H}/n_{el})$ ($n_c{}^{D,H}$ is an empirical coefficient for D or H plasmas). The ripple loss of beam ions is not taken into account at present, whose power loss fraction may be less than 10%.

We consider that these plasmas are enough to be tested for the isotope effect on the energy confinement. Figure 2 shows the stored plasma energy obtained by diamagnetic measurement, W_d, vs total heating power, P_h, for various I_p values (I_p=1MA; triangle, 2MA; circle and 3MA; square). The stored energy of D plasmas (open symbols) exceeds that of H plasmas (closed symbols) a little for almost the same condition. A comparison of energy confinement time, $\tau_E{}^{exp} = W_d/P_h$ with that predicted by ITER89P L-mode scaling, $\tau_E{}^{ITER89P}$ [2] is shown in Fig.3, where values of M_i being 1 for H plasma and 2 for D plasma are adopted for simplicity. The confinement time of JT-60U plasma for higher I_p regime becomes smaller compared with $\tau_E{}^{ITER89P}$. This tendency has been observed on the former JT-60 divertor experiments [4].

Though the energy confinement of D plasmas is generally better than that of H plasmas, it is seen in Fig.2 the reversal of W_d between for D and H plasmas for I_p = 1MA and $P_h \approx$ 6MW. These improved plasmas of hydrogen have higher value of internal inductance, l_i, compared with other discharges. The cause of the higher l_i value is the strong MHD activity during the initial phase of the discharge. When we take into account the effect of internal inductance on the energy confinement, we can correct the stored energy to be one divided by l_i, W_d/l_i [6] The corrected stored energy is demonstrated in Fig.4 as a function of P_h for various I_p values. The scattering in the figure becomes small, and the difference in the confinement time between D plasmas (open symbols) and H plasmas (closed symbols) can be clearly seen. Next, we evaluate the I_p dependence of W_d by using experimental data around P_h = 7MW, and obtain a rough relation, $W_d/l_i \propto I_p{}^{0.8}$, for both D and H plasmas. Figure 5 shows the quantity $W_d/(l_i I_p{}^{0.8})$ vs P_h. In the range of P_h < 13MW, the ratio of $W_d/(l_i I_p{}^{0.8})$ for D plasmas to that for H plasmas is found to be 1.2 - 1.3. By considering the ratio of effective mass, $M_{eff}{}^D/M_{eff}{}^H$, being about 1.3-1.5, the ion mass dependence of the confinement time can be estimated as $\tau_E \propto M_i{}^\alpha$ with α = 0.5 - 1.0, which is rather stronger dependence on M_i compared with former scaling laws; α = 0 - 0.5.

3. Summary and discussion

A comparative study of D and H plasma confinement has been performed in the JT-60U elongated divertor configuration. The confinement time, τ_E, in the JT-60U L-mode

plasmas is found to depend on the ion mass number, M_i, as well as on the plasma current, I_p, and internal inductance l_i : $\quad \tau_E \propto M_i^\alpha \, l_i \, I_p^{0.8}$ with $\alpha = 0.5 - 1.0$.

This result is the first one to show clearly the isotope dependence of L-mode confinement in large tokamak devices.

The isotope dependence obtained here is rather stronger compared with former scaling laws. The component of beam ions plays important role in the global energy confinement time. The slowing-down time of D beam ions against background electrons is larger by twice than that of H beam ion in the same electron density and electron temperature. Therefore, a certain part of the improvement in the global energy confinement for D plasmas compared with for H plasmas is due to the larger stored energy of D beam ions. A linear increase of W_d with P_h, especially for D plasmas, may also be explained by the effect of beam component. Separation of the global energy into the beam component, thermal ion component, and electron component is now in progress, and it will be clear what component is affected by the ion mass number.

References

[1]   JT-60 Team and M. Nagami, "Recent Results from JT-60," JAERI-M 87-205 (1988).

[2]   P. Yushmanov, T. Takizuka, K. Riedel, O. Kardaun, J. Cordey, S. Kaye, D. Post, Nucl. Fusion 30 (1990) 1999.

[3]   J. Christiansen, J. Cordey, O. Kardaun, K.Thomsen, Nucl. Fusion 31 (1991) 2117.

[4]   D. Post et al., "ITER Physics," ITER Documentation Series No.21 (IAEA, Vienna, 1991) p.31.

[5]   J. Christiansen et al., "A Global Energy Confinement H-mode Database for ITER," JET-P(91)46 (1991); to be published in Nucl. Fusion.

[6]   Y. Kamada et al., "Effect of Current Profile on Energy Confinement," ch. 3.5 in this review.
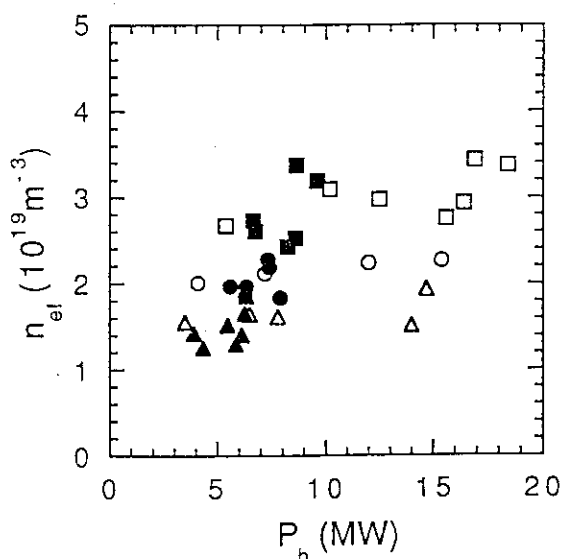
Fig.1 Line averaged electron density n_{el} vs total heating power P_h for $I_p=1MA$ (triangle), 2MA (circle), and 3MA (square). Values of n_{el} are almost the same for D (open) and H (closed) in almost the same condition.
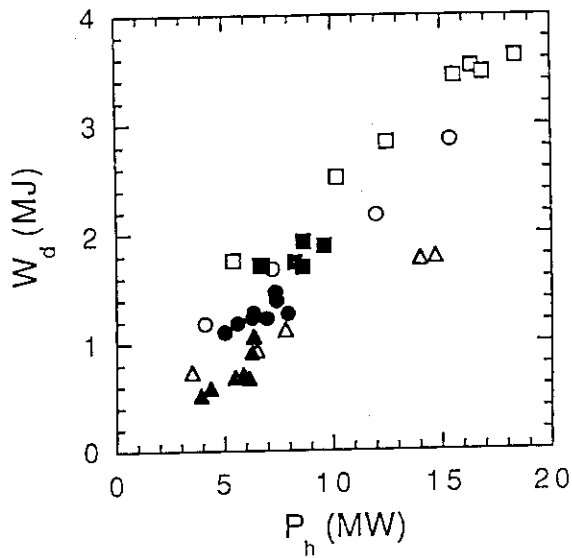
Fig.2 Stored plasma energy W_d vs P_h for I_p=1MA (triangle), 2MA (circle), and 3MA (square). D plasma confinement (open) is better a little than H (closed).
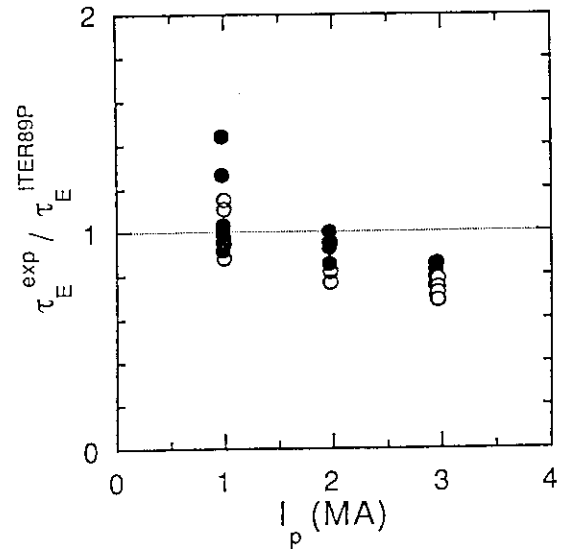
Fig.3 Comparison of τ_E^{exp} with $\tau_E^{ITER89P}$. The ratio becomes smaller than unity with the increase of I_p.
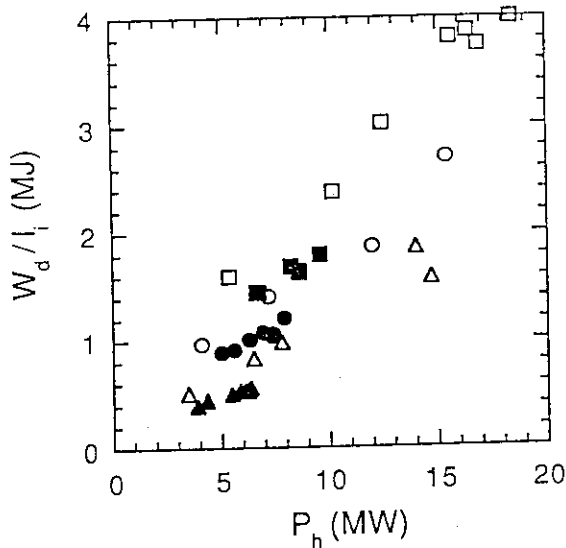
Fig.4 Stored plasma energy W_d divided by l_i vs P_h. Improvement of D plasma confinement compared with H plasma confinement is clearly seen.
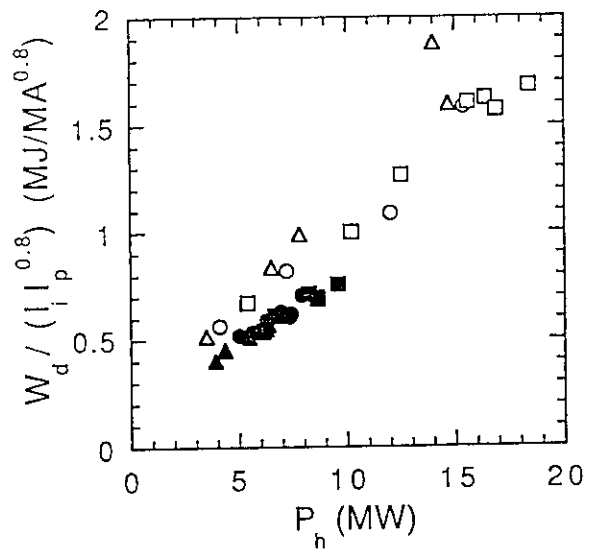
Fig.5 Stored plasma energy W_d divided by $(l_i\, I_p^{0.8})$ vs P_h.. Energy confinement time of D plasmas is larger by 20 - 30% than that of H plasmas.

3.5 Effect of Current Profile on Energy Confinement in JT-60U

Y.Kamada, T.Takizuka and M.Kikuchi

1. Introduction

Many empirical scalings have been reported to explain the energy confinement time τ_E[1,2] using global parameters such as I_p, B_t, P_{in}, R, a, n_e etc. Whereas, it is known that there exists effects of profiles of plasma parameters on τ_E such as n_e profiles [3,4]. While, about the current density profile j(r), in spite of its strong effect on MHD, the effects on τ_E has not been clarified yet. Because, in the tokamak system, there seems to be a strong restriction to keep T_e profile constant even if the heating profile or the n_e profile is changed and j(r) is closely connected with T_e profile. However, recent progress of current drive including the bootstrap current suggests that j(r) is controllable independent of $T_e(r)$. Practically, such control is essential in the reactors and the effect of j(r) on τ_E should be clarified. The peakedness of j(r) is expressed by internal inductance l_i. Some effects of li on τ_E was reported firstly in ref.[5] by the current ramp down experiment. This section expands the discussion into wide ranges of plasma parameters to generalize the understandings. Another important value is the safety factor to understand the effects of the toroidal current. In particular, τ_E in the law q region (q<3) is sometimes observed to be degraded compared to that in the high q region [6]. The explanation, however, has not been clear [7]. In Sec.6. we will discuss effects of l_i and q on MHD. By combining these studies about MHD and confinement, we can achieve the systematic understandings and, then, can separate the roles of macro and micro instabilities on tokamak confinement.

2. Effect of l_i on The Enhanced Confinement in High q Region

Figure 1 shows a high-q (q_{eff}~11) L-mode discharge with Ip=1MA, Bt=4T using hydrogen as working gas by the high elongation mode. Although I_p was ramped down in this discharge, the very high l_i (~1.9) in the initial phase was caused mainly by the instability at t~4s. In Fig.2, τ_E normalized by the ITER-89 power law [2] is platted against l_i where τ_E is given by τ_E=W/(P_{in}-dW/dt), P_{in}=P_{NB}+P_{OH}. In calculation of P_{NB} and P_{OH}, ~5% of re-ionization loss, shine through as a function of n_e and dl_i/dt were included. The effect of ripple loss was not included. We assumed A_i=1.2 in the calculation of τ_E^{ITER} based on the measured ratio of deuterium/hydrogen. The dependence of H-factor on l_i is clear and is almost proportional to l_i. The reason may be explained by two possibilities. The first one is the strength of poloidal field at a certain area where the total confinement is determined. In this case, the responsible area is relatively inner region of the plasma. The second possibility is magnetic shear. In this case, the key area is relatively outer region. The effect of sawtooth seems to be independent of these discussions. Because, as mentioned in Sec.6.3, the sawtooth mixing region increases with l_i, which should lead the inverse dependence of H-factor on l_i. (The effect of sawtooth is discussed below.) We also examined the effects of MHD modes with medium m/n and

observed that these modes dose not correlate with the l_i dependence. Therefore, this dependence may be caused by high m/n modes or micro turbulence.
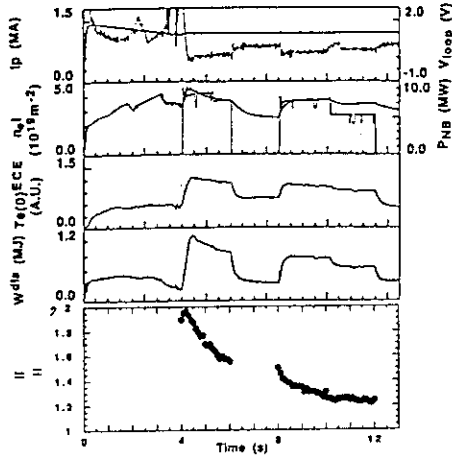
Fig.1: A high-q (q_{eff}~11) L-mode discharge(Ip=1MA, Bt=4T, hydrogen, high elongation mode.)
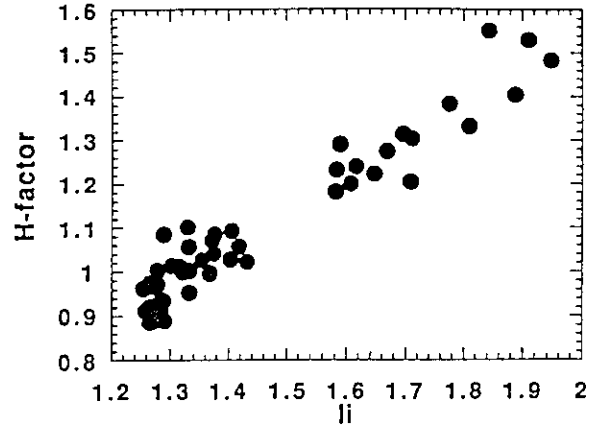
Fig.2:H-factor (τ_E normalized by τ_E ITER-89-P) versus l_i for the discharge given in Fig.1

3. Effect of l_i, q and Sawtooth on H-factor in Low q Region

This section uses L-mode data of deuterium discharges with Ip=3MA, Bt=2.5-4T, Vp=65-75m³, P_{NB}>7MW by high elongation mode. The calculation of H-factor was done by the same way as mentioned above and A_i was assumed to be 1.85. Figures 3(a) and (b) show behaviors of H-factor versus q_{eff} and l_i, respectively. H-factor seems to be degraded with decreasing q_{eff}. While, H-factor increases almost linearly with l_i. Figure 4 shows H/li dose not depend on q_{eff}. This new finding is important to understand the confinement degradation in the law-q region. Generally speaking, equilibrium l_i decreases with decreasing q_{eff} and this dependence is stronger in the lawer-q region (see Sec.2.2.1), then this dependence may be the reason of confinement degradation with decreasing q_{eff}.
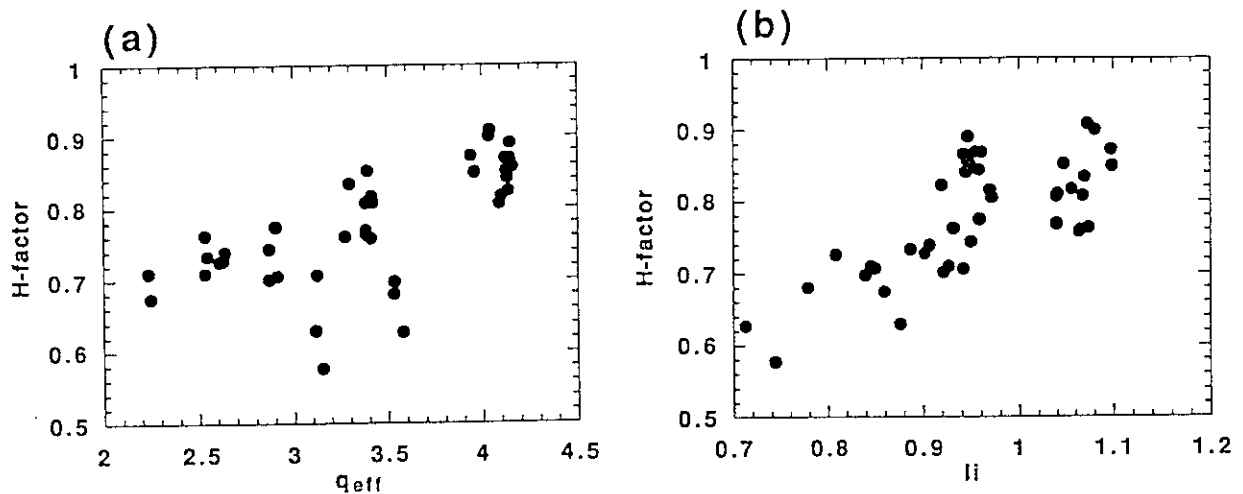
Fig.3:H-factor versus (a) q_{eff} and (b) l_i (Ip=3MA, Bt=2.5-4T, Vp=65-75m³, P_{NB}>7MW, high elongation mode).

Figure 5(a) shows H/l_i and the sawtooth period τ_{sw} in three regions of q_{eff}=2.2-2.6, 3.1-3.5 and 3.9-4.1. Figure 5(b) enlarges the region for q_{eff}=2.2-2.6. In all region, H/l_i increases with τ_{sw}. The dependence (slope) of H/l_i on τ_{sw} increases with decreasing q_{eff}. This tendency may be explained by the dependence of sawtooth mixing region on q_{eff} (see Sec.2.2.3). In Fig.6, τ_{sw} is normalized by τ_E. In case of q_{eff}=3.9-4.1, H/l_i saturates at τ_{sw}/τ_E ~1.5 because H/l_i is ~0.85 for sawtooth free discharges, where l_i is relatively small (Sec.2.2.1) and H-factor itself is small because of small l_i. However, H/l_i of these sawtooth free discharges are large and almost the same as that of long τ_{sw} discharges. The question is the behavior for q_{eff}=2.2-2.6. The slope of H/l_i against τ_{sw} is very steep (Fig.5) and H/l_i~0.9 is obtained even at τ_{sw}/τ_E~0.2. In the pellet injection experiment in JT-60 [8], the saturation of improved confinement occurred at τ_{sw}~τ_E for q_{eff}~2.3. Then, this steep slope is now an open question and may be treated more carefully. The causality of improvement in H/l_i and enhancement of τ_{sw} should be examined by active τ_{sw} control such as co-/counter-injection of NB and ICRH, because τ_{sw} is a strong function of T_e as given in Sec.2.2.3 and T_e is increased by improved confinement.

Figures 7(a) and (b) show that both H and H/l_i are independent of $\bar{n}_e$. However, H and H/l_i clearly depend on l_i (Fig.3(b)) and τ_{sw} (Fig.5), respectively. Therefore, it can be concluded that n_e itself does not affect the confinement improvement discussed here. However, the n_e profile may have some effects. Unfortunately, the effect of n_e profile is not clear in the present status.
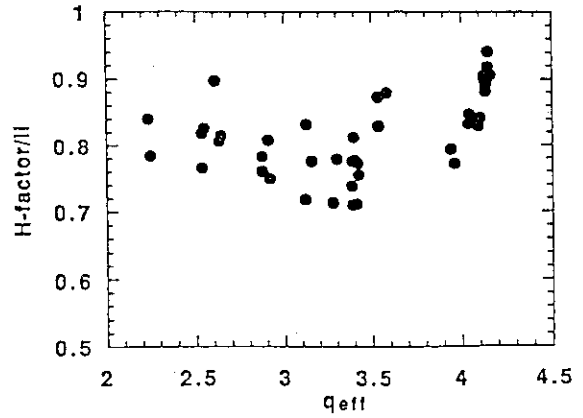
Fig.4: H/l_i versus q_{eff} for the same data as given in Fig.3.
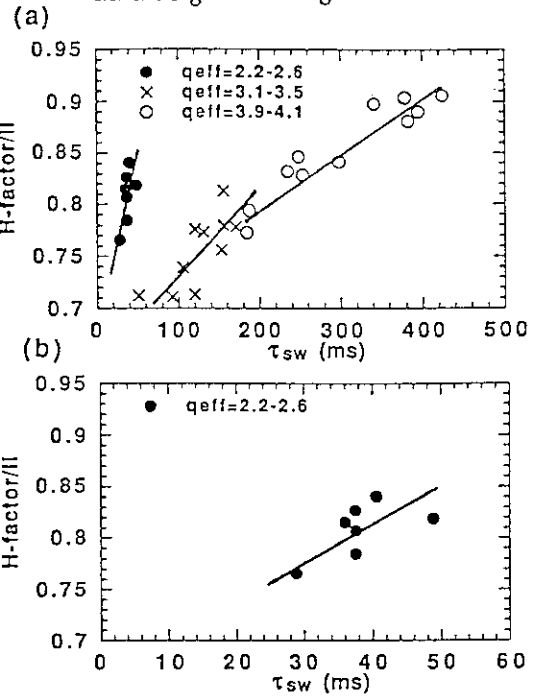
Fig.5: (a): H/l_i and τ_{sw} in three regions of q_{eff}=2.2-2.6, 3.1-3.5 and 3.9-4.1. (b) enlarges the region for q_{eff}=2.2-2.6.
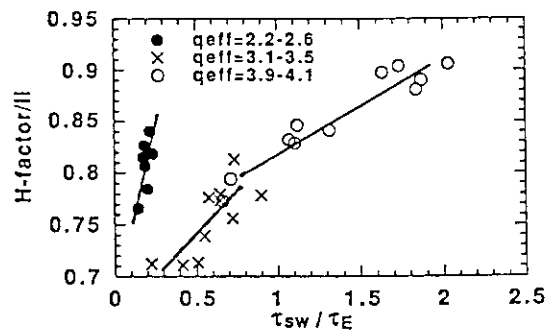
Fig.6: H/l_i and τ_{sw}/τ_E
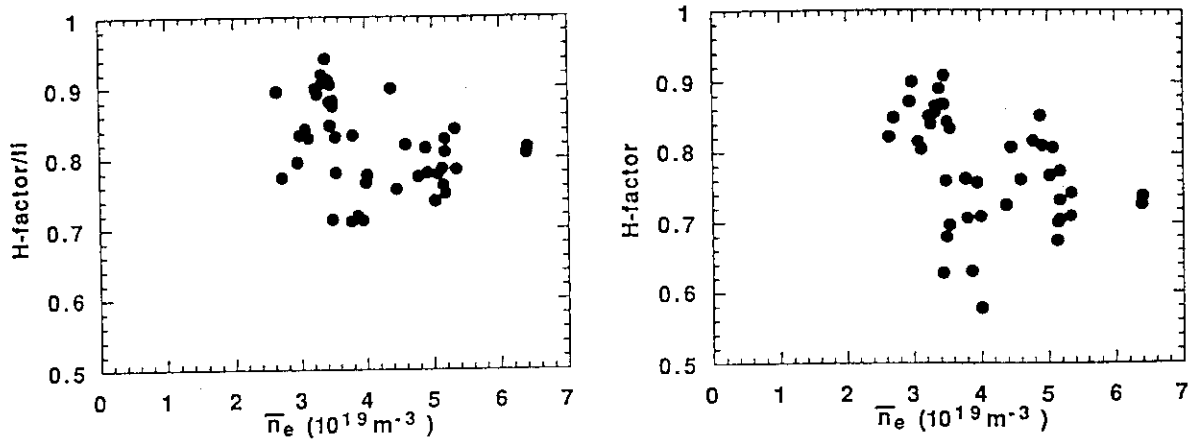
Fig.7:(a) H-factor and (b) H/l_i versus $\bar{n}_e$.

4. H-factor dependence on li in wide ranges of parameters including H-mode

In Figure 8, all data used above are summarized and H-mode data are added. In L-mode, it is confirmed that H-factor is almost proportional to l_i in the wide range of q_{eff}: q_{eff}=2-11.The maxima of H-factor in H-mode also seem to increase with l_i. However, large scatter of data is observed for H-mode. As Kamada et al. pointed out [9], l_i tends to decrease with H-factor in H-mode because of development of edge T_e pedestal. Therefore, the dependence of τ_E on l_i in H-mode should be discussed by separating the current profile in the central region and edge region.

At last, we should note ambiguities in our data set: These H-mode discharges are obtained by the standard configuration and the height of X-point is relatively small, then the ripple loss of injected NB particles are relatively larger than that of other data

Fig.8: H-factor and l_i

by the high elongation mode. Another ambiguity may be caused by the purity of working gas. Both hydrogen and deuterium inventory in the vacuum vessel should be taken into account for more detailed discussion.
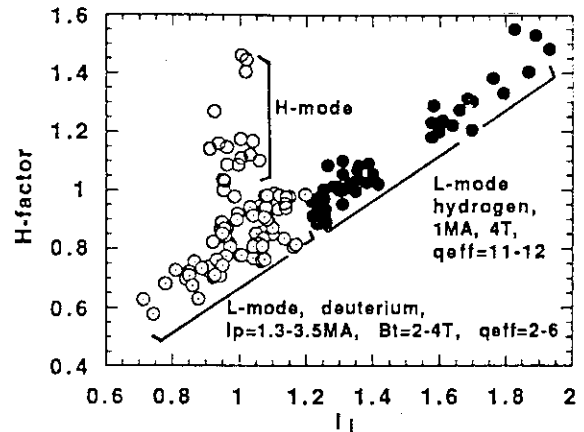
REFERENCES

[1] GOLDSTON, R.J., Plasma Phys. Controll. Fusion 26 (1984) 87.

[2] UCKAN, N.A., et al., in *Plasma Physics and Controlled Nuclear Fusion Research* (Proc.13th Int. Conf.,Washington, 1990) IAEA-CN-53/F-3-1.

[3] KAUFMANN,M., et al., in *Plasma Physics and Controlled Nuclear Fusion Research* (Proc.12th Int. Conf., Nice, 1988) Vol.I, IAEA Vienna (1989) 229.

[4] KAMADA Y., et al., Nucl Fusion 29 (1989) 1785.

[5] ZARNSTORFF, M.C., et al., in *Plasma Physics and Controlled Nuclear Fusion Research* Proc.13th Int. Conf., Washington, 1990, (IAEA, Vienna, 1991), Vol.I, p109.

[6] NAITO, O., et al., Nucl. Fusion 30 (1990) 195.

[7] JET Team presented by TANGA, A., in *Plasma Physics and Controlled Nuclear Fusion Research* Proc.13th Int. Conf., Washington, 1990, (IAEA, Vienna, 1991), Vol.I, p.

[8] KAMADA,Y., et al., Nucl Fusion 31 (1991) 23. see also KAMADA,Y., et al., in *Plasma Physics and Control. Nucl. Fusion Research* (Proc.13th Int.Conf.,Washington, 1990) Vol.I (IAEA, Vienna, 1991) p291.

[9] KAMADA, Y. et al., GA-A20611 General Atomics (1992), submitted to Nucl. Fusion.

3.6 H-mode Regime and ELMs

Y.Kamada, , R.Yoshino, H.Ninomiya, M.Shimada, M.Kikuchi, H.Yoshida, H.Nakamura

1. Introduction

This section treats the initial results of H-mode experiments in JT-60U where deuterium beams are injected into deuterium plasmas. Compared to previous JT-60 where hydrogen was used, the parameter region of H-mode was expanded and the clarification of key parameters for the L-H transition was advanced. In JT-60U, the inner wall of the vacuum vessel is fully covered by carbon tiles and the plasma configuration is open-type divertor. It is widely known that the wall condition (viz. minimization of Z_{eff} and reduction of recycling) is important to achieve high quality H-mode. For this purpose, we use TDC and GDC with D or He. About these effects, Sec.8 reports the details. Here the operation regime of H-mode discharges are summarized.

2. Operation Regime of H-mode

Figure 1 shows the I_p-B_t region of H-mode discharges. Many of H-mode discharges were carried out in relatively low q region (q_{eff}~3~5). In Fig.2, P_{NB} is plotted with B_t for H-mode discharges. The threshold power P_{NB}^{th}(MW) increases with B_t(T): P_{NB}^{th}=1.6~1.9$B_t^{1.5}$ or P_{NB}^{th} =4.5B_t-3, where P_{NB} is calculated including power lost by reionization in injection ports (~5%) and by shine through given by $0.6exp[-\bar{n}_e(10^{19}m^{-3})/1.44]$. It is known that P_{NB}^{th} decreases with reduction of Z_{eff}. In this sense, most of the discharges shown here was not carried out under optimized wall condition. In particular, for data with B_t~4T, radiation loss from the main plasma reached ~70% of the absorbed power. Relatively optimized wall condition was achieved for discharges with B_t~1.7~2T. Therefore, P_{NB}^{th} may possibly decrease by improved wall conditioning planned in the next year. In the present status, the minimum P_{NB}^{th} around Bt~2T is given by P_{NB}^{th}=1.6$B_t^{1.5}$ or P_{NB}^{th}=2.3B_t. In other tokamaks, it has been also reported that P_{NB}^{th} is a function of B_t [1]. In ASDEX, P_{NB}^{th}=0.36$B_t^{1.5}$ or P_{NB}^{th}=0.6B_t. In JET, P_{NB}^{th}=1.5$B_t^{1.5}$ or P_{NB}^{th}=2.4B_t. Figure 3 shows comparison of various tokamaks (JFT-2M, DIII, ASDEX, PDX, DIIID, JT-60 lower X-point, JT60U and JET), where P_{NB}^{th}/Bt$^{1.5}$ is plotted for (a)plasma volume, (b) surface area, (c) $2(ab/R)^{0.75}$[2] and (d) a^2/k [3], respectively. If direction of the ion
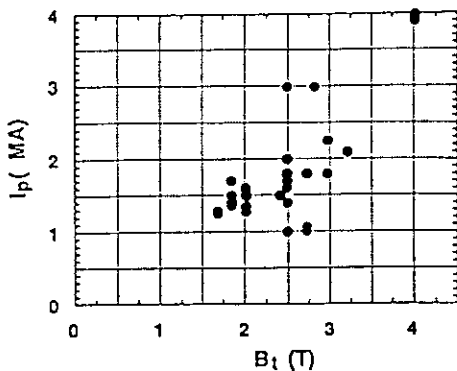
Fig.1: H-mode region on I_p-B_t space.
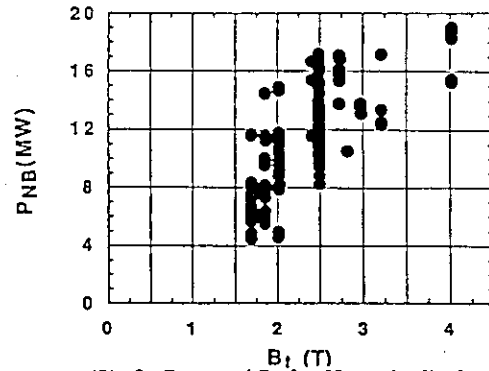
Fig.2: P_{NB} and B_t for H-mode discharges.
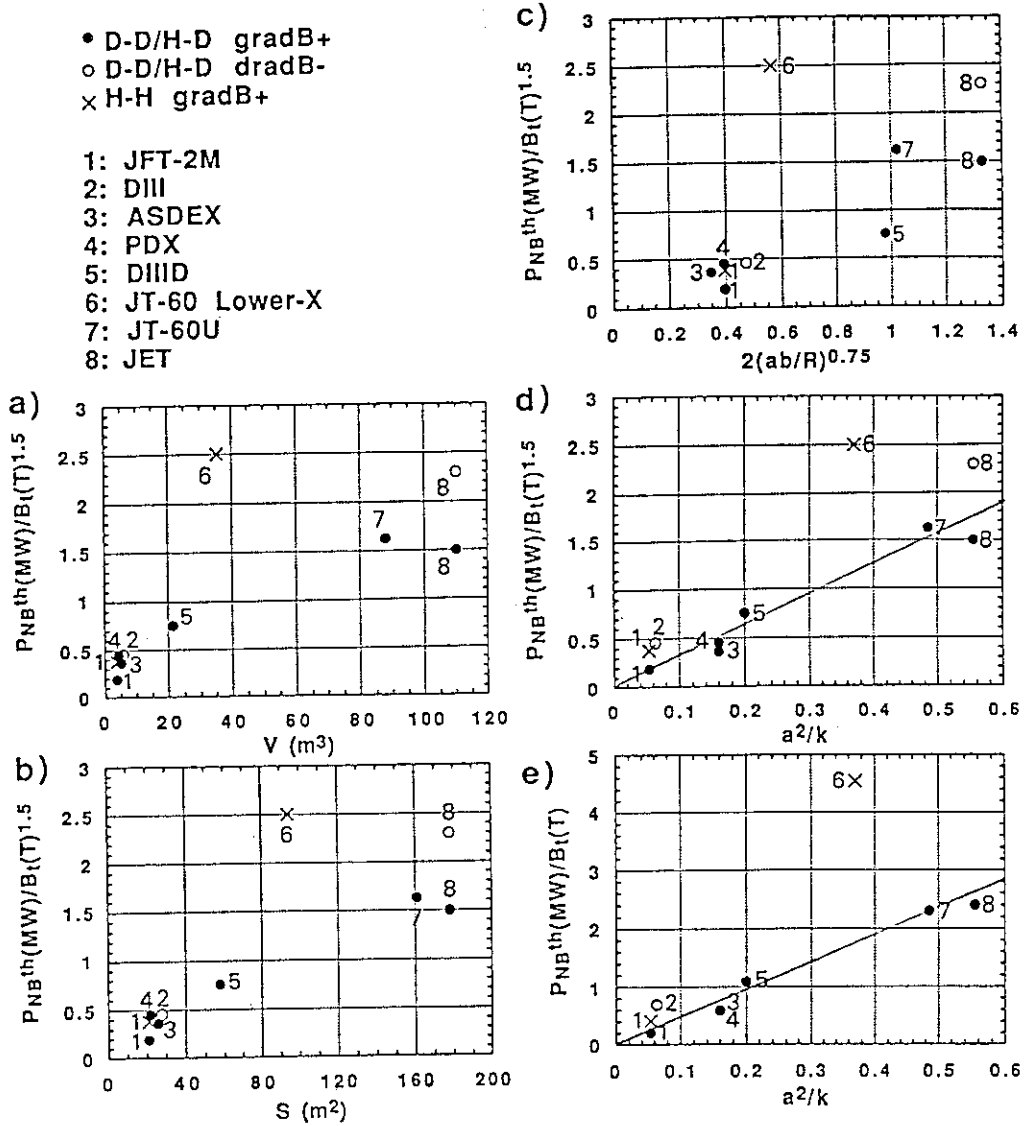
Fig.3: $P_{NB}{}^{th}(MW)/B_t{}^{1.5}$ and (a)plasma volume, (b) surface area, (c) $2(ab/R)^{0.75}$ and (d) a^2/k. In (e), $P_{NB}{}^{th}(MW)/B_t$ and a^2/k.

grad-B drift is not toward the X-point or if the working gas is hydrogen, $P_{NB}{}^{th}$ increases. Among these plots, a^2/k seems to be the best parameter to fit $P_{NB}{}^{th}/B_t{}^{1.5}$. In Fig.3(e), $P_{NB}{}^{th}/B_t$ is plotted for a^2/k, here the linearity is also clear. The dependence on B_t is important to design fusion reactors. Because, if $P_{NB}{}^{th}$ is proportional to $B_t{}^{1.5}$, the required $P_{NB}{}^{th}$ in SSTR is ~150MW. In turn, if $P_{NB}{}^{th}$ is proportional to B_t, the required value is 70MW. In case of the dependence shown in Fig.3(c), the required value is only 28MW.

In Figs.4(a) and (b), P_{NB} and the heating power density per particle $P_{NB}/(\bar{n}_e V)$ is plotted against q_{eff} for fixed B_t of 2.5T. It is observed that the threshold power and power density do not seem to depend on q_{eff}. Therefore, in the present status, the largest dependence of $P_{NB}{}^{th}$ is that on B_t. In Figs.4(c) and (d), P_{NB} is plotted for height of the X-point X_p and the inboard clearance del180, respectively. The quality of H-mode were observed to change with these values. In turn, $P_{NB}{}^{th}$ were independent of these values. Figure 5 shows the dependence of P_{NB} on l_i for 2.5T H-mode discharges for (a) Ip=1~3MA and (b) Ip=1.4-1.5MA. From these figures, P_{NB} to achieve
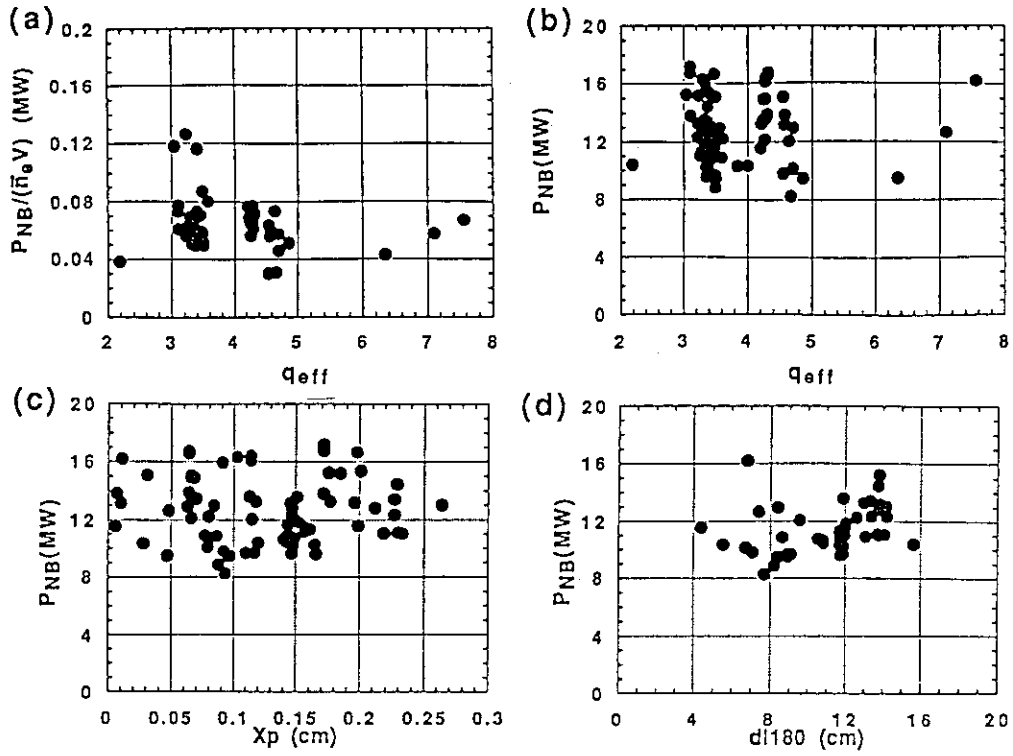
Fig.4: (a) P_{NB} and (b) $P_{NB}/(\bar{n}_e V)$ iversus q_{eff}. P_{NB} and (c)X_p and (d) del180. (B_t =2.5T)
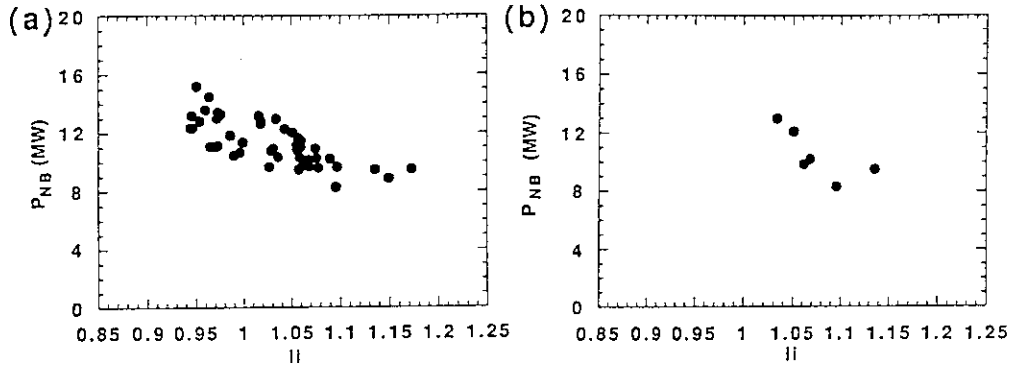
Fig.5: Dependence of P_{NB} on l_i for 2.5T H-mode discharges. (a) and (b) include data with
Ip=1~3MA and Ip=1.4-1.5MA.

H-mode seems to decrease with increasing l_i. However, the causality of this relationship is still unclear, because l_i usually tends to decrease with increasing P_{NB} by modification of T_e profiles.

3. ELM Activity

Behavior of ELM activity is a good measure of quality of H-mode. In our present status, effect of ELMs on confinement has not been systematically analyzed. Because in many discharges behavior of ELM activity was not steady enough to analyze the effects on confinement. Therefore, here, some aspects of ELMs are briefly reported. Figure 6 shows time evolution of plasma parameters in X_p-swing experiment. In this discharge, X_p was modulated between 14cm and 19cm with 2.5Hz. The H transition occurs when X_p decreases below ~16cm, then $\bar{n}_e$ and W_{dia}
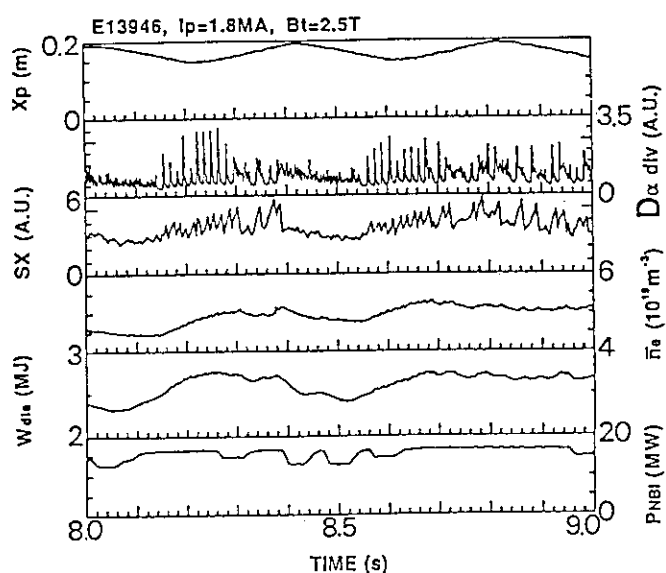
Fig.6:
Time evolution of plasma parameters in Xp-swing experiment.
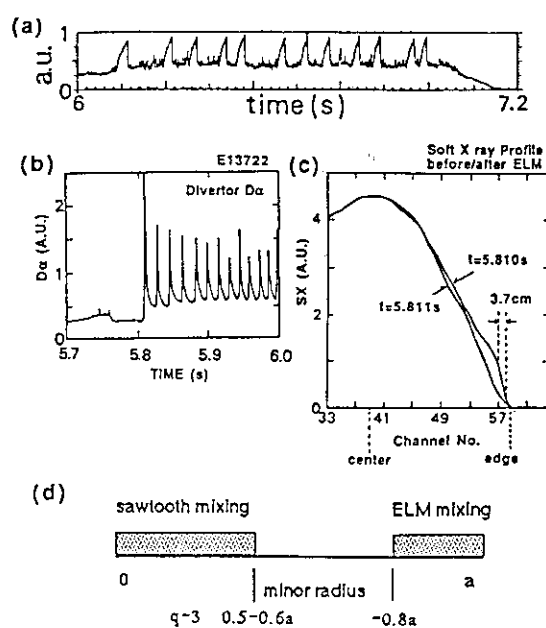
Fig.7: Behavior of ELM activity.

increase. However, clear dependence of P_{NB}^{th} on X_p is not observed (see Fig.4(c)), because at t~8.8s H-phase can be observed even when X_p~19cm. In this portion, quality of ELMs seems to be different from that observed at X_p~15cm (t~8.2s and 8.6s). The change in ELM quality by varying X_p is also still unclear. The change of recycling may be one reason or, as shown in Sec. 2.11, error field produced by the feeder of divertor coil may affect the H-mode quality.

Figure 7 shows behaviors of ELM activity. Figure 7(a) is the trace of soft X ray (SX) signal from the peripheral region, where each spike of SX intensity corresponds to H-phase. An interesting observation is that the amplitude of SX spike is almost constant if the period of H-phase changes, which suggests that the termination of H-phase is caused by a kind of limit of edge pressure. Figure 6(c) gives profiles of SX signal just before and after the termination of H-phase. The sudden change of the profile is localized only in the edge region (r>0.8a) and the width of the transport barrier is less than 3.7cm which is the minimum resolution of the PIN diode array. For low-q (q_{eff}<4) H-mode discharges, the effects of sawteeth and ELMs are particularly important (see Fig.7(d)), because about 70% of the plasma column is governed by sawteeth and ELMs, since the saturated mixing radius of sawtooth reaches about half the minor radius for q_{eff}=4 (see Sec. 6.3) and ELM region is about r>0.8a.

[1] 'Contributions to the 3rd Workshop on H-mode Physics' JET Joint Undertaking, Abington, 10-12 June 1991.

[2] GOLDSTON, R.J. at Workshop on H-mode, GA Technology, San Diego, U.S.A, 9-10 Nov.1987

[3] NAGAMI.M., see ' Review of JT-60 Experimental Results' JAERI-M 88-063 (1988) p178.

3.7 H-mode Characteristics at Low B_t Regime in JT-60U

H. Yoshida, O. Naito, Y. Kamada,

T. Takizuka, H. Nakamura, N. Asakura, S. Tsuji, M. Shimada and M. Kikuchi

1. Introduction

This paper describes a brief summary on H-mode characteristics in the initial experiments of JT-60U deuterium discharges with near-perpendicular NB (deuterium) injection. In these experiments, the ion ∇B drift was toward the X-point located near bottom of new vessel and divertor configuration was so called open type. The H-mode transition was observed in wide parameter ranges of I_p=1~4 MA, B_t=1.7~4 T, $\bar{n}_e$=(1~5) x 10^{19} m^{-3}, and P_{NB}=5~20 MW. The threshold power needed for H-mode transition in B_t~3 T was about 10~12 MW [1], which was reduced by ~20 % in comparison with hydrogen discharges previously performed in lower divertor configuration. Especially in low B_t regime of less than 3 T, the H-mode discharges were characterized by the long-duration H-mode accompanying ELM activity (ELMy H-mode) and the short-duration ELM free H-mode. The former was reproducible, but it was difficult to reproduce ELM free H-mode and to extend its duration time. The long-duration ELMy H-mode discharges showed the improvement of energy confinement of up to ~40 % compared with L-mode ones.

2. Typical H-mode discharges in low Bt regime

Figure 1 shows the difference of discharge characteristics between L-mode and ELMy H-mode. Although the experimental conditions for both discharges were similar in magnetic configuration and operated parameters of I_p=1.8 MA and B_t=2.5 T, the stored energy achieved in ELMy H-mode was higher by around 50 % than in L-mode. The edge electron temperature (r~0.93a) measured by Thomson scattering was 0.9~1.3 keV (P_{abs}=16~17 MW) during H-mode, while 0.5~0.7 keV (P_{abs}=13~15 MW) in L-mode.

The NB power dependence of ELMy H-mode is time-evolutionally illustrated in Fig. 2, where the H-mode transition started with grassy ELM in lower power level (7.5 MW), and giant ELM occurred in higher one (12.7 MW). In the same figure, ELM free H-modes were frequently observed above medium power level (9.2 MW). The maximum duration time of ELM free H-mode obtained with P_{NB}=9 MW was about 80 msec as seen in Fig.3. On the other hand, long-duration ELMy H-mode lasted almost during NB pulse (~1.8 sec) with short intervals of ELMs ($\geq$5 msec) as shown in Fig. 4, where stored energy, electron density and radiation power became near steady state. In the next section, the properties of long-duration ELMy H-mode are discussed from a viewpoint of energy confinement.

3. Energy confinement of long-duration ELMy H-mode

It is well known that H-mode discharges with ELMs reach steady state at a cost of modestly reducing in H-mode energy confinement. In JT-60U, the energy confinement of ELMy H-mode discharges in near steady state was about 20 % degraded compared with that in transient phase. However, as shown in Fig. 5, it was 20 to 40 % improved in comparison with that of L-mode discharges.

For long-duration ELMy H-mode discharges of 1.3 MA and 1.7 T, and also 1.4 MA and 1.85 T, stored energy and energy confinement time are plotted as a function of electron density in Fig. 6 (a) and (b), respectively. In this plot, we selected data carefully : R_p=3.24~3.25 m, a_p=0.78~0.80 m, κ=1.65~1.68, P_{ctr}/P_{tot} (ratio of counter-injection power to total NB power)=0.20~0.21, P_{abs}=8.6±0.2 MW. It seems that with some scatters stored energy as well as confinement time decrease slightly with an increase in density. Figures 7 and 8 show the P_{ctr}/P_{tot} dependence of stored energy, indicating that stored energy decreases with the fraction of counter-injection power. It is noted that in Fig. 7 the reduction of sawteeth frequency and Soft X-ray signal intensity occurred after NB injection with counter component. Taking account of near-perpendicular injection angle and off-axis beam path-line, Figs. 6, 7 and 8 may suggest that the ripple loss of fast ions affects energy confinement especially in higher density. Another possibility is the effect of current profile on energy confinement [2]. In the L-mode scaling study of JT-60U, the linear dependence of stored energy and confinement time on internal inductance, li, was revealed [2,3]. In the same data set as in Fig. 6, current profile became slightly flattened in higher density region : li varied ~1.0 to ~0.9. For this problem of the energy confinement degradation with the density or the fraction of counter NB component, more systematic and precise investigation is needed to obtain the conclusion.

4. Summary

At low Bt operation in JT-60U the feature of H-mode was characterized by long-duration ELMy H-mode and short-duration ELM free H-mode. In long-duration ELMy H-mode discharges the edge electron temperature exceeded 0.9 keV with P_{abs}=15~16 MW, and the energy confinement was improved 20 to 40 % compared with L-mode discharges. The ripple loss effect or the current profile effect seems to be a possible cause of the decrease in energy confinement with higher density or with fraction of counter injection.

References

[1] Y. Kamada et al., "H-mode Regime and ELMs", in this review.

[2] Y. Kamada et al., "Effect of Current Profile on Energy Confinement", in this review.

[3] T. Takizuka et al., "Comparative Study of D and H Plasma Confinement in JT-60U", in this review.

(a) L-mode [E13956]

(b) H-mode [E13958]
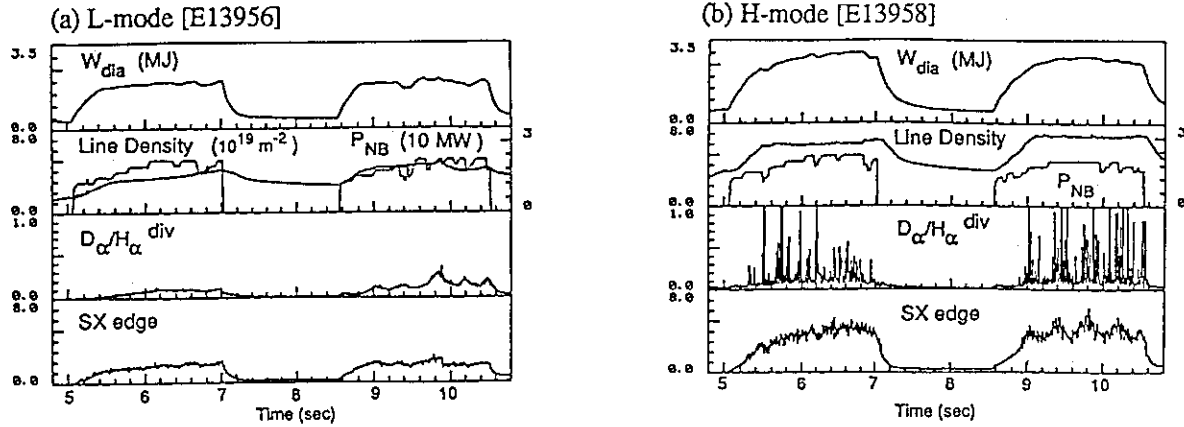
Fig. 1   Comparison of discharge characteristics between (a) L-mode and (b) ELMy H-mode. For similar conditions of Ip=1.8 MA and Bt=2.5 T, achieved stored energy in ELMy H-mode was ~50 % higher than in L-mode.

E13871 (Ip=1.3 MA, Bt=1.7 T)
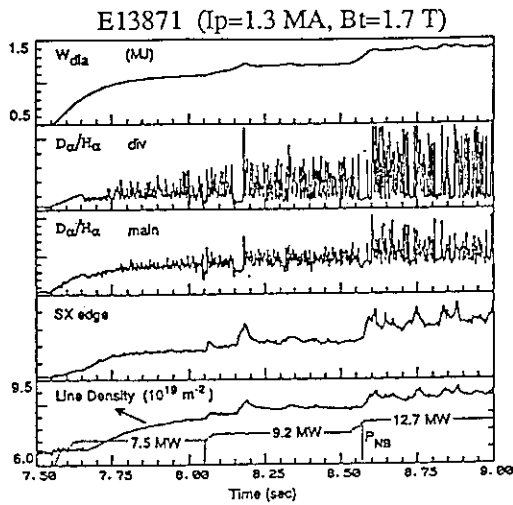
Fig. 2 NB power dependence of ELMy H-mode

E13871 (Ip=1.3 MA, Bt=1.7 T)
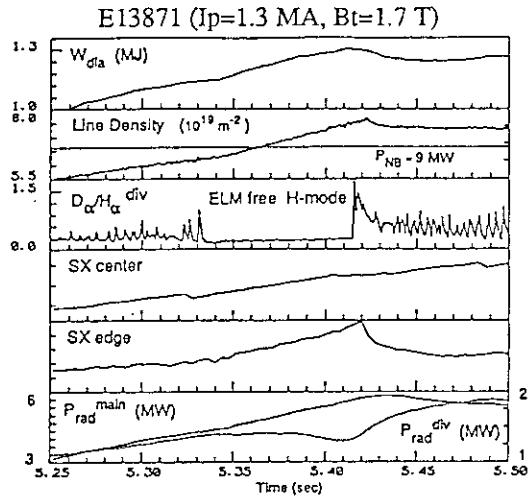
Fig. 3 Typical discharge of ELM free H-mode
Duration time of ELM free H-mode was about 80 msec.

E13951 (Ip=1.8 MA, Bt=2.5 T)
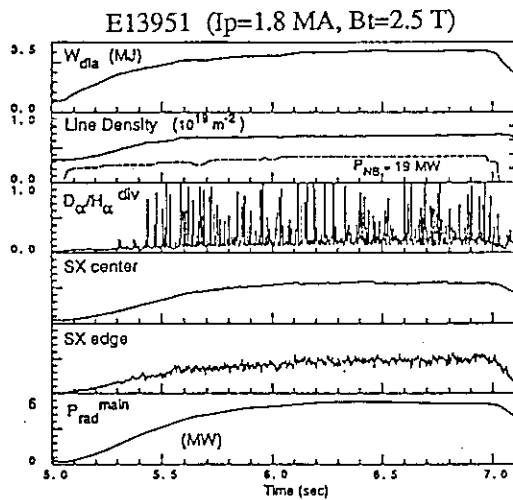
Fig. 4 Typical discharge of long-duration ELMy H-mode
ELMy H-mode lasted almost during NB pulse and reached near steady state.
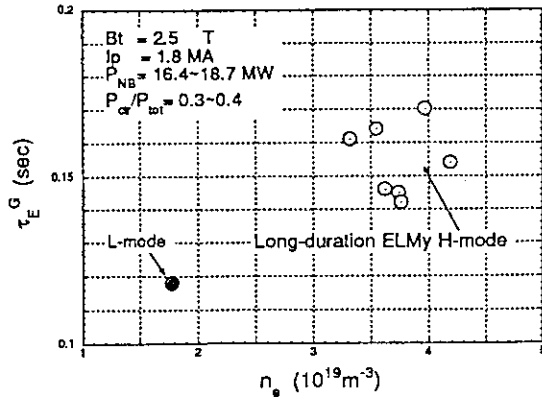
Fig. 5 Comparison of energy confinement time between
L-mode and long-duration ELMy H-mode
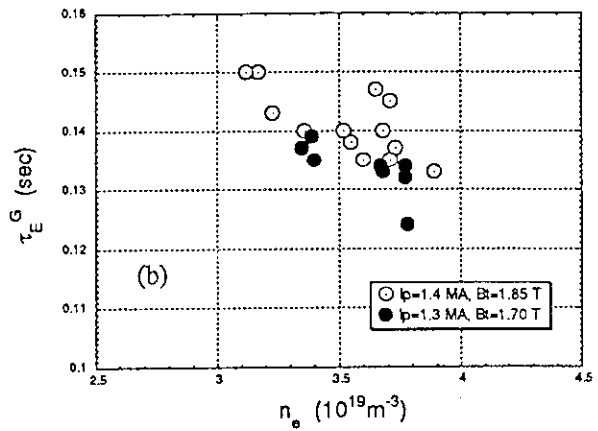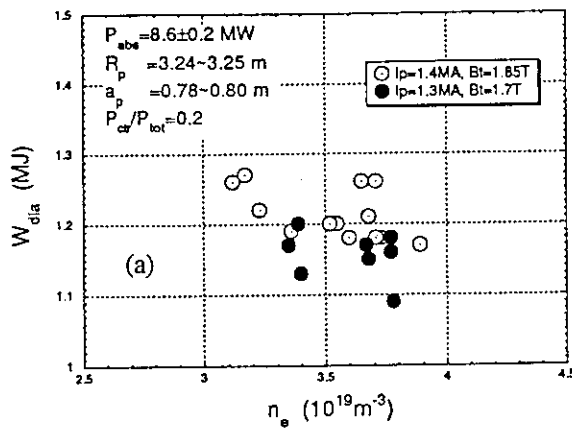
Fig. 6 Density dependence of (a) stored energy and (b) energy confinement time. Data set was carefully selected : Pabs=8.6±0.2 MW, Rp=3.24~3.25 m, ap=0.78~0.80 m, and Pctr/Ptot (ratio of counter-injection power to total NB power)=0.2.

E13927 (Ip=1.3 MA, Bt=1.7 T)
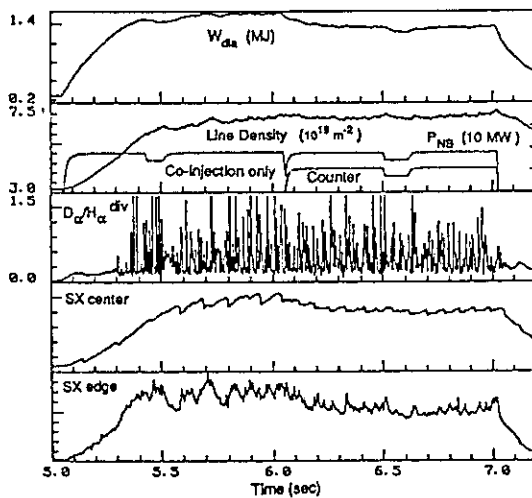
Fig. 7 Discharge characteristics of long-duration ELMy H-mode with and without counter-injection power keeping total NB power of 9 MW constant
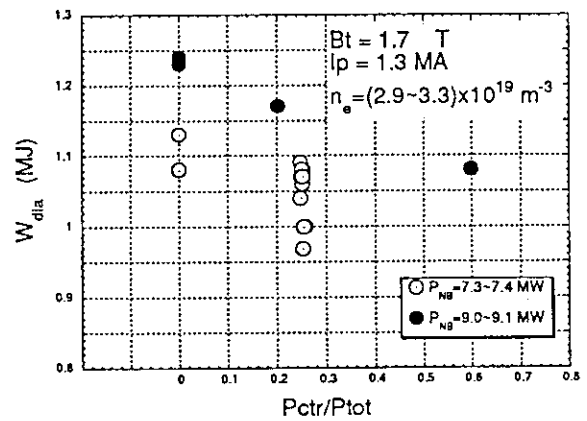
Fig. 8 Fractional counter power dependence of stored energy

3.8 Radiation Loss in NB Heating Discharges in JT-60U

N.Hosogane

1. Introduction

The global characteristics of the radiation loss in the NB heating discharges is presented. The investigation is concentrated on the L-mode NB heated discharges with standard configuration and high elongation configuration with large volume($75m^3$), and on the high T_i NB heating discharges performed in the high elongation configuration with small volume($50m^3$).

2. Global Characteristics of Radiation Loss in NB heating Plasmas
2.1 Standard Configuration(k=1.4)

Figure 1 shows the total, main and divertor radiation loss power plotted as a function of the absorbed heating power. The parameter range is plasma current of 1.3-3.5 MA, toroidal magnetic field of 2-4T and NB heating power of 1.5-15MW. It is seen that the total radiation loss increases with the absorbed heating power in the range of 50-80% of it. The main radiation is less than 20%.

Figure 2 shows the total, main and divertor radiation loss plotted as a function of electron density with parameters of toroidal magnetic field and plasma current. To see the effects of these parameters, the data plotted are limited to the discharges with toroidal magnetic field of 2.5-4T and constant plasma current of 2 MA and the discharges with plasma current of 2-3.3 MA and constant toroidal magnetic field of 4T. Also, the radiation loss observed seems to depend on the height of the X-point. As the height of X-point becomes low, the radiation loss tends to be small. So that, the height of the X-point in this plot is limited to the range of 8-16 cm. It is seen in this figure that both the main and divertor radiation losses increase with electron density through the divertor function. Moreover, it is found that the divertor radiation loss becomes large as the safety factor becomes large.

2.2 High Elongation Configuration(k=1.7) with plasma volume of 50 m^3

The radiation loss measured in the high Ti experiment with small plasma volume of 48-54 m^3 is investigated. The experimental range is plasma current of 1-2 MA, toroidal magnetic field of 4T and NB heating power of 13-22 MW.

Figures 3 shows the radiation loss power as a function of absorbed power. It is seen that the main radiation loss power is 25-45% of the absorbed power and the total radiation loss power is 50-90% of it. However, the radiation loss in the scrape-off layer, which is defined by the difference of signals between the upper and lower bolometer arrays as explained in ref.1), spreads over the lower half of the plasma column for these small plasmas unlike the other configurations. So that, it should be noticed that the main radiation power may be larger than those plotted, although the total radiation loss power remains unchanged.

Figure 4 shows the total, main and divertor radiation losses for the absorbed power as a function of electron density. It is found that both the main and divertor radiation losses increase with the electron density. For a series of 1.1 MA discharges, the main and divertor radiation losses are 35-45% and 20-40%, respectively. The large increase in divertor radiation loss is considered to be due to the non-linear rise in divertor electron density through the divertor function. The maximum neutron yield was attained

in the low density regime of 1.1 MA discharges. The main and divertor radiation losses in this discharge are 35% and 20%, respectively.

2.3 High Elongation Configuration(k=1.7) with plasma volume of 75 m³

The radiation loss measured in the L-mode discharges with plasma volume of 73-80 m³ is investigated. The parameter range is plasma current of 1-4 MA, toroidal magnetic field of 4T and NB heating power of 4-21 MW. The height of the X-point is 6-12 cm.

Figure 5 shows the radiation loss power as a function of absorbed power. The fraction of the total radiation loss power is 50-80%, which is the same level as the discharges with standard configurations. However, compared with those discharges, the main radiation loss power tends to increase with the plasma current.

Figure 6 show the main and divertor radiation loss for the absorbed power as a function of electron density. The main radiation loss increases up to about 50% for 4 MA discharges. Since the change in electron density is accompanied by the change in plasma current in this plot, the main radiation loss seems to strongly increase with electron density. However, compared with the results for the case of the standard configuration, it is clear that the effect of the plasma current is dominant for the increase in the main radiation loss. In contrast with the main radiation loss, the divertor radiation loss decreases with the electron density. The detail is discussed in the next section.

3. Discussion

It is found in sections 2.1 and 2.2 that both radiation losses depend on the plasma current and toroidal magnetic field. So, the radiation losses is expected to be related with a parameter $n_e R q_{eff}$ as found in ohmic discharges[1]. Here, R is major radius and q_{eff} is effective safety factor. Figures 7(a) and (b) show the radiation losses plotted as a function of $n_e R q_{eff}$ for the discharges with standard and high elongation configurations, respectively. From these figures, it is found that the radiation losses may be expressed by some functions of $n_e R q_{eff}$, irrespective of different plasma current and toroidal magnetic field. It is interesting to note that there is the same characteristics as ohmic discharges although the heating power in the NB heating discharges is given irrespective of the safety factor unlike the ohmic discharges. The total radiation losses are almost the same level for both discharges. However, it is noted that the electron density is measured at the different positions for these different configurations through the U2 port. It is necessary to use the electron density commonly defined for the further study.

The above results provide the method for comparing the radiation losses of the discharges with different configurations. Figures 8(a) and (b) show the main and divertor radiation losses as a function of $n_e R q_{eff}$ for the high elongation configurations and the standard configurations. The plot for the main radiation loss (Fig.8(a)) indicates that the main radiation loss for the high elongation configurations is the same level as those for the standard configurations for the 1 MA and 2 MA discharges, but increases as the plasma current increases above 3 MA. On the other hand, the divertor radiation loss, which seems to decrease with the electron density in Fig.6, is found to obey the parameter $n_e R q_{eff}$ like the case of the standard configurations although it is small. The result that the divertor radiation loss is small may be due to the increase in main radiation loss. The reason that the main radiation for the high elongation discharges with above 3 MA increases is under investigation.

4. Summary

The global characteristics of the radiation loss is summarized for three types of NB heating discharges with standard configurations, high elongations with volume of 50 m^3 and 75 m^3. The same parameter dependence $n_e R q_{eff}$ as found in ohmic discharges is found for these NB heating discharges. The result suggests that the connection length is an important role for understanding the characteristics of the radiation losses. However, the main radiation loss in the high elongation configuration with volume of 75 m^3 increases beyond the level evaluated from the $n_e R q_{eff}$ dependence as the plasma current increases above 3 MA.

1) N.Hosogane, 'Radiation Loss in Ohmic Discharges in JT-60U', in this review.
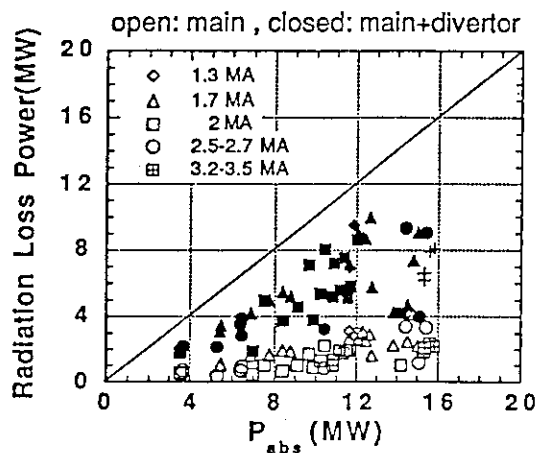
Fig.1 Radiation loss power as a function of the absorbed power in the NB heating discharges with standard configurations.
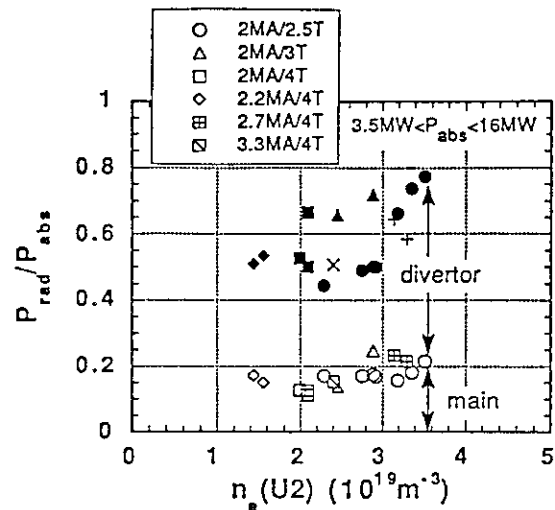
Fig.2 Radiation loss as a function of electron density in the NB heating discharges with standard configurations.
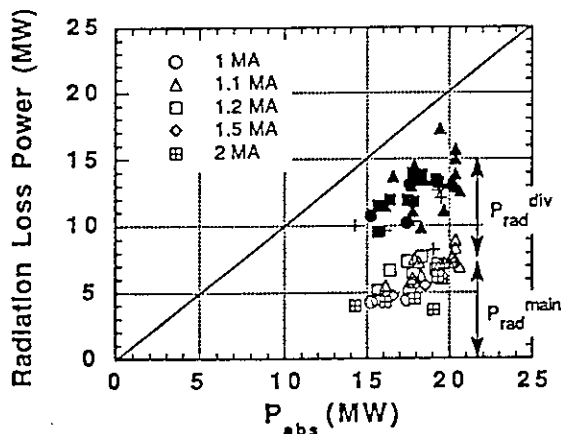
Fig.3 Radiation loss power as a function of the absorbed power in the NB heating discharges with high elongation configurations with volume of 50 m^3.
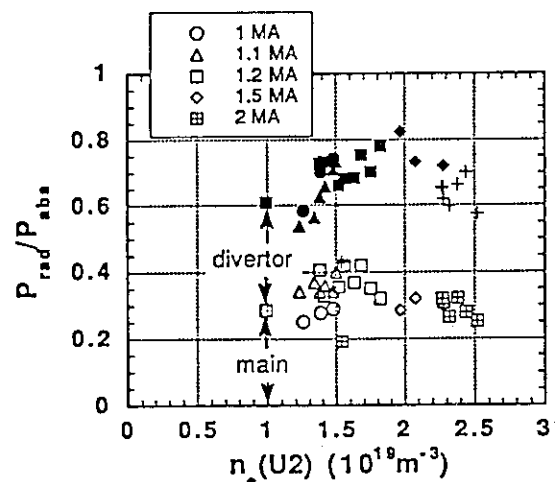
Fig.4 Radiation loss as a function of electron density in the NB heating discharges with high elongation configurations with volume of 50 m^3.
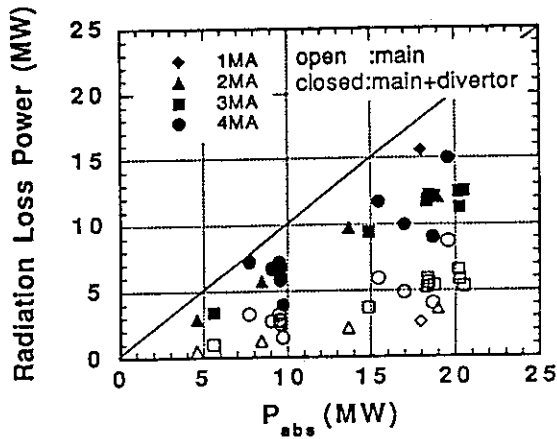
Fig.5 Radiation loss power as a function of the absorbed power in the NB heating discharges with high elongation configurations with volume of 75 m³.
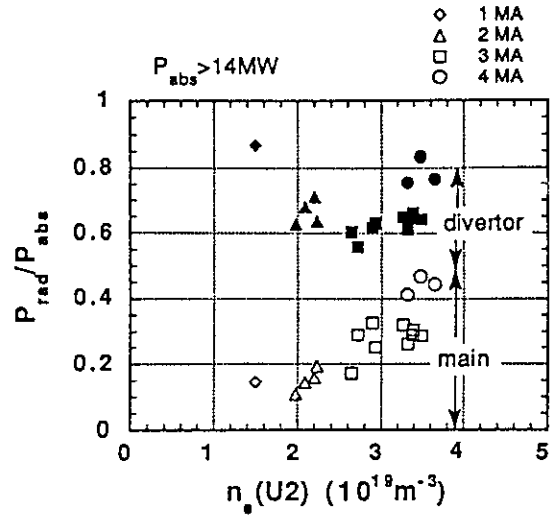
Fig.6 Radiation loss as a function of electron density in the NB heating discharges with high elongation configurations with volume of 75m³.
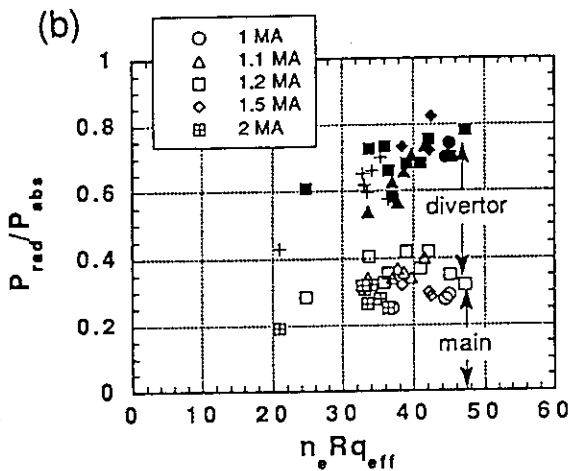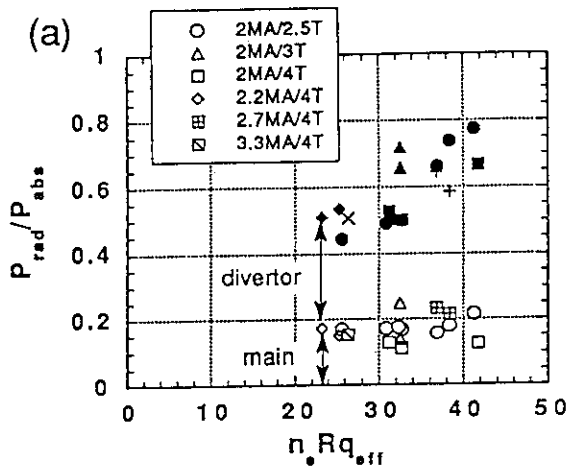
Fig.7 Radiation loss as a function of $n_e R q_{eff}$ in the NB heating discharges
(a) standard configurations
(b) high elongation configurations with volume of 50 m³.
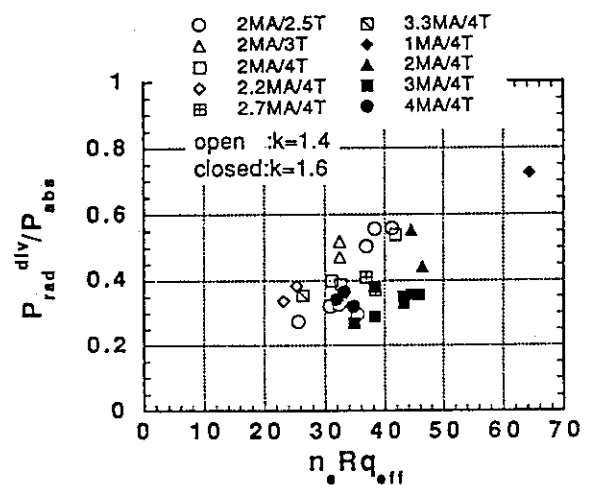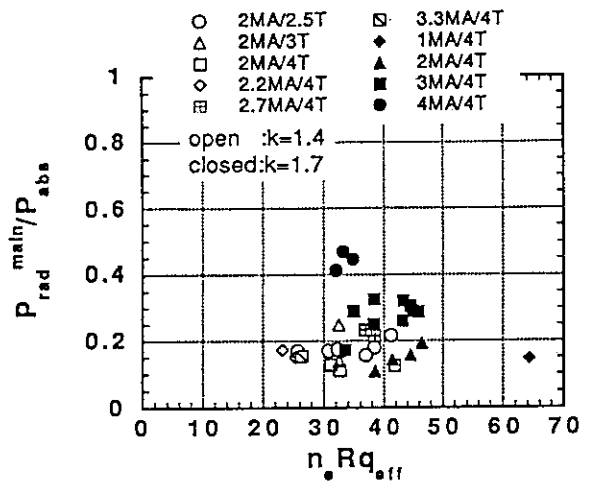
Fig.8 Comparison of the main and divertor radiation losses plotted as a function of $n_e R q_{eff}$ between the high elongation and standard configurations.

3.9 Characteristics of Toroidal Rotation in JT-60U Plasma

Y. Koide, N. Asakura and A. Sakasai

In JT-60 CXRS measurement [1], the basis of rotation velocity is determined by the assumption that line emission from CVI ion is not Doppler-shifted in the period of plasma initiation, and the detector is slightly affected by the leakage magnetic field from the tokamak. The ambiguity of up to 2×10^4 m/sec is expected due to these effects. In JT-60U, a pair of tangential array, which views the opposite direction, and a new type of detector , which is free from the leakage magnetic field. The typical ambiguity is reduced within 2×10^3 m/sec (see section 6.2.1). The number of spatial channel is increased up to 20. In this paper, the characteristics of V_t in JT-60U plasma are described.

Figure 1 shows the $V_t(r)$ with unidirectly injected NBI, where I_p=2 MA, B_t=4 T, $\bar{n_e}$=1.6×10^{19} m^{-3}. Here the positive sign of ordinate means the co-directed rotation. In the case of counter injection (shown with closed circles), the observed direction of $V_t(r)$ qualitatively agrees with the expected one from the direction of the momentum input. However plasma doesn't rotate in the co-direction except in the central region even though only co-directed NBI of the same power is injected (shown with open circles). So we carried out the systematic investigation of $V_t(r)$ on injected momentum input. Experiment has been done with the following conditions : I_p=2 MA, B_t=4 T, $\bar{n_e}$=1-1.8×10^{19} m^{-3} , H^0 beam into H$^+$ plasma. The results are shown in Fig.2, where abscissa is net NBI power and the ordinate is V_t; Fig.2(a) is for the central region and Fig.2(b) for the region at around a/2; NBI system of JT-60U is characterized into four groups from the viewpoint of injection angle i.e. up/down and co/ctr, which is discriminated by different symbols in this figure. It should be noted that V_t is ctr-directed when net NBI power is zero, and V_t doesn't readily rotate in co-direction, whereas it directed easily to ctr-direction. This character remains if I_p and B_t are inverted as shown in Fig.3. The one candidate to drive this counter-directed rotation is the negative potential due to the ambipolar electric field which originates from the ripple-loss of ions. There is some indirect evidence in favor of this view : Ohmic rotation is ~1×10^4 m/sec in ctr-direction, which is measured with short pulse (100 msec) of diagnostic NBI only, but it is not so large as that inferred when the net power is zero in Fig.2 and 3 (2-4×10^4 m/sec) : Detail time evolution of V_t just after the NBI injection (co : ctr =3 : 2) shows that ctr-rotation in the edge region first occurs. However it is doubtful whether ripple loss mechanism can fully explain this peculiar rotation profile because 1) this tendency is observed even with as a small plasma as that in JT-60 where ctr-rotation is not recognized, 2) V_t in the central region seems to be biased in the ctr-direction, where the ripple loss is below 0.01 %. So there might be some unknown

mechanisms e.g. charge separation, which occurs just after the ionization of neutral beam due to the difference in gyro radii of ion and electron. Tangential NBI, which will be operated in July 1992, will enable us to investigate systematically the effect of ripple loss.

Next we compare the V_t measured by CXRS with the inferred one from the frequency of MHD mode oscillation f^{MHD}. If the fluid flow and MHD mode are perfectly frozen to each other and the toroidal mode number equal unity, the following relation is satisfied,

$$V_t = 2\pi R f^{MHD} \quad (1)$$

, where R is the major radius. We must be careful about the former assumption because ions are allowed to flow freely along the magnetic lines of force, whereas the MHD mode is frozen to the magnetic field. Nevertheless, the estimate of poloidal rotation velocity V_p from the difference of the two velocity of measured and estimated one by eq.(1) is meaningful from the viewpoint of checking of the validity of neoclassical theory. Figure 4 shows such a comparison for a discharge free from sawtooth oscillations with $I_p=1$ MA, $B_t=4$ T, $q_{eff}=14.2$, $\overline{n_e} = 2\times10^{19}$ m^{-3}. Odd mode oscillation with f^{MHD} is observed around $r/a=0.14$. Its frequency changes from 4.45 to 2.5 kHz during t=6.8-7.8 sec and the velocity estimated from eq.(1) is plotted with closed circles, where only the absolute value of velocity is considered because the direction of mode rotation is not resolved in our soft X-ray data. V_t at the same radius is plotted in the same figure (open circles). V_t is 2 times larger than that estimated from eq.(1). The two-fold difference in velocity is not so small but this difference can be supplemented by the rotation in the ion-diamagnetic direction with the frequency f_p of 2 kHz. V_p estimated from the following relation, where m=1 is assumed, is only 3 km/sec,

$$V_p = 2\pi r f_p/m \quad (2)$$

, where m is the mode number of poloidal rotation. The similar result is obtained with a discharge with sawtooth and m=1 oscillations and is shown in Fig.5, where $I_p=3$ MA, $B_t=4$ T, $q_{eff}=4.1$, $\overline{n_e} = 3\times10^{19}$ m^{-3}. Investigation to check whether the above poloidal rotation is consistent with the neoclassical theory is in progress.

[1] Y. Koide, et al, in Review of JT-60 Experimental Results from June to October,1988, JAERI-M 89-033 (1989).

E14248, t=6.5 sec E14269, t=6.8 sec
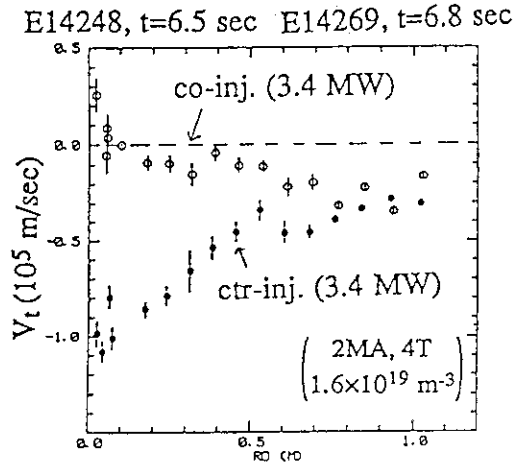
FIG. 1 $V_t(r)$ in co- and ctr-injections.
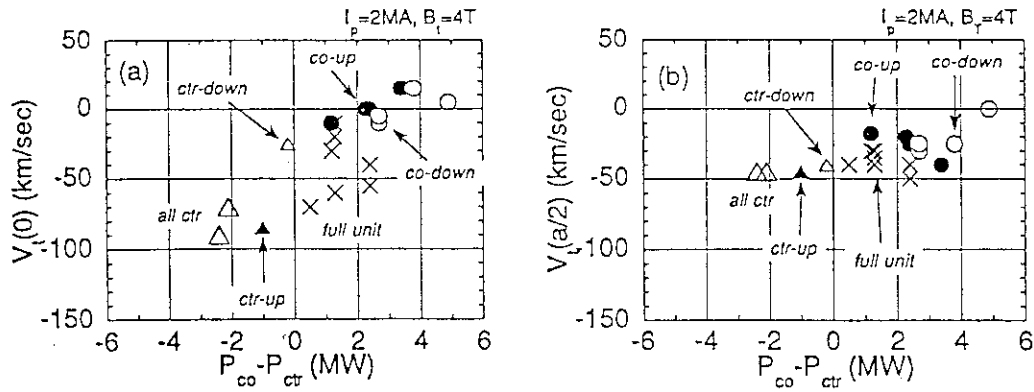
FIG. 2 Power dependence of V_t ($B_t, I_p > 0$).
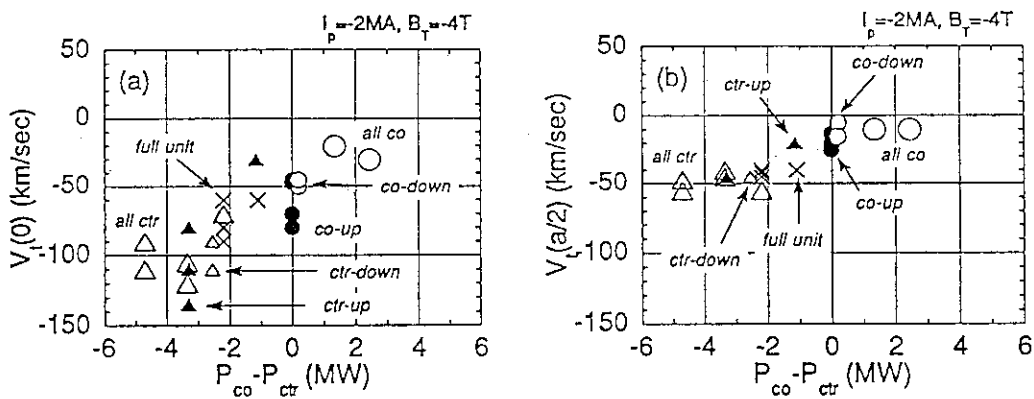
FIG. 3 Power dependence of V_t ($B_t, I_p < 0$).
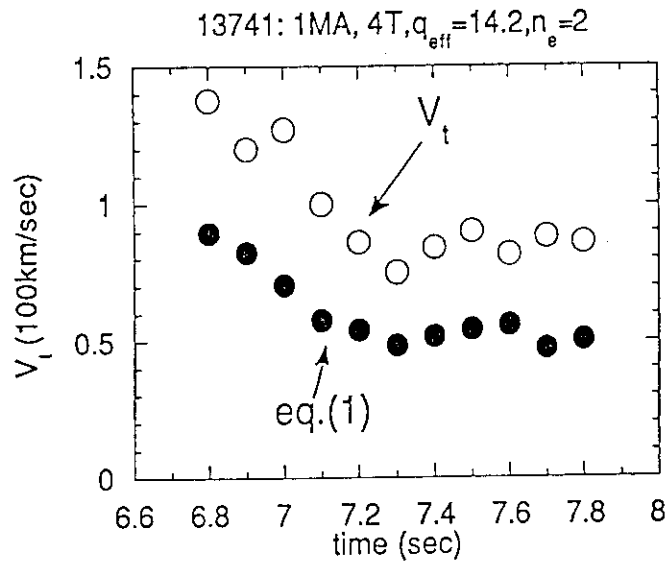
13741: 1MA, 4T,q_{eff}=14.2,n_e=2

FIG. 4 Comparison of V_t and one deduced from
the frequency of m=1 oscillation (without sawtooth).

13736 : 3MA, 4T, q_{eff}=4.1,sawtooth,n_e=3
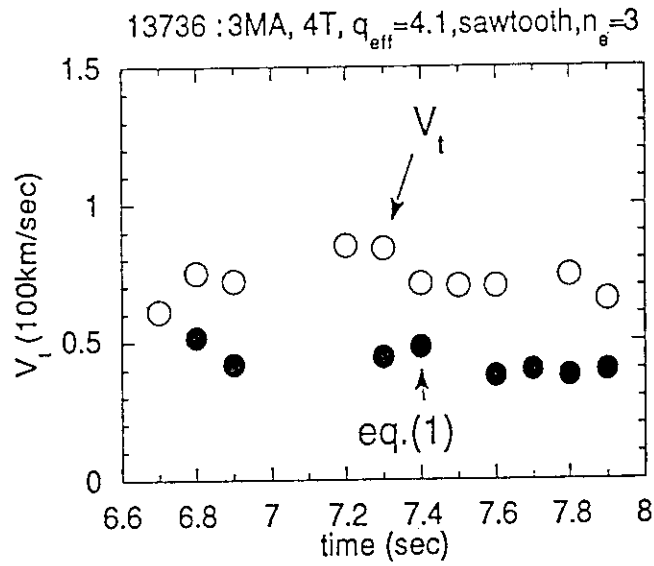
FIG. 5 Comparison of V_t and one deduced from
the frequency of m=1 oscillation (withsawtooth).

3.10　Energy Confinement in Ohmically Heated Plasmas in JT-60U

Hiroshi SHIRAI, Tomonori TAKIZUKA, Masafumi AZUMI

Abstract.　Plasma parameter dependence (density, plasma current, toroidal field and isotope mass) of Ohmically heated JT-60U plasmas are studied. Maximum τ_E of 710 msec is obtained in deuterium plasma. The ration of deuterium τ_E to hydrogen τ_E is about 1.1 in a high elongated configuration and 1.2~1.3 in a standard configuration. Strong dependence of τ_E on toroidal field, or safety factor, is obtained.

Energy Confinement time of Ohmically heated plasmas is calculated as follows;

$$\tau_E = W_{dia} / \left(I_p V_{res} - \dot{W}_{dia} \right) \tag{1}$$

where W_{dia} is stored energy measured by diamagnetic loop and V_{res} is resistive component of one turn voltage, respectively. Dot on the variable denoted time derivative of that variable. Let $V_{surface}$ be the surface voltage. The resistive loop voltage, V_{res}, is described as

$$V_{res} = V_{surface} - I_p L_i / 2, \tag{2}$$

where L_i is the self inductance of plasma current ring, which is expresses as $L_i = \mu_0 R \left[\ln(8R/a) + l_i / 2 - 2 \right]$, where l_i is internal inductance; $l_i = B_\theta^2 / B_\theta(a)^2$. As a result, equation (2) is written as follows;

$$V_{res} = V_{surface} - \pi l_i R I_p(MA)/10 \tag{3}$$

We calculate both hydrogen and deuterium plasmas in the standard and the high elongated configurations. As for hydrogen plasmas, we deal with the plasmas of $I_p = 2$ MA and $B_t = 4$ T for the standard configuration and $I_p = 1 \sim 3$ MA, $B_t = 4$ T for the high elongated configuration. As for deuterium plasmas, we deal with the plasmas of $I_p = 2 \sim 3.3$ MA, $B_t = 2.5 \sim 4$ T for the standard configuration and $I_p = 1 \sim 3$ MA, $B_t = 3.5 \sim 4$ T for the high elongated configuration.

Figure 1 shows the density dependence of τ_E in hydrogen (closed symbol) and deuterium (open symbol) plasmas of $I_p = 2$ MA and $B_t = 4$ T in the standard configuration. Data of hydrogen plasma are gathered in April. Data of deuterium are gathered in July several weeks after the beginning of deuterium experiment. The wall temperature of both data is around 300 degree Celsius. Assuming the electron density profile as some power of parabolic shape; $n_e(r) \approx n_e(0) \left(1 - r^2 \right)^m$, and using two channels of interferometer data, the line averaged electron density, $\bar{n}_e$, is inferred. In this calculation, Shafranov shift of magnetic surface is taken into account. Although this is a very rough estimation of density profile, the value of density peaking coefficient m is close to that of JT-60 plasmas. The m value decreases as the increase of $\bar{n}_e$ like the JT-60 cases.

The maximum τ_E of 2 MA hydrogen and deuterium plasmas in the standard

configuration is 490 msec and 660 msec, respectively. Improvement of τ_E by isotope mass difference is approximately expressed as τ_E (Deuterium) = (1.2~1.3) τ_E (Hydrogen).

In the figure, we show the neo Alcator scaling of τ_E [1]

$$\tau_E(\text{sec}) = R^2 \, a \, q_{cyl} \, \bar{n}_e \times 10^{-21} \tag{4}$$

by solid line. In this case it is roughly expressed as $\tau_E(\text{sec}) = 0.47 \times 10^{-19} \, \bar{n}_e$. Unfortunately, there is no low density data for both hydrogen and deuterium. We cannot conclude whether the τ_E of JT-60U Ohmic data in the standard configuration obey the neo Alcator scaling.

Figure 2 shows the density dependence of τ_E in hydrogen (closed symbol) and deuterium (open symbol) plasmas in the high elongated configuration. Circle, rectangular and triangle indicate the plasmas with I_p of 1 MA, 2 MA and 3 MA, respectively. Toroidal field is 4 T. Data of hydrogen plasmas are gathered in June and October. Data of deuterium are gathered after August. The wall temperature of both data is around 150 degree Celsius. The maximum τ_E of hydrogen plasmas is 670 msec (2MA plasma). The maximum τ_E of deuterium plasmas is 710 msec (1MA plasma). The saturation of τ_E occurs at the very low density region ($\bar{n}_e \sim 1 \times 10^{19}$ m^{-3}). Comparison of hydrogen and deuterium data shows that a confinement improvement with of isotope mass is 1.1 in the high elongated configuration. The diamagnetic loop data shows that there is nearly no difference in the measured stored energy between deuterium plasmas and hydrogen plasmas in 1 MA and 2 MA plasmas. Slightly lower resistive loop voltage of deuterium plasmas comparing to that of hydrogen plasmas makes this small difference in τ_E.

The solid line, the broken line and the dotted line in the figure show the neo Alcator scaling of 1 MA, 2MA and 3MA plasmas in high elongated configurations, respectively. Experimental data scatter around these lines for 1MA and 2MA deuterium data. Unfortunately, there are no low density data for both hydrogen and deuterium plasmas. We cannot conclude whether the JT-60U Ohmic data in the high elongated configuration obey the neo Alcator scaling.

As is mentioned above, the improvement factor of τ_E by mass difference is different between the standard configuration and the high elongated configuration. However, it must be kept in mind that hydrogen data in the standard configuration are obtained at the very beginning of JT-60U experiments. That is to say, these hydrogen data are not well optimized, especially from the view point of wall conditioning. In order to confirm the difference in the degree of τ_E improvement by mass between the standard configurations and high elongated configurations, we must obtain more hydrogen data in the standard configuration.

In ASDEX, τ_E of ohmically heated deuterium plasmas is $\sqrt{2}$ (~ 1.4) times higher than that of hydrogen plasmas in the τ_E saturation region ($\bar{n}_e \geq 2.5 \times 10^{19}$ m^{-3}) [2], which is different from JT-60U cases. Although the H/D ratio of JT-60U plasmas shown in Figure 1 and 2 is about 0.3 for these deuterium plasmas, that is they are not pure

deuterium plasmas, this is not the substantial explanation of small improvement factor of τ_E by isotope mass difference in JT-60U plasmas. We must survey the density and temperature profiles of hydrogen and deuterium plasmas in detail in order to clarify the mass effect.

Figure 3 shows the density dependence of τ_E in deuterium plasmas with different toroidal field of 4T (rectangular) and 2.5T (rectangular with cross) in standard configurations. The wall temperature of both data is around 300 degree Celsius. The solid line and the broken line show the neo Alcator scaling of 4T and 2.5T plasmas in the standard configuration, respectively.

It is clear that τ_E strongly depends on toroidal field (or maybe on safety factor q), which is different from previous analysis results of JT-60 data [3]. It can be assumed that the drift wave turbulence dominates the energy transport of ohmically heated plasmas in JT-60U. This remains to be done in the future work. The stored energy of 4T plasmas is larger than that of 2.5T plasmas. The resistive loop voltage of 4T plasmas is smaller than that of 2.5T plasmas. These facts indicate that the electron temperature of 4T plasmas is higher than that of 2.5T plasmas both in the core and the edge regions. Unfortunately, since the electron temperature data measured by ECE is not available for the low toroidal field plasmas, we cannot compare the electron temperature at the present time.

[1] R. J. Goldston, Plasma Phys. and Controlled Nucl. Fusion Research, **26** (1984) 87
[2] F. Wagner et al., 16th EPS (1989,Venice) Part I, P. 195
[3] M. Kikuchi, Private Communication
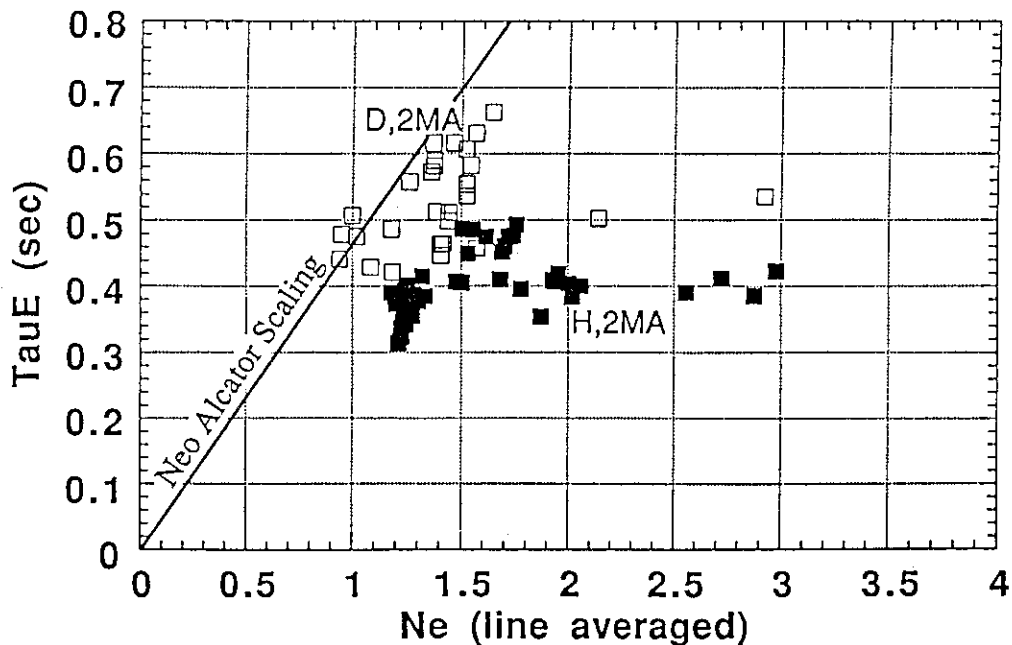
Figure 1   The density dependence of τ_E in hydrogen (closed symbol) and deuterium plasma (open symbol) in standard configuration. Plasma current and toroidal field are 2 MA and 4 T, respectively. The solid line shows the neo Alcator scaling of τ_E.
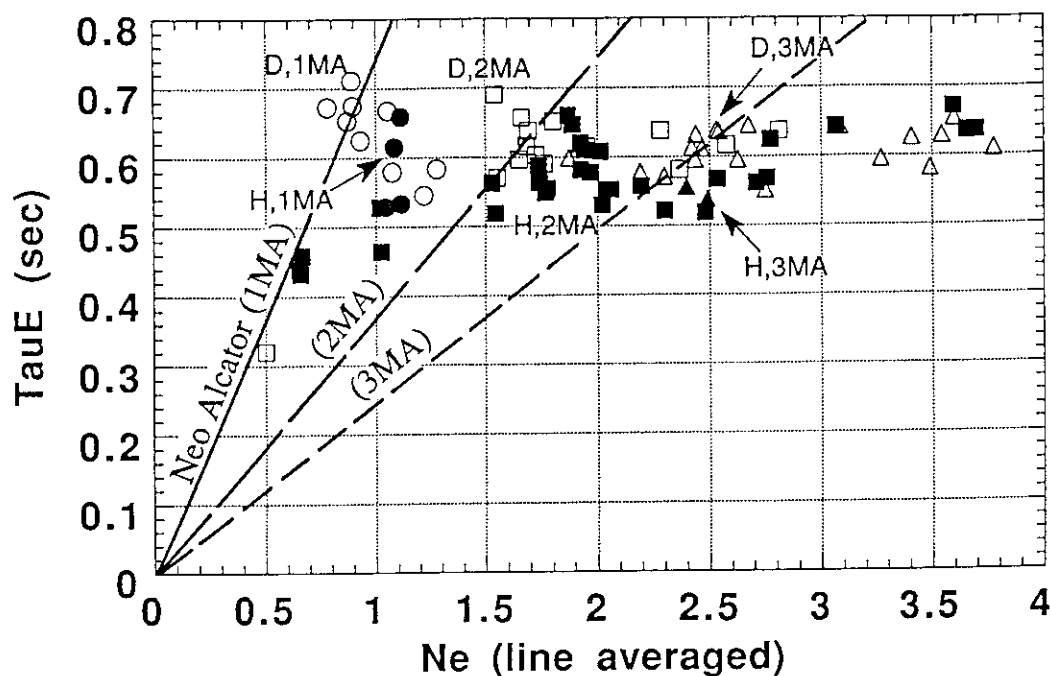
Figure 2   The density dependence of τ_E in hydrogen (closed symbol) and deuterium plasma (open symbol) in high elongated configuration. Circle, rectangular and triangle indicate the plasma with I_p of 1 MA, 2 MA and 3 MA, respectively. Toroidal field is 4 T. The solid line, the broken line and the dotted line show the neo Alcator scaling of 1 MA, 2MA and 3MA plasmas, respectively.
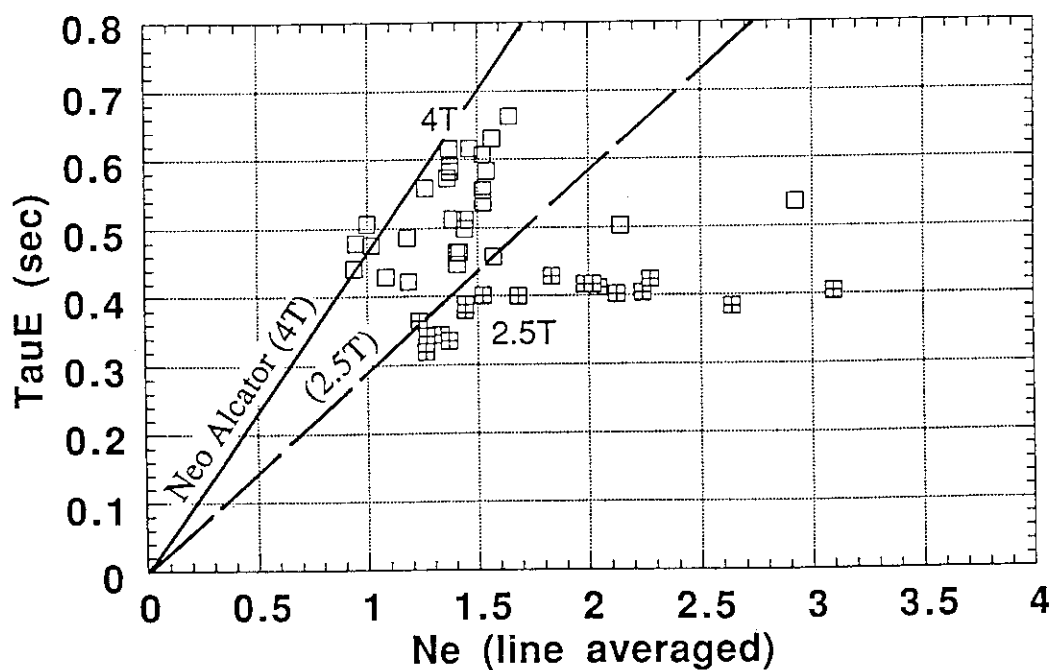
Figure 3   The density dependence of τ_E in deuterium plasma with toroidal field of 4T (rectangular) and 2.5T (rectangular with cross) in standard configuration. The solid line and the broken line show the neo Alcator scaling of 4T and 2.5T plasmas, respectively.

3.11 Electron Temperature Profile and Ion Energy Confinement in Ohmically Heated Plasma in JT-60U

N.Isei, M.Kikuchi and T.Nishitani

1. Electron Temperature Profile

Characteristics of electron temperature profiles for ohmically heated plasmas in JT-60U have been investigated using the data on ECE measurements by Fourier transform spectroscopy[1].

Waltz et al. show that the profile peaking parameter of electron temperature is quantified between $q(a)$ and $q(a)^{2/3}$ assuming Spitzer conductivity and $q(0)=1$; the peaking parameter is defined as the peak electron temperature value normalized by the volume-averaged value, usually written as $T_e(0)/<T_e>$[2].

Figure 1 shows the peaking parameter of the electron temperature profile as a function of the q^* value , the same as the cylindrical q value at the edge. It is found from this result that Waltz's proposal does not apply to ohmically heated plasmas in JT-60U. The similar observations have been also obtained in JT-60[3].

2. Ion Temperature Profile from the Neutron Yield

Ion temperature profile in ohmically heated deuterium plasmas in JT-60U is evaluated from the neutron yield[4][5] as follows. Assuming the profile of ion energy confinement time (τ_{Ei}) is flat, we can write

$$\frac{3/2 n_i T_i}{\tau_{Ei}} = q_{ei} = \frac{3}{2} n_e \frac{T_e - T_i}{\tau_{eq}}$$

where q_{ei} is electron-ion energy equipartition term and τ_{eq} is electron-ion equipartition time. In the above equation, the electron temperature profile from ECE is used and the electron density profile is evaluated from the line average density measurement of the twe-channel FIR interferometer, assuming to have the form $n_e = n_{e0}(1-\rho^2)^\alpha$, where ρ is the normalized flux surface radius in the midplane and n_{e0} is the density on axis, and Z_{eff} is obtained from the visible bremsstrahlung measurement, assuming to have a flat profile.

Such τ_{Ei} value that the neutron yield calculated from which is consistent with the measured one, is determined by iterative calculation. Then T_i profile is calculated from the τ_{Ei}. Figure 2 shows a comparison between the calculated and the measured neutron yield. It can be seen that the solutions are exist, which satisfy a good agreement between the calculated and the measured neutron yield for various values of the neutron yield.

Figure 3 shows T_i profile by the above evaluation method and T_e profile by ECE measurements and Thomson scattering measurements.

3. Comparison of the Stored Energy

A check on the validity of the above assumptions and the accuracy of the measurements can be obtained by comparing the kinetic total stored energy (W_{kin}) with the diamagnetically measured energy content (W_{dia}). This comparison is shown in Figure 4. The agreement between the two evaluations of the total energy contents is good, but W_{dia} is larger about 10% than W_{kin}.

In order to improve the accuracy of the evaluation, it is required to examine internal consistency of the measured T_e, Z_{eff} and V_{loop} values. Figure 5 shows comparison of measured resistive loop voltages and calculated ones from the neoclassical theory. As is clear from the figure, the experimental loop voltage is systematically smaller than the neoclassical prediction. This result indicates the necessity of investigating the validity of the measured T_e and Z_{eff} values.

4. Ion Energy Confinement Time

Figure 6 shows the density dependence of the τ_{Ei} and central ion temperature (T_{i0}) by the above evaluation method and central electron temperature (T_{e0}), Z_{eff}, electron total stored energy (We) and kinetic total stored energy ($We+Wi$). The τ_{Ei} values of about 300 msec to 800 msec are obtained, although the density dependence of τ_{Ei} is not clear. The T_{e0}/T_{i0} value decreases from about 3 to 1 as the increase of $\bar{n}_e$.

5. Conclusion

Ion temperature profile in ohmically heated deuterium plasmas has been evaluated from the neutron yield. The validity of the evaluation was confirmed by comparing W_{kin} and W_{dia}. Then τ_{Ei} values of about 300 msec to 800 msec are obtained. But the experimental resistive loop voltages are not consistent with calculated ones from the neoclassical theory.
An investigation of this cause remains to be done for the future subject.

REFERENCES:

[1] M. Sato et al., Section 12.2, in this review.

[2] R.E.Waltz et al., Nucl. Fusion 26(1986)1729.

[3] S. Ishida et al., Kakuyugo Kenkyu Vol.65 Supplement (1991) 211.

[4] T. Nishitani et al., Section 9.1, in this review.

[5] T. Iguchi et al., Section 9.9, in this review.

$$\frac{T_{eo}}{\langle T_e \rangle} = q^* \qquad \frac{T_{eo}}{\langle T_e \rangle} = q^{*^{2/3}}$$
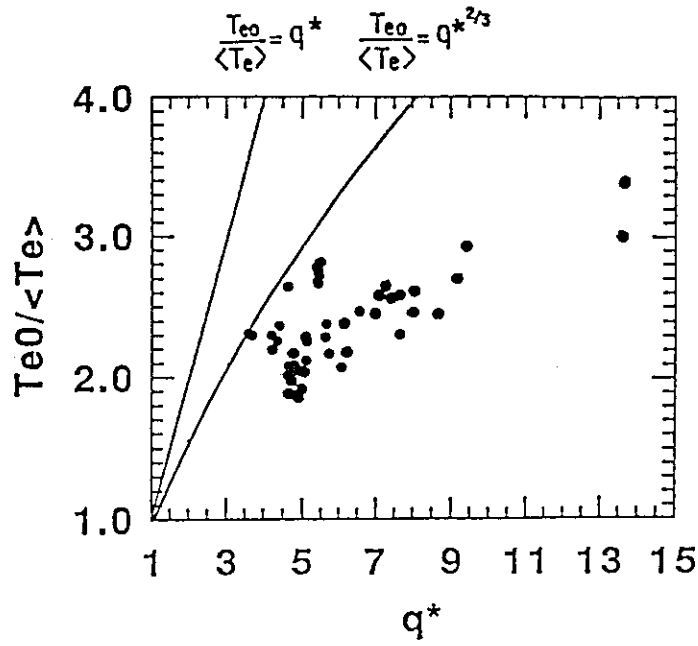
Fig.1 Peaking parameter of the electron temperature profile as a function of q^*
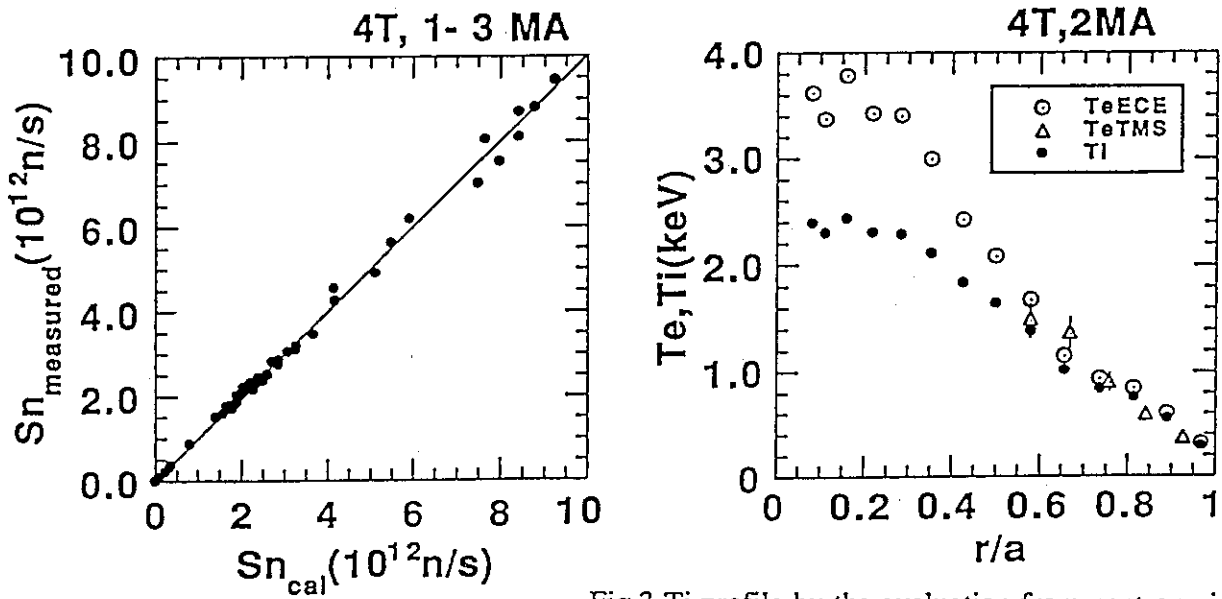
Fig.2 Comparison between the calculated and the measured neutron yield.

Fig.3 Ti profile by the evaluation from neutron yield, Te profile by ECE measurements and Thomson scattering measurements.
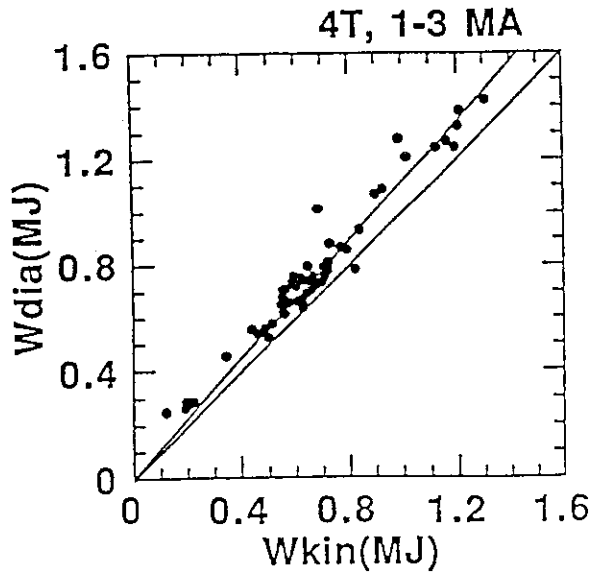
Fig.4 Comparison between the kinetic total stored energy (W_{kin}) and the diamagnetically measured energy content (W_{dia}).
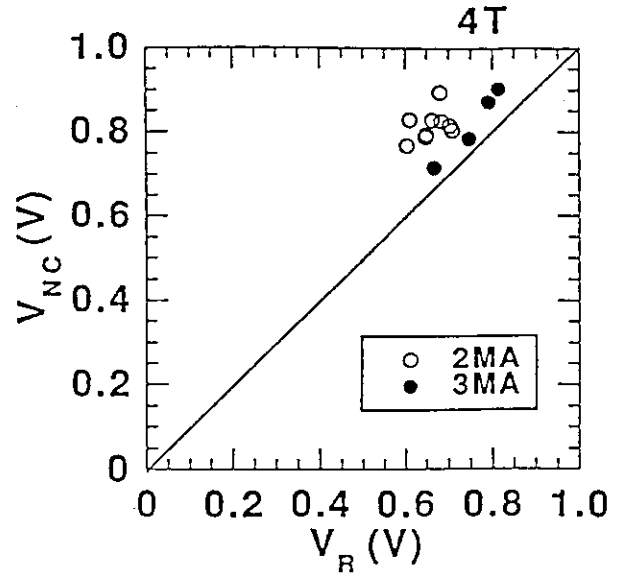
Fig.5 Comparison of measured resistive loop voltages (V_R) and calculated ones (V_{NC}) from the neoclassical theory.
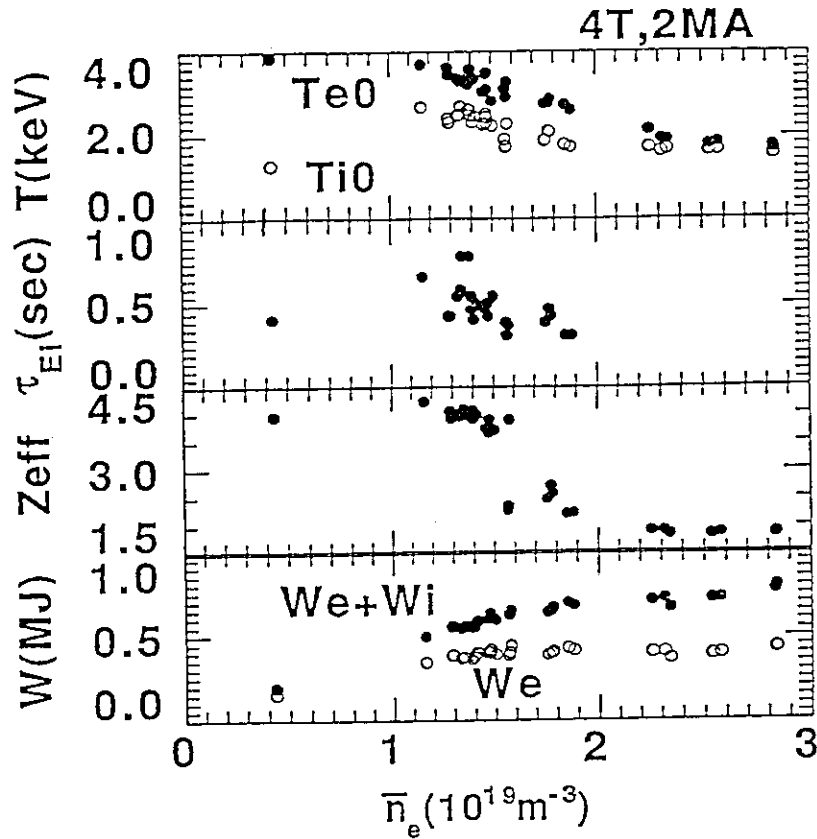
Fig.6 Density dependence of the τ_{Ei}, central ion temperature (T_{i0}), central electron temperature (T_{e0}), Z_{eff}, electron total stored energy (We) and kinetic total stored energy (We+Wi).

3.12 Radiation Loss in Ohmic Discharges in JT-60U

N.Hosogane

1. Introduction

The radiation loss plays an important role in the transport of tokamak plasmas. To obtain improved confinement modes such as H-mode or VH-mode, it is necessary to suppress the main radiation loss at a low level. While, from the view points of the reduction of the heat flux to the divertor tiles, it is essential to establish the enhanced divertor radiation through the divertor function. Thus, it is important to understand the characteristics of the radiation loss. In this paper, the characteristics of the radiation loss in ohmic discharges in JT-60U is presented. The characteristics of the radiation loss in NB heating discharges is presented in ref.1).

2. Measurement System

Figure 1 shows the arrangement of measurement systems for radiation loss. Two bolometer systems with a 16 channel array are arranged to cover the main and divertor region of tokamak plasma. The time response of the system limited by the low pass filter is 10 msec, and the sampling time is 4 msec. The spatial resolution is 0.1-0.12 m at R=3.0 m in the main plasma region, and is about 0.07m in the divertor region (ch.28-32). The absolute value of the radiation loss power was calibrated by regarding the radiation loss of detached ohmic plasmas as 100% radiation. The relative sensitivities of the sensors were determined with the He-Ne laser.

3. Profiles and Calculations of Radiation Loss Power

Figure 2 shows the profile of the radiation loss power in the ohmic discharge with the standard configuration(κ=1.4) shown in Fig.1. The thick solid line stands for the chord integrated radiation loss measured by the bolometer arrays. The channel number 1-16 and 17-32 correspond to the bolometer arrays viewing the upper half and lower half of the plasma column, respectively. The separatrix hit points at the divertor are located around the ch.29 and ch.30. It is seen that there are strong radiation loss power in the region centering around ch.29. The strong radiation loss power comes from the divertor region including the separatrix hit points and the scrape-off layer near the X-point. The radiative region is wide compared with the distance between the two separatrix hit points on the divertor plates. The spread of the radiative region is considered to be due the particle recycling around the X-point, which probably causes the weak up-down asymmetry in the profile of the radiation loss power. According to this understanding of the radiation profiles, the radiation loss from the main plasma region P_{rad}^{main} is calculated with only an upper array (ch.1-16), assuming that the radiating power density in the main plasma is up-down symmetry. The radiation loss from the divertor region P_{rad}^{div} is calculated as a sum of the radiation at the legs of separatrix in the divertor region and the radiation from the scrape-off layer in the lower half region of the main plasma. The latter is defined as the residual radiation obtained by subtracting the signals of upper array from the signals of the corresponding channel in the lower array. The dotted line and thin solid line in Fig.2 respectively show the contributions from the main and divertor radiations calculated in this way.

4. Global Characteristics of Radiation Loss in Ohmic Plasmas

Figure 3 shows the radiation loss of deuterium ohmic discharges as a function of ohmic power. The radiation loss powers are obtained in the ohmic phase of the NB heating experiment for both high elongation(κ=1.6) and standard(κ=1.4) divertor plasmas. It is seen that the total radiation loss power increases with the ohmic power, and reach 1.7 MW for I_p=3 MA. The scattered data points are due to the density dependence.

Figure 4 shows the density dependence of the fraction of the total and main radiation power losses, P_{rad}/P_{OH} and P_{rad}^{main}, for the ohmic power. With increase in electron density, the main radiation loss increases from 15% to 30% and the divertor radiation loss increases up to about 40%. The total radiation loss reaches about 70% of the input power except for the case of Ip=1 MA. Also, it is found in Fig.4 that both the main and the divertor radiation losses depend on the plasma current and toroidal magnetic field. As the plasma current is raised from 1 MA to 3 MA, the curves of the radiation loss shift to the higher density region. For the same plasma current (Ip=2 MA), the radiation loss for the case of 2.5T shifts to the higher density region compared with the case of 4T. These results are understood by the fact that both the edge electron temperature and the divertor electron temperature become low as the plasma current is lowered or the safety factor is raised. This is consistent with the understanding of the density limit in the Hugill diagram.

5. Discussion

There is an idea[2] that the density limit is related with the connection length Rq, where q is safety factor and R is major radius. If the connection length is long, the electron temperatures in the divertor region can be low. As a result, the radiation becomes so large that the thermal instability can grow at the divertor, which leads to the density limit. From this physical picture, the radiation loss is expected to depend on the parameter of n_eqR, including the electron density dependence. This idea is tested for not only divertor radiation but also main radiation. Figure 5 shows the main and divertor radiation loss as a function of the parameter n_eqR. The result is favorable. All the curves of the radiation losses which lie at the different positions in Fig.4 seem to lie on the same curve in a rough sense. It is interesting that the main radiation also obeys the parameter n_eqR.

6. Summary

The global characteristic of the radiation loss in the ohmic discharges is investigated. The main radiation loss is 15-30%, and the divertor radiation loss is up to 40%. Both the radiation losses increase with electron density. It is also found that both the radiation loss depend on the plasma current and toroidal magnetic field. From the parameter dependence obtained, it is suggested that the radiation loss is related with the connection length Rq.

1) N.Hosogane, 'Radiation Loss in NB Heating Discharges in JT-60U', in this review.
2) K.Borrasa, Nucl. Fusion 31(1991)1035

FIR Interferometer
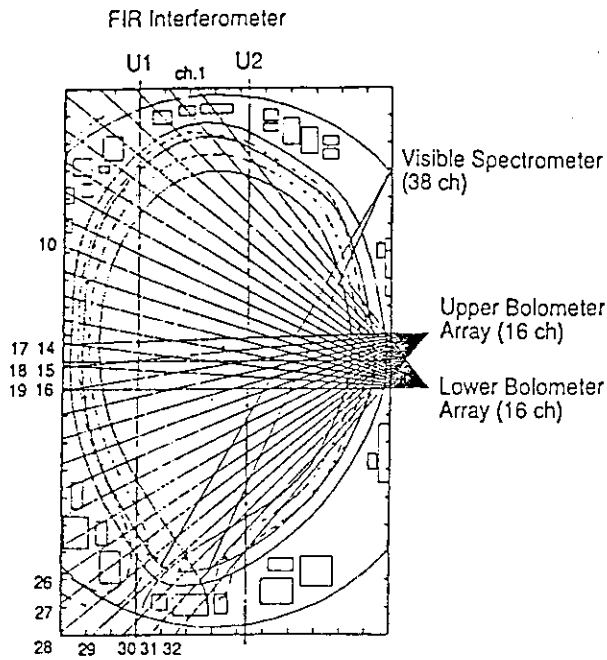
Fig.1 Measurement system
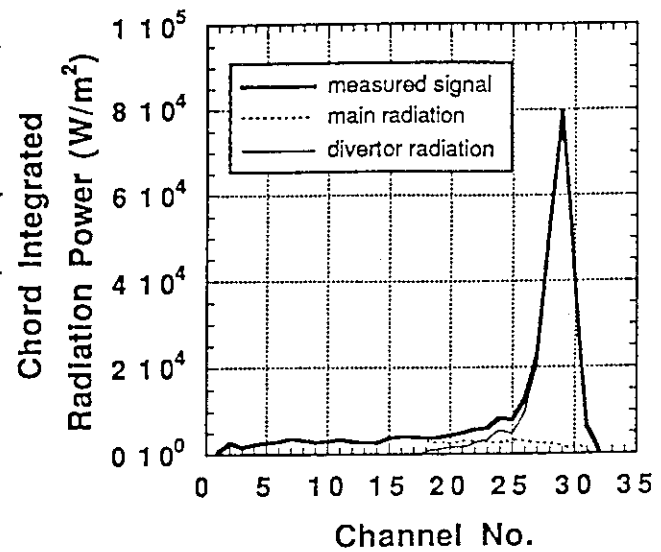
Fig.2 A typical profile of chord integrated
radiation loss power.
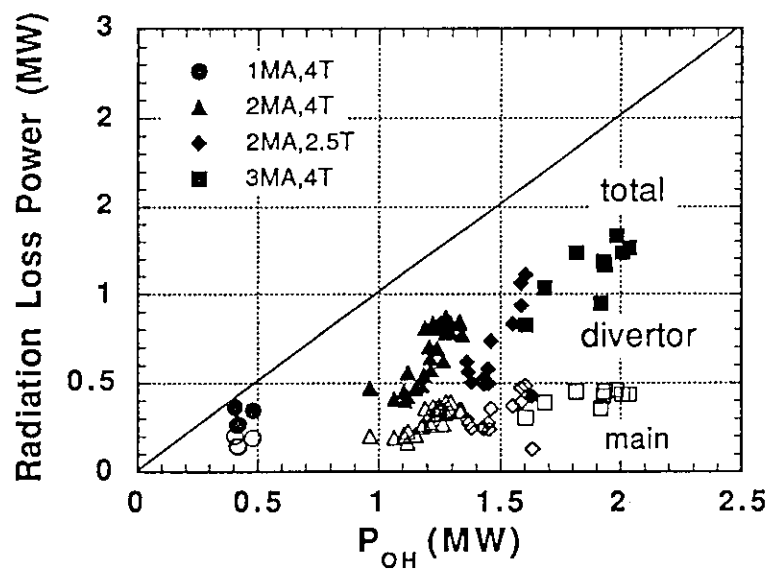
Fig.3 Radiation loss power as a function of
ohmic power
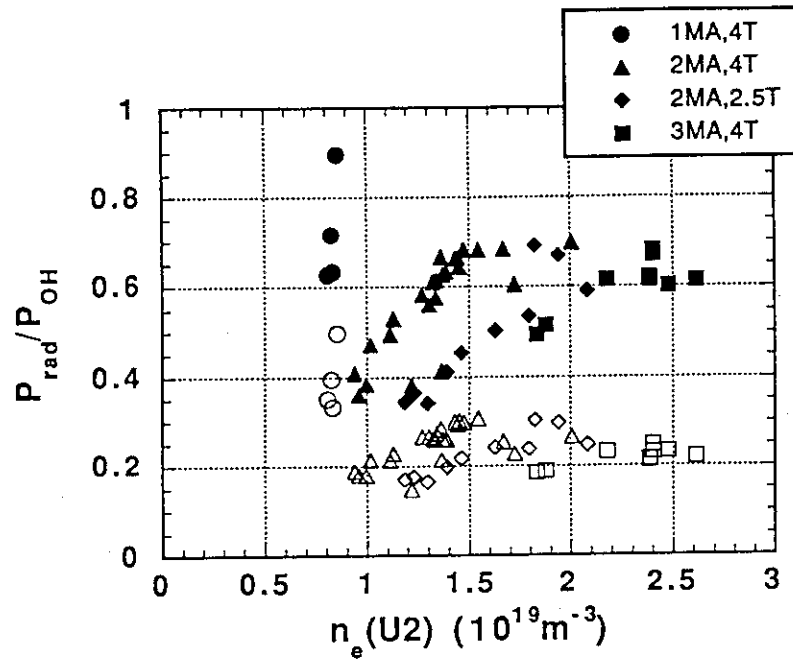
Fig.4 Density dependence of the radiation losses
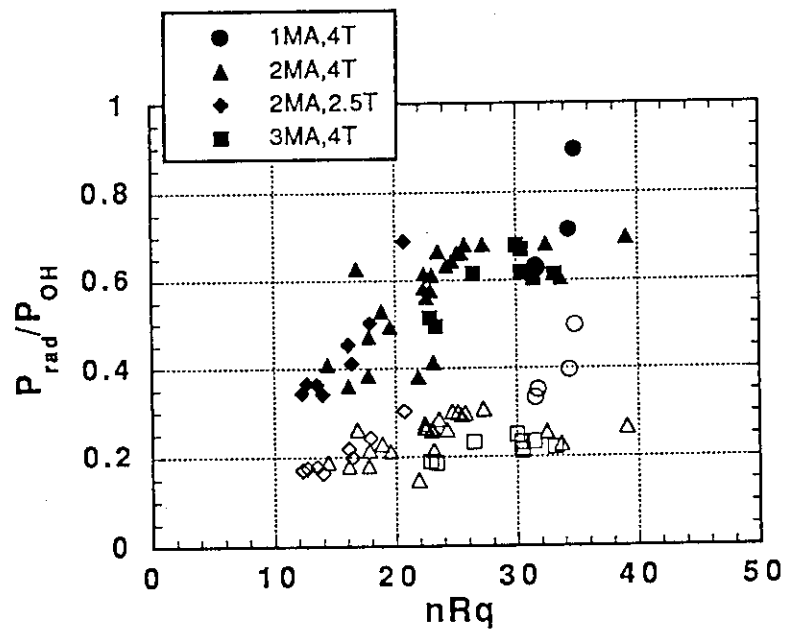
Fig.5 Radiation losses plotted as a function of n_eRq_{eff}.

4 High β_p Confinement

4.1 Overview of High Poloidal-Beta Experiments in JT-60U

S. Ishida, S. Tsuji, M. Kikuchi, Y. Koide, T. Nishitani, H. Nakamura and JT-60 Team

1. Introduction

In nuclear fusion research, the high β_p regime in tokamak operation is potentially of interest as it may offer an alternative route to the development of an ignition device in which the requirement for external sources of non-inductive current-drive is very much reduced[1,2]. In JT-60, high β_p regime has been extensively explored by significantly reducing the plasma current below 1 MA, in which highly bootstrapped discharges with I_{BS}/I_p up to ~0.8 have been demonstrated and a lower limit of the Troyon factor has been revealed as a fast β collapse at $\beta_p \sim 3$, which was named a "β_p collapse" [3]. Succeeding to the JT-60 high β_p experiments, the purpose of the high β_p experiments in JT-60U is to demonstrate the basic feasibility of a high β_p tokamak reactor under a standard reactor-relevant configuration in a large tokamak as addressing to a number of critical issues for steady state operation.

In JT-60U, the experiments for the high β_p research has been programmed so as to suit the plans for additional installations of auxiliary heating devices. At this first period of the JT-60U operation, objectives of the initial high β_p experiment are set: (1) optimization of a high β_p plasma in terms of hot-ion mode features, neutron yields and enhanced confinement; (2) overall survey of the operational regimes and β limits.

2. Experimental Arrangements and Discharge Optimization

In the same way as the high β_p operation in JT-60, optimization of the high β_p discharges in JT-60U was accomplished with the central neutral beam injection into low density target plasma with a small volume under the first wall sufficiently conditioned to suppress the recycling. The target plasma was produced with a highly elongated configuration shifted as possible as inward for obtaining the central beam deposition, because the plasmas with the nominal "standard" and "high elongation" configurations are situated significantly off-axis against the present beam lines. A typical equilibrium configuration at $\beta_p^{dia} \sim 2.5$ is shown with the beam injection lines in Fig.2.1.

Helium GDC (glow discharge cleaning) is newly applied in JT-60U,
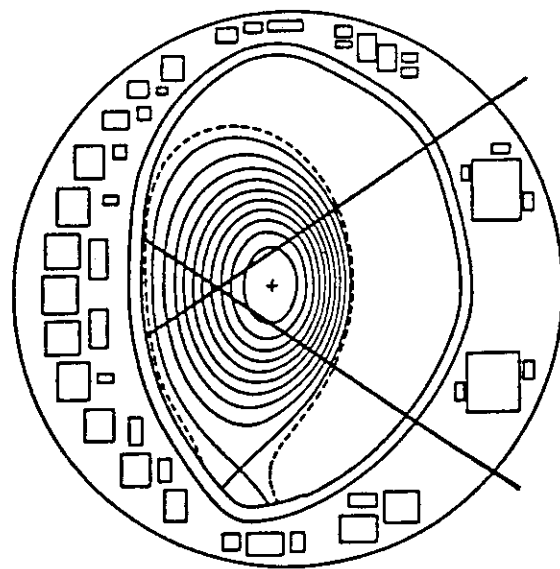
Fig.2.1 High β_p equilibrium and beam lines

which is a powerful tool for wall conditioning as well as helium TDC (Taylor discharge cleaning). The divertor function is also effective for the maintenance of the suppressed recycling condition. Thus, the target plasma with the reduced recycling could be easily obtained in the divertor configuration. Although vertical instability became a problem to sustain the high β_p discharges because of the lower capability of the stability for the high elongation configuration, it was able to be suppressed up to $\beta_p{}^{dia}$~2.5 by regulation of the stability gains for feedback control.

Under the above experimental arrangements, the plasma current scans have been conducted in deuterium beam injection experiments into low density deuterium plasmas in the range of I_p=0.8-2.0 MA. The main parameters are: B_t=4 T, R_p~3.1 m, a~0.75 m, κ=b/a~1.6, the volume of the plasma V_p~50 m^3, the equivalent cylindrical safety factor q^*=5(1+κ^2)a^2B_t/(2R_pI_p[MA])~4-10, P_{NB}~15-22 MW (injection power to torus) and the beam energy of E_b~80-95 keV. The total experimental time of about 4 days (63 shots) has been spent for the series of the experiment.

3. Poloidal-Beta Enhanced Confinement

In the high β_p experiments, an enhanced confinement regime for high β_p plasmas has been discovered. The enhancement factor evaluated from the diamagnetic stored energy against the L-mode ITER-89 power law is shown as a function of the $\varepsilon\beta_p{}^{dia}$ value in Fig.3.1. Significant enhancement in confinement is observed to be about triple times as compared to the L-mode scaling (see Section 4.4). From the fact that the enhancement factor increases with the β_p value as shown in this figure, this regime is here called the "poloidal-beta enhanced confinement" (PEC) regime.
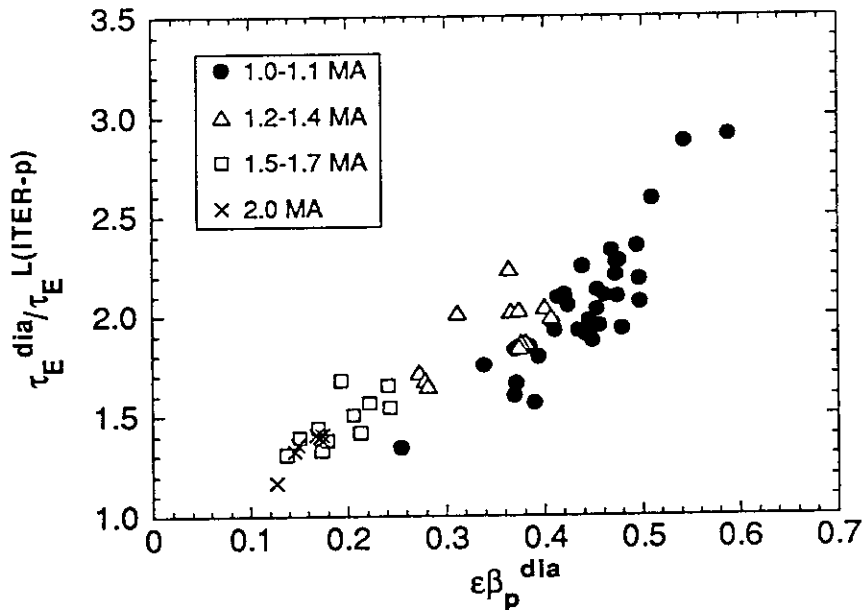
Fig.3.1 Enhancement factor as a function of $\varepsilon\beta_p{}^{dia}$

In the PEC regime, grassy ELMs have been normally observed during the beam injection. On some occasions, a short ELM free-phase appeared during the ELMs, when the stored energy

was increased under the constant beam power. So, the grassy ELMs seem to cause the slight confinement degradation as enhancing the recycling. From the point that the line-density signal at $r/a\sim0.5$ is observed to be slightly decreased during the ELM free-phase, it appears to be somewhat different from the normal H-mode in which the density significantly increases in the ELM-free phase.

The PEC mode plasma appears to be optimized as the ELMs are completely suppressed during the beam injection. In this case, the wall recycling was significantly suppressed in comparison with other similar discharges as the $H\alpha$ emission at the edge was maintained at lower levels (see Section 4.7). In Fig.3.2, the main waveforms are shown of an ELM-free PEC mode plasma obtained for $I_p=1.1$ MA and the injection power $P_{NB}=21$ MW (the absorption power $P_{abs}=17$ MW). In this discharge, the following parameters are achieved; the fusion neutron rate $S_n=1.3\times10^{16}$ n/s, the ion temperature $T_i^{CXRS}(r/a=0.16)=22$ keV, the electron temperature $T_e^{ECE}(r/a=0.18)=6.6$ keV, the line-electron density $\bar{n}_e(r/a=0.6)=1.4\times10^{19}$ m^{-3}, the diamagnetic stored energy $W_{dia}=3.8$ MJ. The discharge encounters the β_p collapse at the peak value of $\beta_p^{dia}=2.5$ and the Troyon factor $g=\beta_t^{dia}[\%]aB_t/I_p[MA]=2.0$ (see Section 4.3). The electron and ion temperature profiles at $t\sim7.85$ s are shown in Fig.3.3, clearly indicating a typical hot ion mode feature as $T_i\sim3T_e$ near the center. The internal MHD activity on the soft X-ray emission (PIN-diode array) and the electron cyclotron emission (grating polychromator) was very small or not detectable before the β_p collapse. This shot records the highest values of Q_{DD} and $n_e(0)\tau_E^{dia}T_i(0)$ in JT-60U to be 0.8×10^{-3} and $\sim3\times10^{20}$ [m^{-3}skeV], respectively, of which plasma performance corresponds to $Q_{DT}\sim0.2$ (see Section 4.6). A key to attain the ELM-free PEC mode is the suppression of the recycling before the beam injection.
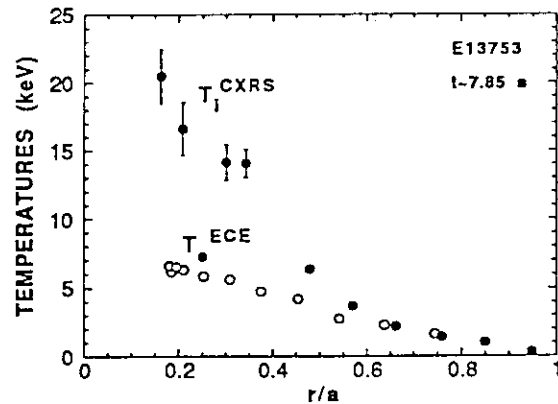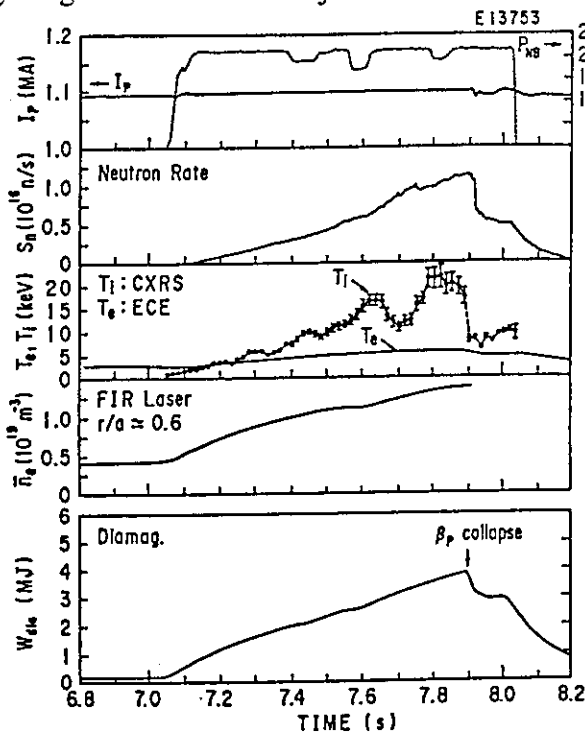
Fig.3.2 Waveforms of the high β_p discharge   *Fig.3.3 Ion and electron temperature profiles*

4. High Neutron Yield and Fusion Amplification Factor

The PEC mode plasma is a so-called two-component plasma made up of thermal and beam components of ions in which the total neutron yield is significantly amplified by the non-Maxwellian ions through beam-beam and beam-thermal reactions. The two-component tokamak operation provides an attractive route to the achievement of a criterion in terms of the fusion amplification factor, $Q_{DT} \sim 1$, in which the requirement for auxiliary heating devices is very much reduced than in a conventional approach based on Maxwellian plasmas. In the aspects for the attainment of the thermonuclear-ignition condition, the two component approach may be also important for optimization of an initial ignition operation in which a natural evolution from the cold-target reactor to the conventional thermonuclear reactor is required.

Since on-axis beam injection allows the beam ions to be efficiently produced in the center where the T_e value is peaked, the on-axis heating is a key technique in increasing the total neutron yield by the beam contributions. In the PEC regime, the measured neutron emission rate S_n is shown as a function of the W_{dia}^2 in Fig.4.1, showing the approximate linear dependences particularly for the $I_p \sim 1$ MA discharges, which implies that the neutron yield is dominated by the beam contributions.
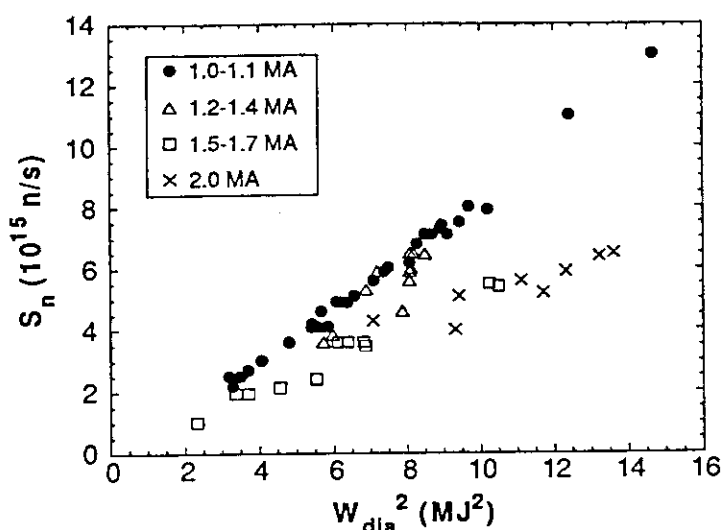
Fig.4.1 S_n as a function of W_{dia}^2

5. Summary and Future Plans

The original objectives of the experiment in this operation period have been accomplished with the discovery of the PEC regime and the attainments of high fusion products and fusion amplification factors in the ELM-free PEC mode in which the L-mode enhancement factor closely approaches ~3. As a next step of the experiment, long-pulse heating and tangential beam injection experiments are planed in which the critical issues for the steady state operation such as effects of current-profile relaxation and beam-driven currents on β limits, impurity accumulation and fuel dilution will be highlighted. The performance of high β_p discharges is expected to be further improved by operating in the higher current region with increasing the beam power.

References

[1] M. Kikuchi, Nucl. Fusion 30(1990)1391; Y.Seki et al., IAEA Washington DC, 1990, paper IAEA-CN-53/G-1-2.

[2] R. Conn et al., ibid, paper IAEA-CN-53/H-1-4.

[3] S. Ishida et al., ibid, paper IAEA-CN-53/A-3-2.

4.2 Equilibrium Analysis of High β_p Plasmas in JT-60U

S. Tsuji, K. Ushigusa, Y. Neyatani, S. Ishida

1. Introduction

The high β_p regime has been attained by means of nearly perpendicular beam injection into deuterium plasmas in JT-60U [1]. It is important to evaluate poloidal beta values accurately to investigate confinement properties and to correlate with MHD activity [2]. This paper describes the MHD equilibrium analysis on JT-60U. We obtain the perpendicular component of β_p from diamagnetic measurement. It is possible to evaluate the equilibrium β_p, which is the average of parallel and perpendicular components, by least-squares minimization techniques to reproduce magnetic data measured outside the elongated plasma [3,4]. Thus the plasma pressure anisotropy can be investigated from the MHD equilibrium analysis. In the case of discharges with isotropic plasma pressure, the β_p values evaluated independently can be cross-checked to estimate systematic errors in the two methods.

2. Magnetic Diagnostics

Fifteen one-turn loops and a poloidal set of 17 pairs of pick-up coils have been installed inside the vacuum vessel to measure poloidal fluxes and tangential and normal components of poloidal magnetic fields. The accuracy of the β_p evaluation can be improved from the previous analysis with 6 pairs of pick-up coils and no flux loops on JT-60 [5].

Diamagnetic loops are are wound along a vessel connecting ring. The details of the diamagnetic measurement are described in a separate paper [6].

3. MHD Equilibrium Analysis

Now we have the flux loops, poloidal flux data can be used as constraints for the MHD equilibrium calculation. Accordingly results from a fast boundary identification (FBI) code which approximates the plasma current as six filaments [7] are required no longer to make the free boundary problem as fixed one. The Grad-Shafranov equation is solved using the fast Buneman method and the Picard iteration scheme. The plasma current density profile is assumed as

$$j(\psi) = j_0 \{ \beta_p^* R / R_p + (1 - \beta_p^*) R_p / R \} f(\tilde{\psi}) \tag{1}$$

$$f(\tilde{\psi}) = 1 + \alpha \tilde{\psi} + \gamma \tilde{\psi}^2 - (1 + \alpha + \gamma) \tilde{\psi}^3 \tag{2}$$

$$\tilde{\psi} = (\psi - \psi_{axis}) / (\psi_{sur} - \psi_{axis}) \tag{3}$$

The edge current density is put to be zero since the effects of the SOL current on the MHD equilibrium was found to be negligible from Langmuir probe measurements at divertor plates. The functional form of $f(\tilde{\psi})$ was adopted by the Doublet III group [4]. Two of the unknown parameters, j_0 and α, are determined by specifying I_p and q_0. The rest two parameters, β_p^* and γ, and resulting $\beta_p^{eq} = (\beta_p^{\parallel} + \beta_p^{\perp}) / 2$ and ℓ_i are scanned to minimize deviations of the calculated poloidal fluxes and magnetic fields from measurements;

$$\chi^2 = \chi_f^2 + \chi_b^2 + \chi_v^2$$

$$= \Sigma \, (\, \psi_i^{cal} - \psi_i^{exp} \,) \,^2 \, / \, \sigma_{fi}^2 + \Sigma \, (\, B_{pi}^{cal} - B_{pi}^{exp} \,) \,^2 \, / \, \sigma_{bi}^2 + \zeta \, (\, I_v^{cal} \,) \,^2 \qquad (4)$$

where σ_{fi} and σ_{pi} are the estimated standard deviation reflecting the measurement uncertainty at sensor i. At the moment, only the tangential probe data are used for χ_b^2. The third term on a virtual current is added to accelerate the minimization procedure. The measured external coil currents are used to calculate the vacuum field. Besides a unknown current of the passive horizontal field coil, four additional fields (even and odd components of dipole and quadrupole of analytic vacuum fluxes) are included by least-squares fit to the measured poloidal fluxes at the flux loops. This procedure facilitates the free boundary calculation. The virtual current in Eq.(4) is chosen to be the even component of the dipole flux. This flux produces a uniform vertical field so that the scan of unrealistic equilibrium with incorrect $\beta_p^{eq} + \ell_i \, / \, 2$ values is avoided owing to the last term. The constant ζ is chosen to make χ_v^2 comparable to χ_f^2.

Figure 1 shows an example of the minimization for a time slice of a high β_p discharge at qeff ~ 9.3 (E13753, 7.9 s) which produced the maximum neutron emission rate in 1991. The values of χ^2 are plotted as a function of ℓ_i with assumed β_p^{eq}. The constrained value of q0 is two since no sawtooth was observed. When the assumed β_p^{eq} is appropriate the three dip points almost agree with one another and hence a minimum of χ^2 is achieved as shown in Fig. 1(b). The minimum χ^2 and resulting β_p^{eq} and ℓ_i are plotted in Fig. 2 as a function of q0. The minimized β_p^{eq} and ℓ_i are insensitive to the q0 assumption. Although the q0 values which give the minima in χ_f^2 and χ_b^2 do not agree with each other, q0 is considered to be in a range of 2.0 $\pm$ 0.4 from the variation of χ^2. Thus β_p^{eq} is estimated to be 2.12 $\pm$ 0.02. The reconstructed magnetic surfaces are plotted in Fig. 3 with q0 = 1.6 and 2.0. The shape of the outer most flux surface is almost the same. However the plasma column shifts slightly upward with lowering q0. Figure 4 compares the reconstructed profiles of the safety factor, current density and plasma pressure along the horizontal plane which passes the magnetic axis. The position of the current density peak shifts outward with increasing q0.

4. Discussion

The poloidal beta estimated from the diamagnetic measurement on the time slice analyzed in the previous section is $\beta_p^{dia} = \beta_p^\perp = 2.5$. The true beta is expressed as $\beta_p = (\, \beta_p^{\parallel} + 2 \, \beta_p^\perp \,)$ / 3 = ($\beta_p^{dia} + 2 \, \beta_p^{eq}$) / 3 = 2.25 taking into account the pressure anisotropy [8]. The data analysis on several high β_p shots indicates that β_p^{dia} differs from β_p by up to 15%. Thus the plasma pressure anisotropy in JT-60U is not so strong as that of the high β_p regime in JT-60 [5]. The parameterization of the pressure anisotropy and the estimation of the systematic errors are under way.

Using a 129 $\times$ 129 grid, an adequate minimization in (β_p^{eq}, ℓ_i) space with the simplex method can be obtained in five to eight minutes of CPU time on the FACOM M-780/10S. The non-linear optimization is not fast enough for routine data analysis. Hence a linearized minimization interleaved with the equilibrium iterations is under development following the scheme devised by Lao et al [4].

The use of the toroidal flux value measured with the diamagnetic loop as an additional constraint to the MHD equilibrium problem has been reported to provide a more precise evaluation of q0 [9]. However our present analysis indicates that the reconstructed toroidal flux

varies only weakly on q_0. The plasma modification of the toroidal field coming mainly from the central region of the plasma depends not only on q_0 but also on the assumption of current density profile shapes. Incidentally the discrepancy in estimating q_0 between the magnetic flux data and magnetic field data as seen in Fig. 2(a) may arise from the incorrect assumption of the current density. Independent specifications of the pressure and paramagnetic functions of the current density is left as future work for more realistic reconstructions.

5. Summary

The poloidal beta values of high β_p discharges are evaluated from the diamagnetic measurement and MHD equilibrium analysis on JT-60U. Not depending on the assumed q_0, β_p^{eq} and ℓ_i are well separated with $\kappa \approx 1.6$. The highest β_p value achieved is calculated to be 2.25. The high β_p plasmas in JT-60U are less anisotropic than those in JT-60.

References

[1] S. Ishida et al., this report, Sec. 4.1.
[2] S. Ishida et al., this report, Sec. 4.3.
[3] J.L. Luxon and B.B. Brown, Nucl. Fusion **22** (1982) 813.
[4] L.L. Lao et al., Nucl. Fusion **25** (1985) 1611.
[5] S. Tsuji et al., JAERI-M 90-066, Sec. 6.3.
[6] S. Tsuji et al., this report, Sec. 12.3.
[7] D.W. Swain and G.H. Neilson, Nucl. Fusion **22** (1982) 1015.
[8] W.A. Cooper and A.J. Wootton, Plasma Phys. **24** (1982) 1183.
[9] E. Lazzaro and P. Mantica, Plasma Phys. Controll. Fusion **30** (1988) 1735.
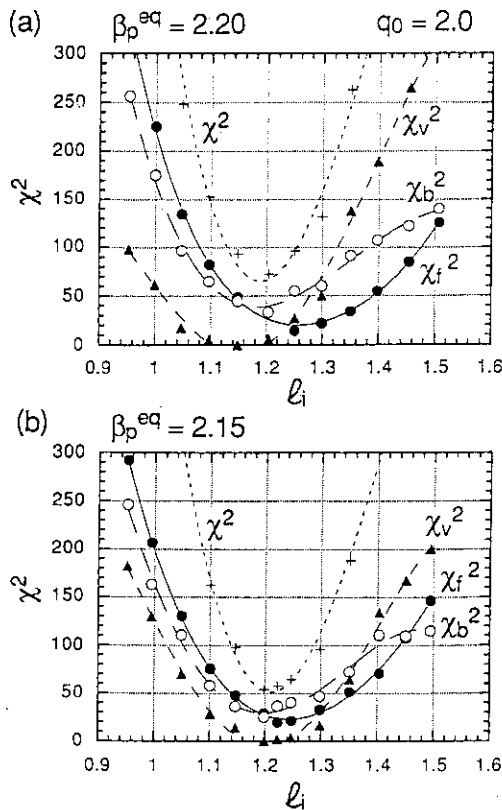
Fig. 1 Deviations defined by Eq. (4) as a function of ℓ_i.
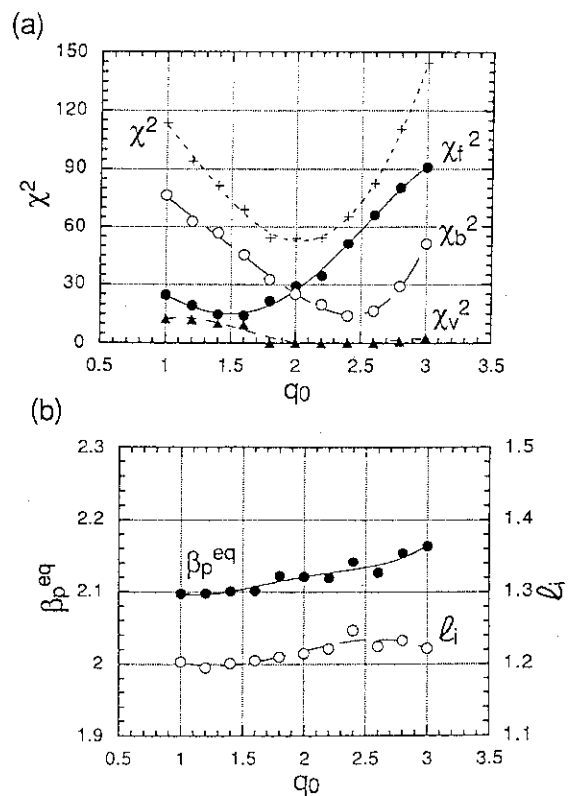
Fig. 2 Variations of χ^2 and minimized β_p^{eq} and ℓ_i as a function of q_0.

E13753 7.9 s
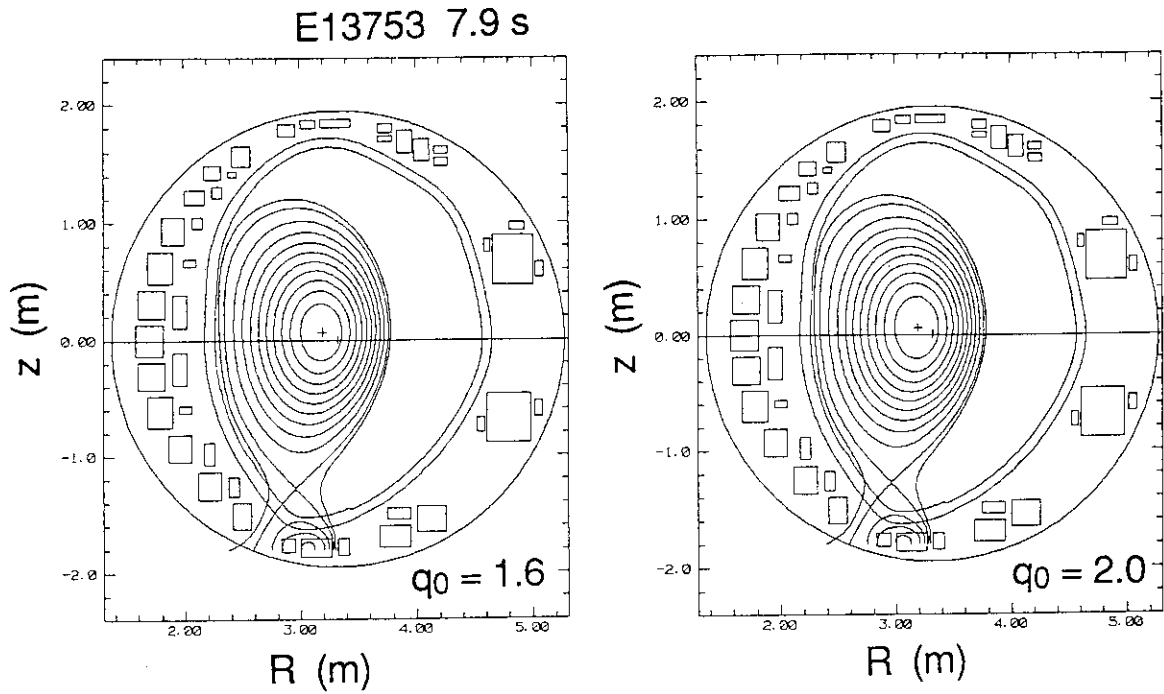
Fig. 3 Comparison of the reconstructed magnetic surfaces with different q_0.
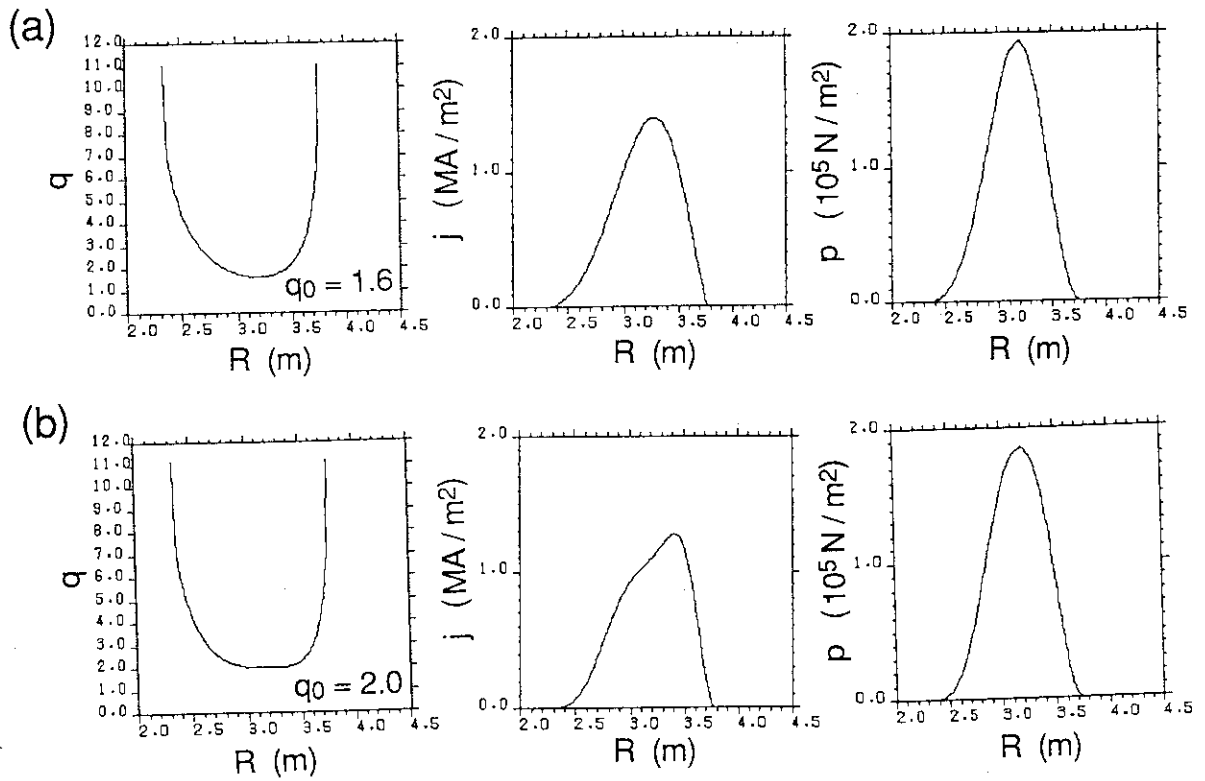
Fig. 4 Comparison of the reconstructed radial profiles of the safety factor, current density and plasma pressure with $q_0 = 1.6$ (a) and 2.0 (b).

4.3 Beta Limits and Poloidal-Beta Collapses in High β_p Plasmas

S. Ishida, S. Tsuji, Y. Kamada and T. Ozeki

1. Introduction

While the discharges in the high β_p regime can be sustained with much lower driven currents than are generally considered necessary, the stability of the high pressure plasmas under a large bootstrap current fraction is crucially important to determine whether the high β_p reactor scenario is workable. Presently, the Troyon limit with a Troyon factor of ~3.5 is widely believed or accepted as an operating β limit as it has been long adopted in the reference designs of a tokamak reactor. However, it may be dangerous to apply it toward a new regime such as the high β_p regime because of the view that the broadened or hollowed current profiles due to a large bootstrap current fraction lead to lower limits of the Troyon factor.

In the high β_p regime, the discharges are free from sawtooth activity which restricts the central q value to be around unity. Large increase in the β_p due to the beam injection causes a slow current relaxation, which allows the toroidal equilibria to be significantly altered during auxiliary heating. In JT-60U, the β limit study directs much attention to the confirmation of β limits in the high β_p regime including the current relaxation effects. The final goal of this study is to control the β limit by a current profile modulation with substantial beam-driven currents for steady state operation.

2. High β_p Regimes in JT-60U and JT-60

The operational β regimes in high β_p experiments are compared between JT-60 and JT-60U with the diagram of β_p^{dia} as a function of β_t^{dia} as shown in Fig.2.1; the JT-60U data are closed circles and the JT-60 data are open squires. In JT-60U, the achieved toroidal and poloidal betas are $\beta_t^{dia}=0.73$ % and $\beta_p^{dia}=2.5$, respectively. As shown in this figure, the prominent improvement in confinement obtained in JT-60U reduces an optimum operational q^* value to q^*~6, which is much lower than in the JT-60 case of q^*~10; where q^* is an equivalent cylindrical safety factor defined as $q^*= 5a^2B_t(1+\kappa^2)/(2R_pI_p[MA])$.
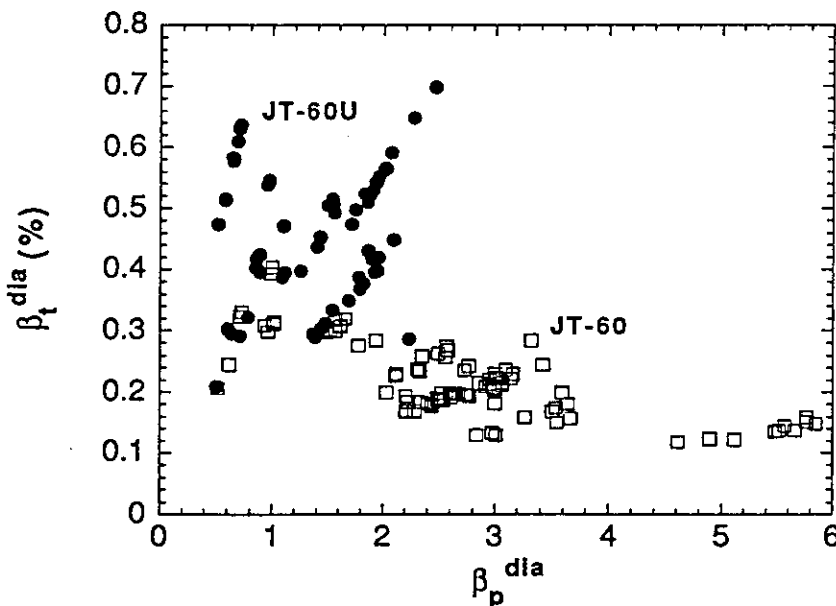
Fig.2.1 β_t^{dia} as a function of β_p^{dia} for high β_p experiments.

3. Beta Limits

A fast β collapse dubbed as the β_p collapse has been first revealed in JT-60 under a large bootstrap current fraction up to ~80 %, and is associated with the β limit substantially below the Troyon limit. A hollow current profile evolution in the high β_p regime plays an essential role on the MHD stability. The experimental evidence of the β_p collapse has a significant impact against the reactor scenario, since it may suggest that the large bootstrap current fraction and the high normalized β tend to be contradictory in tokamak operation to each other.

Various attempts to extend the β values have been carried out in tokamaks and have encountered a variety of β-limiting phenomena: for instance, soft β collapses for high β_t experiments in PBX-M, DIII-D and JET; β_p saturation for high β_p experiments in ASDEX and PBX-M; a disruptive β-limit at β_p~2 for supershot experiments in TFTR. Pressure-driven high-n ballooning modes, resistive ballooning modes or external kink modes have been dealt with to explain the β limits. Most recently, high β_p experiments in TFTR and DIII-D have almost reached equilibrium limits at $\varepsilon\beta_p$ ~1.5 and 1.8, respectively. Nevertheless, the β_p collapse observed in JT-60 is clearly different from any other β-limiting phenomenon reported before and may not be explained by those MHD modes.

Figure 3.1 shows the Troyon factor as a function of $\varepsilon\beta_p$ for high β_p experiments in JT-60 and JT-60U which are indicated with open circles and open squires, respectively. The β_p normalized by the aspect ratio, $\varepsilon\beta_p$, may be preferable to the simple β_p value since it is associated with equilibrium limits, ballooning instabilities and other toroidicity-related high-β MHD activities.
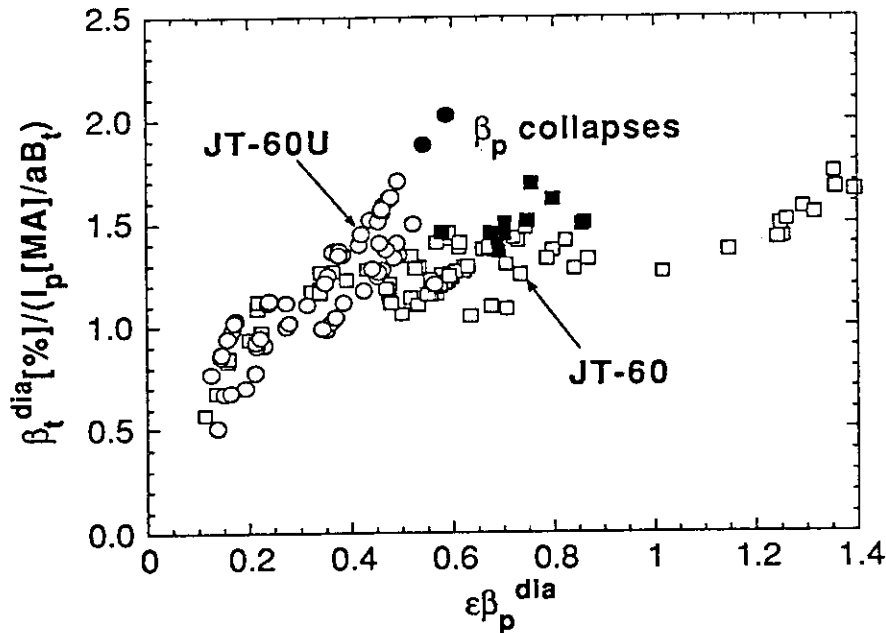
Fig.3.1 Troyon factor as a function of $\varepsilon\beta_p{}^{dia}$ for high β_p experiments in JT-60U and JT-60.

The Troyon factor defined as $g=\beta_t{}^{dia}[\%]/(I_p[MA]/aB_t)$ was achieved to be 2.0 at $\varepsilon\beta_p{}^{dia}$~0.6 (or $\beta_p{}^{dia}$~2.5) in JT-60U. As shown with their closed symbols in this figure, the high β_p plasmas in

JT-60U have encountered the fast β collapses in a highest $\epsilon\beta_p$ and Troyon factor regime, which has the same features as the β_p collapses found in JT-60 as discussed in the next section. The plasma pressure is almost isotropic as $\beta_p^{dia}/\beta_p^{equ}\sim1.1$ (see Section 4.2). While the β_p collapse has been discovered from the specific circumstances in JT-60, it is now considered to provide a possible limit for general high β_p operation under a large bootstrap current fraction. Furthermore, the β limit boundary determined by the β_p collapses would be asymptotically connected with the conventional Troyon limit in the low β_p regime.

4. Poloidal-Beta Collapses

The β_p collapse observed in JT-60 was a non-disruptive β limiting phenomenon, probably because q_0 was well above 1, thus eliminating the m=1/n=1 mode. Significant reduction of the stored energy by 20-30 % was followed by the collapse. The MHD feature was characterized by a large-amplitude partial relaxation with a fast growth time of ~100 μs. The MHD observations were consistent with the ideal n=1 kink/ballooning stability analysis for the hollow current profile showing that an m=3/n=1 mode is dominant near the magnetic pitch minimum.

As shown in Fig.2.1 of Section 3.4.1, a β_p collapse in JT-60U occurred at ~0.9 s after the beam injection and limited the increase in the stored energy, the β values, ion and electron temperatures and neutron yield. For the same discharge, the temporal evolution of the electron temperature at r/a~0.2 is shown in Fig.4.1, which is obtained from the electron cyclotron emission measurement using the grating poly-chromator with a sampling time of 20 μs. The expanded time trace shows the very fast collapse time of ~100 μs with some mode rotating. After that, the temperature gradually decreases for t~7.90-7.97 s, suggesting the incomplete reconnection near the center during the β_p collapse.

Location of the β_p collapse within the plasma can be estimated form the soft X-ray arrays with 64 channels as shown in Fig.4.2(a), showing the lines of sight for the soft X-ray measurements. From the bottom array with a digitizing time of 40 μs, the soft X-ray profiles are obtained during the β_p collapse as shown in Fig.4.2(b): at t=7.90740 s (Δt=0: just before the β_p collapse), t=7.90748 s (Δt=80 μs)and t=7.90752 s (Δt=120 μs).
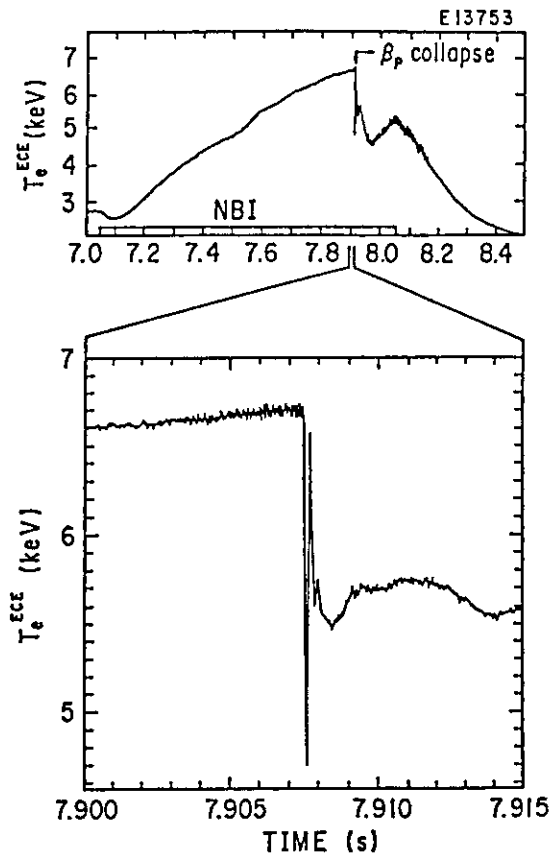
Fig.4.1 Evolution of electron temperature at r/a~0.2.

Figure 4.2(c) shows the profiles of the soft X-ray fluctuation level 80 μs and120 μs after the β_p collapse. It should be noted that, in Fig.4.2, the effects of neutrons on the soft X-ray signals before and after the β_p collapse are eliminated by subtracting the background noise level due to the neutrons from the raw signal for each channel. From the results, it is found that the chord inversion radius is located at r/a~0.37 where the flattening of the pressure initially takes place, leaving the central part of the soft X-ray emission profile during the collapse. Thus, the β_p collapse observed in JT-60U is also characterized by a large-amplitude partial collapse as observed in JT-60.
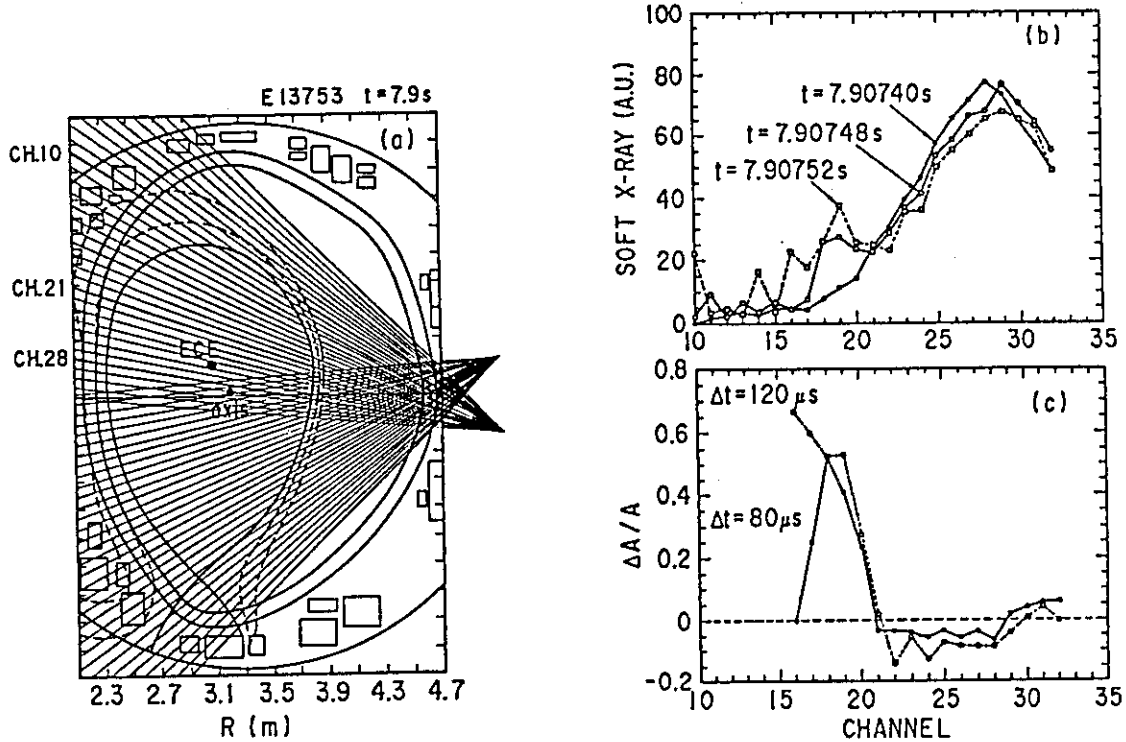
Fig.4.2 Soft X-ray arrays and the measured profiles of soft X-ray emission and fluctuation levels at the β_p collapse.

5. Summary and Future Directions

In JT-60U, the β_p collapses have been observed as a β limit for the plasmas with high Troyon factor (g~2), high poloidal beta (β_p^{dia}~2.5) and high enhancement factor (τ_E^{dia}/τ_E^{L}~3). The MHD features are quite similar to the JT-60 β_p collapses except that the occurrence timing during the beam injection in JT-60U is earlier than in JT-60. The dependence of the β limit on the current profile demonstrated in JT-60 and JT-60U gives hope that it will be possible to operate at high Troyon factor in future devices equipped with mechanisms for current profile control. The slow current relaxation during auxiliary heating must affect the β limit since the stability depends on the details of the current and pressure profiles. Thus, a long-pulse heating experiment is indispensable to investigate whether the plasma can be stable in a steady state. The effects of beam-driven currents by tangential injection on the β limit will be studied in the next experimental period of JT-60U for the future β limit control experiment with negative-ion based beam injection.

4.4 Enhanced Confinement in high βp plasma in JT-60U

M. Kikuchi, S. Ishida, Y. Koide, T. Nishitani, S. Tsuji

Enhanced confinement is observed in a series of high βp discharges. The high βp enhanced confinement is produced via intense NB heating to the low target density ($n_e{}^{OH}$=0.3-0.8x10^{19}m^{-3}) , small volume (V_p~50m^3), low current (1-1.5MA) plasmas. Higher confinement enhancement factor is obtained at higher βp / Ti up to 2.9 times ITER power law. Best τ_E is larger than those of 4MA L mode discharges and TFTR supershots

1. Introduction

Confinement optimization in high βp regime is particularly important for the realization of the steady state tokamak reactor based on the bootstrap current [1]. One of key issues in this regime is whether existence of large bootstrap current degrades energy confinement. In such a regime, radial excursion of the trapped particle is large (δr_{th} ~ 5cm, δr_{beam}~20cm) and the parallel viscous force plays an important role in the particle flow on the flux surface. Moreover, electrons and ions are deeply in the collisionless regime, collisionalities of which are typically ~0.1 and ~0.01, respectively. In such a regime, one may aware of the anomalous transport due to trapped particle instability. In the old JT-60 hydrogen experiments, confinement enhancement factor of ~1.5 has been obtained at low current (Ip=0.5-0.7MA) via intense NB heating (~20MW) into the small volume (~30m^3) lower X point discharges [2]. Similar to this experiment, we have studied the low density hot ion enhanced confinement regime (PEC mode) in deuterium discharges in JT-60U.

2. Energy confinement at high βp

Present experiments are made in the elongated divertor configuration at B$_t$=4T. Fig.1 shows the confinement enhancement factor over ITER-P scaling as a function of plasma current. Open and closed circles show small volume and full size ED data. Confinement optimization is focussed on low current (1-1.1MA) at small plasma volume where the sawtooth activity is suppressed (but is accompanied by continuous MHD modes in most cases). This mode of operation is characterized by the high T$_i$ and
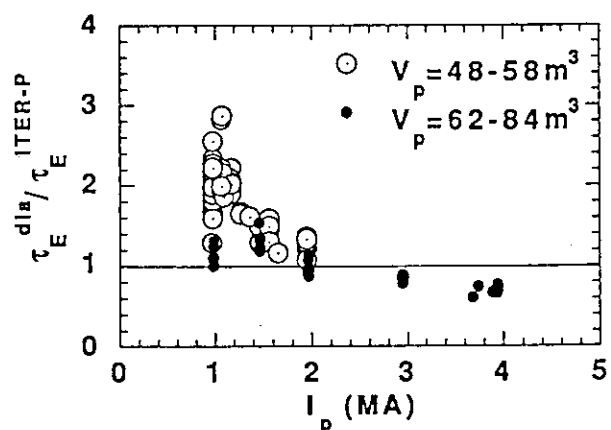
Fig.1 Confinement enhancement factor as a function of plasma current I$_p$.

large neutron yield up to 1.3×10^{16}/s. Fig.2 shows energy confinement time for low Ip regime as a function of the net heating power compared with ITER power law. The energy confinement time of 0.27s at $P_{net}=14$MW is demonstrated much better than that of TFTR supershot [3]. The confinement time of 2-3 times τ_E^{ITER-P} is obtained. Such an enhancement factor is obtained for a wide range of heating power, 10-20MW. Power degradation of the energy confinement is seen in most discharges in contrast to the TFTR supershot. Fig. 3 shows the confinement enhancement factor (H factor) as a function of net heating power. For 1MA plasmas, H factor varies depending on the optimization level. But the H factor for 1.1MA and 1.2MA plasmas is relatively constant as a function of the net heating power showing the existence of the power degradation, except for a few best PEC shots (E13752, 13753) in which very low target density $\sim 3 \times 10^{12}$m^{-3} has been obtained by a reduction of the recycling and continuous MHD modes have been suppressed. These best PEC shots have better confinement time than 4MA L mode discharges. Fig. 4 shows a comparison of the standard 1MA L mode and 1.1MA best PEC mode discharges (P_{NBI}, W_{dia}, n_e, neutron emission S_n, divertor and main D_α intensities are shown). PEC mode appears during the intense NB heating for low target density plasma with a reduced recycling in the divertor region. For higher plasma current (1.5-1.6MA), H factor is low, also insensitive to the heating power.
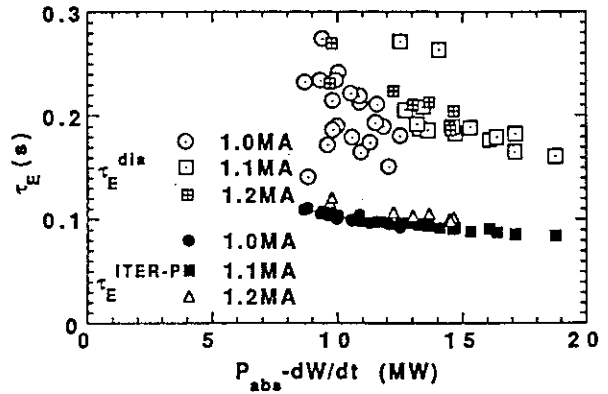
Fig. 2 Energy confinement time tE of PEC modes as a function of net heating power.
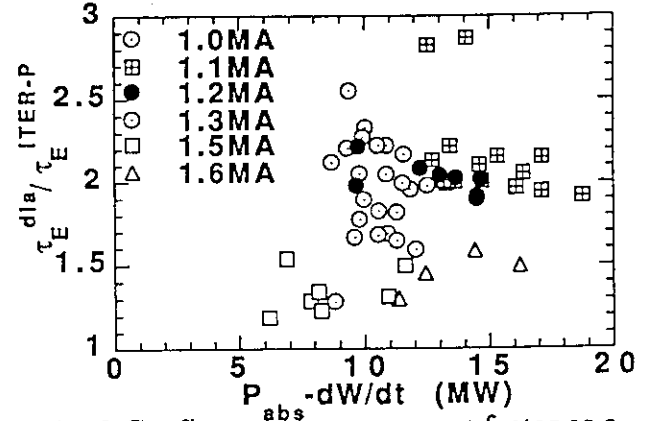
Fig. 3 Confinement enhancement factor as a function of the net heating power.
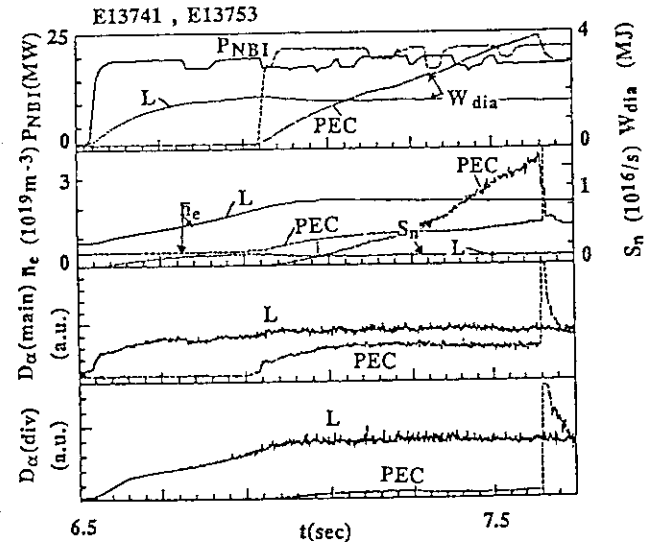
Fig. 4 Discharge waveform for 1MA L mode (E13741) and best PEC mode (E13753).

Appearance of the hot ion mode with $T_i \sim 3T_e$ is associated with this enhanced confinement mode. Fig.5 shows typical temperature profile of T_e and T_i, and the edge temperature is not quite high suggesting confinement improvement mainly comes from the central region. The central ion temperature is plotted as a function of plasma current I_p and safety factor q_{eff} in Fig. 6 and 7. Appearance of the hot ion mode may be related to the sawtooth stabilization at high q operation and the lower density operation at lower plasma current. Systematic study to identify the regime of the hot ion mode is required to clarify the cause of this improvement.

Fig. 5 Typical ion and electron temperature profiles for PEC mode.

Fig. 6 Maximum $T_i(0)$ as a function of plasma current for JT-60 and JT-60U.

2. Correlation of the enhanced confinement with plasma parameters

One of key interests of the high βp mode is whether the enhanced confinement is attainable at high βp where a large fraction of the plasma current is carried by the bootstrap current. Fig. 8 shows the confinement enhancement factor as a function of the

Fig. 7 Maximum $T_i(0)$ as a function of safety factor for JT-60 and JT-60U.
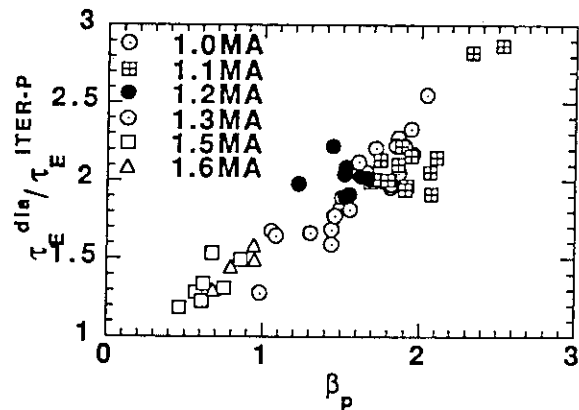
Fig. 8 Confinement enhancement factor as a function of poloidal beta value.

poloidal beta for various plasma current. Higher H factor is obtained at high poloidal beta, relavant for the steady state tokamak reactor concept. But it should be careful to say $\tau_E/\tau_E^{ITER-P} \sim \beta_p$ which is the definition of the H factor itself and results in an energy balance equation like $dW/dt = P_{net} - W/\tau_E = $ const.(with respect to W) and has no steady state solution. Fig. 9 shows the H factor as a function of the maximum ion temperature. This figure may suggest thermal diffusivity χ has favourable dependence on T_i as suggested by TFTR supershot. But it should be carefully examined, as in the case of β_p dependence.
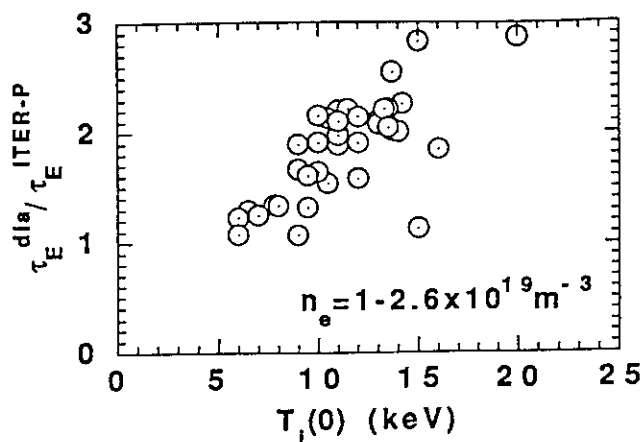
Fig. 9 Confinement enhancement factor as a function of central ion temperature.

3. Summary

Energy confinement properties of high β_p enhanced confinement regime (PEC) is investigated in JT-60U. Confinement enhancement factor up to 2.9 over the ITER power law is obtained. This enhanced confinement is obtained in small volume plasma ($<50m^3$) and low target density plasmas, similar to the TFTR supershot. And there are some differences and similarities. PEC mode has power degradation similar to L&H modes, in contrast to the supershot. Absolute value of supershot τ_E is 120-170ms, insensitive to I_p and heating power which casts a fear on the feasibility in the higher current future machines. Attainment of better confinement time (absolute value up to 270ms) in PEC mode is thus important if it is same kind of improved confinement. Confinement improvement mainly comes from the central part and further improvement should be pursued in combination with the H mode.

References

[1] Y. Seki, M. Kikuchi et al., IAEA-CN-53/G-1-2, (1990,Washington).

[2] S. Ishida, M. Kikuchi et al., IAEA-CN-53/A-3-2, (1990,Washington).

[3] M.G. Bell et al., IAEA-CN-50/A-1-2, (1988, Nice).

4.5 Ion Temperature and Rotation Characteristics in Hot-Ion Mode in JT-60U

Y. Koide, S. Ishida, A. Sakasai, N. Asakura and M. Kikuchi

Hot-ion mode has been continuously studied in JT-60U with deuterium as working gas since we had found it in high β_p regime with JT-60 hydrogen plasma [1]. (Here 'hot-ion mode' is defined as the following : The central ion temperature (T_i) is decoupled from electron temperature (T_e) and is raised above ~10 keV. Comparing with JT-60 hot-ion mode, the maximum central ion temperature is doubled to above 20 keV (See section 3.4.1), and more detail profiles are obtained with new CXRS diagnostic with the improved spatial resolution (See section 6.2.1). This paper deals with the characteristic evolution of $T_i(r)$ and $V_t(r)$ in hot-ion mode.

Figure 1(a) shows the example of measured profile of $T_i(r)$ with I_p=1.1MA, B_t=4 T, q_{eff}=8.3, NB power of 18 MW. Sawtooth activity doesn't appear in this range of q_{eff} and injection power. As seen in this figure, $T_i(r)$ is peaked in the central region and $T_i(0)$ reaches 14 keV. The high T_i and its high peakedness are characteristics of hot-ion mode. $T_i(0)$ is plotted as a function of q_{eff} in Fig.2(a). This q_{eff} scan, in fact, is equivalent to I_p scan (I_p=1.1-3 MA) because B_t is fixed at 4 T in this data set. Data free from sawtooth oscillation are selected because it seems that hot-ion mode doesn't coexist with sawtooth oscillation. $T_i(0)$ increases slowly with q_{eff}. The peaking parameter $T_i(0)/<T_i>$ weakly increases or is roughly constant with q_{eff} as shown in Fig.2(b). The maximum value of $T_i(0)/<T_i>$=6 is higher than that in JT-60 hot-ion mode, where $T_i(0)/<T_i>$ is below 4.5 in the range of q_{eff}=4-16. The close relation of $T_i(0)/<T_i>$ with that of electron density recognized in JT-60 hot-ion mode but it cannot be discussed on JT-60U data with small plasma volume due to the lack of the central density measurement.

The measurement of $V_t(r)$ (Fig.1(b)) shows that plasma is rotating in the counter-direction with the high speed of $\sim 1 \times 10^5$ m/sec. This feature of counter-directed rotation is commonly observed even if the net momentum input is co-directed irrespective of hot-ion or non hot-ion discharges. This peculiar behavior is discussed in section 6.2.1. The special feature of $V_t(r)$ in hot-ion mode is observed in the central region, r<0.2 m, as seen in this figure. It should be noted that the region is almost coincides with the peaking region of T_i, the key factor on the location of peaking region is not clear. Although the peaking region has been studied from the viewpoint of the relation with the rational surfaces inferred from MHD mode of m=1-3 in JT-60 [2], the same method is not applicable because only m=1 oscillation appears in JT-60U at present , which may be partly because q_{eff} is not scanned to the range above 10.

As mentioned above, T_i and V_t peaks in the similar region. However their evolution is not necessarily simultaneous. Figure 3 shows the mutual evolution of $T_i(0)$ and $V_t(0)$. The period of 400 msec from the start of NB injection to the timing when the $T_i(0)$ takes its maximum is plotted (the period of every 50 msec is marked with closed circles). In the first period of 200 msec, $T_i(0)$ and $V_t(0)$ grow together. In the following 100 msec, $V_t(0)$ takes its maximum. Even after $V_t(0)$ entered in the decreasing phase, $T_i(0)$ is still in the growing phase. Because the net momentum input is thought to be co-directed, the tendency in $V_t(0)$ of returning back to co-direction might be attributed to the improvement in the momentum confinement. (As a matter of fact, the measurement of $n_e(r)$ evolution is required for conclusive discussions). From the viewpoint of the momentum balance in a steady state, the change in V_t suggests the change in the radial electric field (E_r) (Strict treatment requires the informations of poloidal rotation (V_p) and pressure gradient.). There is a possibility that the relation of E_r and confinement is systematically understood, combining with the discussion of edge E_r in H-mode.

Next we show the MHD activities in the central and edge regions, which prevents hot-ion mode to grow. Figure 4 compares two discharges with the similar controllable parameters of I_p=1.1-1.2 MA, B_t=4 T, NBI of 18 MW but with difference in the attained plasma performance. Figure 4(a) shows the evolution of the best shot, where the maximum neutron emission rate (S_n) of 1.3×10^{16} n/sec and the highest $T_i(0)$ of 20 keV is obtained at t=7.85 sec . From the start of NBI heating at t=7 sec, plasma stored energy (W_{dia}) and S_n (Fig.4(a)) increase monotonically till the event of β_p collapse at t=7.85 sec $(\overline{n_e}=1.3 \times 10^{19}$ m$^{-3})$. $T_i(0)$ also increases in like manner although it seems to be slowly oscillating in radial direction around t=7.5-7.9 sec. Toroidal rotation velocity is saturated at t=7.5 sec around 1×10^5 m/sec in counter direction. On the contrary in the case of Fig.5(b), $S_n, W_{dia}, T_i(0)$ saturate after t=7.6 sec $(\overline{n_e}=1.8 \times 10^{19}$ m$^{-3})$. This timing is almost simultaneous with the appearance of oscillations observed in the soft X-ray (Fig.5(d)) and D_α/H_α in divertor region (Fig.5(e)). $T_i(0)$ is kept saturated after t=7.7 sec when the central MHD decreases. So hot-ion mode, which improvement is mainly in the central region, is largely affected by the peripheral condition.

[1] S. Ishida, et al, in Proceedings of the Thirteenth International Conference on Plasma Physics and Controlled Nuclear Fusion Research, Washigton, D.C., United States of America, 1990.

[2] Y. Koide, et al, The Role of Integer-mode Rational Surface on Peaked Profile Formation in Toroidal Rotation Velocity and Ion Temperature, JAERI-M 91-041 (1991).
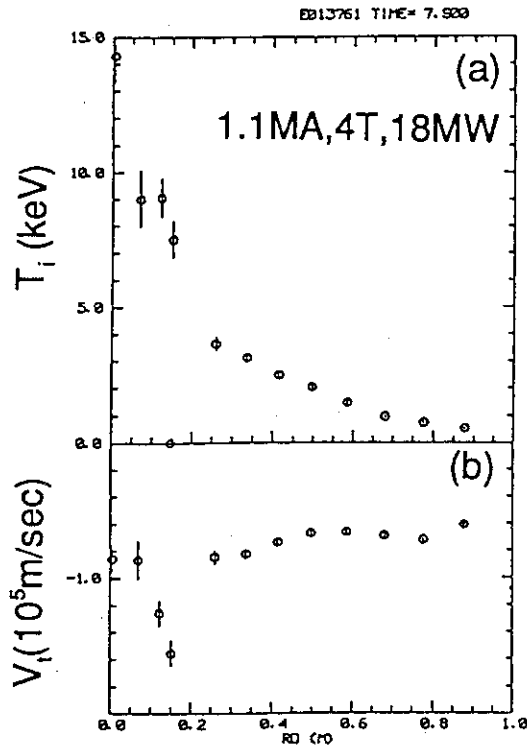
FIG. 1 $T_i(r)$ and $V_i(r)$ in hot-ion mode.
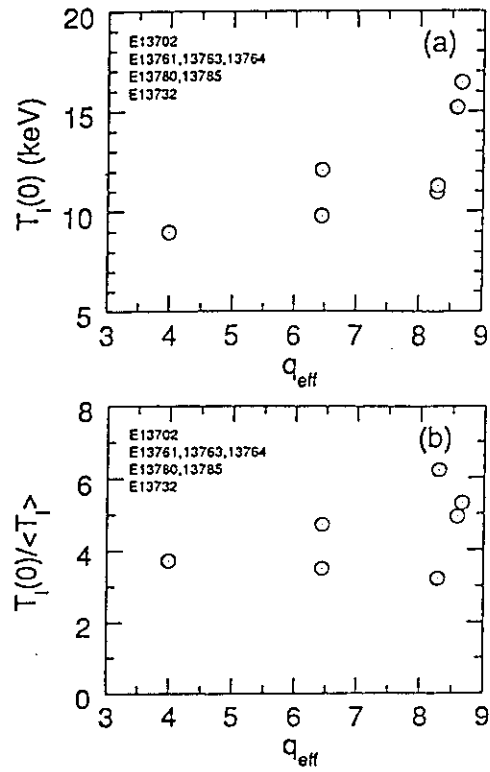
FIG. 2 q_{eff} dependence of $T_i(0)$ and $T_i(0)/<T_i>$
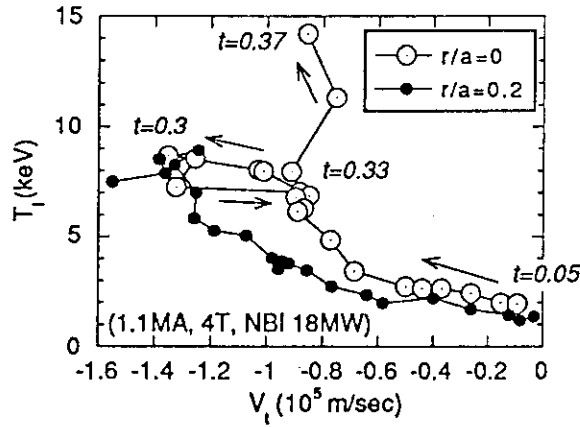
FIG. 3 Correlative evolution of $T_i(0)$ $V_t(0)$ during hot-ion mode.

FIG. 5 Evolution of hot-ion mode with MHD activities.
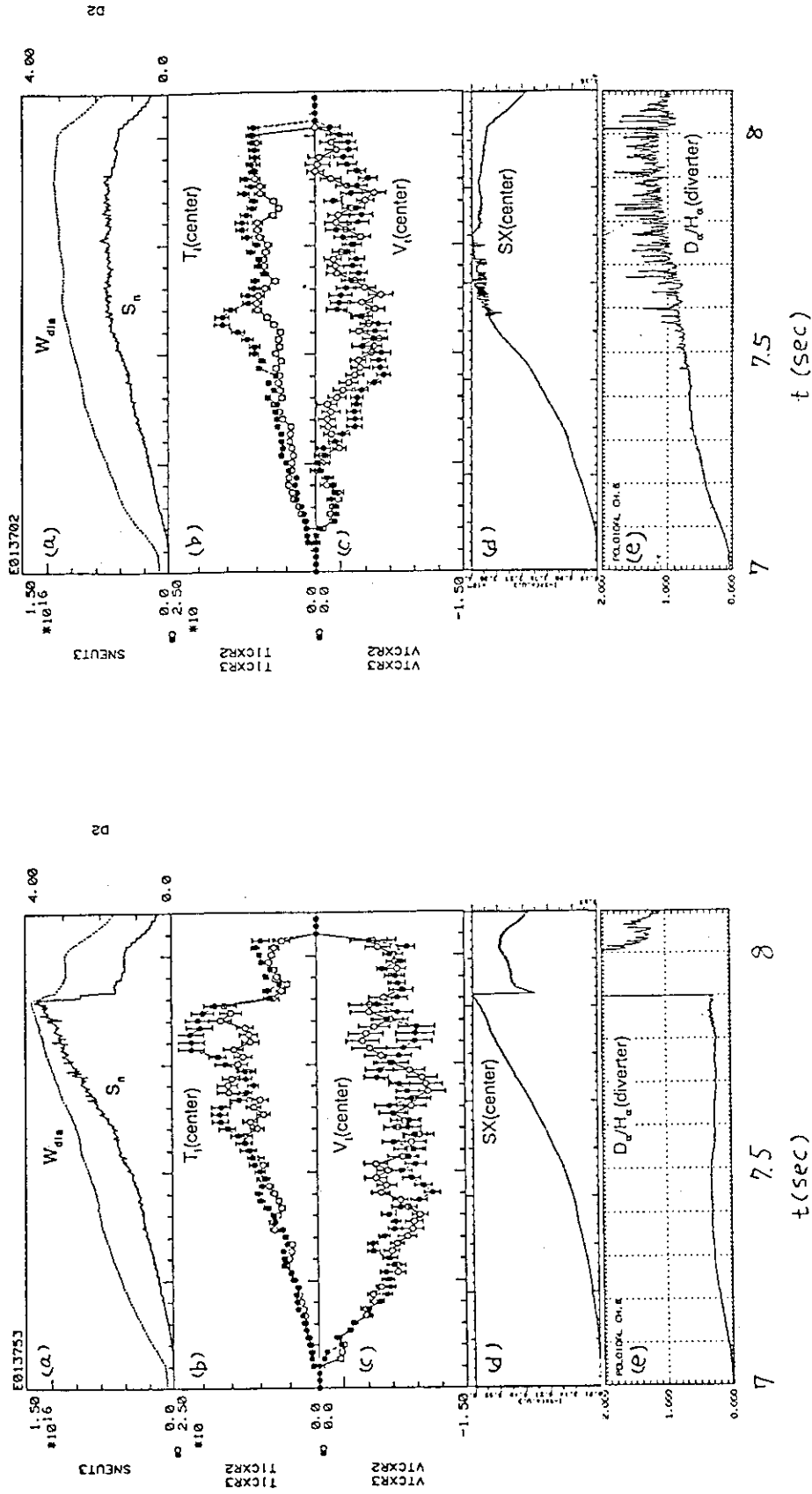
FIG. 4 Evolution of hot-ion mode without MHD activities.

4.6 Neutron Production and Q Value Evaluation in High βp Plasmas

T. Nishitani, S. Ishida, M. Kikuchi, S. Miura and M. Azumi

1. Introduction

The fusion power multiplication Q_{DD} of the D-D plasma has been used to evaluate the plasma performance as well as the energy confinement time τ_e. It has different dependence or sensitivity on certain plasma parameters. For example, it is more sensitive to the deuterium dilution through Z_{eff} of the H/D ratio. In the high βp regime, the fast ion component generated by the beam injection has an important role on the enhancement of the confinement and the fusion reactivity. The Q_{DD} or the fusion reactivity is more sensitive to the fast ion component than the τ_e or the stored energy, so that the Q_{DD} is a suitable parameter to evaluate the plasma performance in the the high βp regime. Whereas, the fusion power multiplication Q_{DT} extrapolated from the D-D plasma to the D-T one is more attractive than the Lawson parameter to criticize the breakeven condition. Here the measured Q_{DD} and the Q_{DT} analysis of the high βp plasmas are presented. The neutron yield characteristics of the NB heated discharges including high βp ones is presented section 9.2.

2. High Neutron Yield by the high βp plasmas.

We obtained the high neutron emission rate, two shots of $1.1- 1.3 \times 10^{16}$ n/s and several shots of $7- 8 \times 10^{15}$ n/s, in the high βp plasmas with almost same plasma condition. Figure 1 shows the neutron emission rates of a couple of the typical βp discharges. The best neutron emission rate, 1.3×10^{16} n/s, was obtained in E013753, and 7×10^{15} n/s was obtained in E013750.
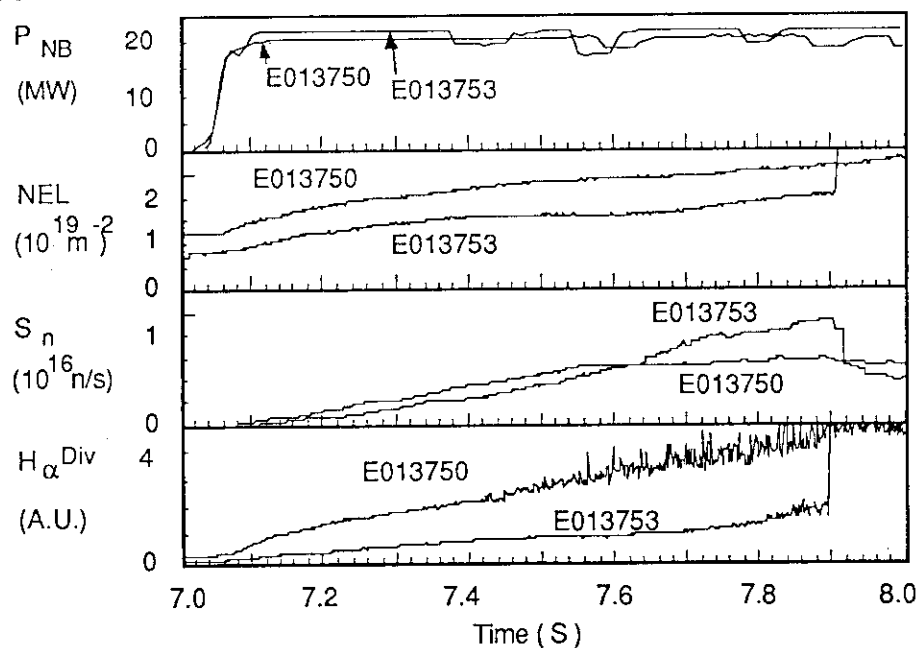
Fig. 1 Time evolutions of NB power, line electron density, neutron emission rate and Hα intensity in the divertor region for discharges E013750 and E013753.

Both discharges have same Ip of 1.1 MA, and almost same NB power of 21-22 MW and the equilibrium configuration. The electron density of E013753 is approximately two thirds of that of E013750. The Hα intensity of E013753 is approximately one third of that of E013750, which is consistent with the difference of the electron density because the Hα intensity is proportional to the square of the electron density. The neutron emission rate S_n of E013750 is grater than that of E013753 before 7.6 sec., but is saturated associated with the growth of the ELM fluctuation appeared in the Hα intensity. The S_n of E013753 increases steeply after 7.6 sec. according with the increase of the ion temperature which indicates that the ion heating regime is performed where the critical energy E_C ($\approx$ 19 T_e) is higher than beam energy E_B so that the NB is heating ion directory. The increase of the S_n is terminated by the βp collapse (see Section 4.3).

3. Q_{DD} of the high βp plasmas.

In the D-D plasma, dominant fusion reactions are follows; (1) d + d → t (1.0 MeV) + p (3.0 MeV) and (2) d + d → ^{3}He (0.8 MeV) + n (2.5 MeV). The reaction blanch (1) and (2) have almost same reactivity in the interesting energy range for a fusion study. A unit neutron yield corresponds to the fusion output power of (4.0 + 3.3) MeV = 1.2×10^{-12} J. Therefor the D-D fusion power multiplication Q_{DD} is defined as follows;

$$Q_{DD} = \frac{P_{Fusion}}{P_{Input}}$$
$$= \frac{1.2 \times 10^{-12} \ S_n}{P_{Input}} \tag{1}$$

where S_n is the neutron emission rate and the P_{Input} is the $P_{OH} + P_{NB}$ for NB heated discharges. The is the net NB power injected to the plasma with correction of the re-ionization loss in the injection ports and the shinethrough. Figure 2 shows the Q_{DD} obtained in the NB heated discharges as a function of the heating power. The Q_{DD} increases with the heating power.
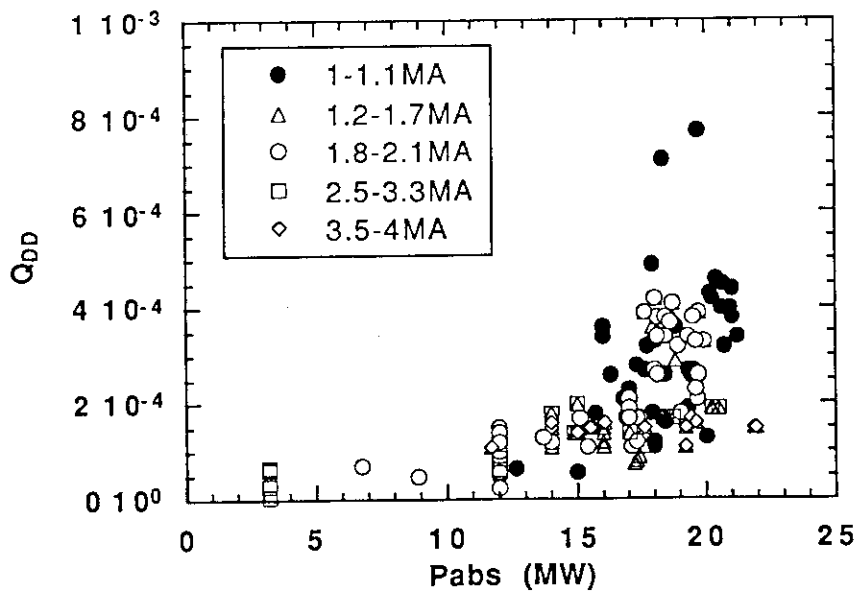
Fig.2　Q_{DD} of the NB heated discharges as a function of the heating power.

The maximum of 8.9×10^{-4} is obtained in the best neutron yield discharge E013753. The Q_{DD} of the discharges with the P_{NB} of 15-20 MW is scattered in the range 1.0×10^{-4} to 5×10^{-4} except a couple of the best neutron yield discharges. Those Q_{DD}s are larger than twice of other ones but consistent with the those of TFTR supershot [1,2], $Q_{DD} = 7.0 \times 10^{-4}$ to 1×10^{-3} for P_{NB} of 15-20 MW, which indicates that those two discharges are similar to the supershot of TFTR.

3. Neutron Production Analysis and Projection of D-T Plasma Performance.

The neutron production analysis and the projection of the D-T plasma performance have been carried out for the best neutron yield discharge by using a steady-state 1.5 D tokamak code with a multi-pencil-beam model is used beam of beam deposition. The confined beam-ion distribution function is calculated by a steady-state Fokker-Planck solution in the code.

The ion temperature profile measured with the CXRS and the electron temperature profile with the ECE shown in Fig. 3.2 of Section 4.1 are used in the calculation. The Thomson scattering measurement is not available for this equilibrium configuration because the FIR beam is passing only the plasma edge region. A couple of sight line of the FIR interferometer have almost same tangent radii for the configuration so that the electron density profile could not be estimated. Therefor the electron density profile is assumed to be parabolic as $n_e0\ [1 - (r/a)^2]^m$, and the power m is determined to reproduce the stored energy and the neutron emission rate within their measurement uncertainties, where anisotoropy corrected stored energy as $W = (W_{dia} + 2\ W_{In})\ /3$.is used. In this calculation, the deuterium enrichness D/(D + H) is 0.85, Zeff is 3, and the impurity is assumed to be carbon. Figure 3 shows the stored energy and the neutron emission rated as a function of the power m, where the line electron density of U1 pass is foxed to be measured value. The power m of 1.4 has good agreement with both the stored energy and the neutron emission rate. Thus, the electron density profile of $(4.8 \times 10^{19})\ [1 - (r/a)^2]^{1.4}\ m^{-3}$ is obtained.
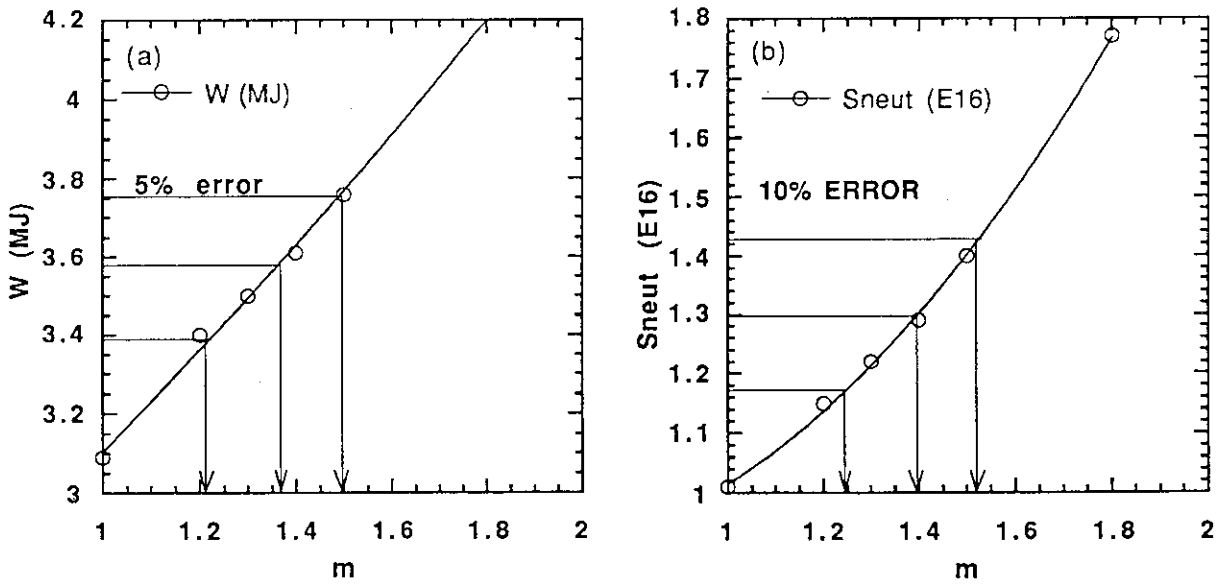
Fig.3　Calculated (a) stored energy and (b) neutron emission rated as function of power m in the parabolic electron density profile $n_e0\ [1 - (r/a)^2]^m$.

The calculated neutron emission profile is shown in Fig.4. The calculation indicates that for the discharge with the highest Q_{DD}, 27 % of the neutron yield is due to thermal-thermal reactions, 53 % due to beam-thermal and 20 % due to beam-beam reactions. The thermal-thermal component has a peaked profile due to the high ion temperature in the core region. The profiles of beam-thermal and beam-beam reactivities are slightly hollow provably because the beam lines do not pass just the plasma center.

The performance of equivalent D-T discharge was simulated by assuming D^0 beam injecting and 50/50 D/T target plasma.using same temperatures and electron density profile, Zeff, beam power, and other parameters as a comparable D-D discharge. The neutron emission profile extrapolated to D-T plasma is shown in Fig.5. The total neutron emission rate is expected to be 1.4 $\times$ 10^{17} n/s in the equivalent D-T discharge, which corresponds to Q_{DT} value of $\sim$ 0.20. Here Q_{DT} is defined by $Q_{DT} = P_{Fusion(DT)}/P_{Input} = 2.8 \times 10^{-12}$ S_n/P_{Input}. In this case the thermal-thermal reactions contribute 37 % while the beam-thermal beam-beam reactions are 63 % of the total neutron yield. The ratio of Q_{DT}/Q_{DD} is 225 which is near the results of TFTR $Q_{DT}/Q_{DD} \sim 180$ - 200 [1], but much smaller than JET results $\sim$300 [3].
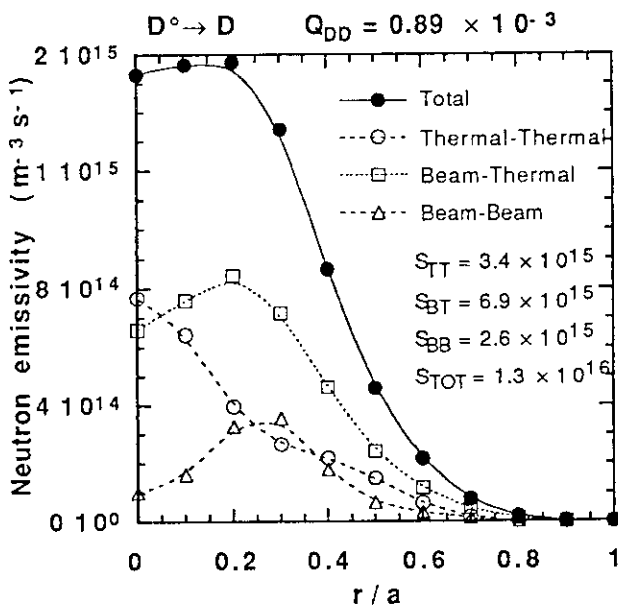
Fig.4   Neutron emission profile calculated for the shot E013753.
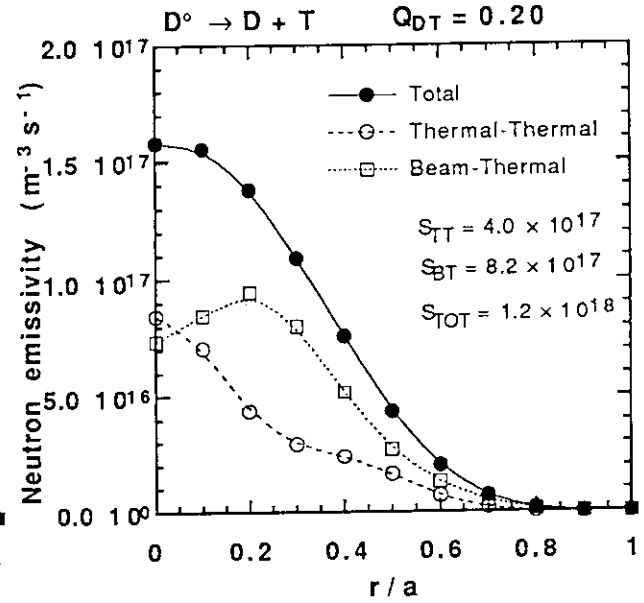
Fig. 5   Neutron emission profile extrapolated from the comparable D-D shot.

References

[1]   M.G. Bell, A. Arunasalam, C.W. Barnes, et al.,in Plasma Physics and Controlled Nuclear Fusion Research, IAEA-CN-50/A-1-2, IAEA, Vienna (1988).

[2]   D.M. Meade, A. Arunasalam, C.W. Barnes, et al.,in Plasma Physics and Controlled Nuclear Fusion Research,IAEA-CN-53/A-1-1, IAEA, Vienna (1990).

[3]   B. Balet, J.G. Cordy, P.M. Stubberfield, et al., Proc. 17th Europ. Conf. 14B, Part I, (1990) 65.

4.7 Recycling and H/D Ratio in High βp Discharges in JT-60U

Hiroo Nakamura, Shinichi Ishida, Akira Sakasai

1. Introduction

Controle of hydrogenic particle recycling is one of key issues in present plasma device to improve energy confinement characteristics. In JT-60U, the maximum values of enhancement factor of energy confinement time (2.9) and neutron production rate (1.3×10^{16} s^{-1}) have been attained in high βp experiments. In this paper, recycling characteristics in the high βp discharge is described. Also, hydrogen/deuterium ratio is described.

2. Recycling characteristics in high βp discharges

In the shots with the highest plasma performance, the electron density of target plasma is relatively low. However, for precise discussion on the particle recycling, much work is needed to measure particle confinement time and recycling coefficient. Therefore, global characteristics of the particle recycling is evaluated using the line integral electron density. Figure 1 shows typical wave forms of the line integral electron density during initial ohmic heating phase and NB heating phase. In standard divertor operation of JT-60U, plasma shape is changed from limiter configuration to divertor one at t = 2 s. During the divertor phase, decay of the line integral electron density is observed. This decay is considered to be caused by wall pumping of graphite divertor plate. In a shot No.13753 with the highest neutron production rate, line integral electron density just before NB heating is also low. Dischrarge of shot No. 13754 is a repeat shot of No. 13753. Line integral electron density of the shot 13754 is relatively high due to increase of wall recycling. Figure 2 shows relation between the line integral electron density at 2 s and one just before NB injection. Good correlation between these values is observed.
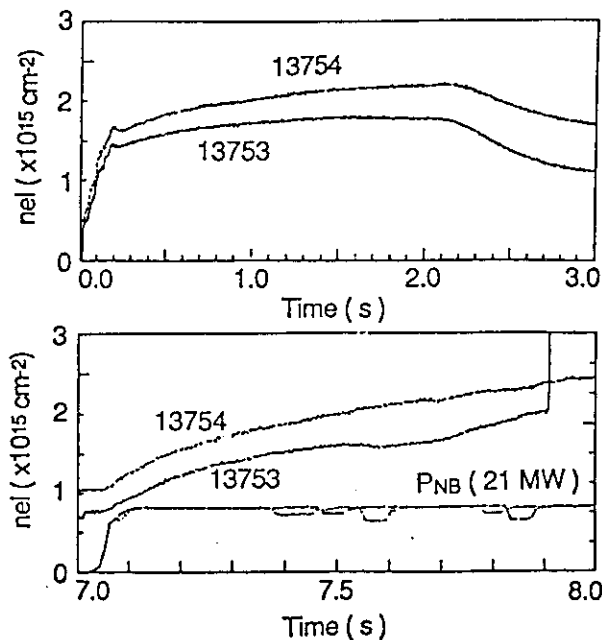
Fig.1 Temporal behaviors of the line integral electron density in high βp discharges.
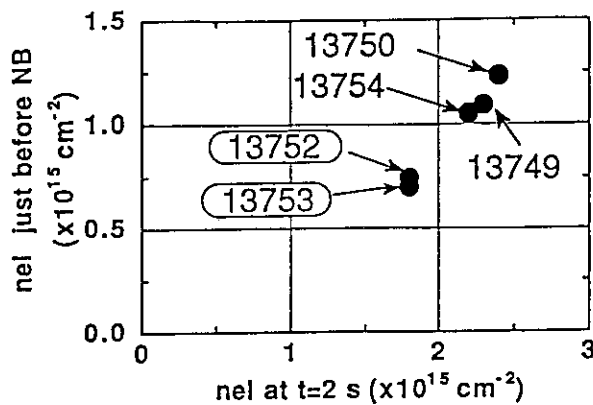
Fig.2 Line integral electron density at t = 2 s vs. line integral electron density just before NB heating in high βp dischrges.

Figure 3 shows that trend of the neutron production rate and the decay time of the line integral electron density at t = 2 s on a day when the highest neutron production rate was obtained. The decay time is defined by $n_e/(-dn_e/dt)$ and used to compare recycling characteristics. Plasma current is 1 MA and neutral beam heating power is about 21MW. Shot No.13753 show highest neutron production rate. During lunch time during 12am to 1pm, He GDC was done. In a first shot after the He GDC (E13751), the neutron production rate is 8×10^{15} s^{-1}. In this shot, the electron density was not obtained. Before a shot of E13752, He TDC was done. Density decay time is 1.2 s. This value is relatively low comparing standard value. Before a shot of E13753, He TDC was also done. Interval time between shot E13752 and shot E13753 is about 2 hrs. During such a long interval time, vacuum pumping is also effective for degassing of graphite tile. In the both discharges of E13752 and E13753, high neutron production has been obtained. However, a shot of E13754 does not show high neutron production rate. In this shot, decay time of the line integral electron density increases up to 3 s. In the repeat shots of E13755 and E13756, the neutron production rates decrease around 8×10^{15} s^{-1}. In these shots, the decay times are not obtained because the electron densities were not measured. However, wall recycling in the repeat shots of E13755 and E13756 is considered to be similar to the shot E13754. According to these observation during E13749 to E13756, low recycling condition which the density decay time is about 1.2 s is necessary to achieve high neutron production rate.
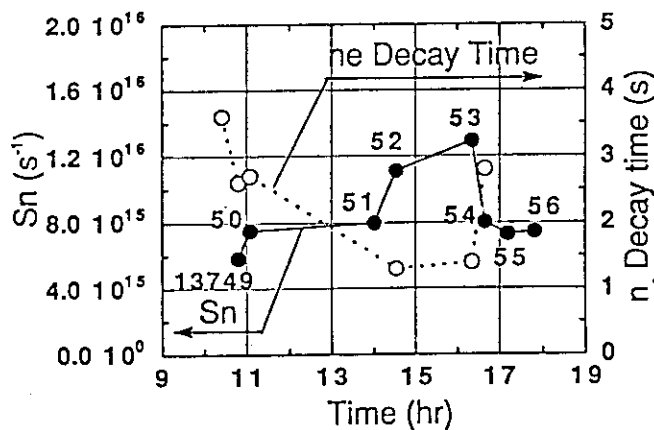
Fig.3 Trend of the neutron production rate and the decay time of electron density.
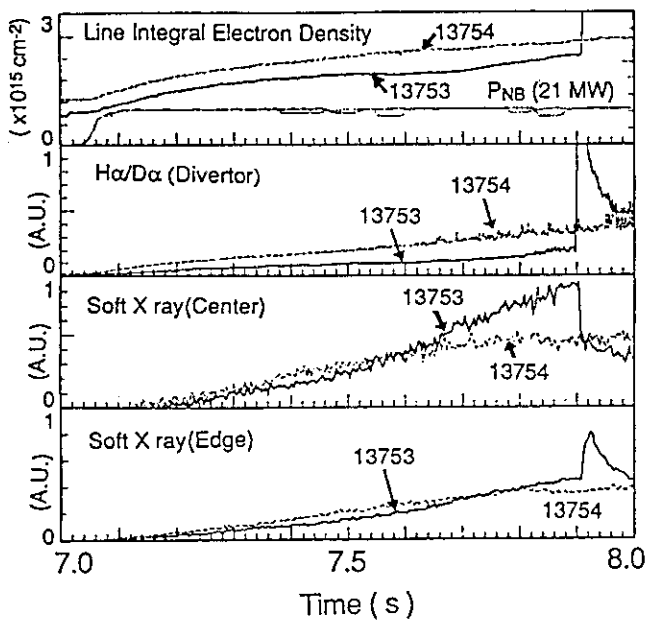
Fig.4 Typical wave forms of high βp dischrges of E13753 and E13754 during NB heating phase.

Typical wave formes of t he line integral electron density,divertor $H\alpha/D\alpha$ and soft X-ray intensity are shown in Fig.4. At $t = 7.9$ s of shot E13753, βp collaps occrred. Above 1.5×10^{15} cm^{-2} to 2×10^{15} cm^{-2}, fluctuation similar to ELMs is observed in divertor $H\alpha/D\alpha$ signal. In a shot of E13753, soft X-ray in center region end to increases from $t = 7.4$ s until the βp collaps. On the other hand, in case of shot E13754, significant increase of the soft X-ray in the central region is not observed. Fluctuation similar to ELMs is observed from $t = 7.5$ s. Therefore, low recycling condition to obtain low density target plasma is necessary to suppress these fluctuations. However, further study on effect of recycling on plasma characteristics is necessary.

3. Hydrogen/Deuterium ratio in high βp discharges

During the deuterium discharge, hydrogen dilution was observed. As preceding plasma discharges, ratio of hydrogen increases gradually. Moreover, beam heated discharges show higher hydrogen dilution than ohmically heated discharges. These characteristics implies that source of hydrogen is graphite tile. For example, typical value of H/(H+D) is 20% in September 1991. To increase DD neutron production rate, extensive reduction of the hydrogen dilution is necessary.

4. Summary

Highest performance of enhanced confinement and neutron production rate in JT-60U has been obtained in the discharges with lowest recycling. Decay time of the electron density at transition from limiter configuration to divertor one is about 1.2 s although the decay times in the standard shots are a few second. Study on correlation between recycling and plasma parameters is also necessary in future study.

4.8 Bootstrap Current in High βp Discharge

M. Matsuoka, M. Azumi, S. Ishida, Y. Kamada, M. Kikuchi,

H. Kubo, M. Kuriyama, M. Nemoto and H. Takeuchi

1. Introduction

The amount of bootstrap current in tokamaks have been well confirmed to agree with the prediction by the neoclassical theory in such an experiment performed in JT-60, where up to 80% of the total plasma current was driven by the bootstrap current [1]. On the basis of these experimental facts, steady state tokamak demonstration reactor SSTR with bootstrap fraction of 75% was proposed [2]. However, few observations on the profile of bootstrap current and temporal evolutions relating to this current are reported. In JT-60U, efforts are focused to obtain these data with the enhancement of the parameter regime. In this report, preliminary experiment on bootstrap current made in this period is described.

2. Typical Results

Figure 1 shows temporal evolutions of a poloidal beta βp and an estimated bootstrap current Ibs when deuterium beams of 16 MW absorbed power were injected into deuterium plasma with 1.1 MA plasma current. Ibs was estimated with 1.5 D transport analysis code using an electron temperature profile from ECE, an ion temperature profile from CXRS, two line-integrated electron densities from interferometers, and $Zeff$ from visible bremsstrahlung. An ion temperature profile before and after beam injection was assumed to be equal to that just after beam initiation and that of an electron temperature, respectively, since no data were available in these time spans. An electron density profile was fitted by 0.5 power of parabola as two line-integrated electron densities agree with measured values. $Zeff$ of this shot was not measured but was assumed to be 3.5, which was deduced from a series of data of the shots before and after the shot. The plasma surface voltage and the plasma stored energy calculated with these profile data agreed well with the measured values. Beam driven current was estimated to be less than several kilo amperes and can be ignored since beam were injected to quasi-perpendicular directions. As seen in Fig. 1, a bootstrap current was maximized at t=7.9 sec and was about 820 kA (75% of total plasma current). This bootstrap current is about a factor of two higher than that observed in JT-60. A poloidal beta at that timing was about 2.0. A volumed averaged electron temperature $<Te>$ was 4.9 keV. The other discharge parameters at the timing were: $<ne>=2.6\times10^{19}$ m^{-3},

$<Ti>=10.0$ keV, $R_{maj}=3.05$ m, $R_{min}=0.63$ m, ellipticity=1.88. The plasma configuration was a single null diverter with a toroidal field of 4 T.

Figure 2 shows a temporal evolution of the profile of bootstrap current in the same shot. The current density is higher at the outer side of the plasma and exceeds the joule current density. In fact, the plasma surface voltage was maintained negative throughout beam injection. The total current profile seemed, however, almost unchanged. Though sawtooth activity was not observed in joule heating phase due to high q operation, the safety factor at the plasma center should be nearly unity at beam initiation since joule phase lasted for seven seconds. After beam initiation, sawtooth-like MHD activity with small inversion radius ($\rho \approx 0.05$) was observed at every 0.25 seconds. This activity was not an usual sawtooth since the crash time was very long. The inversion radius was unchanged with time. Around the inversion radius, high frequency oscillation with odd poloidal mode number was observed. These observations indicate the total current profile did not vary in the time scale of Fig. 2 and consequently rational surface with safety factor of unity did not move at all.

3. Summary

Bootstrap current in JT-60U reached about 800 kA (75% of the total plasma current), which is about a factor of two higher than that obtained in JT-60. As usual in high q operation, the plasma energy confinement time was as good as two times of the ITER-89 L-mode power law. For further improvement of the plasma confinement characteristics, combined current drive experiments with LH and NB are planned.

References

(1)   M. Kikuchi et al., Nuclear Fusion 90 (1990) 343.
(2)   Y. Seki et al., 13th IAEA Meeting, Washington, 1990, IAEA-CN-53/G-1-2.
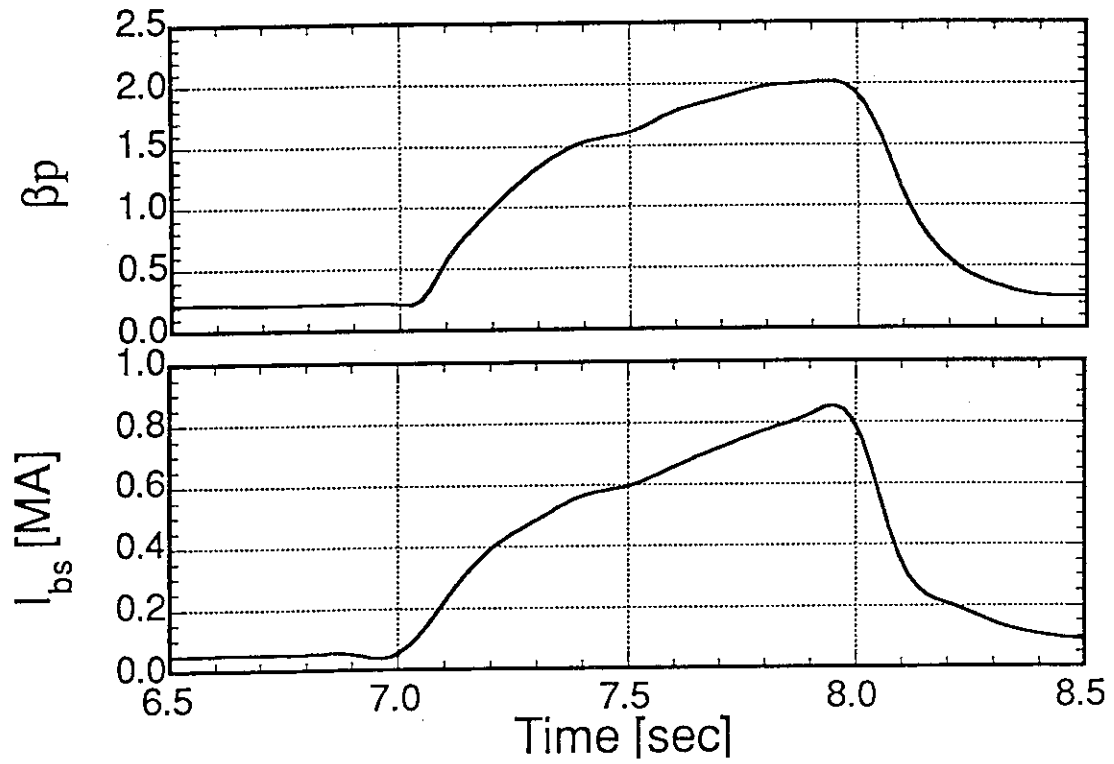
Fig.1 Temporal evolutions of a poloidal beta βp and an estimated bootstrap current Ibs
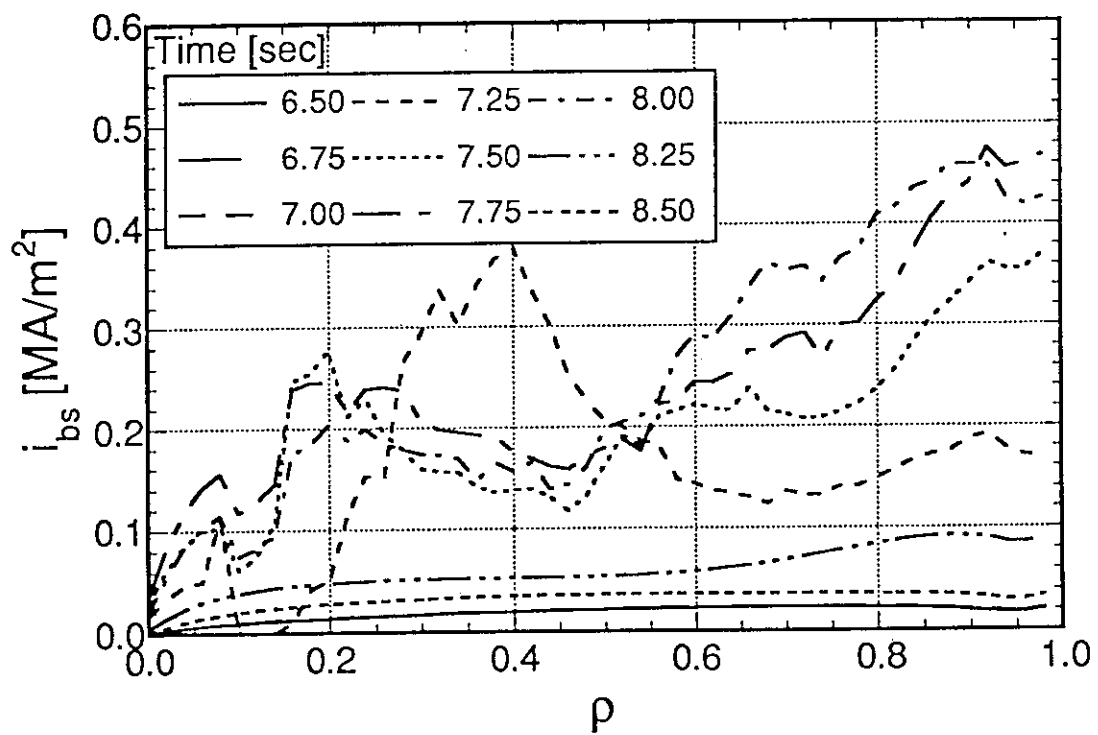
Fig. 2 Temporal evolution of the profile of bootstrap current.

5 Transport Studies

5.1 Transport Analysis of Ohmically Heated Plasmas in JT-60U

Hiroshi SHIRAI, Toshio HIRAYAMA, Masafumi AZUMI

Abstract. In ohmically heated plasmas, the neutron emission rate and the stored energy easily change with density peakedness factor, effective charge number and ion thermal diffusivity. No direct measurement of ion temperature and ambiguity of diagnostics data, especially density profile data, make the transport analysis very difficult.

In this section, we evaluate the plasma parameter dependence of neutron emission rate and stored energy in ohmically heated, deuterium plasmas in JT-60U as the first step of transport analysis. Assuming the electron density profile as some power of parabolic shape; $n_e(r) \approx n_e(0) \left(1 - r^2 \right)^m$, and using two channels of interferometer data, the line averaged electron density, $\bar{n}_e$, is inferred taking into account of Shafranov shift of magnetic axis. We use Electron Cyclotron Emission (ECE) data for the electron temperature, which is calibrated by Thomson scattering data. Effective charge number, Z_{eff}, is calculated by visible Bremsstrahlung data.

Since we do not have direct measurement of ion temperature data in ohmically heated plasmas, we must assume ion thermal diffusivity, χ_i. We often adopt neoclassical diffusivity proposed by Chang & Hinton, χ_i^{CH} [1], as χ_i. The profile of χ_i^{CH} is almost spatially constant in the bulk plasma but its value increases rapidly toward plasma center like $\chi_i \approx \varepsilon^{-1.5}$, where $\varepsilon = r / R$ is inverse aspect ratio. This feature of χ_i^{CH} profile may cause the suppression of central ion temperature and give rise to the underestimation of neutron emission rate.

In order to check the validity of adoption of χ_i^{CH} as χ_i, we compare the neutron emission rate calculated by some multiple of χ_i^{CH} with that calculated by spatially constant χ_i. We adopt shot E13807 (plasma current 2 MA, toroidal field 4 T, high elongated configuration, t = 9.75 sec) for this calculation. The measured neutron emission rate and the stored energy of this shot are 1.68×10^{12} s^{-1} and 0.73 MJ, respectively. The H/D ratio of this shot is about 0.3. We modify the calculated neutron emission rate (thermal-thermal reaction) by multiplying 0.59 (= $1/1.3^2$) because the calculation code deals with pure deuterium plasmas.

The calculation result shows that both χ_i models shows considerably good agreement of neutron emission rate (Fig.1). The central T_i values calculated by both χ_i models turn out to be almost the same. In this shot, both five times of χ_i^{CH} and constant $\chi_i = 1$ m^{2}sec^{-1} well reproduces the neutron emission rate and stored energy which are measured experimentally. Since the neoclassical diffusivity has q dependence, we must adjust the multiplication factor of χ_i^{CH} when we analyze the plasma of different current range. In this section, we assume spatially constant χ_i.

Now, there are lots of ambiguity factor about the profile data. The ambiguity of the electron density profile affects the stored energy and also affects neutron emission rate through the ion density profile. The ambiguity in the Z_{eff} value affects the ion density population and affects the stored energy and neutron emission rate. For these reason, we

must check the dependence of stored energy and neutron emission rate on the density profile peakedness factor, the Z_{eff} value and the χ_i value at first. We select shot E13807 again for these sensitivity check.

Figure 2 shows the dependences of stored energy and neutron emission rate on the density peakedness factor m. Originally, the calculated m value by using the interferometer data at U1 and U2 port is 0.32. When we change this peakedness factor, we use only the density data at U1 port. The line averaged electron density increases as m value. The Z_{eff} value is set 2.1 by visible Bremsstrahlung data. We assume spatially constant χ_i of 1 m^2sec^{-1}. Both stored energy and neutron emission rate increases as the peaking factor. Especially, the neutron emission rate is very sensitive to m; in other words, very sensitive to the density in the plasma core region. We need whole electron density profile data in order to evaluate accurately the neutron emission rate of ohmically heated plasmas.

Figure 3 is the Z_{eff} value dependence of stored energy and neutron emission rate. The density profile is given as $(1- r^2)^{0.32}$. We assume spatially constant χ_i of 1 m^2sec^{-1}. The decrease of neutron emission rate as the increase of Z_{eff} value is remarkable, because the ion density is diluted as $n_i/n_e = (Z-Z_{eff}) / (Z-1)$, where Z is the charge number of impurity. The decrease of stored energy as the increase of Z_{eff} value is not so large.

Figure 4 is the dependences of stored energy and neutron emission rate on the ion thermal diffusivity. We assume spatially constant χ_i. The cases of 0.1, 0.2, 0.5, 1.0, and 1.5 m^2sec^{-1} are compared. The Z_{eff} value is set 2.1. The density profile is given as $(1- r^2)^{0.32}$. It is very interesting that the decrease of stored energy due to the increase of χ_i value is very small. On the other hand, the neutron emission rate decreases rapidly as the increase of χ_i value. The small changes of ion temperature in the plasma core region greatly affects neutron emission rate.

As is apparent from these sensitivity check, the shortage of data, especially the electron density profile in the plasma central region, makes the transport analysis very difficult. At the present time, we cannot evaluate χ_e profile of ohmically heated plasma by using electron and ion power balance equation. In order to make reliable transport analysis, we need absolute value of central electron density and ion temperature, at least.

[1] C. S. Chang, F. L. Hinton, Phys. Fluids, **29** (1987) 3314
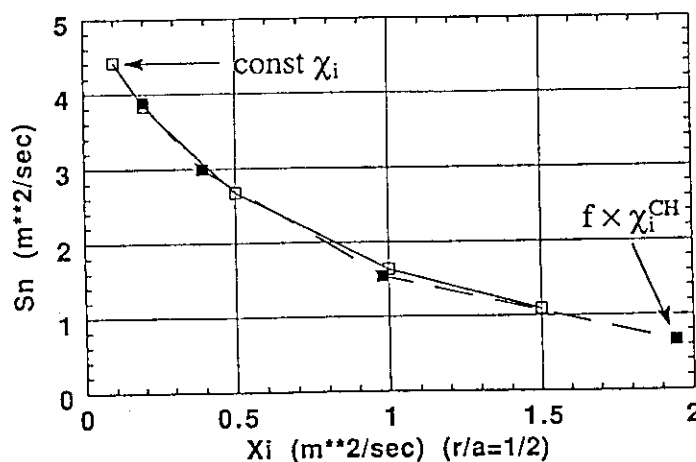
Figure 1   The comparison of neutron emission rate in different χ_i model; the spatially constant χ_i and the multiple of χ_i^{CH}.

Figure 2   The dependence of stored energy and neutron emission rate on the density peakedness factor m in shot E13807. The Z_{eff} value is set 2.1. We assume spatially constant χ_i of 1 m^2sec^{-1}.
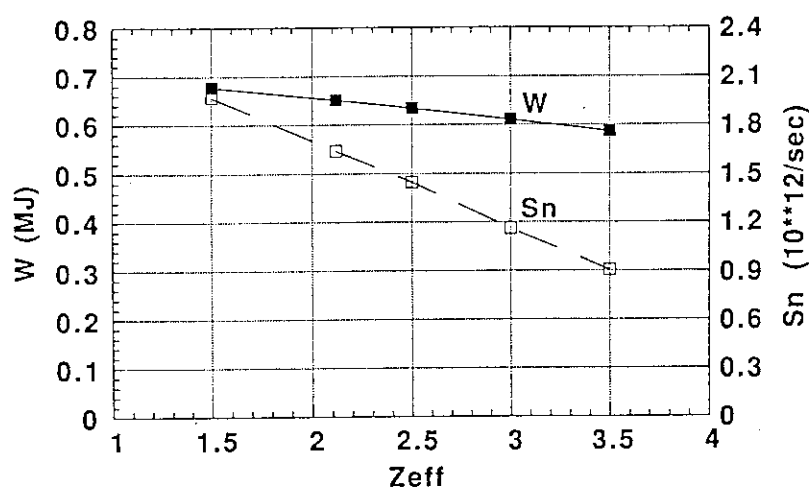
Figure 3   The dependence of stored energy and neutron emission rate on Z_{eff} value in shot E13807. The density profile is given as $(1-r^2)^{0.32}$. We assume spatially constant χ_i of 1 m^2sec^{-1}.
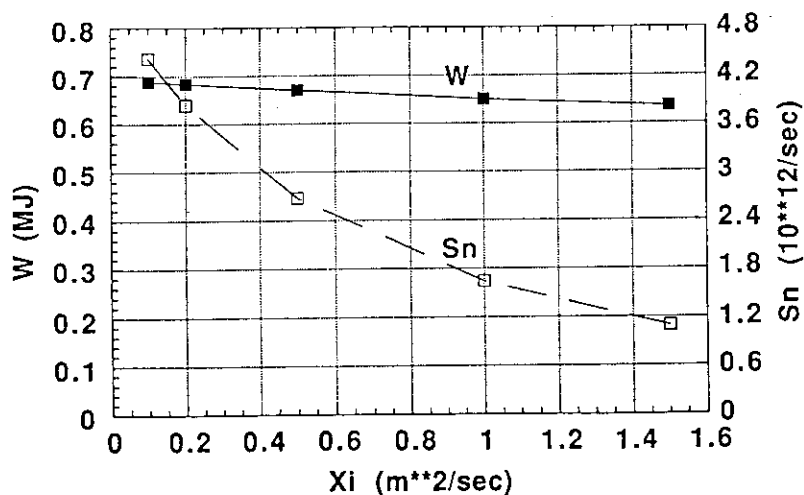
Figure 4   The dependence of stored energy and neutron emission rate on the ion thermal diffusivity in shot E13807. We assume spatially constant χ_i. The density profile is given as $(1-r^2)^{0.32}$. The Z_{eff} value is set 2.1.

5.2 Transport Analysis of Neutral Beam Heated Plasmas in JT-60U

Hiroshi SHIRAI, Toshio HIRAYAMA, Masafumi AZUMI

Abstract. Plasma parameter dependence (plasma current, absorption power and toroidal field) of electron and ion thermal diffusivities in the neutral beam heated JT-60U L-mode plasmas are studied. As plasma current increases χ_i decrease. As absorption power increase χ_i increases. On the other hand, the χ_e value is nearly insensitive to plasma current nor absorption power. This indicates that the ion thermal transport dominates the energy transport. The χ_{eff} value is almost insensitive to toroidal field.

In this section, we evaluate transport characteristics of neutral beam heated JT-60U L-mode plasmas. Plasma current, absorption power and toroidal field dependences of electron and ion thermal diffusivities, χ_e and χ_i, are estimated. As for the high ion temperature plasmas, we will discuss in the following section. The definition of χ_e, and χ_i, are shown as follows;

$$\chi_e(r) = \frac{-\frac{3}{2} T_e \Gamma_e + \frac{1}{r\langle |\nabla r|^2 \rangle} \int_0^r (- P_{rad} + P_{eq} + P_{OH} + P_{NBI}^e) \, r \, dr}{- n_e \frac{\partial T_e}{\partial r}} \tag{1}$$

$$\chi_i(r) = \frac{-\frac{3}{2} T_i \Gamma_i + \frac{1}{r\langle |\nabla r|^2 \rangle} \int_0^r (- P_{CX} - P_{eq} + P_{NBI}^i) \, r \, dr}{- n_i \frac{\partial T_i}{\partial r}} \tag{2}$$

where Γ_i, P_{rad}, P_{eq}, P_{CX}, P_{OH}, P_{NBI}^e and P_{NBI}^i represent the ion particle flux, the radiation loss, the equi-partition energy exchange between electrons and ions, the charge exchange loss, Ohmic heating power, respectively. Since P_{rad} is disregarded in this calculation, the χ_e and χ_i value in the peripheral region is not correct. Bracket is the average over a magnetic surface. Γ_i is defined as follows.

$$\Gamma_i(r) = \Gamma_e(r) = \frac{1}{r\langle |\nabla r|^2 \rangle} \int_0^r dr \, r \, (S + S_{NB}) \tag{3}$$

where S and S_{NB} are a local particle source due to the recycling at the wall and a fast ion birth profile of neutral beam, respectively.

In high density plasmas, it is very hard to estimate P_{eq} correctly. In such plasma, we evaluate effective thermal diffusivity, χ_{eff}, instead of χ_e or χ_i.

$$\chi_{eff}(r) = \frac{-\frac{3}{2} T_e \Gamma_e - \frac{3}{2} T_i \Gamma_i + \frac{1}{r\langle |\nabla r|^2 \rangle} \int_0^r (- P_{rad} - P_{CX} + P_{OH} + P_{NBI}^e + P_{NBI}^i) \, r \, dr}{- n_e \frac{\partial T_e}{\partial r} - n_i \frac{\partial T_i}{\partial r}} \tag{4}$$

First, we study the plasma current dependence of transport. We select plasmas whose absorption power is around 17 MW and toroidal field is 4 T. Line averaged electron density increases with plasma current ($\bar{n}_e = 2.5 \sim 5.2 \times 10^{19}$ m^{-3}). Figure 1(a) shows the plasma current dependence of stored energy component; W_e is the electron stored energy, W_i is the ion stored energy and W_b is the unthermalized beam component. We do not include 2 MA case in this figure, because there is not an appropriate 2 MA shot with the same absorption power range. We can see that W_e and W_i increase plasma current. Figure 1(b) shows the χ_e and χ_i value at half of minor radius. χ_e value does not change for different plasma current. On the other hand, the decrease of χ_i as the increase of plasma current is remarkable.

Figure 2(a) shows the absorption power dependence of stored energy component. Plasma current and toroidal field of these shots are 3 MA and 4 T, respectively. Line averaged electron density increases with absorption power ($\bar{n}_e = 2.6 \sim 3.6 \times 10^{19}$ m^{-3}). W_e, W_i and W_b increases as the absorption power. The χ_e value at half of minor radius is almost insensitive to the absorption power (Fig.2(b)). On the other hand, the χ_i value increases drastically with the absorption power. This trend was also observed in JT-60 plasmas (hydrogen plasmas) [1]. We can assert that the energy transport in the L-mode plasma is dominated by ion conduction loss.

Figure 3(a) shows the toroidal field dependence of W_e, W_i and W_b with plasma current of 3 MA and absorption power of 17 MW. Each stored energy component is independent of toroidal field. Since the line averaged electron density is fairly high for these three shot; $\bar{n}_e = 5.4 \times 10^{19}$ m^{-3} for 3 T shot, $\bar{n}_e = 4.9 \times 10^{19}$ m^{-3} for 3.5 T shot and $\bar{n}_e = 3.6 \times 10^{19}$ m^{-3} for 4 T shot, it is hard to estimate both electron and ion energy flows due to the large equi-partition loss channel. Instead of studying the characteristics of χ_e and χ_i, we examine the toroidal field dependence of χ_{eff} profile (Fig.3(b)). We can see that the dependence of χ_{eff} value on the toroidal field is very weak. This is consistent with the weak toroidal field dependence of energy confinement time in the ITER power law; $\tau_E \approx B^{0.2}$.

It is very interesting results that energy confinement time of neutral beam heated plasma is nearly independent of toroidal filed, while the τ_E of ohmically heated plasmas strongly depends on toroidal field. There must be transition in absorption power or density regime at which the toroidal field effect on the energy confinement changes. We must study this by making experiments with low density and law absorption power NBI plasmas.

We cannot compare the transport of hydrogen beam injected hydrogen plasma with that of deuterium beam injected deuterium plasma. This remains to be done for the future subject.

[1]   T. Hirayama, H. Shirai, M. Yagi, K. Shimizu, Y. Koide, M. Kikuchi, M. Azumi, Nucl. Fusion **32** (1992) 89.
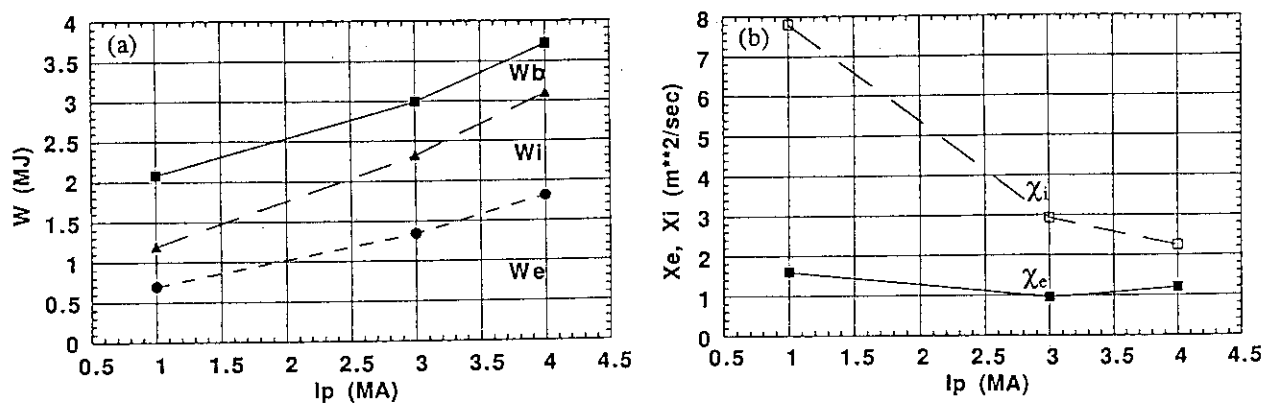
Figure 1   The plasma current dependence of (a) stored energy component and (b) χ_e
and χ_i value at half of minor radius. Absorption power and toroidal field of
these shots are 17 MA and 4 T, respectively.
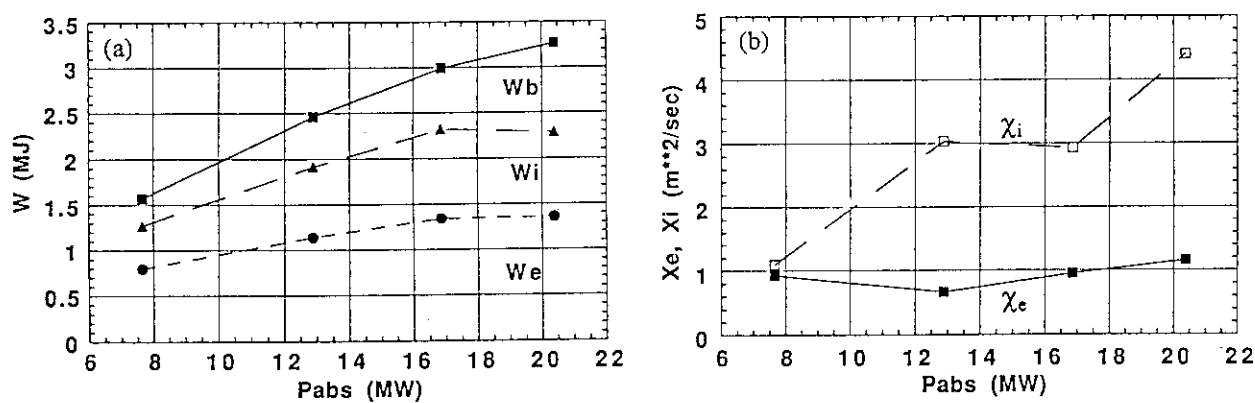
Figure 2   Thee absorption power dependence of (a) stored energy component and (b) χ_e
and χ_i value at half of minor radius. Plasma current and toroidal field of these
shots are 3 MA and 4 T, respectively.
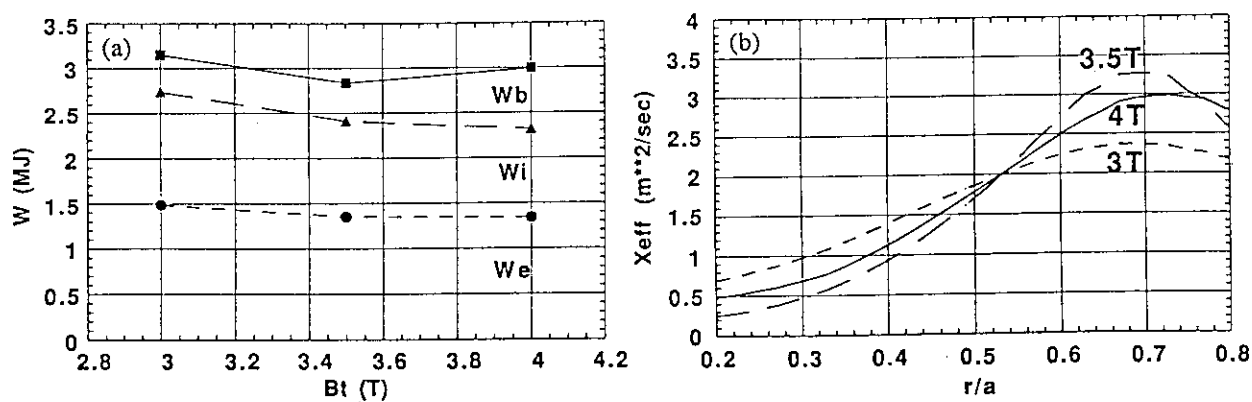
Figure 3   The toroidal field dependence of (a) stored energy component and (b) χ_{eff}
profile. Plasma current and absorption power of these shots are 3 MA and 17
MW, respectively.

5.3 Transport Analysis of Hot Ion Mode in JT-60U

Hiroshi SHIRAI, Toshio HIRAYAMA, Masafumi AZUMI

Abstract. The electron and ion thermal diffusivities of hot ion plasmas in JT-60U are calculated by using power balance equations. Lack of density profile data makes the estimation of thermal diffusivity very difficult, because the neutron emission rate easily changes with density peakedness factor and effective charge number. We cannot make clear conclusion on the plasma current dependence of χ_e and χ_i of hot ion plasmas at the present time.

In this section, we analyze the electron and ion thermal diffusivity, χ_e and χ_i, of high ion plasmas in JT-60U. We select plasmas whose central ion temperature is around 10 keV and more. We also make sure that diagnostics data such as two channels of interferometer data, ECE data and CXRS data are completed in these shots. The plasma current of analyzed hot ion plasmas are 1.1 MA, 2 MA and 3 MA. The 1.1 MA high T_i plasma is obtained with the condition of small volume (~ 50 m^3) and small minor radius which allows the central neutral beam deposition. The high T_i plasmas of 2 and 3 MA are obtained in the high elongated configuration (~ 75 m^3).

The characteristics of high T_i plasmas in JT-60 were that not only the T_i profile but also the density profile is highly central peaked pedestal one [1]. We can also expect such central peaked density profile in JT-60U hot ion plasmas. However, it is impossible to know the entire density profile because there is no density data in the central region. In this case, the assumption that the electron density profile is expressed by some power of parabolic shape; $n_e(r) \approx n_e(0) (1 - r^2)^m$ is entirely misleading. Actually, the obtained density peakedness factors m of hot ion plasmas are 0.1 ~ 0.6, at most 1.1. This value means very flat density profile, which is entirely different from high T_i plasmas of JT-60. With this very flat density profile, calculated stored energy and neutron emission rate becomes much lower than measured values.

We use Electron Cyclotron Emission (ECE) data which are normalized by Thomson scattering data for electron temperature profile and use Charge Exchange Recombination Spectroscopy (CXRS) data for ion temperature profile. Effective charge number, Z_{eff}, is calculated by visible Bremsstrahlung data.

Before calculating χ_e and χ_i by using the electron and ion power balance equations, we check the dependence of stored energy and neutron emission rate on the density profile peakedness factor and Z_{eff} value just as we executed in the transport analysis of ohmically heated plasma. We select shot E13777 (plasma current 1.1 MA, high elongated configuration, t = 7.7 sec) for these sensitivity check. The stored energy and the neutron

rate is 2.26 MJ and 3.89×10^{15} s^{-1}. The H/D ratio of this shot is about 0.3. We modify the calculated neutron emission rate by multiplying 0.59 (= $1/1.3^2$) to thermal-thermal reaction and 0.77 (= 1/1.3) to beam-thermal reaction because the calculation code deals with pure deuterium plasmas.

Figure 1 shows the dependences of stored energy and neutron emission rate on the density peakedness factor m. The calculated m by using interferometer data of both U1 and U2 port is 1.11. When changing the peakedness factor, we use only the density data at U1 port. The Z_{eff} value is fixed 3. Both stored energy and neutron emission rate increases as m value.

Figure 2 shows the dependences of stored energy and neutron emission rate on Z_{eff} value. The density profile is assumed to be parabolic. The decrease of neutron emission rate with increasing of Z_{eff} value is remarkable because of the sudden decrease of ion density. On the other hand, the decrease of stored energy is not so large.

As is apparent from these sensitivity check, the shortage of data, especially the electron density profile in the plasma central region, makes the transport analysis quite difficult. The following local transport analysis is subject to many ambiguity of measurement, although the stored energy and neutron emission rate are adjusted to the measured value as much as possible by modifying the density peakedness factor m, Z_{eff} value.

The definition of χ_e and χ_i is the same as are shown in the previous section. We select three plasmas in the high elongated configuration with different plasma current; 1.1 MA (shot E13777, t = 7.7 sec), 2 MA (shot E13785, t = 7.3 sec) and 3 MA (shot E13732, t = 6.85 sec). We modify density profile considering the stored energy and the neutron emission rate by measurement.

Figure 3 shows the χ_e and χ_i profiles of these shots. They are obtained on the assumption of parabolic shape of density profile and Z_{eff} value of 3. The χ_i value at the plasma central region becomes very small like JT-60 high T_i plasmas. The χ_i value of 1.1 MA plasma is lower than that of 2 MA or 3 MA plasma. However, we cannot take this result as it is because there is large difference in the plasma volume and there are lots of assumption to determine the profile data. In order to make clear the plasma current dependence of χ_e and χ_i in the high T_i plasmas, we need absolute value of central electron density and electron temperature, at least.

[1]   S. Ishida, M. Kikuchi, T. Hirayama, et al., in Plasma Physics and Controlled Nuclear Fusion Research 1990 (Proc. 13th Int. Conf. Washington D.C., 1990), Vol. 1, IAEA, Vienna (1991) 195
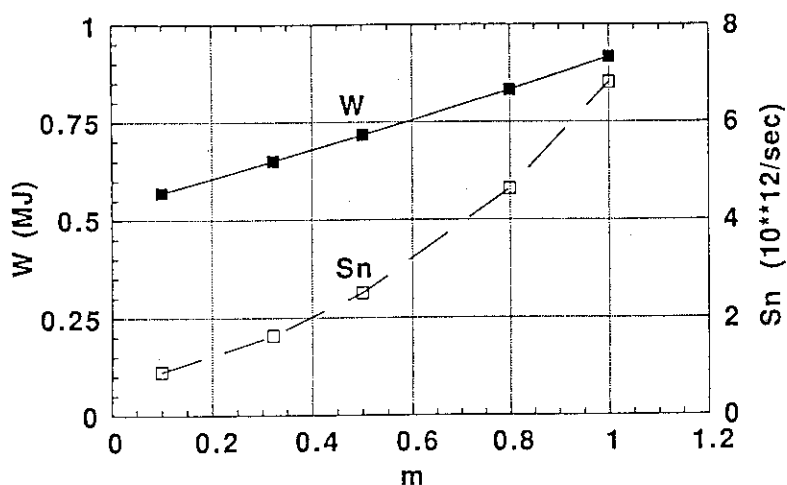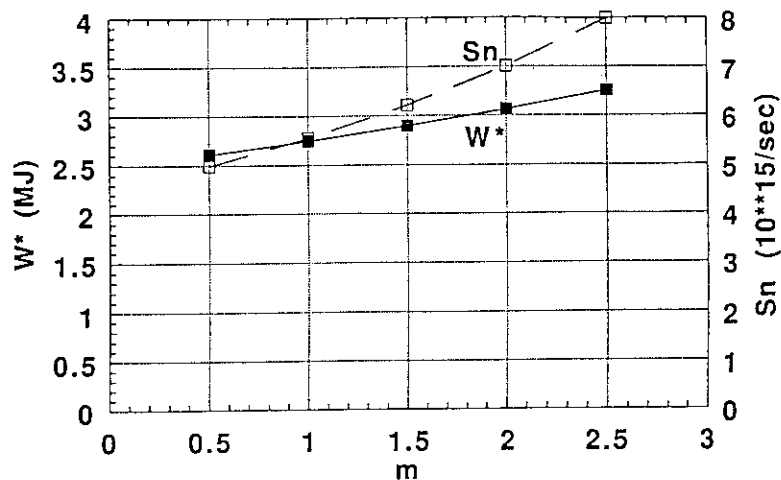
Figure 1   The dependence of stored energy and neutron rate on the density peakedness factor m. The Z_{eff} value is set 3.
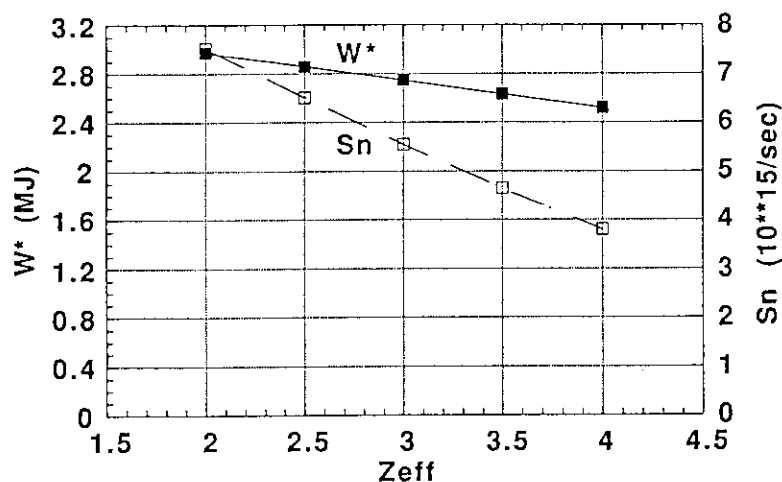
Figure 2   The dependence of stored energy and neutron rate on Z_{eff} value. The density profile is assumed to be parabolic.
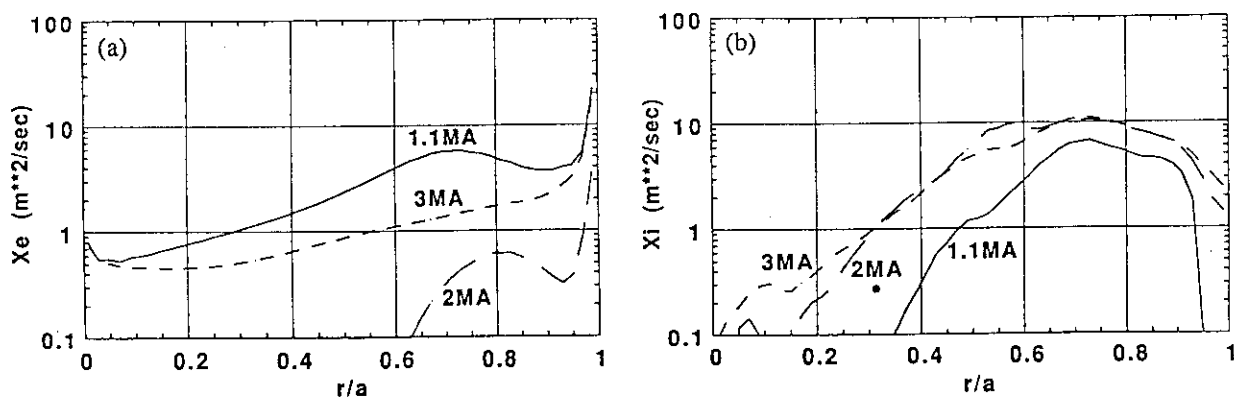
Figure 3   The profile of χ_e and χ_i with different plasma current; 1.1 MA (shot E13777, t = 7.7 sec), 2 MA (shot E13785, t = 7.3 sec) and 3 MA (shot E13732, t = 6.85 sec) in the high elongated configuration.

5.4 Transport Analysis Based on the Drift Wave Theory.

M. Yagi and M. Azumi

1. Introduction

The anomalous energy transports in a tokamak are considered to be caused by microturbulences of electrostatic drift wave type, and the linear stability and nonlinear state of these instabilities have been extensively studied from the theoretical points of view. The validity of these theories is usually tested by the comparison with experimental results at some specific radial points or by the transport code simulation. In this paper, we try different approaches to test drift wave theories by using the experimental data of JT-60 L mode discharges. We consider trapped particle turbulences for the electron anomalous energy transport and ion temperature gradient turbulences (η_i mode turbulences) for anomalous ion energy transport, respectively. We discuss electron and ion transports separately in the following, although the interaction between these two transport processes may be important.

2. Electron Transport Analysis

The anomalous thermal conductivity due to trapped electron turbulences has the different dependence on the electron temperature, depending on the regime of electron collisionality parameter, $\nu_{ei}/\epsilon\omega_*$, so that it may be one of good measures for testing the validity of theoretical models to check whether the global electron energy confinement time has the different dependence on the collisionality regime. We have evaluated the ratio of radial widths, where dissipative trapped electron (DTE) modes and collisionless trapped electron (CTE) modes are unstable; $\lambda = w_{CTE} / (w_{CTE} + w_{DTE})$. In JT-60 L-mode discharges, the collisionality parameter is almost always in the banana regime and it decreases with increasing plasma current. Figure 1 shows the electron energy confinement time τ_E^e versus the parameter l both for divertor and limiter discharges, where closed circle and triangle correspond to the divertor and limiter ones, respectively. The radial width w_{CTE} of collisionless trapped electron regime is wider for the divertor discharges, higher plasma current and lower input power. Although l changes in the wide range for discharge conditions, the data points of energy confinement time are scattered only in the bounded range and it is difficult to see the some correlation between the parameter l and the energy confinement time τ_E^e. In Fig. 2, the radial profiles of thermal conductivity χ_e based on the mixing length theory of trapped electron modes are compared with those evaluated from experimental data for both configurations of limiter (solid line) and divertor (dashed line). The regions of CTE and DTE modes are also

plotted in the figure. The mixing length theory gives roughly the value of the same order as experimental analysis but its tendency is opposite to the experimental one; that is, the wider CTE region gives the lower χ_e .

3. Ion Transport Analysis

Next, we consider the ion energy transport. Shirai et al. have tested the mixing length theory of η_i mode turbulence on JT-60 plasmas[1]. They have concluded that η_i mode turbulence is the good candidate of ion energy transport anomaly in the main region of the plasma, except central and peripheral regions. To confirm this conclusion in more quantitative sense, we perform the nonlinear simulation of η_i mode turbulence by using Hong/Horton model [1] and evaluate the absolute value of the thermal conductivity χ_i to compare with experimentally analyzed one. We perform the simulation for both cases of slab and toroidal η_i mode. Figure 3 shows the example of the simulation results for both cases. In this figure, the shaded region corresponds to the experimentally analyzed χ_i, while the solid line does to χ_i of Domingues-Walts model. Closed circles and triangles correspond to χ_i evaluated from nonlinear simulations by using the plasma parameters at each point and those evaluated from the mixing length model by using the simulation results, respectively. For the slab η_i mode model, χ_i of the mixing length model and simulation result are crucially different. And those values are also quite different from experimental values. The difference between the mixing length model and the nonlinear simulation is because the shear parameter of JT-60 is very small and the mode width of slab η_i mode eigenfunction, which is inversely proportional to the shear parameter, is broad. In this weak shear limit, the model equations should be modified. On the other hand, For the toroidal η_i mode model, χ_i of the mixing length model and nonlinear simulation are of the same order and both show fairly good agreement with experimental values in the half way region of the plasma. In the peripheral region, η_i mode models give χ_i decreasing toward the plasma surface and can not explain the anomaly in this region. Experimentally observed transport anomaly in the peripheral region may attribute other edge turbulences, which are the future subject of anomalous transport analysis.

References
[1] H. Shirai, T. Hirayama, M. Azumi, JAERI-M 91-018 (1991).
[2] B. G. Hong and W. Horton, Phys. Fluids **B** 2 (1990) 978.
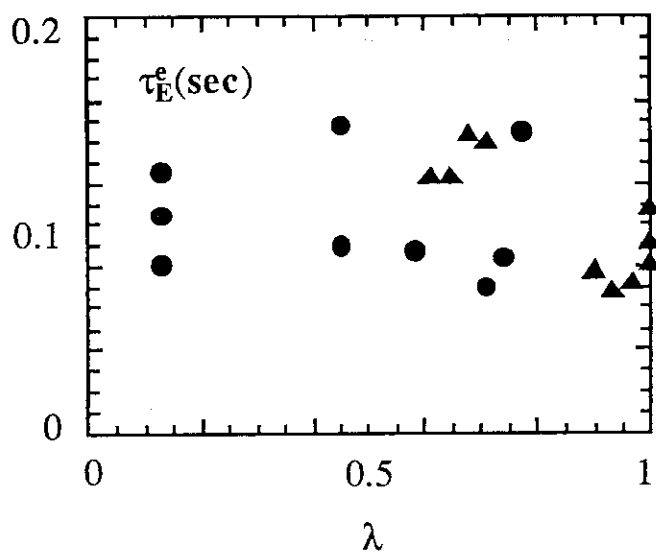
Fig.1 The electron energy confinement time versus the region of trapped electron regime. l = 1 means whole region is laid into DTE regime and l = 0 means whole region into CTE regime. These shots are laid in the rage of 1MA < Ip < 2MA, 1.5 < averaged line density < 5.0, 3MW < Pabs < 16MW.
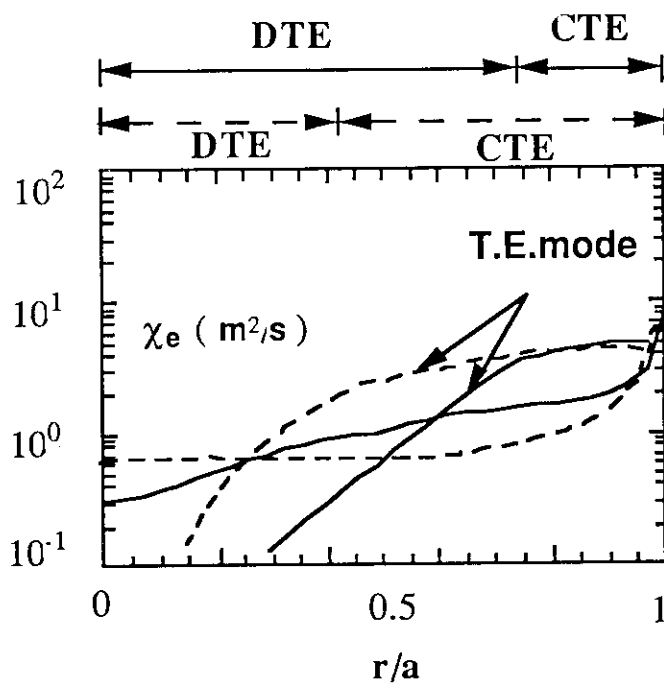
Fig.2 The electron thermal diffusivity versus the radius for limiter (E10643) and divertor (E10761) shots. The typical parameters are Ip = 2MA, Pabs = 10MW, averaged line density = 3.5.
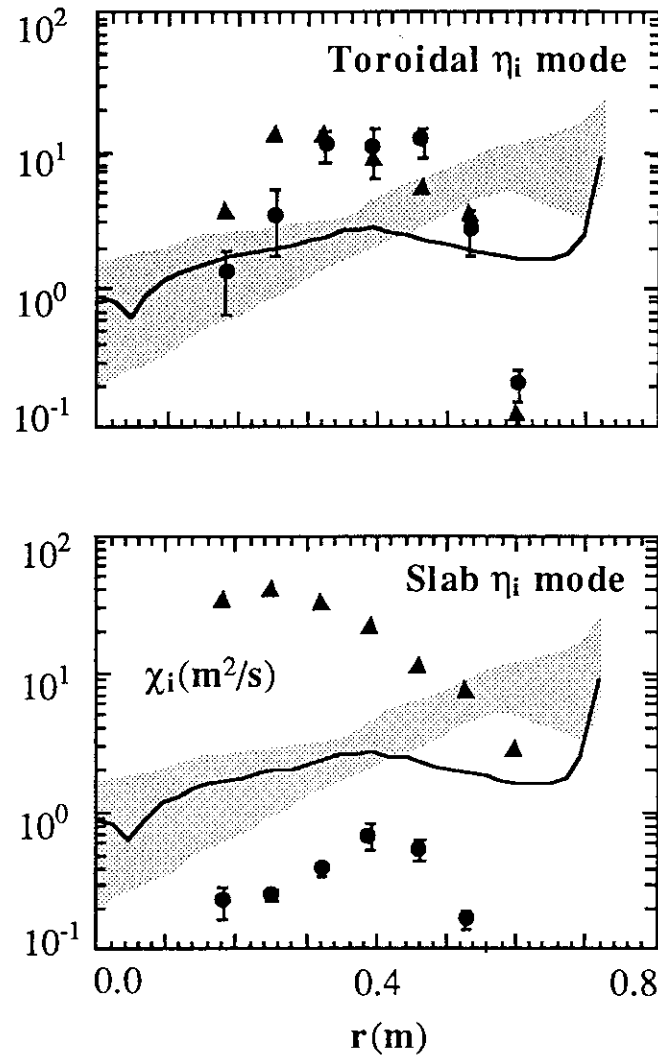
Fig.3 The ion thermal diffusivity calculated from hi mode turbulence simulation for the divertor shot (E11171) versus the radius. The typical parameters are Ip = 1MA, Pabs = 10MW, averaged line density = 3.5.

5.5 Perturbative Heat Transport Experiments in JT-60U

J.C.M. de Haas, K. Nagashima, T. Hirayama, and K. Hirai

I. Introduction

In the next few years, transport analysis at JT-60U will be performed using different perturbations, diagnostics and analysis techniques. The perturbations that could be used are sawteeth, (regular) Elms, gas puffs, modulated gas puffs, switch on and switch off of additional heating, modulated additional heating, and L to H mode transitions. In principle any diagnostic on which a perturbation can be seen can be used. Fast diagnostics with a good time resolution are preferable but, depending on the kind of perturbation and the analysis tools available, other diagnostics could be used as well. The analysis can be done using different methods, depending on the type of perturbation and the kind of diagnostic: Fourier transforms, Laplace transforms, fitting of transport modeling to experimental data, and system analysis of step and or impulse responses.

Some experimental data concerning transient processes and perturbations at JT-60U have been analyzed to obtain information about heat (and density) transport in the plasma. The diagnostics at JT60-U, especially those with good spatial and temporal resolution, are still under development. Using the present diagnostics capabilities, data has been analyzed to test different techniques. In the future more extensive measurements are planned in which systematic comparisons with power balance analysis will be made. In this paper descriptions are given of the development of analysis tools and the experiments performed so far.

II. Sawtooth induced perturbations

Sawteeth induced perturbations have been looked at for a number of ohmic shots and beam heated shots for which power balance analysis has been performed [1,2]. The sawteeth induce both temperature (HP=heat pulse) and density (density pulse = DP) perturbations which are moving out from the so-called mixing radius which is determined by the $q = 1$ surface. The only diagnostics until now with enough spatial and temporal resolution to see these perturbations are the Soft X-Ray (SXR) arrays. The disadvantages of this diagnostic are that the signals depend on both the temperature and the density, and that the signals are line integrated emissivities, not local values. The signals still could be used for e.g. a heat pulse analysis in case the perturbation seen on the SXR signals is mainly caused by the perturbation in the electron temperature [3]. Because the HP is generated near the center of the discharge and its amplitude is largest there, the perturbation of the line integrated data tends to be dominated by the perturbation at the flux surface tangent to the line of sight of the channel. The characteristic shape of a heat pulse perturbation is a relatively quick rise to a maximum value and then a relatively slow decrease back to the original value. The perturbation at a specific spatial location can be characterized by the time between the sawtooth crash and the maximum perturbation (ttp = time-to-

peak). A plot of the ttp versus spatial location gives information about the transport in the plasma. Because the analysis is done just outside the mixing radius, the spatial location of the analysis depends on the plasma current and the magnetic field.

The shots considered have plasma currents between 1 and 3 MA and magnetic fields between 3 and 4 T. Only shots with I > 2 MA have large mixing radii and therefore large enough amplitudes to be seen on the SXR data. In the ohmic shots the amplitudes are still small and therefore the signal to noise level is small. The situation can be improved by averaging over a number of sawteeth but software to do this is not yet available. The neutral beam heated signals have larger amplitudes but the time between sawteeth is very large. This means that the analysis has to be done on the perturbation caused by one single crash. A problem is that, due to the neutral beam heating, the density is rising and the resulting rise in the background of the SXR signal should be subtracted. Because the data acquisition of the SXR cameras is set-up to look at very fast phenomena, there is a lot of high frequency noise which can be filtered out by the application of a smoothing procedure. An accurate determination of the location of the channels with respect to the plasma equilibrium as provided by SELENE still has to be made. The locations can roughly be determined with respect to the outermost flux surface, as determined by FBIU. The best analysis method available at the moment is using both the heat and the density pulse, including coupling between the two [4]. Despite the fact that it can only be applied for a limited number of discharges, development of such an analysis is planned for JT-60U in 1992, because it should yield important experimental information about transport.

III. Modulated Gas Puff Experiments

Gas puff modulation experiments have been done in Ohmic JT60-U plasmas in hydrogen and are described elsewhere in this paper [5]. A valve regulating the introduction of hydrogen into the vacuum vessel just below the outboard midplane, was used. The modulation was sinusoidal with frequencies between 1 and 8 Hz. The H_α signal looking at the x-point is used as a reference for the introduction of particles into the plasma. The perturbation of the density can clearly be seen on the interferometer data and therefore also a modulation of the SXR signal was expected. However, the SXR data does not show a modulation at the same frequency as the gas puff. This means that at least one of the two other quantities which determine the SXR emission, namely the electron temperature and the impurity content, are modulated. The SXR does clearly show the sawtooth activity at a frequency of about 35 Hz which is much faster than the modulation. The electron temperature has been measured using the Fourier Transform Spectrometer (FTS) system which normally has a time resolution which is to low for perturbative transport studies. In this case the modulation frequencies are very low and FTS data has been used. The sawtooth activity is considered to be adding only random noise to the data.

A code has been developed to fit a harmonic oscillation on a linear background to any diagnostic signal [6]. The perturbation induced by the gas puff causes the temperature to go down

while the density goes up. The fit to the FTS data is very good indicating that the gas puff induces two different perturbations namely a harmonic oscillation and a change which is linear in time. The fitting gives four experimentally determined parameters, namely the amplitude and the phase of the modulation, the change in time of the background signal and the background signal itself. The results for the phases are shown in Fig. 1 covering values of r/a between 0.2 and 0.75 for the FTS, the phase of the H_α signal at the edge and the phases of both interferometer channels at the tangent flux surfaces. The phases are defined with respect to the gas valve signal and negative values indicate a phase lag. The perturbation seen on the FTS is plotted with a 180 degrees phases lag. It is clearly moving inward from the edge, started by the source as given by the H_α signal at the x-point. The interferometer data shows that the temperature and the density perturbation are about 180 degrees out of phase, explaining why there is hardly any perturbation visible on the SXR data. The slope of the phase for the FTS data corresponds with a electron heat diffusivity of 1.6 m^2/s assuming there are no perturbed sources or coupling with the electron density perturbation [7]. Both these assumptions are questionable. The data shown here was taken in a ohmic shot and a change in the local ohmic power caused by the temperature perturbation can influence the result. Also there is a clear density perturbation and coupling effects should be taken into account [3]. Note that the value for the heat diffusivity is very close to that for the particle diffusivity [5]. Besides the phase of the modulation, one can also use the amplitude. To avoid uncertainties in the absolute calibration of the FTS, the relative amplitudes with respect to the background signal are plotted in Fig. 2. The relative amplitude of the temperature perturbation is 1% at r/a = 0.3 and 2 % at r/a = 0.8 while this is 7% for the H_α signal. Also the interferometer perturbation has the same magnitude. For comparison the relative change per second of the background signal is given in the same figure, together with the ratio of both data. For r/a > 0.5 the ratio is constant but for r/a < 0.5 the linear perturbation decreases very fast with respect to the harmonic perturbation. One should realize that this does not mean that the data is inconsistent. It is possibly the result of the different natures of both perturbations and might well be described by one transport model. As far as is known, this is the first comparison between two different perturbative methods at the same time in one discharge.

V. Conclusions

Different perturbative transport experiments are planned at JT-60U. These should give important information about transport due to the large variety in both the quantities that can be perturbed and the kind of perturbations that can be applied. The developments of analysis tools to execute a perturbed transport program has been started and should match the increasing availability of experimental data over the coming years. Some preliminary results are shown in this paper, including the comparison between two different perturbative methods at the same time in one discharge.

References

[1] H. Shirai, T. Hirayama, and M. Azumi, "Transport Analysis of Ohmically Heated Plasmas in JT-60U", Sect. 5.1 of this report.

[2] H. Shirai, T. Hirayama, and M. Azumi, "Transport Analysis of L mode Plasmas in JT-60U", Sect. 5.2 of this report.

[3] J.C.M. de Haas, J. O'Rourke, A.C.C. Sips, and N.J. Lopes Cardozo, "Interpretation of Heat and Density Pulse Measurements in JET in terms of Coupled Transport", Nucl. Fusion, Vol. 31, No. 7 (1991) pp 1261-1274.

[4] G.M.D. Hogeweij, J. O'Rourke, and A.C.C. Sips, "Evidence of Coupling of Thermal and Particle Transport from Heat and Density Pulse Measurements in JET", Plasma Physics and Controlled Fusion, Vol. 33, No. 3 (1991) pp 189-198.

[5] K. Nagashima and A. Sakasai, "Gas Puff Modulation Experiment in JT60-U", Sect. 5.6 of this report.

[6] B. Joye, J.B. Lister, J.-M. Moret, A. Pochelon, and C.W. Simm, "Dynamical Plasma Response to Additional Heating", Plasma Physics and Contr. Fusion, Vol. 30, No. 6 (1988) pp 743-762.

[7] J.C.M. de Haas, T.C. Luce, C.C. Petty, and W.M. Meyer, "ECH Modulation Experiments at DIII-D", GA Report, to be published in Physics of Fluids.
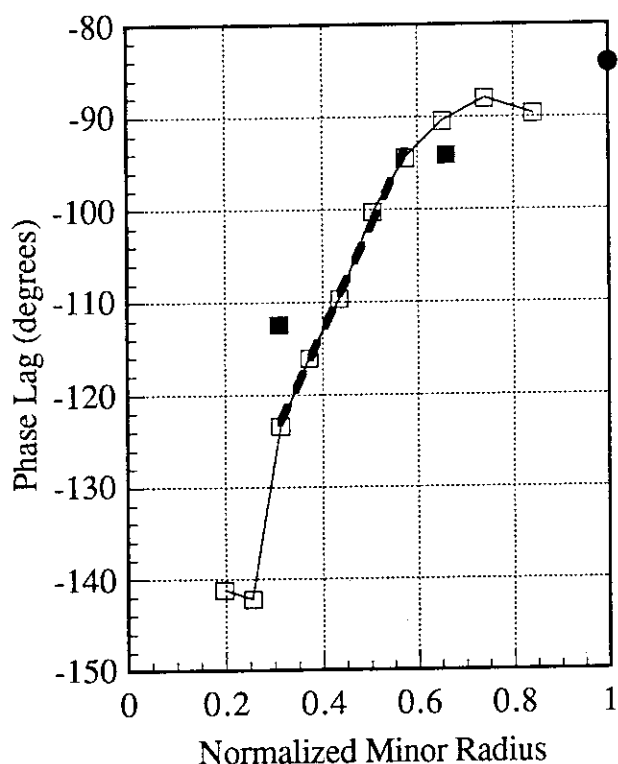
Fig. 1. The phase lag for different quantities as result of a 1 Hz modulation of the gas valve: local electron temperature from the FTS (open squares), H_α signal at x-point (closed circle) and line integrated density from the interferometer (closed squares). The dashed line is a fit to the FTS data between r/a = 0.3 and r/a= 0.6 .
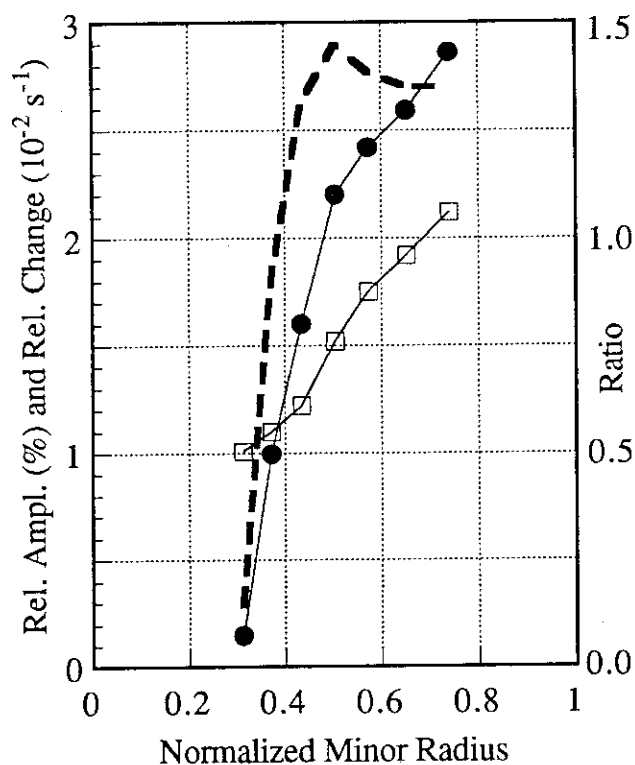
Fig. 2. Relative amplitudes for both perturbations on the FTS data: the relative amplitudes of the harmonic oscillation with respect to the background signal (open squares), the relative change per second of the background signal (closed circles) and the ration of both signal (dashed line).

5.6 Gas Puff Modulation Experiment in JT-60U

K. Nagashima, A. Sakasai

1. Introduction

Using the steady state phase of ohmic heating plasma, gas puff modulation experiment was performed. In this experiment, the injection of working gas was oscillated in the form of sinusoidal and it results in that electron density and the other plasma parameters were modulated in the sinusoidal form with the same frequency. The motivation of this experiment is to estimate the particle diffusivity from the dependence of modulation quantity on the oscillation frequency. The injected gas is ionized in the peripheral region of plasma and becomes the particle source for electron density. As the source profile is highly peaked in the peripheral region, the particle penetrates into the inner region with the characteristic time which is dominated by the transport process. Therefore, the transport coefficient can be estimated from the perturbation level and phase relation of modulation quantity.

2. Experimental Result

The experiment was performed using the ohmic heating discharges with plasma current of 2.5 MA, toroidal magnetic field of 4.0 T, major and minor radii of 3.28 and 0.90 m, plasma ellipticity of 1.58, effective safty factor of 4.5, and the line averaged electron density of 1.8-4.0x10^{19} m^{-3}, using the hydrogen working gas. (But the ratio of H/(H+D) was about 0.6-0.8 in these discharges, because the deuterium absorbed in the first wall was not fully removed.) The modulation frequency of gas puff was scanned from 1 to 7 Hz with the same injected quantity. However, as there is finite conductance between the gas puff valve and the vacuum chamber of JT-60U, it is thought that the supplied gas to the plasma depends on the modulation frequency.

The perturbation quantities of electron density and H-alpha intensity were measured using the FIR interferometers and the H-alpha monitor using interferometric filter. In this experiment, we used H-alpha intensity as the particle source signal. The bulk electron density (not modulated quantity) was not constant throught the scanning of modulation frequency. As the H-alpha intensity is mainly dependent on the peripheral electron density and neutral particle density, the effect of the difference of bulk electron density must be subtracted from H-alpha intensity to use as the particle source signal. To do this, H-alpha intensities were divided by the values of line averaged electron densities, because the bulk density profiles were almost same in these experiments. The perturbation levels and relative phases of electron density and H-alpha intensity were analyzed using the FFT procedure.

In Fig.1, the perturbation level of line integrated electron density divided by the

normalized H-alpha intensity is plotted as a function of the modulation frequency. The open and solid circles represent the measured values obtained from the outer and inner viewing chords of U-1 and U-2 ports, which are arranged at the radii normalized by minor radius of 0.68 and 0.30, respectively. In the figure, perturbation levels decrease with the modulation frequency and become a half value at the frequency of about 5 Hz (U-1) and 3 Hz (U-2). The relative phase between electron density and H-alpha intensity is shown in Fig.2. The clear difference of the dependence on the modulation frequency can be seen between the two different chords. The relative phase of inner chord (U-2) is larger than the one of outer chord (U-1) in the low frequency region, but this relation becomes opposite in the high frequency region. In these experimental results, it should be noted that the measured electron densities are the chord integrated values.

3. Analysis

The dynamics of plasma density is described using the particle diffusion equation with any source profile[1]. Using this equation, modulation of electron density can be calculated numerically. If it is assumed that the source profile is a delta function at the most external magnetic surface, the analytical solution can be obtained easily[2]. However, in the modulation experiment of JT-60U, the electron density was measured as a chord integrated value and it include the effect of source profile. In this analysis, we assumed that the half width of the particle source profile is 5 cm from the outermost magnetic surface. Using the appropriate particle diffusion coefficient, we calculated the dependence of density perturbation on the modulation frequency, including the effect of chord integration. The calculated results are shown in Fig.3 and 4, which are the cases of measurement chord at r/a=0.68 and 0.30 (a is minor radius), respectively. From the conparison between Fig.1 and Fig.3, 4, the particle diffusion coefficient can be estimated and it result in that D/a^2 is about 0.5 sec^{-1}. Considering the ellipticity is 1.58 in the above discharges, the diffusion coefficient is inferred to be 0.6 m^2/sec.

References
1) K. Nagashima, T. Fukuda, M. Kikuchi, T. Hirayama, T. Nishitani, H. Takeuchi,
    Nucl. Fusion 30 (1990) 2367
2) K. Krieger, G. Fussmann, and the ASDEX Team, Nucl. Fusion 30 (1990) 2392

Fig.1 Measured Electron density perturbation divided by the normalized H-alpha as a function of the modulation frequency. Open and solid circles represent the values of U-1 and U-2 ports.
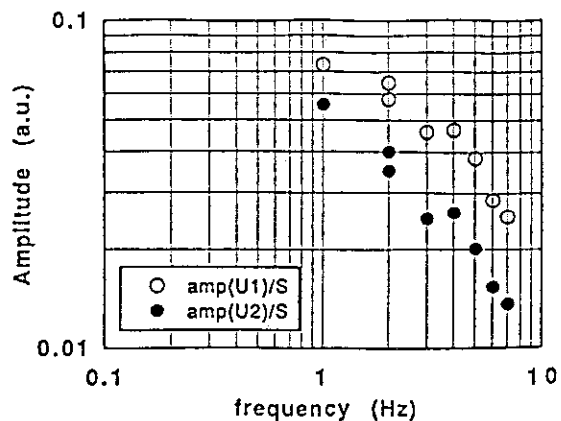
Fig.2 Relative phase between electron density and H-alpha intensity as a function of the modulation frequency. Open and solid circles are same in Fig.1.
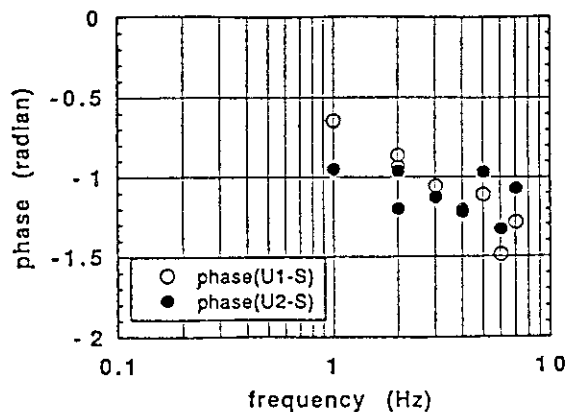
Fig.3 Calculated density perturbation at the radius of r/a=0.68 (U-1) as a function of the modulation frequency. The plots represent the four cases of $D/a^2 = 0.25$, 0.5, 1.0 and 2.0 sec^{-1} from upper line in the graph.
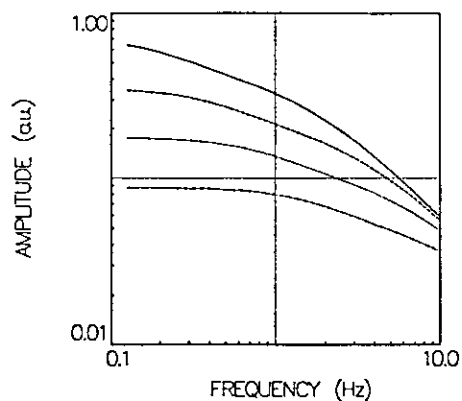
Fig.4 Calculated density perturbation at the radius of r/a=0.31 (U-2) as a function of the modulation frequency. The plots represent the four cases of $D/a^2 = 0.25$, 0.5, 1.0 and 2.0 sec^{-1} from upper line in the graph.
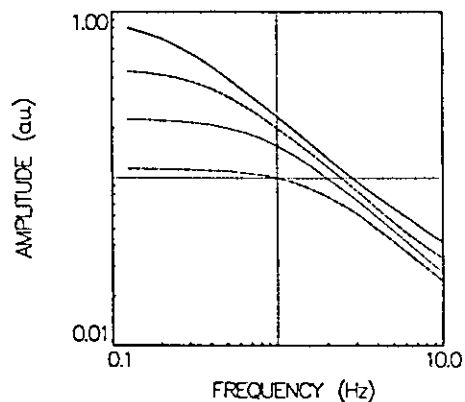
6. MHD

6.1 Characteristic MHD Regions in JT-60U

Y.Kamada, H.Ninomiya, S.W.Wolfe, S.Ishida and R.Yoshino

1. Introduction

The macroscopic MHD activities affect the tokamak confinement in many of characteristic discharge regions such as L-mode, improved L-mode, H-mode, high-Ti-mode and high-β_p mode etc. Discharge regions of these modes can be characterized by values of safety factor q, internal inductance l_i, β and pressure gradient. While, these physical values are the fundamental values determining the MHD stability. If these values are close to the stability limit, MHD instabilities play principal roles in the energy and particle confinement by disruptive (major or minor) events. If the instability is not disruptive, in turn, some of the MHD activities can affect confinement by the enhancement of diffusivity or repetitive release of kinetic energy. Generally, in order to realize the good confinement with high fusion reaction rate, profiles of the plasma parameters should be optimized to improve the transport properties and, at the same time, they should be selected to avoid disruption, to suppress the central MHD activity, to control the edge MHD including ELM activity. The purposes of the MHD studies in JT-60U are i) to identify the characteristic MHD activities in the discharge regions and ii) to clarify the relation between MHD and confinement in the tokamak system. In particular, the latter point is our final goal, for which safety factor and internal inductance play very important roles.

Many types of MHD behavior have been reported in the history of tokamak research [1]. However, unfortunately, there is no systematic foundation of MHD activities and the relation to global/local confinement including wide range of plasma parameters. Many of previous papers reported only some fragments of the MHD characteristics. What is important here is to study the dependence of MHD characteristics using the constructed MHD database and not to focus on the characteristics of some individual fragments. This type of database can suggest us the direction of tokamak study toward the fusion reactor. Without the fundamental database, for example, we cannot evaluate the effects of "MHD suppression" by the effects of hot ions, local change in the pressure and current density (by using NB, IC, ECH and LHCD) etc.

The energy confinement observed in many tokamaks seems to be degraded by decreasing edge safety factor [2]. Some evidence of improvement of confinement with increasing l_i has been also reported [3]. For identification of these effects, we have to separate the macroscopic instability and micro-turbulence. In other words, for the precise analyses of micro turbulence, the study on macro instabilities is indispensable.

For the first step of this study, this review paper reports the results of initial experiment in JT-60U. In this subsection, we introduce the MHD database and discuss the characteristic

MHD regions. Based on this discussion, more detailed study are reported in the following subsections (6.2-6.6). Roles of current profile and ELMs on confinement are given in Sec.3.5 and Sec.3.6, respectively. Detailed discussions of high-βp discharges are presented in Sec.4. Change of MHD by LHCD is reported in Sec.11.

2. Examples of MHD effects on Confinement in JT-60 and JT-60U

Examples of disruptive event observed in JT-60 and JT-60U are:

i) high l_i disruptions including high density disruptions,

ii) major or minor disruption at lower l_i usually observed during the plasma current ramp-up,

iii) low-q disruption and

iv) βp-collapse observed in high-q and low-li region. The important aspect of the βp-collapse is that the collapse is not followed by major disruption.

The non-disruptive degradation in transport is caused by sawtooth and m=1 related activities, ELMs and balloon limit. The results of the ballooning analyses in ref.[4] suggests that the ideal ballooning limit is a soft limit which only saturates the pressure gradient. The effects of ELMs on confinement is discussed in Sec.3.6. The effects of the central MHD activities is particularly apparent when the discharge has a peaked pressure profile (pellet injected discharges, high Ti discharges.) For the achievement of high-Ti and/or high-β_p discharges, avoidance of the central MHD is indispensable (see Sec.4). According to ref.[5] which reported characteristics of the central MHD activities for pellet fuelled plasmas, reduction in the sawtooth frequency has a strong relationship with enhanced confinement and peakedness of the electron density profile, where the contribution of the sawtooth activity to the global energy confinement increases systematically with decreasing q(a). An analytical treatment [6] also reported that the sawtooth activity can change τ_E especially for low-q discharges. However, it is impossible to discuss the general role of sawtooth on confinement without the basic scaling of r_{inv} (the sawtooth inversion radius) and τ_{st} (sawtooth period). In this aspect, Ref.[7] tried to discuss the relationship between τ_{st} and τ_E including the effects of ELMs which can change τ_{st} through the change in the current distribution.

3. MHD regions in JT-60U

Toward the final goal mentioned above, we have constructed the MHD database. The database includes ~300 discharges and ~1100 data sets. Regions of plasma parameters are: I_p=1-5MA, B_t=1.7-4T, q_{eff}=2-15, V_p(plasma volume)=45-90m^3. Using this database, Fig.1 shows the discharge regions on the l_i-q and β_p-β_t diagrams. Figure 1(a) reviews the discharge regions for β_p<1 discharges for the identification of current driven instabilities. From this figure, we can clearly understand the characteristic MHD regions: Large closed circles indicates the high-l_i (high-n_e) disruptions. Open circles and small closed circles correspond to sawtoothing discharges and sawtooth free discharges, respectively. It can be observed that

minima of li for appearance of sawteeth is characterized by a clear boundary (dotted line). The open squares correspond to low-li locked mode (major and minor disruptions) and low-q disruptions. Figure 2 shows a schematic characterization of MHD regions for a fixed q_{eff}. In the sawtoothing region, we can observe a boundary of profile consistency given by the dashed line in Fig.1. Experimentally, if I_p is kept constant, l_i increases asymptotically toward the boundary and cannot increase beyond this line. In other words, the boundary corresponds to the fully penetrated current profiles. Open circles above this boundary in Fig.1 were obtained during current ramp down. Along this boundary, the sawtooth inversion radius (r_{inv}) can be written by $r_{inv} \sim a/q_{eff}$, where a is the minor radius (Detailed discussions are given in Sec.6.3). This profile consistency may be caused by sawtooth activity itself in low-q region where sawtooth mixing radius is large ($r_{mix} \sim a/2$) , and may be caused by some
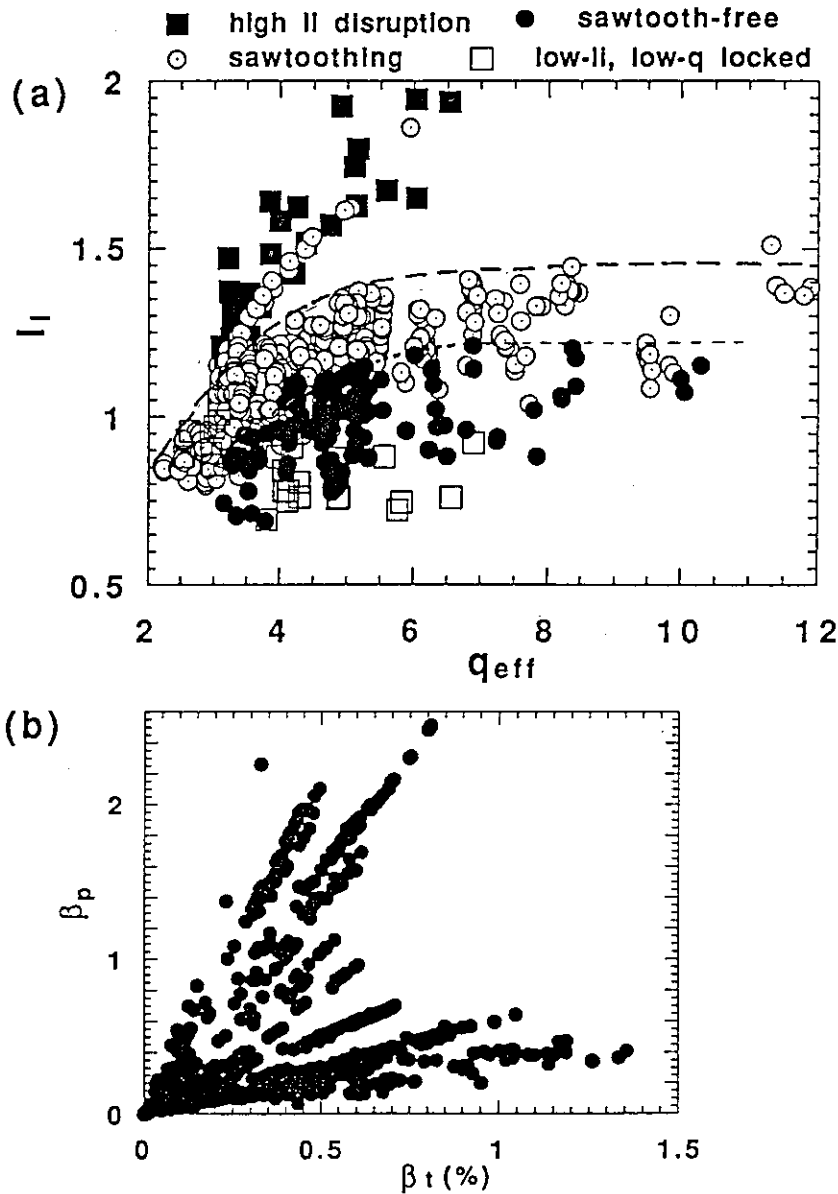
Fig.1: MHD Regions in JT-60U on (a) the li-q diagram and (b) the β_p-β_t diagram.

low l₁
locked   **Sawtooth**   **Sawtooth**   **high l₁ (high n_e)**
mode   **free**   **disruption**

l_i

Profile
Consistency?
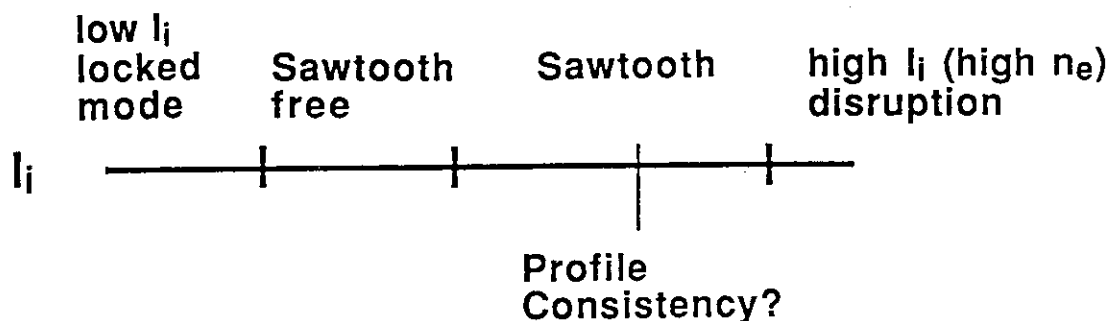
Fig.2: Schematic characterization of MHD discharge regions with l_i for a given q_{eff}.

transport effects in higher q region where effects of sawteeth or other MHD activities are small. High density and high l_i disruptions can be observed in the lower l_i region below the boundary given by large closed circles in Fig.1. In those cases, detachment of plasma column are usually observed before the MHD modes responsible to the major disruption evolves. The precise calculation of q and li for the detached plasmas has not been completed yet.

The basic characterization of the current driven instabilities on the li-q diagram was given by Cheng et al. [8] and, in many tokamaks, the l_i-q diagram is used to express the discharge conditions [9,10]. Generally, high-l_i disruption is believed to be caused by tearing modes and low-l_i locked modes are related to external kink activities or double tearing modes. The identification of the locked mode is given in Sec.6.2.

[1] to review the MHD research, WESSON, J., in ' Tokamaks ' (Oxford Science Publication, 1987). see also AZUMI, M., Kakuyugo Kenkyu 66 (1991) ???

[2] JET Team, in *Plasma Physics and Controlled Nuclear Fusion Research* Proc.12th Int. Conf., Nice, 1988, (IAEA, Vienna, 1989), Vol.I, p159.

[3] ZARNSTORFF, M.C., et al., in *Plasma Physics and Controlled Nuclear Fusion Research* Proc.13th Int. Conf., Washington, 1990, (IAEA, Vienna, 1991), Vol.I, p109.

[4] OZEKI, T., et al., Nucl. Fusion 31 (1991) 51.

[5] KAMADA,Y., et al., in *Plasma Physics and Controlled Nuclear Fusion Research* Proc.13th Int. Conf., Washington, 1990, (IAEA, Vienna, 1991), Vol.I, p219. and KAMADA,Y., et al., Nucl. Fusion 31 (1991) 23.

[6] CHENG, Z. and CALLEN,J.D., Nucl Fusion 30 (1990) 219.

[7] KAMADA, Y., et al., ' Sawtooth Frequency Studies in DIII-D Tokamak' GA-A20611, General Atomics(1992) , submitted to Nucl. Fusion.

[8] CHENG, C.Z., et al., Plasma Physics and Controlled Fusion 29 (1987) 351.

[9] SNIPES, J.A., et al., Nucl. Fusion 28 (1998) 1085.

[10] SCOVILLE, J.T., et al., Nucl. Fusion 31 (1991) 875.

6.2 Locked Modes in JT-60U

S W Wolfe, Y Kamada, R Yoshino, N Hosogane, K Itami, K Ushigusa

1. Introduction

Plasma disruptions remain a fundamental problem in tokamak operation. In their most benign form they cause momentary losses of confinement and performance degradation, while at their worst, rapid termination of the discharge results, causing large forces on the vacuum vessel. Therefore, from the standpoint of obtaining the best plasma parameters and extending a machine's lifetime, controlling or avoiding disruptions is a critical issue for a Next Step device. Since the large majority of disruptions in today's large tokamaks are preceded by unstable coherent MHD modes which grow in amplitude and phase-lock [1-3], the study of such "locked modes" is essential for this purpose.

In JT-60U, locked modes have been observed under conditions when the discharge is pushed to its limits of density, current, and ramp rate. Their behaviour and effects on the discharge vary depending on these conditions, and these will be described here, along with the consequent limitations on operation.

2. Detection

Locked modes are visible on many diagnostics, and if the mode has a rotating phase before locking, detection is made simpler. The most useful diagnostics for this study are shown schematically in Figure 1. The FIR interferometer measurement of line-averaged electron density, although usually unable to resolve the mode directly, often reveals related phenomena such as MARFE activity preceding the mode or ensuing particle loss. The H_α emission is affected by the locked mode, and spectral measurements made along lines of sight near the edge reveal these effects, although the time resolution of 1 ms means that only slowly rotating modes are visible. Two PIN diode arrays with 64 channels in total view the plasma cross-section through a 250 μm Be filter and give profiles of line-averaged soft x-ray emission every 40 μs (lower array) and 80 μs (upper array). If the edge plasma is sufficiently hot, the rotating mode is clearly visible.

The most useful information, however, was obtained from the magnetic probe systems. There is a Mirnov coil set measuring the time derivative of the field component tangential to the vacuum vessel. It consists of a poloidal array of 22 probes and a toroidal array with probes at six other positions around the torus. These are fast probes, with an adjustable sampling time down to 2 μs, but usually over a restricted time interval. There are also probes used for gross plasma control, and, because they are integrated, they were useful for detecting locked modes which were not rotating. They are arranged in three poloidal sets: two sets of 17 probes each measure field tangential to the vessel with 1 ms resolution at two toroidal locations separated by 180°. Another set of 16 probes measures the field normal to the vessel at 0.25 ms resolution. The slow sampling is not a problem for detecting the locked mode. Using the magnetic data, poloidal mode numbers m up to about six and toroidal mode numbers n up to about three can be resolved.

To determine the poloidal structure of a mode which is not rotating, the perturbation in an equilibrium magnetic field component is calculated as $\tilde{b}(\theta) = B(\theta)/B_0(\theta) - 1$ where $B(\theta)$ and $B_0(\theta)$ are the perturbed and unperturbed field components, respectively. If plasma equilibrium parameters such as shape, position, and Shafranov shift do not change appreciably during the growth of the mode, then B_0 may be assumed to depend on current only, and its value inferred from that at the onset of the mode. $\tilde{b}(\theta)$ is then plotted in polar form.

3. Evolution of the Locked Mode

In JT-60U, as in other large tokamaks, locked modes appear during the current rise and before major disruptions at high density or low surface safety factor. Each type has certain distinguishing characteristics. A typical density limit disruption is shown in Fig. 2a. This one occurs during a 1.2 MA hydrogen discharge with a toroidal field of 3.8 T. The electron density increases until instability sets in and the plasma terminates after a series of minor disruptions. Before these disruptions begin, the H_α emission from the divertor drops and the soft x-ray emission gradually rises. This indicates that the divertor is no longer functioning, and the plasma is essentially detached from the divertor. (See Section 7.4 of this report for further discussion of divertor plasma behaviour prior to disruption). The profiles which result are peaked and unstable, because soon afterwards a rotating mode appears. It is most clearly seen on the plasma position signals. This mode, on closer inspection, is seen to grow in amplitude and slow in frequency until locking. From the polar plot, an m=4 structure is clear. n was not measured in this case. It should be noted that m=2 or 3 with n=1 is more commonly observed in density limit disruptions.

Fig. 2b shows a locked mode occurring during the current rise. In contrast to the density limit case, the plasma does not detach from the divertor prior to the onset of the mode. In fact the mode appears soon after the divertor configuration is established at about 2 s. The polar plot of the mode shows an m=5 structure; other cases of this type have shown poloidal mode numbers from 3 upwards, and usually n=1. The poloidal wavelength of the mode is seen to be smaller on the high-field side, as expected. The minor disruptions which ensue do not lead to large energy losses from the plasma, as evident in the soft x-ray signals. The discharge survives these disruptions, and only terminates in a major disruption much later. This late disruption may be related to the earlier activity, as discussed below.

Sometimes a locked mode is seen to grow without a rotating phase. An example of this is shown in Fig. 2c. Again, there is no detachment from the divertor. The minor disruption which follows about 30 ms after the mode onset is quite severe, as evident from the large drop in the central soft x-ray signal. Density drops substantially throughout the whole process. m=3 is clear from the polar plot, and again the plasma survives until a major disruption in the current ramp-down.

4. Limitation to Operation

The development of a locked mode and the subsequent disruptive events place severe limitations on tokamak operation. These limits appear most clearly in a plot of plasma internal inductance l_i vs surface safety factor q_{eff}. Here, q_{eff} is given by

$$q_{eff} = \frac{5a_p^2 B_T}{R_p I_p(MA)} \frac{1+\kappa^2}{2}\left[1+\left(\frac{R_p}{a_p}\right)^2\left(1+\frac{(\beta_p + l_i/2)^2}{2}\right)\right]\left[1.24 - 0.54\kappa + 0.3(\kappa^2 + \delta^2) + 0.13\delta\right]$$

where κ and δ are the plasma elongation and triangularity, and the other symbols are standard. The equilibrium parameters are obtained from a fit to the magnetic and diamagnetic data (see Section 2.4 of this report). The results are shown in Fig. 3 for a selection of JT-60U discharges. The data were taken when the mode first became visible on the magnetic signals.

The locked modes have appeared under a wide range of plasma conditions: plasma currents from 1 to 4 MA, toroidal fields from 2 to 4 T, and line-averaged densities in hydrogen or deuterium from 0.5 to 8×10^{19} m^{-3}. Divertor configuration was used. Most of the modes have occurred in Ohmic plasmas, but a few have appeared during NB heating at powers up to 20 MW. Because of the rapidly changing conditions just after NB switch-on and switch-off, locked modes occurring around these times are not included.

The low inductance limit is encountered during the current rise. There is usually a rotating phase before the mode locks, although there are some cases between q_{eff} of 4 and 5 where this was not detected. Since the data are quite sparse, it is

difficult to resolve any structure in the low inductance boundary, such as the theoretically expected "sawtooth" shape [4].

The high inductance boundary is encountered when the plasma detaches from the divertor, either as a result of operation at the density limit or during the current ramp-down. In these cases, the plasma boundary calculated from the equilibrium code is sometimes a poor representation of the true boundary since the code assumes a well-diverted configuration still exists. Therefore, q_{eff} is often overestimated, as evident for some data points in the figure. There are also a few cases where detachment was not observed, and the locked mode grew without rotation.

The points for which no mode rotation was observed generally appear at low q_{eff}, with $q_{eff}=3$ being a probable condition for instability. In many cases the activity has been preceded by a locked mode with rotation which has occurred in the current rise. m/n for this earlier activity has been observed to match the q_{eff} at the later disruption, implying that the earlier locked mode saturates and persists until conditions are such that loss of confinement is inevitable.

5. Discussion and Summary

Theory predicts that the tearing mode should determine the high inductance limit in a tokamak while at low inductance either the surface kink mode or double tearing mode should become unstable. More work is required to precisely determine the instabilities responsible for locked modes in JT-60U, but some preliminary insights can be obtained based on their topology and the resulting disruptive behaviour.

Rotating modes which lock in the current rise have been seen to have m≥3/n=1 structure. Initial mode frequencies range from 0.1 to 1.5 kHz with growth rates of about 50 s^{-1}. m/n is usually less than q_{eff}, indicating an internal mode. Such a locked mode leads to minor disruptions (at least in the short term), and soft x-ray profiles indicate only a small energy loss near the edge. These observations may be explained by a broad current profile with large shear near the edge.

Modes which appear after detachment from the divertor, as in density limit experiments, usually exhibit m=2 or 3 with n=1. Initial mode rotation ranges from 0.7 to 2.5 kHz, and the growth rate ranges from 50 to 500 s^{-1}. Locking is usually followed by a series of minor disruptions and discharge termination. m/n is less than q_{eff}, but, as mentioned, the q_{eff} measurement may not be reliable. Soft x-ray observations show energy loss confined to the edge, at least for the minor disruption immediately following the mode lock.

Disruptions which are preceded by a locked mode with no rotational phase are severe and usually terminate the discharge. In these cases, m/n=q_{eff}, indicating a surface mode. For low q_{eff}, soft x-ray observations have occasionally showed that m=1 activity and sawtooth behaviour are also affected, indicating that mode coupling may be important.

Error fields from the coil systems are generally believed to be important in causing such instabilities. In JT-60U, locking occurs when $\tilde{b}_\theta$ at the wall is about 0.5%, corresponding to $\tilde{B}_\theta$ of about 10 G, and the minor radial field fluctuation at the wall is about 5 G. The error field from the Ohmic heating coil feeder has at least this magnitude at some points within the vessel, so it could play a role. The possible contribution of the divertor coil error field has been revealed in a study of the stable operation region of JT-60U (see Section 2.11 of this report). It was found that the height of the x-point above the divertor plates and the ratio of divertor coil current to plasma current were critical parameters for determining whether certain discharges would disrupt.

6. References

[1] Scoville, J T et al, Nuclear Fusion **31** (1991) 875.
[2] Ninomiya, H et al, Nuclear Fusion **28** (1988) 1275.
[3] Snipes, J et al, Nuclear Fusion **28** (1988) 1085.
[4] Cheng, C Z et al, Plasma Phys. & Contr. Fusion **29** (1987) 351.

13113

Fig. 2a -- Density limit locked mode.

Fig. 1 -- Diagnostics: U1 and U2 -
FIR interferometer; V - visible
spectrometer (1 of 38 lines); XU and
XL - SX detector arrays; semicircles -
positions of tangential probes.

13582

Fig. 2b -- Locked mode in the current
rise.

13160
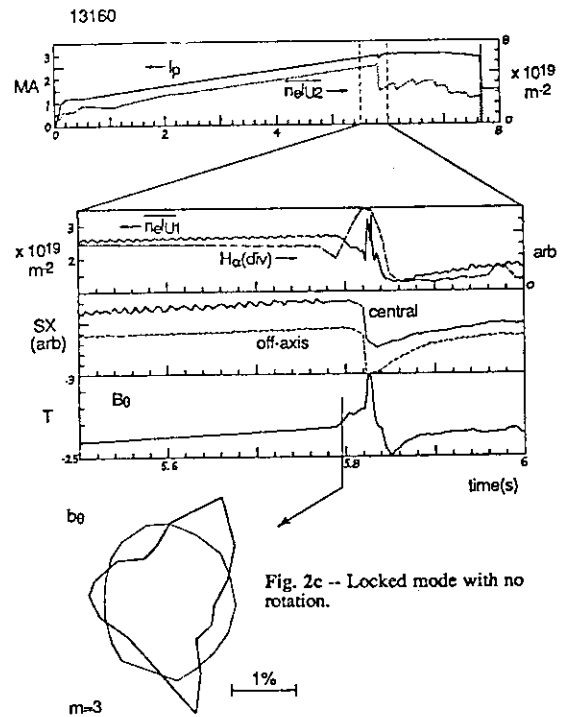
Fig. 2c -- Locked mode with no
rotation.

Fig. 3 — Plasma internal inductance vs
effective surface safety factor at the
onset of locked modes.

6.3 Sawtooth Characteristics and m=1 Activities

Y.Kamada

1. Introduction

This section treats the basic behavior of sawtooth activity such as inversion radius r_{inv}, mixing radius r_{mix}, sawtooth period τ_{sw} to achieve the systematic understanding of sawtooth instability itself and the effects of sawtooth on confinement. The sawtooth activity plays principal roles in limiting the attainable central pressure and in determining the central transport properties. In addition, sawteeth may have a beneficial effect by removing impurities, including He ash, from the plasma center. Because of these importance, the studies on sawtooth have been carried out on many tokamaks. However, the theoretical explanation consistent with the experimental observations has not been completed [1]. For the trigger mechanism, the observed structure exhibits complexity after the introduction of the three large tokamak devices,TFTR, JET and JT-60, where the sawtooth can occur without observed precursor oscillations and the crash time of sawtooth τ_{crash} is much faster than the conventional prediction based on the fully reconnecting structure of the magnetic field [2]. In JT-60, we have been studying the crash mechanisms. According to ref.[3], for lower-β_{p1} (β_p defined inside the q=1 surface) discharges, the sawtooth crash behaves following the fully reconnecting style. Such sawteeth often have precursor m=1 oscillation and small or no successor oscillation. In contrast, for higher-β_{p1}, the crash tends to follow incomplete reconnection and the successor oscillation becomes larger: With increasing β_{p1} or steepening of the density (pressure) gradient in the core region, τ_{sw} increases, the release of the central kinetic energy by the sawtooth crash decreases and the sawtooth changes its characteristics from reconnecting type to non-reconnecting type.

Concerning τ_{sw}, many works have been done to examine the methodology of the sawtooth suppression with neutral beam (NB) heating, ion cyclotron (IC) heating (see Sec.10.4), lower hybrid-current drive (LHCD; see Sec.11), electron cyclotron heating (ECH) and pellet injection [4]. In previous works, the enhanced τ_{sw} was discussed without a basic scaling of τ_{sw} and the sufficiently quantitative analyses of the sawtooth suppression were not completed. Although, the scaling of τ_{sw} has been discussed in some works [5], there has been no systematic experimental scaling of the sawtooth period in wide ranges of plasma parameters. Reference [6] reports this kind of the systematic analyses of τ_{sw} on DIIID and the observation supports the results given this section. Without the scaling, we cannot evaluate the effects of "sawtooth suppression" by the effects of hot ions, local change in the pressure and current density.

For the first step of this study, this paper reports the results of initial experiment of JT-60U.

2. Sawtooth

In Sec.6.1, we clarified the discharge regions where sawtooth activity appears on the l_i-q diagram. In this section we discuss more detailed feature of sawtooth activity using q_{eff} and l_i. Figure 1 shows the plot of r_{inv}/a (the sawtooth inversion radius r_{inv} normalized by the plasma

minor radius a) versus $1/q_{eff}$. This figure covers wide ranges of plasma parameters: Ip=1-5MA, Bt=1.7-4T, $\beta_p<1$ and $\beta_N<1.5$. The maximum value of r_{inv}/a is almost proportional to $1/q_{eff}$ as given by the dotted line. Here the important finding is that the dotted line is almost identical to the line of the profile consistency given in Fig.1 in Sec.6.1. This very clear proportionality of r_{inv}/a to $1/q_{eff}$ suggest there exists a strong restriction of current density distribution in the tokamak system. In lower q region, sawtooth activity itself may be the reason of this restriction. In turn, in higher q region where the mixing radius of sawtooth is small compared to minor radius, the restriction may be caused by transport properties which keep electron temperature profile constant. In Fig.1, it is observed that there are many sawteeth having smaller r_{inv}/a than that given by the dotted line. These sawteeth correspond to data where the current profile has not been fully penetrated. This observation can be understood when r_{inv}/a is plotted against l_i for fixed q_{eff}-values. In Fig.2, closed and open circles correspond to data sets with q_{eff}=0.30-0.32 and q_{eff}=0.24-0.26. It is also clear that r_{inv}/a increases with increasing li for a given q_{eff}. In Fig.3, r_{inv} and r_{mix} normalized by a are plotted against l_i for q_{eff}=0.24-0.25. It is also observed that r_{mix}/a increases with li and it should be noticed that the maximum value of r_{mix} reaches about half the minor radius even for q_{eff}=4. To evaluate the effect of sawtooth on confinement, another important parameter is the sawtooth period. Figure 4 shows the observed sawtooth period τ_{sw} against W(MJ)/$\bar{n}_e$($10^{19}m^{-3}$)V(m^3) which is nearly proportional to the volume averaged electron temperature <Te>, where W, $\bar{n}_e$ and V are the plasma stored energy measured by a diamagnetic
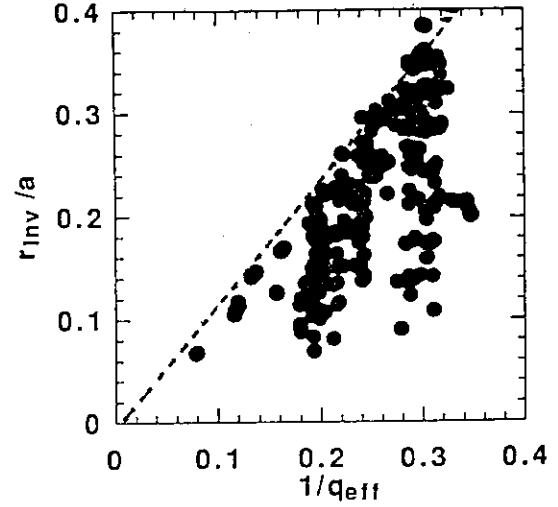
Fig.1: r_{inv}/a and $1/q_{eff}$
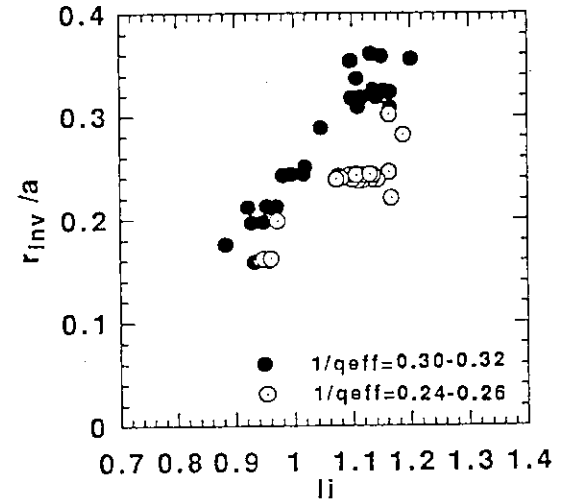
Fig.2: r_{inv}/a and l_i for $1/q_{eff}$=0.24-0.26 and $1/q_{eff}$=0.30-0.32.
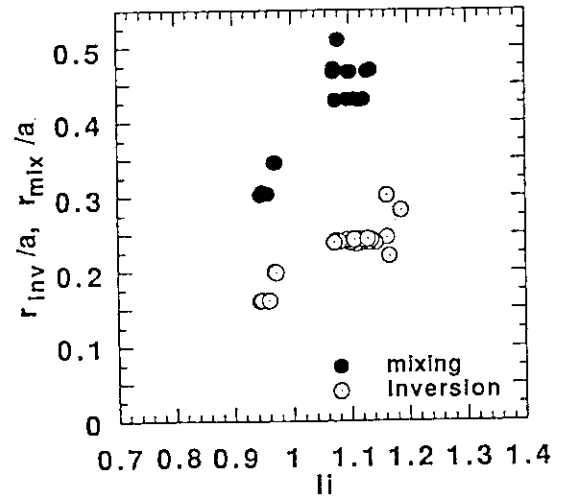
Fig.3: $rinv/a$ and $rmix/a$ and l_i for $1/q_{eff}$=0.24-0.26.

loop, the line averaged electron density measured by a FIR interferometer (~1/3a off-axis) and the plasma volume, respectively. In Fig.4, data with Ip=3MA, Bt=3.5-4T, V=70-76m^3 are plotted. The dependence of the sawtooth period is τ_{sw}~$<T_e>^{3/2}$. This clear dependence is almost the same as that obtained by Kamada et al. in DIIID [6]. The scaling including JT-60U and DIIID results suggests that the sawtooth period is explained by the resistive diffusion time of the current profile. These observations (Figs.1-4) give the quantitative base to discuss the effect of sawteeth on the global confinement.
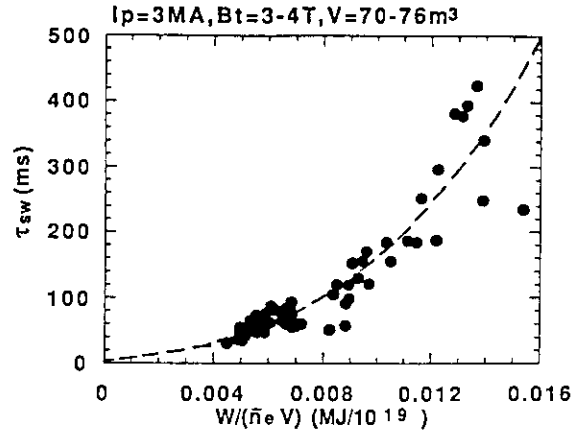
Fig.4: Dependence of τ_{sw} on the volume averaged Te for Ip=3MA.

3. m=1 Activity and Fishbone

In some discharges, nearly steady m=1 continuous oscillation without sawtooth is observed. Figs.5(a)-(c) show the change of the central MHD behavior with increasing β_p. For lower β_p, usual sawtooth activity accompanied by m=1 oscillation is observed. For medium β_p, sawtooth disappears but long continuous m=1 is observed. For high β_p, both sawtooth and m=1 continuous oscillation disappears and central MHD oscillation is dominated by higher m/n modes and sometimes large amount of the central energy is released by β_p-collapse (see Sec.4.3) when β_p-value reaches a limiting value (~2.5). In case of Fig.5(c), about 20% of the total stored energy is released by very fast crash (~100μs) of the central pressure profile. The important feature of the β_p-collapse is that the collapse has never been followed by major disruption.
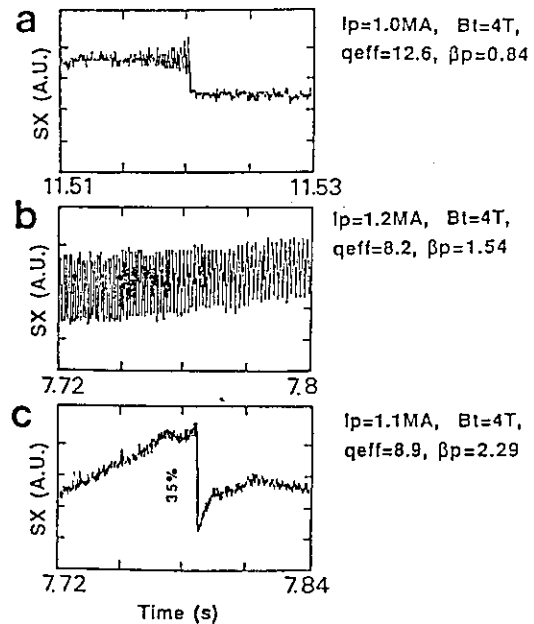
Fig.5: Change of the central MHD with increasing β_p.

(a)

Ip=1.4MA, Bt=4T,
qeff=6.9, βp=1.02

(b)
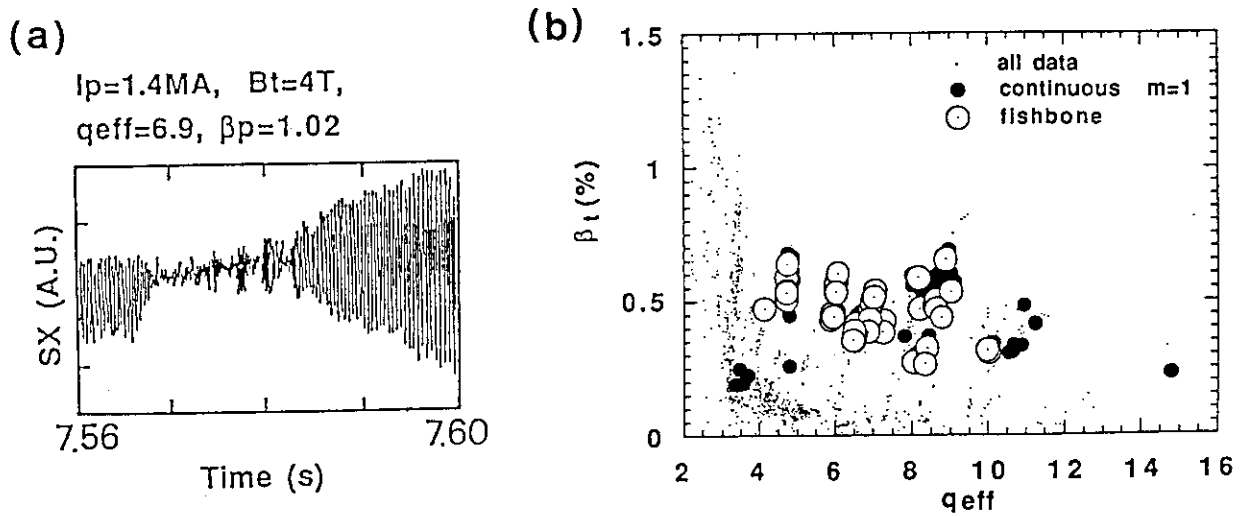
Fig.6: (a) fishbone activity and (b) discharge region of continuous m=1 and fishbone oscillations.

In JT-60U, fishbone type m=1 burst [7,8] is sometimes observed. Figure 6(a) is the example of the soft-X ray signal of the center chord. During one burst, frequency of the oscillation is larger in the early stage, then slows down. The typical frequency is ~3~4kHz which is in the same frequency range as the precession frequency of the nearly perpendicular injected NB particles with energy of ~100keV. Unfortunately in this year density profile cannot be measured in the central region and we cannot evaluate the ion diamagnetic frequency. This type of fishbone activity can be observed during sawtoothing phase. In some cases of sawtooth free phase, fishbone activity is observed during usual continuous m=1 oscillation as shown in Fig.6(a). In this type of discharge, it is difficult to distinguish fishbone and usual m=1 oscillation because both activity observed is continuously connected. Figure 6(b) shows the region of fishbone activity (open circles) and continuous m=1 oscillation without sawtooth (closed circles). Small dots in this figure correspond to all the data included in the MHD data base. From this figure, fishbone activity is observed when $q_{eff}\beta_t > 2\sim 3\%$.

REFERENCES
[1] WESSON, J., ' Theory of Sawtooth Oscillations', JET-P(87)55, 1987.
[2] CAMPBELL, D. J., et al. Nucl Fusion 26 (1986) 1085.
[3] KAMADA,Y., OZEKI,T., AZUMI,M., Phys.Fluids B 4 (1992) 124.
[4] KAMADA,Y., et al., Nucl Fusion 31 (1991) 23. see also KAMADA,Y., et al., in *Plasma Physics and Controlled Nuclear Fusion Research* (Proc.13th Int. Conf.,Washington, 1990) Vol.I (IAEA, Vienna, 1991) p291.
[5] PARK,W. and MONTICELLO,D.A., Nucl Fusion 30 (1990) 2413.
[6] KAMADA, Y. et al., GA-A20611 General Atomics (1992), submitted to Nucl. Fusion.
[7] McGUIRE, K., et al., Phys. Rev. Lett. 50 (1983) 891.
[8] HEIDBRINK, W. W., et al. Nucl Fusion 30 (1990) 1015.

6.4 Non-circular Tomographic Method Based on Fourier-Bessel Expansion Considering Magnetic Surfaces

T. Kondoh, Y. Kamada and K. Nagashima

1. Introduction

Tomography techniques to determine local emissivity from line integral measurements have been used in many devices. The Cormack inversion[1,2] has been used to investigate production mechanism of hot electrons in tandem mirror[3] and MHD phenomena in tokamaks or in stellarator. Nagayama modified the Cormack inversion by replacing the Zernicke polynomials to the Bessel function in radial expansion.[4] This method reduces spurious noise in the edge and the number of radial expansion terms.

It has been required to consider noncircular shape of flux surfaces. Though, we require an inversion method that is applicable to more complicated plasma shapes such as plasma in JT-60U with divertor configuration.

We therefore modified the Fourier-Bessel expansion method that is taken into account the shape of magnetic surfaces. This modified method of tomography has been carried out in JT-60U plasma using soft x-ray detectors. We assume that plasma rotates along the magnetic surfaces.

2. Tomographic method

We briefly review the tomographic method based on the Fourier-Bessel expansion. The brightness, $f(p,\phi)$, is a line integral of the emissivity along the viewing chord $L(p,\phi)$.

$$f(p,\phi) = \int_{L(p,\phi)} g(r,\theta)dl \tag{1}$$

Here, (p,ϕ) represent the polar coordinates (Fig. 1), p is the chord radius, and ϕ is the angle between the normal to the chord L and the axis given by $\theta = 0$.

Next, the emissivity $g(r,\theta)$ is expanded in the Fourier harmonics and Bessel function.

$$g(r,\theta) = \sum_m \sum_l \left[a_m^{c,l} \cos m\theta + a_m^{s,l} \sin m\theta \right] J_m(\lambda_m^{l+1} \cdot r) \tag{2}$$

where $a_m^{c,l}$ and $a_m^{s,l}$ are the expansion coefficients. J_m is m-th order Bessel function and λ_m^{l+1} is (l+1)th zero-value of the m-th order Bessel function. Then, the brightness $f(p,\phi)$ is reduced to

$$f(p,\phi) = \sum_m \sum_l \left[a_m^{c,l} f_m^{c,l}(p,\phi) + a_m^{s,l} f_m^{s,l}(p,\phi) \right] \tag{3}$$

$$f_m^{c,l}(p,\phi) = \int_{L(p,\phi)} \cos m\theta \cdot J_m(\lambda_m^{l+1} \cdot r) \, dl \tag{4}$$

$f_m^{c,l}(p,\phi)$ is constant value. In the above mentioned methods, if the expression $g(r,\theta)$ in the entire region in $0 \leq r \leq 1$ and $0 \leq \theta \leq 2\pi$ is obtained, we can get source function $f(p,\phi)$ exactly. Nevertheless, we can get only discrete values of $f(p_i,\phi_i)$ these are line integral data of detector i along the chord $L(p_i,\phi_i)$.

The expansion coefficients, $a_m^{c,l}$ and $a_m^{s,l}$, are calculated by least squares method, that is, minimizing S,

$$S = \sum_{i=1}^{Ndetector} \left\{ \sum_{m=0}^{Mmax} \sum_{l=0}^{Lmax} \left[a_m^{c,l} \cdot f_m^{c,l}(p_i,\phi_i) + a_m^{s,l} \cdot f_m^{s,l}(p_i,\phi_i) \right] - y_i \right\}^2 \rightarrow \text{miminum} \quad (5)$$

where y_i is a line integral data along the chord $L(p_i,\phi_i)$, $N_{detector}$ is the number of the detector, M_{max} and L_{max} are the number of the expansion terms.

This reconstruction method requires the data from many different directions. But it is difficult and we can get only in the discrete point according to restricted port access or technological problem.

This method is based on the expansion along coaxial circles and is suitable for a tokamak having circular cross section. But JT-60U has more complicated cross-section. Now, we consider the expression of magnetic surfaces. To simplify the calculation, we only use the data of outermost -magnetic surface measured by magnetic probes. We approximate the outermost magnetic surface by $r = r_{mag}(\theta)$ (Fig. 2) with an equation,

$$r_{mag}(\theta) = \sum_{n=0}^{N} \left[b_n^c \cos n\theta + b_n^s \sin n\theta \right] \quad (6)$$

Where b_n^c and b_n^s are the expansion coefficients determined by a least squares method and N is the number of the expansion terms.

Then, inner magnetic surfaces can be approximately expressed by following expansion,

$$r(x,\theta) = x \cdot \left\{ b_0 + k(x) \cdot \sum_{n=1}^{N} \left[b_n^c \cos n\theta + b_n^s \sin n\theta \right] \right\} \quad (7)$$

where x is a radius of the flux surface at $\theta = 0$, and $k(x)$ is a function for convenient approximation of flux surfaces. In our experiment, we choose $k(x)=x$ because the magnetic surfaces become circular near the magnetic axis.

Next step, we expand the functions $f(p,\phi)$ and $g(r,\theta)$ along the flux surfaces $r(x,\theta)$.

$$g(r,\theta) = \sum_{m} \sum_{l} \left[a_m^{c,l} \cos m\theta + a_m^{s,l} \sin m\theta \right] J_m(\lambda_m^{l+1} \cdot x(r)) \quad (8)$$

$$f_m^{c,l}(p,\phi) = \int_{L(p,\phi)} \cos m\theta \cdot J_m(\lambda_m^{l+1} \cdot x(r,\theta)) \, dl \quad (9)$$

where the function x(r) is the inversion function of r=r(x,θ).

3. Experimental result

The viewing chord of x-ray imaging system using PIN photodiode is shown in Fig. 3(a). Two detector arrays are carefully arranged at same toroidal location to cover the entire poloidal cross-section. It is required to measure the radial profile of the plasma edge for tomographic reconstruction. Each array has 32 detectors with spatial resolution of 3.5 cm at the plasma center. The signals are digitized every 40 μs in the lower array and 80 μs in upper array during 15 s, and time response of the system is about 40 μs. To introduce higher expansion term Mmax in eq. (5), rotation frequency must be less than 1 kHz.

Figure 3 (b) represents contour plot of time evolution. We assume uniform rotation along the flux surfaces. Rotation frequency is calculated by maximum entropy method (MEM). Fourier expansion terms from m = 0 to m = 2 and Bessel expansion terms from l = 0 to l = 9 are taken into account. The number of terms is decided so as to minimize AIC (Akaike's Information Criterion). The tomographic reconstruction of the emissivity is presented in Fig. 4 that shows the m=1 structure rotating around the + point.

The following is the subject for a future study: (i) Sampling time of 40 μsec is too late to analyze MHD phenomena like a sawtooth crash. (ii) Multiplexor of the system is not simultaneous sampling between the channels. (iii) Detector arrays are installed only in the horizontal port. Measurements from the other ports are required to reconstruct emissivity without assuming uniform rotation.

References
1 A. M. Cormack, J. Appl. Phys. 34 (1963) 2722.
2 A. M. Cormack, J. Appl. Phys. 35 (1964) 2908.
3 T. Kondoh, T. Cho, M. Hirata, N. Yamaguchi, T. Saito, Y. Kiwamoto, S. Miyoshi, J. Appl. Phys. 67 (1990) 1694.
4 Y. Nagayama, S. Tsuji, K. Kawahata, N. Noda, S. Tanahashi, Jpn. J. Appl. Phys., 20 (1981) L779.
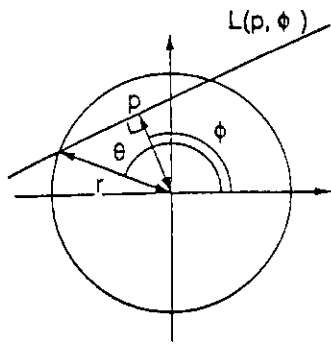
Fig. 1 Co-ordination system for tomographic reconstruction. Function f(p,φ) in the line integration of source function g(r,θ) along the line L(p,φ).
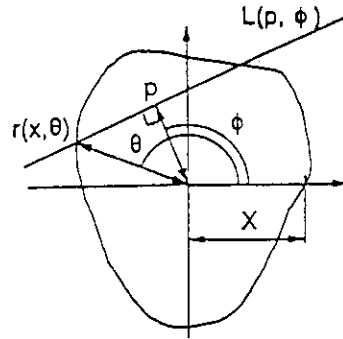
Fig. 2 Co-ordination system for non-circular tomography.
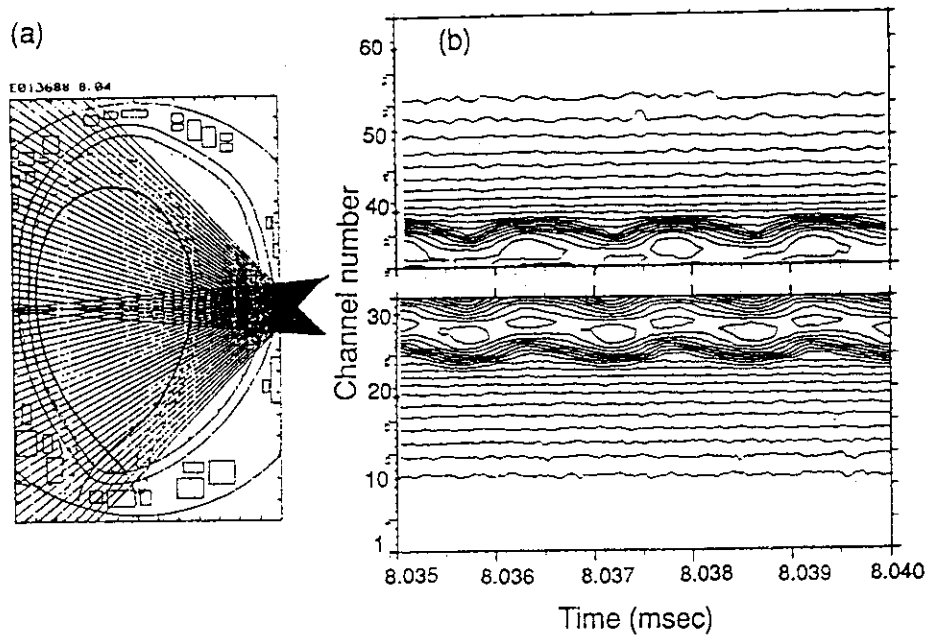
Fig. 3 (a) Arrangement of PIN photodiode arrays and outermost magnetic surface. (b) Contour plot of the soft x-ray signal.
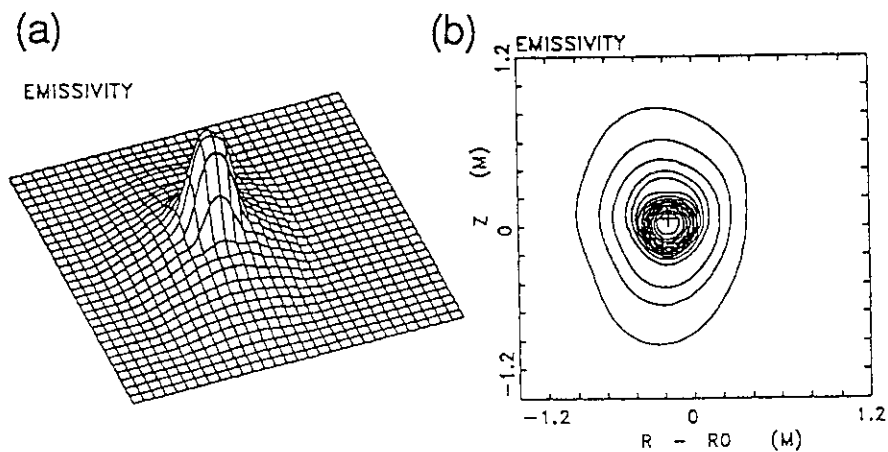
Fig. 4 (a) 3-dimensional plot and (b) contour plot of the reconstructed x-ray emmisivity showing m =1 structure rotating around + point.

6.5   Energetic Ion Behaviors during the Internal Disruption

M. Azumi, G. Kurita, K. Tani, M. Yagi

1. Introduction

The confinement of energetic ions is one of the most important subjects in the fusion research. In an axisymmetric tokamak, energetic ions produced by fusion reactions, neutral beam injection or RF heatings are well confined in a quiescent plasma except spontaneous orbit loss near the peripheral region. The micro-turbulence with $k_\perp \rho_s \approx 1$, where ρ_s is the ion larmor radius evaluated with the electron temperature, has also little effects on these ions. However, the large scale perturbations may cause serious effects on the confinement of the energetic ions. The nonaxisymmetric modification of the magnitude of magnetic field, like toroidal and helical field ripples, is well known as the loss process of energetic ions and has been extensively studied with numerical simulations. The MHD activities also affect the energetic ion orbits. The topological change of magnetic surface changes the passing particle orbit, while the perturbed electric field has the effect on trapped particles. Resonant interaction of energetic ions with MHD perturbations is also the important process from both view-points of energetic ion loss and kinetic MHD mode excitation. In order to have the understanding of this process, the behavior of energetic ions should be studied consistently with the temporal evolution of MHD modes.

In this paper, we study the energetic ion behavior during the internal disruption due to the m=1/n=1 resistive mode by using the MHD-particle hybrid simulation code, which solves the time evolution of particle orbits and MHD modes simultaneously, taking into account of the interaction between energetic ions and MHD modes. And mechanisms for MHD modes to expel ions are studied.

2. Simulation Model

The interactive behavior of energetic ions and MHD activities can be studied by the combination of the drift kinetic equations of energetic ions and the MHD equations including the anisotropic pressure tensor produced by energetic ions. In a low beta tokamak plasma with large aspect ratio and finite electric resistivity, the MHD activities are expressed by the following reduced set of MHD equations:

$$\frac{dU}{dt} = [\psi, J] - [X^2, p + (p_{//}^f + p_\perp^f)/2] \tag{1}$$

$$\frac{\partial \psi}{\partial t} = [\psi, \phi] + \eta J \tag{2}$$

$$\frac{d}{dt} X^{2\gamma} p = 0 \tag{3}$$

where

$$\mathbf{B} = B_0 \nabla \varphi + \nabla \varphi \times \nabla \psi, \quad \mathbf{V} = X^2 \nabla \varphi \times \nabla \phi$$

$$U = X^2 \Delta_\perp \phi, \quad J = X^2 \nabla_\perp X^{-2} \nabla_\perp \psi, \quad X = R/R_0$$

Parameters γ and η are the adiabatic constant and the electric conductivity, respectively. The bracket denotes the Poisson bracket, consisting of the cross product of the radial and poloidal angle derivatives. p is the plasma pressure composed by electron and thermal ions, while $p_{//}^f$ and $p_\perp^f$ are the parallel and perpendicular component of energetic ion pressure, respectively. It is noted that, under the assumption of the incompressible fluid motion, energetic ions give their effect on the MHD perturbation only through the temporal evolution of the averaged value of the anisotropic pressure, which is evaluated by using the distribution function of energetic ions, F_f, as follows

$$p_{//}^f + p_\perp^f = m \int d^3v \, (v_{//}^2 + v_\perp^2/2) F_f$$

F_f is determined by the drift kinetic equation

$$\frac{\partial F_f}{\partial t} + (v_{//} + v_E + v_D) \cdot \nabla F_f$$

$$+ \frac{e}{m} \left(\frac{\partial \Phi}{\partial t} - v_{//} \frac{\mathbf{B}}{B} \cdot \frac{\partial \mathbf{A}}{\partial t} \right) \frac{\partial F_f}{\partial W} = 0 \tag{4}$$

$$W = v_{//}^2/2 + \mu B + \frac{e}{m} \Phi$$

For simplicity, the collision term is neglected. The electric scalar potential Φ is related with the fluid steam function ϕ by the relation $\phi = \Phi / B_0$. This drift kinetic equation is solved by following guiding center orbits under temporal evolution of electric and magnetic fields determined by the reduced MHD equations (1-3). All quantities are normalized by the poloidal Alfven velocity $v_{pA} = B_a / \sqrt{\mu_0 \rho}$, $B_a = a B_0 / R_0$.

We employ the standard technique for solving the MHD equations; the predictor-corrector time integrating scheme, the finite difference scheme in the radial direction and the Fourier expansion in the poloidal and toroidal angle. The perturbed fields are fitted in the radial direction by the cubic spline method and particle orbits are followed by the predictor corrector method in the flux coordinate system, in which equilibrium field lines are straight lines.

3. Simulation results

We consider the alpha particle behavior during the internal disruption in ITER tokamak. The Kadomtsev model is employed for simulating the MHD dynamics and the disruption time is assumed to be around 200 μsec, which corresponds to the magnetic Reynold number of 10^5, or $\eta = 10^{-5}$. The radial grid number of 200 and 9 Fourier modes are employed in the following simulation. The toroidal coupling of MHD modes is neglected in the following, for simplicity, because it is not essential for the dynamics of Kadomtsev type reconnection and our purpose is to study the direct effect of m=1 mode evolution on energetic ion dynamics. In this case, MHD modes has the helical symmetry of $\zeta = \theta - \varphi$, where θ, φ and ζ are the poloidal, toroidal and helical angle, respectively. We also neglect the rotation of MHD modes so that the resonant interaction of energetic ions with m=1 modes can be neglected. Typically 5000 alpha particles are followed to study the modification of particle orbits in the typical ITER equilibrium.

Figures show typical examples of (a) the magnetic surface in the poloidal plane of $\varphi=0$, (b) particle positions in the three dimensional space and (c) their projections to the poloidal plane. The equilibrium q-profile is chosen such that the q=1 surface and the reconnection point are at r=0.5 and r~0.6, respectively, and particles are initially located at (r=0.2, θ=0) and uniformly in the φ direction (Fig. 1). Figure 2 shows the result for the untrapped alpha particles just after the internal disruption. These particles follow the topological change of magnetic surface and are expelled through the reconnecting point in the same way as the fluid element. As the result, particles are redistributed in the region outside of the equilibrium q=1 surface after the internal disruption. On the contrary, trapped alpha particles do not follow the change of magnetic surface (Fig.3). These particles are suffered both from the ExB drift and the toroidal precessional drift. The motion of the banana center is expressed by

$$< \frac{dR}{dt} > = | v_E | \cos \varphi , \; < \frac{d\varphi}{dt} > = v_{D\varphi}$$

In the case of the trapped particle with low energy, the precessional drift $v_{D\varphi}$ can be neglected and the particle moves by the ExB drift in almost the same poloidal plane as the initial position. We note that the turning point also moves at the same velocity as the banana center because of the energy gain (or loss) due to the electric field acceleration (or deceleration). As the result, some particles, which move inside of the torus, are free from the trapping by the magnetic field. On the other hand, energetic trapped particles are swinged in

the major radius direction by the combination of ExB and $v_{D\phi}$ drifts and their orbits are randomized in the poloidal plane after the internal disruption except the extremely high energy particles, for which the ExB drift is averaged out by the $v_{D\phi}$ drift. Figure 3 shows the trapped alpha particles are uniformly distributed outside of the torus after the internal disruption.

4. summary

Behavior of alpha particles during the internal disruption in ITER tokamak has been studied by using the MHD-particle hybrid code under development, and the difference between behaviors of passing and trapped alphas has been clarified. The behavior of energetic ions produced by parallel / perpendicular NBI and ICH heating in JT-60U is now studying by using the same code and results will be reported elsewhere. In this paper, we have made several assumptions for simplification. The toroidal mode coupling produces the stochastic magnetic field and may randomize the energetic ion orbits. The mode rotation can make the MHD mode resonant with energetic ions. These problems are also under investigation with the improvement of the hybrid code and results will be reported.

Figure 1
Initial condition
(before disruption)

Figure 2
Passing alphas
after the disruption

Figure 3
Trapped alphas
after the disruption

(a) magnetic surface at $\phi = 0$
(b) three dimensional plot
    of particle positions
(c) projection of particle positions
    to the poloidal plane (r, θ)
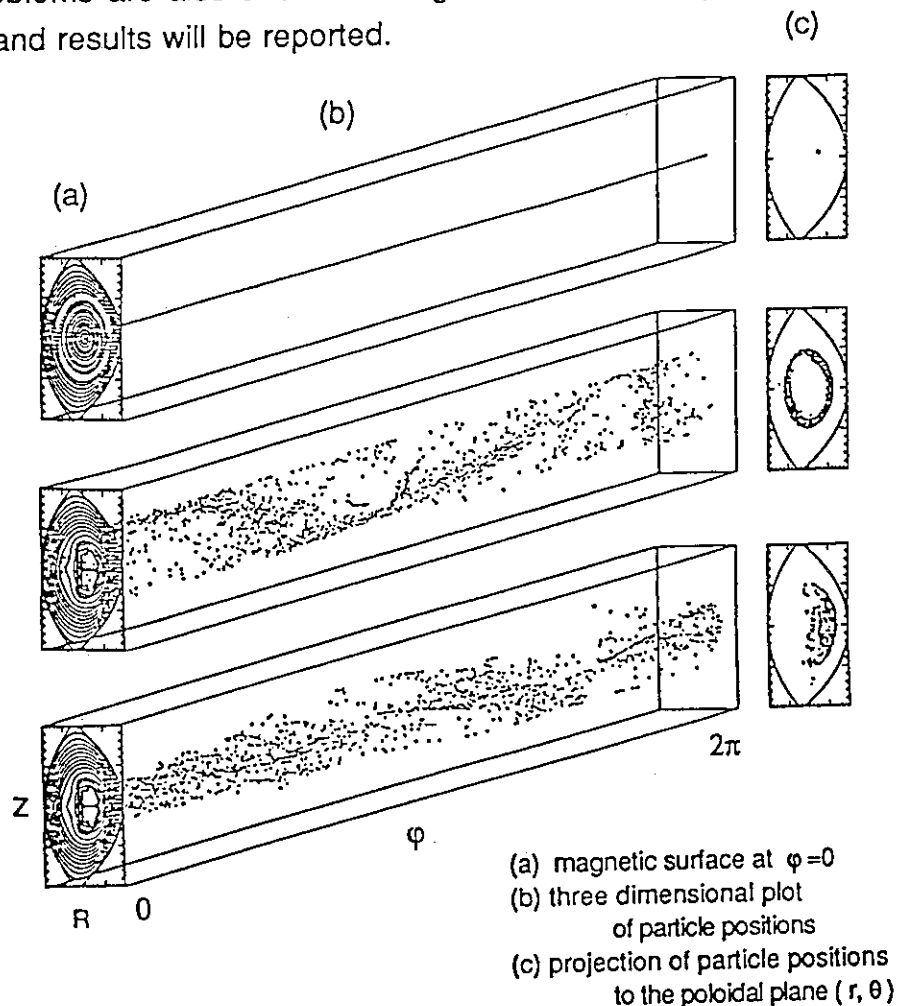
6.6 Ideal Ballooning Instability near the Separatrix in JT-60U

T. Ozeki, M. Azumi, and Y. Kamada

1. INTRODUCTION

In the H-mode plasmas in JT-60U, ELMs (Edge Localized Mode) are observed in the wide rage of operations. In ELMs of JT-60U, large spikes of H_α and the rapid degradation of the edge pressure gradient are observed and the restriction of the increase in the stored energy is appeared [1]. The ELM study in DIII-D shows that the most plausible candidate of the giant ELM is the ideal ballooning instability[2]. Therefore, in this section, we study the ideal ballooning mode near the separatrix in the JT-60U divertor configuration. The detailed pressure gradient near the separatrix is not observed, so that the maximally obtainable pressure gradient is numerically discussed by using the up-down asymmetry equilibrium code MEUDAS.

2. BASIC CONSIDERATION OF BALLOONING MODE

The stability diagram of the ballooning mode is generally shown by the s-α diagram, where s is the global shear defined by $(r/q)(dq/dr)$ and α is the normalized pressure gradients defined by $-(2\mu_0 R q^2/B^2)(dp/dr)$. Wesson and Sykes[3] described that α of the first ballooning limit is approximately proportional to the s, i.e., $s = A\alpha$ where A is 1.67 in the circular flux surface. From this result, the maximally allowable pressure gradient can be estimated as follows,

$$\frac{dp}{dr} = -\frac{1}{A}\frac{B_t^2}{R}\frac{s}{q^2}. \tag{1}$$

Because the ballooning mode is localized mode, the limit pressure gradient near the separatrix is determined the parameters near the separatrix, i.e., the shear s, the toroidal field B_t and the safety factor q. Equation (1) shows the high shear, the high B_t and the low q are preferable for the stability of the ideal ballooning mode. Consequently, the following results are obtained. 1) The high shear near the separatrix is correspond to the low internal inductance ℓ_i or the low pedestal current. This is not acceptable for the H-mode plasmas. 2) The high B_t is good for ballooning mode but it might increase the threshold power of the H-mode transition. 3) The low q is preferable to both the ballooning mode and the transition to H-mode. The constant A of Eq. (1) might be changed by the configuration, for example, the elongation, the triangularity and

the X-point. In the next section, therefore, we consider the more realistic equilibrium numerically.

3. NUMERICAL ANALYSES

The MHD equilibria are obtained by solving the Grad-Shafranov equation for the prescribed plasma shape and the profile data. To determine the two free functions, i.e., the plasma pressure $dP/d\psi$ and the toroidal field function $F(\psi)$, in this study, we use the following function,

$$\frac{dp}{d\psi} \propto (1 - \kappa)\psi^{\nu} + \kappa, \tag{2}$$

$$< J_{\parallel} \cdot B > \propto (1 - \sigma)\{(1 - \tilde{\psi}^{\alpha_1})^{\alpha_2}\} + \sigma. \tag{3}$$

where $\tilde{\psi} = (\psi - \psi_{axi})/(\psi_{bun} - \psi_{axi})$ is the normalized poloidal flux to $0 < \tilde{\psi} < 1$. In the following calculation, we use ν of 10 and κ of 0.1 to make a high pressure gradient near the separatrix. The amount of σ represents the pedestal of the plasma current. As the pedestal increases, the shear near the separatrix decreases. In the parameter survey of the shear, we changed σ from -0.2 to 0.2. $\alpha1$ is fixed to 1.0 and $\alpha2$ is determined to adjust the q_0 to 1.05.

The results are shown in Fig. 1 - Fig. 4. We choose the typical three configuration, i.e., (a) the high elongation configuration, (b) the standard configuration, and (c) the circular configuration without X-point. Figure 1 shows the typical configuration for three plasmas. The aspect ratio, R/a, in three configurations are 3.1m/0.75m, 3.4m/1.0m, and 3.0m/1.0m for the high elongation, the standard and the circular configurations, respectively. The elongation and the triangularity ϵ/δ are 1.67/0.1, 1.39/0.32 and 1.0/0.0, respectively.

Ballooning stability analysis was carried out by solving the ordinary infinite n ballooning equation [4]. The flux function shape and the pressure and current profiles, which have been constructed by the equilibrium code, are used for stability analysis. The marginal pressure gradient $dp/d\psi$ is determined on each flux surface by fixing that the growth rate be zero. Figure 2 shows the results of the ideal ballooning mode, where the pressure gradient dp/dr is plotted for the minor radius r/a. Here, we use the value of dp/dr for the pressure gradient, because this pressure gradient is a experimentally observed value. The dp/dr is reduced as the minor radius r increase near the separatrix, though the $dp/d\psi$ (or α) increases as the minor radius.

Figure 3 shows the marginal pressure gradients dp/dr at the 95% flux surface for the high current ($I_p = 3MA$) and the high toroidal field ($B_T = 4.8T$) with the safety factor of $\sim$ 3. In three configurations, the marginal pressure gradient increases with the global shear as to be estimated from Eq. (1). The marginal pressure gradient also increases on the low shear region. This is due to the effect of the negative local shear. The marginal pressure gradient in the high elongation configuration is higher than that in the standard configuration. This seems to be mainly effects of the decrease of the major radius (from 3.4m to 3.1m) and the increase of B_t ($\propto 1/R$).

Figure 4 shows the marginal pressure gradients $dp/d\psi$ at the 95% flux surface for the low current ($I_p = 1.5MA$) and the low toroidal field ($B_t = 2.5T$) with the safety factor of $\sim$ 3. The differences of the marginal pressure gradient is almost same as the high field plasma. The values of the pressure gradient of B_t (= 2.5T) is about four times as less as the values of the high field plasma (= 4.8T). This is consistent to Eq. (1).

4. SUMMARY

The high elongation plasma can have a higher pressure gradient near the separatrix, so that the high elongation seems to be preferable to suppress the ELMs in JT-60U. As the shear decreases, the marginal pressure gradient becomes higher after the degradation. The pedestal current is preferable to make a higher ballooning limit. To ascertain this conclusion, the detailed measurements of the edge pressure gradient and the current profile near the separatrix are important.
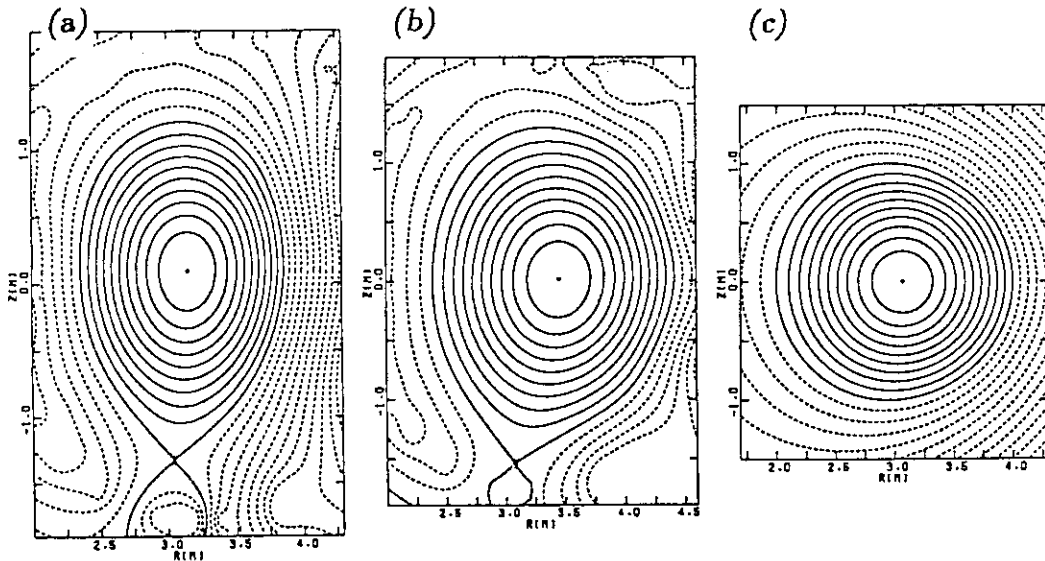
Fig. 1 Configurations of (a) the high elongation, (b) the standard and (c) the circular plasmas.

REFERENCES

[1] KAMADA,Y., et al., (in this paper, section 3.3.5).

[2] GOHIL,P., et al., Phys. Rev. Lett. **61** (1988) 1603.

[3] WESSON,J.A, SYKES,A., Nucl. Fusion **25** (1985) 85.

[4] CONNOR,J.W., HASTIE,R.J., TAYLOR,J.B. Phys. Rev. Lett. **40** (1978) 396.
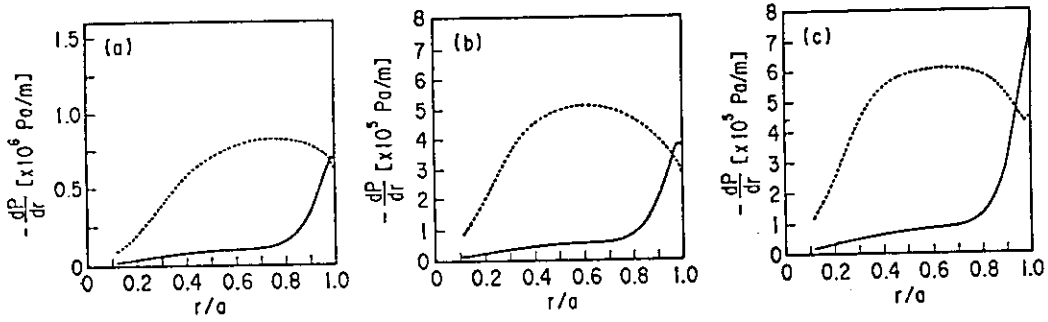
Fig. 2 *Marginal pressure gradient (broken line) and pressure gradient of the equilibrium (solid line) as a function of the minor radius for three configuration in Fig. 1.*
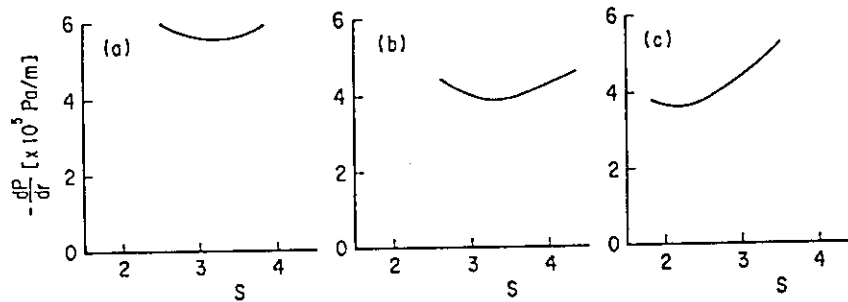
Fig. 3 *Marginal pressure gradients at the 95% flux surface as a function of the shear for B_t of 4.8T and q of 3.0.*
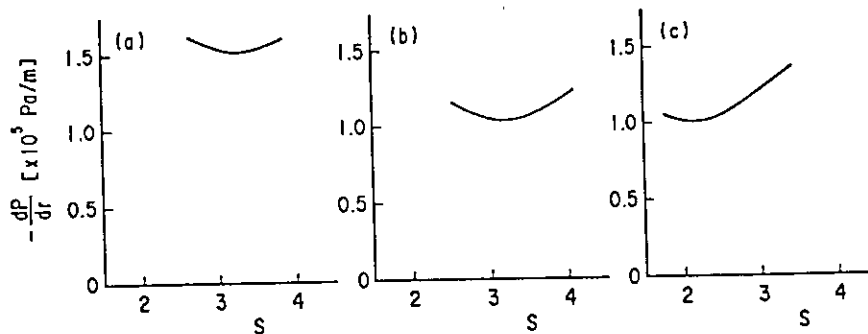
Fig. 4 *Marginal pressure gradients at the 95% flux surface as a function of the shear for B_t of 2.5T and q of 3.0.*

7 Disruptions

7.1 Statistical Analysis of Disruptions

Y. Neyatani and N. Hosogane

1. INTRODUCTION

In tokamak devices, the maximum electromagnetic loads are induced during the disruptions on the vacuum vessel, poloidal field coils etc. For the reason, it is important to evaluate statistically the frequency and the discharge phase of the disruptions in order to continue the plasma operations without catastrophic damages. In this paper, a statistical survey of the disruptions is described in the JT-60 upgrade (JT-60U) operation. In the next section, frequencies of the disruptions are described for each operational period. The decay rate of the plasma current is discussed in the following section. The summary is described in the last section.

2. FREQUENCY OF THE DISRUPTIONS

The experiment of the JT-60U was started at April 1991. The total shots of 1283 were discharged during April to October. The first Deuterium operation of 706 shots was performed from June to September. The average frequency of the disruptions is 19.7% of total discharge during the operation as shown in Fig.1. In 1991, experiments divides three periods by its operational gases. Figure 2a shows the histogram of the discharges in the first period from April to June with Hydrogen gas. Many discharges were spend to obtain the condition of the plasma initiation and have a most part of the discharges in this period. The frequency of the disruptions is 16.4% which is relatively less than the average value. In the next period from July to September, Deuterium was fueled as a operation gas. As a results of continued study of the plasma initiation and the wall conditioning, a number of no build up shots reduced about a half. The disruptions occurred 24.2% of the total shots (Fig.2b). The large frequency is mainly due to increase the number of total good shot, not Deuterium operation. In the last period of 1991 experiments, Hydrogen was also utilized for the plasma operation in order to reduce deuterium atoms adsorbed in the first wall. The frequency becomes 15.2% which is least value during the three periods (Fig.2c).

The average frequency is less in the case of JT-60U than in the case of original JT-60 of 30% or less [Ref.1]. Some reasons of this reduction are described as follows; (1)The disruption due to locked mode has been studied in the experiment of JT-60 and can be effectively avoided to add the input power [Ref.2]. (2) The plasma TV was utilized in order to build up the plasma current effectively by monitoring the location of the initial plasma and the impurity influx for each shot. It is powerful diagnostics for the discharges successed. (3) The glow discharge cleaning (GDC) [Ref.3] had large effect for the wall conditioning and reduced impurity

concentration in the first wall. (4) The glowing plasma method [Ref.4] is also dramatically reduced no build up discharges. For the reasons, the low frequency of the disruption is atchieved, especially, in the last period. As several shots were disrupted on purpose to check the response of the plasma control in this period, the frequency of the unexpected disruptions would be attributed 10% or less and the rate of the completed shots without troubles reached 74% or more.

The 48% of the disruptions took place in the flat top phase of the plasma current. This rate is roughly comparable in the case of original JT-60. The 31% and 21% took place in the ramp up and ramp down phases respectively. This ratio is almost constant during the whole experimental periods. The electron density just prior to the disruption is relatively low ($n_e < 3 \times 10^{19} \ m^{-3}$) in the ramp up and down phases.

3. DECAY RATE OF PLASMA CURRENT

The electromagnetic force induced by the disruptions is increased with the decay rate of plasma current. Hence, it is important to estimate the maximum decay rate for the design of the next generation devices. Figure 3 shows the maximum decay rate of the disruptions with the flat top, Ip ramp up and down phases. The maximum rate has 780 MA/s in the 4 MA disruption and proportionally increases with plasma current. The fastest decay have IP/(dIP/dt)max ~ 5ms. No difference of the decay rate is obtained for each discharge phases. The disruption with low density appears to have relatively large decay rate but the density dependence is not clear. The difference of Deuterium and Hydrogen discharges is also not clear.

The eddy current in the vacuum vessel is arose the further force on the vacuum vessel by the inductive voltage from the plasma current decay; Iv ~ (Lv/Rv)(dIP/dt), where Lv is the effective inductance and Rv is the toroidal resistance of the vacuum vessel. The maximum value of the eddy current reached approximately 50% of plasma current [Ref.5]. Figure 4 shows the relation between the eddy current (Iv) and the plasma current decay (dIP/dt). The typical time of the eddy current determined by Lv/Rv is approximately 1.9 to 4 ms. The range suggests the distribution of the eddy current on the vessel differs for the disruptions due to plasma location, shape, and plasma movement. The disruption conditions with low Lv/Rv suggests the low electromagnetic loads conditions.

4. SUMMARY

The average frequency of the disruptions of 19.7% is surveyed at the JT-60U experiment in 1991. This frequency has less than that of original JT-60. It is because that the plasma TV, the glow discharge cleaning and the glowing plasma method are powerfully used to reduced the disruptions and no build up discharges. Using these tools, the frequency of the disruption reached 10% or less in the last experimental period.

The fastest decay have IP/(dIP/dt)max ~ 5ms and it is almost constant with plasma current. No difference is observed for some discharge phases and operational gases. The typical time of the eddy current in the vacuum vessel is 1.9 to 4 ms.

ACKNOWLEDMENT

The author would like to thank Dr. R. Yoshino for his helpful discussions.

REFERENCES

[1] JT-60 team : JAERI-M 89-033 p.34-37.

[2] H. Ninomiya et al. : Nucl. Fusion, 28 (1988) p.1275-1281.

[3] M. Shimada et al. : In this review paper.

[4] R. Yoshino et al. : In this review paper.

[5] Y. Neyatani et al. : In this review paper.
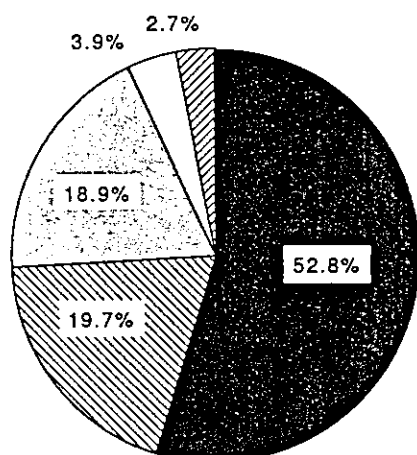
Fig.1 Histogram of the Discharge in 1991 (12779-14306)
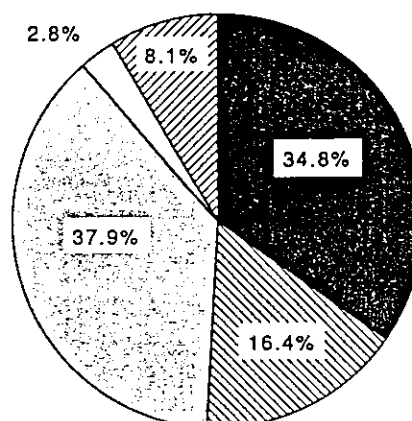
H dischrge (April - June)

Fig.2a Histogram of the Discharge in 1991 (12779-13239)

■ Good shot
▨ Disruption
☐ No build up
☐ Interlock
▨ Others
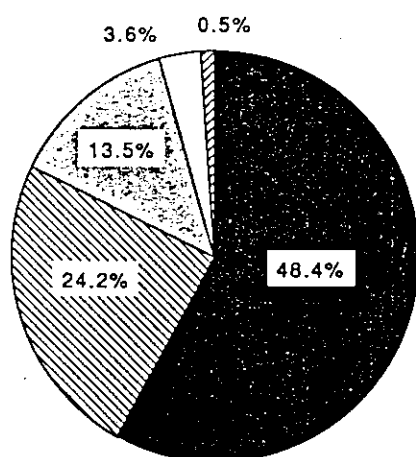
D discharge (July - September)

Fig.2b Histogram of the Discharge in 1991 (13292-13963)
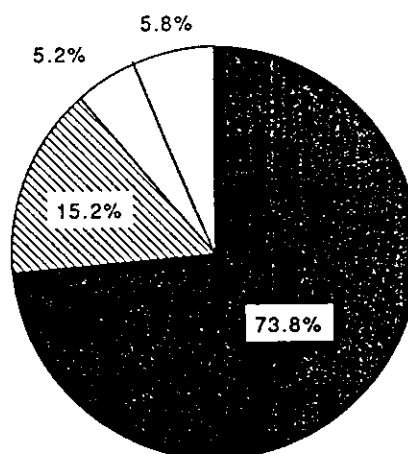
H discharge (October)

Fig.2c Histogram of the Discharge in 1991 (13998-14306)
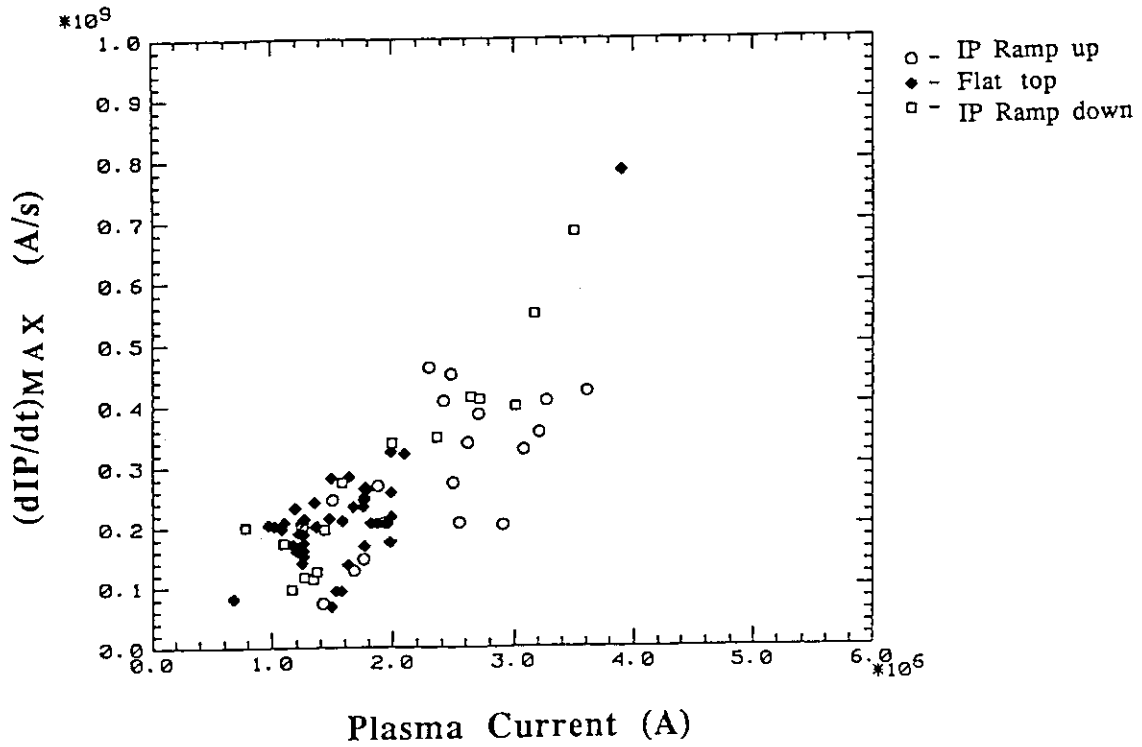
Fig.3 The maximum value of dIP/dt during the current decay
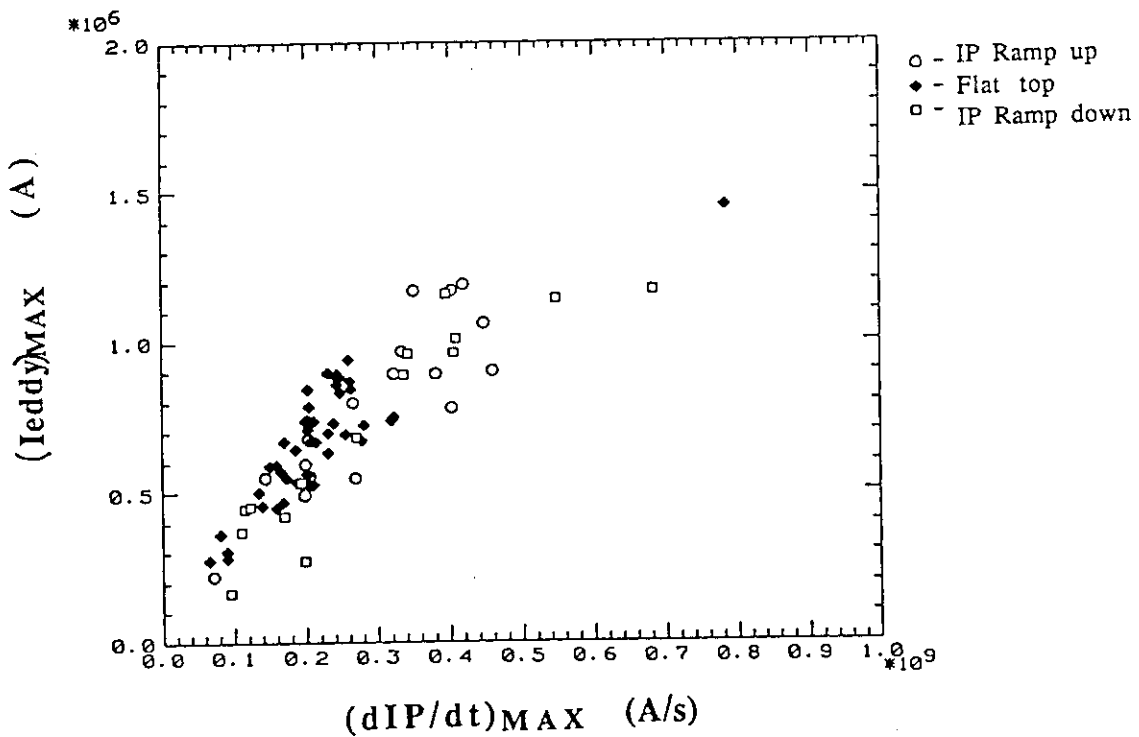
Fig.4 Maximum eddy current on the vacuum vessel as a function of maximum dIP/dt.

7.2 Profiles of Eddy Current and Electromagnetic Force on the Vacuum Vessel in Major Disruption

K. Ushigusa, M. Matsukawa and Y. Neyatani

The toroidally symmetric eddy current and the electromagnetic force on the vacuum vessel in major disruptions on JT-60U have been analyzed by using a magnetic fitting code (see Sec. 2.4).

1. Vertically unstable discharge

Figure 1 shows an example of a vertically unstable discharge. By increasing the poloidal beta during the neutral beam pulse, the vertical oscillation of the plasma column grows and finally the discharge is terminated by a major disruption at $t \sim 6.8s$. The bottom two traces in Fig. 1 show the amplitudes of Fourier components of the fitted eddy current. The $m = 1$ component of the eddy current increases when the vertical displacement velocity is large and this indicates the strong shell effect of the vacuum vessel. The profiles of the eddy current during the plasma displacement are also shown in Fig. 1, where outside and inside bars mean that the direction of the eddy current is the same as and opposite to the plasma current, respectively. Figure 1 clearly shows that the eddy current flows so that the electromagnetic force acts to prevent the plasma displacement. The velocity of the vertical displacement is $\sim 20m/s$ in this case.
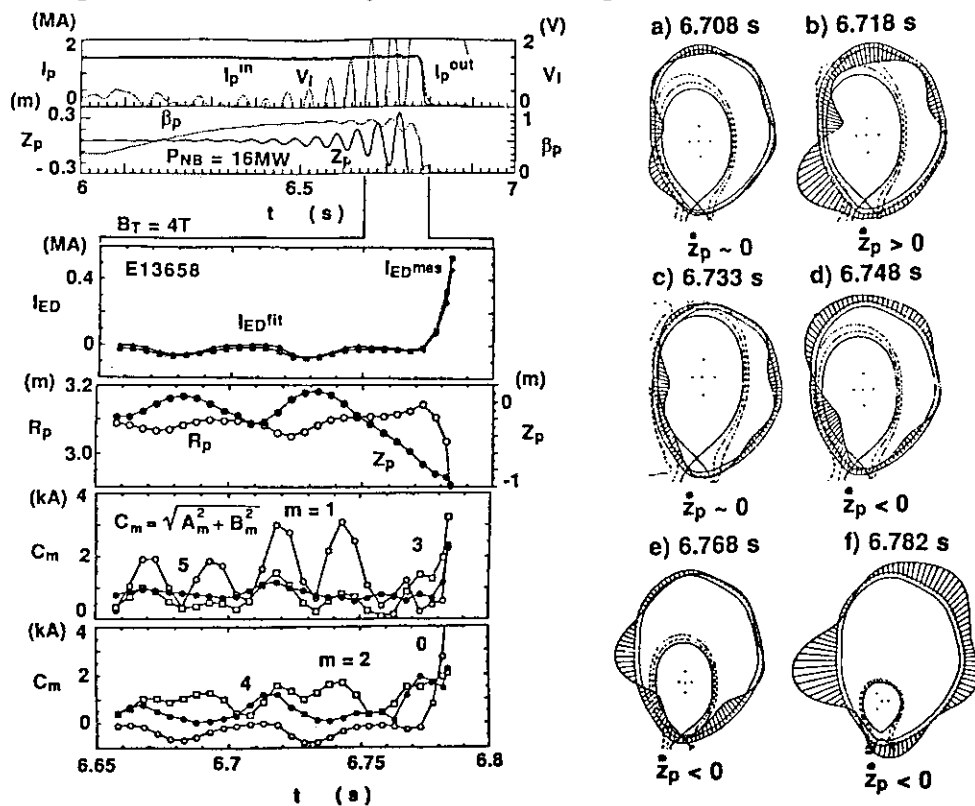
Fig.1 Eddy current on the vessel on the vertically unstable discharge

Recently a poloidal current which flows in first wall (halo current) was observed in some tokamaks during a vertical displacement event (VDE). We can not confirm the halo current in a VDE because no diagnostic tool is available on JT-60U. We can say only that there was no large difference in the magnetic probe signals located at two different toroidal sections. A very simple modelling shows that the halo current can be estimated[1] by

$$I_{pol} = \frac{f(\kappa, \delta)}{2\pi R} B_{tor} \left| \frac{dz}{dt} \right| t_{sh}\sigma \ (C/q)^2 \qquad (1)$$

where $f(\kappa, \delta)$ is geometrical factor in the range of 0.65 (elliptical) to 1 (circular) which depends on the ellipticity κ and triangularity δ, and R, B_{tor}, C and q are the major radius, the toroidal field, the circumference of the plasma surface and the safety factor, respectively. t_{sh}, σ and dz/dt are the thickness of the sheath where the halo current flows, the conductivity of the sheath and the velocity of vertical displacement, respectively. By using Eq.(1), experimentally observed halo currents have indicated that the product of $t_{sh}\sigma$ is $\sim 1.5 \times 10^4 \ \Omega^{-1}$ for a JET disruption and $\sim 1 \times 10^4 \ \Omega^{-1}$ for DIII-D. When we employ $t_{sh}\sigma$ of $1.5 \times 10^4 \ \Omega^{-1}$ and apply Eq.(1) to the case shown in Fig.1, about 40kA of halo current may flow (E13658, t = 6.743, Btor = 4T, R = 3.1m, C = 6.4m, q = 6.9, f = 0.75, dz/dt = 20m/s).

2. Rapid major disruptions

Figure 2 shows the fastest disruption observed in this series of experiment (4MA divertor discharge).
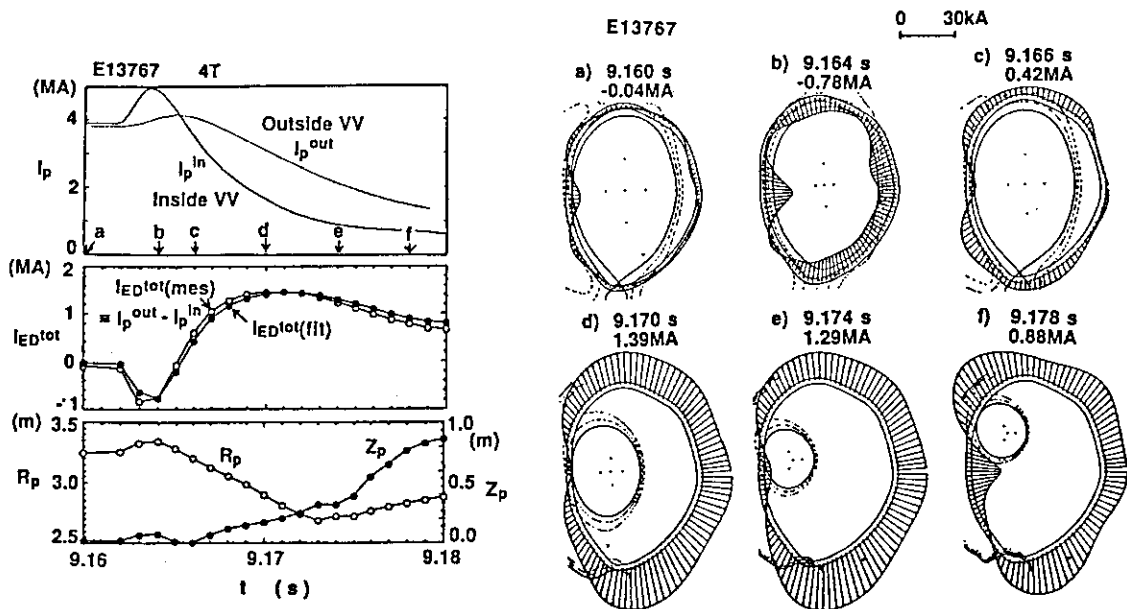
Fig.2 Vessel current profile on the fastest major disruption

The difference between outside and inside Rogowskii signals indicates that about 1MA of vessel current flows opposite to the plasma current just after the disruption event, and then a vessel current of up to 1.4MA flows in the same direction as the plasma current. The total toroidal eddy current estimated by the fitting code agrees fairly well with the measured current. The velocity of plasma displacement is estimated to be $|dz/dt| < 130$m/s and $|dR/dt| < 80$m/s. By using the fitted results, one can easily derive the electromagnetic force on the vacuum vessel. Figure 3 shows time evolutions of the integrated radial, and vertical force on the vessel, and the radial profile of electromagnetic force. About 700 tons of radial force acts on the vessel in this case, and this value is lower than the design limit (2000 tons). The integrated vertical force is not as large as the horizontal force. It should be noted that the direction of the radial force changes according to the direction of the vessel current. This may enhance the large vibration of the vessel.

Figure 4 shows the disruption speed $|dIp/dt|$, the total eddy current I_{ED}, and the integrated horizontal and vertical force (F_r and F_z) against the plasma current just before the disruption event. The characteristic time of the current decay is < 5ms. The total vessel current increases with the initial plasma current Ipo and the ratio of I_{ED}/Ipo is roughly 0.38. The horizontal force may be scaled by F_r(ton) ~ 37.5 Ipo(MA)^2. A low current disruption tends to create an upward force on the vessel while higher current produces a downward force. This may correlate with the direction of plasma displacement.
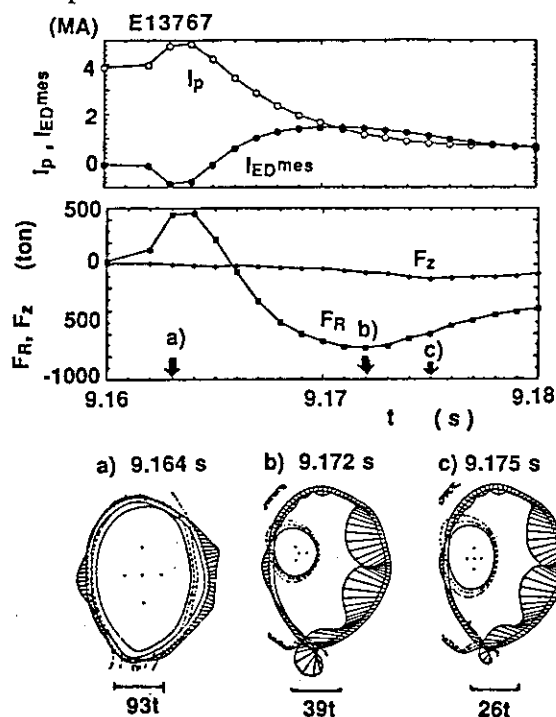
Fig. 3 Electromagnetic force on the vessel during disruption.
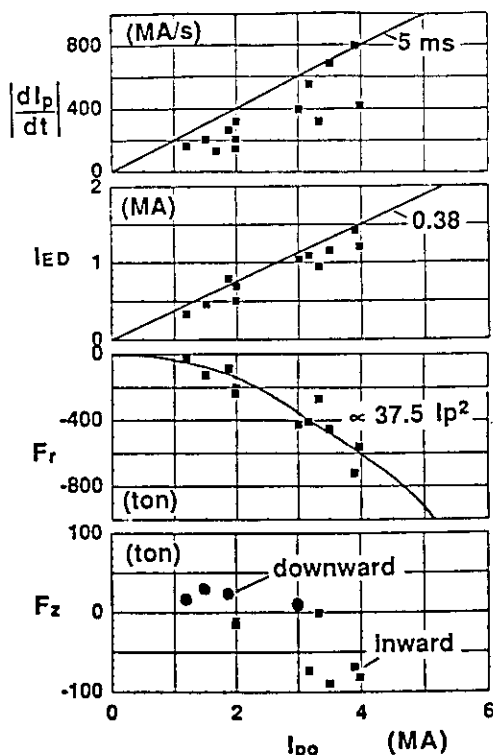
Fig. 4 Disruption speed, total eddy current, radial and vertical forces vs. plasma current.

Solid circles (squares) in the bottom box in Fig. 4 represent discharges which have terminated with downward (inward) displacement. From these data, we predict a disruption of a 6MA discharge to have a disruption speed of ~ 1200MA/s, total vessel current of ~ 2.25MA and horizontal force on the vessel of ~ 1400 ton.

Figure 5 shows the increment of the plasma current just after a disruption event and the disruption speeds against the initial plasma current. Solid and open squares in Fig.5 show the current ramp-up rate and negative disruption speed, respectively. About a 20% increase in the plasma current has been observed, and the current ramp up rate has almost the same value as the following negative disruption speed at current quench. The current jump at the disruption event comes from the change in the internal inductance. If we assume flux conservation , the increase in the plasma current becomes

$$\Delta Ip = - \frac{\Delta l_i'}{l_i} I_{po} - \frac{L_e I_e}{\frac{1}{2}\mu_o R_o l_{io}} = \frac{\Delta(R_p \Lambda) - \Delta(R_p \beta_p)}{R_{po}\Lambda_o - R_{po}\beta_{po}} I_{po} - \frac{L_e I_e}{\frac{1}{2}\mu_o R_o l_{io}} \qquad (2)$$

where Rp, Λ, βp, I_e and L_e are the major radius, the Shafranov lambda, the poloidal beta, the eddy current of the vessel and the external inductance of the vessel. The suffix "o" means the the value just before the disruption event. It was assumed that all thermal energy is lost by the current jump ($\Delta\beta p = \beta po$). Figure 6 shows the increment in the plasma current against the first term of Eq.(2). The increment in the plasma current increases linearly with a decrease in li. Figure 6 suggests that about half of the internal flux contributes to the increase in the plasma current just after the disruption event.
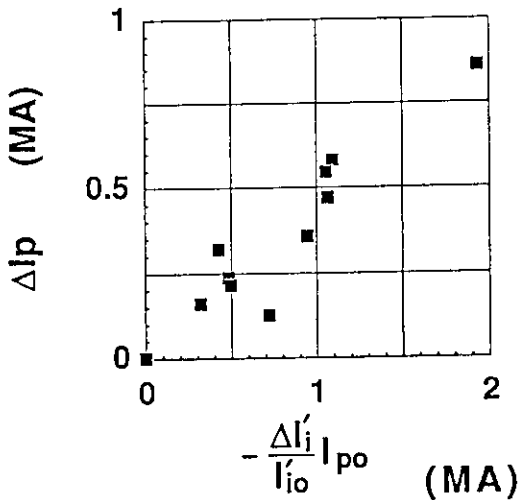
Fig.5 Increment of plasma current and disruption speeds vs. the plasma current
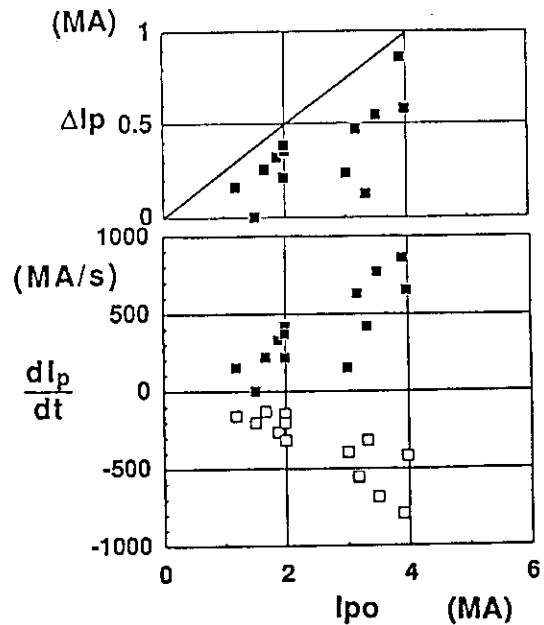
Fig.6 Observed increment current vs. increment current due to flux change

Reference [1] G.W.Pacher, H.D.Pacher and the NET team, ITER-IL-PH-8-0-15.

7.3 Vibration of the Vacuum Vessel during Disruptions

Y. Neyatani, K. Ushigusa, M. Matsukawa and H. Ninomiya

1. INTRODUCTION

Disruption is the most serious problem for Tokamak operations. A large electromagnetic force is generated by the eddy current on the vacuum vessel during disruptions. As the vacuum vessel of the JT-60 Upgrade (JT-60U) is designed to endure the 1000 times 6MA disruptions (2000 cycles of load) [Ref.1], it is important to preclude damage to the vessel by providing limits on plasma operation. The some kind of diagnostics and a analysis code are prepared to estimate the stress, the eddy current on the vessel and the plasma motions during disruptions.

2. DISRUPTION MEASUREMENT

The structural analysis predicts that the JT-60U vacuum vessel has high vibration frequency of 60-100 Hz. Hence, the displacement sensors with laser are attached on the lower spacer of TFC instead of the mechanical sensor as to measure the displacement of the vacuum vessel. The triangulation is applied in order to measure the displacement of the target against the sensor as shown in Fig.1. The frequency response of the sensor is 3 kHz and the range of measurement is ±10mm with the accuracy of 50 mm. The effect of the magnetic field is confirmed by the toroidal field coil tests. The results shows the error due to the magnetic field of 4 tesla is up to 50 mm.

The toroidal eddy current on the vacuum vessel is measured by subtracting the inside and outside Rogowski coils. High speed visible TV is used for observation of the plasma motions. The plasma motions are also evoluated by the FBI code including the eddy current on the vacuum vessel [Ref.2]. This code is also estimated the distribution of the eddy current and the electromagnetic force during the disruptions.

3. RESULTS AND DISCUSSIONS

(1) *Vibration of the vacuum vessel*

Figure 2 shows the vibration of the vacuum vessel during 4MA disruptions. In this case, plasma was disrupted at 9.15 sec and the eddy current of 40% of the plasma current was induced on the vacuum vessel. Plasma moved inward at the speed of 80m/sec during the current decay. The radial electromagnetic force was reached 720 tons which was approximately 35% of the maximum design force. The vertical force was 120 tons. The vessel vibrated with the frequency of 82 Hz and the amplitude of 0.3 mm. The frequency of the vibration is very close to the calculated fundamental frequency of the vessel. The decay time of the vibration is approximately 55-70 ms. At a point of the stress fatigue, it is equivalent 2 cycles of the

electromagnetic loads. Figure 3 shows the maximum displacement of the vacuum vessel during disruptions. The amplitude is within the limit of 2 mm which determined by the stress restriction.

(2) *Disruption behavior*

Figure 4 shows the current decay rate during the major disruptions from July to October 1991. The maximum dIP/dt during disruptions is 780 MA/s which is 1.6 times of the maximum decay rate of the original JT-60. The average dIp/dt is 430 MA/s. The fastest decays have Ip/(dIp/dt)$_{MAX}$ $\sim$ 5 ms and is almost same of the original JT-60 [Ref.3] and JET [Ref.4].

The maximum toroidal eddy current is up to 50% of the plasma current just prior to disruptions as shown in Fig.5. This result is good fit to the eddy current analysis with the vessel resistance of 0.16 mW. The plasma motions during disruptions are almost inward direction. Downward motion is only observed in a case of high beta disruptions with the vertical instabilities.

(3) *Comparison to the structural analysis*

The experimental results are compared the structural analysis to preclude the damage of the vacuum vessel. The model of the structural analysis is the plasma current of 6MA, the decay time of 10 ms and the plasma motions of downward during 10 ms. From the analysis, the maximum stress of 30 kg/mm^2 is generated on the root of the lower large port and the displacemnet of 2 mm is obtained at the top of the port. The real structure of the vacuum vessel has different from the analysis model. The rigidity near the root of the port is 20% higher due to the short welding pitch of the outer skin. The thichness of the port wall near the root is also large, hence the geometrical moment of inertia is incerased 25%. After these consideriations, the displacement of the port is expected 1.3 mm at the 6 MA disruption.

In the case of experimental 4 MA disruptions, the plasma moved inward direction with the average decay time of 12 ms. The maximum stress of the disruption is 70% with moving inward than with moving downward case. As the electromagnetic force is approximetery 35 % of the maximum radial loads, the amplitude of the vibration is expected 0.32 mm with these two effects. It is good fit to the experimental result. This shows that the measured vibration will be properly indicated the maximum stress of the vacuum vessel during disruptions.

4. SUMMARY

The vibration of the JT-60U vacuum vessel is measured to confirm the stress of the vacuum vessel during disruptions by laser sensors. The vibration frequency of the vacuum vessel is 82 Hz, which is very close to the calculated fundamental frequency of the vessel. The maximum amplitude of the vibration is 0.3 mm during 4 MA disruption moving inward of 80 m/sec with

the maximum current decay of 780 MA/sec. During the experiments from July to October 1991, the amplitude of the vibration is within the limit, and is good fit to the result of the structural analysis.

ACKNOWLEDMENT

REFERENCES

[1] Y. Neyatani et al.: Plasma Devices and Operations, 1991, Vol.1, p.183-203.

[2] K. Ushigusa et al.: Sec.7.2, in this review paper.

[3] JT-60 Team : JAERI-M 89-033 p.34-37.

[4] J.A. Wesson et al.: Nucl. Fusion 29 No.4 (1989) p.641-666.
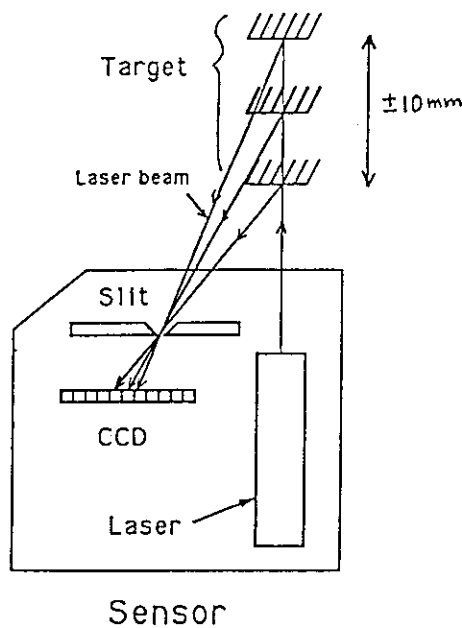
Frequency Responce : 3 kHz
Range : ±10mm
Accuracy : ±50μm

Fig.1 Measurement principal of the laser displacement sensor
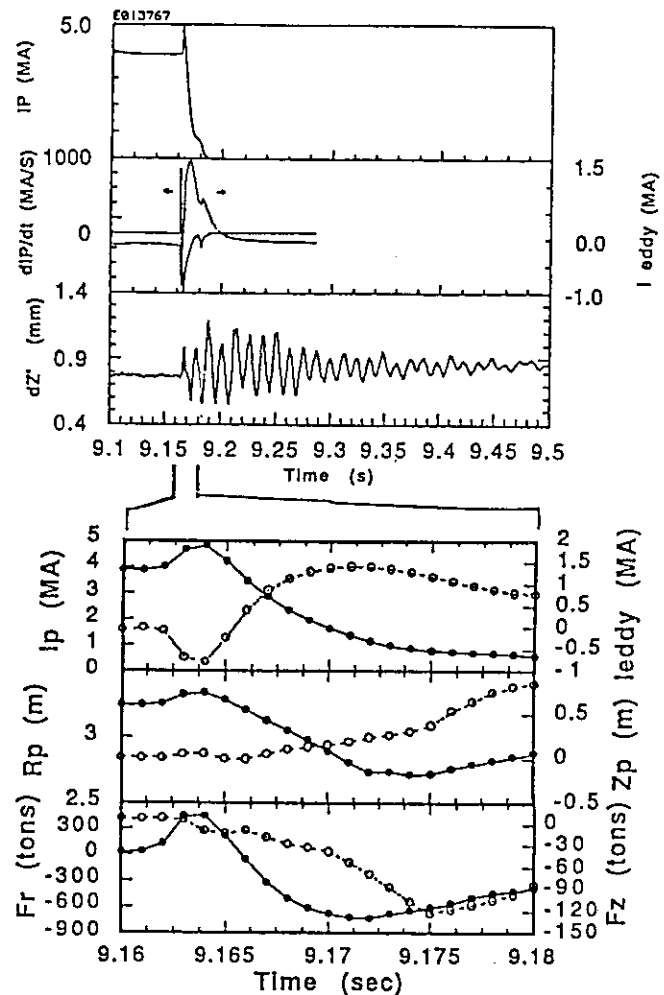
Fig.2 (a) Time history of the vibration of vacuum vessel at the disruption (b) Time history of the eddy current, location of plasma and the electromagnetic force during the current decay.
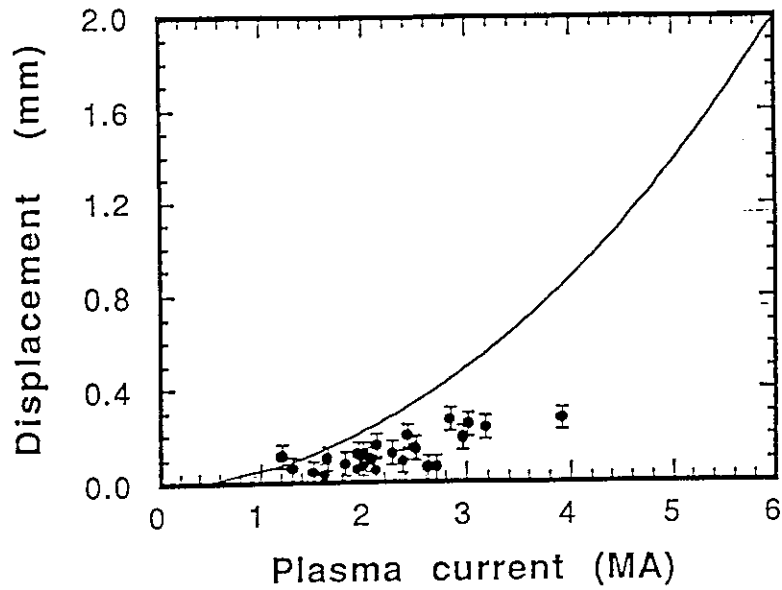
Fig.3 Displacement of the vacuum vessel during disruptions
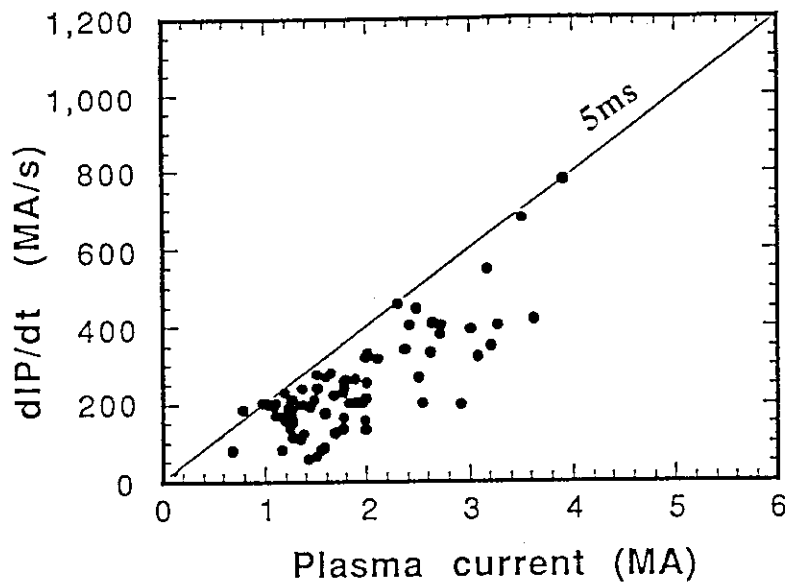
Fig.4 Maximum value of dIP/dt during the current decay as a function of plasma current
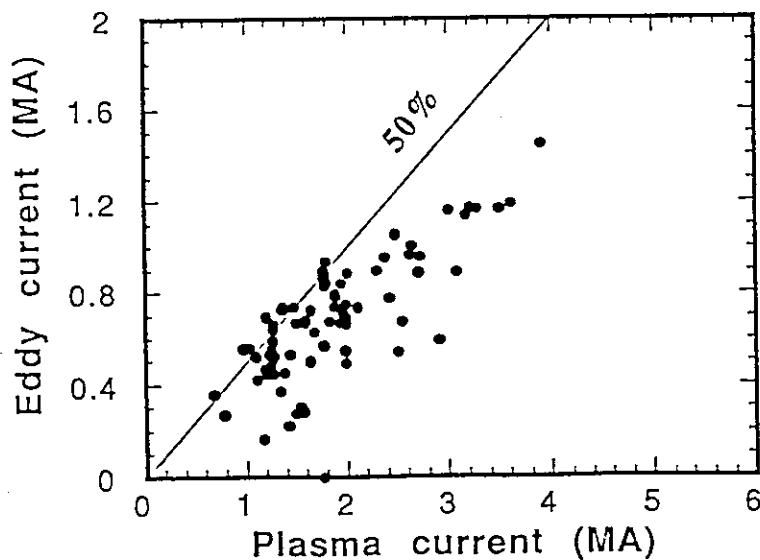
Fig.5 Maximum eddy current in the vacuum vessel as a function of plasma current

7.4 Observation of Divertor Phenomena prior to Density Limit Disruptions in JT-60U

N.Hosogane, N.Asakura, H.Kubo, K.Itami, A.Sakasai, K.Shimizu, H.Nakamura, M.Shimada, Y.Neyatani, R.Yoshino, S.Wolfe, Y.Kamada and H.Ninomiya

1. Introduction

It is well known that the MARFE occurs before the density limit disruptions[1,2]. In the divertor plasmas, the MARFE grows in the divertor region, and develops to the plasma detachment, finally leading to the disruptions[2,3]. This is because the high recycling state with large radiation loss is formed in the divertor through the divertor function. Therefore, to understand the density limit of the divertor plasma, it is important to study the divertor phenomena relating to the MARFE.

2. Measurement system

Figure 1 shows the arrangement of the measurement systems in the divertor region. A 38 channel visible spectrometer arranged to view the divertor plates from the above measures spatial intensity profiles of H_α and visible impurity line CII, CIII and OII in the divertor region. The lines of sight of the bolometer array is arranged to cross those of the spectrometer, which provides the information for the spatial distribution in the direction of the height. The divertor electron temperature measured with the Langmuir probe only at about 7 cm (ch.15) outside of the outboard side separatrix was available in this experiment, but was often unavailable due to the breakdown in the high density regime.

3. Density Limit Discharge

The experiment was performed with hydrogen discharges, NB heating of about 7.5 MW, plasma current I_p of 1.7 MA, toroidal magnetic field B_T of 2.5, 3 and 4 T(safety factor q_{eff} of 3.4, 4.4 and 6.1, respectively) and electron density n_e of (4-6.5)x10^{19}m^{-3}. The direction of gradB ion drift was toward the divertor.

Figure 2 shows the time evolution of the density limit discharge with q_{eff}=6.1. The electron density is raised by the preprogramed gas puff so as to reach the density limit during the NB heating pulse. It is seen that the MARFE occurs in both the ohmic and NB heating phases when the divertor electron temperature falls to the level of 10 eV or less. The main and divertor radiation losses before the start of the MARFE in the NB heating phase is about 20% and 50%, respectively. The heat flow to the divertor at this time is about 20% of the absorbed heating power.

4. Generation and development of the MARFE

Figure 3 shows the spatial intensity profiles of H_α radiation in the divertor region. The separatrix hit points at the divertor plates and the X-point calculated by the MHD code lie on the channels 7,33 and 18, respectively. It is clearly seen that in the NB heating phase, a new peak grows between the two peaks(ch.6 and 30) corresponding to the high recycling places in the divertor. The increase in H_α intensity indicates the build-up of the high density plasma due to the development of the MARFE. The MARFE is found to grow at the place apart from the high recycling places in the divertor.

The comparison between the spatial intensity profiles of the impurity lines and the radiation loss profile which were measured through the different lines of sight as shown in Fig.1 provides the detailed information of the trace of the MARFE in the proximity of the divertor region. Figure 4 shows the spatial intensity profiles of CII lines. A sharp peak is also found at the channel numbers 23-24 which just correspond to the generation place of the MARFE. The peak shifts to the channel 17 in the same way as the peak of H_α. Almost the same behavior was observed for the line radiation CIII and OII of the impurities with higher ionization energies. So that, this peak is considered to correspond to the most radiating place. In the radiation loss profiles shown in Fig.5, the most radiating place before the start of the

MARFE is located on the line of sight of ch.29 viewing just the above of the X-point. This place shifts to the channel 28 as the MARFE grows. The comparison between these behaviors indicates that the MARFE is generated at the surface of the main plasma to the outboard side of the X-point as shown by the shadow area in Fig.1, and moves to the inside of the main plasma in the course of its development.

5. Temperatures before and after the occurence of the MARFE

Figure 6 shows the electron temperature at the outboard side separatrix T_e^{div} plotted as a function of the electron density of the main plasma n_e^{main} for the two discharges with the same NB heating power of 7.5MW and different toroidal magnetic field of 3T and 4T. The open and closed symbols respectively stand for the phases without and with the shift of the radiating place to the proximity of the X-point in the intensity profiles of CII line. For the discharge with $B_T=4T$, the radiating place shifts to the proximity of the X-point when the electron temperature falls to about 10 eV, and the MARFE occurs. After the strong gas puff during the NB heating, the MARFE appears again. At this time, the electron temperature is below 10 eV again. While, for the discharge with $B_T=3T$, the divertor electron temperature remains above 10 eV, so that the MARFE accompanied by the shift of the radiating place does not occur before the additional gas puff during the NB heating.

6. Radiation loss

Since the MARFE is generated in the proximity of the X-point, the divertor radiation loss is an important factor for the power balance. Figure 7 shows the divertor radiation loss during the NB heating plotted as a function of the electron density of the main plasma for the three discharges with $B_T=2.5T$, 3T and 4T. Here, the divertor radiation loss is defined as a sum of the radiation powers at the legs of the separatrix and near the X-point to the main plasma, which can not be separated with the bolometer array shown in Fig.1. The open and closed symbols respectively stand for the phases before and after the start of the build-up of the H_α intensity in the valley of the two peaks indicating the growth of the MARFE. It is found that the divertor radiation loss saturates at the same level of about 50%, and does not increase after the start of the MARFE. In the high-q discharge where the growth of the MARFE is clearly seen, this is observed as a phenomenon that the most radiating place moves to the inside as shown in Fig.5 with the divertor radiation loss almost unchanged as a whole.

7. Particle recycling

The difference in the development of the MARFE for the case of $B_T=3T$ and 4T is also seen in the the ion saturation current measured with the Lagngmuir probe shown in Fig.8 indicating the particle recycling in the divertor. The ion saturation current for the case of $B_T=4T$ is larger than that for the case of $B_T=3T$. This means that for high-q discharges, the divertor plasma easily reaches the high recycling state through the divertor function, resulting in the decrease in divertor electron temperature to the level where the shift of the radiating place from the divertor plates to the proximity of the X-point occurs. As a result of the build-up of the high recycling state in the divertor, the neutral pressure around the lower half of the main plasma, which was measured in the lower evacuating port, becomes low compared with the case of $B_T=3T$ as shown in Fig.9. Viewed from the particle recycling around the main plasma, the cooling effect to the plasma surface becomes large as the neutral pressure increases. This is qualitatively consistent with the occurence of the density limit disruptions without the development of the MARFE for low-q discharges.

8. Discussion

In the discharge with $B_T=4T$, in the mean time after the start of the NB heating, the most radiating place still continues to exist in the proximity of the X-point without any sign of the growth of the MARFE. This result probably means that the divertor electron temperature at the high recycling place on the divertor is in the range below 10 eV where the radiating power parameter $L(T_e)$ sharply drops as the electron temperature decreases, and the most radiating place remains near the X-point with higher electron temperature. However, since the power balance for the thermal instability is not satisfied before the strong gas puff at 7.0 sec, the

MARFE does not occur during this period. This suggests that the MARFE occurs through the two sequential events, the shift of the most radiating place to the proximity of the X-point and the satisfaction of the power balance condition for the growth of the thermal instability.

9. Summary

In the density limit disruptions of divertor discharges, the MARFE is generated at the surface of the main plasma to the outboard side of the X-point, and shifts to the inside of the plasma in the course of its development. In the process of the occurence of the MARFE, the most radiating place shifts from the high recycling place on the divertor plates to the proximity of the X-point, and the MARFE successively grows at this place. The electron temperature at the occurence of the MARFE is at a level of 10 eV or less for both the ohmic and NB heating discharges. The divertor radiation loss saturates at about 50% before the start of the MARFE, irrespective of the safety factor of the discharges, and remains unchanged after the start of it. The qualitative property of the particle recycling observed may explain the difference in the occurence of the MARFE for the high and low q discharges.

1) J.A.Wesson et al., Nucl. Fusion 29(1989)641
2) A.Stabler et al., 17th EPS Conf. Europhysics Abstract, Vol.1 p.395,1990
3) N.Hosogane and JT-60 Team, IAEA TCM on the Avoidance and Control of Tokamak Disruptions, Culhum, Sep.10-12,1991
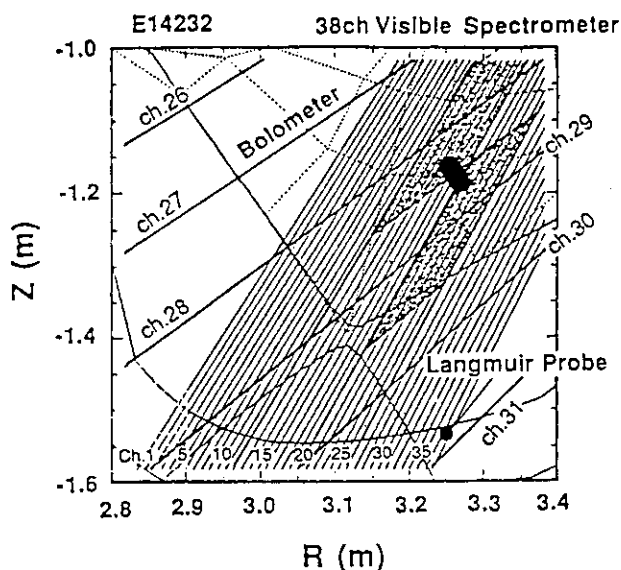
Fig.1 Measurement system in the divertor region. The magnetic surface shown is that of the discharge with B_T=4T discussed in this paper. The shadow areas are the radiating places inferred from the measurement results with the bolometer and the 38 ch visible spectrometer in the course of the development of the MARFE.
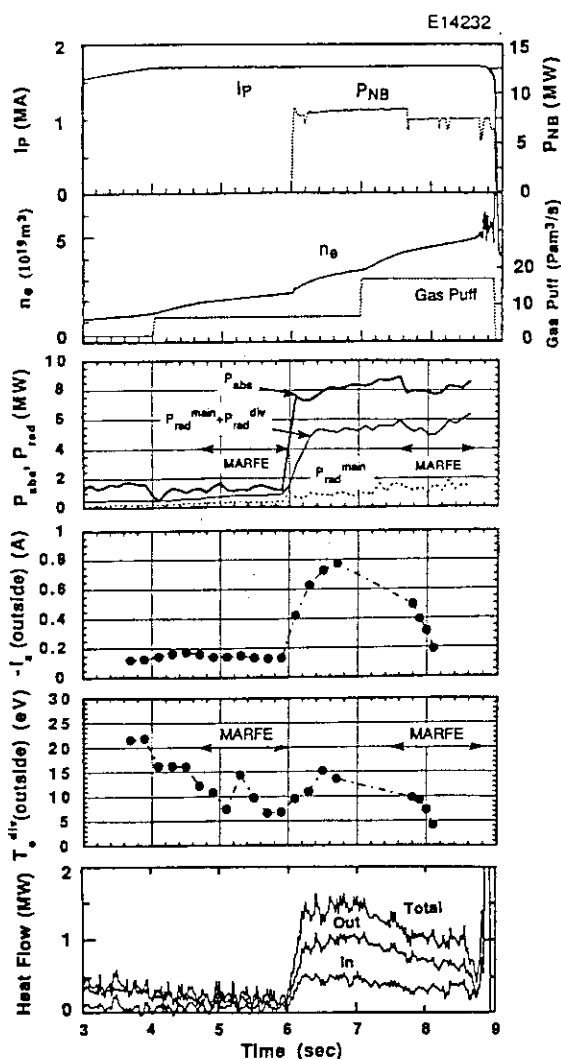
Fig.2 Time evolution of the density limit discharge with B_T=4T (q_{eff}=6.1)
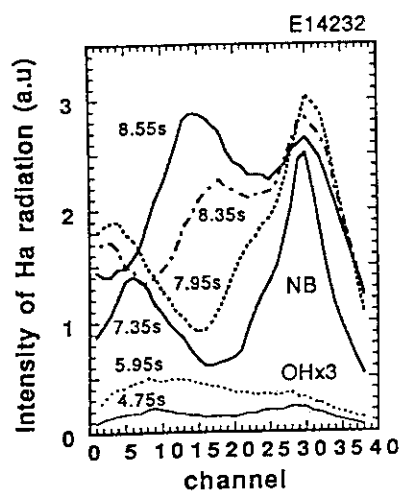
E14232

Fig.3 Time evolution of the spatial intensity profiles of H_α line in the divertor region.

E14232
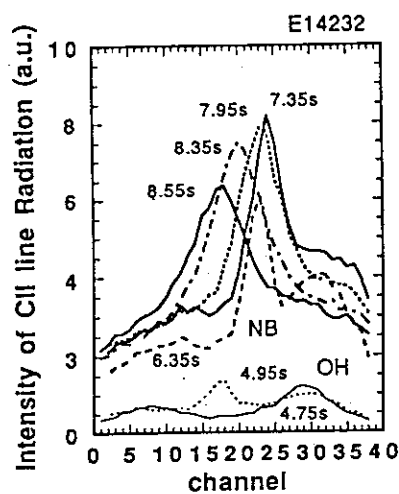
Fig.4 Time evolution of the spatial intensity profiles of CII line in the divertor region

(MW/m²) E14232
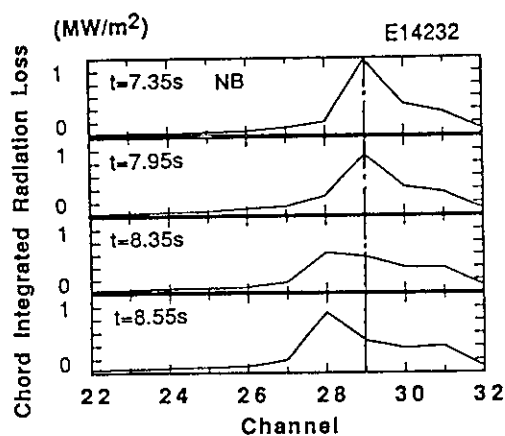
Fig.5 Time evolution of the radiation loss profiles in the divertor region.

open : without a peak of CII
closed: with a peak of CII
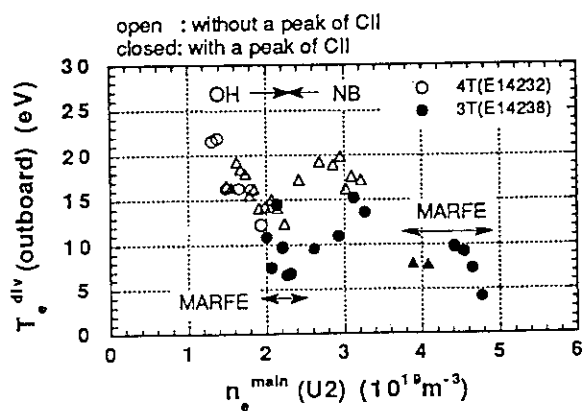
Fig.6 Divertor electron temperature as a function of the main electron density.
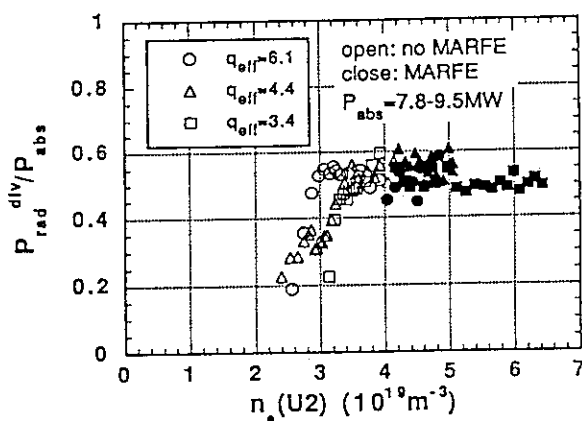
Fig.7 Divertor radiation loss before and after the occurence of the MARFE

Fig.8 Ion saturation currents as a function of the main electron density.

Fig.9 Neutral pressure around the lower half of the main plasma.
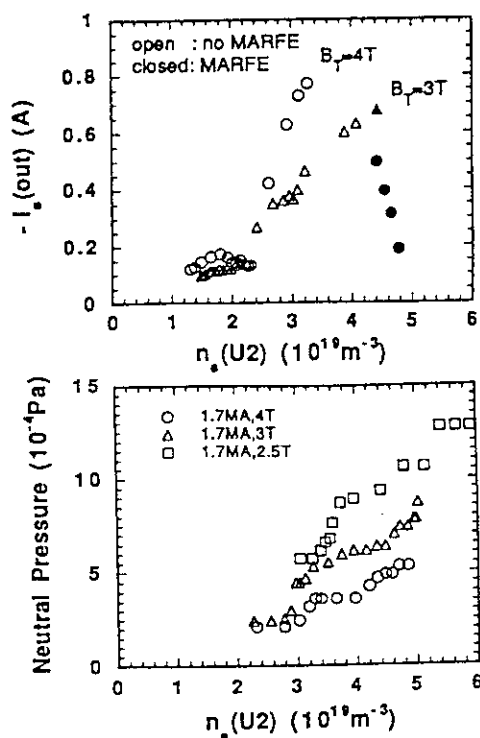
8. Impurity and Divertor Characteristics

8.1 Recycling of Hydrogen and Deuterium in JT-60U

Hiroo Nakamura, Ryuuji Yoshino, Akira Sakasai
Michiya Shimada, Takashi Arai and Astushi Kaminaga

1. Introduction

Controle of hydrogen and deuterium recycling is crucial problem in present plasma device to improve energy confinement characteristics. Recently, experiments with long duration time have been done. To realize steady state discharge, understanding of the recycling characteristics is important. Moreover, these studies are also important as a simulation experiment of DT discharge. In this paper, we describe vacuum properties before discharges and recycling characteristics during discharges in JT-60U.

2. Vacuum Characteristics before Discharges

In JT-60U, a baking temperature of vacuum vessel was varied in the range of 60 °C to 300 °C. Figure 1 shows dependence of neutral particle pressure at vacuum pumping port on the baking temperature. To remove an effect of plasma discharges on vacuum properties, the neutral pressures on Monday morning at 7 am were used. Above 150 °C, the neutral pressure increases as the baking temperature increase. Between 60 °C and 150 °C, no significant change of the neutral pressure was observed. According to observation of these residual gas data at 7am, main peak is m/e=2 (H_2) in spite of deuterium discharge phase. Peak intensity of m/e = 4 (D_2) is a few % of H_2 peak. Therefore, Fig.1 shows effectively characteristics of H_2. According to 1/T plot of the neutral pressure, an activation energy is estimated to be 0.26 eV. This value is similar to an activation energy of hydrogen diffusion in graphite. This implies that mechanism of hydrogen generation is thermal desorption. However, similar temperature dependence is observed in TiC coated Mo wall experiments of JT-60. Therefore, further study is necessary to conclude whether source of hydrogen is graphite or vacuum vessel.
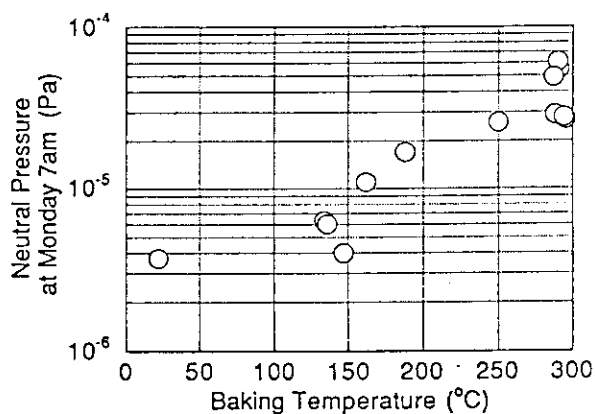
Figure 1 Dependence of neutral pressure before discharges on baking temperature in JT-60U vacuum pumping.

3. Recycling Characteristics during Discharges

Effect of baking temperature on recycling characteristics during discharge was studied. Change of electron density at transition from limiter configuration to divertor one is compared. Above 150 °C, decrease of the electron temperature was observed during divertor configuration phase as shown in Fig.2. Decay time of the electron density is defined by $n_e/(-dn_e/dt)$ and is less than several second. However, in operation with 60 °C of baking temperature, an increase of the electron density was usually observed as shown in Fig.3. Therefore, hot wall temperature operation above 150 °C is necessary from a view point of density controle.
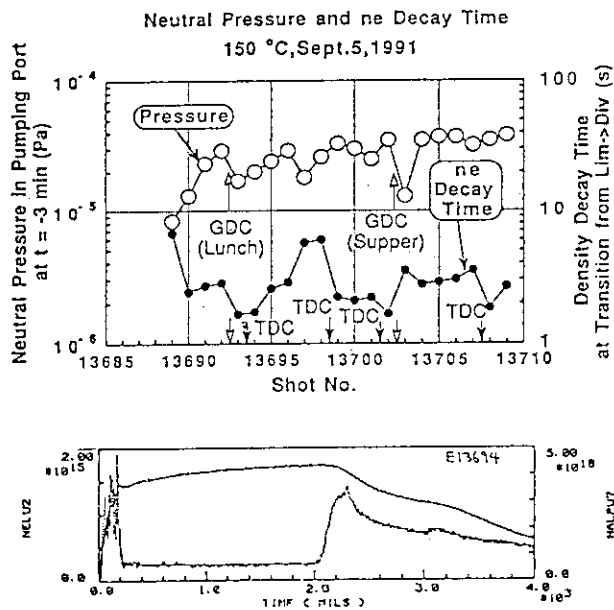
Figure 2 Trend of the decay time of electron temperature and neutral pressure before discharge in 150 °C of baking operation. Typical wave forms of the line integral electron density and Hα/Dα are shown.
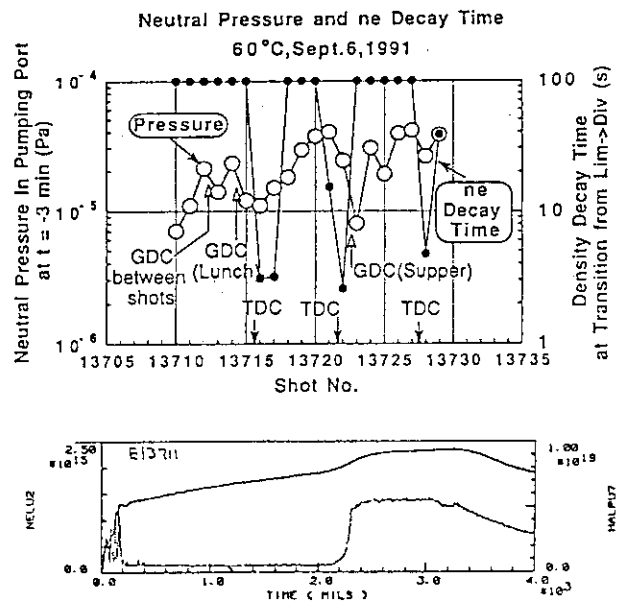
Figure 3 Trend of the decay time of electron temperature and neutral pressure before discharge in 60 °C of baking operation. Typical wave forms of the line integral electron density and Hα/Dα are shown.

During the deuterium discharge, significant hydrogen dilution was observed. As preceding plasma discharges, ratio of hydrogen increases gradually. Moreover, beam heated discharges show higher hydrogen dilution than ohmically heated discharges. These results implies that dominant source of hydrogen during plasma discharges is graphite tile. For example, typical value of H/(H+D) is 20% to 40% in August 1991 as shown in Fig.4. Reduction of the hydrogen dilution is necessary to improve plasma performance.
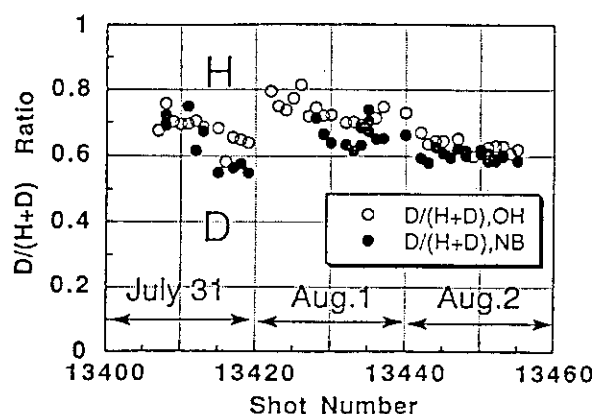
Figure 4 Trend of ratio of D/(H+D) in typical experiments with deuterium gas. Open circles show data in OH phase and closed circles in NB phase. H and D intensities are obtained with spectroscopy measurement.

To obtain H-mode discharges with improved energy confinement, reduction of recycling by wall conditioning is necessary. In JT-60U experiments, He GDC,He TDC, He clean-up shot and plasma shot with disruption are applied. Figure 5 shows trend of the density decay time and the line integral electron density at t = 2 s. After a shot of E13935, He clean-up shot and H-mode shot with disruption were performed. Decay time decreases until E13945 where both wall conditionings were stopped. On the next day, similar reduction of the decay time was observed with wall conditioning by only plasma shot with disruption. Therefore, plasma shot with disruption is most effective for reduction of wall recycling. Under the low recycling condition, quasi-steady state H-mode with continuous ELMs was obtained reproducibly.
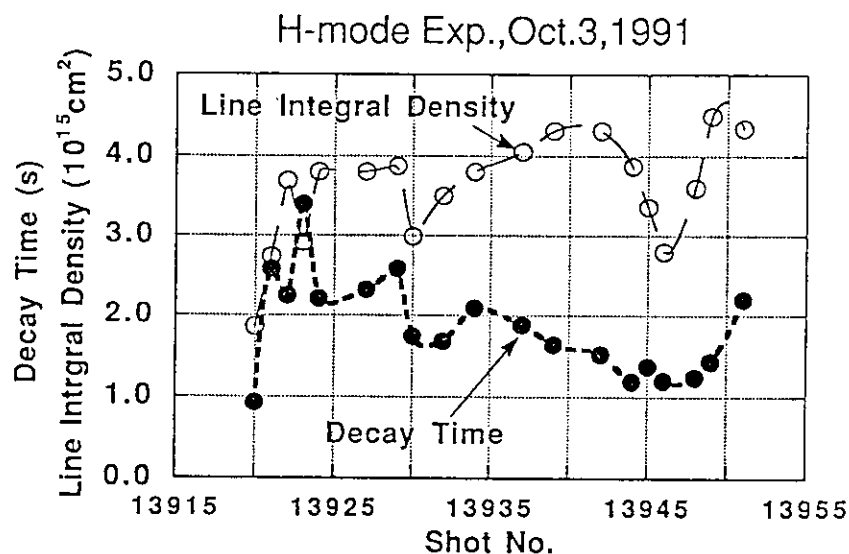
Figure 5 Trend of the line integral electron density and its decay time at t = 2 s in H-mode experiments. At t = 2 s, plasma configuration is changed from limiter to divertor. During the discharges of E13934 to E13946, helium conditioning discharge and H-mode discharge with plasma disruption have been done.

Particle exhaust in H-mode discharge is one of crucial problems. Figure 6 shows dependence of the neutral pressures around the main plasma on the line integral electron density in the quasi-steady state H-mode discharges with continuous ELMs. Closed circle and open one show the neutral pressure around main plasma at lower pumping port and one at upper pumping port, respectively. Neutral pressures of the H-mode with ELMs increases in proportion to n_e^2 to n_e^3. This dependence is same as L-mode discharges observed in previous JT-60 experiments. To obtain more reliable data on particle exhaust characteristics, measurement of the neutral particle pressure near divertor region is necessary. Installation of a fast mass analyzer is now under way.

Figure 6 Dependence of neutral pressures around the main plasma on the line integral electron density in H -mode discharges continuous ELMs. Closed circles show the neutral pressures near divertor region. Open circles show the neutral pressures above midplane.
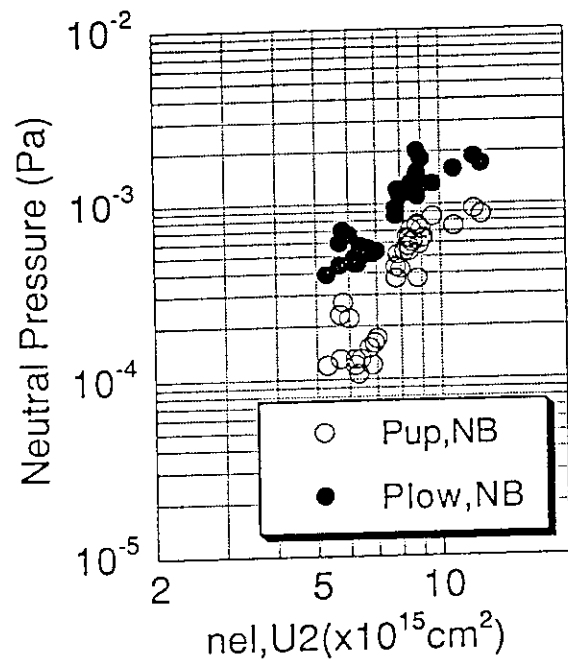
4. Summary

Effect of baking temperature on recycling characteristics was observed. In 60 °C operation, the density controle is difficult. Above 150 °C of baking temperature, density controle is easy. In residual gas analysis at 7 am, main peak is m/e=2 (H_2) in spite of deuterium discharge phase. During plasma discharge, hydrogen dilution was observed. Origin of hydrogen gas is graphite tiles. To reduce wall recycling, plasma shot with disruption is effective. After the wall conditioning, quasi-steady state H-mode with ELMs has been obtained. Dependence of neutral particle pressure on electron density is same as L-mode discharges. This implies that particle exhaust capability of the ELMy H-mode is promising.

8.2   Behavior of Hydrogen-Deuterium Dilution

A. Sakasai, Y. Koide, H. Kubo and T. Sugie

1. Introduction

Deuterium plasma confinement experiment started in the middle of July 1991 in JT-60U. Initial issue was hydrogen-deuterium dilution in deuterium experiments. Knowing the hydrogen-deuterium dilution ratio is important for confinement studies, for example, the effect of effective mass on plasma confinement time.   High neutron rate can be obtained in high temperature plasma of pure deuterium.   We observed the hydrogen-deuterium dilution ratio with spectroscopy of Hα 656.28nm, Dα 656.10nm, H Lyα 121.567nm and D Lyα 121.534nm.

Hα and Dα in main plasma are measured by 1.0m Czerny-Turner spectrometer (dispersion 4.45nm/mm at 656.3nm) with same fiber optics of CXRS system viewing tangentially. Fig. 1(a) shows spectra of Hα , Dα , C II 657.805nm and C II 658.288nm measured by the visible spectrometer at the start of discharge, 0.1s, in OH plasma.   Each spectrum had clearly two Zeeman splitting lines because the small plasma was touching the inside first wall in this time where magnetic field was strong, $B_T \sim 5.7T$.   It was found that only two σ components were clearly observed and π component could not be observable because of tangential view. Fig. 1(b) shows H Lyα and D Lyα in divertor plasma are measured in fifth order by 1.2m normal incidence spectrometer (dispersion 4.54nm/mm at 610nm).

2. Hydrogen-Deuterium Dilution

Fig. 2 shows typical spectra of Hα and Dα in initial phase of deuterium OH experiment. The dilution ratio of H/(H+D) was about 0.1 on the third day after start of deuterium OH experiment to perform discharge conditioning and D2-Taylor Discharge Cleaning. Howeve the dilution ratio went up on a large value H/(H+D)=0.65 after H2-TDC for 1.5 hour as shown in Fig. 3.   It was difficult to remove hydrogen and hydro-carbons absorbed once into the carbon composite first wall by H2-TDC.   Fig. 4 shows shot history of the dilution ratio in OH plasma after after H2-TDC.   He-TDC for 10 minutes between each shot enlarged slightly the dilution ratio.   It seems hydrogen and hydro-carbons were removed from the first wall and made easy to remove to surface from inside by He-TDC. It was found that it decreased effectively by OH discharge for 15s.   Fig. 5 shows time evolutions of Hα and Dα in initial phase of deuterium OH experiment. The dilution ratio of H/(H+D) was about 0.65 at 1.0s and decreased to 0.5 at 10.0s. Amount of hydrogen in the first wall had certainly decreased during OH discharge.

The dilution ratio was effectively decreasing to perform D2-TDC as shown in Fig. 6. However the dilution ratio of H/(H+D) was increasing shot by shot from 0.3 to 0.4 after 20~ 30 shots per one day when D2-TDC was performed for 0.5 or 1 hour. For example, the dilution ratio had decreased 0.6 to 0.3 after D2-TDC for one hour and from 0.4 to 0.2 after D2-TDC for

half an hour. Finally, the dilution ratio was saturated to 0.1~0.2 after 500 shots of deuterium experiment.

Fig. 7 shows time evolution of the dilution ratio during deuterium neutral beam injection. The dilution ratio increased by 0.07 ~ 0.09 caused by wall plasma interaction in initial phase of deuterium experiment. However the time evolution of H/(H+D) in NB heated plasma was not so change when wall conditioning has been performed by He-TDC, OH and NB heated plasma.

While the dilution ratio of H/(H+D) by using charge exchange neutral particle flux of E//B CX neutral particle analyzer was dynamically decreased 0.3 to 0.2 in NB heated plasma. This CX neutral particle analyzer was viewing Deuterium Neutral Beam Line. So the charge exchange neutral particle flux of deuterium has actively behaved during NBI.

3. Summary

The dilution ratio of H/(H+D) was measured with with spectroscopy of $H\alpha$ 656.28nm, $D\alpha$ 656.10nm, H $Ly\alpha$ 121.567nm and D $Ly\alpha$ 121.534nm. The dilution ratio had effectively decreased to perform D2-TDC substituting hydrogen for deuterium. It had been certainly decreasing by repetition of deuterium discharge but it was saturated to 0.1~0.2 after 500 shots of deuterium experiment. It was difficult to remove completely hydrogen and hydro-carbons absorbed into the carbon composite first wall. It is positively undesirable to performed H2-TDC to reduce the dilution ratio.
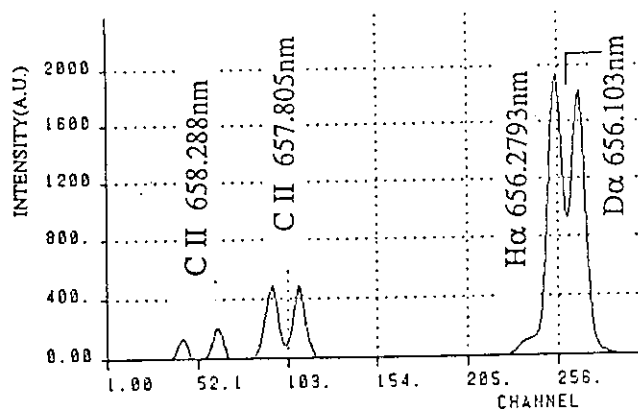
Fig. 1 (a): Spectra of $H\alpha$, $D\alpha$, C II 657.805nm and C II 658.288nm measured by the visible spectrometer viewing tangentially at the start of discharge, 0.1s, in OH plasma.
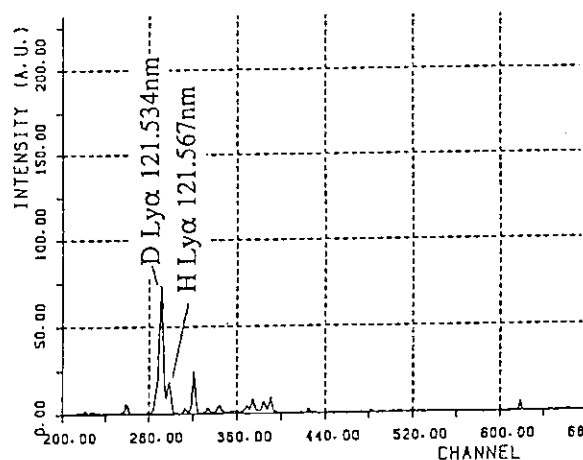
Fig. 1 (b): H $Ly\alpha$ and D $Ly\alpha$ in divertor plasma are measured in fifth order by 1.2m normal incidence spectrometer.
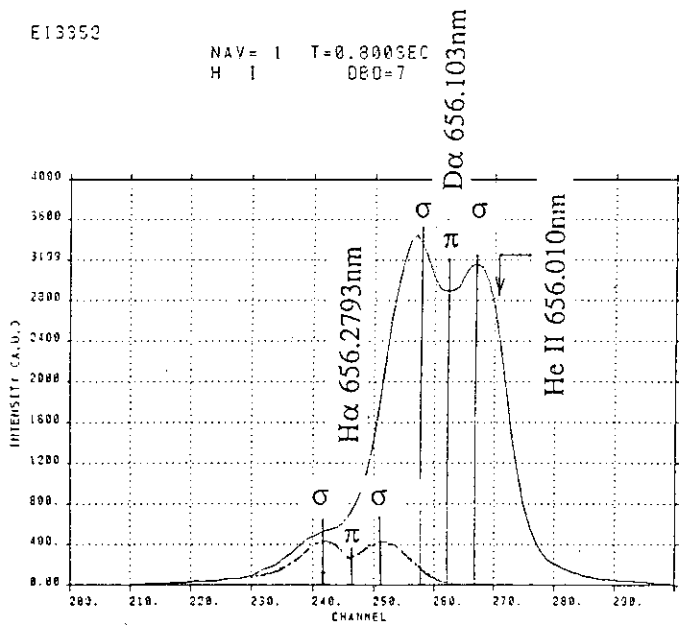
Fig. 2   Typical spectra of Hα and Dα in initial phase of deuterium OH experiment.
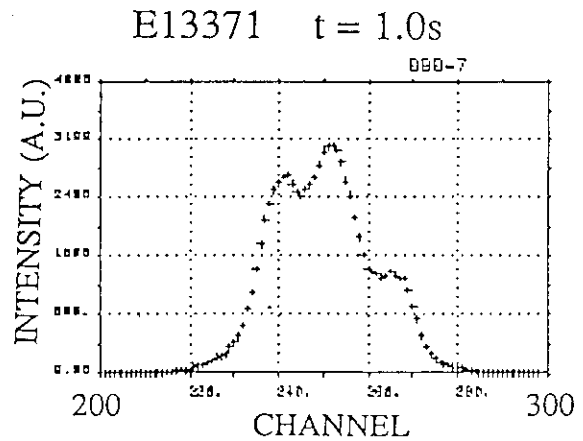
Fig. 3   Spectra of Hα and Dα after H2-TDC for 1.5 hour. The dilution ratio of H/(H+D) went up on a large value of 0.65.
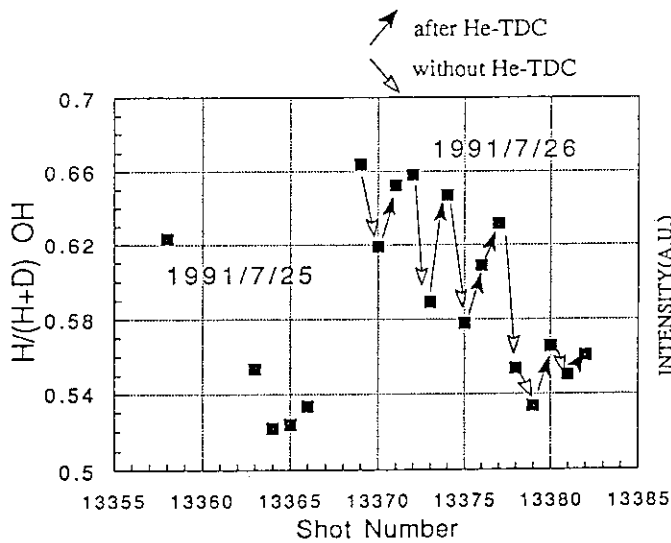
Fig. 4   Shot history of the dilution ratio in OH plasma after after H2-TDC.
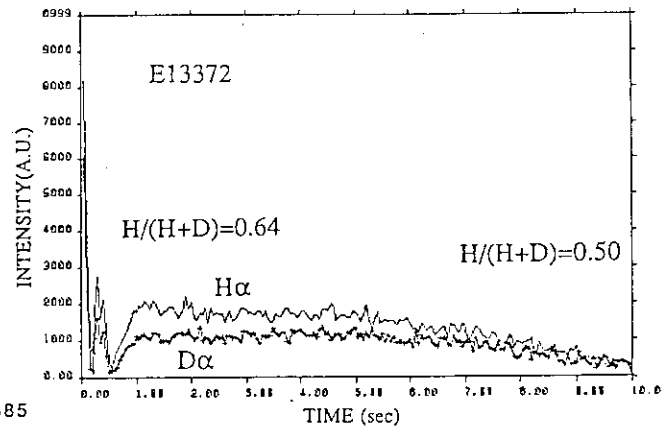
Fig. 5   Time evolutions of Hα and Dα in initial phase of deuterium OH experiment.
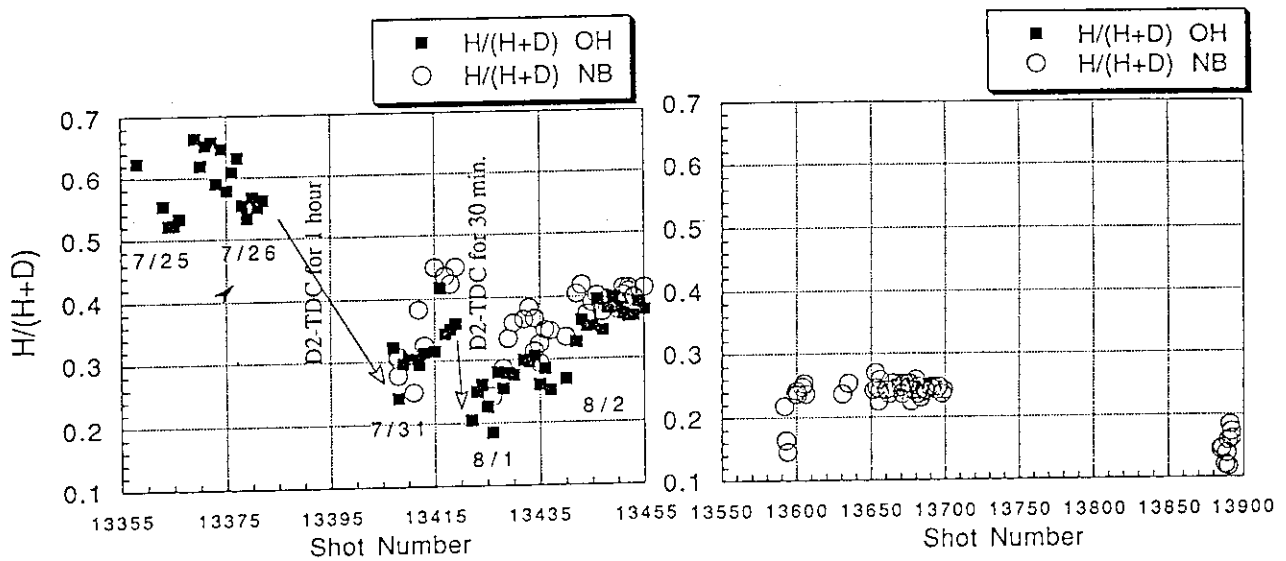
Fig. 6 Shot history of the dilution ratio for about
500 shots in OH and NB heated plasma.
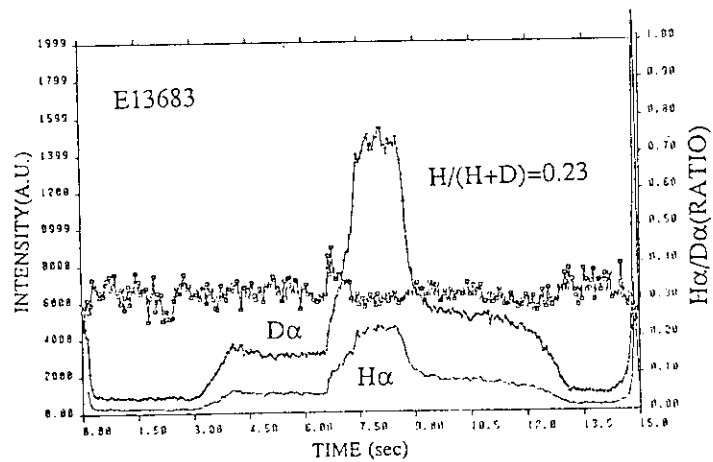
Fig. 7 Time evolution of the dilution ratio during
deuterium neutral beam injection.

8.3 Impurity Generation in the Divertor

H. Kubo, K. Itami, N. Asakura, S. Numazawa, T. Sugie,

H. Nakamura, Y. Kawano, and M. Shimada

The influxes of carbon, deuterium, and oxygen in the divertor region have been measured spectroscopically and the mechanism of carbon production is discussed. For the first time, the measurement and the calculation for the carbon influx in the divertor region are compared quantitatively.

1. Experimental Arrangement and Analysis Procedure

A schematic diagram of the experimental set-up of the diagnostics for particle influx measurement in the divertor region is shown in Fig. 1. Line intensities of Dα and C II 6578 Å were measured by a 0.5-m visible spectrometer with fiber optics. Spatial distribution of line intensities of Dα and O II 4415, 4417 Å were observed by a 38-channel optical fiber array with interference filters. The electron temperature and the electron density were observed by Langmuir probes[1].

Neutral particles are ionized in the divertor region. Under the condition of negligible recombination, the neutral influx equals the ionization rate. The ionization process is accompanied by the emission of spectral lines and the numbers of the ionization events and of emitted photons are closely correlated. Therefore, the neutral particle influx can be derived from the measured intensity of the neutral line emission. In the region of low electron density, the relation between the neutral particle influx Γ and the line intensity I is basically given by the equation

$$\Gamma = 4\pi \frac{S}{XB} I$$

(1),

where, respectively, S and X are the ionization and excitation rate coefficients, and B is the branching ratio for the observed line. This equation is commonly used to derive hydrogen influx from Hα measurement[2], and it can be also used for influx measurement of low-charge-state impurities[3].

In this study, the influxes of deuterium, carbon, and oxygen were derived respectively from the measured line intensities of Dα, C II, O II by using the Eq. 1. The equation is valid in the density region in question ($n_e^{div} < 1 \times 10^{19}$ m^{-3}), because we analyze the data for the ohmically heated discharges in this paper. The ionization events per photon (S/XB) [3] at the electron temperature measured with the Langmuir probe was used in the analysis .

In this paper, we discuss the data for ohmically heated deuterium discharges with the temperature of the vacuum vessel of 290 °C (E13357 - E13628). The data for the divertor region near the outer strike point of the separatrix were analyzed.

2. Results and Discussion

In Fig. 2, the carbon influx relative to the deuterium influx (Γ_C/Γ_D) in the divertor region and the carbon density relative to the deuterium density (n_C/n_D) in the main plasma are shown against the electron density. The relative carbon influx in the divertor region decreased from 9 % to 5 % as the electron density increased from 1.0×10^{19} m^{-3} to 1.8×10^{19} m^{-3}. The relative carbon density in the main plasma also decreased from 5 % to 2 % with increasing electron density. The ratio of the relative density to the relative influx was about 0.6 and it seemed to decrease as the electron density increased.

In a sputtering model, the relative carbon influx can be expressed as

$$\Gamma_C = Y_D \Gamma_D^{out} + Y_O \Gamma_O^{out} + Y_C \Gamma_C^{out} \qquad (2),$$

where, respectively, Γ_D^{out}, Γ_O^{out}, and Γ_C^{out} are the fluxes of deuterium, oxygen, and carbon ions onto the divertor plates. And Y_D, Y_O, and Y_C are sputtering yields of carbon with deuterium, oxygen, and carbon ions[4]. As the sputtering with deuterium, the chemical process is important and the yield depends not only on the incident energy of the deuterium ions, but also on the surface temperature of the carbon plates and the ion flux density. The sputtering yield with oxygen is always nearly unity. And the self-sputtering yield depends on the energy of the carbon ions. The carbon influx was calculated from Eq. 2 by using the influx of deuterium and oxygen obtained from the measured line intensities of Dα and O II. The sheath acceleration energy was assumed to be $3 \times T_e^{div}$. It was assumed that all of the produced carbon returned to the divertor plates with the charges of 4. It was also assumed that the recycling rates for deuterium and oxygen were unity and the fluxes of deuterium and oxygen onto the divertor plates equaled the measured influxes. The charge state of the oxygen ion incident on the divertor plates is not important, because the dependence of the sputtering yield on the ion energy is weak.

In Fig. 3, the calculated carbon influx and the measured influx are shown against the electron density in the main plasma. The both influx show a decreasing trend with increasing density, although the calculated influx is 2.5 times as large as the measured influx. The discrepancy might be due to the error in the estimation of the influx from the line intensity. The sputtered carbon might recycle rapidly near the divertor plates before ionizing up to two times and emitting the observed line[5].

In the low density region ($n_e \approx 0.8 \times 10^{19}$ m^{-3}), the self-sputtering and the sputtering by oxygen are more important than the sputtering by deuterium. The relative carbon influx decreased for higher electron density because of the smaller self-sputtering yield and the decrease of the relative oxygen density. In high density regime ($n_e \approx 1.8 \times 10^{19}$ m^{-3}), the contributions of the sputterings by deuterium, oxygen, and carbon were about 25 %, 40 %, and 40 % of the carbon influx, respectively.

For discharges with T_e^{div} = 39 -45 eV, the relation between the relative carbon influx and the relative oxygen influx is shown in Fig. 4. The relative carbon influx is a linear function of the relative oxygen influx with a offset constant. This trend is explained by Eq. 2. Thus, the sputtering with oxygen is an important process for the carbon production.

3. Summary

For the first time, the measurement and the calculation for the carbon influx in the divertor region were compared quantitatively. The calculated influx was 2.5 times as large as the measured influx. The relative carbon influx decreased for higher electron density because of the smaller self-sputtering yield and the decrease of the relative oxygen density. It was clearly shown that the chemical sputtering with oxygen was important. For reduction of carbon influx, it is effective to decrease the oxygen density by wall conditioning and to lower the electron temperature with the aid of the dense divertor. It seemed that the carbon shielding rate was higher in the high density region.

References

[1] K. Itami et al., in this report.
[2] L. C. Johnson and E. Hinnov, J. Quant. Spectr. Rad. Trans. **13** (1973) 333.
[3] K. H. Behringer, J. Nucl. Mater **145 - 147** (1987) 145.
[4] J. Roth, E. Vietzke, and A. A. Haasz, Suppl. Nucl. Fusion (1991) 63.
[5] W. D. Langer, Nucl. Fusion **22** (1982) 751.
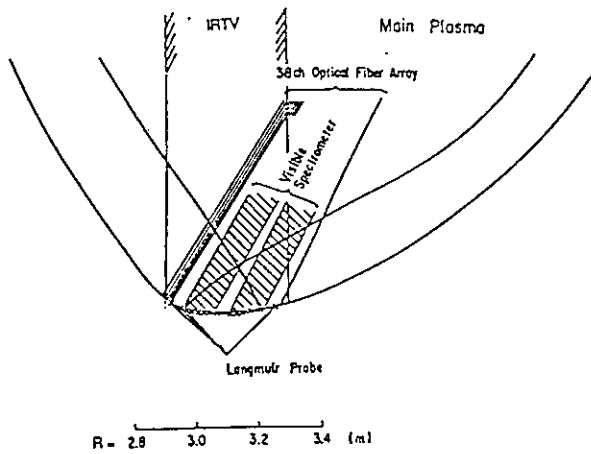
Fig. 1 A schematic diagram of the experimental set-up of the diagnostics for particle influx measurement in the divertor region.
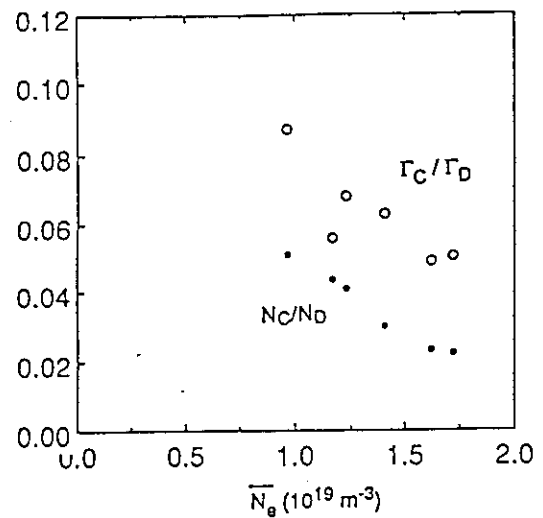
Fig.2 The carbon influx relative to the deuterium influx (Γ_C/Γ_D) in the divertor region and the carbon density relative to the deuterium density (n_C/n_D) in the main plasma against the electron density in the main plasma.
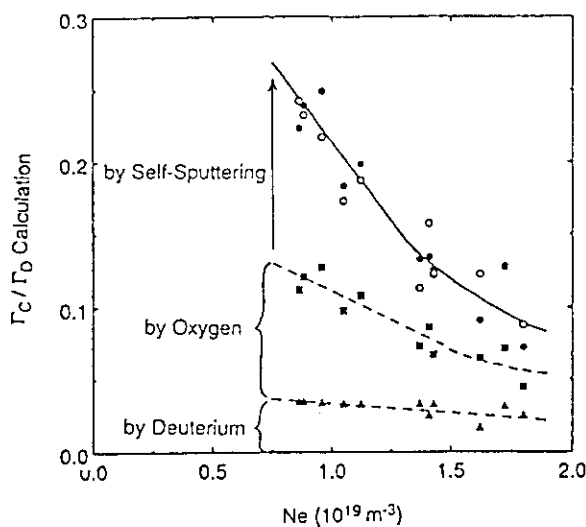
Fig. 3 The comparison between the calculated carbon influx (solid symbols) against the electron density in the main plasma. The open circles show the measured carbon flux multiplied by 2.5.
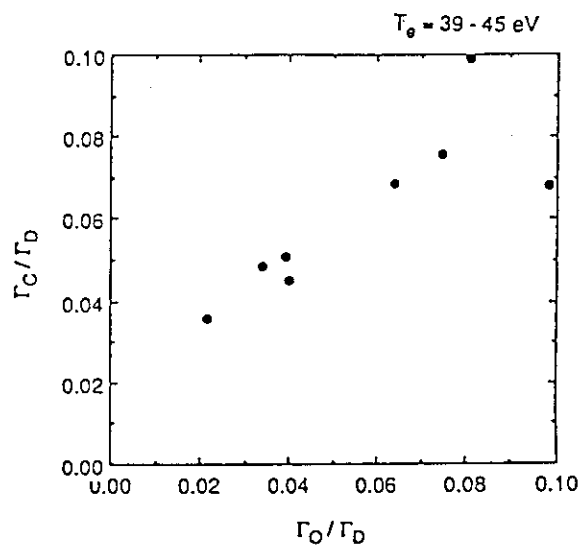
Fig. 4 The relation between the relative carbon influx and the relative oxygen influx for discharges with T_e = 39 -45 eV.

8.4 Transport Analysis of Divertor Plasma

K. SHIMIZU, K. ITAMI, H. KUBO, N. ASAKURA, M. SHIMADA

1. Introduction

It is very important to study the divertor transport experimentally and theoretically in order to predict the particle and impurity control in future tokamaks. To systematically investigate the parameter dependence of divertor plasmas, a simple divertor model has been developed. The fluid equations along the magnetic field are solved with the boundary conditions of the plasma parameter at the divertor plate (n_d, T_d). Profiles of (n_d, T_d) are measured by a Langmuir probe array. The neutral particle transport is simulated in the MHD equilibrium with a real wall geometry by a Monte Carlo code. The interaction between the plasma and neutral particles is solved consistently using the iterative procedure. Using this model, the divertor characteristics in JT-60U ohmic experiments has been investigated.

2. Simple divertor model

The steady state transport equations which describe the divertor plasma are simplified with following assumptions:

* ion temperature is equal to electron temperature,
* the cross field transport effect is negligible,
* the electron heat conduction is the dominant loss in the energy transport.

The simplified transport equations along the field lines are given as follows,

$$\nabla_{/\!/} (nV_{/\!/}) = S_n \qquad (1)$$

$$\nabla_{/\!/} (nm_i V_{/\!/}^2) + \vec{\nabla}_{/\!/} (2nT) = S_p \qquad (2)$$

$$\nabla_{/\!/} q_{/\!/} = \nabla_{/\!/} (- \kappa_{/\!/} \vec{\nabla}_{/\!/} T) = S_E \qquad (3)$$

where S_n, S_p and S_E are the particle, momentum, and energy source due to the interaction with the recycling neutrals; n, and T are the density and temperature; $V_{/\!/}$ is the flow velocity parallel to the field lines; m_i is the ion mass; $\kappa_{/\!/} = \kappa_0 T^{5/2}$ is the classical electron heat diffusivity along the field lines. The differential operator definitions of $\nabla_{/\!/}$ and $\vec{\nabla}_{/\!/}$ should be referred to reference 1. The particle flux parallel to the field lines, $f_{/\!/} = nV_{/\!/}$ and the electron heat conduction parallel to the field lines, $q_{/\!/}$ are calculated by the integration of eq. (1) and (3), respectively. The energy loss term S_E due to electron ionization is expressed by

$$S_E = - E_{ion} S_n \qquad (4)$$

where E_{ion} is the ionization potential. We take the radiation loss of impurities effectively by the enhancement of E_{ion} by a factor of 3 ~ 4. The electron temperature profile along the field

lines is expressed by

$$T^{7/2}(\xi) = T_d^{7/2} + \frac{7}{2\,\kappa_0}\int_\xi^{\xi_d} q_{/\!/}(\xi)\,dl \qquad (5)$$

where l is the distance along the field line. We further assume that the momentum source term is negligible ($S_p = 0$) and $v_{/\!/} \ll C_s$ for simplicity. Under these assumptions, equation (2) is simplified to the condition of constant pressure.

$$n = 2\,n_d\,T_d\,/\,T \qquad (6)$$

The density and temperature are calculated in each flux tube for given source terms (S_n, S_E). The source term S_n is evaluated by the 2-D Monte Carlo code [2]. The interaction between the plasma and neutral particles are iteratively solved. The convergence towards the steady state solution is very fast, because the plasma parameters at the plate (n_d, T_d) are fixed as the boundary condition.

3. Calculation results

We investigate the divertor transport in the ohmic experiments ($I_p = 2$ MA, $B_T = 3.5$ T $\bar{n}_e = 0.8 \sim 3.0 \times 10^{19}$ m^{-3}) using our simple divertor model. Typical radial profiles of n_d and T_d measure by a Langmuir probe array are shown for the high temperature case (shot no # 12953) and the low temperature case (shot no # 12956) in Fig. 1 (a) and Fig. 2 (a), respectively. These data are displayed by the closed symbols at the position corresponding to the radial distance from the separatrix surface at the entrance. The numerical simulations has been carried out for the outside divertor plasma, which is divided into 8 flux tubes. The broken line denotes the smoothed profile which is used as the input data and the solid line denotes the calculated profile at the entrance. Figure 1(b) shows the profiles of the density and temperature in the flux tube close to the separatrix surface for the high temperature case. These profiles are those projected on the poloidal cross section. (z is the poloidal coordinate.) The temperature gradient along the field line is extremely small due to the high thermal conductivity. For the low temperature case, the distribution of plasma parameters along the field line close to the separatrix surface is shown in Fig. 2 (b). The temperature gradient and the high density near the divertor plate are obtained due to the low temperature. The total particle flux, Γ (0) and heat flux, Q (0) at the entranced (z=0) are 2.5×10^{22} s^{-1} and 0.49 MW, respectively. About 40 ~ 50 % of joule input power (~ 1 MW) is lost by the radiation loss in the main plasma. Then Q (0) is consistent with the experimental data. The flux multiplication factor is about 2. But the low temperature at the divertor ($T_d \sim 10$ eV) is realized because of a low heat flux and a large particle flux.

In order to check the validity of our model, comparison of the H_α-intensity with the measurement has been carried out. The H_α monitor viewing the divertor plate consists of 38

channels , as shown in Fig. 3. The closed symbols are measured intensities and the solid line is the calculated profile. They are in good agreement except for the chord passing near the X-point ($R \approx 3.0$ m). This discrepancy is due to the H_α radiation in the main plasma. The agreement in general implies that our simple model is reasonable.

The particle confinement time in the main plasma is estimated normally by the integration of H_α-radiation intensity in the whole plasma [3]. But the H_α radiation near the X-point in the main plasma can not be differentiated from the H_α measurement data of the chords viewing the divertor plate with high accuracy. By using our simple model, the particle confinement time in the main plasma, including the vicinity of the X-point, can be evaluated from the total ionization source inside the separatrix surface. The results of the particle confinement time evaluated are summarized in Table 1. The total particle flux to divertor plates, including the inside plate, Γ_e (L_d) increases with density in the main plasma. The neutral particle flux back flow into the main plasma , Γ_0 (M) shows a tendency to saturate. The particle confinement time including the divertor region, τ_p (D) are nearly constant (45 ~ 50 msec). On the other hand, the particle confinement time in the main plasma, τ_p (M) = V $\langle n_e \rangle$ / $\Gamma_0(M)$, increases from 71 msec to 108 msec with increase of main plasma density. This density dependence of τ_p (M) is generally observed in the low density regime [4].

The cross field diffusion coefficients, ($D_\perp$, $\chi_\perp$) in the scrape off layer are usually evaluated from the e-folding length of the measured profiles of density and temperature [5]. These measurements by Langmuir probes are not easy in large tokamaks because of high edge temperature. We evaluate the cross field diffusivity $\chi_\perp$ averaged in the scrape off layer from the electron temperature and the cross field heat flux at the entrance, which are obtained in our calculations. The heat diffusivity evaluated is almost constant and is ~ 3 m²/s for the density range investigated, as shown in Table 1.

4. Summary

The particle confinement time in the main plasma and the heat diffusivity in the scrape off layer are evaluated for JT-60U ohmic plasma using the Langmuir probe data. As the plasma density increases the particle confinement time increases and the heat diffusivity is almost constant (~ 3 m² / s) in the low density region.

Reference

[1] PETRAVIC, M., KUO-PETRAVIC, G., Nucl. Fusion 30 (1990) 1148.

[2] SEKI, Y., SHIMOMURA, et al., Nucl. Fusion 20 (1980) 1213.

[3] YAMADA, K.., TSUJI, S., et al., the JT-60 TEAM, Nucl. Fusion 27 (1987) 1203.

[4] WOOTTON, A.J., et al., Plasma Phys. Controlled Fusion 30 (1988) 1479.

[5] UEHARA, K., GOMAY, et al., Plasma Phys. 21 (1979) 89.

Table 1 Estimation of particle confinement time
and heat diffusivity

shot no	12953	12956	12959
$\bar{n}_e$	0.8×10^{19} m^{-3}	1.8×10^{19} m^{-3}	2.7×10^{19} m^{-3}
$n_e(L_d)$	1.0×10^{18} m^{-3}	7.1×10^{18} m^{-3}	8.9×10^{18} m^{-3}
$T_e(L_d)$	~84 eV	~9 eV	~9 eV
$n_0(L_d)$	2.0×10^{17} m^{-3}	6.0×10^{17} m^{-3}	7.5×10^{17} m^{-3}
$\Gamma_e(L_d)$	1.6×10^{22} s^{-1}	4.1×10^{22} s^{-1}	5.0×10^{22} s^{-1}
$\Gamma_e(0)$	1.2×10^{22} s^{-1}	2.5×10^{22} s^{-1}	2.8×10^{22} s^{-1}
R	1.4	1.7	1.8
$\Gamma_0(M)$	1.0×10^{22} s^{-1}	2.0×10^{22} s^{-1}	2.3×10^{22} s^{-1}
$\tau_p(D)$	44 msec	40 msec	49 msec
$\tau_p(M)$	71 msec	79 msec	108 msec
$\chi_\perp(x=0)$	3.4 m^2/s	3.3 m^2/s	3.0 m^2/s
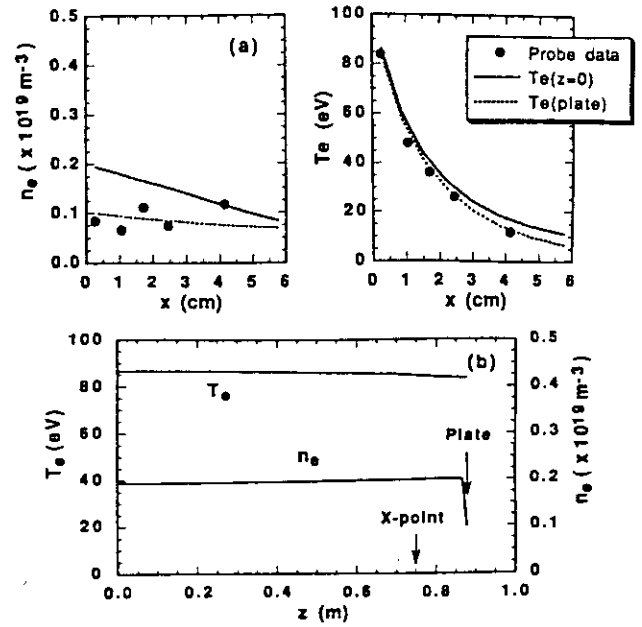
Fig. 1 (a) Radial profiles of temperature and density for
the high temperature case. Closed symbols
denote the Langmuir probe data.

(b) Calculated profiles of Te and ne in the flux
tube close to the separatrix surface.
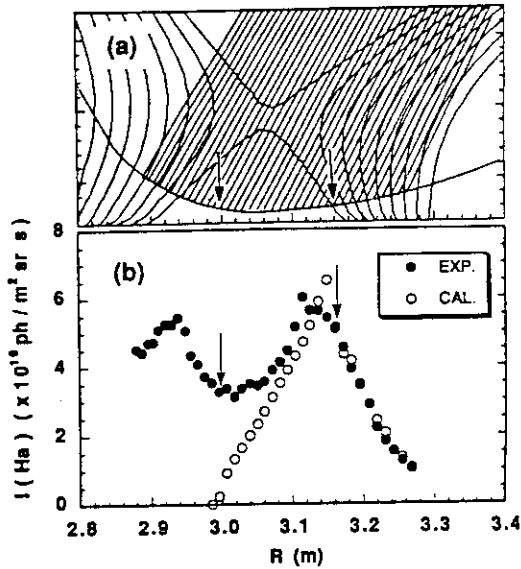
Fig. 3 (a) H_α monitor viewing the divertor plate.

(b) H_α radiation intensity calculated
for the high temperature case.
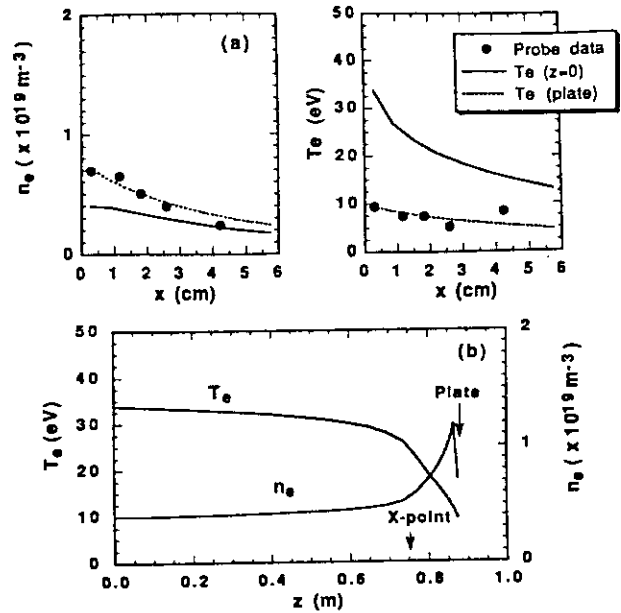
Fig. 2 Spatial dependence of plasma parameter
for the low temperature case.

8.5 Impurity Profiles and Transport Characteristics

A. Sakasai, Y. Koide, H. Kubo, T. Sugie, T. Hirayama and M. Shimada

1. Introduction

Impurity profiles are measured with Charge Exchange Recombination Spectroscopy (CXRS) and transport of impurities is analyzed in JT-60U. Tangential viewing CXRS system provides radial impurity profiles of fully stripped carbon and oxygen. CXR emission of C VI 529.0nm and O VIII 606.8nm is led to 0.5m and 1.0m Czerny-Turner spectrometers by 100m pure quartz optical fibers. We use two type detectors. One is image intensified CCD arrays (767H x 490V pixels) to obtain multi-chord spectra (Each instrument has 24 spectra, maximum 48 spectra). Another is image intensified double linear photodiode arrays (512 pixels) that have high sensitivity (Each instrument has 2 spectra). We have two multi-chordal spectrometers with ICCD detector and four 2-chordal spectrometers. Instrument calibration of the CXRS system was performed by using an integrating sphere. Neutral beam deposition profiles of injection deuterium beam energy components; E_b, $E_{b/2}$ and $E_{b/3}$, were calculated by using effective ionization and charge exchange cross section from electron density profile, electron and ion temperature profiles and effective ionic charge. Density profiles of fully ionized carbon ions C^{6+} and oxygen ions O^{8+} are obtained from CXR emission of C VI and O VIII, neutral beam density profiles and excitation rate coefficients for C VI (n=8-7) and O VIII (n=10-9).

2. Impurity profiles and Transport Characteristics

Density profiles of fully ionized carbon ions C^{6+} are calculated by using 1-D impurity transport code as shown in Fig. 1. Fig. 1 (a) shows density profiles of C^{6+} in the case of diffusion coefficient $D_A=1m^2/s$, peaking parameter $C_V = - V_A(r)a^2 / 2rD_A = 0$, $T_e(r)=2.5$ x (1-$r^2)^{3.0}$ keV, $n_e(r)=3.0$ x10^{19} (1-$r^2)^{0.6}$ m^{-3} and carbon content 0.1%. Fig. 1 (b) shows n^{C6+} (r) in the case of $D_A = 1m^2/s$ and $C_V = 1$ (other conditions are same). These indicate that profile of C^{6+} in $C_V = 0$ is nearly flat at the inside of r~0.7m and n $^{C6+}$ (r) in $C_V = 1$ is a center peaking profile. Steady state analysis of impurity transport suggests that peaking parameter C_V defines effectively profile shape of C^{6+}.

Fig. 2 shows ion temperature profile measured with CXRS and electron temperature profiles measured with ECE and Thomson laser scattering system in typical NB heated deuterium plasma (Ip=2.0MA, B_T=4.0T, P_{NBI}=20MW, $T_{iCXR}(0)$~10keV, $T_e(0)$~4keV,$<n_e>$ =2~3x10^{19}m^{-3}). This plasma had a center peaking profile of ion temperature at the inside of r/a~0.2. Electron density profile was obtained from 2-chord FIR interferometers. The electron density profile was not obtained with accuracy in the case of locally center peaking profile. It seems $n_e(r)$ was locally peaking at the peaking region of ion temperature, for example, in the case of high T_i mode. So density profiles of C^{6+} at the peaking region were not accurately obtained. Fig. 3 shows

deposition profiles $n_{b0}(r)$ of deuterium neutral beam for each beam energy components; E, E/2 and E/3. The beam energy components of $E_{b/2}$ and $E_{b/3}$ were strongly attenuated compared with that of E_b.

Fig. 4 shows density profiles of C^{6+} in the above typical NB heated deuterium plasma measured with CXR emission of C VI. Density profile of C^{6+} at 6.7s was somewhat a center peaking profile. That profile became to peak slowly and the density at 7.1s was about two times as large as that at 6.7s. This result indicates that the peaking parameter Cv is not constant and changes about 0.5 to 1.0. Diffusion coefficient D_A can be given from the time evolution of CXR emission. Fig.5 shows the effect of inaccuracy of effective ionic charge Z_{eff} and electron density profile parameter m [$n_e(r) = n_e(0) (1-r^2)^m$] on the density profile of C^{6+}. The effect of Z_{eff} =3.0~4.0 on n $C^{6+}(r)$ was small in low electron density plasma ($<n_e> \sim 2 \times 10^{19} m^{-3}$). The effect of electron density profile parameter m on $n^{C6+}(r)$ was also small in this plasma. However it seems the effect of Z_{eff} and electron density profile parameter m on $n^{C6+}(r)$ is large so we need accurate electron density profile and Z_{eff} profile to estimate neutral beam deposition profile.

3. Impurity transport of peripheral region from the ratio of O VIII to O VII

O VII 2.17nm and O VIII 1.89nm are measured with a grazing incidence spectrometer viewing plasma center vertically. O^{7+} and O^{6+} localize in the peripheral region of OH and NB heated plasma. Ratio of O VIII to O VII depends on electron temperature, electron density and transport coefficients. We try to obtain information of transport coefficients from the ratio of O VIII / O VII on the basis of accurate $T_e(r)$ and $n_e(r)$. The ratio of O VIII / O VII is about 2 in OH plasma and 1 - 3 in NB heated plasma. The results of impurity transport calculation indicate that increasing peaking parameter Cv gives large ratio of O VIII / O VII than experimental result in OH plasma. It agrees with $D_A=1\sim2$ m²/s and $C_V=0\sim1$ in peripheral region as shown in Fig. 6. The ratio of O VIII / O VII is sensitive to electron temperature in the region where O VIII and O VII exist and emit the observed spectra.

References
1) R. J. Fonk, M. Finkenthal, R.J. Goldston, et al., Phys. Rev. Lett. 49 (1982) 737.
2) K. Ida, T. Amano, K. Kawahata and O. Kaneko, Nagoya University Institute of Plasma Physics Report IPPJ-892 (1988).
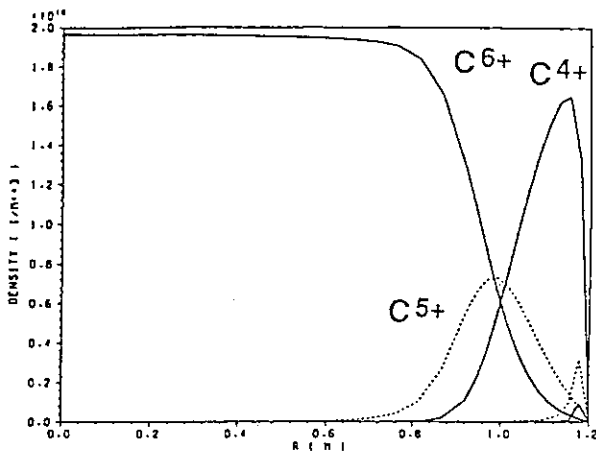
Fig. 1 (a) Density profiles of fully ionized carbon ions C^{6+} are calculated by using 1-D impurity transport code in the case of diffusion coefficient D_A=1m^2/s, peaking parameter C_V = 0.
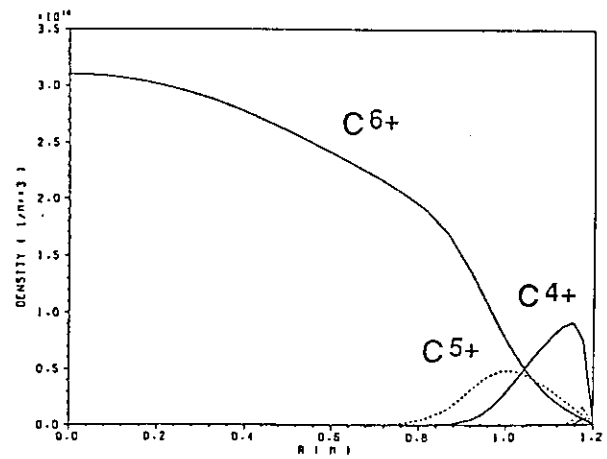
Fig. 1 (b) Density profiles of fully ionized carbon ions C^{6+} are calculated by using 1-D impurity transport codein the case of D_A = 1m^2/s and C_V = 1.
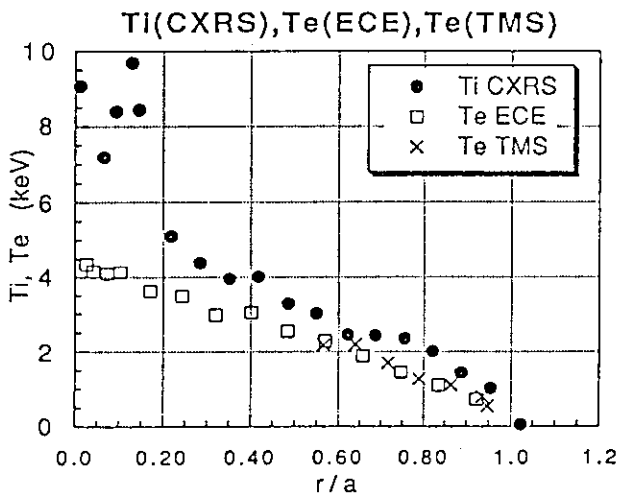
Fig. 2 Ion temperature profile measured with CXRS and electron temperature profiles measured with ECE and Thomson laser scattering system in typical NB heated deuterium plasma (I_P=2.0MA, B_T=4.0T, P_{NBI}=20MW).
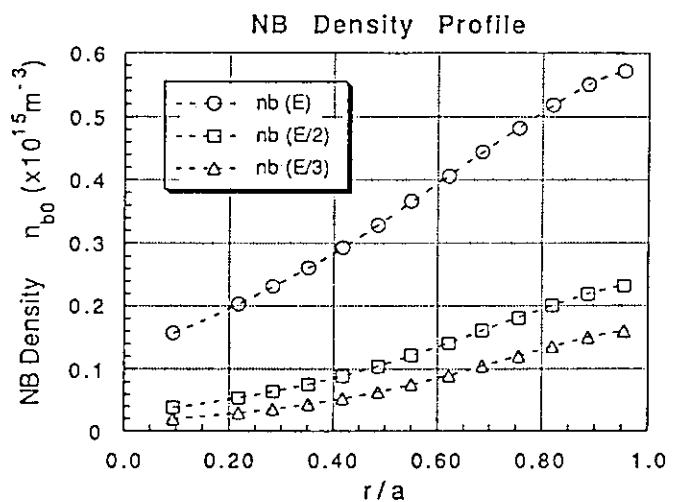
Fig. 3 Deposition profiles of deuterium neutral beam for each beam energy components; E, E/2 and E/3.

C^{6+} profiles from CXRS (E13780)
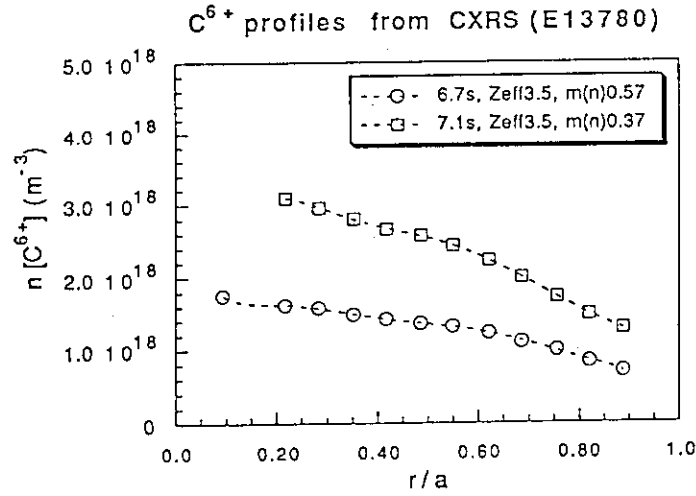
Fig. 4　Density profiles of C^{6+} in typical NB heated deuterium plasma measured with CXR emission of C VI.

C^{6+} profiles from CXRS (E13780,6.7s)
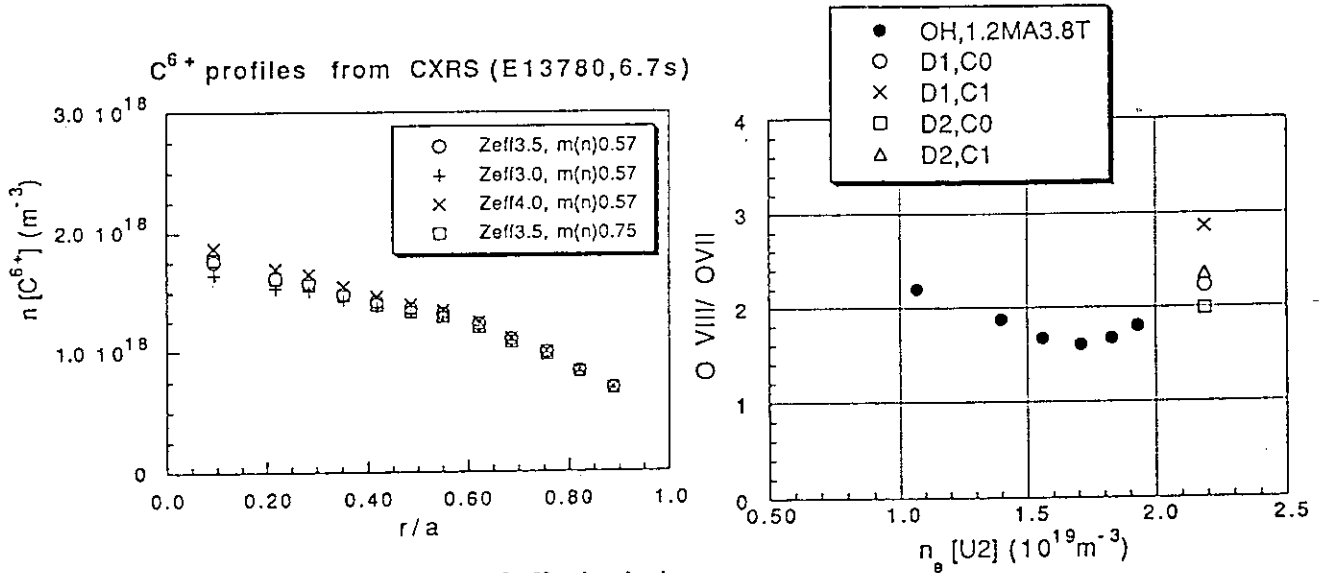
Fig. 5　The effect of inaccuracy of effective ionic charge Z_{eff} and electron density profile parameter m on the density profile of C^{6+}.

Fig. 6　The dependence of the ratio O VIII / O VII in OH plasma on averaged electron density and results of impurity transport calculation.

8.6 Density and Temperature Profiles of Divertor Plasma

K. Itami, N. Asakura

Introduction

The divertor plasma characteristics play an important role on the particle and impurity transport in a tokamak. Particle recycling involves by ionization and charge exchange processes near the divertor plate. Generation and transport of impurity ions change with temperature and density at the divertor and the scrape-off layer plasma. This paper presents characteristics of the density and temperature profile of the divertor plasma in JT-60U and addresses the current transport in the scrape-off layer.

Experimental Set-Up

Two sets of poloidal Langmuir probe array were installed at the divertor plate. A poloidal array consists of fifteen probes which are located 18mm~42mm apart as shown in Figure 1. The probe tip is made of graphite. The mechanical design is based on the probes used in JET. These probes are operated in the single probe mode. The applied voltage was in the range of -200V to 100V and swept by a frequency of 10Hz. The sample frequency to the transient memory was 1kHz. The probe current data is fitted to the biased probe characteristics,

$$I_{probe}(V_{bias}) = -I_s^+(1-exp(\frac{V_{bias}-V_f}{T_{ed}})).$$

Electron temperature T_{ed}, floating potential V_f and ion saturation current I_s^+ are obtained from the probe characteristics. The electron density n_{ed} is obtained from the relation $n_{ed} = I_s^+/A_pec_s$, where the ion acoustic speed is defined as $c_s = \sqrt{2eT_e/M_i}$. A_p is the effective area of the probe.

Ohmic heating measurement

The electron temperature and density profiles has been measured for OH discharges. The electron density and electron temperature show pronounced in-out asymmetry as the main plasma density increases as shown in Figure 2. This asymmetry is reversed when toroidal field is reversed. When the direction of ion grad-B drift is away from divertor, the electron temperature is higher at the outer divertor. The outer divertor is the electron drift side. Although the electron density tends to be higher at the inner divertor, this difference is not large enough to satisfy the electron pressure balance: the electron pressure is higher at the outer divertor.

Figure 3 shows the profiles of electron temperature and heat flux density at the divertor from the discharges for a toroidal field scan where the plasma current, main plasma density and configuration are fixed. This figure shows profiles of electron temperature, electron density, heat flux density and particle flux density. The electron density profile is not sensitive to the safety factor. The electron temperature profile in shot 13186 is more peaked than the profile in shot 13184. Assuming $T_{id} = T_{ed}$, heat flux density is obtained by the equation $P = 7.8IT_e$. The difference in peakedness is more pronounced for the heat flux profile. This result is consistent with the heat flux measurement in JT-60 [1] and can be explained as follows. In higher q discharges, the connection length from the scrape off layer to the divertor is longer than low q discharges and the perpendicular heat flux reaches further across the scrape-off layer.

Total heat load onto the divertor estimated for these shots exceeds the ohmic input power. In

other words the value of heat flux density is overestimated. The heat flux estimation is two to three times larger than the real value. We usually estimate A_p as the projected area normal to the magnetic field. Recently Matthews et al. [2] addressed the problem of fluxes to a surface at grazing angle of incidence. They found ion flux has larger value than $\sin \alpha$ dependence. Here α is the angle between the field line and the wall.

NB heating

With low beam powerm, temperature and density characteristics are similar to those of OH discharges . The profiles of temperature and density were obtained during the initial period of neutral beam experiment. This period is spent for neutral beam aging. Hydrogen and impurity atom are sputtered at the beam duct by beam aging and a large part of neutral beam power is lost at the beam duct. Radiation power is enhanced due to cold neutral particles from the duct. Thus heat flux to the divertor is increased by a factor of two to three. Figure 4 shows the profile of electron temperature and electron density at NB phase in Shot 13603. Electron temperature profile is similar between OH and NB phases except the probe position near the inner separatrix.

Near the end of this experimental campaign, temperature and density near the separatrix was measured during high beam power heating. Figure 5 shows time evolution of plasma parameters during a beam heated discharge. Asymmetry of electron temperature is observed only during the first beam period . After the second beam injection, electron temperature is almost constant (slightly decreasing) while divertor density increases as the main plasma density increases. At t=7.4sec the density at the inner divertor starts to decrease. This is a symptom of detachment and density limit. In a high power heated discharges T_{ed}=9.5eV, n_{ed}=7x10^{19}/m^3 was obtained at the outer divertor. Although asymmetry in the heat flux and particle flux is enhanced in this case, asymmetry of electron temperature between the inner divertor and outer divertor is the same as OH discharges.

Scrape-off Layer Current

Since non-ambipolar current in the scrape-off layer outside the separatrix is measured in JET[3], theoretical and experimental efforts have been made to investigate the mechanism of the non-ambipolar characteristics. Staebler has improved the original Harbour's model and proposed a self-consistent transport model[4]. Up to now no conclusive picture of the scrape-off layer current is obtained, since these model and experiment assumed a temperature asymmetry at the divertor that is crucially important for the non-ambipolar current flow. We obtained the profiles of electron temperature, electron density and non-ambipolar current using Langumuir probe array with a spacial resolution good enough to resolve the difference between each flux tube. Then we have carried out a direct comparison between the experiment and the theory. Figure 6 shows scrape-off current profiles for density scan discharges. The current density at each probe positions is obtained by the probe current when the applied voltage vanishes, $I_{probe}(V_{bias} = 0$). As the main density increases, divertor electron density increases and pre-sheath is formed. The scrape-off current model is applicable in the condition that pre-sheath is well defined. At the discharge with the highest plasma density, the probe current profile shows the current flow from the outer divertor to the inner divertor. Electron pressure asymmetry observed in the experiment modifies the equation given by Staebler. On each flux tube, we have compared the scrape-off layer current with the theoretical

prediction, which is obtained by substituting electron temperature and electron density at the both ends to the equation. The result is shown in Figure 7. When the direction of toroidal field is reversed, the asymmetry of electron temperature is reversed and direction of current is also reversed. Modification to the Stabler's equation reduced the discrepancy between $J_{//}^{theory}$ and $J_{//}^{exp}$ and we found $J_{//}^{exp}$ is explained within a factor of two. We have assumed $Z_{eff} = 1$ and $T_i = T_e$. The discrepancy between $J_{//}^{theory}$ and $J_{//}^{exp}$ suggests that $Z_{eff} > 1$ in the scrape-off layer. Further study of the effect due to hydrogen and impurity ions is in progress.

REFERENCES

[1]ITAMI, K., FUKUDA, T., IKEDA, Y. et al., J. Nucl. Mater. 176-177 (1990) 236.

[2]MATTHEWS, G.F., FIELDING, S.J., MCCRACKEN, G.M. et al., Plasma Physics Contr. Fusion 32(14) 1301.

[3]HARBOUR, P.J., SUMMERS, D.D.R., CLEMENT, S., et al. J. Nucl. Mater. 162-164 (1989) 236.

[4]STAEBLER, G.M., HINTON, F.L., Nucl. Fusion, Vol.29(1989)1820.

Langmuir Probe Array on JT-60U Divertor Plates

15 channels
material: graphite, JET design
6mm(dia), 5mm SR, Protrusion: 1mm
Single probe mode
Sweeping frequency: 10 Hz
Sweeping voltage: -200 to 60 Volts
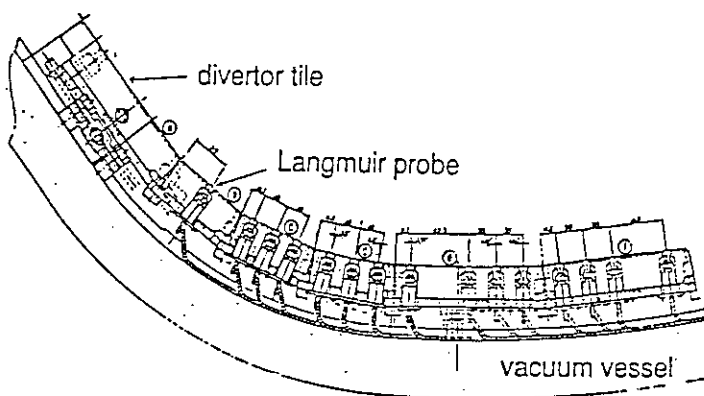
Fig.1 Langmuir Probe Array.
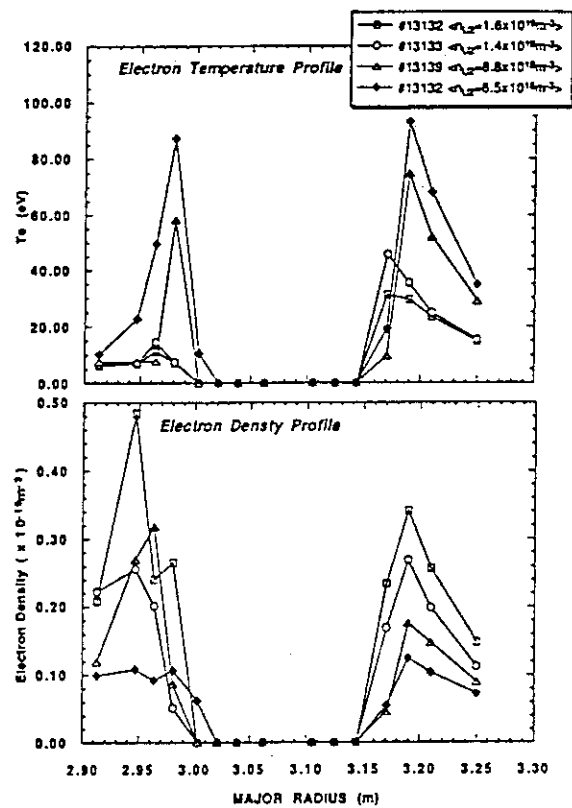
Fig 2 The profiles of electron temperature and electron density are shown from density scan discharges.
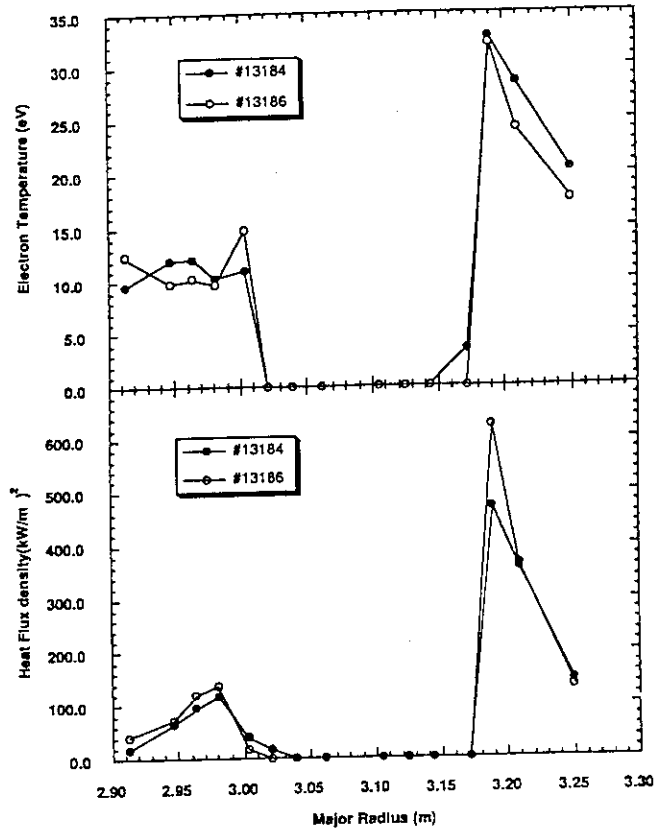
Fig. 3 The profile of electron temperature and heat flux density at divertor from the discharges from a toroidal field scan discharges.
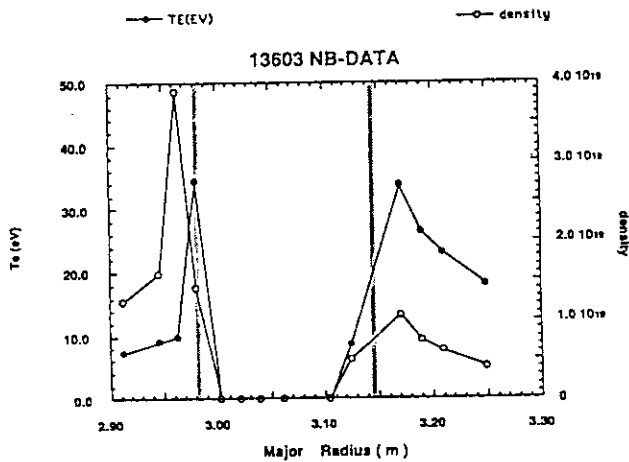
Fig. 4 The profiles of electron temperature and electron density at NB phase in Shot 13603.
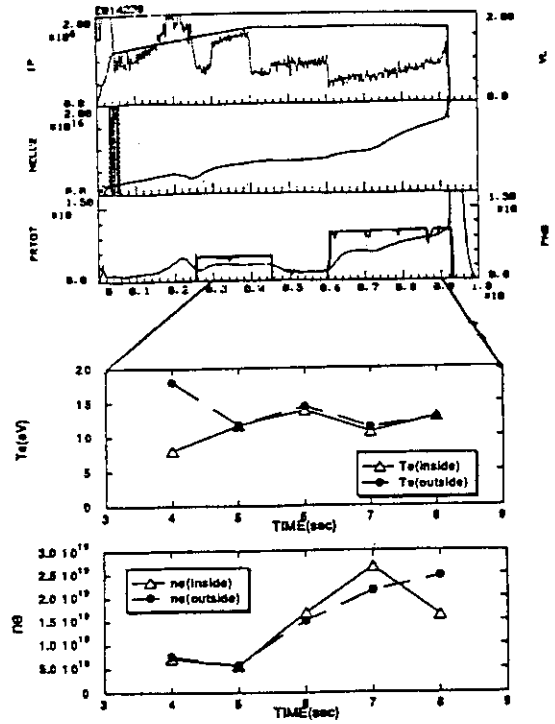
Fig. 5 Time evolution of plasma parameters during the neutral beam heated discharge.
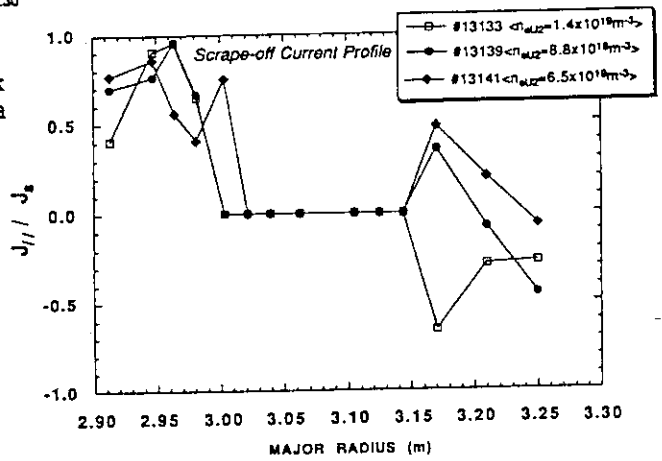
Fig. 6 The scrape-off current profiles.
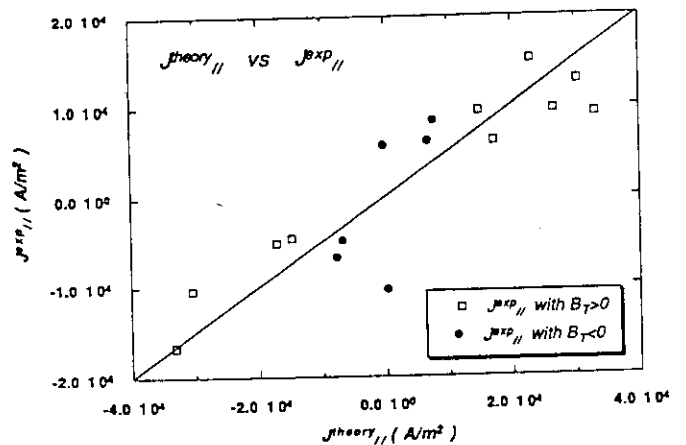
Fig. 7 The measured scrape-off current is compared with the predictions by the modified model.

8.7 Particle Flux and Heat Flux of Divetor Plasma

N. Asakura, K. Itami, M. Shimada, S. Tsuji, K. Shimizu, N. Hosogane

1. Introduction

Performance of the open divertor plasma has been studied relative to the main plasma parameters in JT-60U. Particle and heat flux studies of the SOL and divertor are essential in order to understand the mechanism of plasma edge transport and particle confinement. Meanwhile, the present database for these fluxes and the divertor plasma is not enough to determine the scalings of the divertor performance and particle confinement time τ_p. The particle flux Γ_D and heat flux Q_D to the divertor plates were derived using a Langmuir probe array, and the results of the Γ_D and Q_D determinations are related to the averaged density $\bar{n}_e$, toroidal field B_t, and distance of the X-point from the target plate L_X. This paper concentrates on a series of ohmically-heated hydrogen discharges at a plasma current of 2 MA, which constitutes enough of a database of reproducible discharges.

2. Probe Array Measurement

The Langmuir probe has been the principal edge diagnostic providing most of the data on local n_e and T_e. From the current-voltage ($I - V$) characteristic of the probe biased by external power source, the local values of the ion saturation current I_s^+, the electron temperature T_e and the floating potential V_f can be deduced directly. In JT-60U, a couple of the probe arrays, each of which consists of fifteen identical probes separated by about 2 cm poloidally, are mounted on the divertor plates. The two arrays are separated toroidally at the angle of about 10°. The head of each probe is made of 8 mm diameter carbon fiber composite (CFC) cylinder, and its apex facing the plasma shapes a part of the sphere. The potentials of the probes are swept typically from -100 V to $+30$ V over a period of 0.1 s, from 2 s after the break-down to the end of the discharge (15 s). The results of the particle and heat fluxes to the divertor plates during current flat-top phase in ohmic heating discharges are summarized with related to the main plasma parameters. During neutral beam heating, in particular, the particle flux to the divertor plates are increased about several times than that in ohmic heating case, and arcing between the plates and probes is often observed. The other disturbing sources such as high energy electrons and fluctuations caused by ELM, make it difficult to fit the data to the expected curve.

The profiles of local I_s^+ and T_e are measured along the X-point target plates in the poloidal direction. The local electron density n_e is related locally to the I_s^+ and T_e by the expressions

$$n_e = \frac{I_s^+}{e \, A_p \, c_s} , \qquad (1)$$

where A_p is effective collection area of the probe and $c_s = [k(T_i + T_e)/m_i]^{1/2}$ is the ion acoustic speed. The A_p is a problem to know. Since the "very strong magnetic field" regime ($\rho_i \ll d_{\text{probe}}$) is obtained in JT-60U operations, the area of each probe projected to the local field line, which is 5 to 6 mm^2 depending on the pitch angle of the magnetic field, is used. The value of c_s is an another problem and it is calculated with assuming that $T_i = T_e$.

Particle flux Γ_D and heat flux Q_D are derived as follows,

$$\Gamma_D = \int_{poloidal} \gamma_D(R) \cdot 2\pi R \cdot \cos \theta \; dl \qquad (\text{n} \cdot \text{s}^{-1}), \qquad (2)$$

where $\gamma_D(R) = I_s^+/(eA_p)$ is particle flux density, and

$$Q_D = \int_{poloidal} q_D(R) \cdot 2\pi R \cdot \cos\theta \; dl \qquad (W), \qquad (3)$$

where $q_D(R) = \gamma_s I_s^+ \cdot T_e/(eA_p)$ is heat flux density, respectively. The θ is the angle between the field line and axis of each probe, which is normal to the plate surface. Toroidal symmetry of the profiles are assumed. The sheath energy transmission factor γ_s of 7.8 is used to estimate the heat flux to the divertor in this paper, and the calibration using the infrared sensitive camera system will be performed.

3. HEAT FLUX ESTIMATION

It is difficult to determine γ_s experimentally. Q_D is given by the sum of the electron and ion heat fluxes. Although the electron heat flux is affected by the sheath potential and the secondary electron emission at the target, γ_s^e of 5.0 is usually used. The ion heat flux varies with the ratio of T_i to T_e. Assuming $T_i = T_e$, $7.9T_e I_s^+/(eA_p)$ is a fairly standard estimation of q_D. Figure 1 displays Q_D as a function of $P_{oh} - P_{rad}$, where P_{oh} and P_{rad} are the ohmic input power and total radiated loss, respectively. Since $Q_D = P_{oh} - P_{rad}$ for the steady state phase in ohmic discharges, the conventional value of γ_s should be allowed to range between 10 and 24 for $0.8 \times 10^{19} \le \bar{n}_e \le 1.7 \times 10^{19} \mathrm{m}^{-3}$. To explain the results simply in terms of the difference of the ion heat flux, the corresponding T_i/T_e ratio varies between 1.7 and 6.5. When T_i/T_e is 6.5, c_s is twice larger and the local n_e is decreased to be half values of the above results. γ_s approaches to 7.9 with the increase in $\bar{n}_e$.

4. DENSITY DEPENDENCE

Asymmetries in the T_e and/or n_e profiles have been often seen during divertor discharges, and they depend on $\bar{n}_e$ and the direction of the toroidal field. Figure 2 plots the peak values of n_e on the inboard and outboard divertor plates, and T_e corresponding to the locations of the n_e measurements, as a function of $\bar{n}_e$. B_T is 3.7 T and the direction of the ion ∇B drift is towards the divertor plates. The distance between the X-point and divertor surface is about 10 cm. An increase in $\bar{n}_e$ from 0.6×10^{19} to 2.8×10^{19} m^{-3} results in a reduction of T_e from 80 to $\sim$10 eV, and it corresponds to a rise in n_e from 0.2×10^{19} to 2.8×10^{19} m^{-3}, which is comparable to the density of the main plasma. The maximum T_e on the outboard target (electron side) is always observed to be higher than that on the inboard target (ion side), independent of the main plasma density. The maximum n_e at the inboard plates is larger than at the outboard plates for $\bar{n}_e \le 2.0 \times 10^{19}$. On the other hand, both the peak n_e values rise significantly to be comparable, or is sometimes higher on the outboard plates for $\bar{n}_e \ge 2.5 \times 10^{19}$, where $\bar{n}_e$ is still below the high density disruption limit. Γ_D and Q_D to the divertor plates are also closely related to the main plasma density, and these are shown in Fig. 3. Γ_D to the outer target plates is increased more than that to the inner target plates with the increase in $\bar{n}_e$. Q_D to the outer target plates is superior to that to inside plates in all range of the $\bar{n}_e$.

For the case of the reversed toroidal field, both the T_e and n_e are more symmetric except for $\bar{n}_e \ge 2.6 \times 10^{19}$ m^{-3}. Γ_D and Q_D are shown in Fig. 4. At high $\bar{n}_e$, only the local density at the inboard plates (electron side) rises to be a few times larger than that at the outboard plates (ion side), while the local n_e is only a half the magnitude of $\bar{n}_e$. Neither Γ_D nor Q_D have an asymmetry except in the high density discharges, where the inboard Q_D is twice as large as the inboard one. Contrary to the normal field case, a moderate and balanced increase in Γ_D for both sides with $\bar{n}_e$ results in the "cold" ($T_e < 10$ eV) divertor plasma, and Q_D decreases to a constant level of about 0.1 MW in $\bar{n}_e \ge 1.3 \times 10^{19}$ m^{-3}

5. SOL WIDTH ON DIVERTOR

The width of the divertor or SOL profile is characterized by the decay length, which is obtained by fitting an exponential curve to the profile in the outer magnetic surfaces. Typical decay lengths of T_e, n_e, γ_D ($\propto I_s^+$) and q_D profiles with different plasma density

are shown in Table 1. The amount of data used for the fit is only 3 - 4 points, and the standard deviation δL_{I_s} of 20 − 50% is smaller than δL_{T_e} of more than 50%. It is often difficult to fit a single exponential curve to the T_e profile for low density plasmas, since the T_e profile is flat around 10 eV over 6 cm away from the strike point of the separatrix. The decay lengths of the inboard profiles are smaller than the outboard ones. This result can be explained by the separation of the adjacent flux surfaces, which near the inboard target is 50% narrower than that near the outboard target. While L_{q_D} in the electron side is almost constant with an increase in $\bar{n}_e$, L_{q_D} in the ion side and L_{γ_D}s in both sides decrease gradually.

6. SUMMARY AND DISCUSSION

In contrast to the reversed field case, where Γ_D and Q_D are symmetric except for $\bar{n}_e \geq 2.6 \times 10^{19} \text{m}^{-3}$, when the ion ∇B drift directs toward the divertor plates Q_D rises rapidly at the outboard divertor with density. The asymmetry in Γ_D also reverses from inboard to outboard dominant at $\bar{n}_e = 1.2 \times 10^{19} \text{m}^{-3}$. Both Γ_D and Q_D become extremely substantial for $\bar{n}_e \geq 2.0 \times 10^{19} \text{m}^{-3}$.

It should be noted that these data are measured at the divertor plates, and that the results for Γ_D, Q_D, include not only the outflux from the main plasma, but also the component of recycled neutrals, which are ionized in the SOL/divertor region. It is estimated from the ratio of the H_α emission from the main plasma boundary to the entire plasma and a 2-D divertor model (described in detail in other paper), that the amplification factor of the particle flux in the divertor region (the volume is about 0.3% of the main plasma) is about 2 at $\bar{n}_e \sim 2.5 \times 10^{19} \text{m}^{-3}$. This value is not large enough to change the amplification factor, in particular, at the outboard divertor. This conclusion is supported by the fact that the inboard and outboard ratios of Γ_D and Q_D are constant with L_X, and that the 32 ch. high resolution H_α detector array at the divertor plates does not observe a significant asymmetry in the emission profiles.

$\bar{n}_e$ (10^{19} m^{-3})	B_T (T)	L_{T_e}(mm)		L_{n_e}(mm)		L_{γ_D}(mm)		L_{q_D}(mm)	
		i-side	e-side	i-side	e-side	i-side	e-side	i-side	e-side
1.0	3.7	80~300	70~120	50	87	50	52	49	38
2.0	3.7	~130	60~120	40	63	41	49	37	34
2.7	3.7	~150	50~110	33	42	29	40	23	37
2.0	2.8	~100	70~110	36	63	42	50	42	35

Table 1: Table I: Decay Lengths of Profiles
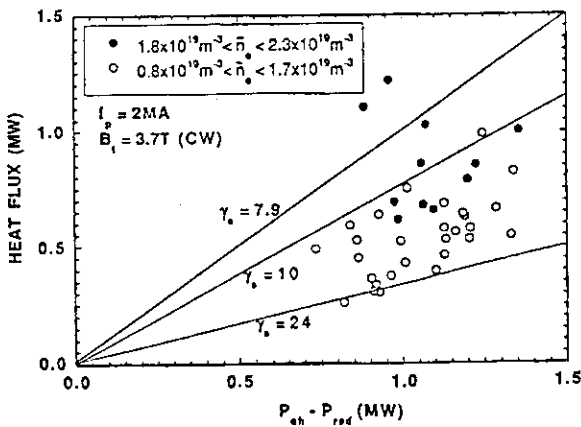
Fig.1 Q_D at high density (closed circles) and in low density (open circles) are plotted as a function of $P_{oh} - P_{rad}$. γ_s of 7.9 corresponds to $T_i = T_e$.
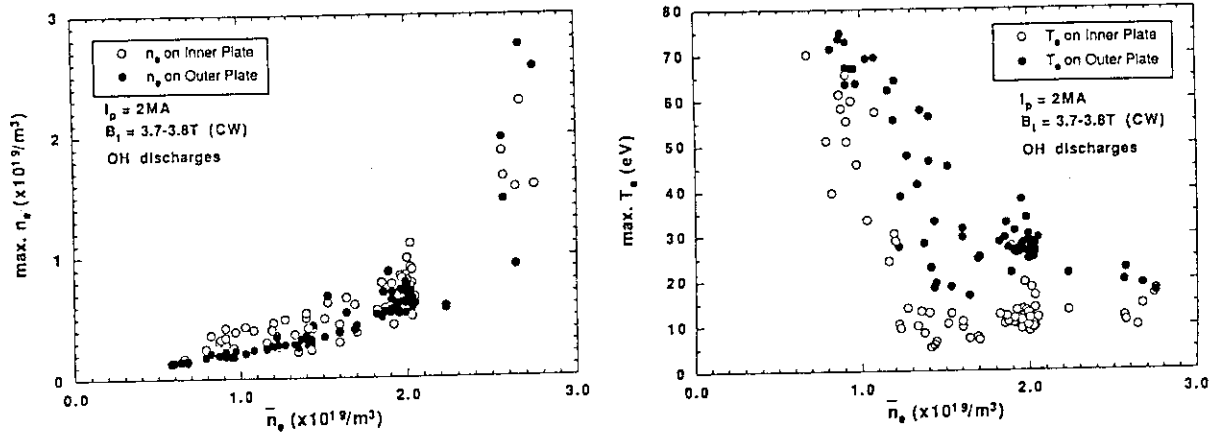
Fig.2 (a); n_es at the inner side and outer side peaks of the n_e profile are plotted by open and closed circle, respectively. (b); T_e, which is measured at the location corresponding to the n_e, is shown.
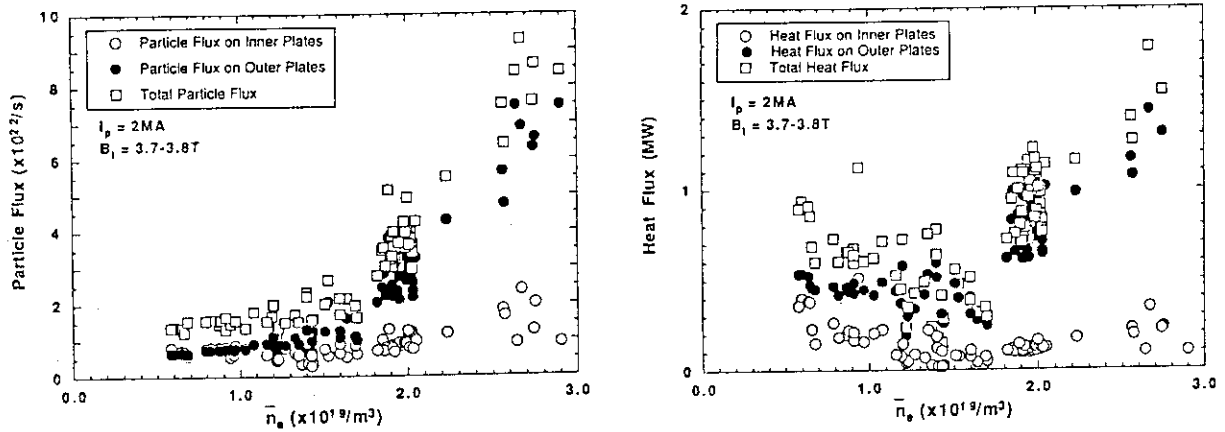
Fig.3 particle flux Γ for (a) and heat flux Q for (b) are plotted as a function of $\bar{n}_e$ for CW toroidal field. Open circle, closed circle and square show fluxes to inner plates, outer plates and total flux, respectively.
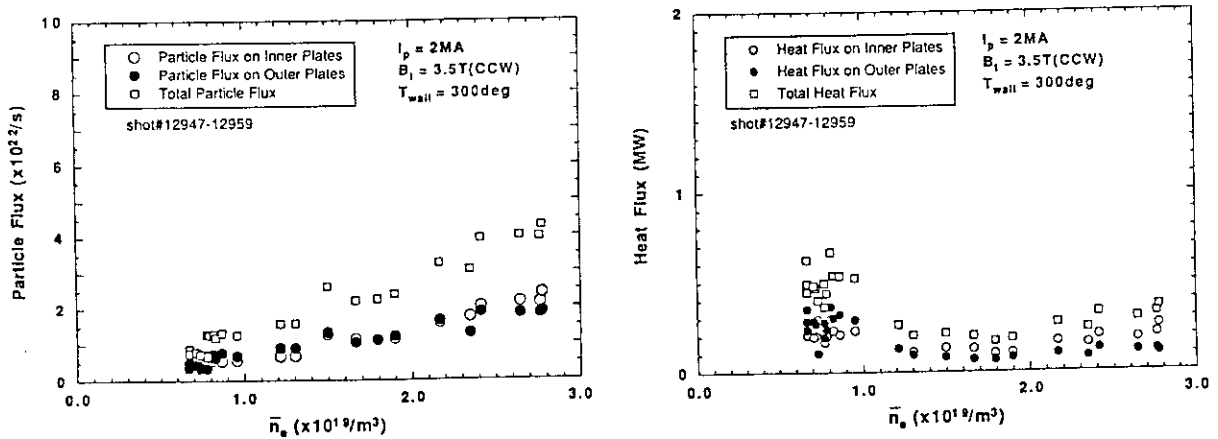
Fig.4 particle flux Γ for (a) and heat flux Q for (b) are plotted as a function of $\bar{n}_e$ for CCW toroidal field. Open circle, closed circle and square show fluxes to inner plates, outer plates and total flux, respectively.

8.8 Particle Confinement

N. Asakura, K. Itami, M. Shimada, S. Tsuji, K. Shimizu, T. Kondo

1. Introduction

In large Tokamak plasma, where the edge density and temperature are fairly high enough to ionize most of the neutral influx within edge region, it has been expected that the particle confinement is less influenced by the transport in the core plasma. The edge plasma conditions including the divertor plasma determine the particle confinement directly, and there have been reported in large tokamaks such as JT60[1], TFTR[2], and JET[3]. Meanwhile, neither the scaling of the particle confinement time τ_p nor the mechanism have been understood systematically[4,5].

In this paper, H_α/D_α measurement in JT-60U and the ionized neutral influx Φ_{in} calculation are described. The Φ_{in} and Γ_D, which is deduced from the Langmuir probe array measurement, are compared for the ohmically-heated hydrogen discharges. τ_p including the SOL/divertor effects is calculated from the Φ_{in} results, and the results are summarized.

2. H_α/D_α Measurement

The H_α/D_α measurement counts the H_α/D_α photons emitted from the plasma, which is proportional to the neutral influx, and the total neutral influx Φ_{in} is determined by integrating the influx over the plasma boundary.

The H_α/D_α scope is installed on a vertical port that provides an oblique view of the plasma. The three H_α/D_α poloidal scopes, which has 30 optical fibers totally, are installed on the same up-oblique port and they view the plasma cross-section perpendicularly. The chords of the sight-line are shown in Fig. 1. The 10 absolutely-calibrated channels are used for the poloidal cross-section measurement. In particular, the best spatial resolution over the divertor plates is designed to be about 4 cm. Other 6 single scopes are installed at the different toroidal section to monitor toroidal asymmetry and they are not absolute calibrated. The signals of line-integrated H_α/D_α emission (656.3 nm) are guided through 200 m optical fibers to the PMT array and an interference filter is placed in front of each PMT. This system is absolutely calibrated in situ by using the standard tungsten-halogen lamp coupled with integrating sphere. The data are sampled from the break-down to the end of the discharge (15 s) with the sampling period of 1 ms, which is restricted by the response of the pre-amplifier.

The total Φ_{in} is calculated by integrating the signals along the poloidal circumference. Although reflected light by the first wall distorts the real image of the H_α/D_α emission, this correction may be small enough in JT-60U, where the first wall is completely covered by graphite tiles. The calculation of Φ_{in} is given as follows,

$$\Phi_{in} = \sum_{j=1}^{13} E_j \cdot \varepsilon_j \cdot 2\pi R_j \cdot \Delta l_j \qquad (n \cdot s^{-1}), \qquad (1)$$

where E_j (photons s^{-1} m^{-2}), ε_j (ionizedneutrals/photon), Δl_j (m) are the H_α/D_α photon signal, the "ionization events per photon" and the representative path over j-th section. The plasma poloidal boundary is divided into 13 sections as is schematically shown in Fig. 2 and the line-integrated emission signals of I_1 to I_{10} are distributed to E_j in each section. Following three assumptions are made for this calculation;

1. The ionization event of ε is influenced mainly by local n_e and T_e. According to the empirical function of $\varepsilon(n_e, T_e)$ [6], ε_j of 15 for the plasma edge condition of $n_e \sim 0.5 \times 10^{19}$ m^{-3} and $T_e \geq 15$ eV, is used for the series of calculations.

2. Toroidal symmetry of the emission profile is relatively satisfied in the ohmically heated divertor discharge with the low or moderate gas fueling.

3. The Δl_j is given by $\Delta s_j \times \cos\theta_j$ if the photon emission is constant over the straight path, where Δs_j and θ_j are the path length and the angle of the sight line normal to the path. Table 1 shows an examples of the elements for each section in the calculation. Here, the inboard/outboard symmetry of the emission is assumed for the sections of $j = 2, 3$ and 4.
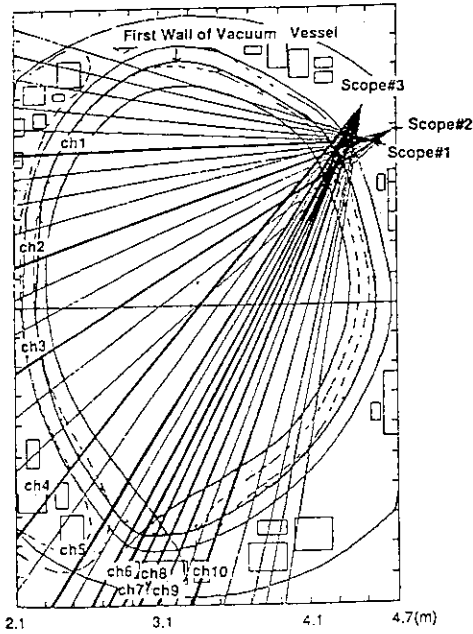
Fig.1 The three H_α/D_α poloidal scopes, which has 30 optical fibers totally, are installed on the same up-oblique port. The spacial resolution of the chord over the divertor plates is designed to be the highest about 4 cm. 10 channels shown by thick lines are prepared for the measurements.
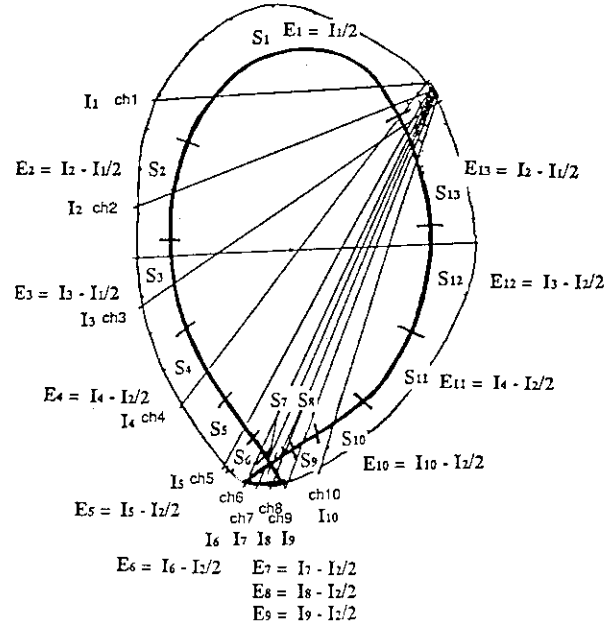
Fig.2 The plasma poloidal boundary is divided into 13 sections to evaluate the neutral influx Φ_{in}. The emission signals of I_1 to I_{10} are distributed to E_j in each section.

Table 1: Example of Influx Calculation

path No. j	path length (m) s_j	view angle θ_j	rep. path (m) l_j ($= s_j \times \cos\theta_j$)	major radius (m) R_j	corresponding signal E_j
1	1.71	45°	1.21	3.30	$I_1/2$
2 + 13	1.47	30°	1.27	3.30	$I_2 - E_1$
3 + 12	1.34	25°	1.21	3.30	$I_3 - E_{13}$
4 + 11	1.25	25°	1.13	3.30	$I_4 - E_{13}$
5	0.500	15°	0.483	2.92	$I_5 - E_{13}$
6	0.120	20°	0.112	3.05	$I_6 - E_{13}$
7	0.120	0°	0.120	3.14	$I_7 - E_{13}$
8	0.120	20°	0.112	3.22	$I_8 - E_{13}$
9	0.210	45°	0.148	3.33	$I_9 - E_{13}$
10	0.640	40°	0.490	3.55	$I_{10} - E_{13}$

3. INFLUX AND OUTFLUX

The signals radiated mainly in the divertor/X-point region, I_6, I_7, I_8 and I_9, are 100 − 200 times brighter than those in the upper half of the plasma such as I_1 and I_2, in the medium and high density discharges ($n_e \geq 1.3 \times 10^{19}$ m^{-3}). While ΔL_j of the divertor sections ($j = 6,7,8$ and 9) are smaller by one order of the magnitude. Therefore, the influx passing through the divertor/X-point sections of $j = 6,7,8$ and 9 is 3 − 4 times larger than that from the other sections of the boundary, and the ratio is increased gradually with $\bar{n}_e$. It should be noted that in the density regime signals of I_4, I_5 and I_{10} (out of view of the targets) also rise significantly, about 20 − 50 times brighter than I_2. This fact suggests that the influx not only from the divertor/X-point sections but also from the close vicinity of the X-point plays a large part in recycling of the neutrals in the higher density operations. In the low density discharge ($n_e \leq 1.0 \times 10^{19}$ m^{-3}), the intensities of I_6, I_7, I_8 and I_9 are about 10 times brighter than I_2, and the influx from the divertor/X-point is decreased comparable to that from the other sections.

Figure 3 plots Φ_{in} and Γ_D as a function of $\bar{n}_e$. The particle flux result Γ_D, which is derived by the probe array, are chosen from the same data base as was described in the previous section. Φ_{in} is calculated using the H_α signals at the corresponding time. The Φ_{in} and Γ_D are in fairly good agreement within the experimental errors. The neutral influx excluding in the divertor/X-point sections ($j = 6,7,8$ and 9), Φ_{in}^m is also shown in Fig. 3. The Φ_{in}^m corresponds to about 50 % and 30 % of the Φ_{in} in the low and high density regions, respectively. More than half of the neutrals are supplied from the divertor/X-point region to the main plasma. While the ratio of Φ_{in}^m to Φ_{in} is decreased gently with the main plasma density in ohmically-heated discharge. The neutral influx of more than 50 % from the divertor/X-point and its vicinity penetrates into the main plasma, and that its relative distribution over the plasma boundary is hardly influenced by $\bar{n}_e$ in the open X-point configuration in JT-60U.

4. GLOBAL PARTICLE CONFINEMENT TIME

The particle confinement time τ_p including the SOL/divertor effect is given by $\bar{n}_e V_p / \Phi_{in}$, and it is plotted as a function of $\bar{n}_e$ in Fig. 4. Here, V_p is the main plasma volume and the volume of the divertor region is small enough to be neglected. τ_p increases with $\bar{n}_e$ for $\bar{n}_e < 1.3 \times 10^{19}$ m^{-3}, and the maximum τ_p of about 80 ms is achieved at $\bar{n}_e = 1.3 \times 10^{19}$ m^{-3}.

In the medium and high density regimes of $\bar{n}_e \geq 1.3 \times 10^{19}$ m^{-3}, τ_p decreases from 80 to 30 ms proportional to $\bar{n}_e^{-1.2}$. the least-squares fit to the normalized Γ_D and τ_p can be reduced to the following expressions; $\Phi_{in}/\Phi_{in}^* = (\bar{n}_e/\bar{n}_e^*)^{2.1}$ and $\tau_p/\tau_p^* = (\bar{n}_e/\bar{n}_e^*)^{-1.2}$, where $\bar{n}_e^*$, Φ_{in}^*, and τ_p^* are 1.3×10^{19} m^{-3}, 1.23×10^{22} n$\cdot$s^{-1}, and 80 ms, respectively. In the reversed field case, the best fits are given by $\Phi_{in}/\Phi_{in}^* = 1.4 \times (\bar{n}_e/\bar{n}_e^*)^{1.2}$ and $\tau_p/\tau_p^* = 0.83 \times (\bar{n}_e/\bar{n}_e^*)^{-0.2}$, for $\bar{n}_e \geq 1.0 \times 10^{19}$ m^{-3}. These results show that the normal B_T direction affects the decrease in the global particle confinement in the high density regime ($\bar{n}_e \geq 1.5 \times 10^{19}$ m^{-3}).

5. SUMMARY

The ionized neutral influx is deduced from the H_α emission signals from the plasma boundary in ohmically-heated hydrogen discharges. The particle flux and ionized neutral influx are in fairly good agreement within experimental errors. The global particle confinement time, τ_p, including SOL effects is derived from the measured influx. When the ion ∇B drift is towards the divertor, the global τ_p decreases with $\bar{n}_e$ in the relatively high density regime ($\bar{n}_e \geq 1.3 \times 10^{19}$ m^{-3}). However, the deterioration is smaller when the ion ∇B drift is away from the divertor.

References:
[1] YAMADA, K., *et al.*, Nucl. Fusion, **27** (1987) 1203.
[2] HEIFETZ, D,B., *et al.*, J. Vac. Sci. Technol. A. **6** (1988) 2564.
[3] MORGAN. P.S., *et al.*, in Controlled Fusion and Plasma Physics (Proc. 12th Eur. Conf. Budapest, 1985), Vol. 9F, PartII, European Physical Society (1985) 535.
[4] WOOTTON, A.J., *et al.*, Plasma Phys. Controll. Fusion **30** (1988) 1479.
[5] TSUJI, S., *et al.*, "Experimental scaling of particle confinement in Tokamaks", Fusion Engineering and Design (1992) (in press)
[6] JOHNSON, L.C., HINOV E., J. Quant. Spectrosc. Radiat. Transfer, **13** (1973) 333.
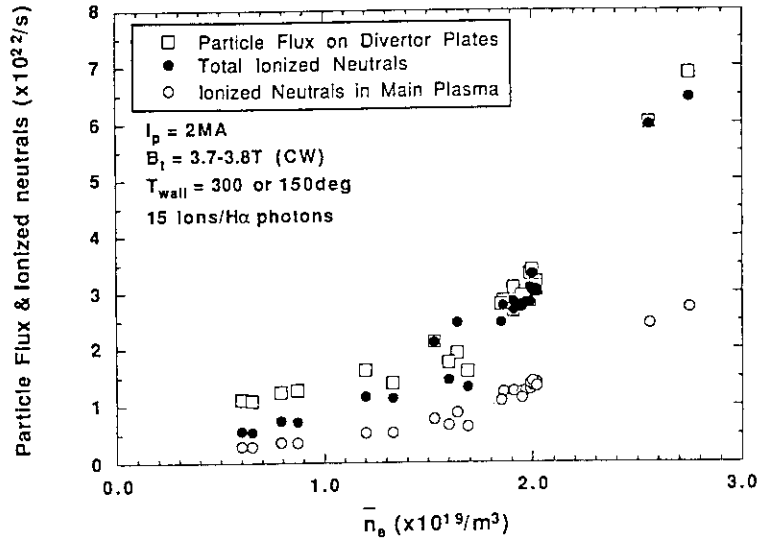
Fig.3 Φ_{in} and Φ_{out} are plotted by squires and closed circles as a function of $\bar{n}_e$, respectively. The particle flux data derived by the probe array are chosen from the same data base described in the previous section. Φ_{in}^m, neutral influx excluding in the most high recycle region, is also shown by open circles.
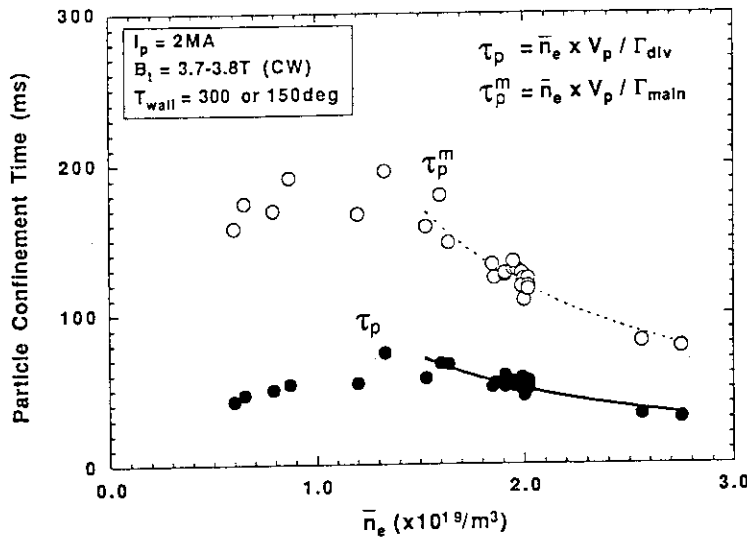
Fig.4 The particle confinement time τ_p including the SOL/divertor plasma is plotted by closed circles as a function of $\bar{n}_e$. The τ_p^m defined by $\bar{n}_e V_p/\Phi_{in}^m$, is also plotted by open circles.

8.9 Heat Load of the Divertor Plates

K.Itami

1. Introduction

One of the major unknown factors in designing a fusion reactor is the heat flux behaviors on the divertor. For predicting the behavior of heat flux in fusion reactors, it is very important to understand the energy balance and the heat transport transport in the scrape-off layer and divertor in large devices, such as in JT-60U. This study is the first study of heat flux behaviors using a thermography in JT-60U.

2. Calculation of Heat Flux

Heat flux to the divertor is calculated from the time evolution of the temperature at the divertor plate. Temperature of the divertor plates is measured by an infrared thermography system. The thermography system developed for JT-60U consists of an infrared TV and two mirrors, viewing the divertor at an angle of 62.5°. Data acquisition system takes radial profiles of temperature with time resolution of 25msec.

In a semi-infinite solid, temperature rise $T(t)$ at the surface exposed to heat flux $\lambda(t)$ is given by

$$T(t) = \varepsilon \pi^{-1/2} \int_{0}^{t} d\tau (t-\tau)^{-1/2} \lambda(\tau)$$

where

$$\varepsilon = (\frac{1}{\rho c K})^{1/2} .$$

Here ρ is the density, c is the specific heat and K is the thermal conductivity of carbon.
Then $\lambda(t)$ is obtained from this equation by substituting the time evolution of surface temperature. (See Figure 1)

3. Heat Fluxes due to ELM activities in H mode

Stationary energy balance is established in L-mode plasmas. In H mode plasmas, heat transport in the scrape-off layer correlates with ELM activities. In case grassy ELMs appear, energy from the main plasma is carried by both the stationary heat flux and the pulsed heat flux due to ELM activities. When ELM activities are weak, the pulsed heat flux is observed only at the inner divertor. As ELM activity becomes stronger, the heat flux due to ELM appears at the outer separatrix, too. When a quiescent phase of H mode is obtained, a large part of energy is carried by the pulsed heat flux due to giant ELMs that appeared at the end of the quiescent phase. Figure 2 shows the case in which the pulsed heat flux dominates the energy transport to the divertor. At t=5.9sec, a clear L to H transition is observed and the heat flux suddenly decreases at both the inner divertor and the outer divertor. An H to L transition occurs 100 milliseconds after the L-H transition and a stationary heat flux recovers. For t=6.2 sec to 7.0 sec, several H-L transitions and L-H transitions are observed and the heat flux to the divertor are strongly correlated with these transitions.

4. Asymmetry of Heat Flux in NB discharges

It has been observed in JT60, DIII-D and JET that the heat flux is larger at the inner divertor than at the inner divertor when the ion drift is toward the divertor plates. The ratio of heat flux at the inner divertor to heat flux at the outer divertor $P^{in}_{HEAT} / P^{out}_{HEAT}$ is plotted against the averaged

plasma density $\overline{n_e}$ for both directions of toroidal field in Figure 3. Changes of the ratio due to the direction of toroidal field is as large as 40%~60%. The mechanism of these asymmetries is not well understood. The ion flux and electron flux due to collisional transport is in opposite directions and a simple estimation indicates these amplitude is not large enough to alter total heat load on the divertor by 10%.

5. Power Balance in OH plasmas, LHCD plasmas and NB heated plasmas

We investigated power balance of OH plasmas, LHCD plasmas and NB heated plasmas using a database. Figure 4 shows the power balance in OH plasmas. The total heat load onto the divertor P_{HEAT}^{tot} and total output power P_{OUT} is plotted against the ohmic input power P_{OH}. P_{HEAT}^{tot} is given by $P_{HEAT}^{tot} = P_{HEAT}^{in} + P_{HEAT}^{out}$. P_{OUT} is given by $P_{OUT} = P_{HEAT}^{tot} + P_{RAD}$. P_{RAD} is the total radiation loss from the main plasma and the divertor plasma. A density dependence of power balance is shown in Figure 5. As the main plasma density increases, the ratio P_{HEAT}^{tot} / P_{OUT} decreases due to the increase in the radiation loss at the divertor.

In LHCD plasmas, up to 1.5MW of LHRF power was injected into the plasma. Since current drive efficiency decreased as the main plasma density increases, fully current driven plasmas were operated in the density range of $\overline{n_e} < 1 \times 10^{19} m^{-3}$. In high density discharges, the loop voltage increased and ohmic input power surpassed LHRF power. The data base includes few points from discharges with $1 \times 10^{19} m^{-3} < \overline{n_e} < 2.7 \times 10^{19} m^{-3}$ and the rest of the data pertains with discharges with $\overline{n_e} < 1 \times 10^{19} m^{-3}$. The power balance in LHCD plasmas is shown is Figure 6. P_{HEAT}^{tot} and P_{OUT} is plotted against the total input power P_{IN}. P_{IN} is given by $P_{IN} = P_{LH} + P_{OH}$. P_{LH} is the LHRF power. As shown in this figure, about 60-70% of input power is deposited onto the divertor.

In NB heated plasmas with high density, the agreement between the input power and the output power is worse than that in OH plasmas and that in LHCD plasmas. Figure 7 shows the power balance in NB heated discharges. P_{HEAT}^{tot} and P_{OUT} is plotted against P_{abs}. P_{abs} is the total absorption of the beam power. The heat flux onto the divertor is ~50% of P_{abs} at maximum.

6. Statistical Analysis of Peaking Factor of The Scrape-off Layer

The scaling of the scrape-off layer thickness is needed for prediction of the boundary plasmas in fusion reactors. Such a scaling has not been obtained experimentally yet. The models of the scrape-off layer, given by Harrison et al. [1], are often used to obtain theoretical predictions. According to the model the scrape-off layer thickness is given by competition between the thermal conduction along the scrape-off layer and the perpendicular thermal diffusion and it is described by the function of the plasma parameters at the scrape-off layer and at the divertor. These local plasma parameters is not easily obtained experimentally and the simple relation between the plasma parameters in the scrape-off layer and those in the main plasma is assumed to apply the Harrison's formulation for estimating those in the fusion reactor. In reality, particularly in high power beam heated discharges, the particle recycling plays an important role in determining the plasma parameters in the scrape-off layer and no simple relation between the main plasma parameters and the scrape-off layer plasma parameters is expected.

We have established a scaling law of the peaking factor of heat flux that is applicable to beam heated discharges in JT-60U with a wide range of plasma parameters. A database was assembled from discharges with $1.2MA \leq I_P \leq 3MA$ (plasma current), $1 \times 10^{19} m^{-3} \leq \overline{n_e} \leq 7 \times 10^{19} m^{-3}$ (averaged density of main plasma), $1MW \leq P_{NB} \leq 16MW$ (NBI heating power), $2.5 \leq q_{eff} \leq 13$

(effective safety factor). The peaking factor Y, defined by $Y = 2\pi R \, f^{out} q_{max} / P_{HEAT}$, is the inverse of the thickness of the scrape-off layer. Here $2\pi R$ is the toroidal circumference, Here R is major radius of the plasma and f^{out} is an expansion factor of flux tube at the divertor to the scrape-off layer at midplane. The parameter q_{max} is the maximum value of heat flux density at the outer divertor and P_{HEAT} is heat flux integrated over the outer divertor. Since the peaking factor is determined by the competition of transport along the magnetic field and perpendicular diffusion of particles and heat, it depends on the parameters P_{HEAT}, $\overline{n}_e$ and q_{eff}, which determine the temperature and density in the scrape-off layer and the divertor plasma. From a statistical analysis, we found the peaking factor Y scaled as $P_{HEAT}^{0.49\pm0.18} \, \overline{n}_e^{-0.45\pm0.22} \, q_{eff}^{0.67\pm0.18}$ as shown in Figure 8. This scaling is much different from the scaling estimated from the Harrison's model[1] ($P_{HEAT}^{5/9} \, \overline{n}_e^{-7/9} \, q_{eff}^{-4/9}$), as shown in Figure 9.

The density dependence of the peaking factor in LHCD plasmas is shown in Figure 10. This database consists of discharges with a limited range of the LHRF power ($P_{LH} < 1.5$MW), the plasma current (most data with $I_P = 1.2$MA, few data with $I_P = 2$MA), and thetoroidal filed ($B_T = 4T$).

REFERENCES

[1] Harrison, M., Analytical Modeling of Divertor and Scrape-Off Layer: ITER-IL-PH-13-9-E12(1989).
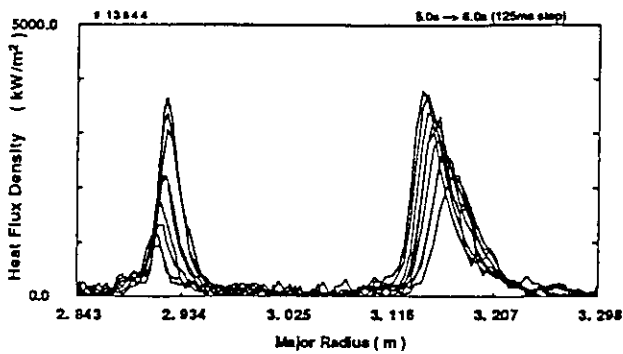
Fig.1 Time evolution of heat flux profile in a NB heated discharge.
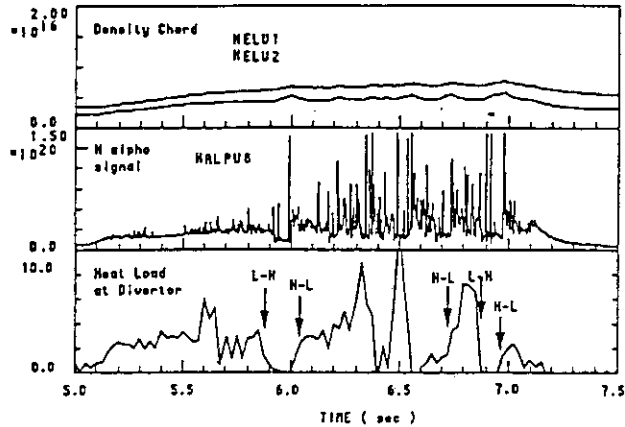
Fig. 2 Heat flux behaviors in a H-mode discharge.
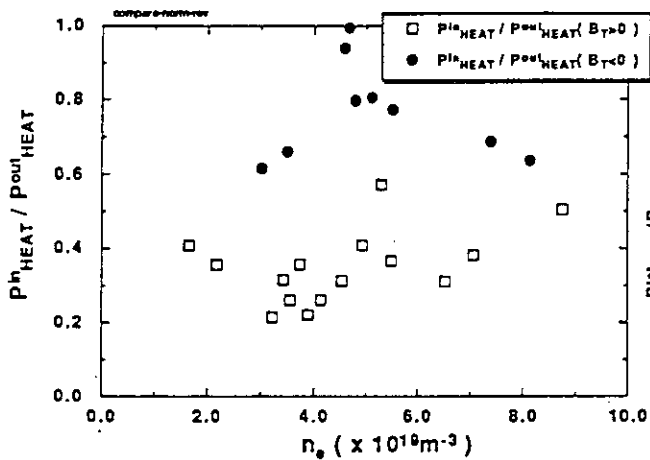
Fig.3 The ratio of heat flux at the inner divertor to heat flux at the outer divertor is plotted against the averaged plasma density for the both direction of toroidal field.
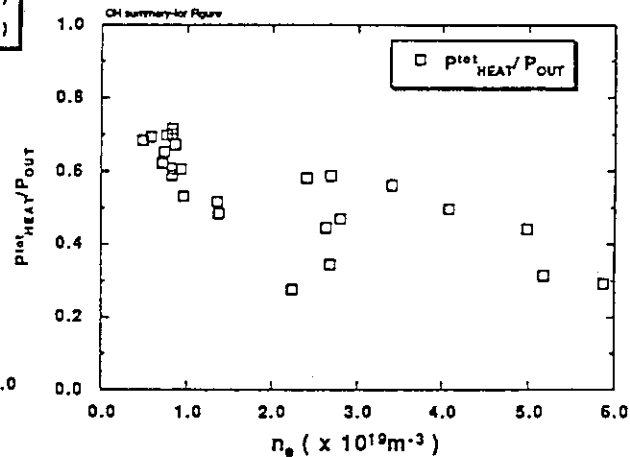
Fig.4 The power balance in OH plasmas.
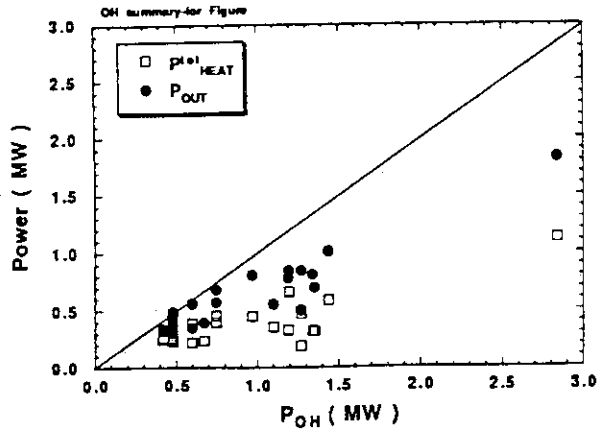
Fig.5 The density dependence of power balance in OH plasmas.
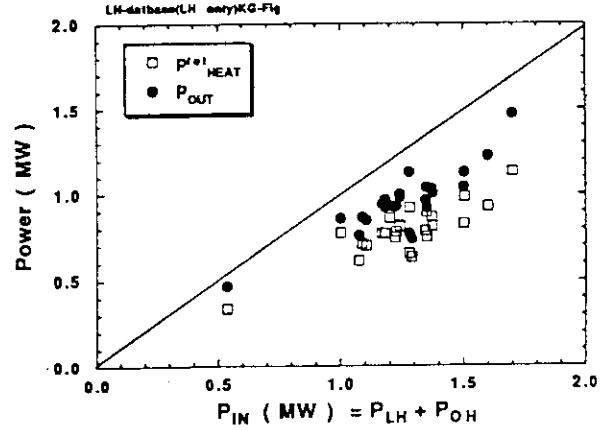
Fig.6 The power balance in LHCD plasmas.
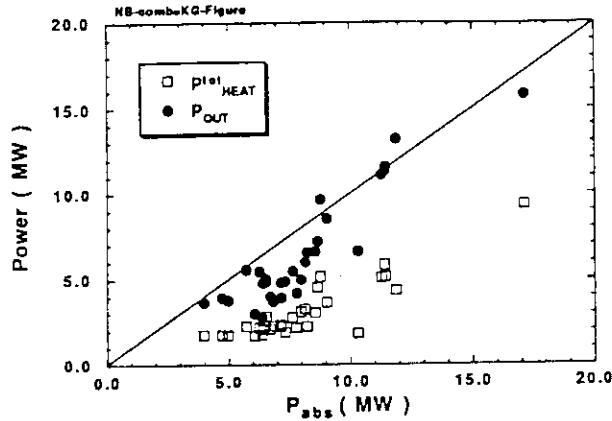
Fig.7 The power balance in NB heated discharges.
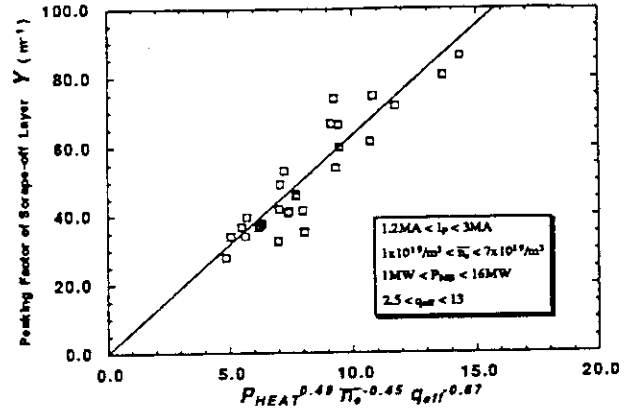
Fig.8 The peaking factor of the heat flux plotted against the statistically obtained scaling.
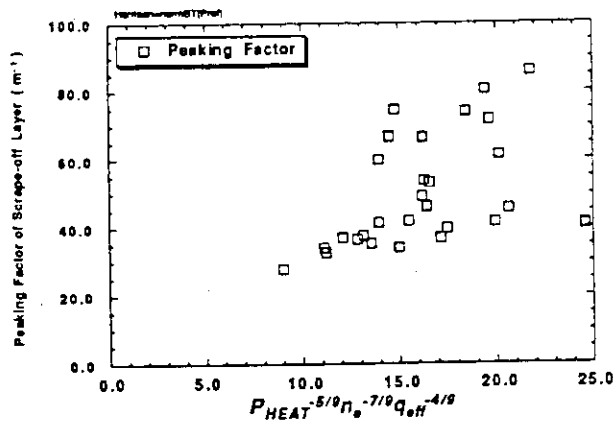
Fig.9 The peaking factor of the heat flux plotted against Harrison's model.
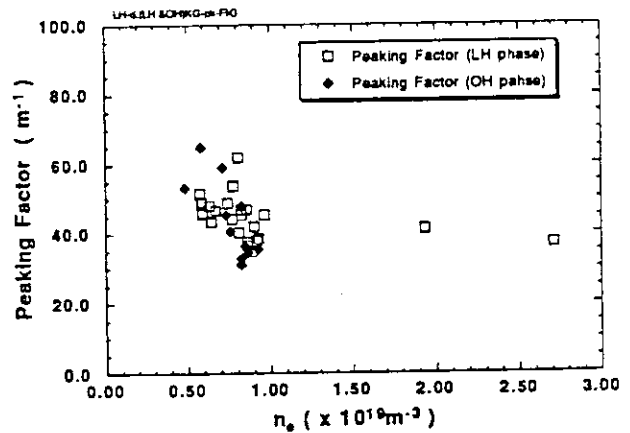
Fig.10 The density dependence of the peaking factor in LHCD plasmas.

8.10 Wall Conditioning in JT-60U

M. Shimada, R. Yoshino, Y. Kamada, H. Kubo, T. Sugie, S. Tsuji,

H. Nakamura, H. Ninomiya, and H. Horiike

1. Introduction

Wall conditioning plays an essential part in improving the quality of discharges in confinement and stability[1,2]. Besides baking, four types of wall conditioning are used in JT-60U: helium glow, helium/deuterium TDC, low-density tokamak discharge and disruptive cleaning.

2. Procedure of Wall Conditioning

After closing the machine vacuum, the vacuum vessel is baked to 300 degree C, followed by deuterium TDC of 30-40 hours long. Tokamak discharges are then attempted, combined with the inter-shot helium TDC, and disruptive cleaning. Disruptive cleaning is a technique of cleaning a particular area of the first wall (divertor plates in the JT-60U case) by making the plasma hit the first wall during the ramp-down phase. Low density conditioning shots are used particularly after a disruption shot. He TDC is often used with other techniques: disruptive cleaning, low density shot, and He GDC. Inter-shot He GDC has not been implemented yet, since glow current is rather low compared with other tokamaks(3A/anode in DIII-D), making short-time GDC inefficient.

3. Effects of Wall Temperature

Figure 1 shows carbon and oxygen emissivities normalized by electron density, with wall temperatures of 300 and 150 degree centigrade. This indicates that carbon and oxygen concentration is reduced by a factor of two by lowering the wall temperature, suggesting importance of chemical processes in impurity generation. Reduction of impurities results in expansion of the electron density range by a factor of two. However, reduction of wall temperature also slows down the process of wall conditioning by baking and TDC; hydrogen pressures are lower by a factor of 5-30 between shots, by a factor of up to 2 during helium TDC and partial pressures of water is lower by a factor of 2-10 between shots and by a factor of 5-20 during helium TDC. This result suggests that after initial periods of baking and cleaning, best results would be obtained by a combination of low wall temperature and helium GDC.

4. Glow System

A glow anode has been installed on the JT-60U machine. Its head is made of graphite,

measuring 16cm x 16 cm. The head position is 2 cm behind the first wall. Anode voltage is 400-700 V, glow current is 1-2A. A preionization filament[3], biased at -300 V with respect to the vessel, initiates glow discharges at low pressure(0.1Pa). Glow discharge cleaning is routinely done during lunch hour (12-1pm), during dinner hour(6-7pm), and overnight(10pm-9am).

5. Reduction of Impurity and Particle Recycling by Helium Glow Cleaning

Figure 2 compares Zeff, oxygen concentration, and carbon concentration before and after the first glow cleaning. Zeff was reduced by 1-2 by helium glow cleaning(Fig. 2(a)). Oxygen was reduced by a factor of two from the level prior to the first glow discharge(Fig. 2(b)). Furthermore, reionization of neutral beam in the neutral beam ports were reduced by helium glow. These results suggest that oxygen and hydrogen/deuterium particles in the graphite wall as well as on the port wall can be reduced by helium glow. 40 hours of TDC reduced oxygen level by a factor of two; however, reionization of neutral beam in the neutral beam ports were enhanced by a factor of two to four. Carbon levels show little effect of glow cleaning(Fig.2(c)). Even after four months of tokamak operation and wall conditioning, Zeff during NBI was still high even in high density(2.2 at $4.4 \times 10^{19} m^{-3}$)(Fig. 3) and confinement improvement by H-mode was still modest(40%). This suggests that further wall conditioning is necessary and more powerful wall conditioning methods(such as boronization) are required.

Figure 4 compares two shots in series(13899 and 13900). Between these two discharges, 1 hour of helium GDC was performed, followed by 10 minutes of helium TDC. Operation parameters(toroidal field, plasma current, gas puff, neutral beam heating) were fixed for these two discharges. Electron density and Dalpha emission clearly showed reduction of particle recycling by helium GDC/TDC.

6. Conclusion and Future Plans

(1) Helium glow discharge cleaning was effective in reducing oxygen and particle recycling. Carbon showed little reduction after helium glow.

(2) Both carbon and oxygen impurities were reduced by a factor of two by reducing the wall temperature from 300 to 150 degrees centigrade.

(3) After four months of tokamak operation and wall conditioning, Zeff during NBI heating(up to 18 MW) was still high 2.2 in high density($4.4 \times 10^{19} m^{-3}$) and confinement improvement by H-mode remained modest(40%). This motivates us to do more wall conditioning and implement powerful conditioning techniques(boronization).

Reference

[1] H.F. Dylla, P.H. LaMarche, M. Ulrickson, R.J. Goldston, D.B. Heifetz et al., Nucl. Fusion 27 (1987) 1221.

[2] G.L. Jackson, T.S. Taylor, S.L. Allen, J. Ferron, G. Haas et al., J. Nucl. Mat.162-164 (1989) 489.

[3] K.M. Schaubel and G.L. Jackson, "Electron Assisted Glow Discharges for Conditioning Fusion Tokamak Devices", General Atomics Report #GA-A19809 (1989).
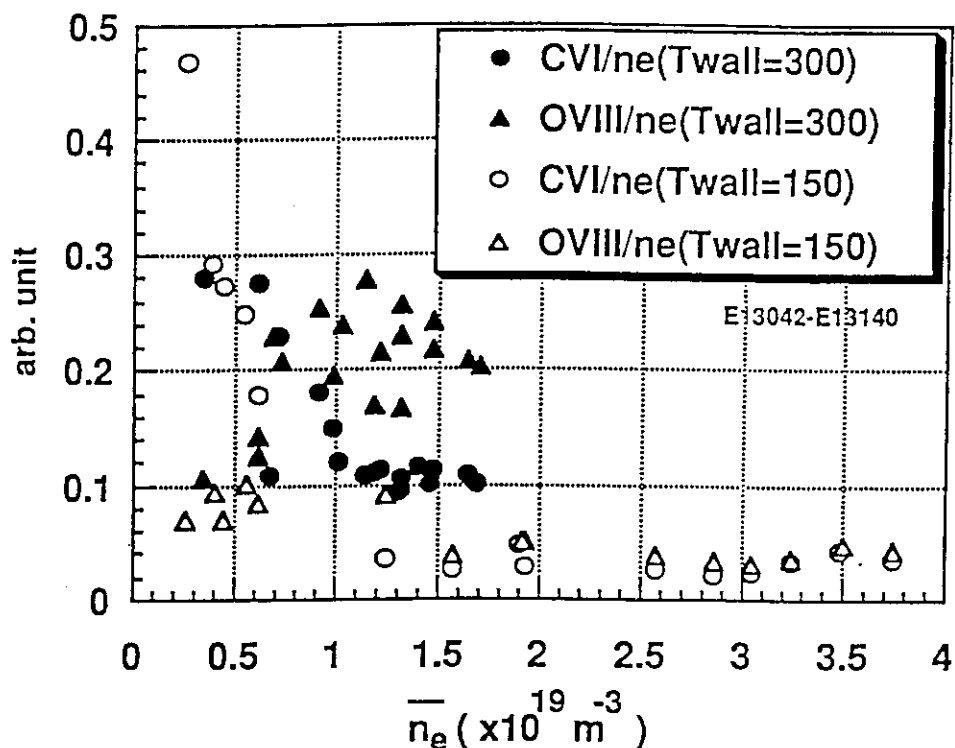
Figure 1 Carbon and oxygen emissivities normalized by electron density, with wall temperatures of 300 and 150 degree centigrade. Carbon and oxygen concentration was reduced by a factor of two by lowering the wall temperature,

OH, Ip=2 - 2.5 MA, Tw=280 deg., E13434-594
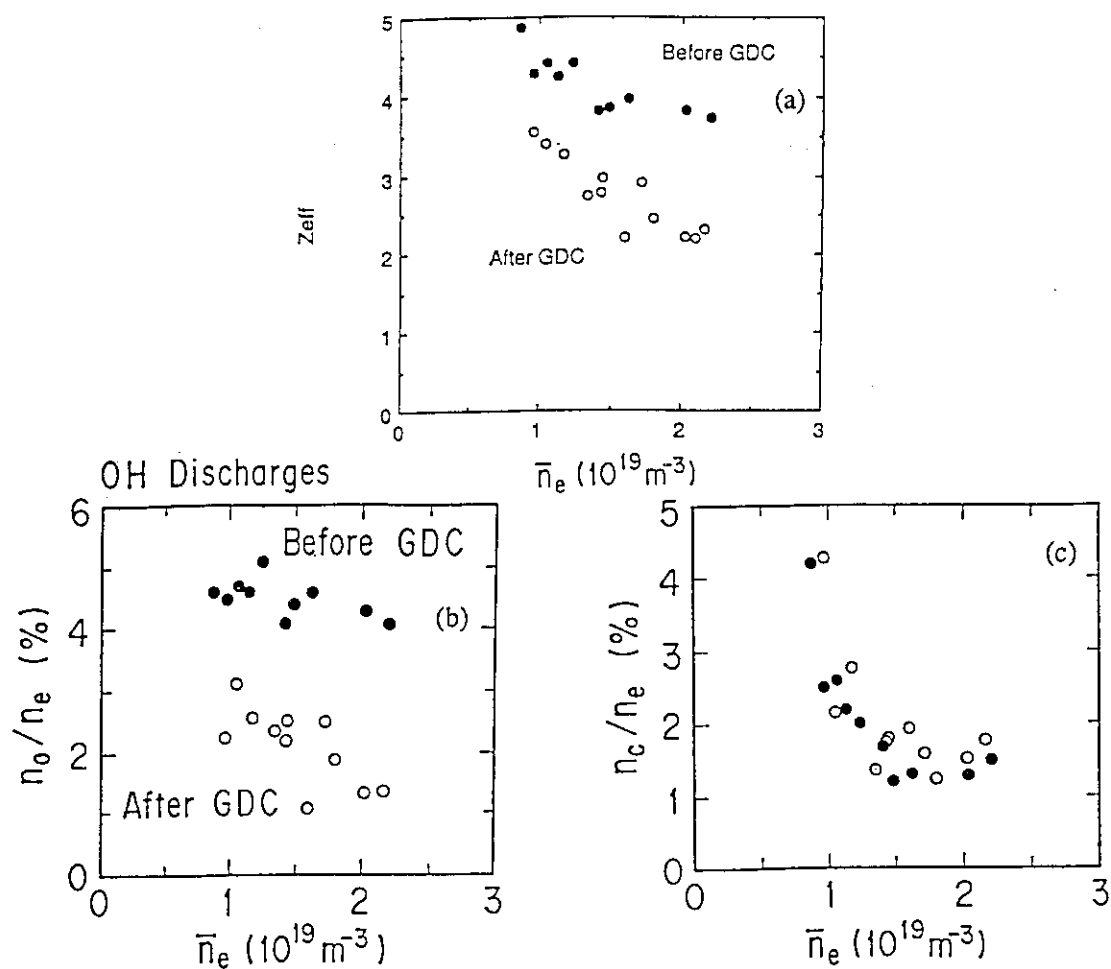
Figure 2 Comparison of (a) Zeff, (b) oxygen concentration, and (c) carbon concentration before and after the first glow cleaning.
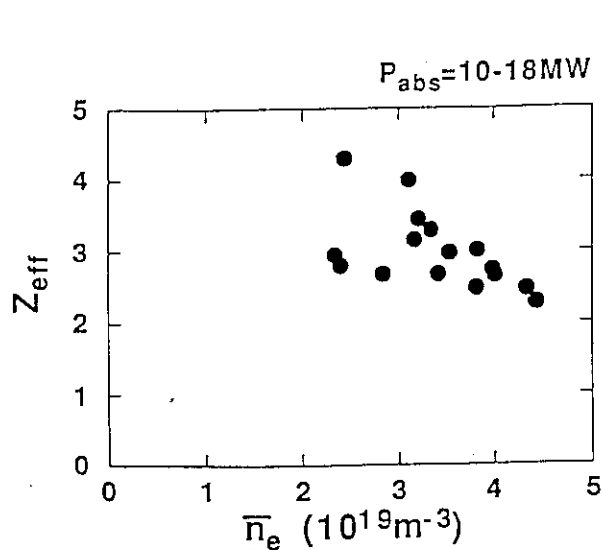
Figure 3 Zeff during NBI heating vs. line-averaged electron density.
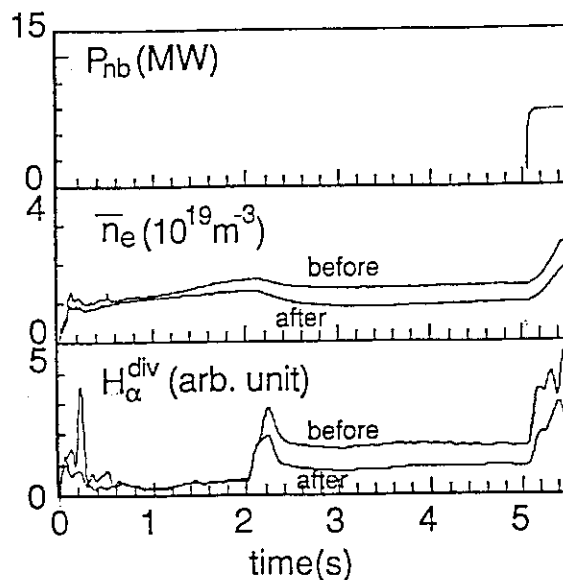
Figure 4 Comparison of two shots before and after 1 hour of helium GDC, followed by 10 minutes of helium TDC.

9 Study on D-D Reaction Particles

9.1 Neutron Calibration Experiment

T. Nishitani, H.Takeuchi, Cris W. Barnes*[1] and T. Iguchi*[2]

1. Introduction

The fusion neutron yield is most important parameter to estimate Q, because the generated fusion power is proportional to the neutron yield. Therefor the accuracy of the neutron yield is needed in the DD or DT operational fusion devices.The absolute calibration of the relation between the neutron source strength in the whole plasma and the output of neutron monitor is a most important problem in the measurements of the neutron yield. The calibration is rather difficult because the neutron source is distributed in the plasma which is surrounded with many complicated structures such as first wall, vacuum vessel poloidal and toroidal coils. Many efforts and time are devoted to the calibration at many tokamaks [1-7]. An moderated ^{235}U fission chamber is popular for the neutron yield measurement with temporal resolution in large tokamaks such as TFTR and JET. In TFTR [1-3] the calibration of the fission chambers has been performed by moving a ^{252}Cf neutron source, and each DD and DT neutron generator in the vacuum vessel. JET [4,5] has employed the calibration using ^{252}Cf neutron source.

2. Physical Description of Detectors and Calibration Apparatus

We employed three types of the neutron detector; ^{235}U and ^{238}U fission chambers, and ^{3}He proportional counter. Fission chamber, which is a ionization chamber of which wall is coated by fissile material such as ^{235}U and ^{238}U, is suitable for the neutron yield measurements for the DD plasmas. The ^{235}U detector is used in the low and medium neutron yield discharges and the ^{238}U detector is used in the high neutron yield discharges such as high-power NB heating experiments. The ^{3}He proportional counter has high detection efficiency. So the detector can obtain sufficient statics in the ^{252}Cf source calibration and plays a role of "temporary detector" to cross-calibrate less sensitive detectors using DD tokamak discharges.

Those detectors were placed on the torus midplane, just outside the toroidal field coils, at three different toroidal bays out of 18 Bays total: P-3 ; P-7 ; and P-13 . At P-3 and P-7 were located one each of a ^{3}He proportional counter, a ^{238}U fission chamber with 1.5 grams, and a ^{235}U fission chamber . At P-13 were another 0.3 gram ^{235}U detector by Toshiba, and another Reuter-Stokes ^{238}U detector, for 8 detectors total. The detectors have all long cylinders in geometry. The ^{235}U detector is surrounded 50 mm thick polyethylene of moderator, and 1 mm thick cadmium of thermal neutron shield, whose neutron sensitivity is estimated to be almost constant in the energy range of 0.55 eV to 2.5 MeV. The ^{238}U detector is surrounded by 50 mm thick lead of gamma shield only. The detectors were oriented vertically and place just beyond the outer diameter of the toroidal field coils to reduce the effects of the magnetic fields. Being in line with midplane ports,

the detectors had a minimum of shielding between themselves and the plasma neutrons. We use ^{235}U and ^{238}U fission chambers in both pulse counting mode and Campbell (MSV) mode, former is suitable for low count rate less than 10^6 cps and later is for high count rate more than 10^5 cps. A pair of the ^{3}He detector are operated in pulse counting mode only.

A remotely controlled source transfer system positioned the neutron point source in the vacuum vessel of JT-60 U. The source transfer system consisted of `train and track" is shown as shown in Fig.1. The ^{252}Cf source was lowered by a fishing line into a funnel into a vertical pipe where it was supported at a height 15 cm above the midplane of the torus (corresponding to the height of the magnetic axis for the lower-divertor plasmas of JT-60U). The pipe was then mounted on a flat ``train" that drove around a ``track" mounted inside the vacuum vessel. Actually the train was more like a moon rover car that travelled a road, with the car about 2 feet long and one foot wide. The source pipe was at one end of the car, and a TV camera was at the other end, with a broadcast unit mounted in the middle of the car. The road had an inverted ridge that the car steered along. The source pipe could be placed at two radial locations, corresponding to 3.42 m and 3.22 m major radius (typical equilibrium positions of the magnetic axis for standard and high elongated configurations, respectively). Most of the mass of the train and track was located below the midplane. The TV signal was broadcast out of the vacuum vessel to a receiver in the adjacent clean room, and then piped by wire into the diagnostic control room where a digital clock was added to the signal and recorded on a VTR.

The track was labelled every 0.5^0 with the toroidal angle from the center of Bay P-1 (the entrance port) of the source when the TV camera was looking at the label. The calibration was done point by point by moving the car to an angle, stopping, and counting for 1000 seconds (with a few points for 2000 seconds). The last 18 hours of calibration were an attempt to calibrate activation and track detectors, with the car kept in constant toroidal motion.

The ^{252}Cf source of 400 MBq manufactured by Amersham was used here. It had a calibrated source strength of 5.14×10^7 n/sec on March 25, 1991, and had decayed (with an assumed half-life of 966.1 days) to 4.78×10^7 n/sec by July 4 when the calibration began. The intensity remained constant during 5 days duration of the calibration. The ^{252}Cf source was sealed by stainless steel capsule of 7.8 mm diam. $\times$ 10 mm height. The angular emission is isotropic. The energy spectrum can be represented by a simple Maxwellian distribution of the form whose averaged neutron energy is 2.14 MeV, which is near 2.45 MeV for the DD neutron energy.

All eight detector signals were acquired into a LeCroy 8590 scaler under computer CAMAC control. The data from all the detectors except the ^{238}U ones were also acquired onto 6-digit manual scalers. The triggering of the computer and manual scalers was manual, with a count down used to synchronize the three buttons to be pushed. All of the sets of numbers (CAMAC and manual scalers values) were tabulated. The manual synchronization worked well enough, with good agreement between the various tabulations.

3. Calibration Results

The point efficiencies, counts per neutron from a point at a single angle, of the detectors at Bay P3 are shown in Fig. 2. Not only high-sensitive ^{3}He detector but also 0.3 g ^{235}U detectors have sufficient statistical certainty. The noise of the detectors at Bay P3 and P7 is quite low, so that meaningful data was obtained for the point source opposite side of the detectors. The point efficiencies can be integrated and averaged with angle to provide toroidal line efficiencies. Multiple data points at a single angle are first averaged together; the integrals using a simple Simpson's rule a cubic spline fit do not differ. The obtained toroidal line efficiencies are summarized in Table. 1. The data from the two major radii are very similar, with a typical reduction of only 2% for the 20 cm difference. The toroidal line efficiencies could also be obtained from the constant revolution of the source during the activation calibration. During a 1160 second revolution (16 turns) the scalers could be triggered, and over 9000 counts obtained in the 0.3 gram ^{235}U detectors. The resulting line efficiencies were indentical to the integrated point efficiencies.

Table 1.　　　Detector efficiencies for toroidal line source

| | Line efficiencies (counts/ source neutron) | | |
| | Integration of point efficiencies | | Constant revolution |
Detector	R= 3.42 m	R = 3.22 m	R = 3.42 m
^{235}U1	5.34×10^{-8}	5.26×10^{-8}	5.34×10^{-8}
^{235}U2	1.78×10^{-8}	1.74×10^{-8}	1.78×10^{-8}
^{235}U3	1.92×10^{-8}	1.88×10^{-8}	$(2.09 \times 10^{-8})*$
^{3}He1	3.27×10^{-6}	3.22×10^{-6}	3.27×10^{-6}
^{3}He3	2.83×10^{-6}	2.78×10^{-6}	2.83×10^{-6}

*　　　Including noise counts

4. Measurement Uncertainties for Neutron Yield

Neutral beam experiments are mainly interested in JT-60 Upgrade. In those experiments, the neutron yield exceeds 10^{14} n/s, where the pulse counting mode is not available due to pulse pile-up. In the range of neutron yield, we have to use Campbell mode or current mode. Campbell mode is employed for the high neutron yield in JT-60 Upgrade. The intensity of our ^{252}Cf source is too low to calibrate the fission chamber in Cambelling directly. So the cross calibration of the ^{235}U detector from the pulse counting mode to the Campbell mode was performed during the ohmically heated tokamak discharges in the rage of neutron yield 10^{11} - 10^{13} n/s, where the Campbell signal overlaps the pulse counting signal. Good linearity between the pulse counting and Campbell modes was obtained in the range of the neutron yield. Above the neutron yield of 10^{13} n/s, the count rate was saturated by the pulse pile-up and the dead time of the electronics. The standard deviation between the pulse counting and Campbell modes was 5% including the Fractuation of the Campbell electronics.

The sources of the calibration and measurement uncertainties are listed in Table 2, where uncertainties by the calibration hardware scattering, and the energy difference between ^{252}Cf and DD neutrons are estimated by the MCNP calculations. The linearity of the Campbell mode was investigated using a fission reactor by changing the output power step by step. The The total uncertainties are derived from the root-mean-square of each source uncertainty. The expected uncertainties in the neutron yield measurement are 10% for the pulse count mode (Sn $\leq 10^{13}$ n/s) and 11% for the Campbell mode (Sn $\geq 10^{12}$ n/s).

Table 2   List of measurement uncertainties for neutron yield

^{252}Cf source intensity	± 1.5 %
Statical error	± 0.3 %
Calibration hardware scattering	± 5 %
Energy difference between Cf and DD	± 6 %
Neutron source profile	± 5.5 %
Plasma position variation	± 2%
Statistical error in pulse counting mode	± 2%
Cross calibration pulse counting to Campbell mode	± 5 %
Campbell mode linearity	± 1 %

*1   Los Alamos National Laboratory
*2   University of Tokyo

References

[1]   H. W. Hendel, D. L. Jassby, H. S. Bosch, et al., Rev. Sci. Instrum. 59 (1988) 1682.

[2]   E. B. Nieschmidt, T. Saito, C. W. Barnes, et al., Rev. Sci. Instrum. 59 (1988) 1715.

[3]   H.W. Hendel, R.W. Palladino, et al., Rev. Sci. Instrum. 61 (1990) 1900.

[4]   O. N. Jarvis, J. Källne, G. Sadler, P. van Belle, et al., JET Report, JET-IR(85)06(1984).

[5]   O.N. Jarvis, G. Sadler, P. van Bell, T. Elevant, Rev. Sci. Instrum. 61 (1990)   3172.

[6]   G. Zankel, J. D. Strachan, R.Lewis, et al., Nucl. Instrum. Methods 185 (1981) 321.

[7]   M. Angelone, P. Batistoni, L. Bertalot, et al. Rev. Sci. Instrum. 61 (1990) 3157.
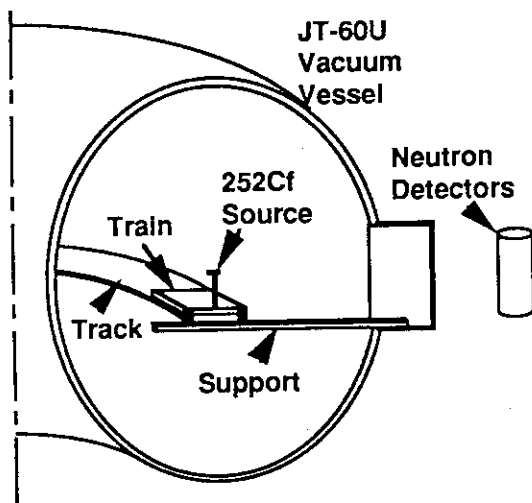
Fig. 1   Schematics of the source transfer system in the vacuum vessel of JT-60 Upgrade.
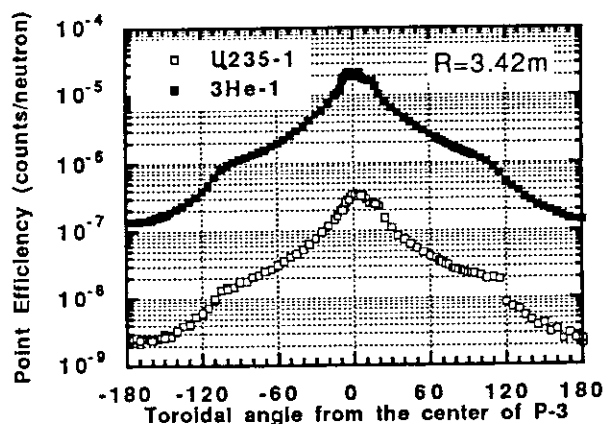
Fig. 2 Point efficiencies for ^{235}U and ^{3}He detectors in Bay P-3 versus toroidal angle of the point source.

9.2 Fusion Reactivity in D-D Plasma

T. Nishitani

1. Introduction

The initial D-D experiments were undertaken from July 18 to October 4 in 1991. The fusion reactivities of The D-D plasma have two major fusion reactions of $d(d,n)^3He$ and $d(d,p)t$ which have almost same reactivity. Therefor the D-D fusion reactivity R_{DD} is almost twice of the 2.5 MeV neutron yield S_n produced by $d(d,n)^3He$ reaction. Here the neutron yield S_n for the ohmically and NB heated plasmas have been investigated with the neutron monitors employing ^{235}U and ^{238}U fission chambers described in section 9.1. The R_{DD} (or S_n) and the fusion power multiplication Q_{DD} have been used to evaluate the plasma performance as well as the energy confinement time τ_e. It seems that the R_{DD} and Q_{DD} are more valuable than τ_e as a parameter of the plasma performance since those are more sensitive to the dilution of the core plasma. The R_{DD} of 7.0×10^{16} s^{-1} and 8.8×10^{16} s^{-1} were obtained in JET [1,2] and TFTR [3] , respectively, until the IAEA conference in Washington, DC. In JT-60U, many efforts have been devoted to optimize the fusion reactivity in this experimental period. Figure 1 shows the progress of the neutron yield on the initial D-D experiments of the JT-60U. The neutron yield increased gradually according to the degasing of the NB injection ports. Re-ionizing losses of the neutral beam in the injection ports were suppressed to be less than 10 % by the GDC which became available August 1991. Maximum neutron yield of 1.3×10^{16} neutrons / s was obtained in the high-Ti and hi-βp plasma (see section 4.6).
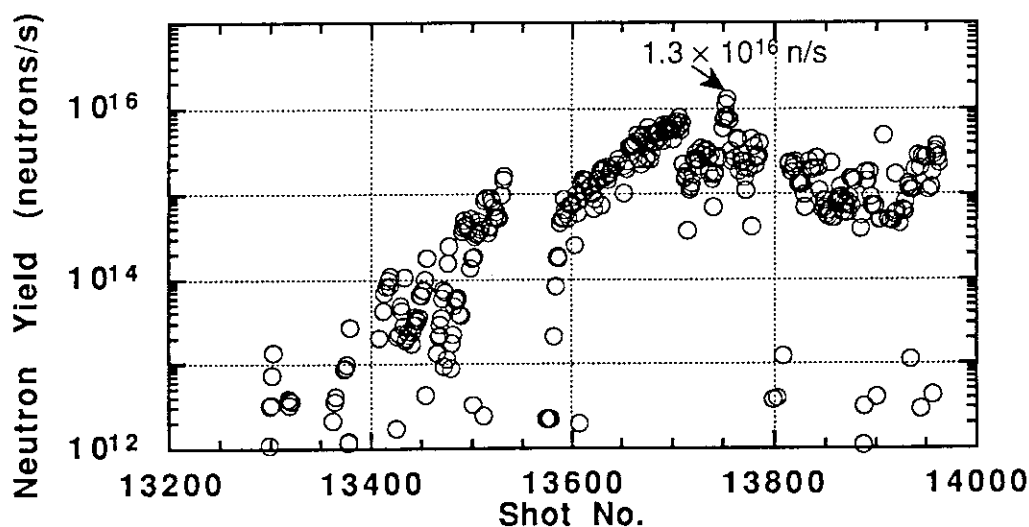
Fig. 1   Progress of the neutron yield on the initial D-D experiments of the JT-60U.

2. Fusion Reactivity of the Ohmically Heated Plasmas.

In JT-60U during 1991, the D-D discharge experiments have been made with the plasma current Ip in the range 1.0 to 3.5 MA. Figure 2 shows the neutron yield obtained in the ohmically heated discharges as a function of Ip. The neutron yield has a strong dependence on Ip, which is seems that higher Ip results in higher ion temperature and density. It reaches up to 10^{13} n/s at the Ip of 3 MA.

Figure 3 shows the neutron yields as a function of the stored energy measured with the diamagnetic loop for the ohmically heated discharges. The neutron yield has a strong dependence on the stored energy and is proportional to $\sim W_{dia}^2$ in the range of Ip from 2 to 3 MA. The neutron yield of the ohmically heated discharge is represented by

$$S_n = \int_0^a \frac{1}{2} n_D^2 \langle \sigma v \rangle 2\pi r \, dr$$

$$= \int_0^a \frac{1}{2} \left(\frac{n_D}{n_D + n_H} \frac{Z_{imp} - Z_{eff}}{Z_{imp} - 1} n_e \right)^2 \langle \sigma v \rangle 2\pi r \, dr \tag{1}$$

where $n_D/(n_D + n_H)$ is a deuterium enrichness, Z_{imp} is a impurity charge number, and $\langle \sigma v \rangle$ is a D-D fusion reactivity which is the strong function of the ion temperature. The has a dependence on $\sim T_i^4$ around the 2 keV of Ti which is a typical ion temperature of the ohmically heated discharges with Ip of 2 to 3 MA. Therefor, the relation between the neutron yield and the stored energy for the ohmically heated discharge is obtained by

$$S_n \propto n_D^2 \, T_i^4 \propto W^2 \quad \text{(for Ip 2 - 3 MA)} \tag{2}$$

where $T_i \propto T_e$ and $n_D \propto n_e$ are assumed. The experimental results showed in Fig. 3 agree with the prediction by Eq. (2).
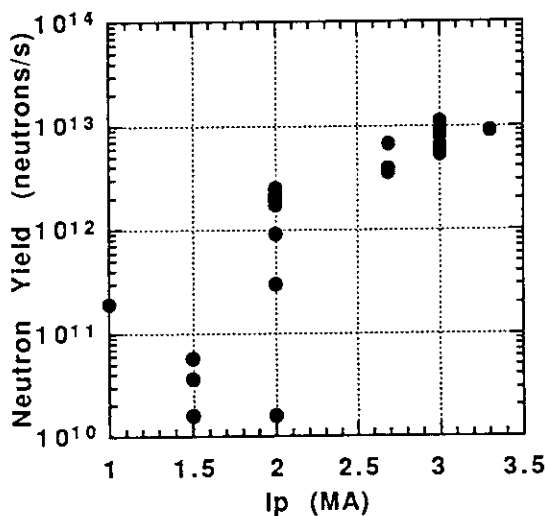
Fig. 2 Neutron yield plotted against the plasma current for the ohmically heated discharges.
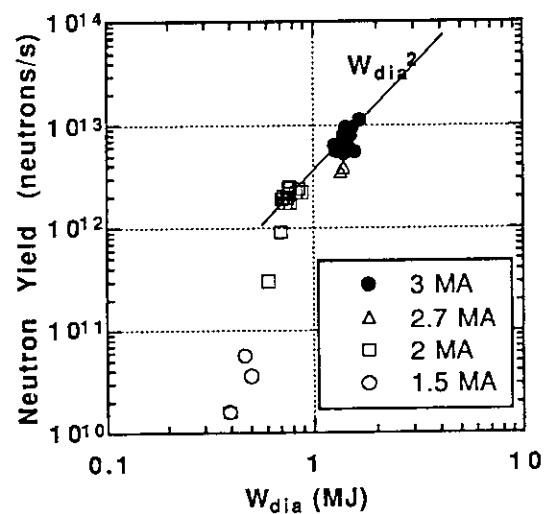
Fig. 3 Neutron yield plotted against the stored energy for the ohmically heated discharges.

3. Fusion Reactivity of the Neutral Beam Heated Plasmas.

The experiments of the fusion reactivity optimization have been made by using deuterium NB injection heating with the power level up to 22 MW. The beam energy was in the range 80 to 95 keV. The highest fusion reactivity was obtained in a high βp plasma in terms of high Ti mode features provided by relatively small radius plasmas with the NB injections passing through the core region , where following parameters were achieved; the neutron yield Sn = 1.3 × 10^{16} n/s, the ion temperature T_i^{CXRS} (r/a = 0.16) = 22 keV, the electron temperature T_e^{ECE} (r/a = 0.18) = 6.6 keV (see section 4.1).

The total neutron yield from the NB heated plasma is made up of these contributions: the thermal-thermal contribution, the beam-thermal contribution and the beam-beam contribution. The three terms scale in the following manner:

$$S_n = \frac{P^2\,T_e^3}{\langle n_e^2\rangle V} K_1 (E_0 , T_e) + \left\langle\frac{n_D}{n_e}\right\rangle P\,T_e^{3/2} K_2 (E_0 , T_e, T_i) + n_D^2\,V\,K_3 (T_i) \tag{1}$$

where Sn is the neutron source strength, P in the input power, V is the plasma volume, and the function Ki is the fusion reactivity <σv> averaged over the respective distribution functions. The relatively weal dependence of K_2 on T_i aries mainly through the thermal distribution function. The beam-thermal contribution is dominant in the steady state phase of the most of the JT-60U operation condition. To maximization of the beam-thermal contribution, both electron and ion temperature need to be high which implies low density operation. The T_e needs so high that the injected deutrons slow down on ions and heat them. Once the critical energy E_C ($\approx$ 15 T_e) becomes higher than beam energy, the neutron yield becomes essentially independent of T_e. The benefit of high T_i values is mainly due to the increase of the thermal-thermal reactivity as well as the beam-thermal one with T_i. The low density target plasma, low plasma current and the wall conditioning by the GDC were required.
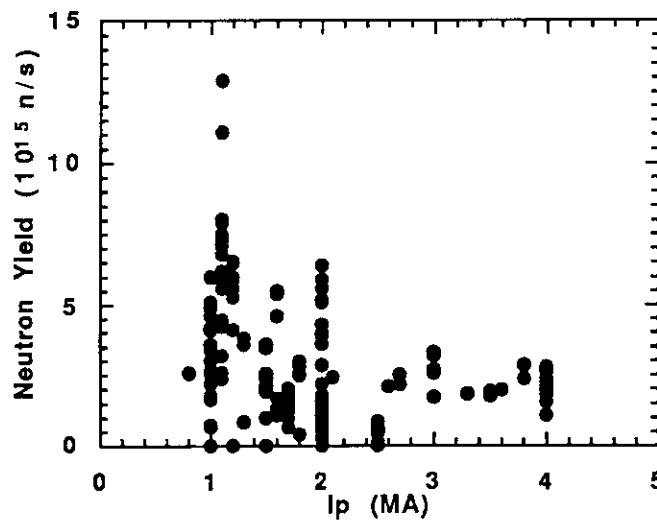
Fig. 4   Neutron yield plotted against the plasma current for the NB heated discharges

Figure 4 shows the neutron yield obtained in the NB heated discharges as a function of Ip, over most of the injection power. The neutron yield was maximized at relatively low plasma current Ip = 1.1 MA, which associated with low initial target density. This is very similar to the result of the initial supershot experiments in TFTR [4]. The neutron yield of the discharges with Ip $\leq$ 1 MA is limited by the interlock of the armor tile temperature due to the NB shinethrough which terminates the discharge. In the discharges with Ip = 1.1 MA, the neutron yield was limited to be ~ 7 $\times$ 10^{15} n/s in the ELMy phase but increased linearly until the βp collapse occured.

The maximum neutron yield during a pulse increases strongly with the heating power as shown in Fig. 5. The upper boundary of the neutron yield varied as ~ P$^{1.8}$ where P is the heating power in the TFTE super shots [3]. In JT-60U, it looks like to vary as P$^{2.5-3}$. It is provably because that the neutron yield has not been maximized in the medium and low heating power regime (Pabs < 15 MW). The variation of the neutron yield and the stored energy are well correlated also in the NB heated discharges. When the neutron yield is plotted against the stored energy, the linear dependence of the Sn on W^2 is found for each plasma current as shown in Fig. 4.1 of section 4.1.
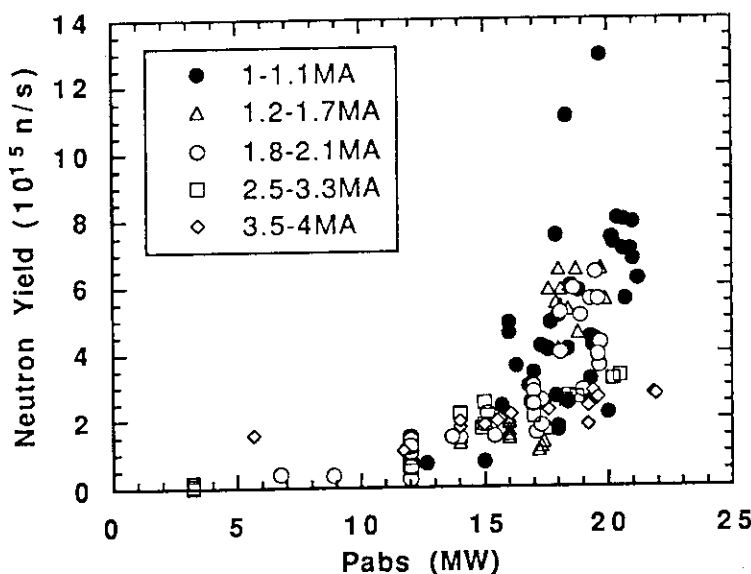
Fig. 5   Neutron yield as a function of the absorbed heating power.

References

[1]   G. Sadler, J.M. Adams, et al., Proc. 17th Europ. Conf. 14B, Part I, (1990) 117.

[2]   The JET team,in Plasma Physics and Controlled Nuclear Fusion Research,IAEA-CN-5 3/A-1-2 IAEA, Vienna (1990).

[3]   D.M. Meade, A. Arunasalam, C.W. Barnes, et al.,in Plasma Physics and Controlled Nuclear Fusion Research,IAEA-CN-53/A-1-1, IAEA, Vienna (1990).

[4]   H.W. Hendel, D.L. Jassby, et al., Proc. 14th Europ. Conf. 11B, Part I, (1987) 53.

9.3 Triton Burn-up

T. Nishitani and Y. Ikeda

The time resolved triton burnup was measured by the 14 MeV neutron detector. The triton burnup ratio was 0.2-2%, in the NB heated plasma. The triton burnup ration averaged in the period July 18 to October 4, 1991 was measured with the foil activation technique employing $^{93}Nb(n,2n)^{93m}Nb$ and $^{58}Ni(n,p)^{58}Co$ reactions. The averaged triton burnup ratio of 0.5% is consistent with the result from the time resolved measurements. The 1 MeV triton slow down is investigated by the 14 MeV neutron detector, which shows reasonable agreement with the classical theory within the measurement uncertainties.

1. Introduction

The behavior of the 1 MeV triton produced in the D(d,p)T reaction is important to prospect the that of DT produced 3.5 MeV alphas because the 1 MeV Triton and 3.5 MeV alpha have similar confinement properties such as larmor radius and presetion frequency. The confinement and slowing down of the fast tritons are investigated by measuring the ratio of 14 MeV and 2.5 MeV neutron production rate. Tritons of 1.0 MeV are produced in the D(d,p)T reaction at the same rate as the 2.5 MeV neutrons from the $D(d,n)^3He$ reaction. The majority of these tritons will remain confined in the plasma and slow down to thermal energies through Coulomb collisions with electrons and ions. A fraction will undergo fusion reaction $T(d,n)^4He$, in which the 14 MeV neutrons are emitted. Strachan[1] shows that the slowing down process of the 1 MeV Triton are not anomalous in TFTR[1]. JET people indicates that the triton confinement and slowing down in the JET plasma are consistent with the classical prediction within the 20 % uncertainties and that triton diffusion coefficient is very small, << 0.1 m^2/s[2-4]. In JT-60U, time resolved and averaged triton burnup measurements were carried out by the 14 MeV neutron detector and the foil activation technique, respectively.

2. Time Resolved Triton Burnup Measurements

The 14 MeV emission rate is measured with silicon surface barrier diode (SBD). The 14 MeV neutrons entering a silicon diode may undergo the following nuclear reactions:

$^{28}Si (n,p) ^{28}Al$ Q = -3.85 MeV

$^{28}Si (n,a) ^{25}Mg$ Q = -2.65 MeV

The high Q-value and the Coulomb barrier inhibiting the escaping of charged particles from the compound nucleus combine to produce effective thresholds of about 7 MeV. Thus, the above reaction channels are not open to the far more abundant 2.5 MeV neutrons.

Figure 1 shows the schematics of the 14 MeV neutron detector on JT-60U. The SBD is mounted in the 20 cm-thick lead cylinder to shield gamma-rays from neutron capture events in the surrounding structure. The detector is installed just outside of the JT-60U vacuum vessel and on

the midplane but inside the toroidal field coils, as close to the plasma as possible. The SBD used in this work has a are of 300 mm^2, a nominal depletion depth of 1500 μm, which is sufficient to stop the 10 MeV protons and alphas made by above nuclear reactions, and a bias voltage of 275 V. A disk with ^{241}Am alpha particle source is mounted in front of the SBD to make energy calibration of the detector by 5.486 MeV alphas.

Signals from the SBD is transmitted to the conventional pulse counting electronics (preamplifier, linear amplifier and single channel analyzer). The discrimination level of the single channel analyzer is set just above the alpha particle energy of the ^{241}Am source. The pulse counting signals are acquired into CAMAC multi-time-bin scalar with typical accumulation time of 10 ms.
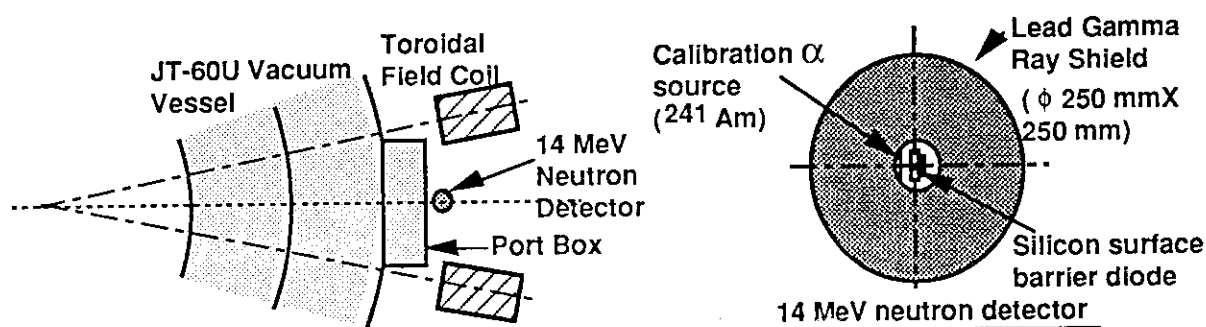
Fig. 1 Schematics of the 14 MeV neutron detector on JT-60U

We have a plan of the detector calibration for the 14 MeV neutrons using the 14 MeV neutron generator of the FNS facility. So far the detector is not calibrated by the neutron source, we make cross-calibration by the fission chambers which have same detection efficiencies for 2.5 MeV and 14 MeV neutrons. The decay of the neutron emission rate after the NB turn off has fast and slow component. The former is due to the decay of the beam fast ions, and later is 14 MeV neutrons. The 14 MeV neutron detector was calibrated by the fission chamber in the slow component dominant phase after the NB turn off.

Figure 2 shows the time traces of the 2.5 and 14 MeV neutron yield in the deuterium beam heated discharge. The 2.5 MeV neutron emission is measured with three pairs of ^{235}U and ^{238}U fission chambers. The cross-section of the T(d,n)^{4}He reaction has a maximum value around the triton energy of 170 keV. The 1 MeV tritons generated by T(d,n)^{4}He reaction slow down and burn around the energy of 170 keV. Therefor the time trace of 14 MeV neutron yield is delayed for slowing down time from 1 MeV to 170 keV, ts (1 MeV, 170 keV). In this case, the ts is derived to be 300±50 ms (9.7 s) and 350±50 ms (10.2 s) from the time delay between the negative spike of 14 MeV neutron yield and the NB power due to the break down of the ion sources.

Figure 3 shows the shot-averaged triton burnup ratio obtained in the NB heated discharges with relatively high electron density. The data dose not include the ones of the high Ti mode discharges. It is seen that the triton burnup ratio increases with the plasma current, which is probably because that the prompt orbit loss of the 1 MeV triton is reduced with the plasma current.
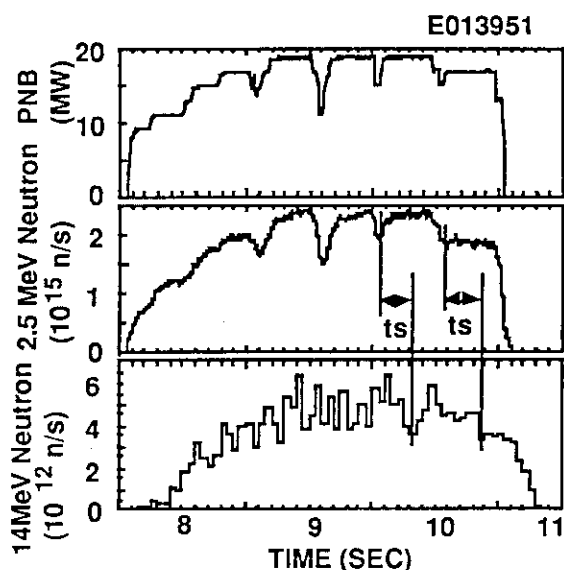
Fig. 2 Time traces of NB power, 2.5 and 14 MeV neutron yield in the deuterium beam heated discharge.
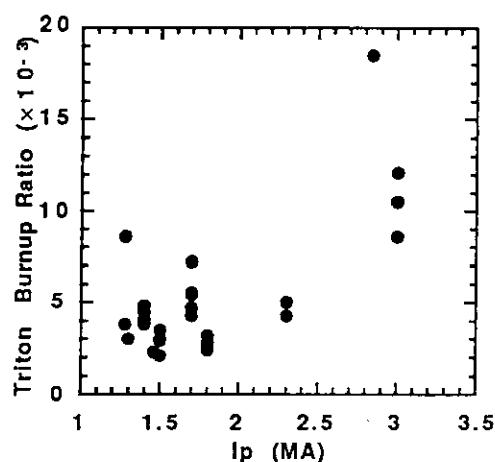
Fig. 3 Triton burnup ratio plotted against the plasma current.

3. Averaged Triton Burnup Measurement with the Foil Activation Technique

The triton burnup ration averaged in the period July 18 to October 4, 1991 was measured with the foil activation technique. The reaction of $^{63}Cu(n,2n)^{62}Cu$ ($T_{1/2}$ = 9 min) is popular to determine the 14 MeV neutron flux from the triton burnup among other tokamaks such as JET and TFTR. No sample transfer system is available at the present moment in JT-60U, we have to chose the activation reaction with rather long half-life. Thus the $^{93}Nb(n,2n)^{92m}Nb$ was used as the detector for the 14 MeV neutrons because the the reaction has high threshold energy of 9 MeV, flat response around 14 MeV, and considerably large cross-section. However, the half-life of 10.15 days is too long to match the measurement shot by shot. but seems better for long period irradiation in the present DD-discharge experiments. In the same reason, the $^{58}Ni(n,p)^{58}Co$ ($T_{1/2}$ = 70.2 days) was assigned as the detector for 2.5 MeV neutron flux.

Foils of Ni and Nb were placed in the re-entrant port for the TV camera of the P-3 section. The foils were irradiated throughout the first series of DD discharge experiment from July 18, 1991 to October 4, 1991 for 6,385,100 sec. The activation reaction rates were obtained by using the gamma-ray counts measured with a Ge detector. It is necessary to correct for saturation of the activity during the long period of the operation. In particular, the reaction rate of $^{93}Nb(n,2n)^{92m}Nb$ suffered from the rather short half-life of the products ^{92m}Nb being 10.15 day. Using the same manner described in section 9.4, the reaction rates were corrected. The cross-section values at 2.5 Mev and 14 MeV corresponding those reactions were taken from JENDL Dosimetry File. Assuming the cross-section, the neutron fluxes of 2.5 MeV and 14 MeV were calculated by using the reaction rated of $^{58}Ni(n,p)^{58}Co$ and $^{93}Nb(n,2n)^{92m}Nb$, respectively. The averaged triton burnup ration was derived to be 0.54 ± 0.03 % in this experimental period. This value showed reasonable agreement with the results of the time resolved measurements.

4. Analysis of the 1 MeV Triton Slowing Down

A full calculation of the time dependent triton burnup should include the variation of the plasma parameters in space and time. Here simple analysis of the triton slowing down is made. If the 1 MeV triton slowing down is classical, the energy loss rate is represented by following formula:

$$\left(\frac{dE}{dt}\right)_{classical} = -\frac{\alpha}{\sqrt{E}} - \beta E$$

$$\alpha = 1.81 \times 10^{-13} \ln \Lambda_{ii} A^{1/2} Z^2 \sum_j \frac{n_j Z_j}{A_j}$$

$$\beta = 3.18 \times 10^{-15} \ln \Lambda_{ei} \frac{Z^2}{A} \frac{n_e}{(T_e)^{1.5}} \qquad (1)$$

where E is the triton energy , Te is the electron temperature both in eV, ne is the electron density in m^{-3} and $\ln \Lambda$ is the Coulomb logarithm. A and Z are the triton mass and charge number; n_j, A_j, and Z_j are the impurity density in m^{-3}, mass and charge numbers, respectively. First term of R.H.S. of the Eq(1) is the slowing down in electrons and second on is on ions. Analytical solution of the Eq(1) gives the slowing down time of the triton from E1 to E2, ts(E1,e2), as,

$$t_s (E1,E2) = \frac{2}{3\beta} \ln \left| \frac{\beta E1^{3/2} - \alpha}{\beta E2^{3/2} - \alpha} \right| \qquad (2)$$

In this work E1 = 1 MeV and E2 = 170 keV. Because the E2 is larger than critical energy Ec ($\approx$ 24 Te) in almost case, slowing down term on ions of Eq.(1) can be neglected. Therefor Eq(2) is rewritten to simple form as

$$t_s(E1,E2) \approx \tau_{se} \ln (E1/E2)$$

$$= 1.78 \ \tau_{se} \qquad \text{(for E1 = 1 MeV and E2 = 170 keV)}, \qquad (3)$$

where τ_{se} is slowing down time on electrons defined by $1/\beta$.

The slowing down time ts cording to Eq. (2) for the discharge sown in Fig. 2 was 300 ms which was coincide with the experimental values within the measurement uncertainty. Here, we used the plasma parameters such as ne and Te for the averaged minor radius defined by

$$\langle r \rangle = \frac{\int_0^a r \, Sn \, (r) \, dr}{\int_0^a Sn \, (r) \, dr} \qquad (4)$$

where Sn(r) is the neutron source profile calculated by the 1.5 D tokamak code.

References

[1] J.D. Strachan, S.J. Zweben, C.W. Barnes, et al.,in Plasma Physics and Controlled Nuclear Fusion Research,Vol.1, IAEA, Vienna (1990) 257.

[2] S. Conroy, O.N. Jarvis, G. Sadler, G.B. Huxtable, Nucl. Fusion **28** (1988) 2127.

[3] S. Conroy, O.N. Jarvis, et al., Proc. 17th Europ. Conf. 14B, Part I, (1990) 98

[4] O.N. Jarvis, J.M. Adams, et al., Proc. 18th Europ. Conf. 15B, Part I, (1991) 21

9.4 D-D Neutron Production Measurement by Foil Activation Technique

Y. Ikeda, N. Miya, T. Nishitani and H. Takeuchi

1 Introduction

The foil activation technique has been applied to measure D-D plasma burning rate as a part of burning plasma diagnostics in JT-60U D-D discharge experiment. As the absolute sense, it is worthwhile to establish the foil activation method as a complemental technique for the fission chamber. Foil activation technique is inherently the integral method which is insensitive to time dependency of the neutron yield. Pneumatic sample transfer system is essential to realized the data acquisition for each shot. Unfortunately, the system is under planning for the installation. We have to wait until next fall in 1992. Considering that the present stage was a testing phase of the technique, we focused on feasibility test on giving the reasonable agreement of the neutron data with that of the fission chamber. Depending on the operation schedule, we had to leave sample at the position over one or two weeks, because the access into the machine room was so limited from the health physics point of view.

2 Activation Foil Detector

In order to detect the D-D neutrons with mean energy of 2.45 MeV, the cross section of the activation reaction should have low threshold. In this context, two standard dosimetry reactions were chosen; $^{58}Ni(n,p)^{58}Co$ and $^{115}In(n,n)^{115m}In$. The profile of two reactions are summarized in Table 1 along with reactions which were used in the D-D discharge experiment to add the information of the neutron spectrum.

Table 1. Reactions and associated decay data

Reaction	Abundance	$T_{1/2}$	Eg(keV)	I_γ	Threshold(keV)
$^{115}In(n,n')^{115m}In$	0.9577	4.49 h	336.24	0.467	0.336
$^{58}Ni(n,p)^{58}Co$	0.6776	70.8 d	810.76	0.994	1.0
$^{47}Ti(n,p)^{47}Sc$	0.0732	3.35 d	159.4	0.68	1.0
$^{64}Zn(n,p)^{64}Cu$	0.4889	12.7 h	511	0.358	1.5
$^{197}Au(n,\gamma)^{198}Au$	1.0	2.696 d	411.80	0.955	---

3 Calibration run for the determination of source neutron intensity

Thick foils of Ni (50 mm in dia. x 5 mm in thickness) and In (30 mm in dia. x 3 mm in thickness) were placed at several position inside an outside of vacuum vessel of JT-60U and irradiated for 18 hours with neutrons of ^{252}Cf (4 x 10^7/s), the source of which was moved along the rail of circular orbit fixed at the middle of the tours. After irradiation, gamma-rays emitted from

the samples were measured with Ge detectors. As expected, counting rate was very weak. The reason why we used such a large foils was due to the extremely low neutron flux. The measured reaction rates were 1.35 x 10^{-23}/s and 6.80 x 10^{-24}/s for ^{115}In(n,n) and ^{58}Ni(n,p), respectively.

Assuming neutron spectrum measured at FNS as the DD neutron spectrum, which had the peak at 2.45 MeV with some low energy tail, a conversion coefficient (CF) for the neutron source intensity from ^{252}Cf neutron to DD neutron was calculated using the spectrum of ^{252}Cf spontaneous fission spectrum and reaction cross sections. The differential sensitivity of reactions to both spectra are illustrated in Fig. 1. The determined CFs are listed in Table 2.
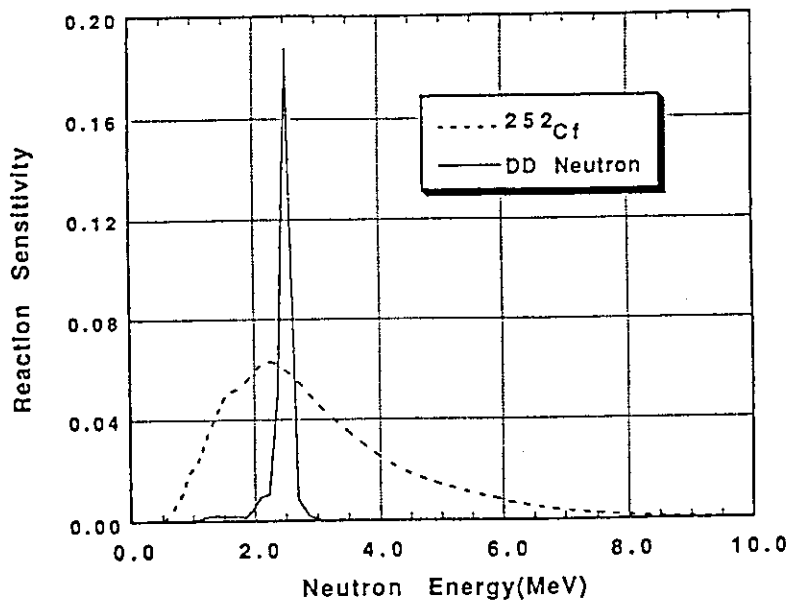
Fig. 1 Differential reaction sensitivities of ^{115}In(n,n')^{115m}In for ^{252}Cf and DD neutron spectra.

Table 2. Calculated reaction sensitivity per source neutron

Reaction	252Cf	D-D	CF(D-D/252Cf)
115In(n,n')	0.1824	0.2851	1.563
58Ni(n,p)	0.1147	0.07903	0.6912

CF=conversion coefficient

The statistical error dominated the total experimental errors. The systematic error in the neutron spectra for both ^{252}Cf and DD are also considered not to be negligible. The uncertainty associated with the assumption of neutron spectrum could range within 10 %. Of cause, a further analytical calculation is needed to make it more accurate.

4 Neutron production determination during DD-discharge experiment

Basic idea was measurement of total neutron productions during 4 days operation. At the beginning of the week, foils were set at the position corresponding to the location where the conversion coefficient was calibrated in the calibration run; at the bottom of the camera port in P3 section. The foil package including Ni, In, Ti, Zn and Au sealed with KAPTON film was attached at the end of bar pilex glass and inserted so as to make the end touched on the bottom camera port of P3. On the next day of the last shot in the week operation, the packaged was taken out and the activation rates were measured with Ge detectors. The correction of the reaction rates for the saturation of radioactivity during the shots was essential since the half-lives of ^{115m}In, ^{47}Ti, ^{64}Cu and ^{198}Au, products of the reactions of interest, are shorter than the length of irradiation period. We have measured five different operation periods for a week or two successive weeks. In Table. 3, the irradiation time, total neutron yields obtained from fission chambers are summarized.

To arrive at the final neutron production rate, Y_n, the relation with the calibrated conversion coefficient given as,

$Y_n = I*RR_{dd}/(RR_{cali}*CF)$,

where,

I: source intensity of ^{252}Cf (/sec),

RR_{dd}: reaction rate during D-D discharge,

RR_{cali}: reaction rate during calibration,

CF: conversion coefficient,

was used.

Table 3 Irradiation time and total neutron yield

Run #	Irradiation Time(sec)	Total Neutron
1	3.3775E+5	1.384E+15
2	3.3726E+5	1.889E+16
3	3.3667E+5	2.643E+17
4	3.3648E+5	1.420E+17
5	9.4194E+5	3.018E+17

The results are tabulated in Table 4 along with the data given by fission chambers for comparison. The large part of the experimental error was attributed to the counting statistics in the calibration experiments. All data except one measured by activation method are in good agreement within experimental error with data of the fission chamber. The exception was attributed to the allocation of the foil position during the irradiation. Figure 2 gives ratios of total neutron production by activation measurements to those by fission chamber.

The mean energy of D-D neutron has been estimated based on the reaction rate ratio of ^{64}Zn(n,p)^{64}Cu and ^{115}In(n,n')^{115m}In using relationship between the neutron energy and reaction

rate ratios measured at FNS. Low energy tail in the neutron spectrum should be taken into account for the correction of the reaction rate. However all of reaction cross section have the threshold

Table 4   Summary of average Neutron Yield

Run #	$^{115}In(n,n')$	$^{58}Ni(n,p)$	Fission Chamber
1	4.31E+9	4.55E+9	4.10E+9
2	2.53E+9	3.19E+10	5.60E+10
3	7.11E+11	7.16E+11	7.85E+11
4	--------	4.84E+11	4.22E+11
5	--------	2.92E+11	3.20E+11
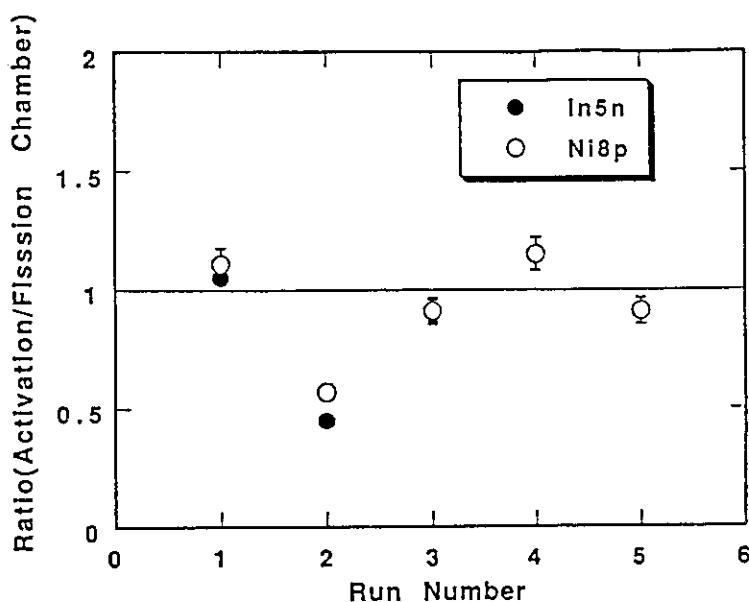
Fig. 2   Comparison of neutron yield between activation technique and fission chamber.

energy closely below the D-D peak energy at 2.5 MeV, it was expected that the contributions were not so large. It should be less than 10 % at most for the $^{115}In(n,n')^{115m}In$ with lowest threshold energy. The ratio of 0.079±0.003 is corresponding to the neutron energy of 2.45 MeV showing a remarkable agreement with the energy expected from reaction kinematics.

5 Summary

The foil activation technique has been applied to measure the D-D plasma burning rate in JT60-U DD-discharge experiment. Although it should be the integral measurement of neutron production rate over a week or two weeks, the activation method gave excellent results consistent to the data taken by the fission chamber. The present test demonstrated the feasibility of the activation technique. In order to obtain the data of each shot, however, a pneumatic sample transfer system will be essential.

9.5 Spatial Profile of Neutron Flux in Torus Hall

Y. Ikeda, N. Miya, K. Oishi*, N. Toyoshima, T. Nishitani and H. Takeuchi

1 Introduction

It is of importance to measure the neutron flux spacial distribution in the machine room during the JT-60U DD discharge experiment in terms of assessment of induced activity and dose rate after shutdown. In addition, the data is valuable for the testing the calculation code capability with a model of extremely complicated configuration. The foil activation technique was employed to measure the neutron flux distribution.

As the primary energy of neutron of 2.5 MeV is generated in the plasma, two partes of spectrum were considered; high energy neutrons around 2.5 MeV and low energy neutrons near thermal energy. As the activation detectors sensitive to those energy regions, $^{58}Ni(n,p)^{58}Co$ and $^{59}Co(n,\gamma)^{60}Co$ were chosen. In addition to $^{59}Co(n,\gamma)^{60}Co$, the detector of $^{197}Au(n,\gamma)^{198}Au$ was used to measure the distribution in a particular direction.

2 Foil Activation Measurement

A numbers of sets of foils were deployed around JT-60U machine room. A schematic arrangement of position where the foils were placed is given in Fig. 1. In the present measurement, two spacial directions, namely Horizontal and Vertical, were considered to get typical profile for the neutron flux distribution.

Schematic drawing of Activation Detector Positions in JT-60U
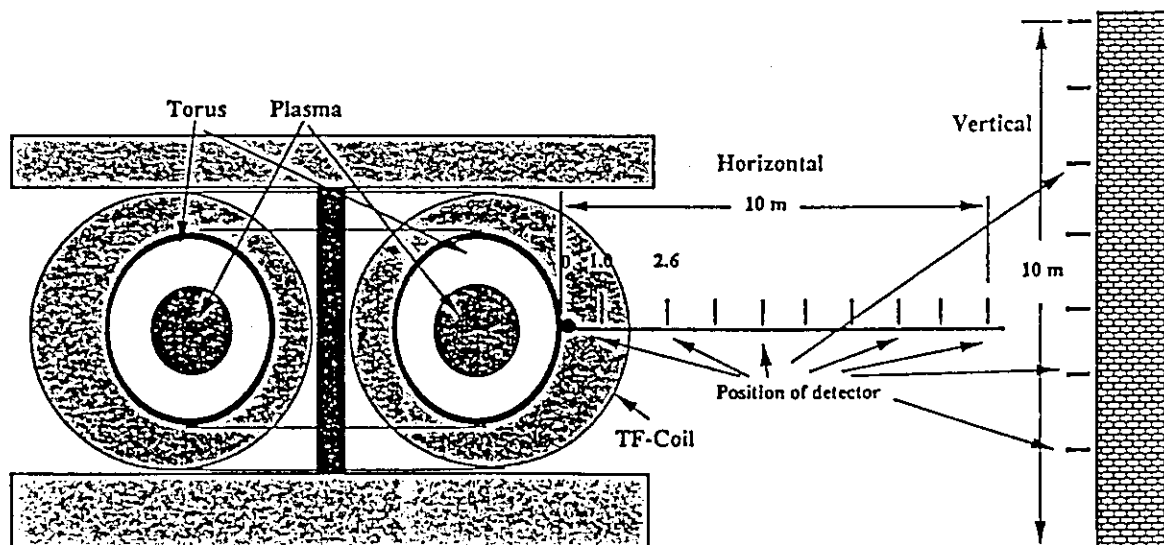
Fig. 1 Schematic drawing of locations of foil packages in JT-60U torus hall.

The foils were irradiated by neutrons from the first DD shot to the last shot. The number of total neutron production was 7.2844×10^{17} throughout the irradiation. After irradiation, the activity of each foil was measured with Ge detectors. It took about two month to almost finish the counting because of a large number of foils and week activities due to relatively long half-lives of ^{58}Co ($t_{1/2}$=70.8 d) and ^{60}Co ($T_{1/2}$=5.4 y). Still counting of some foils are underway. The reaction rate was obtained in a unit per atom on the assumption that the neutron production rate was uniform over the irradiation. As described in Section 5.3.4, the correction for the saturation of activities was necessary, in particular, for $^{197}Au(n,g)^{198}Au$ ($T_{1/2}$=2.7 d), because of long irradiation period for about 2.5 months (6,385,100 sec). At present moment, no self-shielding effect in the foils was considered. The experimental errors range from ± 3 to ± 10 % depending on the γ-ray counting statistics.

3 Discussion of Neutron Flux Distribution

Figure 2 shows the reaction rate distributions along Horizontal direction. The reaction rate of $^{58}Ni(n,p)^{58}Co$ exhibited a steep decreasing profile in the distribution with the distance of position from the torus. This is due to the threshold type reaction of $^{58}Ni(n,p)^{58}Co$. However, the distribution curve shows slower decrease than that by $1/r^2$. This is because of distributed D-D neutron source around the torus. Moreover, it could be expected that some local attenuation of the primary D-D neutron by massive structural materials such as TF-Coil. As for the reaction of $^{197}Au(n,\gamma)^{198}Au$ and $^{59}Co(n,\gamma)^{60}Co$ as shown in Fig. 2, reaction rates decrease slowly as the distance increases. The distributions become almost flat at distances further than 5 m. The results indicated that the low energy neutrons distributed all around the machine room. The difference in the absolute reaction rates between $^{197}Au(n,\gamma)^{198}Au$ and $^{59}Co(n,\gamma)^{60}Co$ is simply corresponding to difference in the cross sections at the resonance regions and thermal energy.
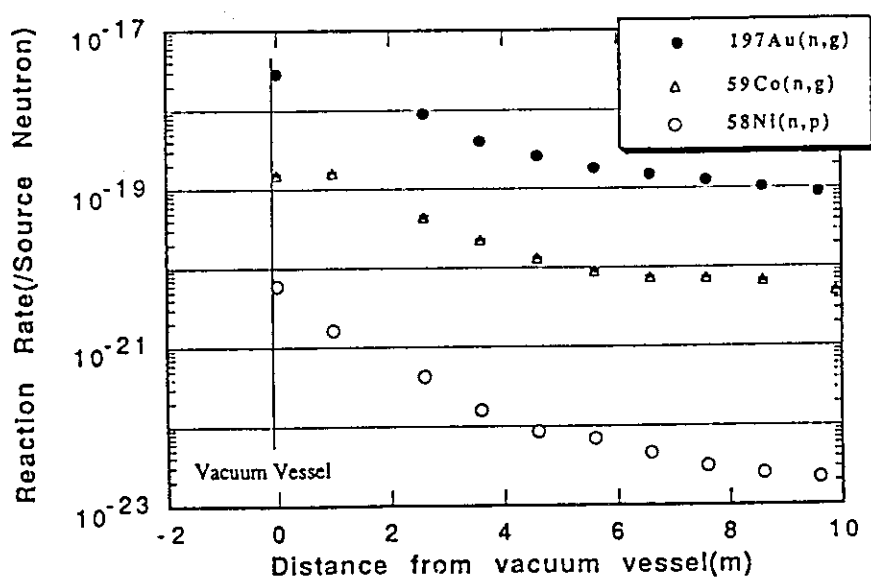
Fig. 2 Reaction rate distribution along the horizontal direction.

The distribution along Vertical direction is shown in Fig. 3. Since measurements for remained Ni foils are now in progress, only three data are available. For this reaction, only a sign for the increase in the reaction rate as positions become mid-plane could be observed. The $^{59}Co(n,\gamma)^{60}Co$ gives very flat distribution throughout the positions. The absolute values of reaction rate are almost same as those at 10 m distance in Horizontal direction. This also supported the the uniform distribution of low energy neutron around the machine room. Very rough estimation for the flux levels for D-D and thermal neutrons was carried out by using the reaction rates and cross sections: 0.1 barn for $^{58}Ni(n,p)^{58}Co$ and 10 barn for $^{59}Co(n,\gamma)^{60}Co$, resulting in low energy neutron flux dominated primary D-D neutron flux by a factor of 2 to 3 at the position far from the torus. This results clearly suggested that low energy neutrons play an important role through neutron capture reactions on the induced activity production and successive dose rate estimation after shutdown.
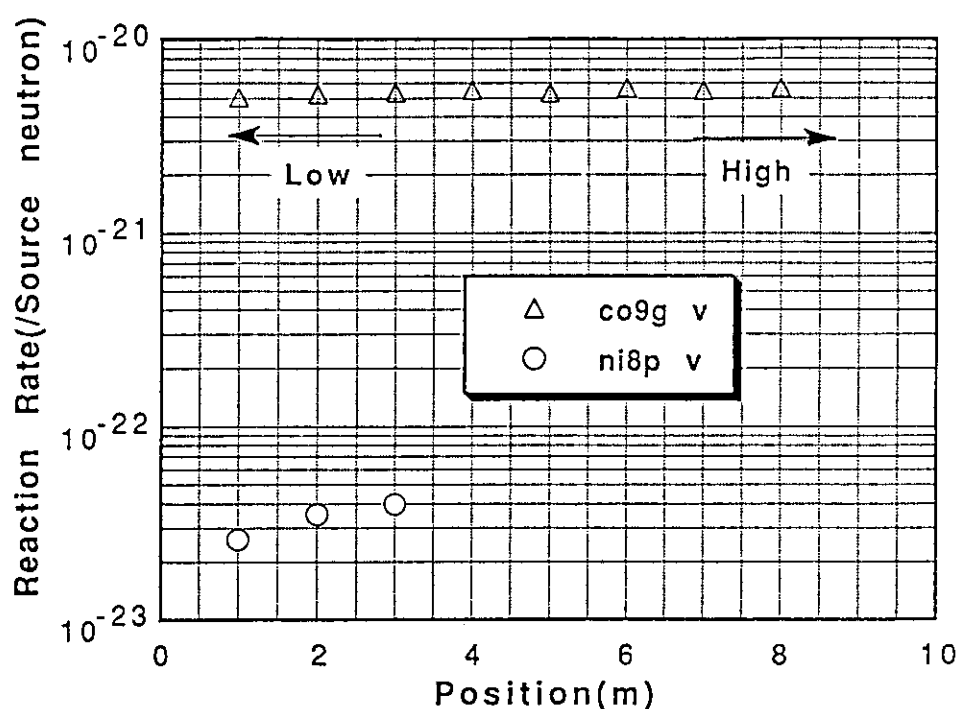
Fig. 3 Reaction rate distribution along the vertical direction.

4 Summary

The present measurement gave a basic idea for the neutron flux distribution during the DD discharge experiment in JT-60U. Although the distribution trend for both primary D-D and low energy neurons was well expected from the simple consideration with the rough model of system configuration, the data measured were valuable in order to examine the neutron transport calculation with complicated large scale model. The data are also very useful to analyse the dose rate distribution data described in section 9.8. The analytical calculation are now in progress to be verified by the present experimental data.

* Shimizu Corporation

9.6 Activation of JT-60U Machine

Y. Ikeda, K. Oishi*, N, Miya, N. Toyoshima, T. Nishitani and H. Takeuchi

1 Introduction

Identification of radionuclides is of importance to assess the level of radioactivity induced by the neutrons associated with the DD plasma discharge. In order to realized the activation problem in JT-60U, in-site measurements of γ-ray spectra was performed.

2 Measurement

A portable Ge detector was used to measure γ-ray spectra at time of 0.5 day after shutdown. Three spectra at positions (1) close to vacuum vessel, (2)near TF-coil and (3) near the wall of torus hall. Spectrum data were stored in a portable multi-channel analyzer.

Also a γ-ray spectrum of type 316-SS a stainless steel, the basic structural material, was measured with a Ge detector at two months after the last shot:. The sample were irradiated over throughout DD discharge from July 18 to October 4 at a position near TF-coil of P3.

3 Results and discussion

Gamma-ray spectra at positions near torus, TF-coil and the wall measured are shown in Figs. 1 to 3. The spectrum at the positions near the torus and TF-coil gave the clear γ-ray lines due to ^{56}Mn which was the major contributor, intensity of which was more than 90 % in all lines. The ^{56}Mn is generated by ^{55}Mn(n,γ) in the high Mn steel used a considerable part of the machine. The other prominent γ-lines were due to ^{99}Mo, ^{51}Cr, ^{59}Fe, ^{60}Co and ^{24}Na, as shown in Fig. 1. They were produced via reactions of ^{98}Mo(n,γ), ^{50}Cr(n,γ), ^{58}Fe(n,γ), ^{59}Co(n,γ) and ^{23}Na(n,γ), respectively.
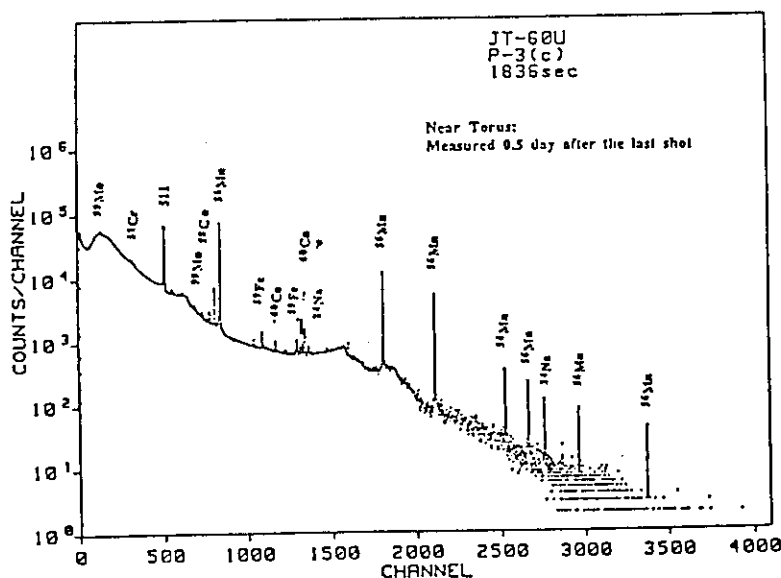
Fig. 1 Gamma-ray spectrum at the position near JT-60U torus measured with Ge detector.

In the spectrum measured at the position mear the wall, ^{24}Na gave highest intensity. It contributed by more than 80 % of the total. The activities was produced in the concrete of wall via the ^{23}Na(n,γ)^{24}Na. The ordinary concrete has considerable fraction of ^{23}Na in the composition. The intensity ratio of 1368 keV γ-line to 2754 keV γ-line was 1.5. When the activity of ^{24}Na is measured using a standard point source, the ratio should be about 2.0. This difference is attributable to the difference in the attenuation coefficient of the gamma-rays; the ^{24}Na activities are distributed deeply in the concrete wall. The depth in the concrete made such a attenuation difference. In this case, also the (n,γ) reaction played a major role on the production of activities. Again, the main concern for the radioactivities should be placed in the (n,γ) reaction because of high low energy neutron flux distributed all around the torus hall.
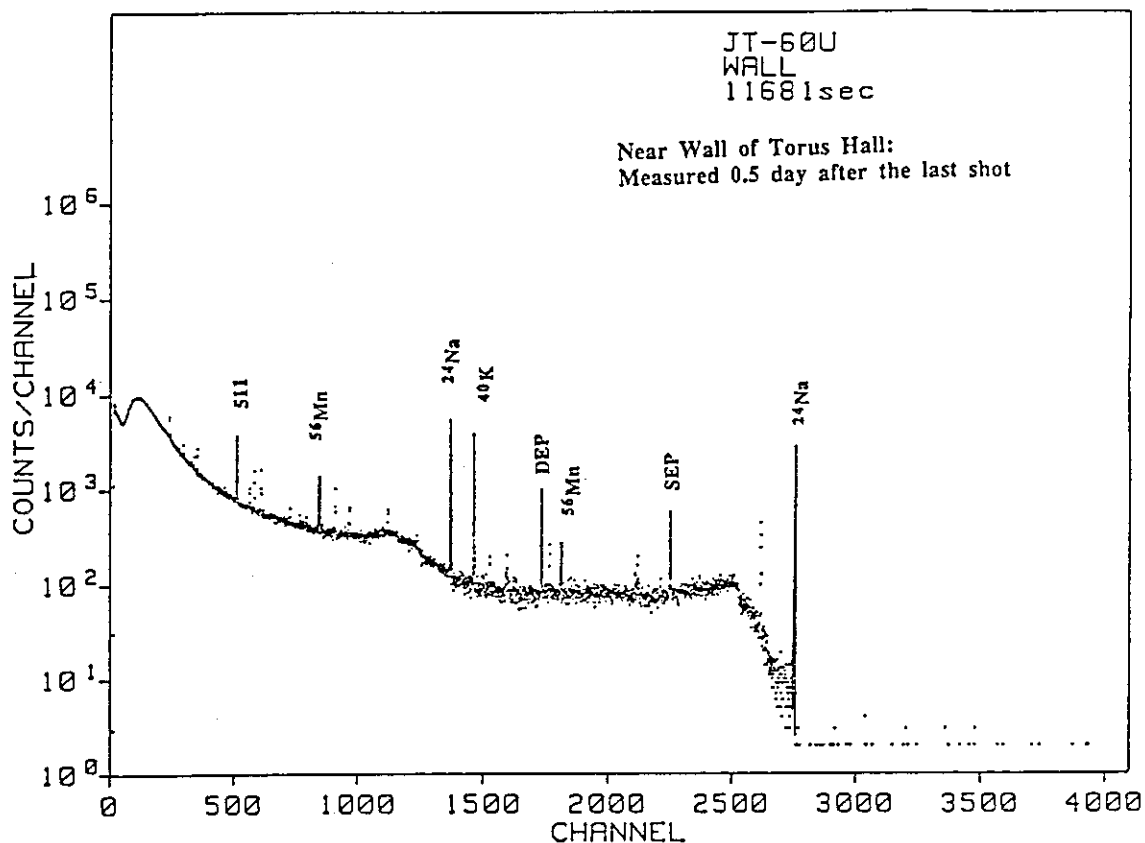
Fig. 2.   Gamma-ray spectrum at the position near wall measured by the Ge detector

The spectrum of 316-SS sample is shown in Fig. 4. Radioactivities of ^{51}Cr, ^{58}Co, ^{59}Fe, ^{60}Co were identified. They have relatively long half-lives of 27 d, 70.8 d, 45 d and 5.4 y, respectively. The (n,γ) reactions dominated in the production of activities. Cobalt-58 was the only visible activity which was produced via the threshold reaction of ^{58}Ni(n,p)^{58}Co. The others were due to (n,γ). This indicated that the large amount of low energy neutron were distributed as shown in section 9.5.
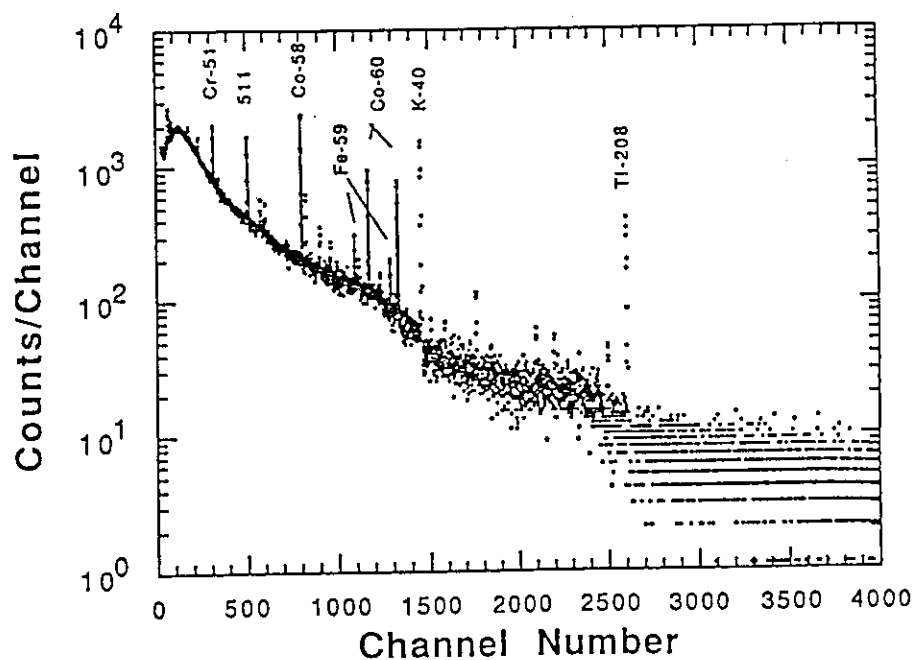
Fig. 3 Gamma-ray spectrum of 316SS stainless steel sample

4 Summary

In the next step for the induced radioactivity measurement, more systematic approach is now under planning; ever materials even their fractions are small are prepared to be the sample for the activation . The in-situ measurement will be more powerful to identify the source of radioactivity in place by place.

*   Shimizu Corporation

9.7 Dose Rate Measurement after JT-60U Discharge

Y. Ikeda, K. Oishi*, N. Miya, N. Toyoshima and T. Nishitani

1 Introduction

Dose rate after shutdown of DD-discharge operations associated with neutron production is of importance to estimate personal exposure during maintenance of the machine. Considering that this D-D discharge experiment is the first, extensive work on th measurements of the dose rate should be addressed to establish the substantial data base providing the guide line of the successive experiment. Dose rate around the JT-60 machine was measured after DD-discharge experiments by using common Thermoluminsescent Detector (TLD) and a gamma-dosimeter (GM survey meter). This section describes the experimental procedure and data focusing on the safety.

2 Dose rate measurement

Dose rates have been measured by TLD in two case: Case#1 at a time 12 hours after operations from June 18 to August 9, and Case#2 at a time 13 hours after operations from September 24 to October 7, 1991. In Case#2, a GM survey meter was also used in order to compare the data with TLD measurement. The corresponding total neutron production and averaged neutron yields are listed in Table 1.

Table 1. Neutron production data.

Case	Total Neutron Yield	Duration (sec)	Averaged Yield(/sec)
#1	2.0423E+16	1.46046E+6	1.3984E+10
#2	7.0802E+17	2.75634E+6	2.5687E+11

Locations of TLDs deployed around JT-60U machine are the same as those of activation foils as illustrated in Fig. 1 in Section 9.5. Additionally, the TLDs were placed along the line in the upper part of torus. For distribution of the radial direction, TLDs were placed at ten to fourteen positions along line on the station at P-15(Horizontal). The TLDs were mapped at twenty six positions along the line just above the top of JT-60U (Ceiling). The TLDs were set at ten positions along the line from the top of tower near the entrance of the machine room (Vertical). Several other TLDs were placed at positions close to vacuum vessel of P-3, TC-17 and Wall of machine room. At each position, two TLDs were set to reduce the error due to characteristics of TLD. In the first case, the measurement of TLD started at around 10:00 on August 10, 1991 for 48 hours, and the two TLD measurements for the second case started at 11:00 on October 5 for 46 hours and at 9:45

on October 7, 1991 for 100 hours. After one day from the end of exposures, dose rates of TLDs were read by TLD reader, National UD-502B. The dose rate was given in an unit of μSv/hr.

3 Results and discussion

The results of dose rate measured by TLD along the horizontal axis are shown in Fig. 2 for both case#1 and case#2, corresponding to the exposure rate at a half day after the last shot. Dose rates near the vacuum vessel decrease radically with distances from the torus increases and become almost same value at distances further than 5 m. The dose rates for case#2 are higher by a factor of 2 to 4 than those of case#1 throughout all positions. The higher value reflected to the higher neutron production during the DD-discharge experiment. The highest value of 5.9 μSv/h averaged for successive 48 hours was observed inside of the coil in the case#2. As it is shown in in Section 9.6, the more than 90 % contribution to the gamma-ray dose at this moment is dominated by the ^{56}Mn with half-lives of 2.6 h.
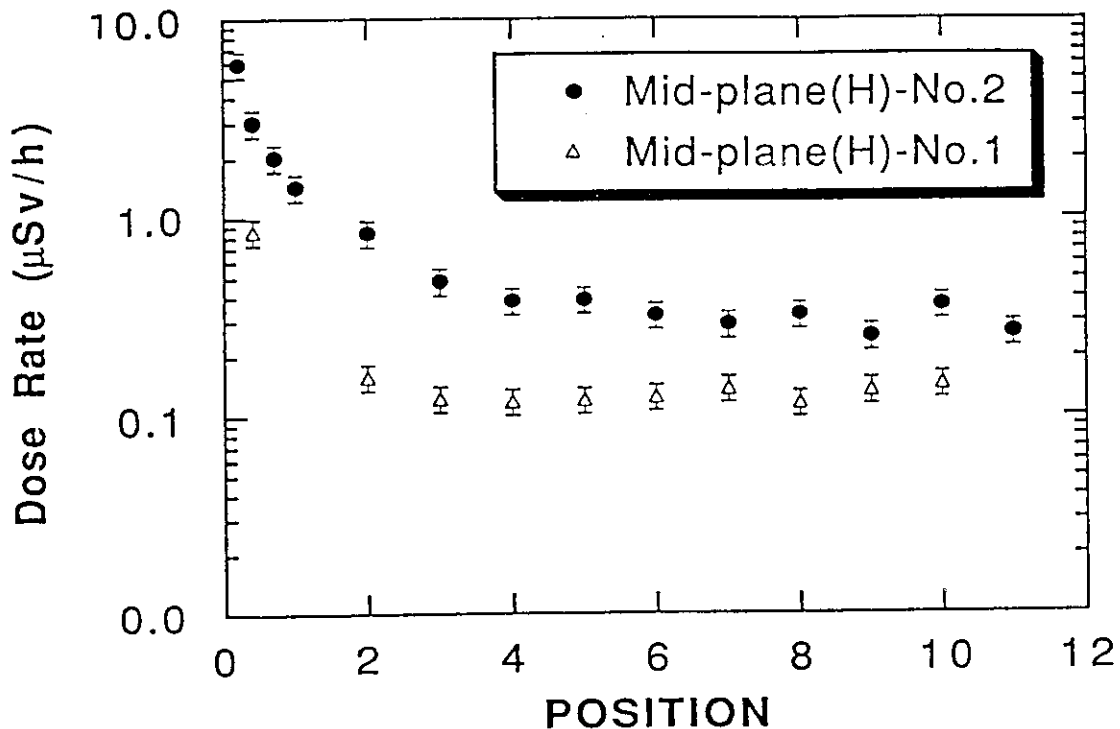
Fig. 1. Radial distribution of dose rates measured by TLD at 0.5 day after D-D operations for Case#1 and 2.

The measure dose rates at positions inside and outside of TF-coil at P-15 are listed in Table 2 for case#2. This Table shows that dose rate inside decreases faster with cooling time than that outside. The ratios of dose rate at 2.5 day to those at 0.5 day are 0.12 and 0.30 for the positions inside and outside, respectively. This result indicates indirectly that ^{56}Mn contributed largely to the dose rate inside.

Table 2. Change of dose rate with cooling time near the TF coil.

Location	Dose rate(μSv/h)		
	after 0.5 day	after 2.5 day	Ratio(2.5day/0.5day)
Inside of TF coil	5.92	0.73	0.12
Outside of TF coil	1.4	0.43	0.30
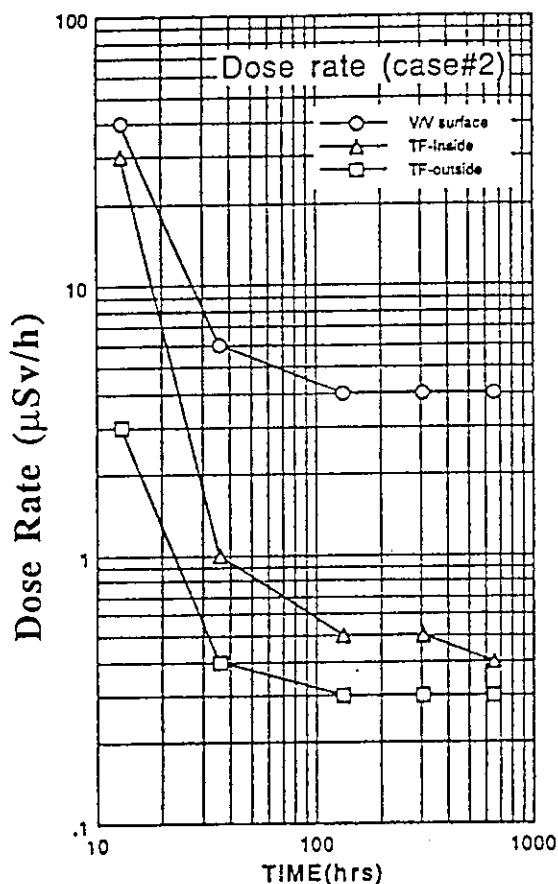
Fig. 2. Time dependent dose rate change measured by GM at the three positions of surface inside and outside TF-coil.

Figure 2 shows time dependencies of dose rates measured by GM at positions of vacuum vessel surface, inside and outside of TF-coil of mid-plane in P3 section. Dose rate on the surface of vacuum vessel shows 40 μSv/h at 0.5 day and decreases to 0.7 μSv at 2.5 day after operation. After 100 hrs, the dose rate has kept almost constant of 4 μSv/h which is contributed dominantly by ^{58}Co with half-life of 71 days, products of ^{58}Ni(n,p) reaction. The dose rate inside TF-coil decreased faster than that outside of TF-coil. It is note that the dose rate inside at 0.5 day is almost equal to that of surface. This indicates the contribution of ^{56}Mn is enhanced inside TF-coil, position of which is close to the support structure of JT-60U device; high manganese steel is a major constituent.

The value of 5.9 μSv/h measured by TLD could suggest that dose rate would be smaller that an the limit of personal exposure of 10 μSv one day after shutdown. The present result clearly indicates that one day after operation, maintenance work near the vacuum vessel could be possible very safely without any protection devises as long as the preset level of neutron production is concerned.

Figure 3 shows the dose rate distribution measured along the vertical line (Vertical). The values are almost the same throughout the positions; 0.13 μSv/h in case#1 and 0.28 μSv/h in case#2. The case#2 gives about a factor of two higher values than the case#1. This also correspond to the total number of neutron production in each case.

JT60U-TLD

JT60U-TLD
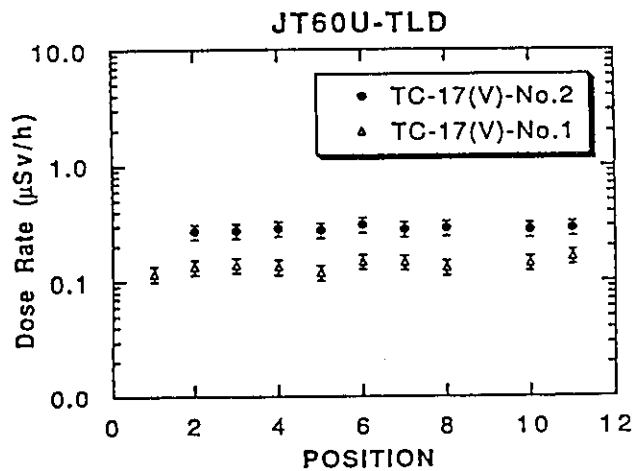
Fig. 3 Dose rate distribution measured by TLD along the vertical direction.
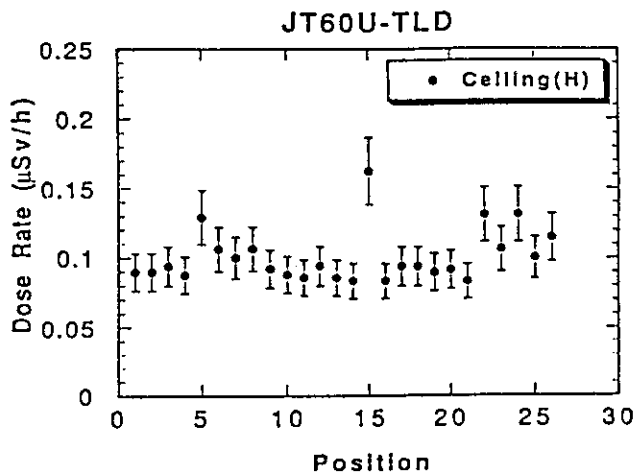
Fig. 4..Dose rate distribution measured by TLD along the line in ceiling.

The result for Ceiling in case#1 is shown in Fig. 4. Dose rates are very low, almost equivalent to the background level of about 0.1 μSv/h. This is possiblly due to the large attenuation for neutron and gamma-ray by thick TF coils by which middle area of upper part of torus is fully shielded.So that, no significant contribution of gamma-ray was detected. In other words, the upper part of the torus is the most safe area in the JT-60U machine.

4 Summary

The present measurement have shown a clear indication to be serve as the base data for the estimation of dose rate distribution in some particular position in the JT-60U facility. Of cause, there are a lot of data to be measure concerning the spacial and time dependent profile in the dose rate. Concerning the importance to establish the data base, corresponding measurements are precisely scheduled in the next phase of the DD-discharge experiment in 1992.

* Shimizu Coporatin

9.8 Tritium Monitoring in the JT-60U Clean up Operations

N. Miya, N. Toyoshima, H.Nakamura, T.Nishitani and H.Takeuchi

1. Introduction

Tritium concentration in exhaust gases from vacuum vessel is measured by an ion chamber and a liquid scintillation counter in order to investigate the tritium retention in JT-60U. From July 19 to Oct.4 1991 approximately 7×10^{17} DD fusion neutrons were produced in JT-60U operations. These reactions would be expected to produce ~1.3GBq of tritium. JT-60U has performed the clean-up operations from Oct.14 to Nov.1 1991 to deplete the activation and tritium concentration inside the vessel. Clean up operations have been conducted with hydrogen OH and NB discharges, TDC and He glow discharge cleaning shots with 150-300°C baking of the vessel.

In this paper we describe some preliminary measurements of tritium monitoring and the results in JT-60U clean up operations.

2. Experimental apparatus

In order to measure the tritium concentration, the experimental apparatus was equipped with an ion chamber (vibrating reed electrometer type) and a detritiation system composed of a catalytic oxidizer (Cu_2O) and two traps (silica gel). Tritiated water is produced from the silica gel samples which is then mixed with a liquid scintillator and the disintegrations are measured using conventional scintillation counter. The major diagnostics used for the following study are shown in Fig.1.

3. Experimental results

3.1 Characteristics of tritium concentration

Figure 2 shows time evolutions of the surface temperature on the divertor plates (thermo couples) and tritium concentration measured in the clean up operations on Oct.30. The high power NB heated hydrogen divertor discharges (P_{NB}=9.3MW, Ip=3MA, Bt=4.5T), He GDC (1-2hrs, E=500V, I=1A) and He TDC (10min.) with 300°C baking are adopted on the day. The neutral pressure inside the vessel during the NB heated discharge is in the range of 10^{-4}-10^{-2}Pa. GDC and TDC have performed in the pressure of 3×10^{-2}Pa and 2×10^{-3}Pa respectively. As NB heated divertor discharge is advanced, maximum surface temperature increases gradually up to 450°C while the base temperature at the beginning of discharge kept almost constant during the operation. It is shown that the concentrations also increase gradually during the plasma discharges.

Figure 3 depicts the dependence of tritium concentration on the baking temperature. Data has plotted at 6:00 in the every morning before the plasma operations in order to except the effect of heating by plasma discharges. It is shown that the concentration is almost constant within 1Bq/cc during the phase in which temperature goes up from 150°C to 300°C on Oct.18-20.

In JET and TFTR experiments, tritium distribution in the graphite walls shows a marked poloidal asymmetry of the torus, with showing a maximum near the divertor plates or the point in which high heat flux concentrated [1,2]. These observations of tritium concentration in Figs.2 and 3 suggest that the high power NB heated divertor discharges with high temperature baking (300°C) enhanced the tritium release in the divertor plates in JT-60U. This is reasonable consideration with the report of the observation of rapid reduction of deuterium gas retention in graphite tiles at higher surface temperature over than 500°K[1,3].

As shown in Fig.2, tritium concentrations during He GDC show sharp increasements while the turnover are observed during the operation. Its peaks depend on the surface temperature of divertor plates at the beginning of each GDC. It is shown that a high efficiency of tritium release can be expected by He GDC with high temperature walls although its duration time is short of around 1 hour. On the other hand, He TDC with 10 minutes has not give a tritium release at all.

3.2 Detritiation results

The results of measurement with detritiation system for 24 hours are summarized in Table 1. A simple silica gel trap was then used to measure tritiated water (HTO) . By the way, elemental tritium (HT) are measured by utilization of an ion chamber and a catalytic oxidizer. The ratio of HT/HTO in averaged concentrations determined by an ion chamber and a catalytic oxidizer indicates 21:1 and 25:1, respectively. The ratio with an ion chamber is slightly larger than that of the detritiation system. It is considered that the difference between two methods depends on an accuracy of a conversion of HT to HTO in the catalytic oxidizer. The regeneration of NBI cryopanels and the pump oils taken from various vacuum pumps show small contributions less than 0.7Bq/cc and 3.6Bq/cc, respectively.

It is estimated that approximately 160MBq of tritium , which is corresponds to 12% of the total generated tritium of ~1.3GBq, were recovered from JT-60U vacuum vessel during the clean up operations using the ratio of 21:1 (HT/HTO) and 8×10^4Bq of HTO from a simple silica gel trap.

4. Summary

Major results in this work are summarized as follows; 1) The high power NB heated divertor discharges with high temperature (300°C) baking enhanced the tritium release from the vessel in JT-60U, 2) It is shown that a high efficiency of tritium release can be expected by He GDC, 3) Approximately 160MBq of tritium which is corresponds to 12% of total generated tritium of ~1.3GBq were retrieved from JT-60U vacuum vessel during the clean up operations.

5. Acknowledgments

The authors would like to acknowledge Mr. T.Okamoto and Mr. F.Niino of Safety Division of Department of Administrative Services for their collaboration and support.

6. References

[1] D.H.J. Goodall et al, J. of Nucl. Mater. 162-164(1989)1059

[2] H.F.Dylla et al, Princeton Phys. Lab. and Sandia Rep., PPPL-2523/SAND 88-8212(1988)

[3] W.Moller et al, J. of Nucl. Mater., 162-164(1989)138

Table 1   Detritiation data in monitoring system.

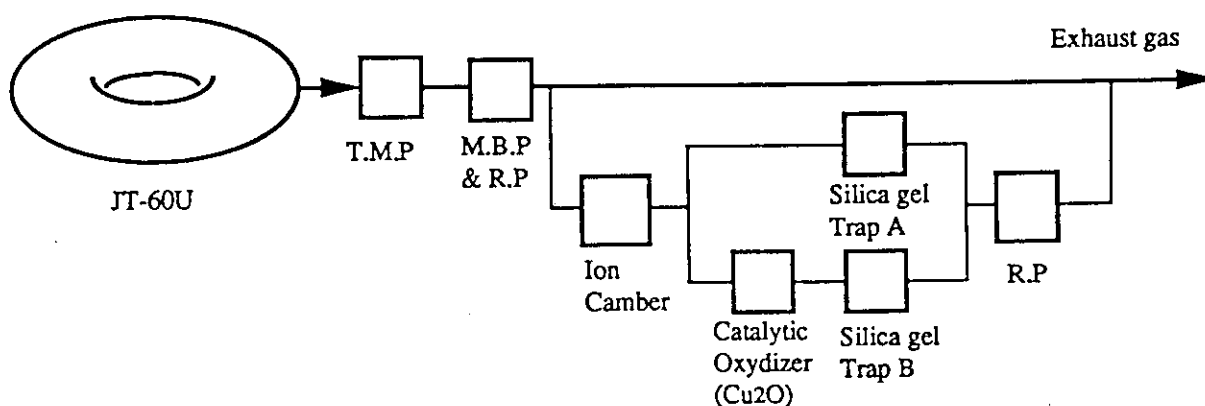|	HT + HTO		HTO
	Ion Chamber	Silica gel Trap B	Silica gel Trap A
Tritium detritiation (Bq)	2.5×10^5	1.2×10^5	5.5×10^3
Monitoring Flow in 24 hrs. (cc)	3.61×10^5	1.87×10^5	1.89×10^5
Averaged Concentration (Bq/cc)	0.72	0.64	2.9×10^{-2}

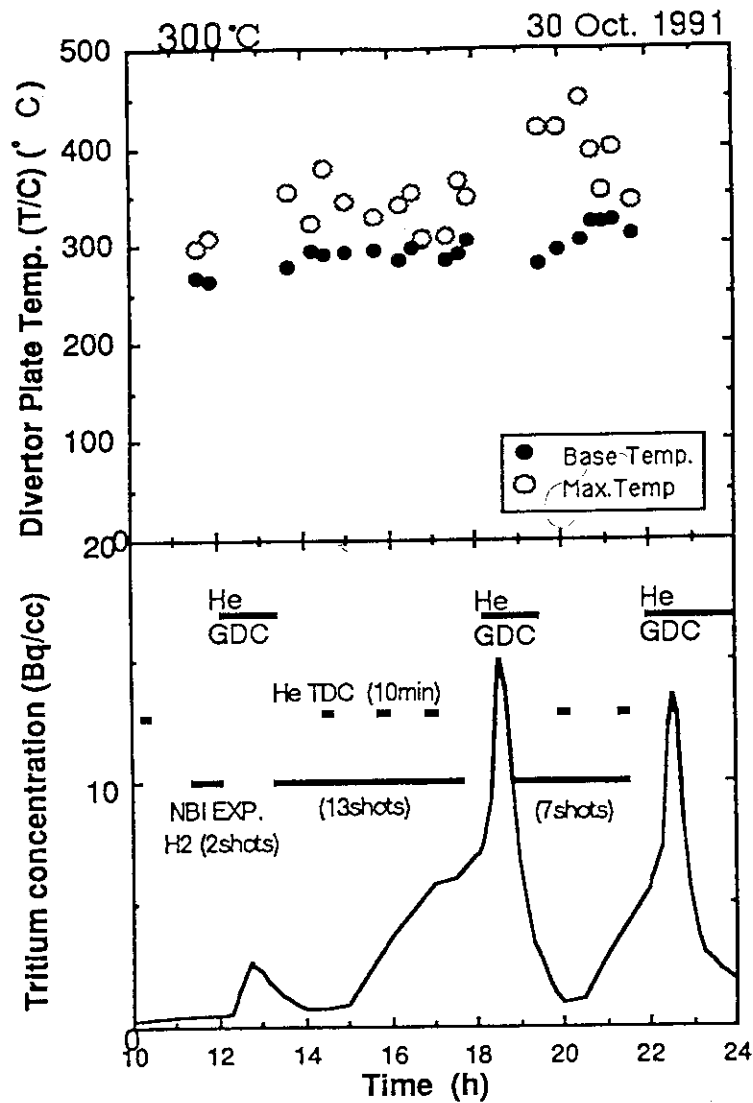Fig. 1 Tritium monitoring system in JT-60U exhaust gases .

Fig. 2 The time evolutions of surface temperature on the divertor plates and tritium concentration in the clean up operations.
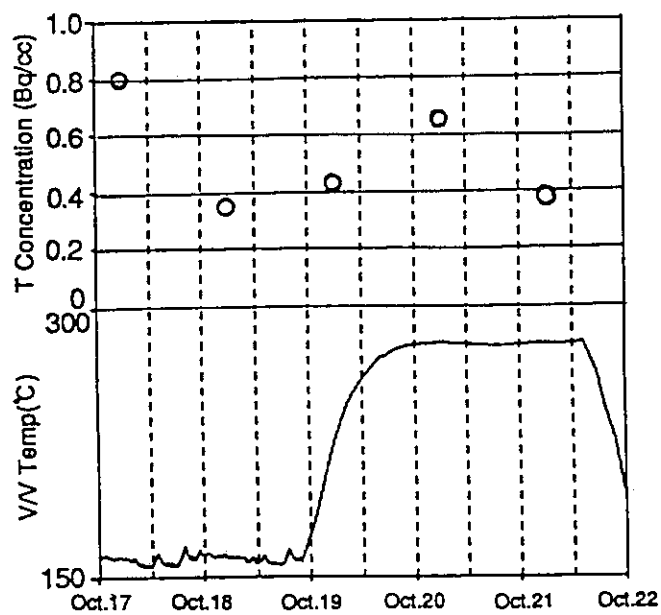
Fig. 3 Tritium concentration v.s. baking temperature of vacuum vessel.

9.9 Neutron Yield and Spectrum Measurement Using a ³He Gas Proportional Counter in JT-60U D-D Discharges

T. Iguchi*, N. Nakayamada*, N. Tanaka, H. Takahashi, Y. Ikeda and T. Nishitani

1. Introduction

Neutron yield monitoring systems in JT-60U consist of three types of neutron detectors; a ³He gas proportional counter, ^{235}U and ^{238}U fission chambers, to cover a wide dynamic range of neutron yield in various operational schemes for D-D discharges. Among these three detectors, the ³He counter system is designed as the most sensitive detector in pulse counting mode operation, which can obtain much better counting statistics than that of the ^{235}U and ^{238}U fission chambers in an in-situ calibration experiment using a ^{252}Cf neutron source. On the other hand, the signal pulse pile-up effect makes it almost impossible for the ³He counter to operate in pulse counting mode under the ordinary D-D discharge experiments. To improve the dynamic range of this ³He counter without changing the present signal processing system, the multi-discrimination level counting technique has been introduced. As another application of a ³He gas proportional counter, neutron spectrum measurement has been also tried for the D-D discharge experiments.

2. Wide dynamic range neutron yield monitoring based on multi-discrimination level counting technique

The ³He gas counter for neutron yield monitoring in JT-60U is operated only in pulse counting mode, of which the maximum count rate keeping the linearity to neutron yield is limited about 5×10^4 cps. To expand this dynamic range, the multi-discrimination level counting (MLC) technique has been introduced into the present signal processing system of the ³He neutron yield monitor. The operational principle of the MLC technique in a pulse pile-up state is based on the following relation [1];

$$\overline{q^2}n \cong k\sum_i N_i \Delta V_i^2 \approx k'\sum_i N_i V_i (V_i - V_{i-1})$$

$$(1)$$

where

    n : signal pulse rate from a counter

    $\overline{q^2}$: mean square charge of a signal pulse

    V_i: i th discrimination level voltage

    N_i: count rate crossing i th discrimination level

    k, k': constant of proportionality

By detecting pile-up pulse signals from the ³He counter through different discrimination levels, the MLC technique can switch over a pulse counting mode for low pulse rate continuously to a mean square voltage mode for high pulse rate through only simple signal processing on a computer. Fig.1 shows a block diagram of the present system to realize the MLC signal processing. The time interval for data sampling is set 100 ms. The performance tests have been made in an accelerator

D-D neutron source at JAERI-FNS and in D-D discharges of JT-60U. Figure 2 shows the result of FNS experiments comparing the MLC output with associate particle count rates, which is directly proportional to neutron yield. It is found that the MLC output is linear to neutron yield up to 10^7 cps, while pulse count rate is saturated over 10^5 cps. Figure 3 demonstrates that neutron yield monitoring of less than 10^{12} n/s in JT-60U D-D discharges would be possible with the present ^{3}He counter by using the MLC signal processing. However it has been also found that this system does not work well when the signal amplitude from the counter is almost saturated due to excessive pulse pile-ups under strong neutron production rate, such as around 10^{15} n/s corresponding to NBI heating.

3. Neutron spectrometry for D-D discharges using a ^{3}He gas proportional counter

A ^{3}He gas ionization chamber (^{3}He I.C.) is often used for D-D plasma neutron spectrometry because of its good energy resolution [2], while a ^{3}He gas proportional counter (^{3}He P.C.) is a little bit inferior to the ^{3}He I.C. in energy resolution and efficiency but has some advantages on a better signal to noise ratio, easier handling, much cheaper cost etc. The applicability of this ^{3}He P.C. has been checked in JT-60U as a complementary neutron spectrometer for D-D discharges. The ^{3}He P.C. used here is XERAM Q24NH25 type, which is about 2.5 cm dia. x 15 cm in sensitive length filled with ^{3}He(4 atm) and Kr(2 atm) gas mixture, and is surrounded with a B_4C filter and Cd cover to eliminate thermal neutrons. The response function of this counter has been prepared by adjusting the previous data [3] of the equivalent detector (TEXLIUM-9341) to the measurement of standard neutron spectrum of ^{252}Cf source. Neutron spectrum unfolding is made with the maximum likelihood and the maximum entropy method [4]. Fig. 4 gives the measured neutron spectrum for 2.4 MeV monochromatic neutrons produced from a D-D accelerator, comparing with the result of a ^{3}He I.C.. The D-D neutron peak shape obtained from the ^{3}He P.C. is found consistent with that of the ^{3}He I.C.. Fig. 5 is a preliminary result of ohmic D-D plasma neutron spectrum in JT-60U, measured with the ^{3}He P.C. placed near the fission chamber port. From comparison with the calculated result of the Monte Calro neutron transport code MCNP, the accuracy of neutron peak analysis using a ^{3}He P.C. is considered sufficient to put into practical use.

4. Summary

The applicability of a ^{3}He gas proportional counter has been experimentally verified to neutron yield and spectrum measurement in JT-60U D-D Discharges. The multi-level discrimination counting technique is useful to improve the dynamic range of the ^{3}He neutron monitor without changing the present pulse counting system and makes it possible to extrapolate the calibration result from a ^{252}Cf source directly to the D-D discharge experiment. Neutron spectrometry using a ^{3}He gas proportional counter is also concluded a promising one in practical use for JT-60U experiments.

---

*   University of Tokyo

References

[1]   K.Hasegawa, Y.Kimura and A.Sekiguchi, IEEE Trans. Nucl. Sci. **NS-23**, (1976) 833.

[2]   O.N.Jarvis, G.Gorini, M.Hone, J.Kallne, et al., Rev.Sci.Instrum. **57** (1986) 1717.

[3]   T.Kosako, M.Nakazawa, H.Wakabayashi and A.Sekiguchi : "Spectral Characterization of Fast Reactor Neutron Fields", J. Fac. Engrg., Univ. of Tokyo(B), Vol.34 (1977) 409.

[4]   S.Itho and T.Tsunoda: J. Nucl. Sci. Tech., **26** (1989) 833
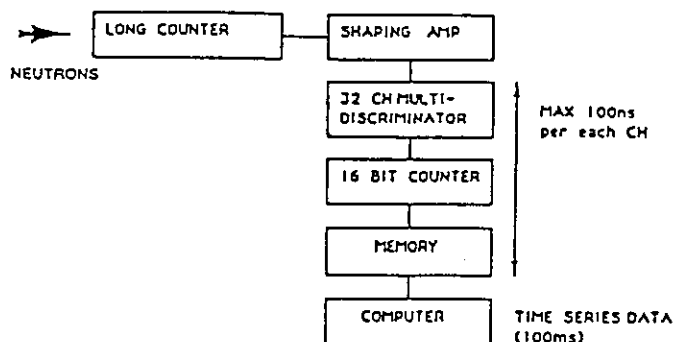
Fig. 1   Block Diagram of the multi-level discrimination counting system for a ^{3}He neutron monitor.

Associate Particle Counting Rate [cps]
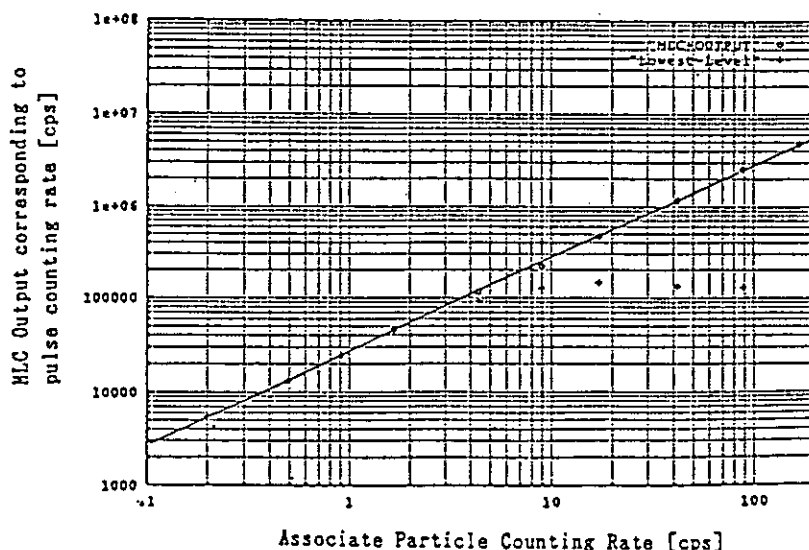
Fig. 1   Linearity check of the MLC output to the neutron yield from a D-D accelerator.
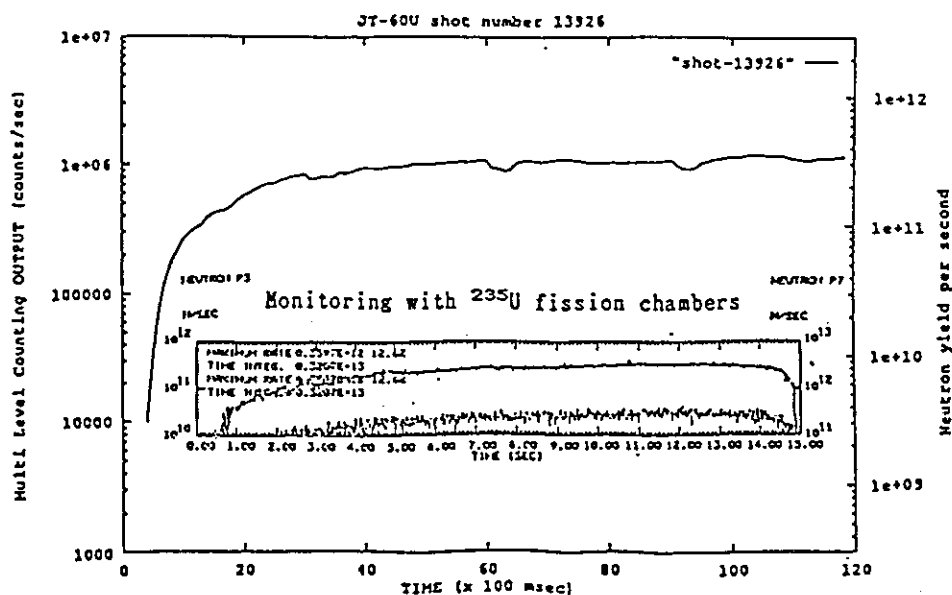
Fig. 3   Results of neutron yield monitoring in JT-60U with the MLC system of a ^{3}He counter.
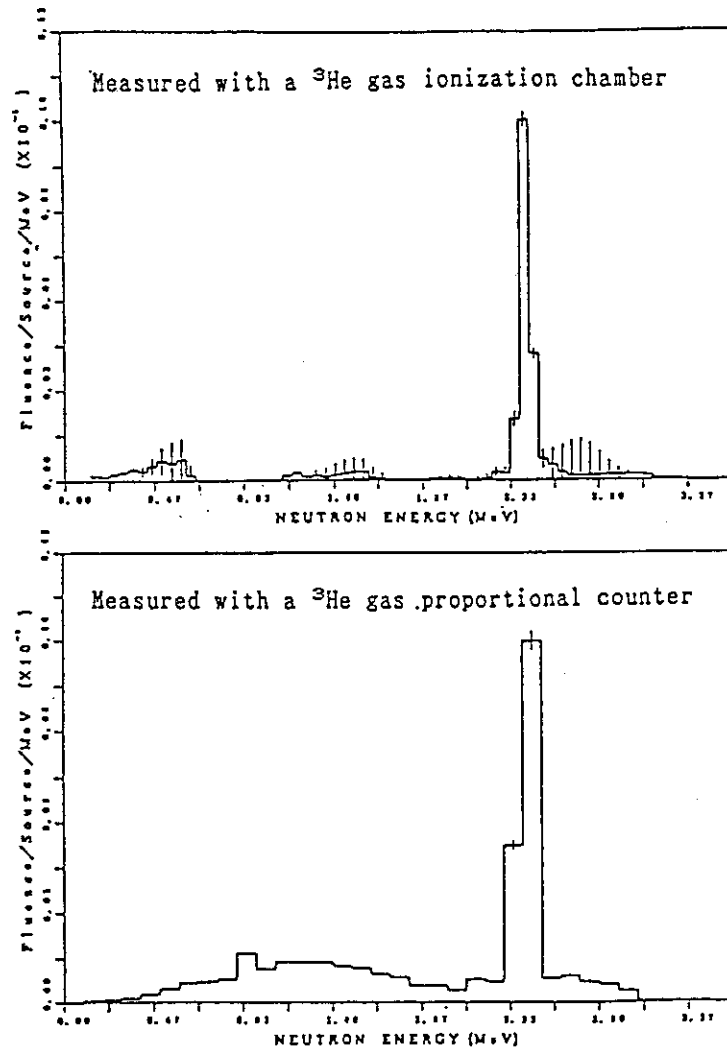
Fig. 4 Measured neutron spectrum of 2.5 MeV monochromatic neutrons from a D-D accelerator.
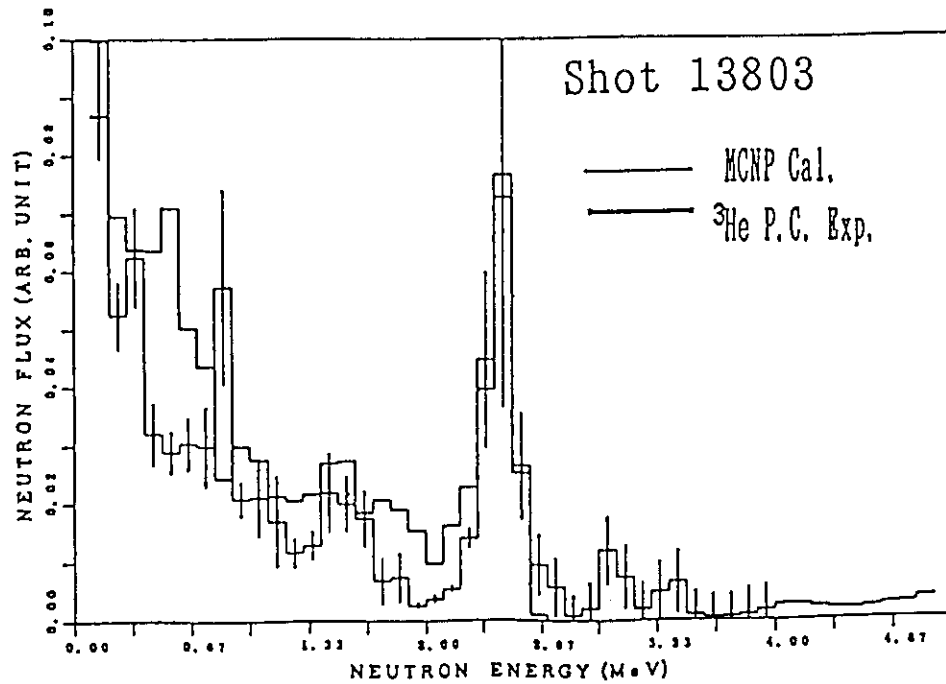
Fig. 5 Neutron spectrum of the ohmic D-D discharge in JT-60U measured with a ^{3}He gas proportional counter.

10 Ripple Loss and High Energy Particles

10.1 Estimation of Ripple Loss by Thermocouple Arrays

K. Tobita, Y. Neyatani, S. Miura, H. Takeuchi, T. Arai, K. Tani, M. Matsuoka

Toroidal field ripple deteriorates plasma performance by enhancements of ion thermal transport [1,2,3] and fast ion loss [4]. Between these undesirable effects due to ripple, fast ion loss induced by toroidal field ripple has an impact on the realization of a fusion tokamak reactor because of its serious heat deposition on the first wall. Up to now, the problem has been treated by some simulation codes. They have provided helpful predictions about permissible ripple size in ITER (International Thermonuclear Experimental Reactor) as well as α particle loss due to ripple [5]. In spite of their usefulness, concerns about the reliability of the codes have not been completely swept away yet because of the complexity of problem and doubts about extremely time-consuming computation, and the experimental confirmation is still at the early stage[6]. In this section, we describes some experimental features of fast ion ripple loss in JT-60U.

JT-60U is a tokamak which has the major radius $R_0 = 3.4$ m, the average minor radius a = 0.9 m. Its toroidal field is produced by 18 circular coils and the toroidal ripple (δ) goes up to 2.2% at the outer edge. The experiment was performed under the conditions of plasma current $I_P = 1.0$-2.0 MA and toroidal field $B_T = 2.7$-4.0 T. The neutral beam injection (NBI) system is operated with about 15 MW near-perpendicular injection (D^0, 80-85 keV). The power fraction of NBI is E : $E_{1/2}$: $E_{1/3} = 78\%$: 15% : 7%. Throughout the experiments, B_T and I_P are directed clockwise and hence the ∇B ion drift direction orients downward. Fast ion ripple loss can be substantial in JT-60U with high toroidal field ripple and near-perpendicular NBI. The ripple magnitude is somewhat high on the upper side compared with the lower side in the divertor operation as shown in Fig. 1.

Heat load on the first wall is deduced from the temperature rise of thermocouples (TC) mounted on the wall. A 3-dimensional heat conduction code is used to deduce the heat flux from the temperature rise. On basis of the OFMC computations, the toroidal and

poloidal TC arrays are aligned on the ∇B ion drift side, i.e. the lower side, so as to measure the heat flux of hot spot due to fast ion ripple loss. The toroidal TC array is mounted between two toroidal coils at the poloidal position (PP) No. 139.5 with toroidal angles of 0-20°: this range of the angles corresponds to one pitch of ripple and the toroidal coils are located at the angles of 0° and 20°. The poloidal TC array is aligned in PP No. 133-147 at the toroidal angle of 13°. The PP No. is illustrated in Fig.1. There are two types of orbit losses due to ripple: ripple-trapped loss and banana drift loss. The heat load due to the former is localized in both toroidal and poloidal directions. The ripple-trapped loss can cause a crucial heat load on the first wall because of its localization. In contrast with the ripple-trapped loss, the heat flux due to the latter is not localized so much. According to OFMC, the ripple-trapped loss is dominant in the typical operations of JT-60U with near-perpendicular NBI.

Figure 2 shows the spatial distribution of heat flux measured by the TC arrays. Here the toroidal angle is taken in the plasma current direction. The conditions of this shot are $I_P = 1.7$ MA, $B_T = 2.5$ T, $q_{eff} = 3.9$, $P_{NB} = 10$ MW, $E_b = 85$ keV and $\bar{n}_e = 2.6 \times 10^{19}$ m^{-3} and the outermost magnetic surface is shown in Fig.1. Here q_{eff} denotes the effective safety factor which is introduced to avoid singularity at the null point [8]. Figure 2 indicates that the heat load due to the ripple loss is localized in both toroidal and poloidal directions.

By changing the plasma size, we obtained the relation between the ripple magnitude ($\delta = \delta B_T / B_T$) and the heat load. As shown in Fig.3, the heat load for normalized input quantity of heat ($P_{NB}\Delta t$) decreases with δ_{max}. Here δ_{max} represents the maximum ripple size on the outermost magnetic surface. In the considered shots the maximum ripple is obtained at the null point or near the low field side. From increase in heat heat with δ_{max}, the observed heat deposition is thought to be due to ripple loss.

Ripple wells are formed in the region where the effective ripple well parameter ($\alpha^* \equiv |r\sin\theta| / NRq\delta$) satisfies $|\alpha^*| < 1$. Here, N is the the number of toroidal coils and other symbols denote conventional definitions. This condition shows that the ripple well region extends with q. The poloidal distribution of heat load in highly elongated

configuration [8] which has a vertically elongated cross section with smaller R_0, is shown as a parameter of q_{eff} in Fig. 4. In the configuration, the peak of heat load is located on the inside (higher PP No.) compared with that in standard configuration shown in Fig. 1. The increase in the poloidal heat load with q_{eff} implies that the observed heat load is mainly due to the ripple-trapped loss, because the banana drift loss is not so sensitive to q_{eff}.

In summary, the heat load due to ripple loss of NB-injected ions was localized in both toroidal and poloidal directions, and the location of the heat spot was in good agreement with the OFMC calculation. The heat load increased with both ripple size and safety factor.

References
[1] T.E. Stringer, Nucl. Fusion 12 (1972) 689.
[2] J.N. Davidson, Nucl. Fusion 16 (1976) 731.
[3] S.D. Scott, et al., Nucl. Fusion 25 (1985) 359.
[4] K. Tani, H. Kishimoto, S. Tamura, in Plasma Physics and Controlled Nuclear Fusion Research (Proc. 8th Int. Conf. Brussels, 1980) Vol.1, IAEA, Vienna (1981) 631.
[5] S. Putvinskij, et al., ITER-IL-PH-1-9-1 (1989).
[6] M. Tuszewski, J.P. Roubin, Nucl. Fusion 28 (1988) 499.
[7] K. Tani, M. Azumi, H. Kishimoto, S. Tamura, J. Phys. Soc. Japan 50 (1981) 1726.
[8] H. Ninomiya, JT-60 Team, submitted to Phys. Fluids B.
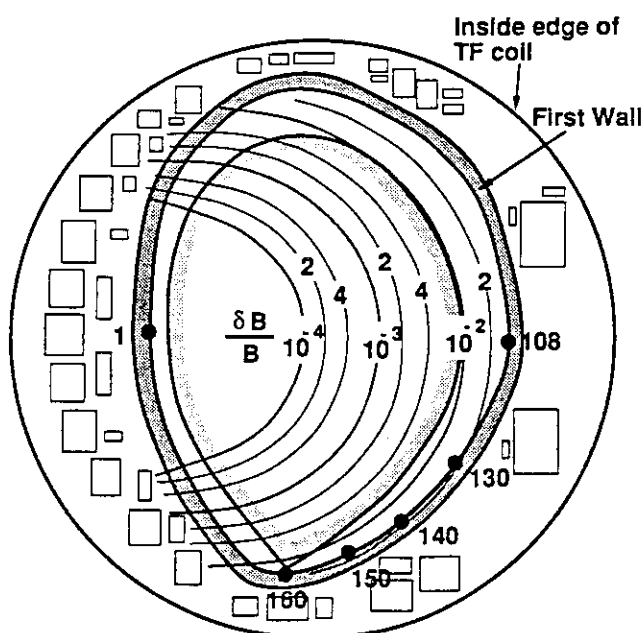
Fig.1 Poloidal cross section of JT-60U plasma and the toroidal ripple distribution. Also shown are the poloidal position numbers (PP No.) of the first wall. The poloidal thermocouple array is aligned in PP No. 133-147 and the toroidal one is located at PP No. 139.5.
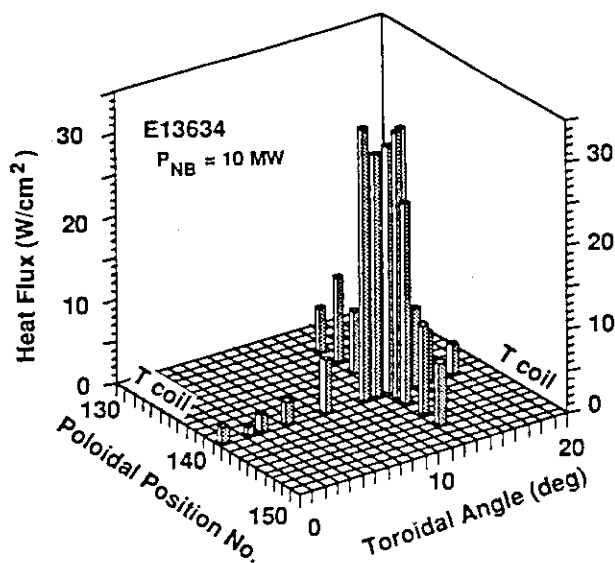
Fig.2 The toroidal and poloidal distribution of the heat flux measured by the thermocouple arrays.
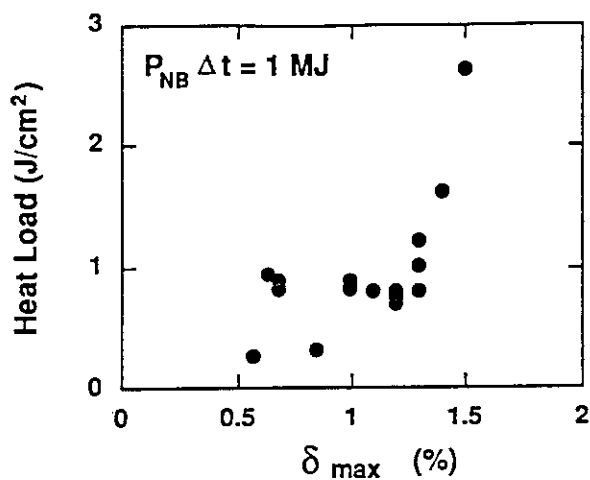
Fig.3 Relation between the heat load and the maximum ripple size δ_{max}.
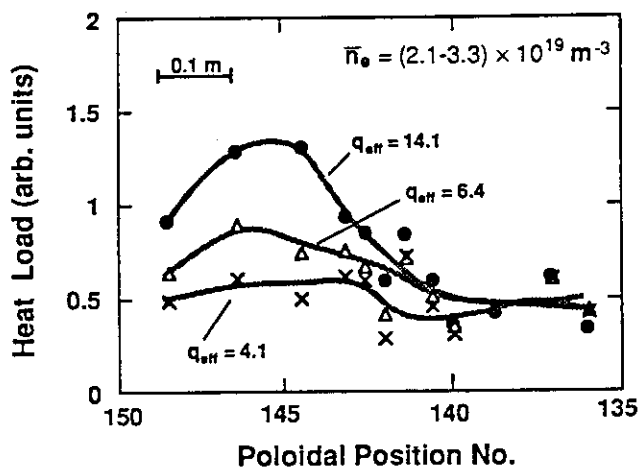
Fig.4 The poloidal heat flux as a parameter of q_{eff}.

10.2 Numerical Analysis of Ripple Losses of Fast Ions Produced by NBI in JT-60U

K. Tani, K. Tobita, Y. Neyatani, S. Miura, H. Takeuchi and M. Azumi

Ripple-induced loss of alpha particles has a very strong impact not only on the specification of toroidal field coils but also on the design of plasma facing components such as the first wall and divertor plates. In order to estimate the ripple losses of alpha particles, many kinds of simulation codes have been developed [1].

The next important step is to make a cross-check of the simulation results with experimental data. In order to support the simulation results, experimental investigations of ripple losses of fast ions produced by quasi-perpendicular NBI are now in progress in JT-60U.

Detailed experimental results are shown in the last section. In this section, a brief explanation of our simulation code and the comparison of the simulation results with those experimental data are presented.

An orbit-following Monte-Carlo (OFMC) technique is adopted in our simulation code. Our OFMC code consists of four parts;

1) calculation of ionization of neutral beams,

2) simulation of Coulomb collisions,

3) calculation of guiding center orbit, and

4) simulation of charge-exchange reactions of fast ions and reionization of fast neutrals in succession.

Monte-Carlo techniques are adopted to the calculation of beam ionization. Distribution of fast ions produced by the ionization of neutral beams with elliptic cross section can be obtained. Computations for multi-beam lines as well as multi-energy

species of neutral beams can be made with our code.

The collisional processes of fast ions are also simulated by a technique of Monte-Carlo. The longitudinal and the transverse components of velocity change by Coulomb collision, Δv_l and Δv_t, are calculated by generating normal random numbers with respective mean values, $< \Delta v_l >$ and $< \Delta v_t >$, and mean square deviations $< \Delta v_l^2 >$ and $< \Delta v_t^2 >$. Assuming that the phase of Larmor motion of fast ions is random, Δv_l and Δv_t are converted into velocity components parallel and perpendicular to the magnetic field line $\Delta v_\parallel$ and $\Delta v_\perp$. Ion trajectories are followed by numerical integration of the standard guiding center equation in a non-axisymmetric system. A second-order Runge-Kutta method is adopted for the numerical integration. The axisymmetric magnetic field is given by the derivatives of poloidal flux function ψ which is obtained by the widely used MHD equilibrium code "SELENE" [2]. The current of toroidal field coils is assumed to be a sheet current with ripple component. Using the model coil current, the field ripple is derived by the Biot-Savart method. The charge-exchange process is also simulated by a simple hit-or-miss Monte-Carlo method. If a fast ion is once charge exchanged, the orbit of fast neutral (straight flight) is followed until it is reionized by field plasma particles or escapes from the plasma. In the above described OFMC code, the fast ions produced by the ionization of injected neutral beams are launched from the birth points and are followed until all of them are thermalized or lost to the first wall.

Calculations were made for a specific shot number E13634. The MHD equilibrium, constant contours of the field ripple and the first wall with poloidal position numbers are shown in Fig.1 in section 5.4.1. About 2000 test particles were employed for one calculation case, and 5 cases of computations were executed with different random numbers. Through the series of calculations, about 2200 loss particles were accumulated. Power fractions of banana-drift (ripple-untrapped) loss, ripple-trapped loss and charge exchange loss particles are 1.4%, 12%, and 1.6%, respectively. The power fraction of ripple-trapped loss particles measured by the thermocouple arrays described in

the last section is about 10%. Both results fairly agrees. Figure 1 shows the two

-dimensional heat load on the first wall diagnosed with those 2200 loss particles. Both

toroidal and poloidal distributions of the heat load derived by the OFMC code are

compared with experimental data measured by the thermocouple arrays. As shown

in Fig.2, numerical results agree very well with experimental data in both toroidal and

poloidal distributions.

References

[1] Putvinskij, S., Uckan, N.A., Borrass, K.,*et al.*, ITER-IL-PH-1-9-1.

[2] Azumi, M., Kurita, G., in Computing Method in Applied Sciences and Engineering (Proc. 4th Int. Symp. Paris, 1979) 335.

```
NE=0.35E+20/M**3
TI=4.00KEV
RT=3.33M
RP=0.93M
BT=2.47T
b =2.20%
OA=4.1S
N =18.0
```
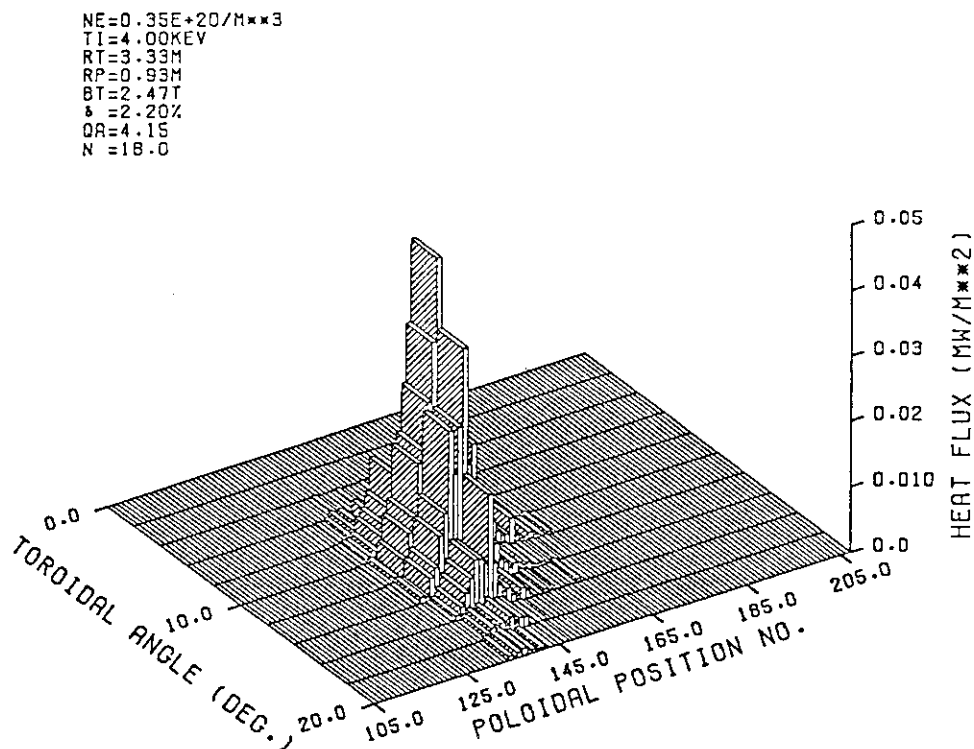

Fig. 1 Two-dimentional heat load on the first wall for ripple-trapped loss particles derived by OFMC code.
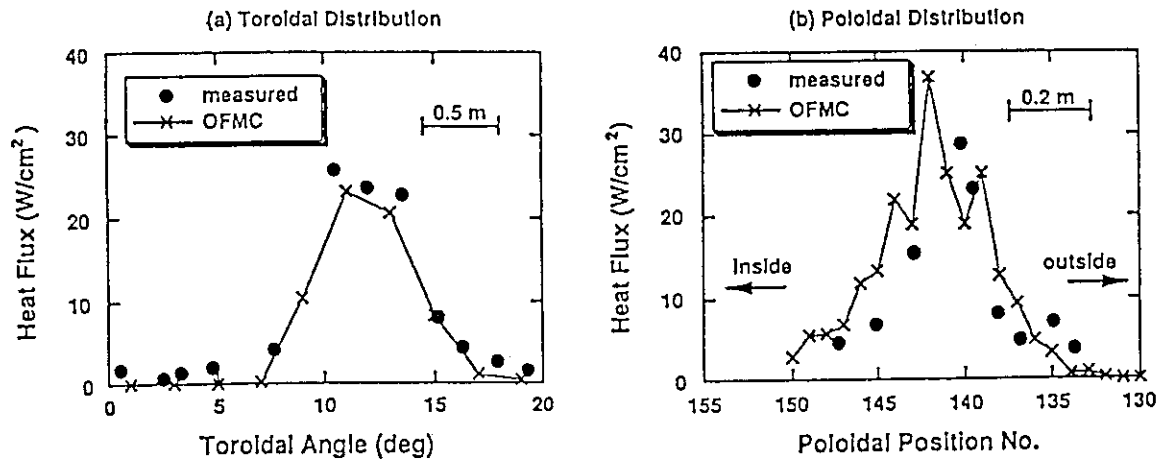
Fig. 2 Toroidal (a) and poloidal (b) distributions of heat load. The histograms and the solid lines show the numerical and the experimental results, respectively. Poloidal position numbers are shown in Fig.1 in the last section.

10. 3 Experimental Plan of α Particle Simulation by D-³He Reaction

T. Fujii, Y. Kusama, H. Kimura, K. Nagashima, M. Yamagiwa, M. Nemoto, K. Tobita,
H. Takeuchi, M. Saigusa, T. Imai,

1. Introduction

In a D-T reactor, high energy α particles are generated and heat D-T plasmas so as to maintain a nuclear fusion reaction expressed by the formula,

$$D + T \rightarrow He\,(\,3.52\,\text{MeV}\,) + n\,(\,14.06\,\text{MeV}\,) \tag{1}$$
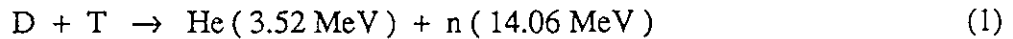
if they bring about no serious MHD instabilities and are confined in a sufficient time. Thus, the study on behaviours and confinement of high energy α particles is one of the most important issues in JT-60 U. However, if we use the D-T plasma, we have a radioactivation problem because neutrons are generated on the reaction. On the other hand, if we use the D-³He reaction given by

$$D + {}^3He \rightarrow He\,(\,3.67\,\text{MeV}\,) + p\,(\,14.67\,\text{MeV}\,), \tag{2}$$
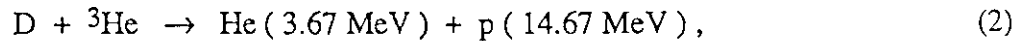
we can investigate behaviours and confinement of α particle with similar energy to the D-T

reaction without actual difficulties with respect to the radioactivation. Experiments of α particle generation have been performed in JET by fundamental minority ICRF heating to heat ³He and then rise the reactivity of D-³He [1]. A frequency range (110 - 130 MHz) of the JT-60U ICRF heating system is fourth harmonic of ³He at $B_T = 3$ T to avoid the second harmonic absorption by hydrogen near the plasma center, as shown in Fig. 1. Fourth harmonic heating is insensitive to minority ³He concentration in contrast with fundamental heating. ICRF power in the fourth harmonic regime is coupled efficiently to high energy ³He. So that we plan to perform experiments of fourth harmonic ICRF heating in combination with ³He NBI.

Cyclotron resonance layers

D - He³ Exp.

f = 116 MHz
$B_T = 3$ T
at R = 3.32 m

ICRF
Antenna

1.0 m

R = 3.5 m
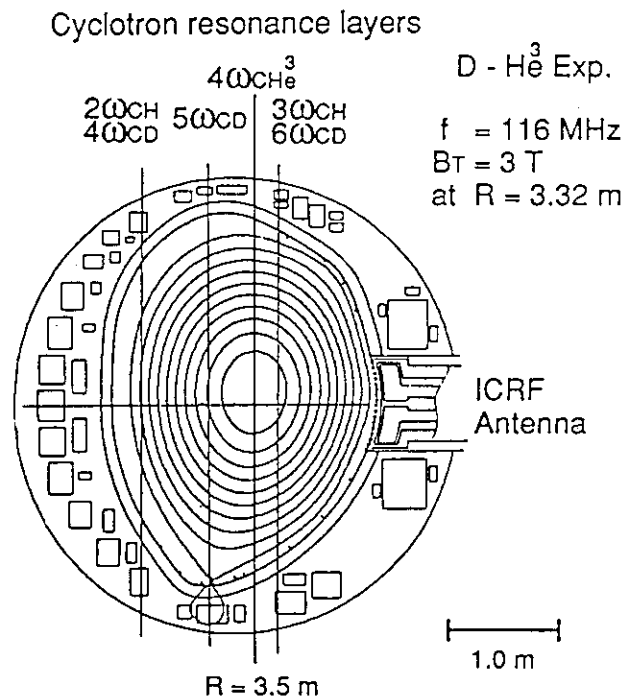
Fig. 1 Positions of cyclotron resonance layers at B_T = 3 T for D-³He plasma heated by ICRF of 116 MHz.

2. Calculated Results by One-Dimensional Fokker-Planck Code

A one-dimensional Fokker-Planck code including a quasi-linear ICRF diffusion term has been developed [2]. Numerical calculation studies are done to compare combined fourth harmonic ICRF and ^{3}He NBI heating with D + (^{3}He) fundamental minority ICRF heating. Figures 2 (a) and (b) show the calculated contours of fusion power yield ratio ΔQ at $T_e = 5$ keV and $n_e = 10 \times 10^{19}$ m^{-3} for each heating as functions of ICRF and NBI power densities. The fusion power yield ratio is defined as $\Delta Q \equiv \{ p_f (p_H) - p_f (p_H = 0) \} / p_H$, where p_f is the fusion power density and p_H is the heating power density. In the fourth harmonic heating ΔQ of 2 % is predicted for more than 0.2 MW/m^3 of relatively low ICRF power density. This value corresponds to fusion power of 100 kW and α particle generation rate of 3×10^{16} s^{-1}. On the other hand, ΔQ of 1.6 % is predicted for a narrow power density range of ~ 0.4 MW/m^3 in fundamental minority heating. The calculated results show that the maximum fusion power yield ratio is scaled by

$$\Delta Q_{max}\ (\%) = 4.3\ T_e\ (10\text{keV}) \{n_e\ (10^{20}\text{m}^{-3})\}^{1.5}\ \text{ for fourth harmonic heating },$$

and

$$\Delta Q_{max}\ \propto\ T_e^{1.5} n_e^{-1} \qquad\qquad \text{for fundamental minority heating.}$$

Then ΔQ_{max} increases with density for the fourth harmonic heating while that decreases for fundamental heating. The experiment in JT-60U will be performed in high density region. Moreover, it is found that ΔQ_{max} for the fourth harmonic heating is obtained for $p_{NB}/p_{IC} \sim 1/5$. According to this prediction we can evaluate the required ICRF power and ^{3}He beam power in the experiment.

Fig. 2   Contours of DQ in the p_{IC} and p_{NB} plane at $T_e = 5$ keV and $n_e = 10 \times 10^{19}$ m^{-3} for (a) the fourth harmonic heating and (b) fundamental heating.

3. Consideration of Experimental Conditions and Setup

First, we discuss ICRF power density which is expected to be absorbed in plasma center region (r < 1/4 a). The available injected power of the JT-60U ICRF heating system is 4.5 MW. If all the power is absorbed homog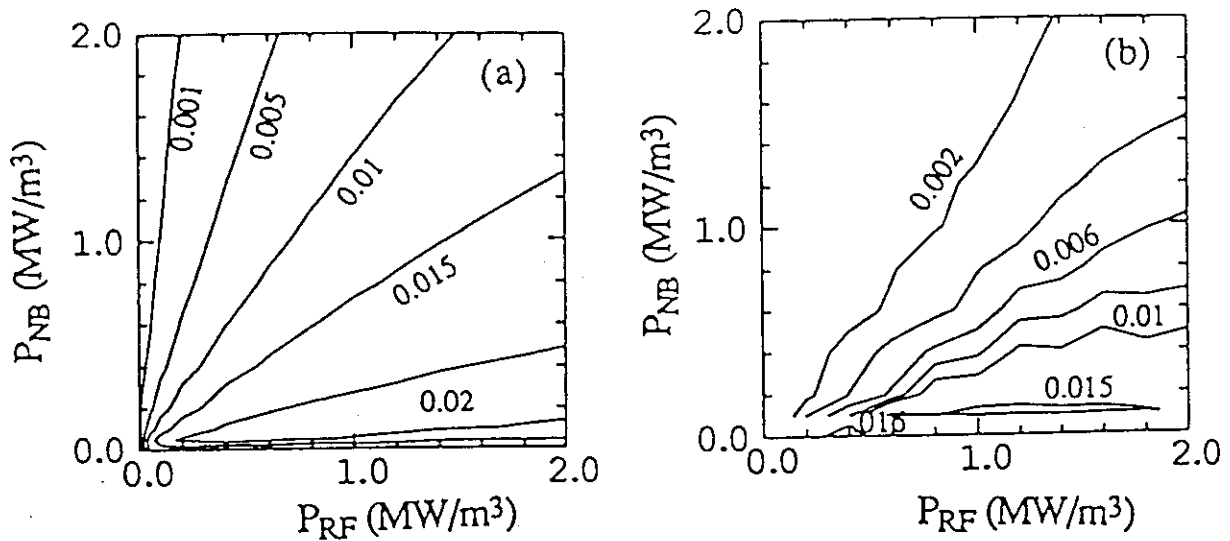eneously in r < 1/4 a, the power density is estimated to be 0.8 MW/m^3 for a = 1 m , R = 3. 5 m, κ = 1.3. This value is suggested to be close to the maximum power density. Also, we may check the absorbed power from the experimental results in JT-60. Figure 3 shows the energy spectra of minority proton measured by charge exchange neutral particle analyzer sighting the plasma center for third harmonic ICRF heating in combination of H beam NBI with beam energy of 65 keV. The absorbed power density is estimated to be 1 MW/m^3 by fitting the tail part of the calculated spectrum to the measured one. The power absorption radius is ~ 0.2 m for P_{IC} = 2.3 MW if the injected power is absorbed completely and uniformly, and is consistent with the calculated absorption radius. Thus, maximum ICRF power density is expected to be 0.5 - 1 MW/m3.

Fig. 3 Energy spectra measured by CX neutral particle analyzer for combined third harmonic ICRF and NBI heating, and calculated by the self-consistent wave code.

Next, we evaluate the deposition power of ^{3}He beam injected at 80 keV. Figure 4 (a) and (b) show the calculated deposition power profile for an upper beam line I and for a lower beam line III. Injection power of each beam line is 0.75 MW. Twenty beam lines are located symmetrically around the horizontal plane at z = 0 m. However, the plasma is asymmetrical and shifts to upper side by 0. 1 - 0.2 m , as shown in Fig. 1. Beam trajectory from the upper beam line passes closer to the plasma center than the lower beam line and therefore the upper beam line has higher deposition power densities near the plasma center. But its value averaged over r < 1/4 a is only 0.009 MW/m^3 for n_{c0} = 5 × 10^{19} m^{-3}.The power density of 1/5 p_{IC} is necessary for p_{NB} as discussed previously. The demanded power density is at least 0.1 MW/m^3. Accordingly, all ten upper and two lower beam lines should be used as a ^{3}He beam injector and their total power is 9 MW.

The following diagnostics relevant to the D-^{3}He experiment have been prepared: a γ ray measurement system to estimate the fusion power because the γ ray of 16.6 MeV is emitted in the other process of D-^{3}He reaction with probability of 3 x 10^{-5} of the formula (2), a CX

analyzer sighting the plasma center and intersecting the beam trajectory to measure the energy spectrum of ^{3}He, H and D, and an active beam system to measure slowing-down α particles with energy of less than 400 keV. Development of the active beam system which can measure α particles up to 3.5 MeV by using a detector fabricated in Ioffe institute is under consideration.
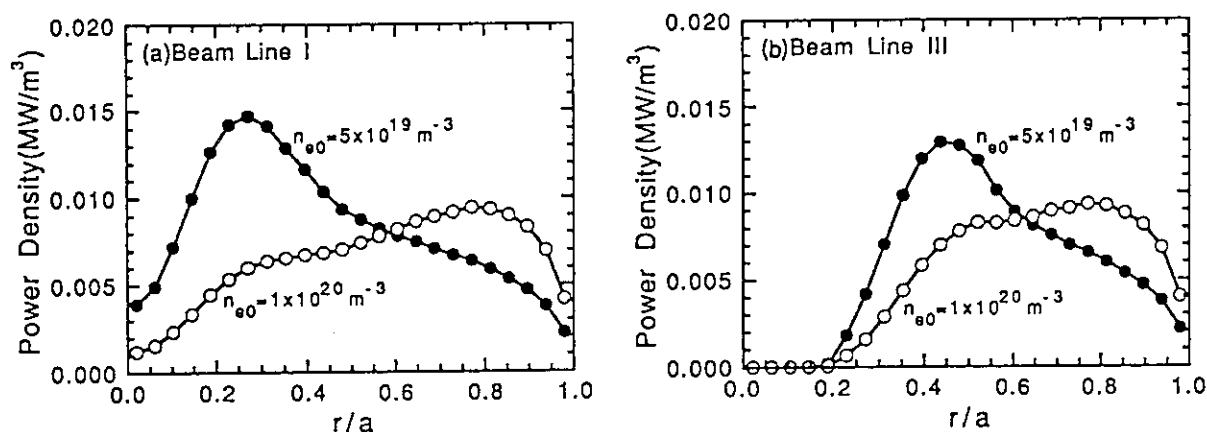
Fig. 4 Calculated power deposition profiles of ^{3}He beam (E_b = 80 keV) for (a) an upper beam line I and (b) a lower beam line III. Power of each beam line is 0.75 MW.

4. Summary

The experiment of the combined fourth ICRF and ^{3}He NBI heating with D plasmas in JT-60U is planned to investigate the behaviours and confinement of high energy α particles without difficulties to the radioactivation. The available ICRF power is 4.5 MW and NBI power is 9 MW. The fusion power yield ratio of ~ 1 % is expected, corresponding to fusion power of 100 kW and α particle generation rate of 3 x 10^{16} s^{-1}. A γ ray measurement system, a CX analyzer sighting the plasma center and intersecting the beam trajectory and an active beam system to measure slowing-down α particles with energy of less than 400 keV have been prepared as diagnostics relevant to the D-^{3}He experiment. Development of the active beam system which can measure α particles up to 3.5 MeV by using a detector fabricated in Ioffe institute is under consideration.

References

[1] JET team, Proc 13th Int. Conf. on Plasma Physics and Controlled Nuclear Fusion Research, Washington, Vol. 1 (1991) 679.

[2] M. Yamagiwa, H. Kimura, Nucl. Fusion 31 (1991) 1519.

10. 4 Sawtooth Stabilization by Trapped Fast Ions Heated by ICRF

T. Fujii, H. Kimura, M. Saigusa, M. Nemoto, K. Tobita, H. Kubo,

K. Hamamatsu, Y. Kishimoto

1. Introduction

Mechanism of sawtooth oscillation has not yet been understood completely although the sawtooth oscillation was first observed in ST tokamak in 1970's. However, the energy confinement time, especially in the plasma center region, is degraded by the sawtooth oscillation. Then suppression or control of sawtooth oscillation is investigated intensively in many devices by additional heating of ICRF, LHRF and ECH. As for application of ICRF heating, it was first reported from JET that a sawtooth period is extended up to 0.9 s during fundamental minority ICRF heating [1]. Up to the date, the extended period sawtooth is observed in JT-60, TFTR and so on. Rough parameter regions of $\bar{n}_e$ and q_{eff} for the extended period sawtooth during ICRF heating alone are summarized in Fig. 1. There is obvious difference in density region of JT-60 data from JET and TFTR data. This is inferred to be due to difference in heating regime. Theoretical models where m = 1 MHD instabilities are suppressed by hot ions heated by ICRF are proposed as one of mechanisms for sawtooth period extension

Fig. 1   Rough parameter regions for extended period sawtooth during ICRF heating alone.

[2, 3]. ICRF power is absorbed by higher energy ions in the second harmonic regime than fundamental regime and therefore hot ions are generated at higher densities in the second harmonic regime. Then, the sawtooth period extension at high densities in JT-60 is consistent with theoretical prediction mentioned above. We have analyzed the JT-60 data for combined second ICRF and NBI heating from this view point as well as second harmonic ICRF heating alone and then we plan to investigate the sawtooth period extension intensively in high power experiments on JT-60U to establish the control of the sawtooth oscillation at high density in a reactor-grade tokamak.

2. Results of Combined Second Harmonic ICRF and NBI Heating in JT-60

Figure 2 shows time evolution of the intensity of soft x-ray I_{SX} at high densities of $\bar{n}_e$ = 5.3 - 5.5 x 10^{19} m^{-3} for combined second harmonic ICRF and NBI heating when NBI power P_{NB} increases form 0 to 2 MW step by step while ICRF power P_{IC} is constant at 2.3 MW. Sawteeth with extended periods of ~ 300 ms are observed for second harmonic ICRF heating alone (P_{NB} = 0 MW) or for combination with very small P_{NB} of 0.5 MW. But the sawtooth period dramatically decreases to ~ 100 ms for combination with P_{NB} of 2 MW.

Figure 3 shows the sawteeth period as a function of $P_{NB}/\bar{n}_e$ at P_{IC} = 2.2 - 2.4 MW, P_{NB} = 0 - 6.7 MW and $\bar{n}_e$ = 5.3 - 6.5 x 10^{19} m^{-3} for heating methods of the combined second ICRF and NBI, second ICRF alone and NBI alone. There is the threshold value of $P_{NB}/\bar{n}_e$ ~ 0.1 x 10^{19} MW m^3 that terminates the sawtooth period extension. When $P_{NB}/\bar{n}_e$ excesses the threshold value, the sawtooth period during the combined ICRF and NBI heating is similar to those of NBI heating alone. The beam energy of 70 keV is much smaller than the energy of ~ 1 MeV of the ions coupled to second harmonic ICRF. Then the average energy of hot ions becomes small as $P_{NB}/\bar{n}_e$ increases. Therefore, the effect on suppression of the m = 1 mode instabilities suppression by hot ions becomes weak and the sawtooth period becomes short with increasing $P_{NB}/\bar{n}_e$.

Fig. 2 Time evolution of the intensity of soft x-ray I_{SX} at $\bar{n}_e$ = 5.3 - 5.5 x 10^{19} m^{-3} and PIC = 2.3 MW for combined second harmonic ICRF and NBI heating as a parameter of P_{NB} = 0, 0.5, 2.0 MW.

Fig. 3 Sawteeth period as a function of $P_{NB}/\bar{n}_e$ for various heating methods.

3. Analysis of Extended Period Sawtooth

As discussed in the previous section, a key point on the role of hot ions for the sawtooth period extension is their average energy $<E_h>$. In theoretical 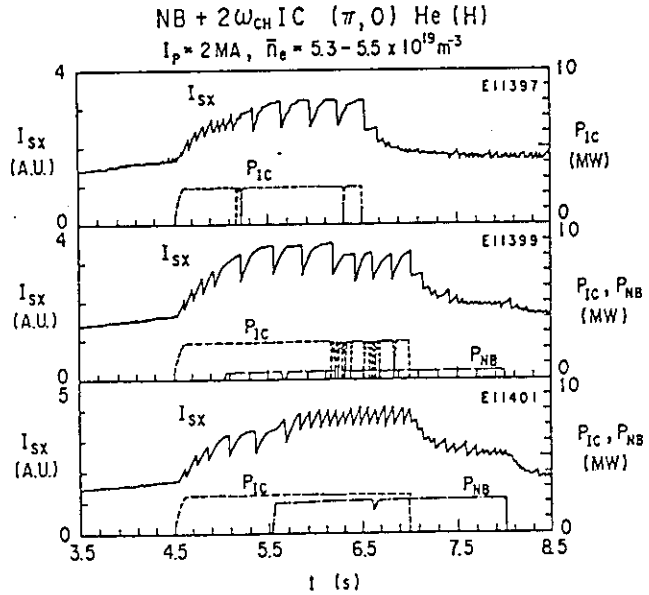models, the stabilization of the MHD oscillations of low n modes depends on currents formed by precessional drift of the trapped particles [4]. The precession frequency ω_{Dh} of the hot ion is defined as $\omega_{Dh} = <E_h>/Z_h BR_0 r_s$, where Z_h is the charge number of the hot ion, R_0 the major radius and r_s the radius of the q = 1 surface. Figure 4 shows the sawtooth period as a function of $1/\omega_{Dh}$ for the data shown in Fig. 3. The sawtooth period decreases with increasing $1/\omega_{Dh}$ and then decreasing $<E_h>$. The period extension disappears above $1/\omega_{Dh} \sim 1.5$ 10^{-4} s/rad, i. e. , $<E_h> \sim 30$ keV. Thus, the sawtooth period depends on the precession frequency of the hot ions.

Figure 5 shows the calculated results of $1/\omega_{Dh}$ as a function of density n_e for fundamental, second and third harmonic ICRF heating regimes. The absorbed power of 0.56 MW/m^3 and minority ion concentration of $n_H/n_e = 0.1$ are assumed for each regime. The calculated results shows that higher $<E_h>$ is obtained with higher harmonic ICRF heating for n_e fixed. This infers that the extension of the sawtooth period even at high densities in JT-60 different from JET and TFTR, as described in introduction, is attributed to the second harmonic heating regime. Therefore, higher harmonic ICRF heating is effective for high density plasma.

We have conducted the calculation of stability of the MHD oscillations of the m = 1 internal modes and the fishbone mode for the plasma including hot ions heated by ICRF waves.
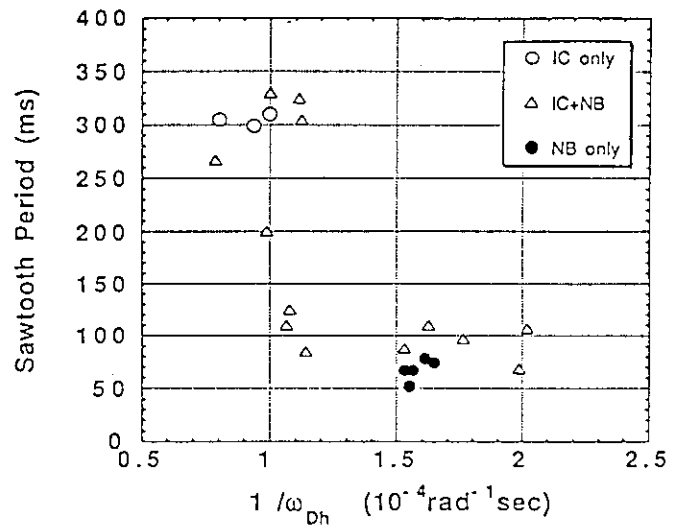
Fig. 4 Sawteeth period as a function of $1/\omega_{Dh}$ for the data shown in Fig. 2.
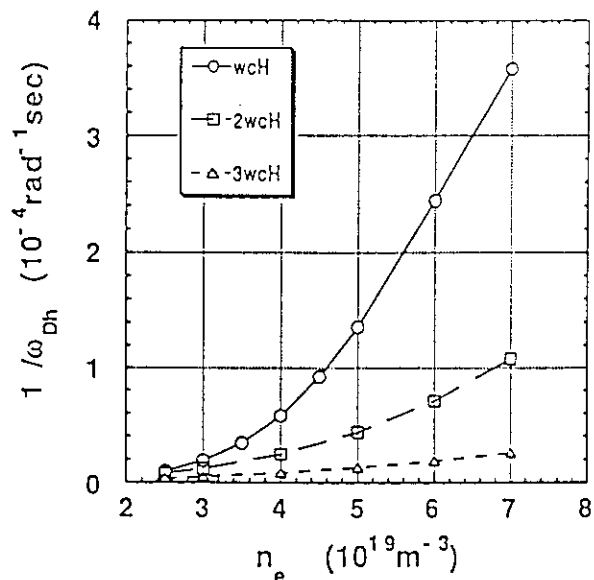
Fig. 5 Calculated results of $1/\omega_{Dh}$ as a function of density n_e for fundamental, second and third harmonic ICRF heating regimes. The absorbed power of 0.56 MW/m^3 and minority ion concentration of $n_H/n_e = 0.1$ are assumed for each regime.

Preliminary calculated results on the growth rate of the MHD modes show that there is a stable region for the beta value of the hot ions for those modes. However, we have a few experimental data of the hot ion stored energy, and then we have a difficulty to compare in detail the experimental results with the calculated ones. Further investigations are left for JT-60U ICRF experiments.

4. Conclusions

The sawtooth period dramatically decreases to ~ 100 ms in second harmonic ICRF heating for combination with small power of $P_{NB} = 2$ MW while ~ 300 ms for second ICRF heating alone at high densities $\bar{n}_e \sim 6 \times 10^{19}$ m^{-3}. It is found that the sawtooth period extends with decreasing $1/\omega_{Dh}$ and then with increasing $<E_h>$. The calculated results shows that higher $<E_h>$ is obtained with higher harmonic ICRF heating for n_e fixed. This infers that the extension of the sawtooth period even at high densities in JT-60, different from JET and TFTR results, is attributed to the second harmonic heating regime. Therefore, higher harmonic ICRF heating is effective for high density plasma. However, we have a few experimental data to compare in detail with the calculated results. Further investigations are left for JT-60U ICRF experiments.

References

[1] JET team, Proc. 11th Int. Conf. on Plasma Physics and Controlled Nuclear Fusion Research, Kyoto, Vol. 1 (1987) 449.

[2] R.B. White, M.N. Bussac, F. Romanelli, Phys. Rev. Lett. 62 (1989) 539.

[3] B. Coppi et al., Phys. Rev. Lett. 63 (1989) 2733.

[4] F. Porcelli, Plasma Phys. and Controlled Fusion 33 (1991) 1601.

11. LHCD Experiments

11.1 LHCD Experiments on JT-60U

T. Imai, K. Ushigusa, Y. Ikeda, O. Naito, S. Ide, M. Seki, T. Kondoh
M. Nemoto, S. Wolfe, , M. Sato, H. Takeuchi

1. Introduction

Steady state operation of the Tokamak Reactor is the most desired scenario for commercial reactor. Development of the non-inductive current drive method is the necessary condition to achieve the steady state operation. In the last half decade, Lower Hybrid Current Drive (LHCD) in JT-60 demonstrated notable results of non-inductive current drive of 2 MA, efficient current drive performance with efficiency η_{CD} ($\equiv$ $\bar{n}_e R_p I_{RF}/P_{LH}$) = $0.34 \times 10^{20} m^{-2} A/W$ and high power LHCD up to ~5 MW[1,2]. In JT-60 Upgrade, plasma current is increased up to 6 MA in divertor discharge and deuterium plasma operation is possible. By use of the same RF system with the modification of the launcher, LHCD program in JT-60U aims further progress of LHCD to explore steady state tokamak reactor and study the profile control.

2. JT-60U LHCD Program

Major objectives of the LHCD in JT-60U are (1) to demonstrate high performance LHCD in reactor relevant plasma, (2) to confirm engineering feasibility concerning thermal load and coupling, (3) to clarify the LHCD physics. High driven current (> 4 MA), high efficiency (> $0.4 \times 10^{20} m^{-2} A/W$), high density (> $3 \times 10^{19} m^{-3}$) and high reliability to control current profile including the demonstration of the ITER and SSTR scenarios are aimed in the item (1). In the item (2), data base for reactor design on heat load to coupling structure and first wall, especially, divertor in quasi steady state condition and disruption phase. The item (3) includes variety of the research like the propagation and absorption of the LH wave, power deposition
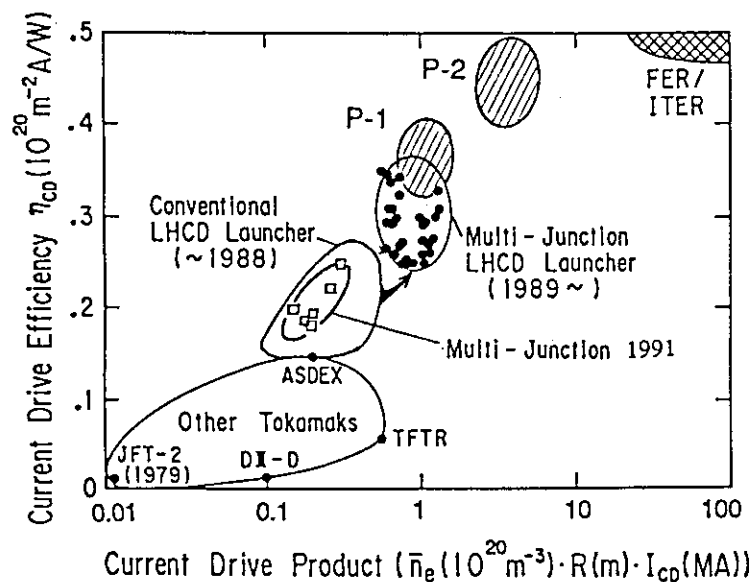
Fig. 1 Achievements of the JT-60 LHCD and other non-inductive current drive. P-1 and P-2 are the aimed region on JT-60 U and shaded region is target for ITER and FER.

profile, RF driven current profile, confinement and transport of the fast electrons, effect to the MHD activity and its mechanism and confinement of LHCD plasma. These are being planned to examine in next half decade in JT-60U.

RF system of the JT-60U LHCD is the same as that of the JT-60 except the launcher and the small modification of the transmission lines for Deuterium operation. Frequency is around 2 GHz and RF source is consist of 24 klystrons. In the early part of the program from 1991 to '92 (phase 1 period), only one third of the whole RF system can operate, where 2~3 MW of launched LHCD power is expected with one 24x4 waveguide multi-junction(MJ) launcher which is almost same as that in JT-60[3]. In phase 2 from 1993, ~10 MW launched power is planned by adding 48x4 waveguide MJ launcher.

Achievements of the performance of the non-inductive current drive in JT-60 and other tokamaks together with the expected performance in JT-60U are shown in Fig. 1, where the achieved current drive efficiency and current drive products ($CDP \equiv \bar{n}_e R_p I_{RF}$) are plotted in vertical and horizontal axes, respectively. Target for FER and ITER is shown with shaded region in the same figure and is still far away from the present achievement ($\sim 0.34 \times 10^{20} m^{-2} A/W$ and $1.2 \times 10^{20} m^{-2} MA$, respectively). It is found that the planned LHCD program in JT-60U, especially in phase 2 experiment, fills the gap between the present achievement and the reactor. Since the power level in the phase 1 is low, we placed the emphasis on the physics understandings of the LHCD in the present studies.

3.Outlines of the LHCD Results

(1) Overview: In the first campaign of the JT-60U experiments in 1991, 1.5 weeks in hydrogen discharge phase were assigned for LH experiments. Since the expected power level in this period was low around 2 MW, as mentioned before, the emphasis of the experiments was placed on the physics of the LHCD.

Fig. 2 Progress of the launched power during the conditioning and LHCD experiment.

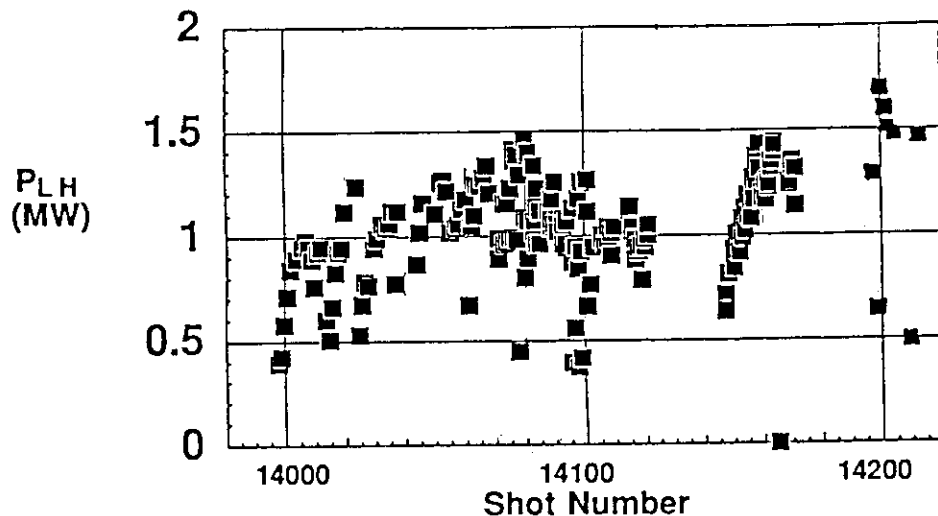There were about 200 shots for LHCD experiments and launcher conditioning, as shown in Fig. 2. Maximum LHCD power of ~1.5 MW has been injected into JT-60U plasma with $B_t = 4T$, $I_p = 1 \sim 2$ MA and hydrogen gas in divertor discharge. In spite of the carbon first wall, density control was easy and very low density plasma far less than 1×10^{19} m^{-3} was routinely possible in this series of experiment by keeping the wall temperature 150 °C and overnight GDC. This enabled driven current of ~2 MA with 1.1 MW in low density plasma (~3×10^{18}m^{-3}). The η_{CD} at present is ~0.25 $\times 10^{20}$m^{-2}A/W and is still low, compared with previous results in JT-60 with the similar launcher. Maximum CDP was 0.3×10^{20}m^{-2}MA. These values are still lower than aiming values in the phase 1, shown in Fig. 1. As described in the section 5.1.2, there are some reasons for the degradation of the current drive efficiency. One of them is the error of the phase adjustment which reduced the directivity of the unidirectional wave by about 30%, as discussed in 5.1.14. The correction of the phase adjustment has already completed during the shut down period just after this series of experiments. The second is the high Z_{eff} due to the low density less than 0.7×10^{19} m^{-3} in the present operational region. Direct loss of the fast electron to the first wall also affects the efficiency in such a low density . Moreover, discharge near the $\omega = 2\omega_{ce}$ region was sometimes observed. We still need further conditioning of the launcher together with the phase correction to get higher performance in the higher density and current region and reach to the target of the phase 1.

(2)Coupling; The reflection coefficient of 10~20% was obtained even if the distance between launcher and outer most magnetic surface (Δ_x) was 8 cm. In case of the combination with NBI, good coupling could be kept up to $\Delta_x = 15$ cm, which suggests possibility of the distant coupling of LHCD launcher. These are described in 11.9.

(3) Efficiency; $N_\parallel$ dependence of current drive efficiency roughly agrees with theory, but the observed maximum efficiency ~ 0.25 $\times 10^{20}$m^{-2}A/W is still low, compared with previous results in JT-60, as mentioned above. Detail discussion will be given in 11.2.

(4) Heat load to the divertor; Heat load to the divertor in the presence of the fast electrons produced by the LHCD power is the one of the most interesting engineering topics concerning the ITER/FER design. In the very low density region far less than 1×10^{19}m^{-3}, the heat load of the electron side of the divertor was amplified by the factor of ~2, but the density dependence of the heat load suggest it is similar to other heating scheme in higher density case. In case of onset of the instability which enhances the diffusion of the fast electrons, the localization of heat load due to the fast electrons is strong but it happens in case of the very low density only. (11.3, 11.8, 11.11)

(5) Sawtooth and MHD activities; $N_\parallel$ dependence of the suppression effect of the sawtooth is studied and the lowest $N_\parallel$ which satisfies the accessibility condition has the strongest effect. The mechanism of the suppression is still under discussion.

(6) Profile, energy spectrum and confinement of the fast electrons; Some HX profile data were obtained which indicate the change of the power deposition profile with change of the phasing of the launcher. Confinement of the fast electrons in the core plasma is dominated by the slowing down time except some particular case. (11.4, 11.5)

(7) Wave propagation and absorption; Identification of the dispersion relation of the lower hybrid wave in tokamak was studied using the NBI as a probe. The experimental result agrees well with theoretical one. Accessibility limit of the lower hybrid wave is studied by HX and ECE measurement. Results obtained qualitatively agree with theoretical prediction, but quantitative agreement requires some $N_{\parallel}$ upshift, as clarified in JT-60[4,5]. (11.6, 11.12, 11.13)

(8) Confinement and plasma rotation; Energy confinement time of the LHCD plasma is slightly better than usual L-mode scaling. Stored energy of the fast electrons seems to contribute to the improvement. Rotation of the LHCD plasma is also measured by CXRS. Application of the LHCD power drove the plasma slightly to co-direction. (11.7)

4. Prospect

We've not reached to the Phase 1 target of LHCD yet, but the major obstacles have been clarified or been solved during the shut down period. Though further conditioning of the launcher is required, the achievement of the phase 1 target seems to be in our hand during the 1992 experiment. Diagnostics to measure the fast electrons, Te(r), J(r) are also improved in the next period. Further physics studies of LHCD by use of these diagnostics are planned, though the power level of the 1992 is still low(=2~3MW). Progress and schedule of the recent decade of the LHCD experiment in JT-60 /60U is shown in Fig. 3.

| 86 | 87 | 88 | 89 | 90 | 91 | 92 | 93 | 94 | 95 |

--------- JT-60 -- ------>   <--------- JT-60U --------------------

* First LHCD   * High efficiency CD   <--- phase 1---> <---- phase 2 -----------
                      with M.J. Launcher   2~3 MW   ~ 10 MW
* 2 MA CD   (η_{CD}=0.34x10^{20}m^{-2}A/W)

* η_{CD}-scaling   * H-mode by LH   * Physics Studies
                                              * High Performance
                                                LHCD Demonstration
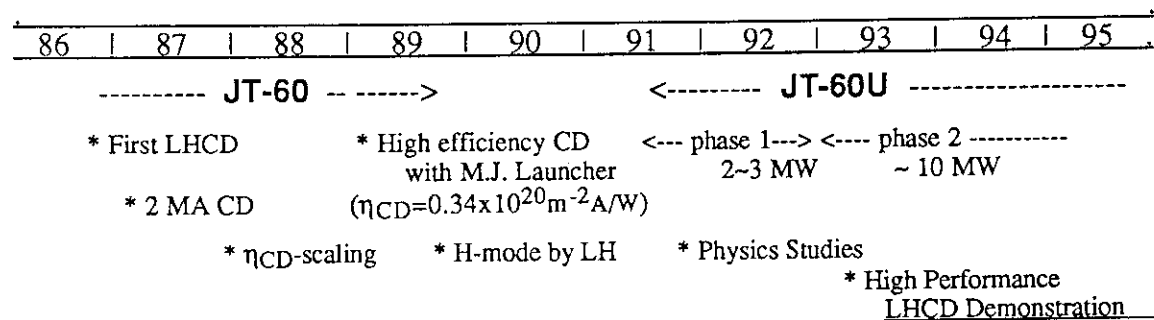
Fig. 3 Progress and Schedule of the JT-60& 60U LHCD experiments in the recent decade.

References
[1] T. Imai, et al. Nuclear Fusion 28(1988)1341.
[2] K. Ushigusa, et al., PlasmaPhys. and Contr. Fusion 32(1990)853.
[3] Y. Ikeda, et al., Nuclear Fusion 29(1989)1815.
[4] M. Nemoto, et al., Phys. Rev. Lett. 67(1991)70.
[5] S. Ide, et al., Nuclear Fusion to be published.

11.2 Current Drive Efficiency in JT-60U

K. Ushigusa, S. Wolfe, T. Imai, Y. Ikeda, O. Naito, S. Ide, H. Kondo, M. Seki, H. Nemoto, M. Sato and H. Takeuchi

The current drive efficiency in lower hybrid current drive (LHCD) experiments in JT-60U is summarized in this section.

1. Typical example and the operated regime

Most LHCD experiments were carried out in hydrogen divertor plasmas with a low density. A typical example of an LHCD discharge is shown in Fig.1, where the LH power was injected in three steps with a peak parallel refractive index $N_{||}{}^{peak}$ of ~1.34 (the phasing between adjacent multijunctions $\Delta\phi_m$= 135°). Fully non-inductive plasma ($|\Delta V/V|$ >1) is achieved with LH power of ~1.3MW, and this corresponds to a current drive efficiency η_{CD} of ~1.8 x 10^{19}m^{-3}A/W. With P_{LH} ~1MW, the decrease in the loop voltage is moderate ($|\Delta V/V| \sim 0.5$), and this corresponds to η_{CD} of ~1.2 x 10^{19}m^{-2}A/W. It should be noted in Fig.1 that the drive efficiency of a fully non-inductive plasma is higher than that with a residual DC electric field. However, in other experiments, it has been commonly observed that the existence of a DC electric field enhances the current drive efficiency. Therefore there is some mechanism which prevents driving RF current at low power injections. This phenomenon will be discussed again in Sec. 11.11. The bottom trace in Fig.1 shows the time evolution of the loop voltage without smoothing. One can find large negative spikes on the loop voltage. This is thought to be a kinetic instability such as the anomalous Doppler effect, which is caused by a large anisotropy in the electron velocity distribution. There is no large difference in the temperature with and without LH as shown in Fig.1. This indicates that the change in the thermal energy is not so large in this density regime.

Figure 2 shows the current drive product $n_eR_pI_{RF}$, and the operated electron density against the LH power, where data with $|\Delta V/V| >$ 0.8 are used. The experiments were carried out in the following parameter range: $\bar{n}_e$ = 0.3 - 0.7 x 10^{19} m^{-3}, I_p = 1.2 - 2MA, P_{LH} = 0.7 - 1.5MW and q_{eff} = 5.2(2MA) - 9(1.2MA). The distance between the launcher and the plasma surface δ_L was 6 - 10 cm, and the total (divertor) radiation power was smaller than 40% (20%) of the total heating power. The current drive product of 3 x 10^{19} m^{-2}MA was obtained with 1.2MW of LH power at $\bar{n}_e$ = 0.5 x 10^{19}m^{-3} and the maximum drive efficiency is around 2.5 x 10^{19} m^{-2} A/W. Compared to the JT-60 results, ~25% of the current drive product and ~70% of the drive efficiency were achieved with the low parameter regime during 1.5 weeks of experiments.

2. Parameter dependence of efficency

Figure 3 shows the density dependence of the drive efficiency and $Z_{eff}/T_e{}^{0.5}$ with $\Delta\phi_m$ = 135°. The efficiency is improved by increasing the density. This comes from the decrease in Z_{eff} as confirmed in JT-60 experiments. The efficiency of 2MA discharge is higher than that of 1.2MA by a factor of ~1.5. A higher efficiency can be
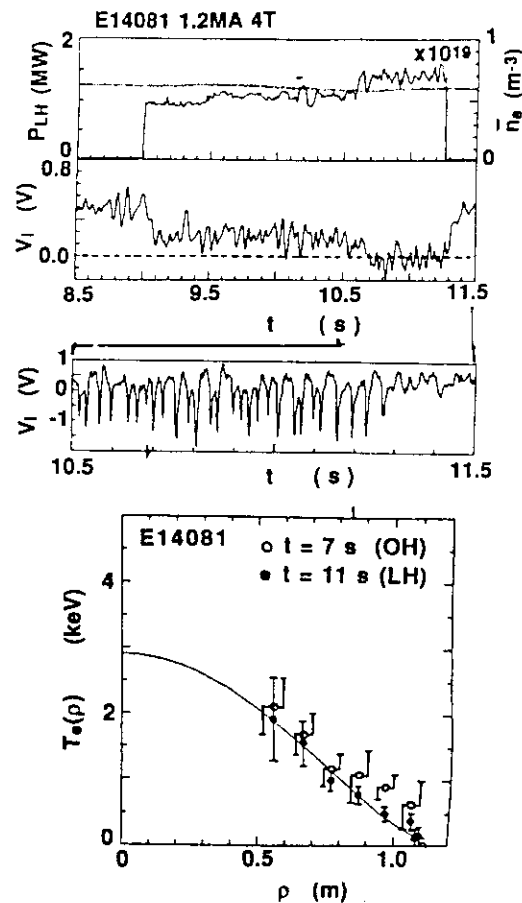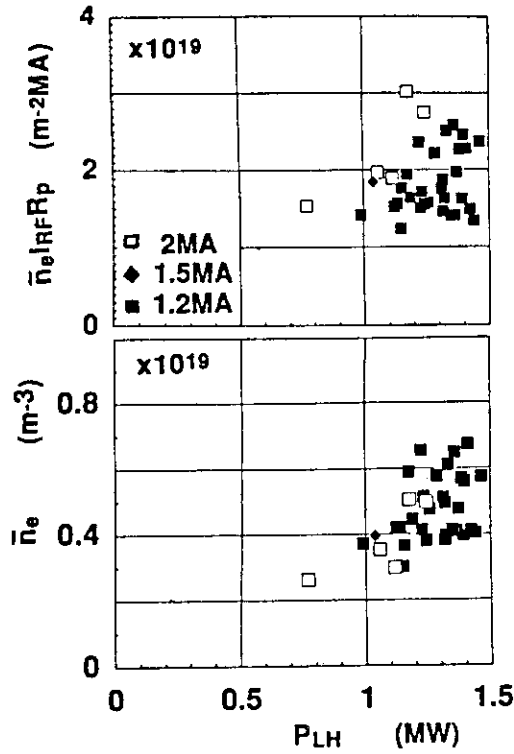

Fig.1 Example of full CD discharge

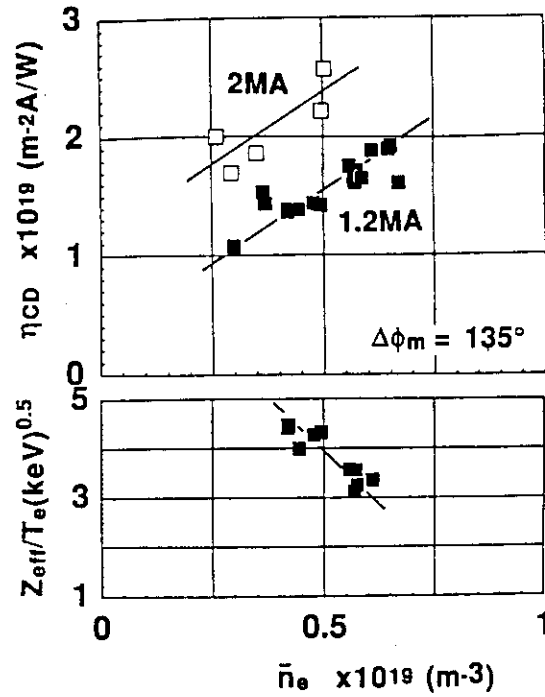Fig. 2 The CD product and the density against the LH power.

Fig.3 Density dependence of the efficiency and $Z_{eff}/T_e^{0.5}$.

expected in the next series of experiments.

The current drive efficiency is plotted against the phasing between adjacent multijunction modules in Fig.4, where $I_p = 1.2MA$ and $\bar{n}_e = 0.4 - 0.6 \times 10^{19}$ m^{-3}. The efficiency has a maximum at around $\Delta\phi_m = 135°$ and this is a similar dependence to the JT-60 results. The simple quasi-linear Fokker-Planck theory says that the current drive efficiency is proportional to $1/N_{||}^2$ for a narrow spectrum width ($\Delta N_{||}/N_{||} \ll 1$). The spectrum weighted $1/N_{||}^2$, which is introduced by J. Stevens[3], regards the efficiency of the launched wave spectrum as the sum of the narrow limit efficiency weighted by the spectrum;

$$\eta_{CD} \propto \frac{1}{<N_{||}^2>} \equiv \frac{1}{\int_{-\infty}^{\infty} P(N_{||})dN_{||}} \left\{ \int_{N_{||ac}}^{\infty} \frac{P(N_{||})}{N_{||}^2}dN_{||} - \int_{-\infty}^{-N_{||ac}} \frac{P(N_{||})}{N_{||}^2}dN_{||} \right\} \tag{1}$$

This is very convenient because the wave spectrum, the accessibility and the directivity are automatically included into one form. It has been confirmed that observed current drive efficiencies in PLT, ASDEX and JT-60 experiments were well scaled with $1/<N_{||}^2>$. If we employ the spectrum weighted $1/N_{||}^2$, the current drive efficiency of the quasi-linear Fokker-Planck theory becomes $\eta^*_{CD}(10^{19}m^{-2}A/W) = 1240 / \ln\Lambda/(5 + Z_{eff})/<N_{||}^2>$, where $\ln\Lambda$ is the Coulomb logarithm. The broken line in Fig. 4 shows the efficiency $\eta^*_{CD}(d)$ which is calculated with the designed launcher spectrum; the pitch of the waveguide is 1.3cm, the phase of adjacent sub-waveguide in a module is 60° at 2GHz and the phase difference between adjacent modules is exactly $\Delta\phi_m$. It was assumed that $Z_{eff} = 8$.
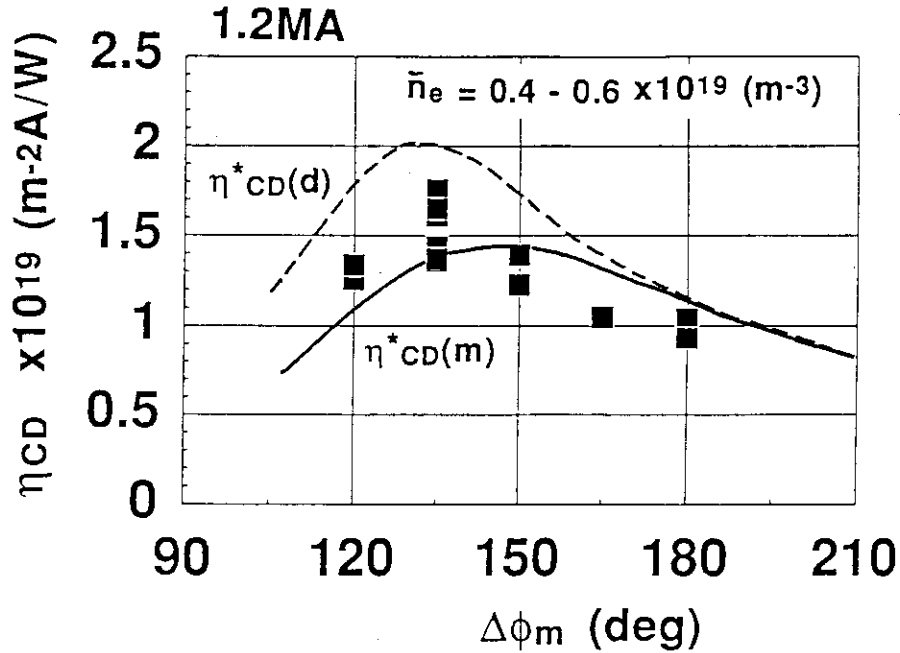
Fig. 4 The current drive efficiency versus the phase difference between modules

Compared with the experimental efficiency, the theoretical efficiency $\eta^*_{CD}(d)$ has a similar dependence on $\Delta\phi_m$ but is slightly higher. After the first experimental campaign of JT-60U, the relative phasings of each multijunction module and each sub-waveguide were measured. There were some differences of the phasing from the designed value. This affects the launched wave spectrum significantly. This influence of the phase difference on the wave spectrum is discussed in Sec. 11.10 in detail. The solid line in Fig.4 shows the theoretical efficiency $\eta^*_{CD}(m)$ where the spectrum weighted $N_{||}^2$ is calculated by using the measured relative phasing of each multijunction and sub-waveguide. It is assumed in the calculation of $\eta^*_{CD}(m)$ that the phase difference between modules in the second column of the poloidal multijunction array is exactly controlled to be $\Delta\phi_m$ (but we cannot exclude a possibility that the phasing of modules in the second column is not periodic exactly). The theoretical efficiency $\eta^*_{CD}(m)$ has similar value to the experimental efficiency, but has a slightly different phase dependence. From the phase dependence, we may say that the excited wave spectrum in the plasma is close to the designed spectrum.

3. Comparison with JT-60 results and discussions

The operated electron density in the first campaign of JT-60U LHCD experiments is lower than that in JT-60. The density dependence of the current drive efficiency between JT-60U and JT-60 experiments is compared in Fig.5 where solid and open symbols are data in JT-60U and JT-60, respectively. The obtained current drive efficiency in JT-60U shows relatively high current drive efficiency at a very low density. The temperature dependence on the current drive efficiency has been shown in JT-60 experiments and this was confirmed recently in the JET experiments. The experimentally observed efficiency is normalized by $\eta^*_{CD}(d)$ and plotted against the volume averaged electron temperature in Fig. 6. Since there is large ambiguity in the electron temperature in JT-60U experiments because of the very low density, the range of measured average temperature is plotted. It is seen that JT-60U data is less than JT-60 results by a factor ~ 0.7.

There are several possibilities to explain this. First, this series of experiments has an uncertainty about the wave phasing. Phase differences between multijunction modules were measured except for the second column, which is used in the feed back control on the wave phasing. We found that the other three columns are not completely periodic. Since the

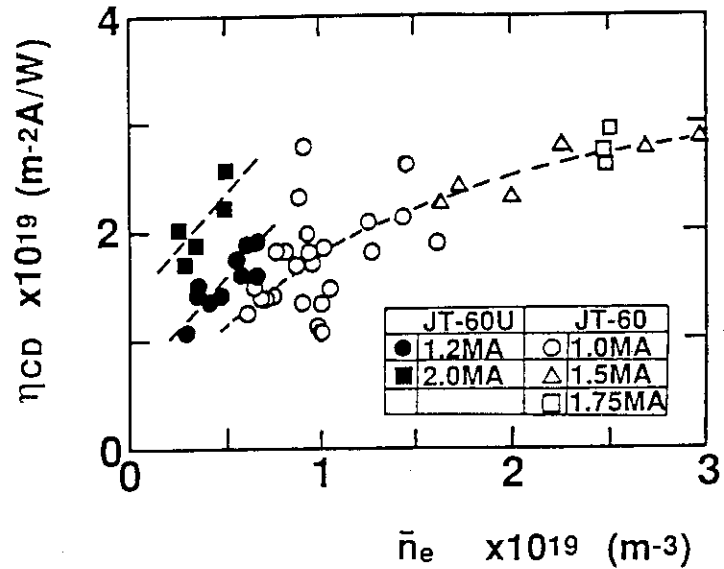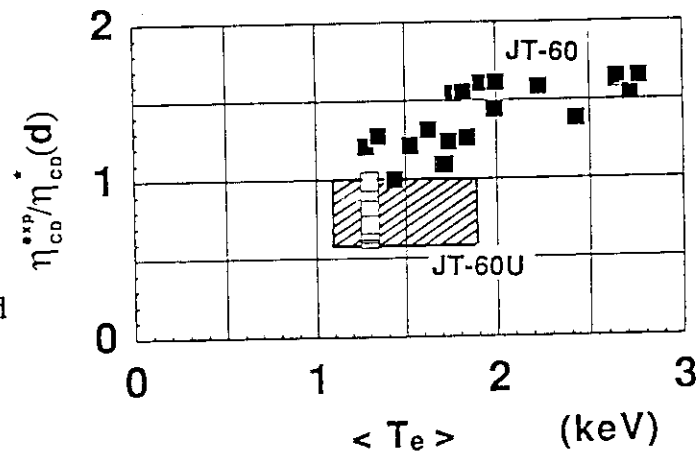Fig. 5 The drive efficiency versus the density.

Fig.6 Normalized efficiency versus the volume averaged electron temperature.

second column of the launcher may have the same problem as previously mentioned, the wave spectrum, which is employed here to estimate $\eta^*_{CD}(m)$, may not be the correct spectrum. The second explanation is about some power losses related to the extremely low density regime. The slowing down time of energetic electrons with an energy corresponding to the accessibility condition($N_\parallel^{acc} \sim 1.15$), is about 0.3 s at a density of $\sim$ $0.5 \times 10^{19}m^{-3}$. Some fraction of power may be lost before they are thermalized by slowing down process. Indeed we have observed significant X-ray emission from the divertor plates during LHCD. Some fraction of the divertor heat load measured by IRTV, which is about half of input LH power (see Sec. 11.3), must be due to the loss of high energy electrons. Furthermore, we observed large negative spikes on the loop voltage during the LH pulse and this suggests a kinetic instability. Rapid loss of parallel energetic electrons may be accompanied by this instability. This is one factor which degrades the current drive efficiency in addition to the ambiguity in the measurements of Z_{eff} and $<T_e>$.

In the first campaign of LHCD experiment in JT-60U, the current drive efficiency of $2.6 \times 10^{19}m^{-2}A/W$ was achieved at very low density ($\bar{n}_e \sim 0.5 \times 10^{19}m^{-3}$) and this is highest value in this density regime. Although there were some factors to degrade the efficiency, we can remove these factors by setting the launcher phasing correctly, and operating at higher density and current. Higher drive efficiency can be expected in the next series of experiments.

Reference
[1] Stevens, J. et al., Nuclear Fusion 28(1988)217.

11.3 Heat Load on Divertor Plates and Power Balance in LH, LH + NBI

Y. Ikeda, T.Imai, K.Ushigusa, Y. Itami

1. Introduction

A major consideration in the achievement of steady state fusion reactor is the handling of the heat load on the divertor plates. With high-power, long-pulse additional heating, the occurrence of impurity bloom from divertor plates is a significant factor limiting the best fusion performance. This bloom sometimes limited the maximum injection RF power in JT-60 LH experiments, because it led to modification of the plasma boundary, resulting in a deterioration of the coupling in launchers. While the measurement of the heat load on the divertor plates and the radiation loss gives the determination of the energy loss channels of the plasma.

We investigated the heat load on the divertor plates by IRTV in LH and LH + NBI discharge. Experiments were carried out in the standard divertor configuration with I_p=1.2 - 2 MA, B_t = 4.0 T. Lower hybrid waves were injected by a multijunction launcher with P_{LH} ≤1.5 MW, f = 1.74-2 GHz.

2. Results

Figure 1(a) shows the typical heat load on the divertor plates in LH discharge, where P_{LH} ~ 1.4 MW, f=2GHz, ϕ = 135°, Ip=1.2 MA, n_e ~ 0.5x10^{19} m^{-3}. A loop voltage is ~ 0 V during LH injection. The distance of the separatrix point and divertor plate (δ_x) is about 0.2 m. A total heat load on the divertor plate (Q) is about 0.8MW, and the peak temperature reaches from 195°C to 220°C. The heat flux profiles in this discharge are shown in Fig. 1(b). The peak heat flux on inner and outer sides are about same value, 0.36 MW/m^2, respectively. While the half width of the heat flux (HWHF) of outer side is about twice larger that of the inner side in this case, which is the same characteristic as reported in JT-60 [1].

The density dependences of the HWHF are shown in Fig. 2. The density is varied from
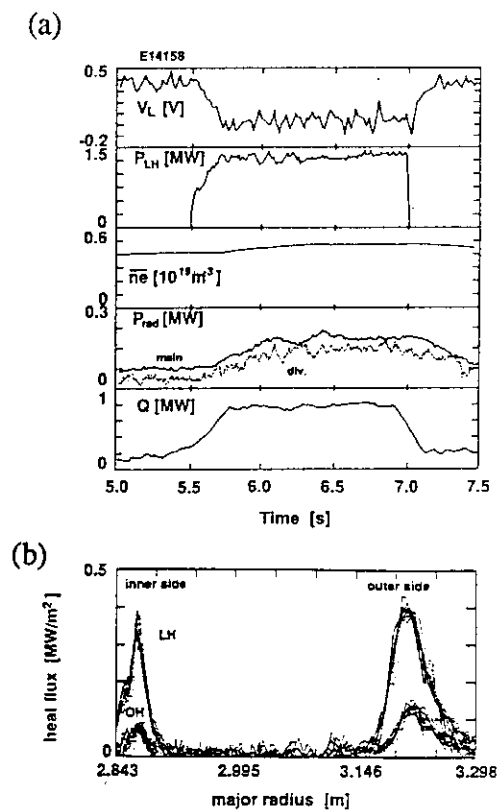
(a)

(b)

Fig. 1(a) typical LH shot,
(b) heat flux profile.

0.8×10^{19} m^{-3} to 2×10^{19} m^{-3} at fixed plasma parameters of Ip $=2$ MA, $\delta_x = 0.2$ m, P$_{LH}$ ~ 0.8 MW, f=2GHz. $\phi = 120$ °. Though the input Ohmic power essentially increases due to the increment of the loop voltage with increasing density, it changes from 0.7 to 0.9 MW. It is found that the HWHF does not change strongly, especially at n$_e$ > 1×10^{19} m^{-3}. The week density dependence of the peak heat flux was also observed in LH +NBI discharge at n$_e$ > 1×10^{19} m^{-3}. Figure 3 shows the peak heat flux normalized input power (q$_{peak}$) in the power range of 1~ 2 MW (P$_{LH}$ ~1 MW, P$_{NBI}$ ~ 1 MW) at Ip =1.2MA. Here, the density dependence of shine through of R = 0.8e$^{-n_e}$, [n$_e$;10^{19} m^{-3}] is assumed. Open and closed symbols are for LH (f=2GHz, $\phi = 135°$), LH + NBI (f=1.74GHz, $\phi = 140°$) discharge, respectively. The drop of loop voltage is more than 0.8 for LH case in this figure, however, there is no data set of fully current drive discharge at n$_e$ > 1×10^{19} m^{-3} for LH + NBI discharge. In LH discharge, the heat flux on the inner side is 0.3 MW/m^{2}MW, which is considerably higher than that of LH + NBI discharge (0.1 MW/m^{2}MW), though the density range is different. The normalized heat flux is approximately constant at n$_e$ > 1×10^{19} m^{-3} for the inner and outer sides in LH + NBI discharge, and the heat flux on the outer side is about twice higher than that of the inner side. Since the higher power is required to sustain plasma current at higher density, it has not been possible to study in detail the question of whether the difference of the heat load in LH, LH + NBI can be explained by the operational density / heating mechanism (beam acceleration).
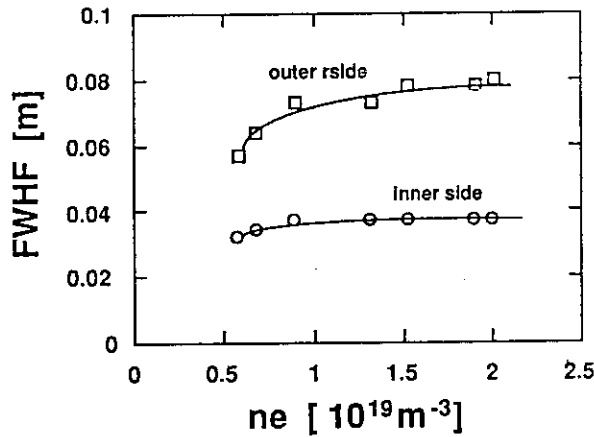
Fig. 2 density dependence of
half width of heat flux.
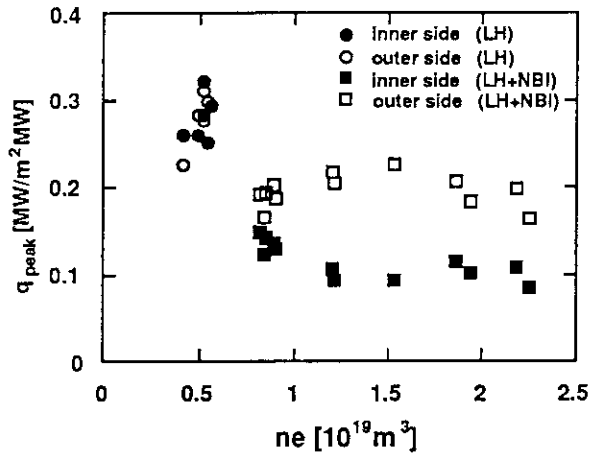
Fig.3. density dependence of
peak heat flux.

The global power balance in LH are shown in Fig. 4. This figure gives the heat load and radiative loss as a function of input power (OH + LH power). These data are in the density range of $0.4 \text{-} 0.6 \times 10^{19}$ m^{-3}, f=2GHz. $\phi = 135°$. The heat load on the divertor plates and radiative loss are in proportion to the input power, the total heat load on the divertor plates, the radiative loss from divertor plasma and main plasma are 60 ~ 65%,

~15% and ~15%,respectively. About 90 ~ 95% of the input power is identified. The ratio of the heat load on divertor plates is slightly higher than that in OH case. The dependence of power balance on the wave spectrum at f=2GHz, ne ~ 0.4-0.6x10^{19} m^{-3} is shown in Fig. 5. Though the experimental data are rather scattered, the heat load on the divertor plates is not sensitive to the wave spectrum. This result shows that the fast electrons produced by LH waves do not seem to be main source of the heat load on the divertor plates.
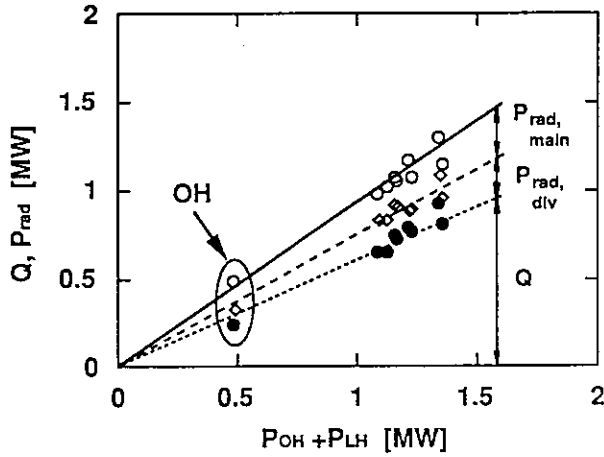
Fig. 4 power balance in LH.
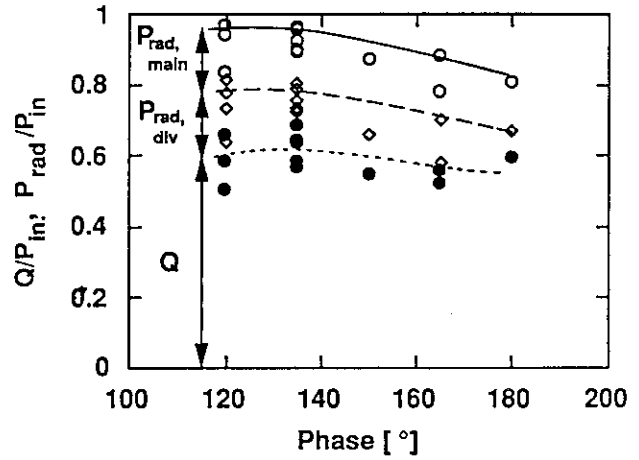
Fig.5. phase dependence of power balance in LH.

In LH +NBI discharge, where P_{LH} ~ 1 MW, P_{NBI} ~ 1-5 MW, the power balance ratio on the divertor plates and the radiative loss is about 35-45 %, 30%, respectively, in the density range of 0.8 - 2.3x10^{19} m^{-3} as shown in Fig. 6. Since the ripple loss is considerably high in the standard NBI-heated plasma configuration, the degradation of power accounting is probably due to the ripple loss in the standard NBI-heated plasma configuration.

In the Harrison model, the heat load is approximately given by [2],

$$Q \approx \frac{P^{14/9}}{n_e^{7/9} \chi_\perp^{7/9}}$$

where, P is input power, $\chi_\perp$ is perpendicular heat conductivity in scrape off layer. On assuming $\chi_\perp$ is constant, heat load is in proportion to $P^{14/9} n_e^{-7/9}$. On the contrary, if $\chi_\perp$ is a Bohm type (Itoh model),

the heat load is given by [3],

$$Q \approx \frac{P}{n_e^{0.4}}$$

therefore, the heat load weekly depends on the density.
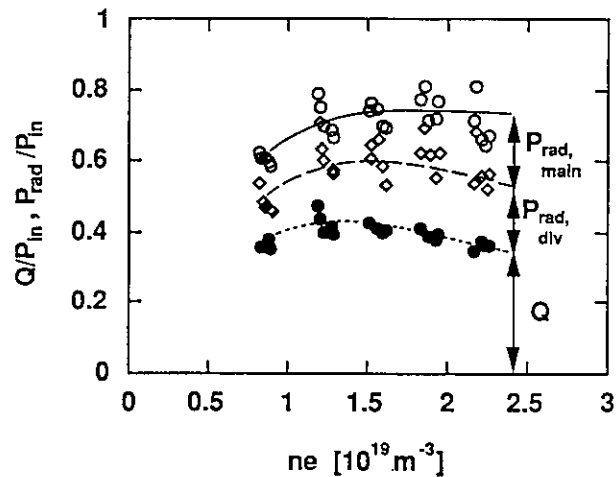
Fig. 6 density dependence of power balance in LH + NBI.

The experimental data show that the density dependence of HWHF and the heat load is week in the range of ne = 0.8 - 2.3x10^{19} m^{-3}, therefore, it seems that $\chi_\perp$ is not constant, and the Itoh model is more suitable to explain these data.

3. Summary

Measurements of heat load were made during LH, LH +NBI , using IRTV. The following observations were made. (a) density dependences of HWHF and the peak heat flux are week in the density range of 1 - 2.3x10^{19} m^{-3}. These results can not be explained by the simple Harrson model, in which the heat load is in proportion to $P^{14/9}ne^{-7/9}$. (b) In LH, the heat load normalized input power is about 0.3MW/m^{2}MW for inner and outer side at ne ~ 0.5x10^{19} m^{-3} . In LH + NBI, they are 0.1, 0.2 MW/m^{2}MW at the density range of 1 - 2.3x10^{19} m^{-3} (c) Global power balance studies lead to the observation of fairly good power accounting. About 90 ~ 95 %, and 70 % of input power are identified in LH, LH + NBI discharge. The heat load on divertor plates are about 60-65% in LH, 35-45% in LH + NBI case.

The heat load of full LH at high density will be carried out in next campaign after sufficient RF conditioning.

References
[1] Y.Itami et. al., J. Nuclear Materials 176&177 (1990) 504-511.
[2] M. Harrison et. al., ITER-IL-PH-13-9-E12.
[3] S.Itoh et. al., ITER-IL-PH-13-0-J-7.

11.4 Distribution of High Energy Electrons in a JT-60U LHCD Plasma

S.Ide, T.Kondoh, K.Nagashima, M.Sato and T.Imai

1. Introduction

For the understanding of the physical mechanisms of Lower Hybrid Current Drive (LHCD), it is very important to get informations about high energy electrons created by the Lower Hybrid Wave (LHW). Although the distributions of high energy electrons in both real and momentum spaces are of interest, they are quite difficult to know[1]-[5]. In this paper, the preliminary result of the investigation of the high energy electrons in the JT-60U LHCD plasma with hard X-ray (HX-ray) measurement is shown.

2. HX-ray apparatus

HX-ray is measured with 7 channels of NaI(ϕ 2 inc. $\times$ 2 inc.) scintillation detectors. Measuring chords are the right angle to the toroidal field B_T, on the same ploidal plane, and are shown schematically in Fig.1. Each signals from photo multipliers are pulse height analyzed every 100 ms for 12.8sec.

3. Experiment

The target plasma was a hydrogen plasma with a lower single null point. The plasma current $I_P = 1.5$ MA, the line averaged electron density $\bar{n}_e \approx 6 \times 10^{18} m^{-3}$ and $B_T = 3$ T. Into this plasma, LHWs of different wave refractive indices parallel to the magnetic field $N_{//}$ were fed through a 24 $\times$ 4 multi-junction launcher. In Fig.2, I_P , the one turn voltage V_L, $\bar{n}_e$, and the intensity of electron cyclotron emission (ECE) I_{ECE} at f = 120 GHz (1.5 times the electron cyclotron frequency at the plasma center) are plotted. The LH powers are shown schematically at the top. They are about 1.2 MW, and the values of $N_{//}$ of each LHWs are, 1.51, 2.12 and 1.19 respectively. And the full width of the spectra are about 0.72. I_{ECE} is detected by a Michaelson interferometer along a chord perpendicular to B_T and from the low field side. Therefore it is difficult to analyze I_{ECE} in such a case where high energy electrons exist in a plasma, because of the radial variation of B_T and frequency down shift caused by the relativistic effect. However, if we assume that the ECE signal is dominated by the down shifted second harmonic emission from the plasma center, then this signal is attributed to the emission from electrons of its kinetic energy about 160keV. Therefore, I_{ECE} indicates tail electron information. By the injections, I_{ECE} increases while V_L decreases. Those show that tail electrons are formed by the injection and then plasma current is partly carried by them.

Results of the HX-ray measurement are shown in Fig.3. Fig.3 (a) is a time evolution of the HX-ray intensity I_{HX}, photon count $\times$ photon energy (100 - 500keV), at 0.2a. I_{HX} responds to each LHWs and is largest for the lowest $N_{//}$ wave. Line averaged I_{HX} profiles are plotted in Fig.3 (b) for each waves. It is clearly seen that the lower $N_{//}$ is the deeper wave penetrates into plasma. HX-ray spectra at 0.2a and 0.57a corresponding to each waves are also shown in Fig.3 (c). A steepness of a spectrum is smaller for lower $N_{//}$ wave and for smaller r.

3. Discussion

Figs.3 (b) agree well with a simplified LHW characteristics as follows. A lower $N_{//}$ (faster phase speed) wave tends to interact with bulk electrons at a region where bulk temperature is higher, in other words bulk thermal speed is faster. Therefore, the lower $N_{//}$ is, the deeper a wave penetrates into the plasma as seen in Figs.3 (b). However it is difficult to tell with what temperature of bulk electrons a wave interacts most strongly. It is because of so called "spectrum gap" problem. The "spectrum gap" problem is that launched wave phase speed is much faster than bulk thermal speed in usual experimental condition. Accordingly, there must be some physical mechanisms of filling the gap[6]. Many theoretical approaches have been made[7]-[10]. However, few cross investigation of theories and experiments have done. In our results, the peak position in Figs3. (b) may indicate a position where strongest interaction occurs. Comparing the results with theories is our future issue on JT-60U.

In Fig.4, e folding energies (T_{HX}) for each spectra at 0.2a shown in Fig.3 (c) are plotted against resonant parallel energy, $E_{res}=m_0c^2 \times ((1 - N_{//}^{-2})^{-0.5} - 1)$ (keV). Fig.4 shows strong dependence of T_{HX} on E_{res} of injected wave. In these LHCD cases T_{HX} is expected to be sensitive to the typical energy of the tail electrons in the direction perpendicular to B_T (i.e. perpendicular temperature $T_\perp$), since HX-ray is measured perpendicular to B_T. Therefore we can say that $T_\perp$ is higher for lower $N_{//}$ wave injection. However because of the accessibility condition a wave of $N_{//} < 1.35$ is not able to penetrate into central region of $r < 0.2a$. In Fig.5 shown are calculated electron energy distribution function using the experimental parameters for each $N_{//}$. For $N_{//} = 2.12$ the tail extends up to about 60 keV, this value is almost the same as E_{res} for $N_{//} = 2.12$. For $N_{//} = 1.51$ and 1.19 the extents are almost the same and are about 250 keV. The value of $N_{//}$ of which $E_{res} = 250$ keV is about 1.35. Accordingly the maximum extension of the electron distribution function is expected, from this calculation, to be the same for both $N_{//} = 1.19$ and 1.51 cases. Nevertheless T_{HX} is larger for $N_{//} = 1.19$ wave injection. The reason can be because $N_{//} = 1.19$ wave has more power in low $N_{//}$ spectrum than $N_{//} = 1.51$ wave does. I_{ECE} is also sensitive to $T_\perp$, and assuming the position of emission and the harmonic number kinetic energy of the resonant electrons is available. In Fig.6 I_{ECE} divided by $I_{ECE}(N_{//} = 2.12)$ against frequency normalized to the electron cyclotron frequency at the plasma center are plotted for $N_{//} = 1.19$ and 1.51 cases. The plotted range of frequency is expected not to be affected by the bulk electrons. In the figure, the peak of the curve is larger and at lower frequency for the lower $N_{//}$. The lower frequency I_{ECE} corresponds to the electrons of higher kinetic energy, if the harmonic number and the position of emission are kept unchanged. Assuming second harmonic resonance at the plasma center, $f/f_{ce0} = 1.25$ corresponds to the kinetic energy of 300keV. Although the spatial profile of the tail electrons varies with $N_{//}$ as HX-ray measurement shows, Fig.6 may support that $T_\perp$ is higher for lower $N_{//}$ wave injection. The results show that a low $N_{//}$ wave which can not penetrate into plasma core directly because of the accessibility condition makes center peaked tail profile. This suggests more flexibility of profile control by LHW at high density region. It is noted that the absolute number of the calculated tail electrons has less information because the calculated driven current and absorbed power are less in $N_{//} = 1.19$ case. The maximum parallel extent of the tail electrons and spatial distribution of the energy of the tail electrons

4. Summary

On the JT-60U tokamak, hard X-ray emission profiles during LHCD are measured. The dependence of the profile on $N_{//}$ agrees with the LHW characteristics. However quantitative discussion about the profile is difficult, since any information about the mechanism of filling the spectrum gap is not clear yet. The slope of the HX spectrum depends strongly on $N_{//}$. This suggests that the average perpendicular energy of the tail electrons is larger for lower $N_{//}$ injection, even though the accessible $N_{//}$ is almost the same.

References

[1] VON GOELER, S., STEVENS, J.E., BERNABEI, S., et al., Nucl. Fusion 25 (1985) 1515

[2] STEVENS, J.E., VON GOELER, S., BERNABEI, S., et al., Nucl. Fusion 25 (1985) 1529

[3] KATO, K., HUTCHINSON, I.H., Phys. Fluis 30 (1987) 3809

[4] IDE, S., OGURA, K., TANAKA, H., et al., Nucl. Fusion 29 (1989) 1325

[5] OGURA, K., TANAKA, H., IDE, S., et al. Nucl. Fusion 31 (1991) 1015

[6] IDE, S., IMAI, T., USHIGUSA, K., et al. to be published in Nucl. Fusion

[7] ANDREW,P.L., PERKINS,F.W., Phys. Fluids 26 (1983) 2537.

[8] BONOLI,P.T., ENGLADE,R.C., Phys. Fluids 29 (1986) 2937.

[9] WEGROWE,J.G., Proc. of 14th European Conf., Madrid 1987, Vol.11D, partIII 911

[10] MOREAU,D., RAX,J.M., SAMAIN,A., Plasma Phys. and Controlled Fusion 31 (1989) 1895.
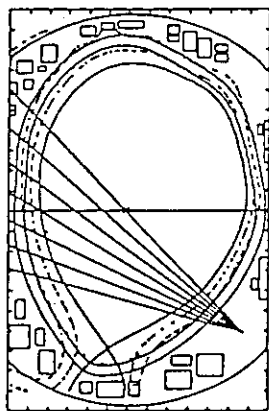
Fig.1 Schematic view of HX-ray measuring chords.
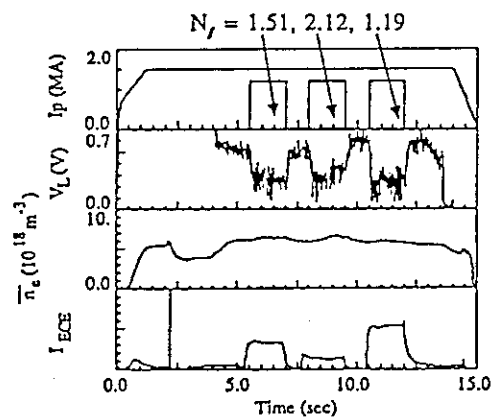
Fig.2 Temporal evolutions of plasma parameters. Ip (MA). V_L (V), $\bar{n}_e$ (10^{19} m^{-3}) and I_{ECE}.

(a)

Time (sec)

N// = 1.51 2.12 1.19

(b)

line averaged I·HX

0.0   r/a   1.0   0.0   r/a   1.0   0.0   r/a   1.0

r/a = 0.53   r/a = 0.53   r/a = 0.53

ln(keV/kev/sec)

(c)

r/a = 0.2   r/a = 0.2   r/a = 0.2

ln(keV/kev/sec)

0   500   1000   0   500   1000   0   500   1000
Photon energy (keV)   Photon energy (keV)   Photon energy (keV)

$N_{\parallel} = 1.19$

$N_{\parallel} = 1.51$

$N_{\parallel} = 2.12$

E (KEV)
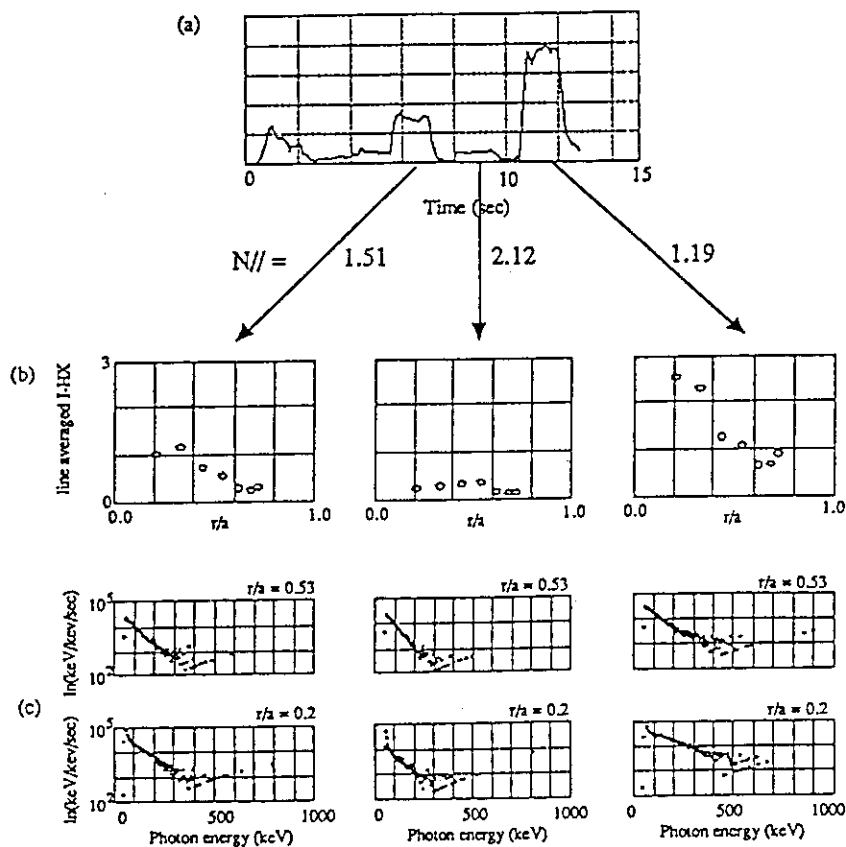
Fig.3 (a) Temporal evolution of HX-ray intensity. (b) Line averaged HX-ray intensity profiles. (c) HX-ray spectra.
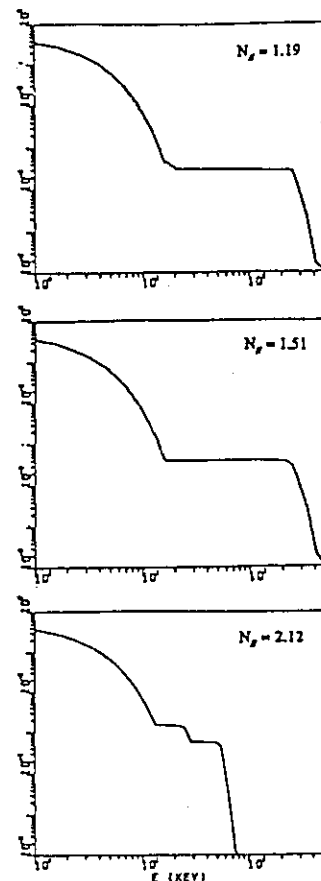
Fig.5 Calculated electron energy distribution functions, f_e ($E_{\parallel}$, $p_{\perp} = 0$).

T_{HX} (keV)

E_{res} (keV)

$I_{ECE}/I_{ECE}(N_{\parallel} = 2.12)$

f/f_{ce0}
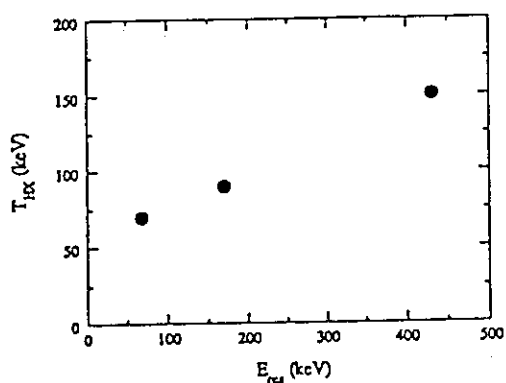
Fig.4 E-folding energy of HX-ray spectrum v.s. the resonant parallel energy of the injected wave.
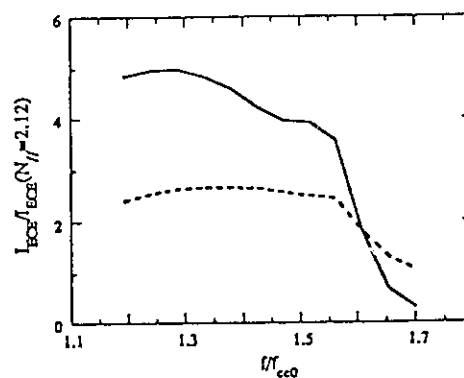
Fig.6 Normalized I_{ECE} against normalized frequency for $N_{\parallel} = 1.19$ (solid line) and $N_{\parallel} = 1.51$ (broken line).

11.5 Absorption Profile Estimation of Lower Hybrid Waves from the Hard X-ray and Soft X-ray Response

T. Kondoh, S. Ide, T. Imai and K. Ushigusa

Time response of hard x-ray and soft x-ray emission produced by modulated lower-hybrid wave (LHW) was measured to estimate the absorption profile of LHW. We estimate the absorption profile in the case of peak refractive index of the excited wave $N_{//} = 1.3$ and 2.1.

1. Experimental apparatus

Radial profile of hard x-rays produced by the fast electrons was detected by 7 channel sodium-iodide (NaI(Tl)) scintillator-photomultiplier combination looking perpendicular to the magnetic field. NaI(Tl) detector, 5.08 cm thick, 5.08 cm in diameter, with 2 mm aluminum vacuum window, is employed to measure the x-ray spectra 30 keV to 1 MeV. Detectors are shielded by 23 cm of lead and 50 cm polyethylene to reduce the γ-rays from (n,γ) reactions produced by fusion neutrons and background x-rays. The photomultiplier tube is shielded against magnetic field by soft iron and μ-metal. The detected x-ray signals are processed by CAMAC and pulse-height analyzed into 256 channels every 100 msec.

In this experiment, sampling time of 100 msec is too long to analyze the time response of hard x-ray signals. To measure the time response, signals are simultaneously digitized in the form of the hard x-ray intensity through an integrator with time constant of 4 msec.

Soft x-ray profile is measured by 64 channel PIN photodiode detector array through 200 μm Beryllium window.

Sight lines of hard x-ray and soft x-ray detectors are shown in Fig. 1.

2. Results

The power of the LHW is modulated by rectangular wave of 10 Hz (repetition of 20 msec power on and 80 msec off) and the phasing between adjacent multijunctions $\Delta\phi$ is varied with shot by shot. This experiment is carried out with $\Delta\phi = 135°$ and $210°$ Parallel refractive index of the excited waves has a peak $N_{//} = 1.3$ and 2.1, respectively. Plasma parameters are $I_p = 1.2$ MA, $B_T = 4$ T, $\bar{n}_e = 4\times10^{18}$ m^{-3}, and $f_{LH} = 2$ GHz.

Time evolution of the hard x-ray intensity (I_{HX}) and the soft x-ray intensity (I_{SX}) is shown in Fig. 2. The continuous LH power is injected from 4.5 to 5.5 sec (CW phase). In this phase, I_{HX} reached to steady state. The modulated power

is injected from 6.5 to 10.5 sec (modulated phase). In this phase, I_{HX} is not reached to steady state. Let the hard x-ray and soft x-ray change during the modulation be ΔI_{HX} and ΔI_{SX}, respectively. $\Delta I_{HX}/I_{HX}$ and $\Delta I_{SX}/I_{SX}$ are 93 % and 8 %, respectively.

The hard x-ray signal is energy integration of bremsstrahlung emission from fast electron through the aluminum window, in the energy range of several tens of keV. Soft x-ray signal is bremsstrahlung emission according to the collision of bulk election and ions.

3. Discussion

The fast electron density, n_f, is governed by the particle balance equation,

$$\frac{\partial n_f}{\partial t} - \nabla(D\nabla n_f + v \cdot n_f) = S - \frac{n_f}{\tau_{sd}}, \tag{1}$$

where S is source term and τ_{sd} is slowing down time of the fast electron.

In the steady state, if diffusion time was much longer than slowing down time, quasi-linear diffusion in the velocity space induced by LHW should be balanced with coulomb collision with the bulk electrons. Decay time of the hard x-ray intensity (e-folding time) just after the RF power switched off in the modulated phase, τ_{decay}, is shown in Fig. 3. We calculate the electron energy E_{sd} that should have slowing down time $\tau_{sd} = \tau_{decay}$. Figure 4 shows radial profile of E_{sd} calculated from τ_{decay} as a parameter of $N_{//}$. From the pulse height analysis of the hard x-ray, the temperature of the fast electron T_f is 40 - 80 keV that is consistent with the energy of E_{sd}. Therefore, the diffusion process of the fast electron may be small compared with the slowing down process.

Because the hard x-ray intensity I_{HX} is proportional to $n_f \, n_i Z^2 \, T_f$ in this plasma parameter considering detection response of the detector, the input power into the fast electron, P_{abs}, can be expressed as follows in the steady state,

$$P_{abs} = (n_f \cdot T_f)/\tau_{sd} \propto I_{HX}/(n_e \cdot Z \cdot \tau_{decay}^{HX}). \tag{2}$$

Figure 5 shows the ratio of the power deposition profile for $N_{//} = 2.1$ to $N_{//} = 1.3$ deduced from equation (2) using the data of τ_{decay}, n_e profile and I_{HX} in the steady state in the phase of CW.

Power deposition for $N_{//} = 2.1$ is broader than $N_{//} = 1.3$. Resonant energy of the electron, E_{res}, with the wave of $N_{//} = 2.1$ and 1.3 are 70 keV and 290 keV, respectively.

The slowing down of fast electron causes an increase of bulk electron temperature. Intensity of the soft x-ray signal is proportional to T_e^α, ($\alpha = 1.5 - 2$) in this plasma parameter. Since line density is not changed during the modulation,

the increase of soft x-ray signal, ΔI_{SX}, is caused by increasing the electron temperature due to the energy flux from LHW power through the fast electrons.

Figure 6 shows the ΔI_{SX} profile with $N_{//}$ as a parameter in the power modulation phase. $\Delta I_{SX}/I_{SX}$ is about 8 % at the center. In the $N_{//} = 2.1$ case, ΔI_{SX} is larger than $N_{//} = 1.3$. This is because of lower slowing down time.

In the bulk electron, diffusion process becomes large, the radial profile is broader than the profile of $P_{abs}(r)$.

$N_{//} = 1.3$ has narrow profile and localized within r/a = 0.5 and $N_{//} = 2.1$ has broad profile. This result is consistent with the absorption profile deduced from HX data. Though deposition profile of r/a < 0.2 is not obtained from the HX data, these results indicate deposition profile in the $N_{//} = 1.3$ case has larger value at the plasma center.

In this experiment, the signal to noise ratio is not so good as to measure the diffusion coefficient from phase shift of the x-ray signal both fast electron and bulk electron. Our next step is to measure the phase shift by improvement of S/N ratio.

4. Conclusion

Absorption profile of LHW is estimated from hard x-ray and soft x-ray response. Power deposition of LHW of $N_{//} = 1.3$ has narrow profile and localized within r/a = 0.5 and $N_{//} = 2.1$ has broad profile.

In the plasma core region, diffusion term can be neglected because the fast electron confinement time τ_f is larger than fast electron slowing down time in contrast with small tokamaks which diffusion time is shorter than slowing down time.

E014213 8.0

Ch 1

Soft x-ray
Array
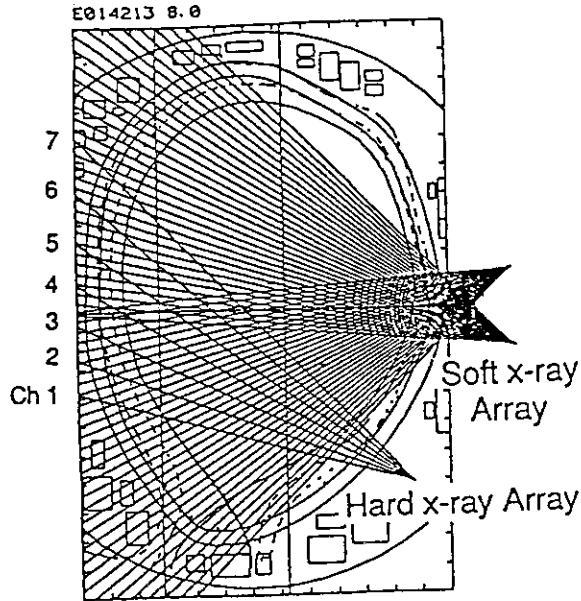
Hard x-ray Array

Fig. 1 Arrangement of hard x-ray
and soft x-ray arrays.

$N_{//} = 1.3$

I_{HX}

I_{SX}

$N_{//} = 2.1$

I_{HX}

I_{SX}

Time (sec)
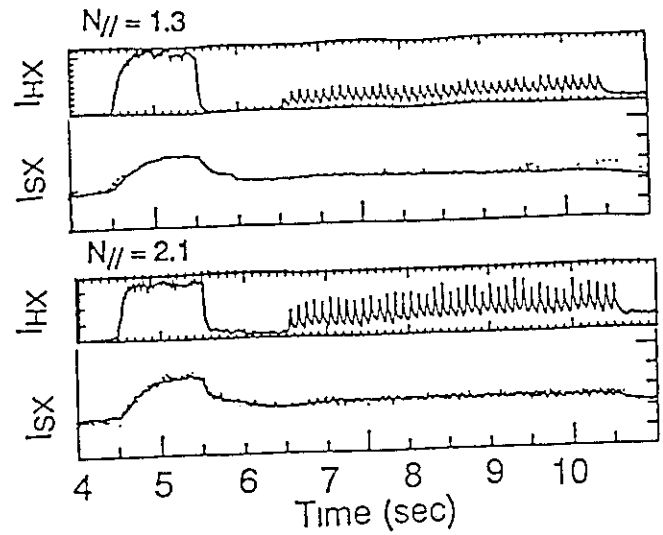
Fig. 2 Temporal evolution of soft x-ray and hard x-
ray signals. Continuous LH power is injected from
4.5 to 5.5 sec and modulated power is injected 6.5 to
10.5 sec.

Fig. 3. Radial profile of decay time of the
hard x-ray signal modulated by LH power.

Fig. 4. Electron energy calculated from
the decay time of I_{HX}.

Fig. 5 Absorped power ratio of $N_{//} = 2.1$
to $N_{//} = 1.3$ calculated from the value of
I_{HX} (r)/τ_{decay}(r).

Fig. 6 Radial profile of $\Delta I_{sx} \propto \Delta T_e$

11.6 Characteristics of the Coupling between LH Wave and High Energy Ion Simulating α Particle

M. Nemoto, T. Imai, K. Ushigusa and M. Sato

1. Introduction

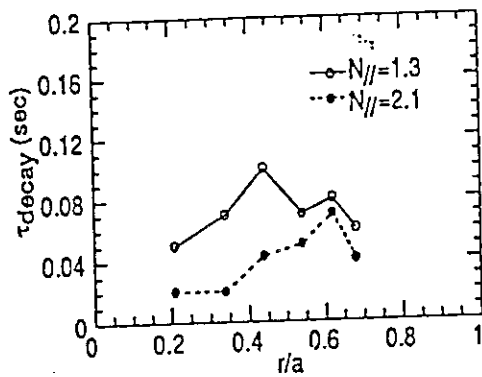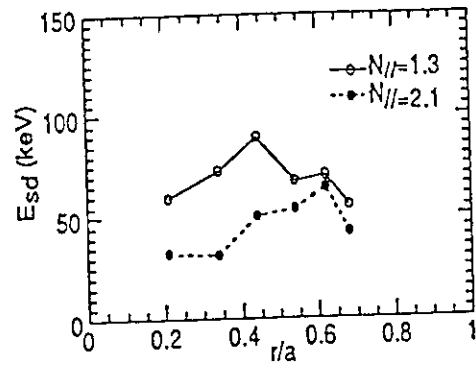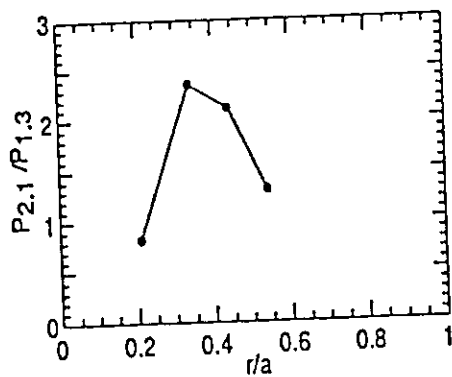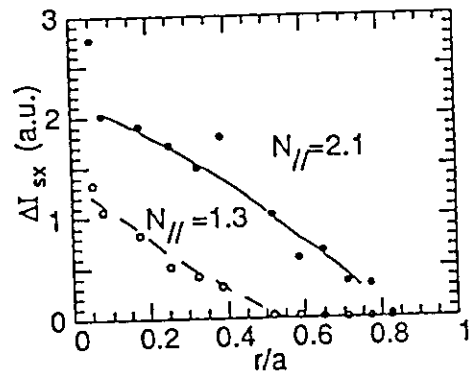Prediction of coupling characteristics between lower hybrid (LH) wave and high energy ion like α particle is one of important subjects in order to establish more efficient LH current drive. We have evidenced the simple theory which was able to predict a critical plasma density where the coupling of the LH wave changes from electrons to ions, depending on LH frequency and ion energy [1]. This result is very simple but striking that high power LH wave follows the linear dispersion relation in Tokamaks. To clarify this fact in more detail, the interaction of the LH wave with ions was further studies here.

2. Experimental Results

We have installed two charge exchange neutral particle mass-energy (CX) analyzers to measure tangential ion behavior in JT-60U plasmas. Both analyzers are viewing plasmas tangentially from counter and co directions on the equatorial plane as shown Fig.1. Since counter viewing one (NPA2) is including #14 neutral beam (NB) line in that sight-line, we can expect observation of beam ion acceleration phenomena in core plasma due to LH wave and ion coupling. Also, that is shielded from neutron flux generated by D-D reaction with polyethylene and lead. Since we are not able to shut off completely from neutron noise with the shield, two micro-channel-plate detectors which are masked by thin metal plates are provided to measure background noise counts in vacuum vessel of the analyzer. Taking these counter measures against neutron, we are able to observe high energy particles production with high S/N.

This experiment was carried out during deuterium degasing plasma operations from the first wall of the JT-60U vacuum vessel, therefore, Joule plasmas were mixture of hydrogen and deuterium ions. Expecting to decrease the critical density, experimental parameters were set at I_p=1.2MA and B_T=4T. We fuelled Helium gas to increase plasma density during simultaneous injection of hydrogen NB and LH wave into divertor plasmas, aiming repeat of time evolution of electron density shot by shot. Range of injected NB energy E_{B0} was from 40keV to 90keV, and injected LH wave conditions were frequency f=1.74GHz and the peak parallel refractive index $N_{//}^{peak}$=1.18~1.83. Fig.2 shows typical time evolutions of the LH absorption when E_{B0} is 60keV and $N_{//}^{peak}$ is 1.39. Those columns show, from the top, electron line density, LH power, NB power and a product of nonthermal frequency signal ($1.5\omega_{ce}$) measured by ECE times electron line density as a measure of the electron absorption. The bottom column shows average energy E_{ave} as a measure of the ion absorption. It is defined as

$$E_{ave} = \int_{E_{B0}}^{E_{max}} E \ln F_i(E) \, dE \Big/ \int_{E_{B0}}^{E_{max}} \ln F_i(E) \, dE \; ,$$

where, $\ln F_i(E)$ is hydrogen ion flux at energy E and E_{max} is measurable maximum energy on a measuring analyzer condition. In this discharge, E_{B0} and E_{max} are 60keV and 143keV, respectively. We define that the critical density is a value which the average energy increase sets in. That is shown with a broken line at t=10.0sec in Fig.2. Typical hydrogen and deuterium ion energy distribution at lower and higher densities, corresponding to t=9.5sec and t=11.0sec, are shown in Fig.3 (a) and (b), respectively. On hydrogen spectra, we can see clearly tail enhancement by the coupling at higher density than the critical density. Besides, deuterium spectra at both densities do not appear high energy ion generation due to the coupling.

3. Discussion

Generally, when ω_{pi} is greater than ω_{ci}, LH resonance frequency ω_{LH} in cold plasma approximation is given by

$$\omega_{LH} = \frac{\omega_{pi}}{\{ 1 + (\omega_{pe} / \omega_{ce})^2 \}^{1/2}} \; . \qquad (1)$$

Dispersion equation of the LH wave in case of $\omega^2/\omega_{LH}^2 \gg 1$ is described as

$$(\frac{\omega}{\omega_{LH}})^2 = 1 + \frac{1}{\gamma} \frac{m_i}{m_e} (\frac{k_{//}}{k_\perp})^2 \; . \qquad (2)$$

In Eq.(2), thermal motion effect of plasma particles is neglected and mass effect due to impurity is considered. ω_{LH} is obtained experimentally with the critical density and other plasma parameters, therefore, we are able to evaluate the left side of Eq.(2) as experimental values.

At the critical density of the LH-ion coupling, the refractive index and the wave number satisfy the following [1]

$$(\frac{N_{//}}{N_\perp})^2 = (\frac{k_{//}}{k_\perp})^2 = \frac{1}{F_\delta^2} \frac{m_e}{m_i} \frac{E_B}{T_e} \; . \qquad (3)$$

The $(k_{//}/k_\perp)^2$ is experimentally obtained from Eq.(3). Central T_e and Z_{eff} evaluating γ are not able to measure in this experiment due to arrangement of Thomson scattering and low S/N of visible spectrometer, therefore, we assume T_e=2.5keV and γ=0.8, refereeing similar plasma discharge data. Moreover, F_δ=2.75 same as the previous prediction and $E_B=E_{B0}$+5keV are substituted into Eq.(3). Since both left and right sides of Eq.(2) can be experimentally obtained from these procedures, it is possible to compare the theoretical dispersion relation (Eq.(2)) and experimental one, as shown in Fig.4. Good agreement means that ion energy dependence of the LH-ion coupling is able to be explained by the simple dispersion equation.

4. Conclusion

Ion energy dependence of the LH wave absorption was studied in JT-60U diverter plasmas. We demonstrated that the obtained ion energy dependence of the absorption was well explained by the simple dispersion theory. This result gives a clear prospect to the coupling of LH wave with α particles in the reactor, where the LHCD is one of the most probable candidates for non-inductive current drive.

We should prove a remaining mass dependence, by occurrence of Helium ion acceleration with Helium NB. Moreover, further detailed and accurate measurements of n_e, T_e and Z_{eff} profiles will bring about a detailed feature and more accurate evaluation of the LH absorption.

References:

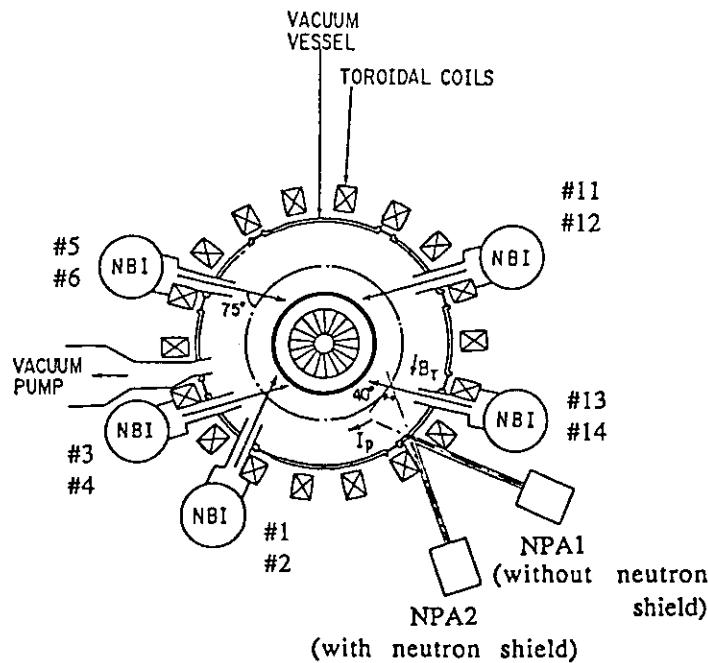[1] M. Nemoto et al., Phys. Rev. Letter 67(1991)70.
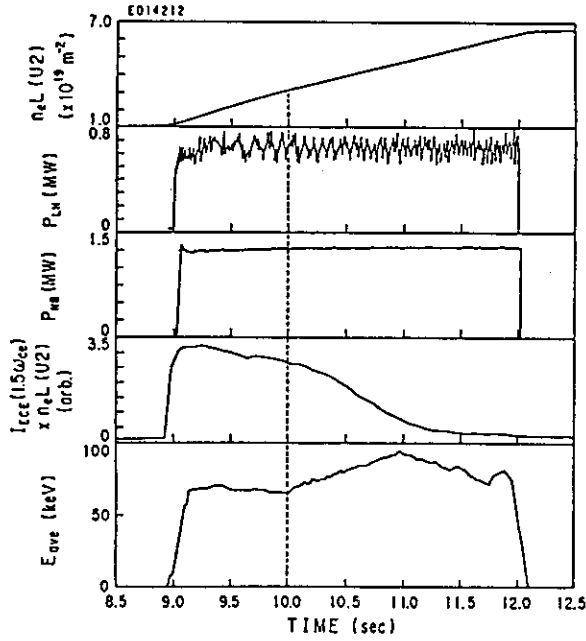

Fig.1 Arrangements of CX analyzers and NBI units.

Fig.2 Typical time evolutions of the simultaneous injection of LH wave and NB.
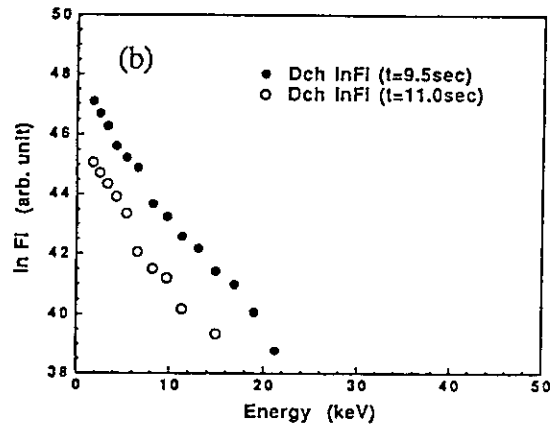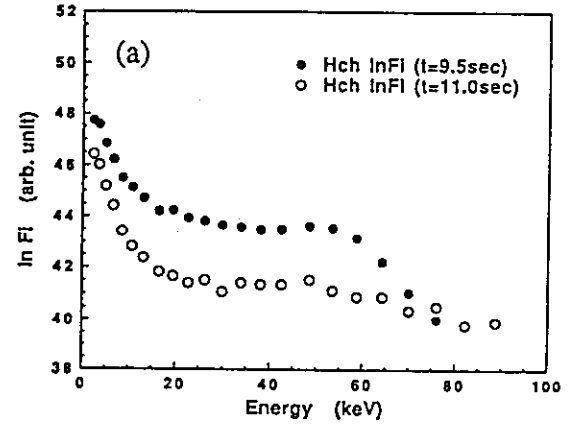

Fig.3(a) Typical hydrogen ion energy spectra at t=9.5sec and t=11.0sec.
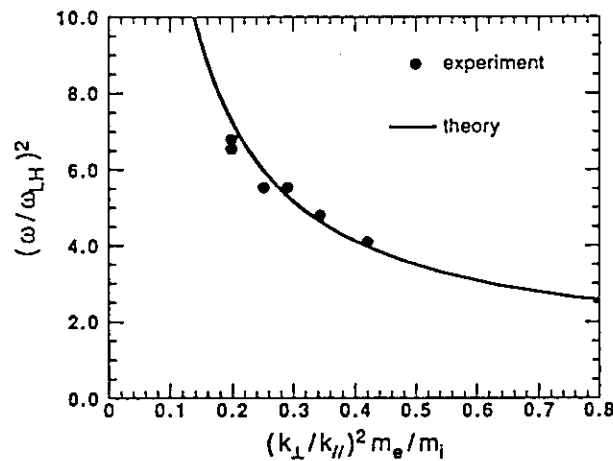(b) Typical deuterium ion energy spectra at the same times.

Fig.4 Comparison between theoretical dispersion relation and experimental data.

11.7 Plasma Rotation with Non-Inductive Current Drive by LHCD

Y. Koide, K. Ushigusa and S. Ide

In recent years there has been a growing interest in the measurement of plasma rotation as an indirect method to know the radial electric field. The formation of negative potential in the H-mode transition, for example, is inferred from this method, which is accounted for the ambipolar electric field due to the ion-orbit loss [1,2]. As for the plasma with LHCD, some special features compared with the usual plasma with non-zero loop voltage have been reported : particle confinement is improved [3] : MHD instability is stabilized [4] : the threshold power required for the H-mode transition is low in LHCD [5]. The measurement of plasma rotation may become one of the approaches to study such characteristics. This is the first report dealing with the plasma rotation in the almost fully current-driven discharge by LHCD.

First we show the characteristic direction of toroidal rotation velocity (V_t) as the response to the LH injection. The two LH pulses (Fig.1(b)), the peak pararel-refractive indices ($N_{//}{}^{peak}$) of which are 1.34 (t = 6-7 sec) and 2.13 (t = 8-9.5 sec), are injected into the plasma with I_p=1.2 MA, B_t=4 T, $\overline{n_e}$=5×10^{18} m^{-3}, $T_i(0)$=2-3 keV. The loop voltage during LH is as small as 0.1-0.2 V in this series of experiment. In this discharge NBI (Fig.1(a)) is not essential but is only needed for the measurement of CXRS (see section 6.2.1). It should be noted that V_t is pushed to co-direction (the same direction as the plasma current) when LH is injected. (Because the NBI power of 1 MW is comparable to that of LH, the measured rotation velocity (Fig.1(e) and (f)) is biased in the counter direction, which is discussed in section 6.2.2.)

Next we investigate the power (0.8-1.43 MW) and $N_{//}{}^{peak}$ (1.18-2.13) dependences on V_t, where the duration of NBI for CXRS is decreased to 100 msec in order to minimize the effect of NBI. Other parameters are almost the same as those in Fig.1. The rotation velocity is plotted as a function of injected LH power in Fig.2. $N_{//}{}^{peak}$ is shown with different symbols in this figure. Because of the poor S/N ratio of CXRS measurement in this series of experiment, the averaged rotation velocity over the half radius is used. The averaged velocity in the inner half region is plotted in Fig.2(a) and the outer one Fig.2(b), respectively. The rotation velocity in ohmic phase is also shown with a line as a reference in the same figures. In the both regions, rotation velocity tends to increase in co-direction as LH power is increased. The phase dependence is not clear in this data set and will be discussed in the future experiment with improved profile measurement and with higher LH power.

The profile of V_t with the maximum LH power of 1.4 MW, $N_{//}{}^{peak}$ of which is 1.66, is compared with the ohmic case in Fig.3. In the ohmic phase, V_t is 1×10^4 m/sec in counter direction. In the LH phase V_t changes its direction to co-direction. The possible mechanism responsible for the resultant co-directed rotation is the formation of outward ambipolar electric field, which is due to the loss of electrons during LH injection. It is clear that information of this type is essential to discuss the current drive efficiency because the direct loss of fast electrons produced by LH degrades it. This will be clear in the coming high power LHCD experiment.

[1] R.J. Groebner, et al, Phys. Rev. Lett. 64, 3015 (1990).

[2] K.C. Shaing, et al, Phys. Rev. Lett. 63, 2369 (1989).

[3] M. Porkolab, et al, Proc. of 10th Int.Conf. on Plasma Phys. and Controlled Nucl. Fusion Research, London (1984), Vol.1 p.463.

[4] D.Van Houtte, et al, Nucl. Fusion 24 (1984) 1485.

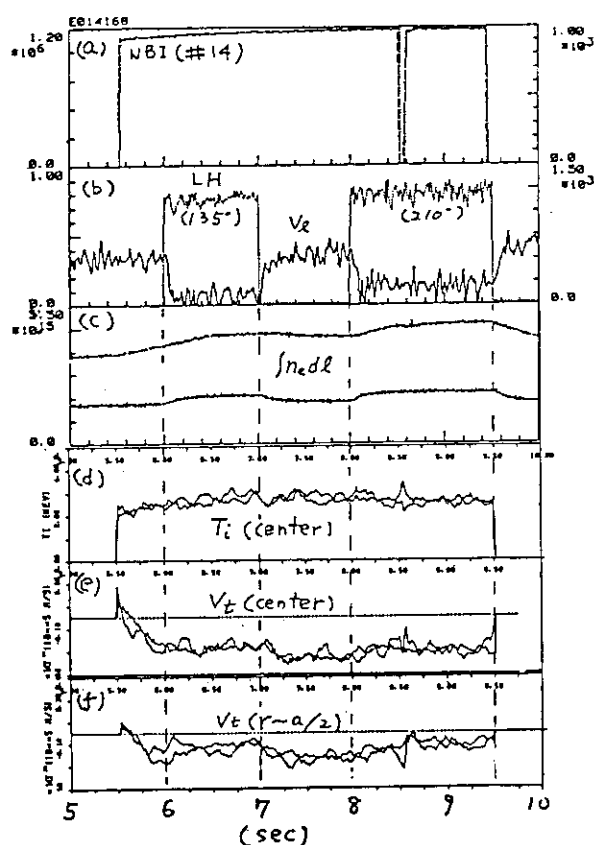[5] S. Tsuji, K. Ushigusa, et al, Phys. Rev. Lett. 64, 1023 (1990).
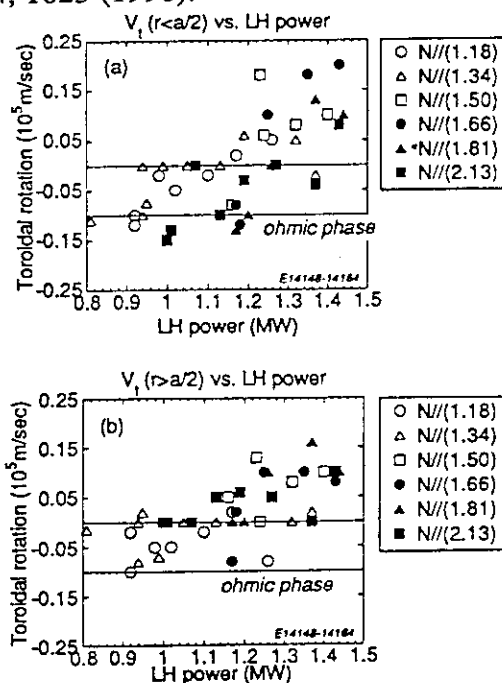
FIG. 1 The responce of V_t to LH injection.
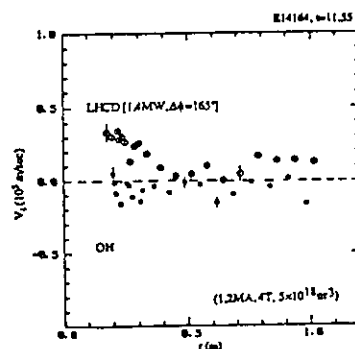

FIG. 2 V_t vs. LH power.

FIG. 3 $V_t(r)$ in LH injection.

11.8 Propagation of Energetic Electron Pulse during LHCD

K. Ushigusa, Y. Kamada and O. Naito

Large loss of high energy electrons has been observed during the current broadening period with high $N_{\parallel}$ wave injection. The loss event occurs at about half radius, the energetic electron pulse (EEP) propagates outward and reaches to the divertor plates with about 30ms of time delay.

Figure 1 shows an example of LHCD discharge with EEP for 3 sec. About 1MW of LH power with the peak $N_{\parallel}$ of 2.2 was injected into a low density plasma($\sim$0.4 x 10^{19}m^{-3}) and decreases the plasma internal inductance l_i gradually. The decrease in l_i of up to $\sim$ 0.4 is achieved for 5sec of LH injection. After LH onset, a slow oscillation with a period of $\sim$0.15 sec is observed in the soft X-ray signal. The diamagnetic beta indicates that a large part of the energy increment by the injected LH power is lost with this oscillation. The divertor heat load measured by IRTV shows this oscillation accompanies about 20% loss of heating power as shown in the 4th trace of Fig. 1. Figure 2 compares the soft X-ray signal with the hard X-ray signal with almost the same radius. This figure clearly indicates that the oscillation in the soft X-ray signal is due to the change in the population in high energy electrons. The oscillation in the soft x-ray signal may reflect the change in population of energetic electrons.
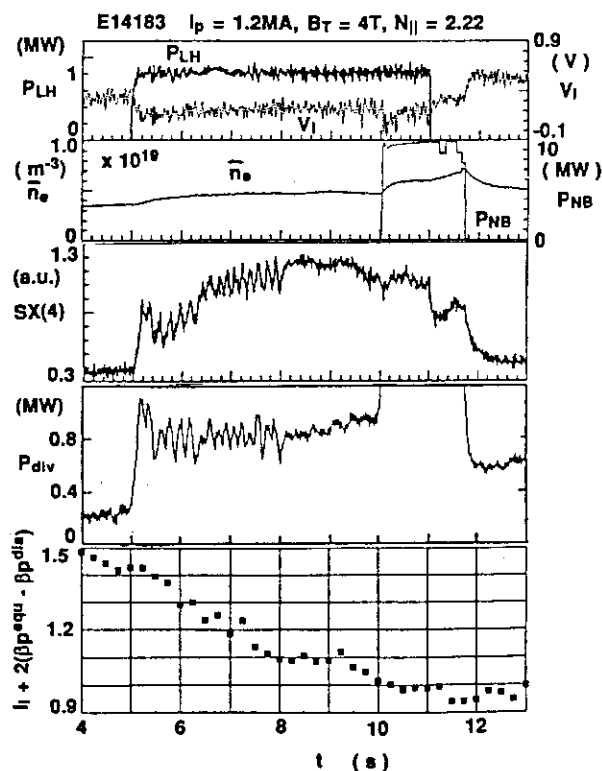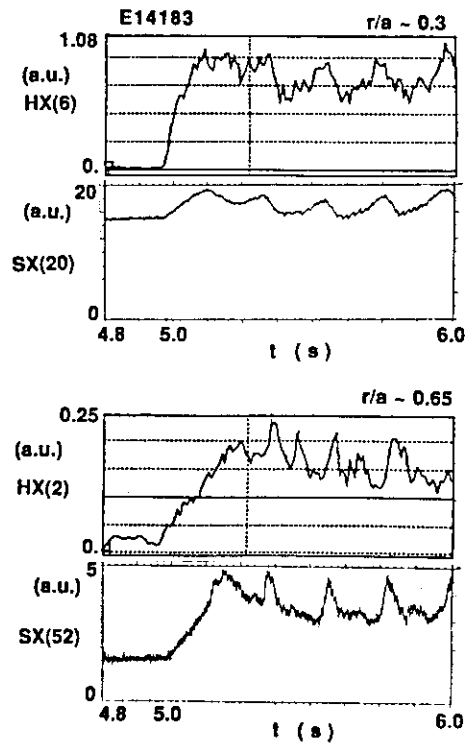

Fig.1 Typical example of EEP

Fig. 2 Comparison of soft and hard X-ray signals for EEP

Figure 3 shows the set-up of soft X-ray arrays. Our soft X-ray(SX) measurement system has two sets of detector array. One of these (the bottom array) detects signals from lower half plasma and several channels (ch. 58 - 64) see the divertor plates. Usually there is no soft X-ray signals in ch.58 - 64 in OH and beam heated plasmas because the electron temperature in the divertor plasma is too low to radiate soft X-ray. However, we observed large SX signal in channel 62, which is very close to the outer leg of the separatrix line, when LH pulse is injected into a low density plasma. High energy electrons may come to the divertor plates from the main plasma before they are thermalized by the collisions since the slowing down time of energetic electrons is long in such a low density plasma. When energetic electrons collide with the divertor plates, the plates radiate the X-ray signal.

Soft X-ray Arrays
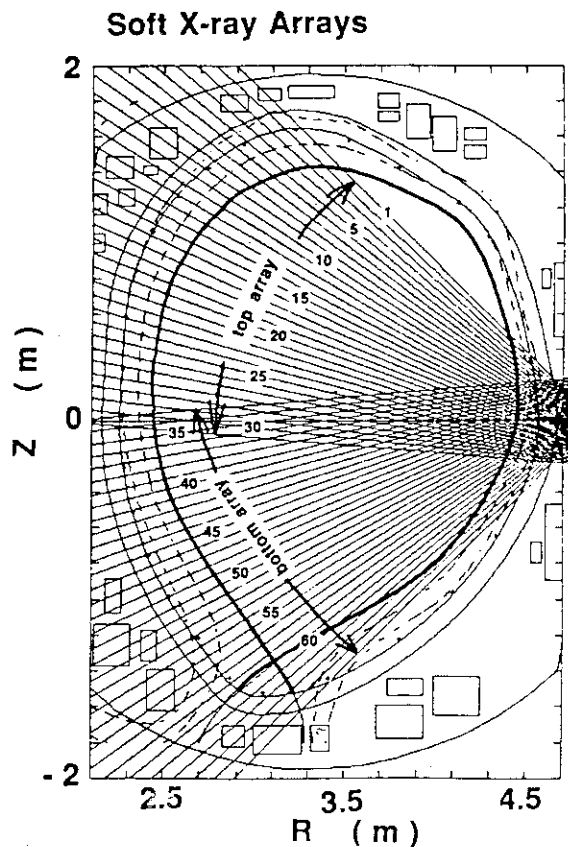
Fig. 3   Set up of SX detectors

The contour plot of SX signal for above mentioned oscillation is shown in Fig. 4(a), where the top (bottom) contour is from bottom (upper) SX array. The plasma center is in around ch.23 on the bottom traces while the divertor plates is in ~ch.62 on the upper box. The peak in the central SX signal appears at t ~ 5.35 s and then decreases slowly. From t = 3.36 s, SX pulse propagates outward and reaches to the divertor plates. Figure 4(b) shows the radial profile of SX signal of upper array and clearly indicates that the only channels from 8 to 13 decrease. These channels correspond to the radius of r/a = 0.35 - 0.6. Since the oscillation in SX signal is due to the change in the population of high energy electrons as shown in Fig.2, Fig.4 indicates that energetic electrons at ~ half radius are released and propagate outward and reaches to the divertor plates with a time delay of around 30msec. It should be noted that there is another SX pulses (small EEP) between large EEPs at t ~ 5.42 s, 5.45 s and 5.8 s in Fig.4. These pulses occur at almost the same position as the large EEP.

Figure 5 shows SX contour plots for several timings. Small EEP appears frequently between large EEPs at early time, however, it appears rarely at t = 7.3 - 7.4 s and then there is only large EEP without small SX pulse at t = 7.8 - 8.0 s. Finally, large EEP is also stabilized at t > 8 s. It should be noted that the central SX island in Fig. 5 becomes slender gradually. At the same time the inversion radius of small EEP shown in the bottom of Fig.5
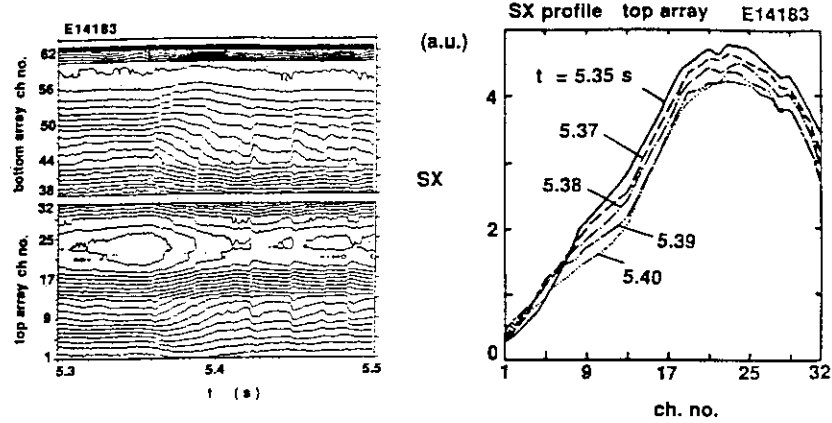
Fig. 4 Contour and radial plot of EEP
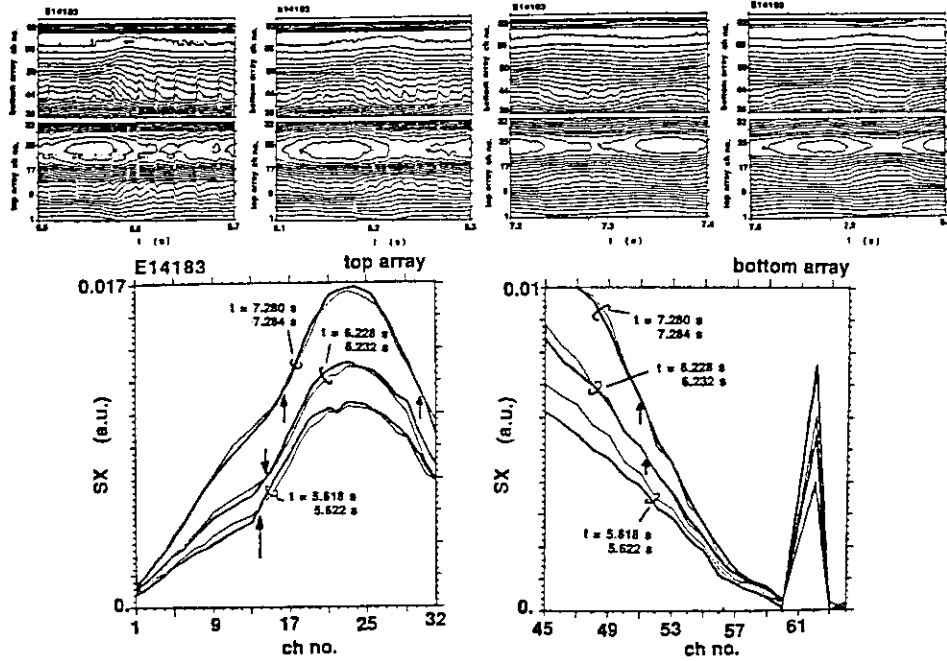
Fig. 5 Time evolution of EEP and Inversion radius of small EEP

shifts inside. This suggests that the location where EEP occurs is correlated to the change in the current profile.

We observed EEP frequently at low density and the relatively high LH power. The injected LH power is divided by the electron density and plotted against the wave phasing $\Delta\phi_m$ in Fig. 6 where solid and open symbols show LHCD without and with large EEP. We did not observe EEP in LHCD with $\Delta\phi_m = 120°$ and $135°$. In such phasings, peaked RF current is driven and the plasma internal inductance does not decrease. The EEP is observed with $\Delta\phi_m \geq 150°$ where LH drives a broad RF current and the power threshold of EEP tends to decrease with $\Delta\phi_m$. The EEP is thought to correlate with some MHD instabilities during the current profile broadening. It is interest that the plasma internal inductance decreases in spite of EEPs. Finally EEP is completely stabilized and a stable
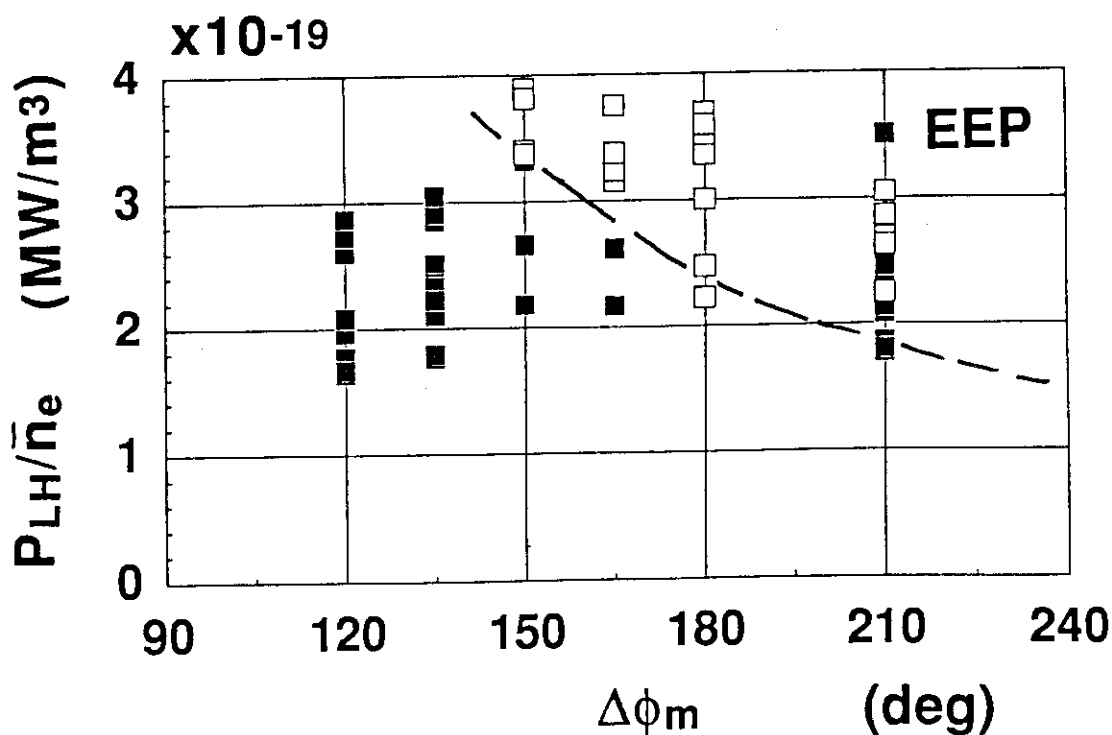
Fig. 6 Threshold for EEP phenomena

steady state current profile can be achieved.

Although EEP is a transient and anomalous phenomenon, it is important because a large loss of energetic electrons is very severe problem for the divertor plates in future steady state tokamak reactor. The JT-60 experiment have probed that the divertor heat load during LHCD can be replaced by the radiation loss at the density larger than $10^{19}m^{-3}$ and the slowing down process of the high energy electrons is dominant. This indicates that the divertor heat load is not due to the high energy electrons. However, when some anomalous loss of energetic electrons such as EEP occurs during high power LHCD, the radiative cooling is no longer effective to reduce the divertor heat load. The divertor plates may suffer a large heat load by energetic electrons. The EEP contains valuable informations, too. We can study the behaviors of high energy electrons by using the propagation of energetic electrons. This will be studied in near future.

There are still many open questions about EEP. We have to find out key MHD activities for EEP. We have to pay attentions to the target OH current profile because a rapid current ramp up technique (growing up method, see Sec. 2.6) was employed in this series of experiments. Further studies will be continued.

11.9　The Distant Coupling of LHCD Launcher in JT-60U

M. Seki, Y. Ikeda, T. Imai, K. Ushigusa, K. Suganuma,
A. Takasa, M. Sawahata, and, S. Takahashi

1.　Introduction

Lower Hybrid Current Drive (LHCD) is one of the most powerful, efficient and promising schemes to drive non-inductive current in Tokamak reactor. It is often pointed out that the weak point of the LHCD is the coupling structure. The front end of the LHCD launcher must face to the plasma surface to drive slow wave in a tokamak whose refractive index parallel to the magnetic field ($N_{||}$) is larger than 1. To couple RF power to the plasma efficiently, the distance between launcher head and plasma must be small, usually, a few cm, similar to the case of the ICRF coupling. Therefore the heat load to the launcher head is serious problem, especially, in a reactor. Reduction of the heat flux to the launcher head is the one of the key engineering development points to be the LHCD more practical in the reactor. One way to reduce heat load is to separate the launcher head from the outer most plasma magnetic surface as far as possible. But it reduces coupling, too. If we can remain a tenuous plasma around the launcher head even in case of the distant place, it is possible to achieve both reduction of the heat load and efficient coupling. This is the topic of this section. The efficient coupling of the LH wave was observed with the distance of the launcher head from plasma more than 10 cm in the present experiments, which indicate the active coupling control of the LHCD launcher.

2.　Launcher description and experimental arrangements

The new LHCD launcher is designed to launch optimized $N_{//}$ power spectrum for high η_{CD}. For this purpose, the spectrum must be sharp and directive, and its phase velocity must be as fast as possible within the accessible condition, which require many waveguides, so that a multi-junction type launcher has been adopted as a new LHCD launcher. Because multi-junction technique serves to attain many effective waveguides in front of plasma without increasing transmission line, and good performances had been obtained by using the multi-junction launcher in the JT-60. The optimized spectrum has the ability of driving current efficiently by ~40 % in compared with conventional one.

Moreover, according to the favorable scaling such as η_{CD} proportional to the square root of averaged electron temperature, the extension of LHCD performance will be expected under the condition of a higher temperature in the JT-60 Upgrade. The main feature of this launcher is to have a wide $N_{||}$ controllability, $N_{||}$ changes from 1.2 to 4.0 by choosing a operational frequency and an adjacent phase difference.

The launcher is composed of a waveguide bundle and a structural jacket. The waveguide bundle is consists of main waveguides and sub waveguides, 8-main waveguide and 4-main waveguide are lined in the toroidal and the poloidal direction, respectively. An rf power are fed by a 1 MW-klystron to 4-main waveguide in the same column. And each main waveguide is divided into 3 sub waveguides, then there are 8x4x3 = 96 waveguides at the grill mouth. The sub waveguides have geometrical phase shifters yielding a phase difference of 60 degrees in order to launch a peak parallel refractive index of 1.3~2.5 at a frequency of 2 GHz. The all waveguides made of stainless steel are copper-plated so as to reduce an rf loss, and 24-waveguide in the same row are constructed by using of the new fabrication technique based on a diffusion boding method [1]. The structural jacket is used to stand up against an electromagnetic force when disruption happens, and has guard limiters to protect the grill mouth against plasma bombardment. There are passive waveguides on the both sides of the grill mouth. The head parts of whole waveguides are carbon-coated for sake of suppression of a breakdown. The height and the width of the grill mouth are about 500 and 470 mm, respectively. The length of a sub waveguide is ~1600 mm.

The launcher has a double-probe located at the grill mouth with a view to measure density in front of the grill. And the probe contains thermocouples in itself. The grill has

many thermocouples, some of them serve as a means of monitoring breakdowns in vacuum waveguides. It is especially important to know whether multipactoring discharge occurs at a zone of the second harmonic electron cyclotron frequency, or not. Since discharge causes the phase difference to change. Tow of thermocouples inserted between a jacket and guard limiters are used as a way of measuring a heat load from plasma. The launcher position can be adjustable shot by shot in order to obtain a good coupling property with a monitoring a heat load.

The LH waves were injected to the plasma in the divertor configuration. The plasma current was 1~2 MA and the toroidal magnetic field was 2~4 T. The averaged electron density was low up to 2×10^{19} m^{-3} and the averaged electron temperature was up to ~1.3 keV. And the temperature of the first wall was mainly sustained at 150 °C.

The experiments were divided into two steps. The coupling characteristics were investigated in the first step. The low rf power up to ~500 kW was injected to OH and NB-heated plasma. The working gas was D$_2$. Conditioning of the graphite tiles of the first wall was not enough, it seemed that out-gassing from tiles occurred when the tiles were heated. The launcher head was located at 1~3 cm behind from the first wall, and the launcher was moved with measuring density. The grill mouth was monitored by using a CCD camera, and temperatures of the grill were also recorded. Then in the second step, launcher conditioning was done and maximum input power of ~1.5 MW was injected to H$_2$ plasma.

3. Results and discussion

In the fig. 1 a reflection coefficient is plotted as a function of the distance between the most outer magnetic surface and the launcher head (δ) . The δ is equivalent to the distance between the magnetic surface and the first wall (δ^{47}) plus between the first wall and the launcher head (δ^{LH}) . This investigation was carried out in the various experimental conditions as written in the figure, in order to search for a good coupling condition with setting a grill head behind the first wall. The low rf power with a phase of 150 degrees was injected as mentioned in section 2. The refection coefficient of 10~20 % was obtained, even though δ was larger than 8 cm. And the good coupling was observed in two regimes as known from fig. 1. The regimes are represented as follows.

First regime; The good coupling of the first regime was obtained in such a case as shown in fig. 2. The incident power of ~500 kW was injected to OH plasma, plasma current was 2 MA and density was low up to 0.5×10^{19} m^{-3}. We have to pay attention to the reflection coefficient (R) during from 3.5 to 6.5 sec., since plasma was approaching the launcher head (see δ^{47}). In the period, the phase difference between main waveguides ($\Delta\Phi$(mod)) was 150 deg. and δ^{LH} was 2 cm. The R gradually decreased with δ^{47}, and R rapidly dropped at 5.2 sec. after that remained constant at ~12 %. The input power subsequently ascended with decreasing R, because of keeping the incident power constant. Emissions from the surroundings of the ports were observed via a CCD camera when plasma was coming near the first wall. However pressure of neutral gas in periphery plasma was not measured, it seemed that out-gassing from the wall occurred if δ^{47} was smaller than a threshold value under the condition of injecting LH power. And Hα fluctuated as shown in the figure, the density in front of the grill changed when a good coupling was observed.

Thus the good coupling condition was obtained during injection of LH power to OH plasma, even though δ was 8~10 cm.

Second regime; The good coupling of the second regime was related to the case of the combination with NB. The typical discharge was illustrated in the fig. 3. The LH power was injected to the NB-heated plasma with Ip = 2.5 MA and $\overline{n}_e$ = $1.9 \sim 2.3 \times 10^{19}$ m^{-3}. The δ^{47} remained nearly constant at ~14 cm, and the δ^{LH} was 3 cm. As known from the

figure, the injection of NB effected the coupling property of LH. A low reflection coefficient of ~14 % was observed during the injection of NB. When the injection of NB was stopped at 7.5 sec., R suddenly rose up to 70 %. Figure 4 allows us to know what had happened in this phenomena. The time evolution of a probe current (Iprobe) is shown, amplitude of Iprobe is associated with density at the grill mouth (n_e^{LH}). Iprobe slightly increased with injection of NB, then n_e^{LH} rose from 4×10^{15} to 2×10^{16} m^{-3} by addition of LH power, after that a good coupling was observed. The reflection coefficient was increasing as n_e^{LH} was decreasing after the stopping the NB injection. This experimental results might indicate that thin plasma in front of the grill was produced by LH power under a certain condition.

Thus the good coupling of 2nd regime was obtained in the case of the combination with NB, even if δ was up to 15~17 cm.

After the attainment of the good coupling, a propagation of an LH wave had been investigated in order to know whether a launched LH wave was used to drive plasma current effectively, or not. This investigations were carried out through the LHCD performances in the second step as mentioned above, the fig. 5 and 6 show obtained data. The reflection coefficient is plotted as a function of normalized temperature increase, which is given by increase in temperature of a probe (ΔT ; °C) divided by an input energy (MJ). As known from figure, the reflection coefficient showed the tendency to decrease with increasing the normalized temperature. This indicated that the increase in normalized temperature was caused by increasing density, and as a result the reflection coefficient decreased. Maximum of ΔT was ~5 °C at an input energy of 5 MJ. On the contrary, the η_{CD} tented to ascend with normalized temperature increase, this illustrated that the η_{CD} was not degraded due to the coupling improvement.

Thus the experimental results indicated that main part of the LH power was not absorbed by periphery plasma, but propagated into main plasma.

4. Summary

The coupling characteristics were investigated with the object of a low heat load on the grill mouth. The experiments had been carried out by using the new multi-junction launcher in the JT-60 Upgrade. It was already found that the head load on the grill mouth was negligible, as far as the grill was set behind the first wall[2]. Hence we searched a good coupling condition with setting the launcher 1~3 cm from the wall. The obtained results is as follows.

The reflection coefficient of 10~20 % was observed during an injection of LH power to OH plasma, even though the distance between the most outer magnetic surface and the launcher head (δ) was 8~10 cm. And the good coupling was obtained in the case of the combination with NB up to δ = 15~17 cm. When good coupling state occurred, the increase of density in front of the launcher head was also observed without the degradation of the current drive efficiency. This experimental results indicated that the main part of the LH power propagated into the core plasma.

The phenomena, however, have not been understood well, it suggests the possibility of the distant coupling of LHCD launcher. After clarifying the mechanism of the phenomena, we should control a coupling property actively.

References ;
　　[1] M.Seki, et al., Symposium on Fusion Technology (1990) 1060
　　[2] Y. Ikeda, et al., Journal of Nuclear Materials 176&177 (1990)306-310.

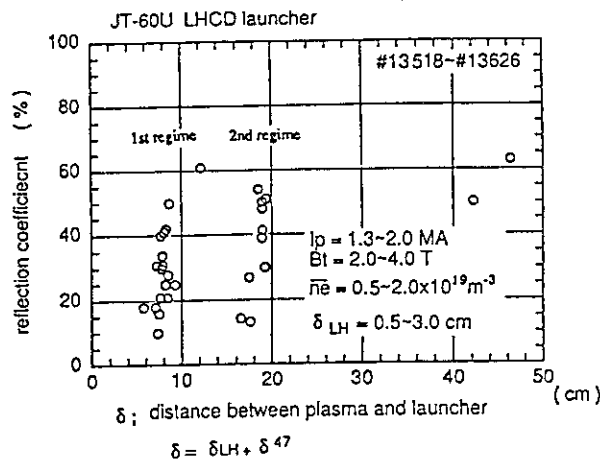Fig.1 The reflection coefficient versus the distance between the plasma and the launcher.
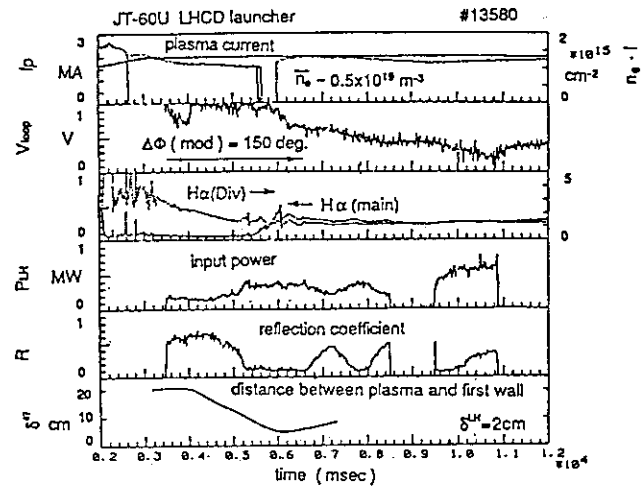

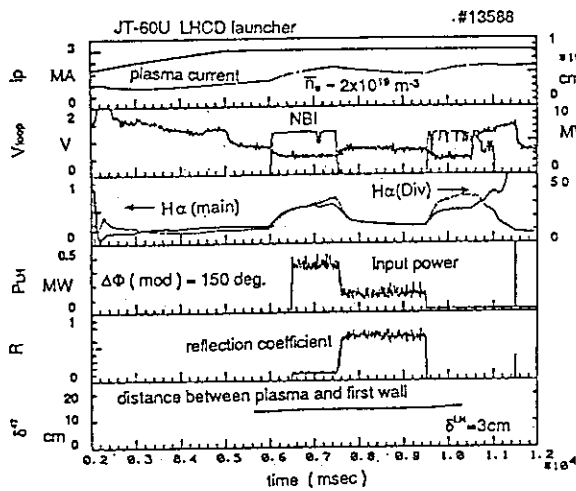Fig. 2 The time evolution in the 1st regime.

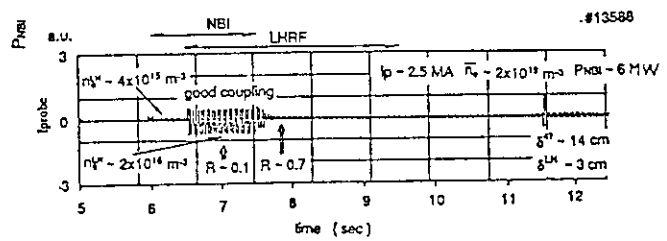Fig. 3 The time evolution in the 2nd regime.

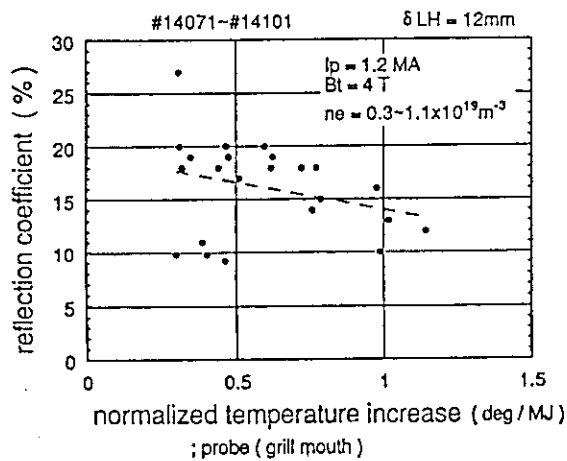Fig. 4 The behavior of the density in front of the launcher head.

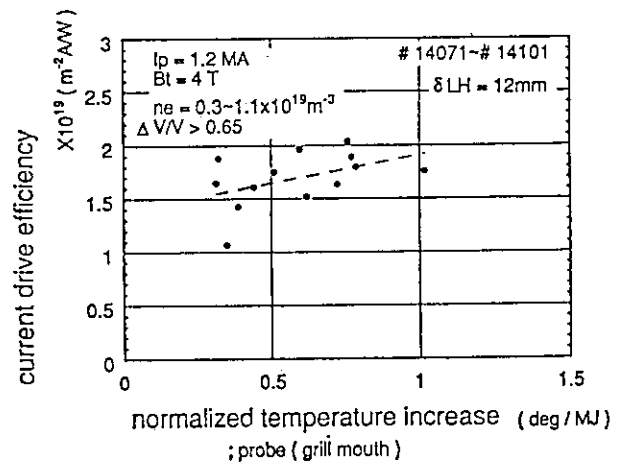Fig. 5 The reflection coefficient versus the normalized temperature.

Fig. 6 The current drive efficiency versus the normalized temperature.

11.10　Effect of Phasing Error in the Current Drive Performance

M. Seki, Y. Ikeda, K. Ushigusa, T. Imai,
M. Sawahata, K. Suganuma, and A. Takasa

1. Introduction

It was pointed out that the current drive efficiency observed in the first campaign of the JT-60U experiments in 1991 was low as compared with previous results in the JT-60. In order to investigate this cause, rf-properties of the launcher used in the lower hybrid current drive (LHCD) experiment were measured after the campaign. It was found that rf-properties, especially phase settings, had errors from intended values from the measured data.

The phase setting of a phased array antenna is essential for LHCD experiment and will determine its performance. Therefore effect of phasing error in the current drive performance is described in this section. The launching spectrum calculated from the rf-properties is firstly mentioned and effect to the current drive efficiency in the JT-60U will be presented. Next the spectrum launched from the launcher with correct phase is shown and a high current drive efficiency in the following campaign is expected after resetting phase correctly.

2. Launcher description

The LHCD launcher is optimized for driving plasma current efficiently and controlling plasma current profile. For the sake of realizing this characteristics, a multijunction type launcher was adopted. Because the multijunction launcher is able to have a sharp spectrum with high directivity and this type launcher in the JT-60 experiments showed high performance. The structure of multijunction launcher in the JT-60U resembles closely the one in the JT-60. And theoretical analysis predicts that this new launcher has higher current drive efficiency by 40 % than that of conventional launcher in the condition of the same plasma parameters.

Outline of the multijunction launcher for LHCD experiments in the JT-60U is briefly described as follows. A waveguide bundle of this new launcher subsystem is mainly modified to obtain a narrow and unidirectional spectrum under the condition that one subsystem of three units in the JT-60 is as remained as possible. The unit consists of eight klystrons generating a total designed power of 8 MW in the frequency rang of 1.74-2.23 GHz and a pulse duration of 10 seconds. A wide $N_{//}$ controllability in launching spectra is a main feature of the launcher. The $N_{//}$ is defined as a ratio of light velocity to phase velocity . A directive and sharp $N_{//}$ spectrum can be changed in the range of 1.2-4.0 by changing frequency and phase difference between adjacent main waveguides (modules) ($\Delta\Phi(mod)$). The waveguide bundle has eight modules lined in the toroidal direction and four in the poloidal direction, then there are thirty two modules. Each module has main waveguide which is divided by thin metallic wall into three sub waveguides in the toroidal direction with geometrical phase shifters yielding phase difference of 60 degrees at a frequency of 2 GHz. Then the launcher results in having 8x4x3=96

waveguides effectively at the grill front without increasing transmission line. The poloidal phase difference, which means a phase shift against the second row in the same column, is attained by changing length of a movable phase shifter shot by shot. This poloidal phase differences are usually set in a phasing of (90,0,0,-90), so as to minimize the reflection to the klystrons by magic Tees. A toroidal phase difference between main waveguides arrayed in the second row is able to be changed by electronic circuit in every 10 milliseconds. For the sake of reducing power density at grill front and reflection power arising at junction point of main waveguide, a thin septum having the thickness of 1.5 millimeters is used to divide main waveguide into three sub waveguides as mentioned above. In order to construct this multijunction module without deformation of a thin septum, which leads an incorrect rf-property from designed one, the new manufacturing technique based on diffusion bonding method has been developed as reported in reference [1]. On the other hand the grill may be weak in thermal strength due to joule loss and rf-discharge, so an injection of a high rf-power should be made carefully in a conditioning process.

3. Phasing calibration

Before starting LHCD experiment in the JT-60U, the rf-properties of the newly constructed multijunction grill had been checked. Then the measured data, phase difference in the main waveguide and power dividing ratio, had shown the allowance of design values. Furthermore after installation the grill on the JT-60U and connection to the transmission line, the each phase of waveguide was set by using data which compensate various phase shifts of cables in measuring system. So at the initial state a launched spectrum was expected to be a nearly designed one. On the contrary, a current drive efficiency (η_{cd}) in the first campaign of JT-60U was still low compared with that of multijunction launcher in JT-60. The experimental result is seemed to be as follows.

To investigate the low η_{cd} , after the campaign an rf-property of every waveguide had been measured by using of an rf-probe and a Network Analyzer in a matched state with dummy loads. The data had shown that the calibration of the second column in the second row, which is the reference of the phase measuring system, was wrong and hence the relative phasing to the reference signal had substantial error. In addition, poloidal phases of from first to fourth columns in the fourth row were mis-set. The measured rf-properties also indicated that there existed phase shift error and power dividing error in the some sub waveguides; namely one third of whole waveguides though the the effect of them is relatively small.

4. Effect of the phasing error

A launching spectrum calculated from measured rf-properties is shown in Fig. 1. The calculation is done under the approximation of vacuum loading. Both data of phase shift and distributed power in the main waveguides are used in this calculation. An N// wave spectrum at a frequency of 2 GHz and a toroidal phase difference of $\Delta\Phi($ mod $) = 135$ degrees is illustrated

in Fig. 1 and designed one is also for comparison. Theoretical analysis predicts that this spectrum should have the highest η_{cd}. As known from this figure, the actual spectrum becomes broader than the designed one, as a result, a peaked power is reduced by $\sim$ 30 %. Moreover a spectrum is not so sharp and directive, and has undesired sidelobe. Therefore spectrum weighted $N_{/\!/}$ ($1/<N_{/\!/}^2>$), indicates the capability of current drive as stated in the section of 11.2 , becomes small. The dependence of $1/<N_{/\!/}^2>$ on $N_{/\!/}^{acc}$ is plotted in Fig. 2 as a parameter of $\Delta\Phi($ mod $)$. $N_{/\!/}^{acc}$ represents the accessibility condition and has been about 1.15 in the campaign. $1/<N_{/\!/}^2>$ is estimated to be $\sim$ 74 % in $\Delta\Phi($ mod $)$ = 135 degrees compared with that of design value. Therefore it seems, as mentioned in 5.1.2 section, that the error of phase setting of main waveguides lead a low current drive efficiency. On the other hand a broad wave spectrum, especially sidelobe, makes a dependence of some physical phenomena on $N_{/\!/}$ indistinct.

The major points of rf-property error are summarized as follows.

    1: mis-calibration of the reference signal.

    2: mis-setting of semi-fixed phase shifter due to incorrect phase compensation of measuring system including the effect of the incomplete cable connection.

    3: deformation of thin septa of multijunction modules

The first possibility seems to be a main cause of phase setting error. The second cause may be possible, but it affects only a few waveguides. The third cause is also possible in some modules, because the RF properties of them are substantially different from that in the initial state, but effect of them is relatively small, as mentioned before.

The calibration error which is the main cause of the mis-phasing ha already corrected. An rf-property of sub waveguide is not able to be changed, but an adjustment of phase shift among main waveguides is possible. Consequently an improved wave spectrum obtained by resetting movable phase shifter is examined for LHCD experiments in the following campaign. The improved spectrum on $N_{/\!/}$ is plotted in Fig. 3. The improved spectrum shows that it is narrow and directive enough to drive current efficiently. And sidelobe is in a low level. Therefore $1/<N_{/\!/}^2>$ at a frequency of 2 GHz and $\Delta\Phi($ mod $)$ = 135 degrees , as illustrated in Fig. 4, is estimated to be $\sim$ 92 % of designed value.

5. Summary

The current drive efficiency with the new multijunction type launcher in the JT-60U is found to be low compared with that of in the JT-60. To investigate this cause, an rf-property of the launcher had been measured after the first campaign. The measured data indicated that the calibration of the reference signal is incorrect. It is also found that there existed some phase setting error of a few modules and the distortion of a few MJ modules. These errors lead launched spectrum into being different from designed one. The spectrum weighted $N_{/\!/}$ shows the efficiency is $\sim$ 74 % of designed value. This may explain a part of the low current drive

efficiency with multijunction launcher in the JT-60U experiments. And a launched spectrum is able to be improved with up to ~ 92 % of the designed one by calibrating the reference signal and resetting phase shift in each main waveguide. Therefore the LHCD experiments using the improved spectrum are expected to approach to the theoretical prediction in the following campaign,1992.

Reference

[1] M.Seki, et al., Symposium on Fusion Technology (1990)1060

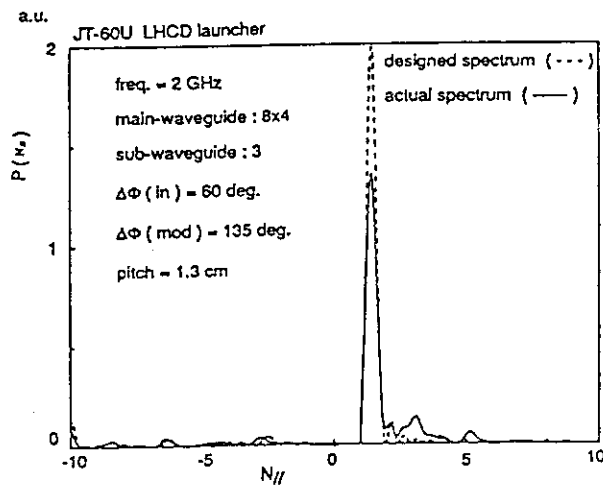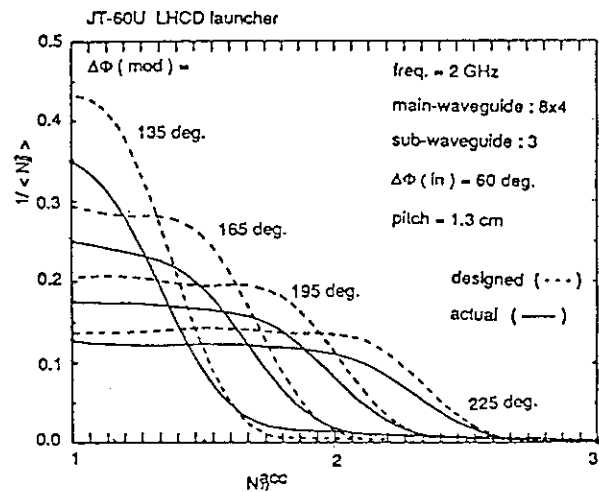Fig. 1 Actual power spectrum is shown.
Designed spectrum is also.

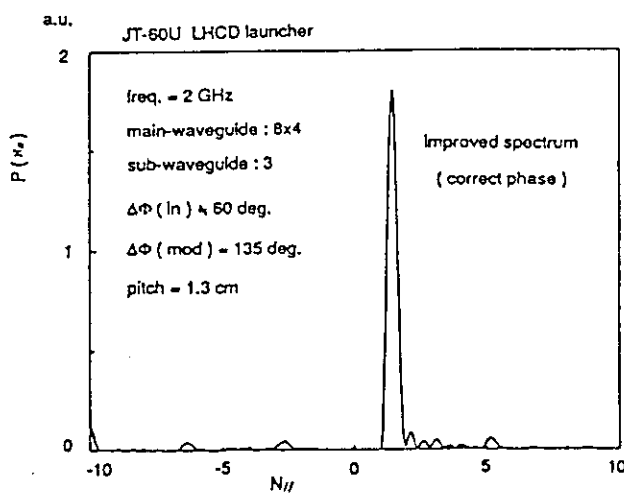
Fig. 2 The dependence of $1/<N_{||}^2>$ on $N_{||}^{acc}$.

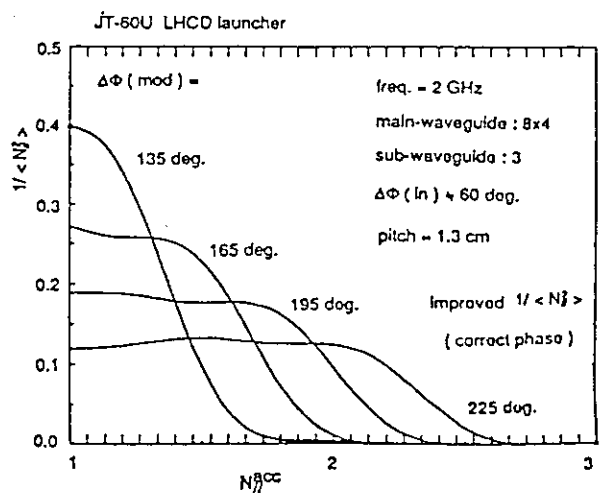Fig. 3 Improved spectrum by means
of setting phase correctly.

Fig. 4 Expected $1/<N_{||}^2>$ versus $N_{||}^{acc}$.

11.11 Estimation of the Fast Electron Power Loss to the Divertor

K. Ushigusa

The soft X-ray (SX) signal from the divertor plates has been observed in low density LHCD plasmas. As discussed in Sec. 11.8 , this is due to high energy electrons which come to the divertor plates from the main plasma before they are thermalized by the collisions since the slowing down time of energetic electrons is long in such a low density plasma. This section will discuss the power loss through fast electrons by using the SX signal from the divertor plates.

Figure 1 shows a time evolution of the SX signal (ch.62) from the divertor plate SX_{62} and the divertor heat load measured by the IRTV. The LH power with phasing of $\Delta\phi_m = 150°$ is injected from t = 5.5 s to 7.0 s. In the employed divertor configuration, the 62th channel of SX array is very close to the outer leg of the separatrix line. There is no signal in this channel in OH phase as shown in Fig. 1. The large spikes on SX and the divertor heat load at t ~ 6.3s is due to the energetic electron pulse (EEP). As discussed in Sec.5.1.13, the change in SX signal, which is related to the EEP, is thought to be due to the change in the population of energetic electrons. For EEP phenomena, the SX signal SX_{62} is compared to the increment in the divertor heat load in Fig. 2. The SX signal from the divertor plates is well correlated to the increase in divertor heat load by anomalous loss of energetic electrons. Therefore we can treat the SX signal from divertor plates as a measure of the fast electron power loss.
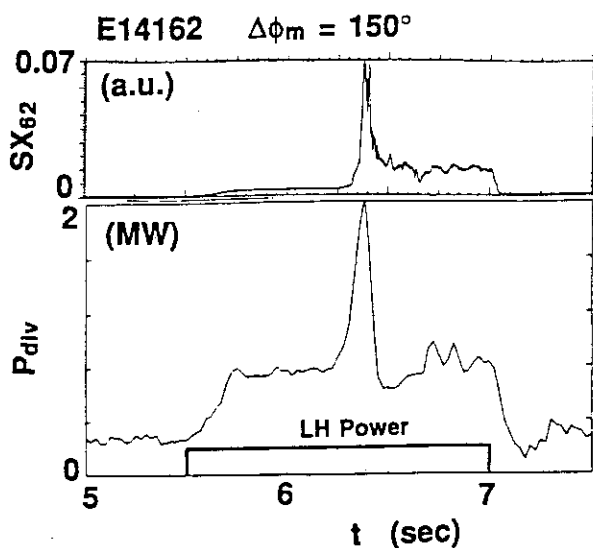

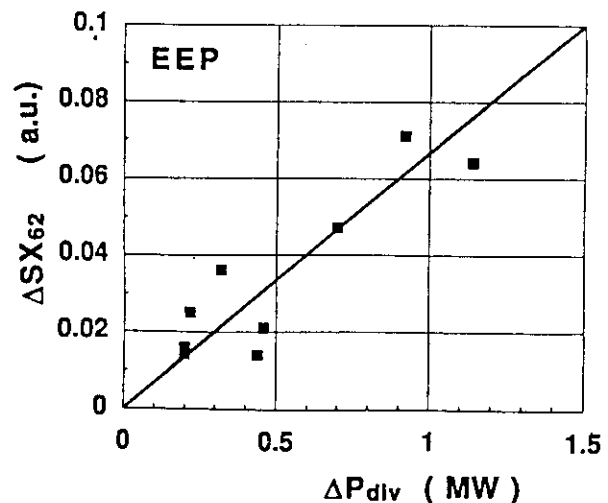Fig. 1 Heat Spike of EEP phenomena

Fig.2 Divertor SX signal vs. Heat Spike on the divertor plates
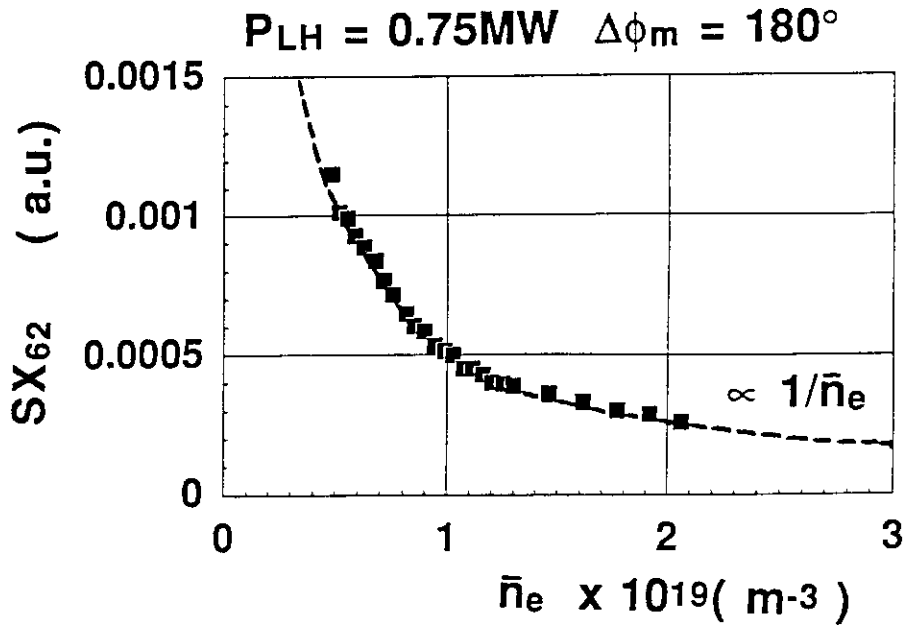
P_{LH} = 0.75MW $\Delta\phi_m$ = 180°

Fig. 3 The SX signal from divertor plates versus the line average density

Based on the above discussion, the fast electron power loss for normal LHCD plasma without EEP phenomena will be analyzed. Figure 3 show the density dependence of the SX signal from the divertor plates SX_{62} with P_{LH} = 0.8MW and $\Delta\phi_m$ = 180° where only data without EEP are plotted. The SX signal deceases with increasing the density and is well fitted by $1/\bar{n}_e$. Hence we can say that the fast electron power loss is inversely proportional to the electron density in the main plasma. This result is quite reasonable because the loss of energetic electrons must be proportional to $1/n_e$ when the slowing down of energetic electrons is dominant process in the main plasma. This results indicates that the loss of energetic electrons can be negligible when the characteristic time of particle confinement is much longer than the slowing down time of energetic electrons.

Figure 4 shows the SX_{62} against the LH power where solid and open symbols show data with $\Delta\phi_m$ = 120° and 135°, respectively. The SX signal increases linearly with the injected LH power. The SX signal SX_{62} is divided by the LH power and plotted against the wave phasing $\Delta\phi_m$ in Fig.5. Although there is large scatter in SX_{62}/P_{LH}, which is mainly due to the difference in the electron density, we can see some dependence of the ratio SX_{62}/P_{LH} on the wave phasing. Larger power loss by energetic electrons is observed in the lower $N_{||}$ wave injection. This is again reasonable because the slowing down time of energetic electrons depends on the velocity v_e ; $\tau_{SD} \propto v_e^3 \propto 1/N_{||}^3$.

The slowing down time of high energy electron accelerated by the wave with $N_{\parallel}$ can be described by

$$\tau_{SD}(s) = \frac{3.368/\ln\Lambda}{\bar{n}_e(10^{19}m^{-3})} \frac{N_{\parallel}^{-3}}{1-N_{\parallel}^{-2}+\sqrt{1-N_{\parallel}^{-2}}} \tag{1}$$

where $\ln\Lambda$ is the Coulomb logarithm. Figure 6 shows the ratio SX_{62}/P_{LH} against the slowing down time where the slowing down time is estimated by Eq.(1) with the launched peaked $N_{\parallel}$. When the slowing down time of energetic electrons is long, the fast electron power loss becomes large and high energy electrons are lost before they are thermalized by collisions. As a measure of the characteristic time of energy confinement, we use the diamagneticalyy measured one; $\tau_E^{dia} = W_{dia}/P_{abs}$. This confinement time is lower than the true total energy confinement time because the energy content W_{dia} does not contain a large parallel electron tail energy. In the parameter rage of $\bar{n}_e = 0.4 - 0.6 \times 10^{19}m^{-3}$, $I_p = 1.2MA$ and $P_{LH} = 1.2 - 1.4MW$, τ_E^{dia} is about 0.3 s and decreases slightly with the wave phasing. The slowing down time estimated at $N_{\parallel}^{peak}$ has a comparable value to τ_E^{dia} for the case with low $N_{\parallel}$ wave injection.

It is very difficult to say the absolute value of lost power through energetic electrons. In order to estimate the energetic electron lost power roughly from SX_{62} signal, we use the correction factor of SX_{62} from results in Fig. 2 ($\Delta P_{div}/\Delta SX_{62} \sim 15$), which were derived for EEP. If we use this factor directly, the maximum on the vertical axis in Fig. 6 corresponds to $P_{loss}/P_{LH} \sim 0.1$. It should be noted that results in Fig.2 is deduced from a transient phenomena. It may be difficult to estimate the peak heat load correctly in such fast phenomena by using the IRTV measurement. To remove this uncertainty, we compared the time integrated SX_{62} with the integrated P_{div} for EEP phenomena and obtain $\Delta P_{div}/\Delta SX_{62}|_{integrated} \sim 30$. If we use this factor, the maximum on the vertical axis in Fig. 6 becomes $P_{loss}/P_{LH} \sim 0.2$.
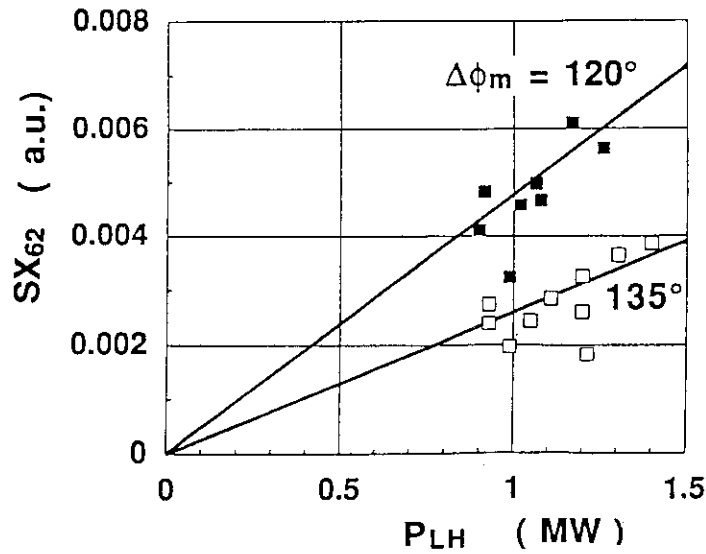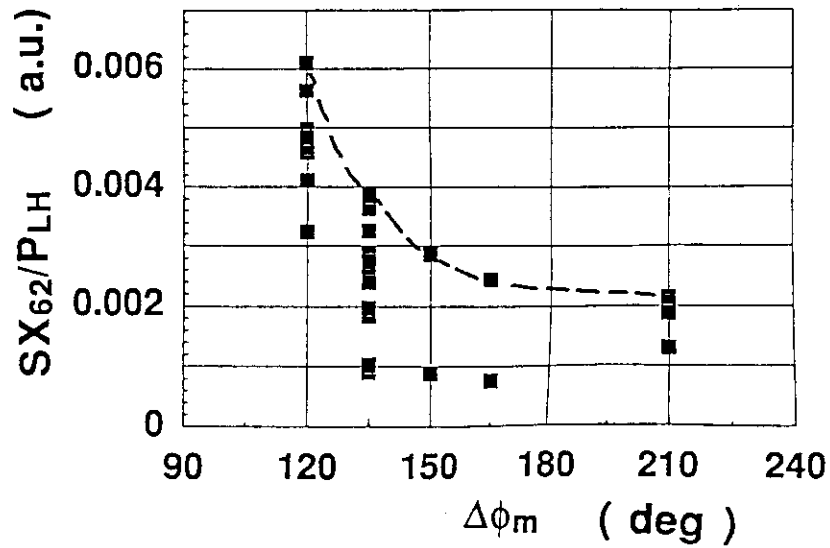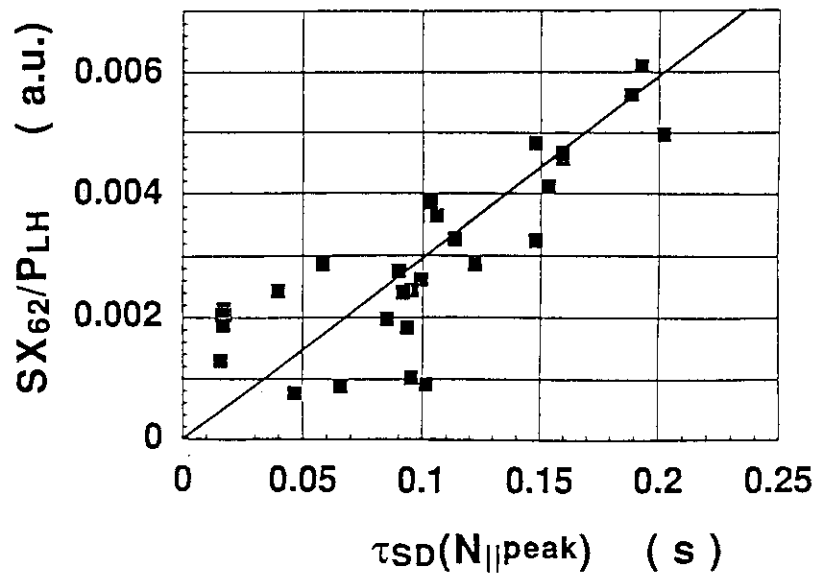
Fig. 4 Power dependence of the diverto SX signal

Fig. 5 Phase dependence of the ratio SX$_{62}$/P$_{LH}$

Fig. 6 The ratio SX$_{62}$/P$_{LH}$ against the slowing down time

11.12 Accessibility Limit in LHCD Discharges

K. Ushigusa and M. Sato

In an application of LHCD in a future steady state tokamak machine, the most of launched wave power may be very close to the accessibility condition because a high wave velocity with a narrow spectrum has a high current drive efficiency and the maximum parallel phase velocity is limited by the accessibility condition. Under such circumstances, the most of launched power may become easily an unaccessible power when some perturbations such as an unforeseeable density increase occur. This is very dangerous because a large RF power (order of 100MW) is not absorbed by the plasma and stay in the vacuum vessel. This power may enhance the impurity influx and finally terminate the discharge (we call this as the accessibility limit). In this section, the accessibility limit which observed in the first champaign of LHCD in JT-60U is reported.

A typical example, in which the most of launched wave power is unaccessible, is shown in Fig.1 where the wave phasing is set to be $\Delta\phi_m = 95°$. In this phasing, the main component of launched spectrum has a $N_\parallel$ range of $N_\parallel = 1.0 - 1.5$ and a peak at $N_\parallel^{peak} \sim 1$.
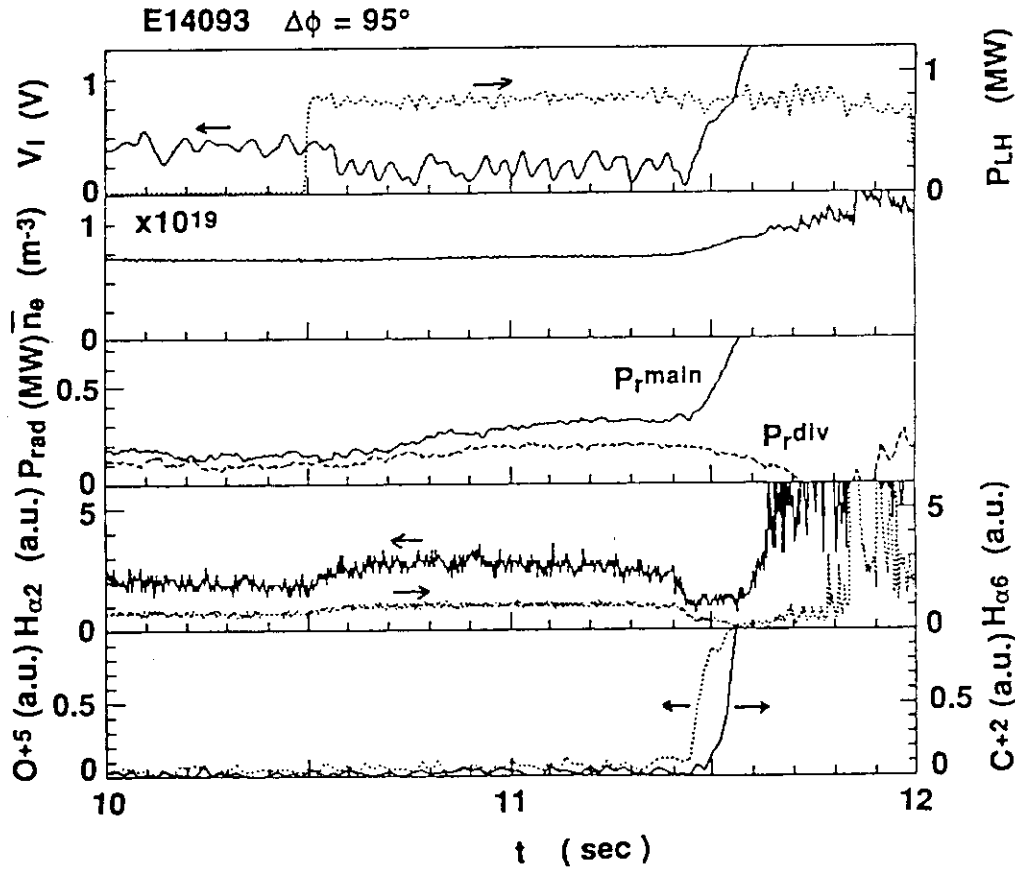

Fig. 1 A typical example of the accessibility limit

The accessibility condition, which is estimated with the line average density n_e and the center toroidal field $B_T(0)$, shows $N_{\parallel}^{acc} = 1.21$. About half of the launched power is unaccessible in these conditions. At $t = 11.4$ s, the H_α signals drop abruptly and the oxygen impurity with a low charge state O^{+5} increases. Then the radiation power from the main plasma and the density increase gradually and finally the discharge becomes disruptive. A similar phenomenon has been observed in ASDEX experiments.

The product of the non-thermal ECE ($1.5\omega_{ce}$) signal and the electron density is plotted against the launched peak $N_{\parallel}^{peak}$ divided by the accessibility condition $N_{\parallel}^{acc}$ in Fig. 2 where the data have a parameter range of $N_{\parallel}^{acc} = 1.13 - 1.19$ and $\bar{n}_e = 0.27 -$ 0.63×10^{19} m^{-3}. The product $n_e I_{ECE}(1.5\omega_{ce})$ increases with decreasing $N_{\parallel}^{peak}$ for $N_{\parallel}^{peak}/N_{\parallel}^{acc} > 1$. This is reasonable because higher energy electrons, which are created by a higher phase velocity wave, may radiate stronger non-thermal ECE. However, when $N_{\parallel}^{peak}/N_{\parallel}^{acc} < 1$, the signal $\bar{n}_e I_{ECE}(1.5\omega_{ce})$ is constant or decrease slightly with decreasing $N_{\parallel}^{peak}$. This indicates that the accelerated electrons are limited by the accessibility condition and the accessibility condition estimated with the line average density and the central toroidal field is good measure to estimate the accessibility in tokamak plasmas. It should be noted that the current drive efficiency has a peak at $\Delta\phi_m$ $= 135°$ under the condition of $\bar{n}_e < 0.7 \times 10^{19}$m^{-3}, $I_p = 1.2$MA in this series of experiments. This corresponds to $N_{\parallel}^{peak}/N_{\parallel}^{acc} \sim 1.25$ in Fig. 2.

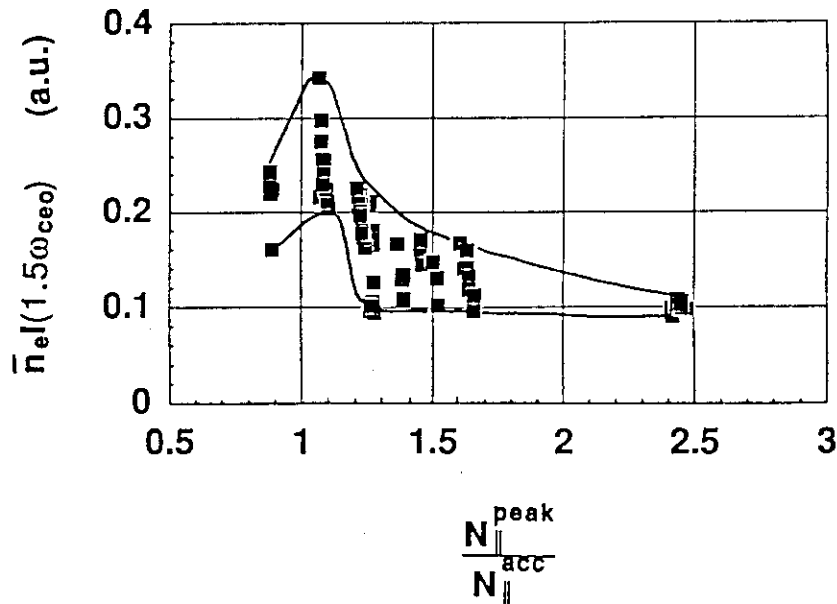
Fig. 2 The non-thermal ECE multiplied by the density versus the launched
$N_{\parallel}^{peak}$ divided by the accessibility condition $N_{\parallel}^{acc}$

In Fig.1, the radiation loss from the main plasma increased when the unaccessible wave was injected. This may be a good measure to characterize the accessibility limit. Figure 3 shows the increment of main plasma radiation against the launched LH power for the unaccessible power injections where $N_{\parallel}^{peak}/N_{\parallel}^{acc} \sim 0.9$ and ~ 1.1 for $\Delta\phi_m = 95°$ and $120°$, respectively. We can see the difference on the power threshold of the accessibility limit between these two phasings; the power threshold of the accessibility limit for $\Delta\phi_m = 120°$ is higher than that for $\Delta\phi_m = 95°$ by a factor of ~ 1.3. The unaccessible power fraction for $\Delta\phi_m = 95°$ is $\sim40\%$ at $N_{\parallel}^{peak}/N_{\parallel}^{acc} \sim 0.9$, while $\sim60\%$ for $\Delta\phi_m = 120°$ at $N_{\parallel}^{peak}/N_{\parallel}^{acc} \sim 1.1$. Therefore the accessibility limit occurs when the unaccessible power reaches to 0.4MW and 0.8MW for $\Delta\phi_m = 95°$ and $120°$, respectively. This indicates that the unaccessible power estimated by the launched spectrum is not suitable to use as the power threshold of the accessibility limit and suggests that the launched waves may be strongly modified near the accessibility limit.
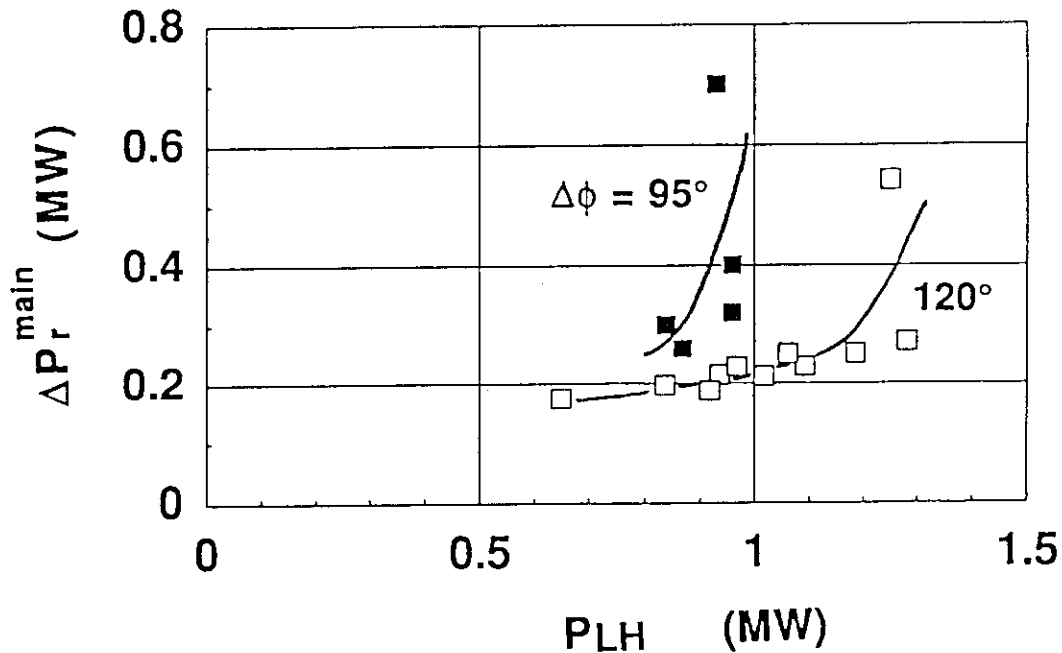
Fig.3 The increment of main plasma radiation against the launched power

The increment in the main plasma radiation ΔP_r^{main} is divided by the injected RF power P_{LH} and plotted against $N_{\parallel}^{peak}/N_{\parallel}^{acc}$ in Fig. 4. This figure clearly indicated that the main plasma radiation rapidly increases when the launched peak $N_{\parallel}$ is close to the accessibility condition. Therefore we can use the parameter $N_{\parallel}^{peak}/N_{\parallel}^{acc}$ as one of the measure of the accessibility limit. When this parameter becomes close to unit by a

density perturbation, the excited wave phasing must be control so that the wave spectrum satisfy an accessibility limit condition (for example $N_{\parallel}^{peak}/N_{\parallel}^{acc} = 1.1 - 1.2$).
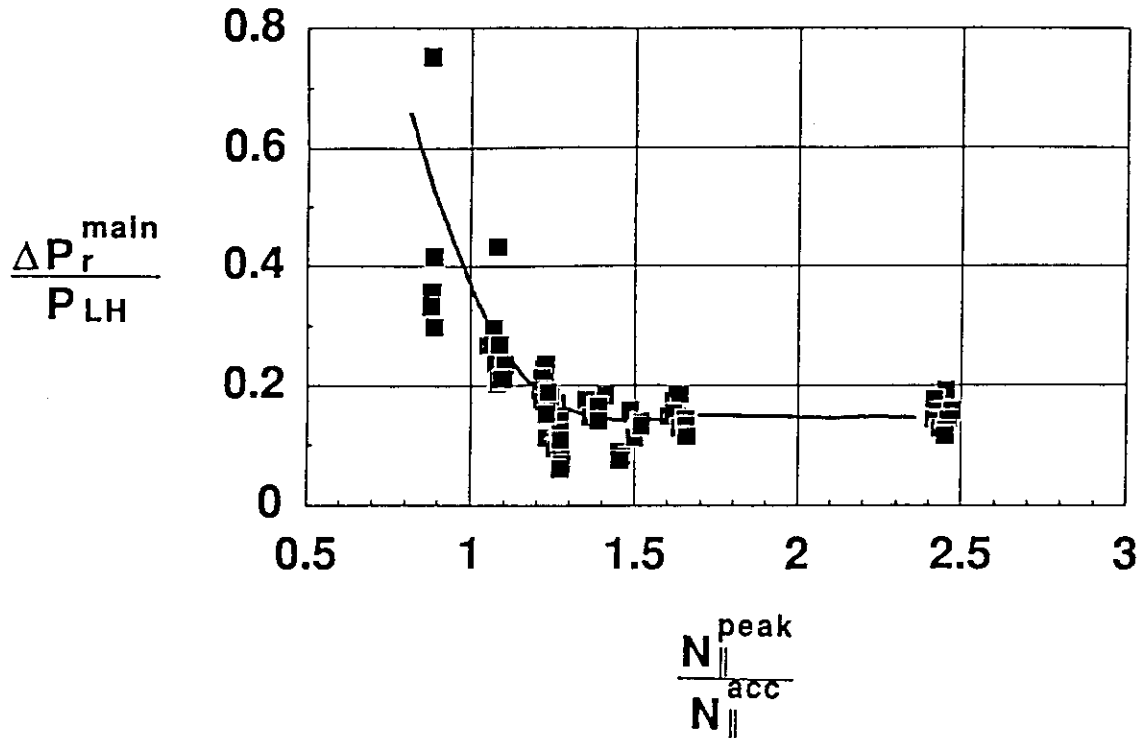
Fig.4 The increment of main plasma radiation divided by the LH power versus $N_{\parallel}^{peak}/N_{\parallel}^{acc}$

There is some open questions about the accessibility limit. In this series of experiments, we changed the wave phasing alone. The accessibility condition depends on the density, the toroidal field and the wave frequency. Other parameter dependence of the accessibility limit should be studied. In order to estimate power threshold of the accessibility limit, the unaccessible RF waves should be measured by several RF probes inside the vessel. These data may give us a measure of the non-accessible power. We have to show a mechanism of the enhancement of impurity influx by the unaccessible wave power.

Reference
[1] F.Söldner, F. Leuterer, in private comminucation.

11.13 Effects of Accessibility on ECE and HX Signal in LHCD Experiments in JT-60

M. Sato, T. Imai, T. Kondoh, S. Ide and K. Ushigusa

1. Introduction

The study of high energy electrons is important for understanding the mechanism of the Lower Hybrid Current Drive (LHCD). One of the interesting feature of the Lower Hybrid Wave (LHW) is the accessibility condition which limits the lowest $N_{||}$ ($N_{||}^{acc}$) to penetrate to the core of the plasma. Accordingly, the high energy electrons produced by the LHW is limited corresponding to the $N_{||}^{acc}$. Therefore the study of the high energy electrons gives how the accessibility works in tokamak plasma. Information of high energy electrons can be obtained from the electron cyclotron emission (ECE) and hard Xray (HX) signal. The description of the HX measurement is given in the sections 11.4 &5. The ECE is measured along a horizontal line of sight in JT-60U. The ECE is measured along a horizontal line of sight in JT-60U. The frequency of ECE from the high energy electrons is relativistically shifted to the lower frequency. The relativistically shifted second harmonic ECE may be absorbed in the frequency region where thermal electrons can emit and absorb the emission. The ECE with frequencies of $1.1< f/f_{ce}^0 <1.6$ is not affected by the absorption, where f_{ce}^0 is the electron cyclotron frequency at the plasma center. Therefore the ECE with $f/f_{ce}^0 =1.1$ & 1.5 are used for the study. If the high energy electrons are located only in the plasma center, the ECE with $f/f_{ce}^0 =1.1$ & 1.5 are emitted by the electrons with energy of 371keV and 222keV, respectively. The energy correspond to $N_{//}=1.22$ & 1.39, respectively. Here, the observed ECE is analyzed from the points of accessibility in LHCD. Here the observed ECE is analyzed from the points of the accessibility of LHW in comparison with HX measurements.

2. Experimental results and discussion

The typical time evolution of the plasma parameters in LHCD are shown in Fig.1. The plasma parameters are as follows; Ip=2MA, Bt=4T, P_{LH}=0.9MW, P_{NBI}=1.5MW, $\Delta\phi=135°$($N_{||}^{peak}$=1.4). The line averaged electron density increases from $0.5 \times 10^{19} m^{-3}$ to $3 \times 10^{19} m^{-3}$, the ECE at $1.1 f_{ce}^0$ and $1.5 f_{ce}^0$ decreases. Physical quantity which is product of line density and ECE emissivity are defined in following equations; $J_{NEC1.1} = n_e dl \times I_{ECE}(1.1 f_{ce}^0)$, $J_{NEC1.5} = n_e dl \times I_{ECE}(1.5 f_{ce}^0)$, where $I_{ECE}(n f_{ce}^0)$ is the ECE emissivity at $n f_{ce}^0$.

The HX spectra viewing the central cord (r/a~0.2) of the same discharge ($\Delta\phi=135°$, $N_{||}^{peak}$=1.4) are shown in Fig. 2(a). The spectra of the center cord extend upto 400 keV until t = 6.0sec and then the maximum energy gradually reduced as the density increases. In case of the higher $N_{||}$ wave injection ($\Delta\phi=180°$, $N_{||}^{peak}$=1.9), the spectra of the center cord do not change much in spite of the density increase in contrast with the case of the $\Delta\phi=135°$ as shown in Fig. 2(b). The maximum energy is less than 300keV and the

intensity and effective temperature are lower than those of the $\Delta\phi=135°$. As shown in table I and II, if the high energy electron dominantly exist within the half radius, the electron energies corresponding to ECE signals of $f=1.5\ f_{ce}$ and $f=1.1f_{ce}$ are 133-302 keV and 308-399 keV, respectively. We can compare the ECE response and HX spectra.

The density dependence of $J_{NEC1.5}$ and $J_{NEC1.1}$ are shown in Fig. 3 (a) and (b). The following two facts are found.

(1)The $J_{NEC1.1}$ and $J_{NEC1.5}$ in case of the $\Delta\phi=180°$ (the highest $N_{||}$)are smallest.

(2) The $J_{NEC1.1}$ and $J_{NEC1.5}$ decrease as the density increase in cases of $\Delta\phi=120°$, $135°$, and $150°$, and the intensity of the lower $N_{||}$ decrease faster.

The power spectra for various LH phases are shown in Fig.4. The ECE with $f/f_{ce}^0=1.1$ & 1.5 is emitted by the electrons at the plasma center with energy of $N_{//}=1.2$ & 1.4, respectively. In the case of $180°$, the power is far from the points of $N_{//}=1.2$ & 1.4 in the spectrum. In the cases of $120°$, $135°$ and $150°$, there are power in the points of $N_{//}=1.2$ & 1.4. Therefore the ECE in the case of the LH phase of $180°$ is smallest. The HX measurements in Fig. 2 (a) and (b) are also consistent with this results.

As for the (2) fact, the power of LH can access under the condition of $N_{//}>N_{//}^{acc}$, where $N_{//}^{acc}$ is the accessibility condition. When the central electron density is changed from $0.6\times10^{19}m^{-3}$ to $2.5\times10^{19}m^{-3}$, $N_{//}^{acc}$ changes from 1.23 to 1.5. If the electrons are located at $R_0-a/2 < R< R_0+a/2$, the energy of the electrons and $N_{//}^{acc}$ which correspond to $f/f_{ce}^0=1.5$ and 1.1 are shown in Table1 and 2. In the case of $f=1.5f_{ce}^0$, $N_{//}$ is from 1.29 to 1.64. The calculated power between $N_{//}=N_{//}^{acc}$ and 1.64 are shown in Fig.5. Decreasing rate of both $J_{NEC1.1}$ and $J_{NEC1.5}$ qualitatively agree well with the density dependence of the $P_{acc1.5}$ and $P_{acc1.1}$. The HX intensity of the $\Delta\phi=180°$ does not change much as seen in Fig. 2(b), while those of energy range corresponding to the $J_{NEC1.1}$ and $J_{NEC1.5}$ in case of the $\Delta\phi=135°$ decrease as density increase. This is again consistent with the above. In both $J_{NEC1.1}$ and $J_{NEC1.5}$ cases, the crossing points of the different $N_{||}$ in the experiments are higher than those of the accessible powers. This fact suggests that actual $N_{||}$ spectrum in the plasma upshifts as evidenced previously in JT-60[1]. It is not clear why the $J_{NEC1.1}$ and $J_{NEC1.5}$ in lower density region reduced substantially, but higher Z_{eff} in the low density region might be responsible for it.

3. summary

Density dependence of the ECE signal and HX spectra were studied to investigate the accessibility condition of the LHW. Both ECE and HX data reflect well accessibility qualitatively. The effect of the $N_{||}$ upshift must be taken into account to explain quantitatively the experimental result. ECE data will be a good cross check of the electron distribution function, if numerical calculation to get ECE emission by use of the HX spectra is compared with the experimental data.

Reference

[1] S. Ide et al; Nucl. Fusion 32 No.2 (1992) (to be published) .

TABLE 1 ; electron energy and $N_{//}$ corresponding to $f=1.5\ f_{ce}^0$

	R_0-a/2	R_0	R_0+a/2
electron energy	302keV	224keV	133keV
$N_{//}$	1.29	1.39	1.64

TABLE 2 ; electron energy and $N_{//}$ corresponding to $f=1.1\ f_{ce}^0$

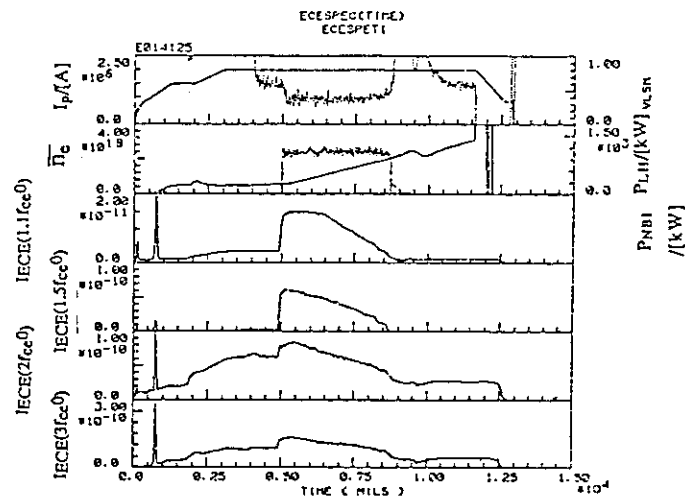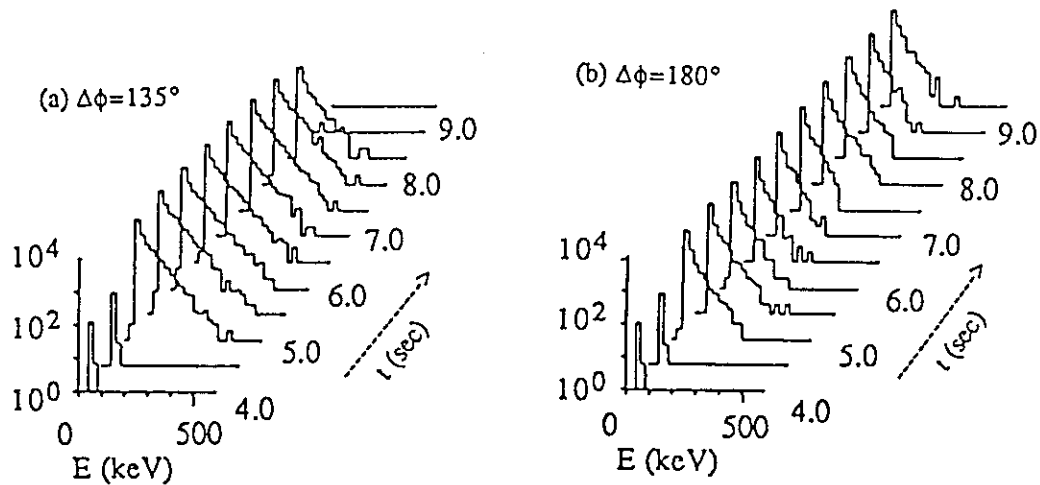|	R_0-a/2	R_0	R_0+a/2
electron energy	399keV	356keV	308keV
$N_{//}$	1.21	1.24	1.28

Fig.1. Typical time evolution of plasma parameters. I_{ECE} unit is $W/Hz/m^2/sr$.
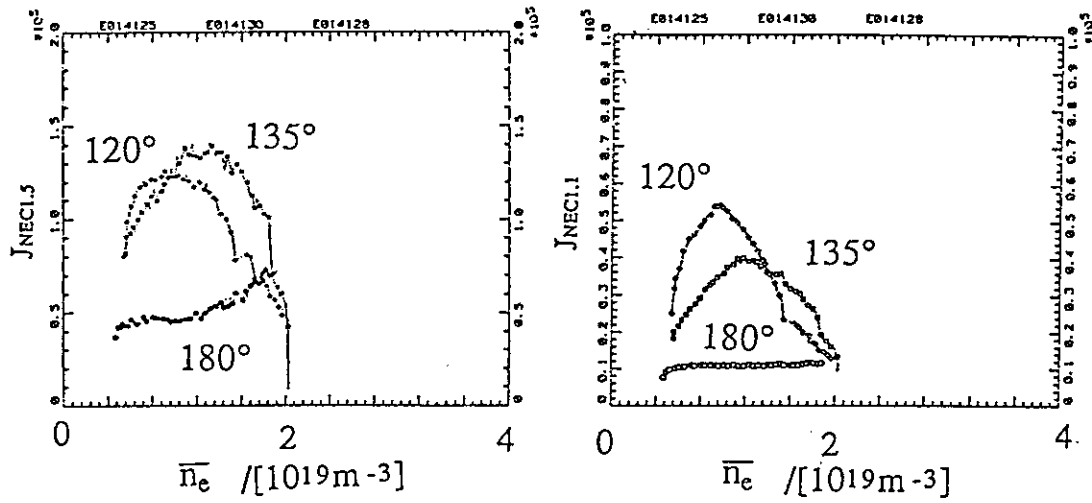

Fig. 2 Time evolution of the HX spectra.

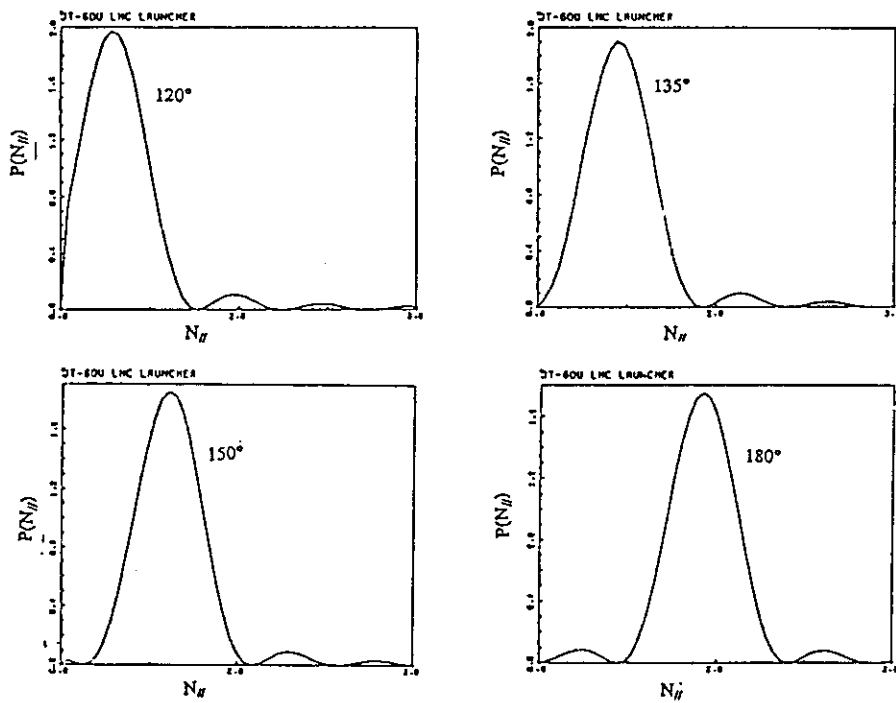Fig.3. Density dependence of $J_{NEC1.5}$ (a) and $J_{NEC1.1}$ (b)

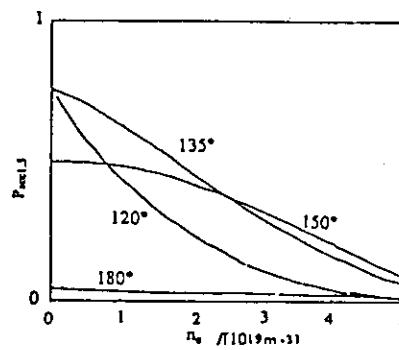Fig.4. Calculated power spectra for different values of LH phase

Fig.5. Calculated power between
$N_{//}=N_{//}{}^{acc}$ and 1.64

11.14 Confinement of the Fast Electrons Produced by LHCD in JT-60U

S W Wolfe, K Ushigusa, T Imai

1. Introduction

The lower hybrid wave drives current in a plasma by collisionless damping on plasma electrons in the tail of the distribution, where the parallel phase velocity of the wave is typically about ten times larger than the electron thermal velocity. Collisional processes, however, counteract this mechanism. The increase in the population of current-carrying tail electrons is balanced by their slowing down due to interaction with the bulk electrons. But these LH-produced fast electrons may be affected by other processes such as spatial diffusion or instabilities. A careful evaluation of these losses, through parameters such as anisotropy and confinement time, may shed light on the physics of the current drive process and will help to determine the applicability of LHCD to future steady-state operation in a tokamak reactor.

2. Experimental Conditions

For these experiments, Ohmic discharges in hydrogen with plasma currents of 1.2 MA were used as target plasmas. A high toroidal field of 4 T and low line-averaged electron density of $\leq 0.5 \times 10^{19}$ m^{-3} were used to allow good accessibility for the lower hybrid wave. The effective ion charge Z_{eff}, measured by visible Bremsstrahlung, was typically 8. The effective safety factor q_{eff} at the surface was about 9. The central electron temperature, extrapolated from off-axis Thomson scattering measurements, was about 4 keV.

Lower hybrid power at 2 GHz was launched into the plasma using a multi-junction waveguide array (see Section 11.9 of this report) of the same design as that used in previous JT-60 experiments [1]. The torus input power ranged from about 1 to 1.5 MW. Various phasings between launcher modules were used ($\Delta\phi$ from 120° to 180°), so that the parallel index of refraction $N_{\parallel}$ at the peak of the launched wave spectrum ranged from about 1.3 to 1.9. For the combination of wave frequency, toroidal field, density, and Z_{eff} used in these experiments, the minimum index for accessibility N_{acc} was about 1.15.

Typical waveforms for the time evolution of plasma parameters during the LH pulse are shown in Figure 1. During the pulse, the electron density rises slightly and the non-thermal ECE signal becomes clear. In the case shown, the one-turn loop voltage drops to near zero. In order for the measurements not to be affected by high energy electrons produced by the residual loop voltage, data were only chosen if less than 20% of the loop voltage remains during LH; that is, more than 80% of the plasma current should be non-inductively driven.

To determine confinement characteristics, information on the change in parallel and perpendicular plasma pressure is needed. This is obtained from a free-boundary equilibrium code

which incorporates data from magnetic probes and flux loops on the vacuum vessel and diamagnetic loops into its fitting algorithm (see Section 2.4 of this report). The calculation produces the evolving diamagnetic β_p and Shafranov Λ (= $\beta_p^{eq} + l_i/2$, where β_p^{eq} is the average of perpendicular and parallel β_p, and l_i is the plasma internal inductance coefficient) shown in Figure 1d. The precision of the calculations is typically about 10%.

The change in $\beta_p^{\perp}$ is obtained directly from $\Delta\beta_p^{dia}$. The change in $\beta_p^{\parallel}$ is contained in $\Delta\beta_p^{eq}$, and inferring this from $\Delta\Lambda$ is usually difficult to do precisely because the change in l_i must generally also be considered. If the measurements taken after the LH switch-on are done within a time interval short enough so that l_i does not change appreciably, then $\Delta\Lambda \approx \Delta\beta_p^{eq}$. Measurements of hard x-ray profiles indicate that this time interval should be about 0.3 s. With this assumption, $\Delta\beta_p^{\parallel}$ is given by $\Delta\beta_p^{\parallel} = 2\Delta\Lambda - \Delta\beta_p^{dia}$. Incremental energies are inferred from these numbers by using the relations $\Delta W_{\perp}(MJ) = (2/3)K\Delta\beta_p^{\perp}$ and $\Delta W_{\parallel}(MJ) = (1/3)K\Delta\beta_p^{\parallel}$, where $K = 0.15\pi R_p[I_p(MA)]^2$, the proportionality constant between W and β_p in the isotropic case.

In order to be able to infer the fast electron behaviour from these equilibrium quantities, we must assume that neither ion pressure nor bulk plasma pressure changes. For an Ohmic plasma at sufficiently low density, LH interaction with the ions is negligible (see Section 11.6 of this report). Also, at the low densities used here, the change in bulk electron parameters is small (see Section 11.2 of this report).

3. Anisotropy and Incremental Confinement Time

A measure of the pressure anisotropy resulting from the LH interaction with the fast electrons is an "incremental" anisotropy defined by $\Delta\gamma = (\Delta\beta_p^{\parallel}-\Delta\beta_p^{\perp})/(\Delta\beta_p^{\parallel}+\Delta\beta_p^{\perp})$. Figure 2 shows this quantity plotted as a function of $N_{\parallel}$ at the peak of the wave spectrum. Surprisingly, the degree of anisotropy shows at most a weak dependence on the parallel index. As $N_{\parallel}$ increases and the phase velocity of the wave approaches the thermal velocity, one would expect that slowing down of the tail electrons on the bulk would become more effective in reducing the anisotropy produced by the LH.

To attempt to determine if some loss mechanism is responsible for this anomalous behaviour, confinement must be quantified. An incremental confinement time for the fast electrons τ_f may be calculated simply as $\Delta W_f/P_{LH}$ where $\Delta W_f = \Delta W_{\parallel} + \Delta W_{\perp}$ and P_{LH} is the LH power input to the torus. Its dependence on $N_{\parallel}$ is shown in Figure 3. Values of τ_f vary from about 40 ms to 90 ms over the range of $N_{\parallel}$ used. There is a large scatter in the data, but there seems to be a tendency toward worse confinement at high $N_{\parallel}$.

Simple collisional considerations are consistent with this tendency. If the slowing-down process is dominant, the fast electron confinement time should follow approximately the slowing-down time, given by

$$\tau_{SD}(s) = \frac{3.368/\ln\Lambda}{n_e(10^{19}m^{-3})} \frac{N_{\parallel}^{-3}}{1-N_{\parallel}^{-2}+\sqrt{1-N_{\parallel}^{-2}}}$$

where n_e is the electron density and $\ln\Lambda$ is the Coulomb logarithm (about 18 in these experiments). At high $N_{\parallel}$, the phase velocity of the wave is too near the electron thermal velocity and the slowing-down time τ_{SD} is small. On the other hand, at low $N_{\parallel}$, the region of interaction is well out in the tail of the distribution, τ_{SD} is large, and fast electron loss will be slow. However, if $N_{\parallel}$ is so low that some portion of the wave spectrum becomes inaccessible, then only a fraction of the torus input power P_{LH} will be absorbed by the plasma. Since this effect is not taken into account here, the calculation of τ_f for $N_{\parallel}$(peak) less than about 1.5 will be artificially lowered.

We can look at these data in a different way by normalising τ_f with the slowing-down time and plotting with the wave phase velocity $v_{p\parallel}$ at the peak of the spectrum normalised by the electron thermal velocity v_{th}. This is shown in Figure 4. For low phase velocities, the confinement seems to be dominated by the slowing down process. As the phase velocity increases, however, the confinement is determined less and less by slowing down. This may be due to other electron loss processes becoming important at low $N_{\parallel}$ such as the recently discovered EEP phenomenon described in Section 11.8 of this report. Of course, part of the degradation could be an artifact of accessibility as described above, but uncertainties in the launched spectrum make it difficult to precisely determine this effect.

The spectrum may also be changed by the plasma -- the so-called $N_{\parallel}$ upshift. This effect becomes more important for a lower $N_{\parallel}$ wave, and the "spreading out" of the spectrum tends to reduce the effective slowing-down time for the fast electron distribution. Thus, $N_{\parallel}$ dependence would be weakened, as observed here.

4.   Conclusion

Preliminary measurements have been made of the fast electron distribution during LHCD on JT-60U. The distribution is anisotropic, as expected, but there is no clear phase dependence observed. The confinement time of the fast electrons at high $N_{\parallel}$ agrees with the slowing down time, but at lower $N_{\parallel}$ the confinement seems to get worse. This may indicate the presence of other loss processes such as the recently observed EEP instability. Other factors which should be carefully considered are the effects of residual dc electric field and the dependence of deposition profile. Also, variations in the wave spectrum from the designed form, due to either launcher uncertainties or $N_{\parallel}$ upshift, may affect the interpretation, especially when working close to the accessibility limit.

5.   References

[1] Ikeda, Y et al; Nuclear Fusion **29** (1989) 1052.

S/N 14161

FIG. 1 - Evolution of a typical LH
discharge:
a) Plasma current and smoothed
one-turn loop voltage;
b) LH power input to the torus
and reflection coefficient;
c) non-thermal ECE signal and
line-averaged electron density;
d) Shafranov Λ from equilibrium
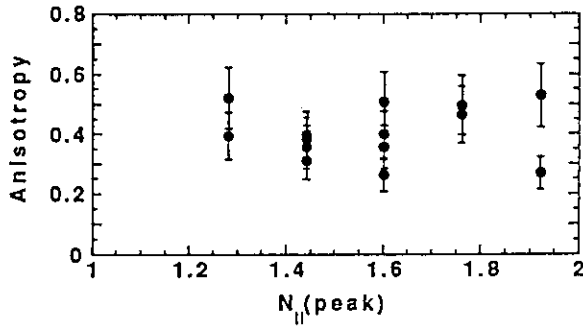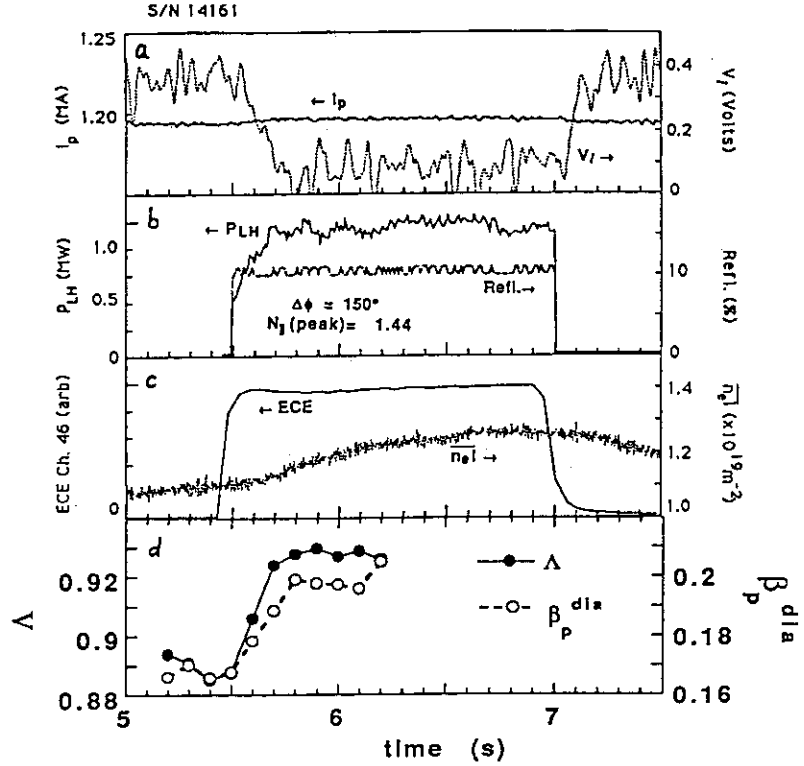fitting and diamagnetic β_p.

FIG. 2 - Variation of anisotropy factor with LH
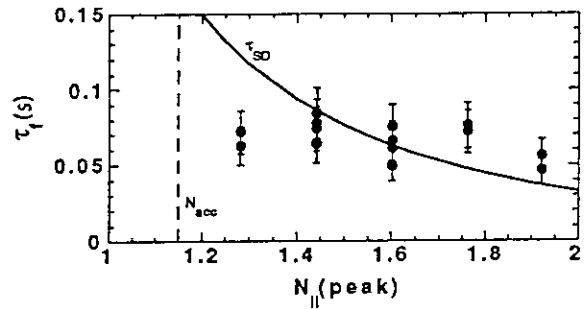parallel index of refraction (taken at the peak of
the spectrum).

FIG. 3 - Incremental confinement time for the
fast electrons vs. parallel index of refraction
at the peak of the LH spectrum. The slowing-
down time is calculated for electrons with speed
corresponding to $N_{||}$(peak) and a density of
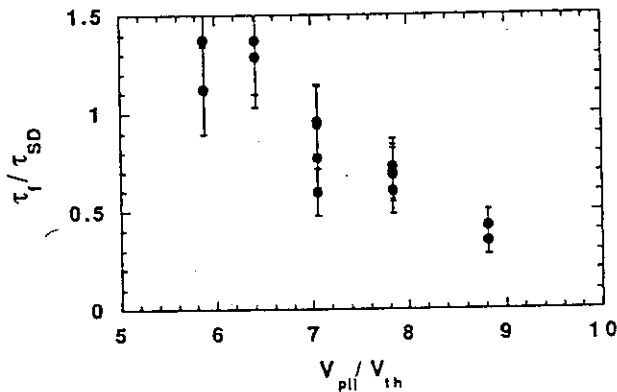
$$0.45 \times 10^{19} \, m^{-3}.$$

FIG. 4 - Incremental confinement time for the
fast electrons normalised by the slowing-down
time as a function of LH parallel phase velocity
at the peak of the wave spectrum normalised by
electron thermal velocity (T_e=4 keV).

NOTE: 20% error bars in these figures are a
guide for the eye only.

12. Diagnostics

12.1 Charge Exchange Recombination Spectroscopy in JT-60U

Y. Koide, A. Sakasai and N. Asakura

In JT-60 experiments, the following problems on CXRS measurement [1] occur, (1)The modulation of diagnostic beam is needed to estimated the background spectrum; (2) The basis of rotation is determined on the assumption that the line emission from CVI ion is not Doppler-shifted in the period of plasma initiation; (3) The leakage magnetic field slightly deforms the spectrum; (4) The number of spatial point is limited. The CXRS system based on CCD camera, which is first developed in NIFS[2], is adopted as the main CXRS system in JT-60U to settle these problems. The formerly used detector (DIMO), which has much larger dynamic range than that of CCD camera, is also used for the measurement of helium and oxygen spectra, which will be discussed in the separate paper. This paper is focused on the CCD system.

Figure 1 shows the new CXRS system schematically. There are three optical heads equipped to the JT-60 vacuum vessel. The diagnostic port, on which optical head is held, is shown in Fig.2. The light from plasma is introduced through a double-sapphire-grazed viewing window (parts 1) to each optical head. This window is protected from the contamination by carbon powder during discharge cleaning by the mechanical shutter (parts 2) connected with the rotation introducer (parts 6), which is driven by the air actuator (parts 4). A shock-resistance test for this diagnostic port has been carried out. Under 1000-times acceleration of 60 G, which is the maximum acceleration anticipated in 7MA disruption, the test port kept its helium leak rate bellow 1×10^{-9} Torr·l/sec [3]. Returning back to Fig.1, the two of the optical heads numbered '1' and '2' have tangential sight lines but their directions are opposite to each other; The system '2' detects composite spectrum of CXR induced spectra and non-CXR spectra from the edge region; The system '1' measures only non-CXR spectra; So we can estimate the net CXR spectrum induced by the diagnostic beam from the difference of these signals. Another system numbered '3' measure poloidal rotation. The light travels through the fiber optics of 60 m to the 50/100 cm visible spectrometers. The spectrum is detected with CCD camera, and the electric signal is digitized and sent to the recorder. The tangential field of view is shown with open circles and the region of poloidal field of view with lines in Fig.3. The specifications are shown in Table.1.

Figure 4(a) shows the relation of optical fiber at the entrance slit of spectrometer and the detective are of CCD. Fibers from system '2' (open circles) and ones from system '1' (closed circles) are detected with one CCD detector. The measured spectra from CVI

ion at the transition of n=8-7 is shown in Fig.4(b). The vertical axis is the signal strength and other two axes have the same meanings of 'spatial direction' and 'wavelength direction' in Fig.4(a). Because this data is at the NBI phase, the signal from beam channel (system '2') is larger by the contribution of CXR reaction. Figure 5(a) shows the procedure of determination of the basis of rotation velocity, where the abscissa is wavelength and the ordinate is signal intensity. In the upper pair of cross and square symbols, the former is from a fiber located at the top of beam channels shown in Fig.4(a) and the latter the top of background channels. From this pair, a basis of rotation is determined. As a matter of fact, we cannot settle the mutual location of detector and the spectrometer perfectly and they may be inclined to some extent to each other. So another basis of rotation is determined from another pair of fibers at the bottom of beam channels and the bottom of background channels in Fig.4(a). The basis of rotation for each fiber is determined from its geometrical relation between the two pair of basis determined previously. The ambiguity of this method estimated from the standard deviation of the spectrum fitting is 2×10^3 m/sec typically. Two spectra during the beam injection are shown in Fig.5(b), where cross symbols are from beam channel and squares from background channel. The spectrum induced by CXR reaction is given by the difference of these spectra (Fig.5(c)). Doppler width (ω_T) and shift (x_i-x_0) are determined by the fitting this to the following Gaussian;

$$y_i = \sqrt{\pi} A \sum_j \frac{\alpha_j \omega_T \omega_j}{\sqrt{\omega_T^2 + \omega_j^2}} \exp\left[-\frac{(x_i - x_0)^2}{\omega_T^2 + \omega_j^2}\right] + B\sqrt{\pi} \sum_j \alpha_j \omega_j$$

, where ω_j is the width of instrumental function. The result is also shown with a curved line the the same figure. In this case, the fitted result is slightly blue-shifted from the basis of rotation (vertical line in this figure) determined as mentioned above.

Figure 6 shows the deduced profiles of ion temperature (T_i) and toroidal rotation velocity (V_t) ((a) and (b), respectively), where Ip=4 MA, Bt=4 T, $\bar{n}_e$~4$\times10^{19}$ m^{-3}, NB power of ~20 MW. Maybe due to the good thermal conduction between ions and electrons in this relatively high density region, T_i agrees well with the electron temperatures from ECE (T_e^{ECE}) and from Thomson scattering (T_e^{TS}). V_t shows the ctr-directed rotation even though the net momentum input is co-directed, which is discussed in section 6.2.2. After the 6-month experiment, the transparency of sapphire windows are reduced by ~30 % for tangential system and the much more for the perpendicular system. The poor S/N ration in poloidal rotation measurement is partly attributable to this contamination of window. The more extensive heating power is injected in the coming experiments so this problem becomes more and more severe.

[1] Y. Koide, et al, in Review of JT-60 Experimental Results from June to October,1988, JAERI-M 89-033 (1989).
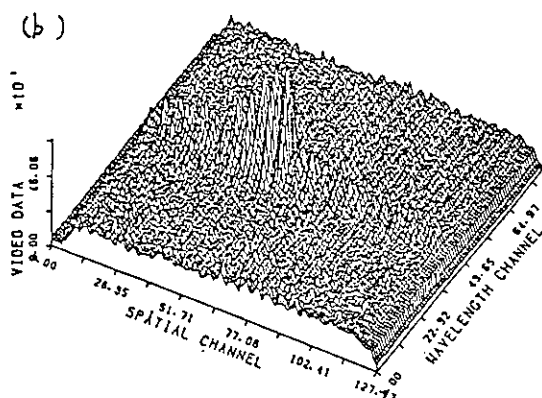
[2] K. Ida, S. Hidekuma, Rev. Sci. Instrm. 60 (1989) 867.

[3] Y. Koide, T. Kondo, A. Sakasai, Shock-resistance Test of Diagnostic Port Made for Visible Light Measurement of JT-60U, JAERI-memo 02-352 (1990) (in Japanese).

Table 1 specifications

CXRS system

spatial resolution

7 cm (toroidal array)   20 points max.

1.5 cm (poloidal array)   8 points max.

time resolution

16.7 msec minimum

50 msec typical

wavelength

400 - 700 nm

FIG. 1 Schematic view of CXRS system.

FIG. 2 Diagnostic port.

FIG. 3 The relation of plasma and the field of view of CXRS system.
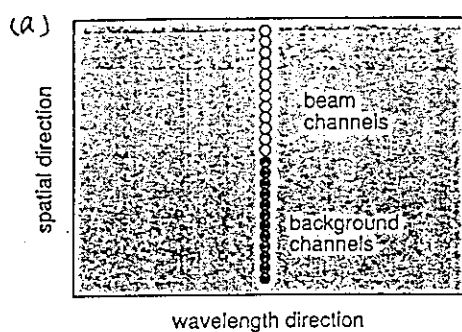
FIG. 4 (a) CCD detector and fiber array
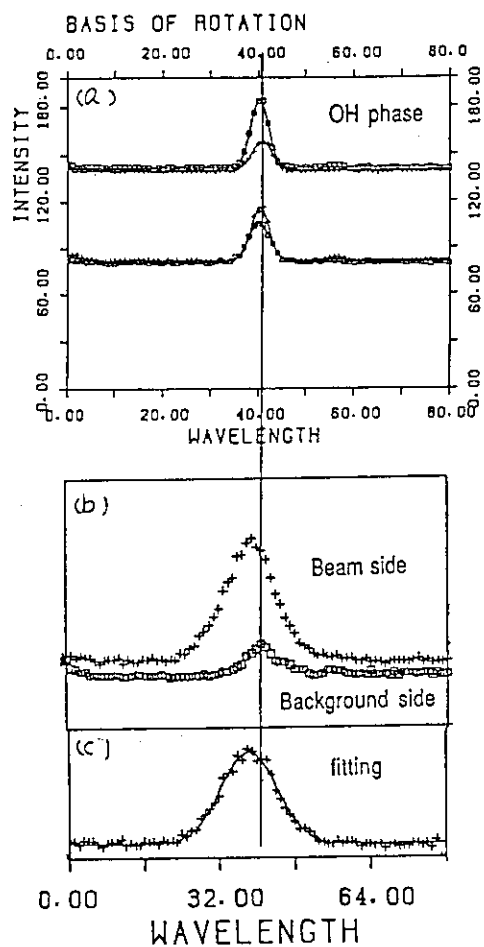(b) Two-dimensional plot of detected signal.

FIG. 5 Determination of the basis of
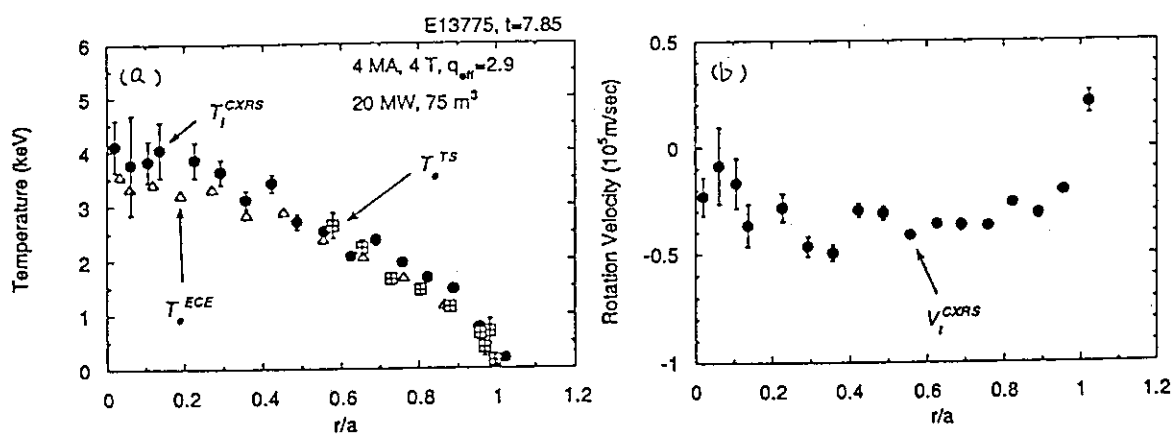rotation and the Gaussian fitting.

FIG.6 An example of deduced $T_i(r)$ and $V_t(r)$.

12.2 Fourier Transform Spectrometer System in JT-60U

M. Sato, N. Isei, S. Ishida, T. Aoyagi and T. Hirayama

1. Introduction

The electron temperature in tokamaks has been measured using the electron cyclotron emission (ECE)[1,2]. A Fourier transform spectrometer system (FTS) was installed in JT-60 for the measurement of ECE. The main parts of FTS in JT-60U were relocated from the torus hall to the diagnostic room, because the necessary shielding of the detector for neutrons is heavy. The schematic diagram of FTS is shown in Fig.1(a). ECE is measured along a horizontal line of sight. The two windows are set at the Brewster angle for the extraordinary mode. The ECE from JT-60U plasma is transmitted to the spectrometer through S-band waveguide which is 42m long and contain 11 bends. The total attenuation of the waveguide, the bends, and the two Brewster windows is 14dB.

2. Calibration of Fourier Transform System

The schematic diagram of the calibration of FTS is shown in Fig.1(b). For the calibration of FTS, the bellows between vacuum vessel and window are removed and a mirror is located on the position of the bellows. The calibration source is Eccosorb used at the liquid nitrogen temperature and at room temperature[3]. 40000 interferograms are integrated. The obtained sensitivity of the FTS is shown in Fig.2.
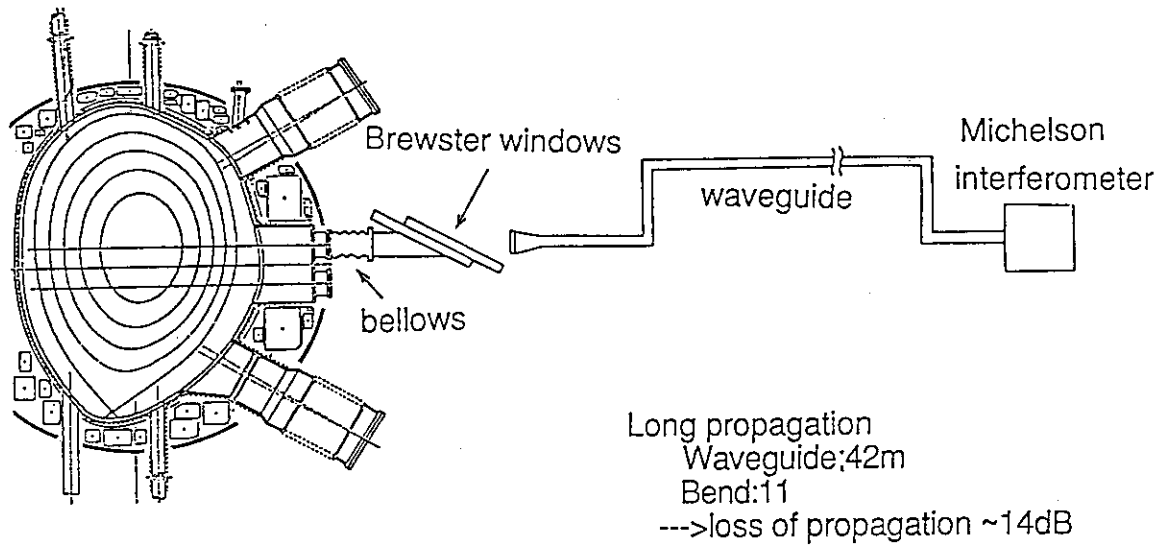
3. Correction of the internal fields

The electron temperature profile is obtained from the second harmonic X mode ECE in tokamak. The position of the electron temperature profile had been obtained on the assumption that the magnetic field in tokamak is mainly toroidal field which is inversely proportional to major radius[1,2]. For JT-60, the preprogramed value of the toroidal field is used for the calculation of the position. The recent study shows that the internal magnetic fields are fairly important and cannot be neglected as before[4]. The internal field is the composed of poloidal magnetic field, diamagnetic field and paramagnetic field, produced by the plasma current, the pressure gradient and the poloidal current, respectively. The results with all correction and with only the preprogramed toroidal field are shown in Fig.3. The measured value of the toroidal field and the ripple field of the toroidal coils are also used in the derivation of the radial position. The poloidal field correction is important in the outer region, the paramagnetic and diamagnetic correction is important in the center region.
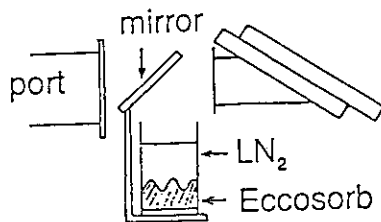
Reference

[1]A. E.Costley et al:Phys. Rev. Lett. 33(1974) 758

[2]M. Sato et al:Jpn J. Appl. Phys. 19 (1980) 577

[3]F.J.Stauffer et al:Proc.4th Conf. on Infrared and Millimeter Waves,Miami, 1979,p74

[4]S. Ishida et al:ITER-IL-PH-07-0-77

Fourier Transform Spectrometer System

(a)

Brewster windows

Michelson interferometer

waveguide

bellows

Long propagation
  Waveguide:42m
  Bend:11
  --->loss of propagation ~14dB

(b)

mirror

port

← LN₂

← Eccosorb

Automatic data acquisition system for
  calibration
  ---> 40,000 integrated data can be
  obtained

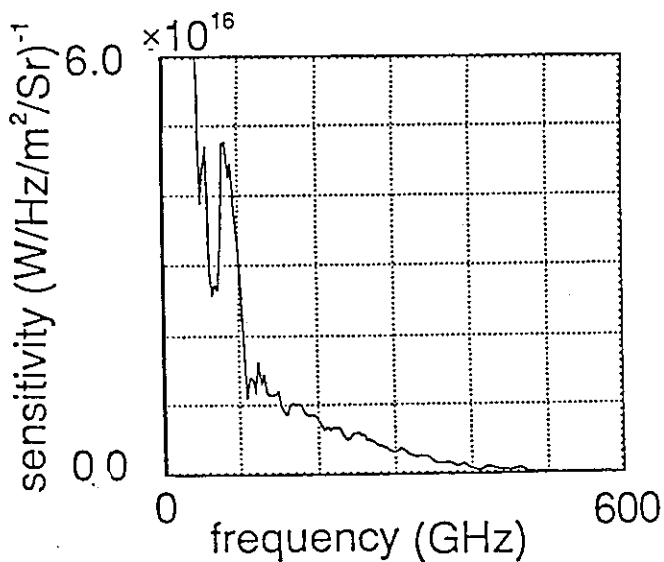Fig.1. (a)Schematic diagram of (a) Fourier transform spectrometer system and (b) the calibration of FTS
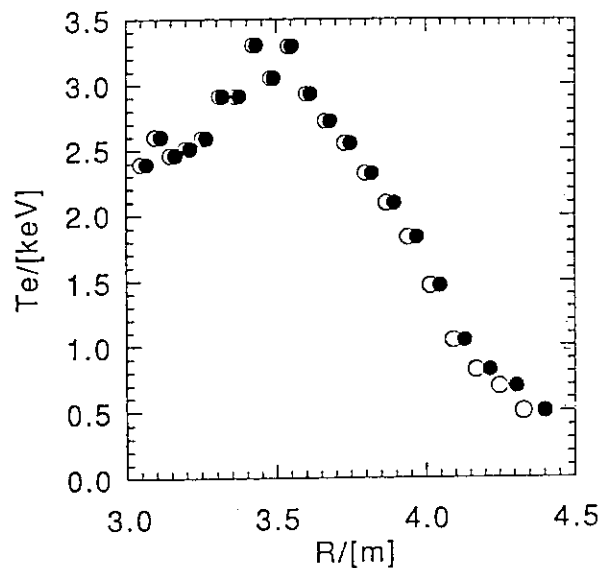
Fig.2. Obtained sensitivity of FTS

Fig.3. Results with all correction (solid circle) and with only preprogramed toroidal field (open circle)

12.3 Diamagnetic Measurement

S. Tsuji, Y. Neyatani, N. Isei, M. Kikuchi

1. Introduction

It is indispensable to evaluate the plasma stored energy accurately in order to investigate energy confinement properties. Although a method based on plasma diamagnetism has difficulties in attaining satisfactory accuracy, it is able to directly measure the time evolution of the stored energy in every shot. The diamagnetic loop on JT-60 picked up horizontal fluxes since the loop plane made an angle of about 5° with the symmetric plane through the torus axis. Consequently the diamagnetic signal was very sensitive to the plasma vertical shift, which was the primary sources of errors [1]. Diamagnetic loops were wound inside the vacuum vessel of JT-60U along more ideal planes to reduce the coupling with the plasma current. The vacuum toroidal flux is compensated by the use of a loop pair with slightly different pick-up areas instead of a Rogowski coil previously adopted in JT-60.

2. Arrangement and Evaluation Method

Figure 1 illustrates the arrangement for magnetic diagnostics on JT-60U. There are four sets of diamagnetic loops; Loops 5, 8, 11 and 14, the numbers of which designate toroidal locations. The best set with least errors is used for routine diamagnetic measurement. The main loop (four turns) and the compensation loop (three turns) are located along a vessel connecting ring as shown in Fig. 2 to be rigid enough to neglect any variation in the toroidal field coupling. The main and compensating loops are separated by 31±1 mm in the radial direction. The toroidal fluxes through the main and compensating loops in the case of $I_t = 52.1$ KA ($B_t = 4.0$ T at R = 3.32 m) are $\phi_t^m = 96.9$ Vs and $\phi_t^c = 76.5$ Vs, respectively. The balancing coefficent for the flux compensation, k is about 0.79. Differential integration is made by an analog circuit with a potentiometer for the adjustment [1]. The output of the integrator is proportional to $(k\, \phi_t^m - \phi_t^c)$ = $(4 k - 3)\, \phi^{dia} \sim 0.16\, \phi^{dia}$ where ϕ^{dia} is the diamagnetic flux. Accordingly the net diamagnetic signal is reduced by a factor of about 6.

The plasma stored energy W_{dia} is calculated from the following equations [2,3] with a fast boundary identification (FBI) code which approximates the plasma current as six filaments [4,5].

$$W_{dia} = 3\, \beta_p^{\perp}\, V\, \bar{B}_p^2 / 4\, \mu_0\ = 3\, \{\, s_1 + s_2\, (\, 1 - R_T / R_p\,)\, \} + \mu\, \}\, V\, \bar{B}_p^2 / 4\, \mu_0 \quad (1)$$

$$s_1 = \pi / (\, V\, \bar{B}_p^2\,)\oint R\, B_p^2\, (\, R\, e_R + Z\, e_Z - R_p\, e_R\,) \cdot n\, d\ell \quad (2)$$

$$s_2 = \pi\, R_p / (\, V\, \bar{B}_p^2\,)\oint B_p^2\, R\, e_R \cdot n\, d\ell \quad (3)$$

$$\mu = 1 / (\, V\, \bar{B}_p^2\,)\int (\, B_{tv}^2 - B_t^2\,)\, d\, V \approx 4\, \pi\, R_0\, B_{t0}\, \phi^{dia} / (\, V\, \bar{B}_p^2\,) \quad (4)$$

$$\bar{B}_p = \oint B_p\, d\ell / \oint d\ell = \mu_0\, I_p / \oint d\ell \quad (5)$$

where the line integral is carried out along the plasma surface, V is the plasma volume and e_R, e_Z and n are unit vectors. For the average poloidal magnetic field energy we use $\bar{B}_p^2$ instead of the usual definition of $< B_p^2 > = \oint B_p\, d\ell / \oint 1 / B_p\, d\ell$ since $1/B_p$ diverges at the separatrix in the case of divertor configurations. The mean radius R_T was numerically found to be approximated by the plasma major radius R_p better than by the mean current radius R_J.

$$W_{dia} \simeq 3 \, \mu_0 \, s_1 \; V \, (\, I_p / \oint d\ell \;)^2 / 4 \; - \; 3 \, \pi \, R_0 \, B_{t0} \, \phi^{dia} / \mu_0 \qquad (6)$$

3. Elimination of Errors

There are several sources of errors in the diamagnetic signal. Thus the output of the integrator can not be directly used as ϕ^{dia}. Note that an error in ϕ^{dia} can be expressed as an absolute error in the plasma stored energy by the second term of Eq. 6.

3.1 Eddy Current

The typical plasma discharge duration of 15 sec exceeds the B_t flattop of 10 sec so that the effects of eddy currents can not be neglected in the initial and/or last phases of each discharge. The error flux due to the dominant eddy current induced in the structures between the main and compensating loops is canceled by an additional circuit to the analog integrator with very low drift. The resulting deviation of zero level is kept within 20 kJ throughout a plasma pulse.

3.2 Stray Flux

The stray coupling of the loops with poloidal magnetic fields were examined by individual coil excitations. The main sources appear to be the stray field generated by neighboring coil feeders. Loop 8 couples mainly with the V-coil current and Loop 14 with the F-coil current, the feeders of which are located at p-6 and p-15 sections, respectively. Major fraction of the stray fluxes are automatically compensated owing to the installation of each loop pair in nearly the same poloidal plane. The residual error fluxes are numerically subtracted assuming the following functional form.

$$\phi_{stray} = (\, C_F + C_{FT} \, I_T \,) \, I_F + (\, C_V + C_{VT} \, I_T + C_{VV} \, I_V \,) \, I_V$$

$$+ \, C_H \, I_H + C_D \, I_D + (\, C_{FV} + C_{FVT} \, I_T \,) \, I_F \, I_V \qquad (7)$$

The stray fluxes arising from F and V coil currents were found to be complicated. The nonlinear terms may reflect the bending of the coil feeders by electro-magnetic force. The coefficients in Eq. 7 were determined experimentally from coil excitations with several combinations of I_F, I_V and I_T like a shot shown in Fig. 3.

Figure 4 displays an example of the integrated signal of a high β_p discharge. The broken trace stands for the elimination of the stray fluxes. The remaining errors at current flat-tops n the stored energy normalized to the plasma current are about 15 kJ / MA and 10 kJ / MA with Loop 8 and Loop 14, respectively.

3.3 Ip coupling

The independent evaluation with Loops 8 and 14 does not agree with each other beyond the errors estimated in the previous subsection. And the discrepancy appear to be depend on the plasma position.Thus Ip coupling with the diamagnetic loops should be taken into account. Figures 5 (a) and (b) show a comparison with the kinetic plasma stored energy [6] of ohmic discharges as a function of the position of the plasma current center (R_J, Z_J). The differences are normalized to I_p since the error is considered to be proportional to the poloidal flux generated by the plasma current. The data points indicate that the diamagnetic stored energy can have offsets which depend on R_J and Z_J.

The I_p-coupling coefficients were determined experimentally by sweeping the plasma column vertically or horizontally during low density discharges and by making computed plasma stored energy not to be so positionally sensitive nor to be negative in extremely shifted cases. The tentative correction in the elongated configuration is made by the following additional terms.

$$\Delta W_{dia}^{Loop\ 8} = (0.4\ Z_J + 0.32\ (R_J - 3.23) - 0.06\ )\ I_p\ (B_t/4.05) \qquad (8)$$

$$\Delta W_{dia}^{Loop\ 14} = (\ -0.60\ (R_J - 3.22))\ I_p\ (B_t/4.05) \qquad (9)$$

The result of the final correction is shown in Figs 5 (c) and (d). The positionally dependent discrepancy between the diamagnetic and kinetic stored energies are almost corrected in the case of Loop 8.

4. Discussion

A systematic error of $0.07\times$ Ip[MA] in the unit of MJ may remain in W_{dia}^{Loop8}. Larger errors exist in W_{dia}^{Loop14} so that it is used as auxiliary data even though the numerical subtraction of the stray fluxes without plasma more successful than that in Loop 8 as can be seen Fig. 2. The I_p-coupling of Loop 14 appear to be too complicated to correct only with linear terms of R_J and Z_J. The similar corrections like Eqs. 8 and 9 are adopted in the standard configuration, too. However the systematic errors are larger than those in the elongated configuration since there are not enough calibration data.

An error in I_p can bring about an offset in the plasma stored energy from the first term of Eq. 6; an error of 1% corresponds to an error of ~ 0.02 in β_p. The use of a poorly calibrated Rogowski coil for I_p (RKC-3) actually produced falsely "improved ohmic confinement". The plasma current was overestimated by $(1 \sim 2)\%$ than fitted I_p values with the FBI code. A more accurate Rogowski coil (RKC11) gives $(0.5 \sim 1)\%$ lower Ip than the fitting. At the moment, we use the fitted I_p since computed β_p agrees with that from a full MHD equilibrium code [7] best.

5. Summary

The evaluation of the plasma stored energy with diamagnetic loops has been established in JT-60U by the elimination of error fluxes. The absolute error [MJ] of W_{dia}^{Loop8} is within $0.07\times$ Ip and $0.10\times$ Ip [MA] in the elongated and standard configurations, respectively. More calibration data are required to improve the accuracy of the measurement.

References

[1] S. Tsuji et al., JAERI-M 91-196.   [2] V.D. Shafranov, Plasma Phys. **13** (1971) 757.
[3] W.A. Cooper and A.J. Wootton, Plasma Phys. **24** (1982) 1183.
[4] D.W. Swain and G.H. Neilson, Nucl. Fusion **22** (1982) 1015.
[5] K. Ushigusa et al., this report, Sec. 2.4.
[6] N. Isei et al., ibid., Sec. 3.11.   [7] S. Tsuji et al., ibid., Sec. 4.2.
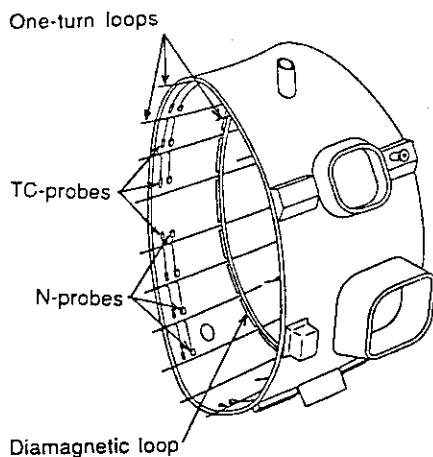
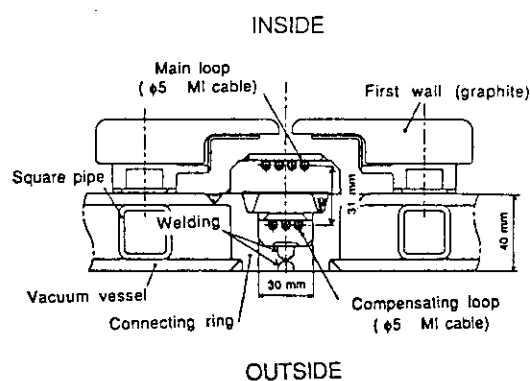Fig. 1   Schematic illustration of the magnetic sensors on JT-60U.

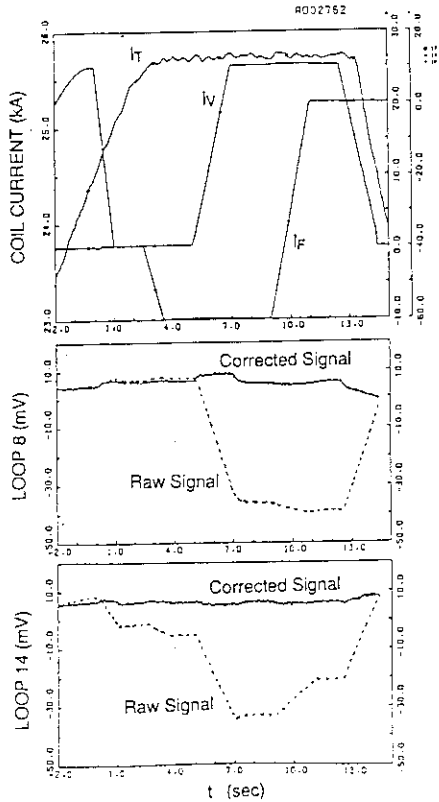Fig. 2   A cross-sectional view of the diamagnetic loops.

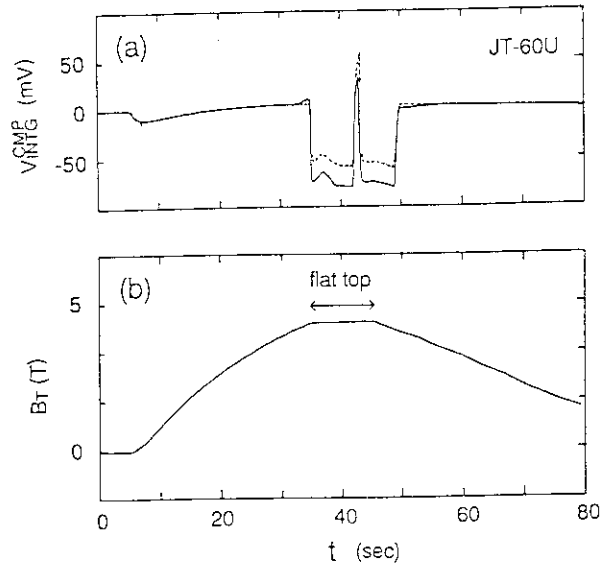Fig. 3 An example of the stray field subtraction.

Fig. 4 The diamagnetic signal of a discharge with $I_p = 1.1$ MA and β_p up to ~2 .
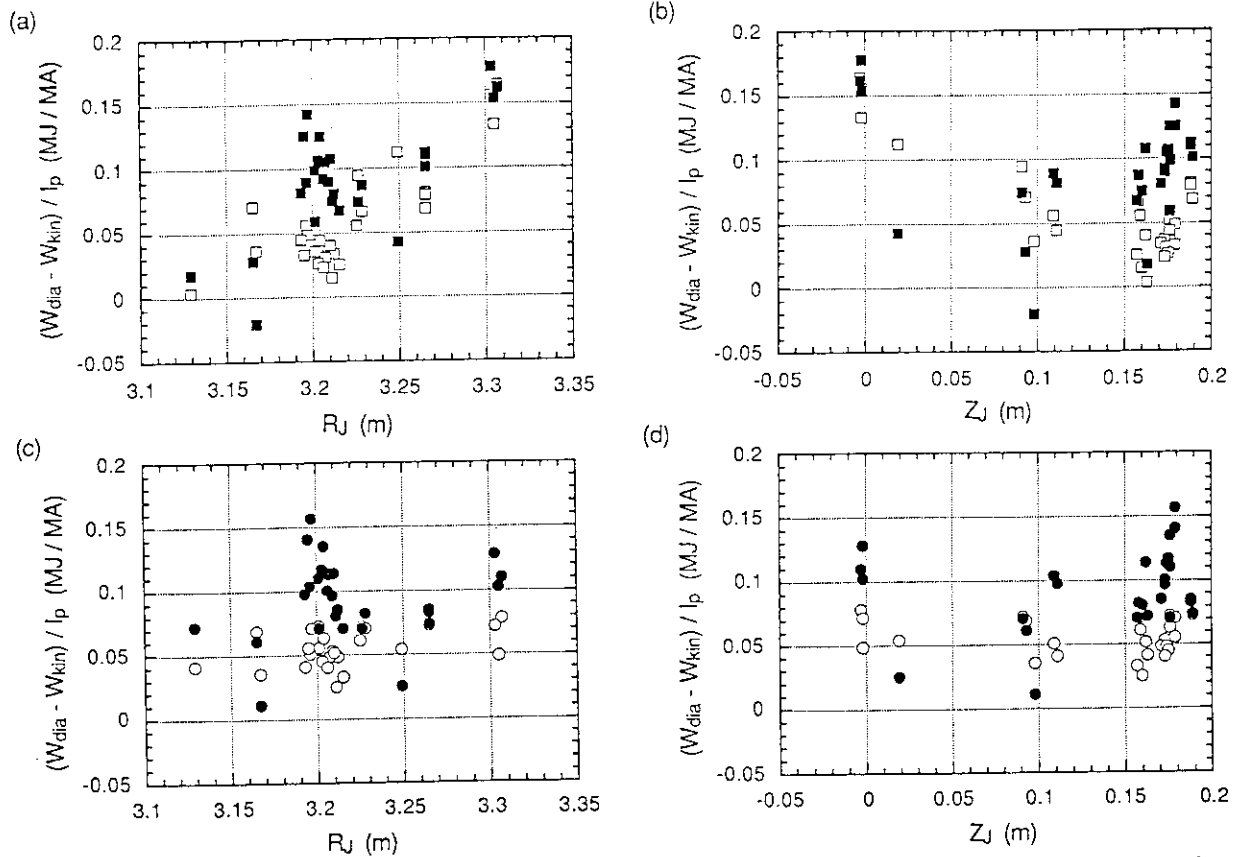

Fig. 5 Difference between diamagnetic and kinetic stored energies normalized to I_p as a function of the plasma current center. Squares and circles stand for without and with the correction by Eqs. 8 and 9. The open and closed symbol denote Loop 8 and 14 data, respectively.

ACKNOWLEDGMENTS